

# POLYMER CHEMISTRY

## EDITOR'S PICK 2021

EDITED BY: Pellegrino Musto  
PUBLISHED IN: Frontiers in Chemistry





# frontiers

## Frontiers eBook Copyright Statement

The copyright in the text of individual articles in this eBook is the property of their respective authors or their respective institutions or funders. The copyright in graphics and images within each article may be subject to copyright of other parties. In both cases this is subject to a license granted to Frontiers.

The compilation of articles constituting this eBook is the property of Frontiers.

Each article within this eBook, and the eBook itself, are published under the most recent version of the Creative Commons CC-BY licence.

The version current at the date of publication of this eBook is CC-BY 4.0. If the CC-BY licence is updated, the licence granted by Frontiers is automatically updated to the new version.

When exercising any right under the CC-BY licence, Frontiers must be attributed as the original publisher of the article or eBook, as applicable.

Authors have the responsibility of ensuring that any graphics or other materials which are the property of others may be included in the CC-BY licence, but this should be checked before relying on the CC-BY licence to reproduce those materials. Any copyright notices relating to those materials must be complied with.

Copyright and source acknowledgement notices may not be removed and must be displayed in any copy, derivative work or partial copy which includes the elements in question.

All copyright, and all rights therein, are protected by national and international copyright laws. The above represents a summary only. For further information please read Frontiers' Conditions for Website Use and Copyright Statement, and the applicable CC-BY licence.

ISSN 1664-8714  
ISBN 978-2-88971-266-3  
DOI 10.3389/978-2-88971-266-3

## About Frontiers

Frontiers is more than just an open-access publisher of scholarly articles: it is a pioneering approach to the world of academia, radically improving the way scholarly research is managed. The grand vision of Frontiers is a world where all people have an equal opportunity to seek, share and generate knowledge. Frontiers provides immediate and permanent online open access to all its publications, but this alone is not enough to realize our grand goals.

## Frontiers Journal Series

The Frontiers Journal Series is a multi-tier and interdisciplinary set of open-access, online journals, promising a paradigm shift from the current review, selection and dissemination processes in academic publishing. All Frontiers journals are driven by researchers for researchers; therefore, they constitute a service to the scholarly community. At the same time, the Frontiers Journal Series operates on a revolutionary invention, the tiered publishing system, initially addressing specific communities of scholars, and gradually climbing up to broader public understanding, thus serving the interests of the lay society, too.

## Dedication to Quality

Each Frontiers article is a landmark of the highest quality, thanks to genuinely collaborative interactions between authors and review editors, who include some of the world's best academicians. Research must be certified by peers before entering a stream of knowledge that may eventually reach the public – and shape society; therefore, Frontiers only applies the most rigorous and unbiased reviews. Frontiers revolutionizes research publishing by freely delivering the most outstanding research, evaluated with no bias from both the academic and social point of view. By applying the most advanced information technologies, Frontiers is catapulting scholarly publishing into a new generation.

## What are Frontiers Research Topics?

Frontiers Research Topics are very popular trademarks of the Frontiers Journals Series: they are collections of at least ten articles, all centered on a particular subject. With their unique mix of varied contributions from Original Research to Review Articles, Frontiers Research Topics unify the most influential researchers, the latest key findings and historical advances in a hot research area! Find out more on how to host your own Frontiers Research Topic or contribute to one as an author by contacting the Frontiers Editorial Office: [frontiersin.org/about/contact](https://frontiersin.org/about/contact)

# POLYMER CHEMISTRY EDITOR'S PICK 2021

Topic Editor:

**Pellegrino Musto**, National Research Council (CNR), Italy

**Citation:** Musto, P., ed. (2021). Polymer Chemistry Editor's Pick 2021.  
Lausanne: Frontiers Media SA. doi: 10.3389/978-2-88971-266-3

# Table of Contents

- 05 Editorial: Polymer Chemistry Editor's Pick 2021**  
Pellegrino Musto
- 07 Advances in Organic Solvent Nanofiltration Rely on Physical Chemistry and Polymer Chemistry**  
Michele Galizia and Kelly P. Bye
- 29 Chitosan Grafted With  $\beta$ -Cyclodextrin: Synthesis, Characterization, Antimicrobial Activity, and Role as Absorbent and Solubilizer**  
Wen-Ya Ding, Si-Di Zheng, Yue Qin, Fei Yu, Jing-Wen Bai, Wen-Qiang Cui, Tao Yu, Xing-Ru Chen, God'spower Bello-Onaghise and Yan-Hua Li
- 43 Thermo-Responsive Molecularly Imprinted Hydrogels for Selective Adsorption and Controlled Release of Phenol From Aqueous Solution**  
Zhenhui Si, Ping Yu, Yanying Dong, Yang Lu, Zhenjiang Tan, Xiaopeng Yu, Rui Zhao and Yongsheng Yan
- 53 Porous Surface Films With Tunable Morphologies and Hydrophobic Properties Based on Block Copolymer Under the Effects of Thermal Annealing**  
Guadalupe del C. Pizarro, Oscar G. Marambio, Manuel Jeria-Orell, Diego P. Oyarzún, Rudy Martin-Trasanco and Julio Sánchez
- 62 Review on Polymer-Based Composite Electrolytes for Lithium Batteries**  
Penghui Yao, Haobin Yu, Zhiyu Ding, Yanchen Liu, Juan Lu, Marino Lavorgna, Junwei Wu and Xingjun Liu
- 79 Fabrication, Investigation, and Application of Light-Responsive Self-Assembled Nanoparticles**  
Juan Pang, Ziyu Gao, Huaping Tan, Xincheng Mao, Jialing Xu, Jingyang Kong and Xiaohong Hu
- 89 Modeling the Kinetics, Curing Depth, and Efficacy of Radical-Mediated Photopolymerization: The Role of Oxygen Inhibition, Viscosity, and Dynamic Light Intensity**  
Jui-Teng Lin, Hsia-Wei Liu, Kuo-Ti Chen and Da-Chuan Cheng
- 103 Preparation of Covalent-Ionically Cross-Linked UiO-66-NH<sub>2</sub>/Sulfonated Aromatic Composite Proton Exchange Membranes With Excellent Performance**  
Penglu Zheng, Quanyi Liu, Donghui Wang, Zekun Li, Yawei Meng and Yun Zheng
- 115 Wet-Spun Trojan Horse Cell Constructs for Engineering Muscle**  
Anita F. Quigley, Rhys Cornock, Tharun Mysore, Javad Foroughi, Magdalena Kita, Joselito M. Razal, Jeremy Crook, Simon E. Moulton, Gordon G. Wallace and Robert M. I. Kapsa
- 126 Electrically Conducting Hydrogel Graphene Nanocomposite Biofibers for Biomedical Applications**  
Sepehr Talebian, Mehdi Mehrali, Raad Raad, Farzad Safaei, Jiangtao Xi, Zhoufeng Liu and Javad Foroughi



**137** ***Fabrication and Specific Functionalisation of Carbon Fibers for Advanced Flexible Biosensors***

Zhang Wenrui, Meng Fanxing, Qin Yanan, Chen Fei, Yue Haitao and Zhang Minwei

**149** ***Poly (Glycerol Sebacate)-Based Bio-Artificial Multiporous Matrix for Bone Regeneration***

Bo Liang, Qiang Shi, Jia Xu, Yi-Min Chai and Jian-Guang Xu

**160** ***Silk Polymers and Nanoparticles: A Powerful Combination for the Design of Versatile Biomaterials***

Cristina Belda Marín, Vincent Fitzpatrick, David L. Kaplan, Jessem Landoulsi, Erwann Guénin and Christophe Egles



# Editorial: Polymer Chemistry Editor's Pick 2021

Pellegrino Musto \*

*Institute on Polymers, Composites and Biomaterials, National Research Council (CNR), Pozzuoli, Italy*

**Keywords:** hydrogel, membrane, surface properties, polymer scaffold, light-responsive materials, biosensors

## Editorial on the Research Topic

### Polymer Chemistry Editor's Pick 2021

The section *Polymer Chemistry* of the journal *Frontiers in Chemistry* was born with the scope of witnessing, disseminating and fostering the advancements of the discipline of macromolecular science in its broadest significance. The opening of a specific section devoted entirely to this subject was justified by the profound impact this discipline and the outcomes of its research efforts have had and continue to have on our everyday life. As stated in the inaugural article (Musto) "Despite the astonishing achievements we have witnessed along the years, many exciting challenges remain to be faced, including green polymer chemistry, environmental pollution issues, polymers for energy storage and delivery, polymers for the human health." Seven years after its launch, we may say that, so far, the section has accomplished the tasks it was created for. The readership is growing, as well as the community of editors and qualified authors. Many interesting papers have appeared, addressing the most relevant challenges currently open, with special emphasis on health related issues. It was therefore decided, according with the editorial office, that the time was mature to realize a Research Topic, assembling a collection of articles that could give to the reader an outlook of the section activity and a summary of its main achievements. The choice among the numerous high-quality contributions was not easy; it was driven by the limited number of articles to be included (thirteen), the readership acceptance as evaluated by the significant bibliometric figures made available by the journal platform and, of course, the personal taste of the Editor, of which he takes full responsibility. The work presented herein witnesses the broad range of activities covered by the section and demonstrates strong advances in theory, experiment and methodology applied to forefront research challenges.

The first contribution Si et al. deals with the development of an innovative hydrogel to be used for selective removal of aromatic pollutants from wastewater. This stimuli-responsive, molecularly imprinted material was characterized by spectroscopic and electron microscopy means and was investigated in terms of adsorption and selective recognition of substituted phenols. It was demonstrated that the hydrogel has good selectivity, temperature switching properties, and is reusable, which makes it a good candidate for controlled separation and release of phenolic pollutants.

In the second paper Ding et al. is described the synthesis of chitosan grafted by  $\beta$ -cyclodextrin. This functional material exhibited strong antimicrobial activity against *E. coli* and *Staphylococcus xylosus*, which was tuned by adjusting the amino content of the polysaccharide. The reported results may be relevant in the livestock industry as a means of reducing the dosage of antibiotics and the antibiotic residues in animal-derived foods.

Next, Galizia and Bye present a detailed review on organic solvent nanofiltration, highlighting the relationship among this process and the underlying physical-chemistry and polymer chemistry. In the first part of the review are discussed the available theoretical models, along with some misleading conclusions commonly encountered in the literature. The following section describes the most

## OPEN ACCESS

### Edited and reviewed by:

Giuseppe Milano,  
University of Naples Federico II, Italy

### \*Correspondence:

Pellegrino Musto  
pellegrino.musto@cnr.it

### Specialty section:

This article was submitted to  
Polymer Chemistry,  
a section of the journal  
*Frontiers in Chemistry*

**Received:** 01 June 2021

**Accepted:** 15 June 2021

**Published:** 30 June 2021

### Citation:

Musto P (2021) Editorial: Polymer  
Chemistry Editor's Pick 2021.  
*Front. Chem.* 9:718755.  
doi: 10.3389/fchem.2021.718755

conventional materials currently in use and identifies a number of alternative materials that may impact this technology in the near future.

The work by Pizarro et al. is an excellent example of the application of precision synthetic routes, in particular, atom-transfer radical polymerization (ATRP), to finely control the surface properties of polymer films. It was demonstrated that parameters such as pore size, roughness, thickness, and wettability of a co-polymer film could be varied by changing the co-monomer structures. Moreover, thermal annealing was found to improve significantly the surface quality, thus providing a further means toward surface engineering.

The review article by Yao et al. is an account of current research on polymer-based composites to be used as electrolytes in Lithium batteries. This is a relevant technological challenge, since substitution of the conventional liquid electrolytes currently in use with solid-state components may allow to overcome numerous weaknesses of Li-ion cells. The survey describes in detail the main classes of composites under consideration, with the relative conductivity mechanisms. The fundamental issues still unsolved are critically discussed.

The research paper by Quigley et al. concerns a relevant health issue, namely the repairing of Volumetric Muscle Loss (VML) as a consequence of trauma (road/industrial accident, war injury) or disease (muscular dystrophy, muscle atrophy). The authors report an innovative biosynthetic material based on the “Trojan Horse” concept. It is an alginate/myoblast construct that was tested successfully as a scaffold for remodelling of diseased and/or damaged muscle.

The work by Talebian et al. deals with electrically conductive hydrogels to be used as biofibers for *in-vivo* stimulation of electrically excitable cells. The biofibers were realized by electrospinning of an alginate/graphene nanocomposite. The graphene-additivated biofibers exhibited better mechanical, electrical and electrochemical properties in comparison to the pristine fibers. In the light of the results obtained, they were also proposed as 3D scaffolds for tissue engineering applications.

Light-responsive materials, e.g., materials that exhibit on-off switching properties when irradiated at specific frequencies, are a hot-topic for an increasing number of high-tech applications. The paper by Pang et al. reports on the realization and the morphological/spectroscopic characterization of one of such systems based on the interaction between  $\beta$ -cyclodextrin and the azobenzene group. This system was shown to self-assemble under the specific stimulus, forming nanoparticles whose dimensions can be carefully controlled by polymer composition and irradiation. Interesting applications were demonstrated as nanocarrier for the precise delivery of anticancer drugs.

Zheng et al. report the preparation and remarkable performances of a proton-exchange membrane made by a composite material. The filler was a MOF (Metal Organic Framework), a recently developed class of molecular structures that is gaining a prominent role in contemporary materials science. The cage structure of the MOF was covalently cross-linked to the polymer matrix, imparting to the composite-membrane excellent thermal and dimensional stability. The

filled membrane showed a proton conductivity considerably improved with respect to the pristine matrix.

Lin et al. present a comprehensive computational study aimed at simulating the kinetics of the photopolymerization process. Taking into account both radical-mediated and oxygen-mediated reaction pathways, the authors were able to account for the relevant process parameters (e.g., photosensitizer concentration, oxygen concentration, light dose and intensity). They derived analytical equations to evaluate curing efficacy and curing depth. These formulas were successfully tested on microfabricated reactive systems.

The review article by Wenrui et al. is an account of the carbon-based composites used in the specialized field of flexible biosensors. The main routes to Carbon Fiber functionalization are reviewed, with special emphasis on those involving noble metals and metal oxides, polymers and MOFs. A final section describes two key-applications of these fibers, e.g., as electrochemical biosensors and as flexible or wearable biosensors.

Liang et al. describe the preparation of a bone repair scaffold made by poly(glycerol-sebacate), a synthetic polymer exhibiting good biocompatibility and high elasticity. Optimizing the photocrosslinking process and the preparation protocol, a sponge-like structure was realized, which improved hydrophilicity and promoted vascularization and osteogenesis. The potential of the proposed material to serve as a bone-mimicking scaffold was demonstrated.

Belda Marín et al. reviewed silk polymer nanocomposites and their applications as biomaterials. Silk fibroin is a versatile material that has found increasing applications for its biocompatibility, biodegradability and excellent mechanical properties. Furthermore, it can be readily processed in various forms at the macro-, micro and nano-scales through additive manufacturing techniques such as 3D-printing bioprinting or stereolithography. Filling the silk fibroin with inorganic nanoparticles provides further versatility and novel functional properties such as antibacterial activity, fluorescence properties, UV protection. The two main routes to bionanocomposite formulation are reviewed, e.g., *in situ* synthesis of INPs in silk materials, and the addition of preformed INPs to silk materials, along with their strengths and weaknesses. In the final section, an overview is provided of the present and perspective applications of these biomaterials.

## AUTHOR CONTRIBUTIONS

The author confirms being the sole contributor of this work and has approved it for publication.

**Conflict of Interest:** The author declares that the research was conducted in the absence of any commercial or financial relationships that could be construed as a potential conflict of interest.

Copyright © 2021 Musto. This is an open-access article distributed under the terms of the Creative Commons Attribution License (CC BY). The use, distribution or reproduction in other forums is permitted, provided the original author(s) and the copyright owner(s) are credited and that the original publication in this journal is cited, in accordance with accepted academic practice. No use, distribution or reproduction is permitted which does not comply with these terms.



# Advances in Organic Solvent Nanofiltration Rely on Physical Chemistry and Polymer Chemistry

Michele Galizia\* and Kelly P. Bye

School of Chemical, Biological and Materials Engineering, The University of Oklahoma, Norman, OK, United States

## OPEN ACCESS

### Edited by:

Pellegrino Musto,  
Consiglio Nazionale Delle Ricerche  
(CNR), Italy

### Reviewed by:

Gloria Huerta-Angeles,  
Contipro Inc., Czechia  
Nonappa,  
Aalto University, Finland

### \*Correspondence:

Michele Galizia  
mgalizia@ou.edu

### Specialty section:

This article was submitted to  
Polymer Chemistry,  
a section of the journal  
Frontiers in Chemistry

**Received:** 01 August 2018

**Accepted:** 04 October 2018

**Published:** 23 October 2018

### Citation:

Galizia M and Bye KP (2018)  
Advances in Organic Solvent  
Nanofiltration Rely on Physical  
Chemistry and Polymer Chemistry.  
Front. Chem. 6:511.  
doi: 10.3389/fchem.2018.00511

The vast majority of industrial chemical synthesis occurs in organic solution. Solute concentration and solvent recovery consume ~50% of the energy required to produce chemicals and pose problems that are as relevant as the synthesis process itself. Separation and purification processes often involve a phase change and, as such, they are highly energy-intensive. However, novel, energy-efficient technologies based on polymer membranes are emerging as a viable alternative to thermal processes. Despite organic solvent nanofiltration (OSN) could revolutionize the chemical, petrochemical, food and pharmaceutical industry, its development is still in its infancy for two reasons: (i) the lack of fundamental knowledge of elemental transport phenomena in OSN membranes, and (ii) the instability of traditional polymer materials in chemically challenging environments. While the latter issue has been partially solved, the former was not addressed at all. Moreover, the few data available about solute and solvent transport in OSN membranes are often interpreted using inappropriate theoretical tools, which contributes to the spread of misleading conclusions in the literature. In this review we provide the state of the art of organic solvent nanofiltration using polymeric membranes. First, theoretical models useful to interpret experimental data are discussed and some misleading conclusions commonly reported in the literature are highlighted. Then, currently available materials are reviewed. Finally, materials that could revolutionize OSN in the future are identified. Among the possible applications of OSN, isomers separation could open a new era in chemical engineering and polymer science in the years to come.

**Keywords:** OSN, sorption, diffusion, transport, polymers

## INTRODUCTION

Polymer technology is of paramount importance in several fields. Petrochemical, materials, food and tissue engineering, as well as medicine, optics and microelectronics are some of the areas where polymers endowed with specific structural or functional properties are sought (Haupt and Mosbach, 2000; Ma et al., 2002; Ulbricht, 2006). In this review we discuss the use of functional polymers to achieve molecular separations in liquid phase.

The vast majority of industrial organic synthesis occurs in solution. Downstream processes, such as solute concentration and solvent recovery, play a crucial role in the chemical industry and pose problems that are as relevant as the synthesis process itself (Marchetti et al., 2014). Often, especially in the food or pharmaceutical industry, traditional thermal separation processes, such as

distillation, cannot be exploited, since exposure to high temperatures would permanently damage thermally labile molecules, such as drugs, active principles and aromas (Kim et al., 2016; Priske et al., 2016). Liquid chromatography may represent, especially on small scales, an alternative to distillation, however it requires large volumes of solvent to be processed (Liang et al., 2008).

Nowadays, separations consume 15% of the energy produced in the world. Specifically, 80% of the energy demanded to separate chemicals is used for distillation (Lively and Sholl, 2017). Membrane separations operate at relatively mild conditions and do not require a phase change, which makes them less energy demanding relative to thermal processes (Galizia et al., 2017a). Moreover, while distillation requires very large equipment and huge investment costs, membrane modules are compact and much easier to assemble and operate. As a case study, let us consider one cubic meter of acetone solution containing a generic solute. Concentrating by a factor 10 this solution by distillation would require an amount of energy equal to 850 MJ. If the same separation is performed at room temperature and 25 bar using a membrane module, the energy consumption would be 2.2 MJ.

The separations mentioned above are generally classified as organic solvent nanofiltration (OSN) and organic solvent reverse osmosis (OSRO) (Koh et al., 2016; Koros and Zhang, 2017). OSN refers to situations in which a bulky solute, whose molecular mass is in the range 200–1000 g/mol, has to be separated from a solvent. OSN membranes generally operate based on the size sieving mechanism (Marchetti et al., 2014). First, the mixture to be separated is compressed to 30–40 atm and fed to the membrane: bulky solute molecules diffuse slowly through the membrane and, for entropic reasons, tend to be sorbed to a small extent by the membrane materials so, based on the solution-diffusion model (cf. section Solution-Diffusion model), they are rejected by the membrane and concentrated in the retentate side. Conversely, small solvent molecules preferentially permeate through the membrane (Marchetti et al., 2014). During the process, the downstream side of the membrane is kept at atmospheric pressure, so the pressure difference across the membrane drives the selective permeation of the solvent over the solute. OSRO refers to membrane separation of two or more liquids of like size. Since the currently available polymer materials cannot accomplish the latter separation, OSRO research efforts are being directed toward inorganic membranes based on carbon molecular sieves (Koros and Zhang, 2017; Lively and Sholl, 2017). Such materials separate molecules of like size based on the so-called entropic selectivity (Singh and Koros, 1996; Koros and Zhang, 2017).

There are several incentives for using OSN in the industrial practice. First, membrane filtration can be used either alone or in combination with traditional processes, such as distillation or liquid chromatography, giving rise to the so-called process intensification. As demonstrated by several techno-economic studies, such practice would reduce significantly the energy consumption of traditional processes, while ensuring high separation efficiency (White, 2006; Van der Bruggen, 2013; Marchetti et al., 2014; Szekely et al., 2014). Another advantage for using membrane filtration is its flexibility. Indeed, three

operating modes are possible for OSN membranes, namely concentration, purification, and solvent exchange. Concentration processes involve the separation of a single solute from a solvent. As mentioned above, solute is concentrated in the retentate side, and solvent is recovered in the permeate side. Purification processes consist in separating two or more solutes, for example the main product of a chemical reaction from the byproduct. Finally, solvent exchange is used to enrich a solution in the solvent B by removing the solvent A.

Although ceramic materials have been also explored, polymers appear more suitable for OSN applications. The large amount of energy required to fabricate defect-free ceramic membranes, as well their intrinsic brittleness, represent the most relevant drawbacks for using ceramics in membrane manufacturing (Li, 2007).

Although OSN membranes are supposed to work based on the size exclusion mechanism, several factors, such as chemical-physical properties of the solute, solute-membrane interactions, solvent-membrane interactions, and membrane structure influence the membrane performance (Tsarkov et al., 2012; Postel et al., 2013; Volkov et al., 2014, 2015; Ben Soltane et al., 2016; Marchetti et al., 2017). However, little research efforts have been devoted to the analysis of these fundamental aspects.

The first attempt to use polymer membranes for organic liquid separation dates back to 1964, when Sourirajan used cellulose acetate to separate xylene from ethanol (Sourirajan, 1964). For almost 30 years, cellulose acetate was considered the standard material for separations involving organic liquids (Kopecek, 1970; Fang et al., 1992). The lack of materials capable to withstand chemically challenging environments has represented, for a long time, the real roadblock to progress in OSN (Cook et al., 2018). Indeed, organic solvents are sorbed to a significant extent by glassy and rubbery polymers. Such very high sorption, which often exceeds 50% by weight, may prejudice the membrane stability. Sometime, polymers can even dissolve in the presence of organic solvents. Several stable materials were developed in the last two decades, so the issue of membrane stability can be considered partially solved. Among these materials, cross-linked Lenzing P84 polyimide (White, 2001, 2002) has been particularly successful and it made possible small scale industrial applications of OSN in dewaxing of lube oil, homogeneous catalyst recovery, and enrichment of aromatics.

In the last decade, research has been focusing on tough polymers. This class of materials includes glassy polymers made of condensed aromatic rings with superior stability in solvents, such as polybenzimidazoles (Vogel and Marvel, 1961; Valtcheva et al., 2014, 2015; Borjigin et al., 2015) and polymers of intrinsic microporosity (PIMs) (Budd et al., 2004; Fritsch et al., 2012; Gorgojo et al., 2014; Ogieglo et al., 2017). Perfluorinated polymers (Chau et al., 2018), polyether ether ketone (PEEK) (Da Silva Bural et al., 2015, 2017), and polyarylates (Jimenez-Salomon et al., 2016) also received significant attention for separations in harsh environments. In this review, we provide a detailed discussion of these materials, including synthesis routes, transport properties and property-structure correlations.

New interesting applications of OSN are in the pharmaceutical industry and, more specifically, in the downstream processing



of drugs, peptides and oligonucleotides. Noteworthy, membrane filtration in pharmaceutical industry can be exploited for separations, extractions, drying and also for particles formation (i.e., crystallization) (Buonomenna and Bae, 2015). For example, oligonucleotides and peptides are synthesized in solution and require a thorough purification before use. OSN represents a valid alternative to other processes, such as distillation or solvent extraction, which could potentially damage thermally and chemically labile biomolecules. Membranes based on cross-linked polybenzimidazole were successfully used to purify peptides and oligonucleotides, opening a new avenue in the area of oligo therapeutics (Kim et al., 2016).

Although membrane separation of organics has been indicated as one of the seven molecular separations that could change the world in the next decades (Lively and Sholl, 2017), OSN is currently one of the most poorly understood processes at a fundamental level. Specifically, the lack of fundamental knowledge about molecular factors governing solute and solvent transport in OSN membranes hampers OSN to take off the ground. Fundamental understanding of transport phenomena in OSN membranes would help not only to develop guidelines for the rational design of materials with pre-assigned transport properties, but also to select the optimal operative conditions to maximize the productivity and selectivity of existing membranes. Such aspect constitutes an essential prerequisite to make OSN competitive with traditional processes.

In this review we provide the state of the art of OSN using polymeric membranes. First, theoretical models useful to interpret experimental data are discussed and some misleading conclusions commonly reported in the literature are highlighted. The correct interpretation of OSN data is an essential prerequisite to identify the key factors affecting solute and solvent transport in OSN membranes. Specifically, the individuation of a general framework to interpret transport data in OSN membranes represents the first step toward the development of structure-property correlations useful for the rational design of OSN membranes. A general theoretical framework for OSN is presented in section Transport Phenomena in OSN Membranes: Mechanism and Challenges. Then, currently available materials are reviewed. Finally, materials that could revolutionize OSN in the future are identified. For each of them, synthesis routes and structure-property correlations are presented and discussed.

## TRANSPORT PHENOMENA IN OSN MEMBRANES: MECHANISM AND CHALLENGES

### Solution-Diffusion Model

The solution-diffusion model sets the mechanism by which gases, vapors, liquids, and ions diffuse through dense (i.e., non-porous) polymers (Paul, 1973, 2004; Wijmans and Baker, 1995). Leveraging on an elegant series of experiments and a purposely built theory, Paul and coworkers, in the early 70's, demonstrated that the solution-diffusion mechanism rules the pressure driven transport of organic liquids in rubbery polymers (Paul and Ebra-Lima, 1971). The pioneering studies conducted by Paul can be

considered the first attempt to understand OSN at a fundamental level, although, at the time, OSN was not recognized as such.

According to the solution-diffusion model, penetrant molecules first partition between the feed and the upstream face of the membrane. Then, sorbed molecules diffuse through the membrane thickness, down a concentration (or chemical potential) gradient. Finally, they desorb from the downstream face of the membrane. When considering the transport of liquids through dense polymer membranes, the permeability coefficient, which is an intrinsic property of the membrane material, is defined as the pressure and thickness normalized flux (Paul, 1973):

$$P_1 = \frac{n_1 l}{\rho_1 \Delta p} \quad (1)$$

where subscripts 1 and 2 stand for the penetrant and the membrane species, respectively. In Equation 1,  $n_1$  is the steady-state penetrant mass flux relative to the fixed frame reference, i.e., the membrane,  $\rho_1$  is the penetrant density,  $\Delta p$  is the pressure difference across the membrane, and  $l$  is the membrane thickness. To simplify the matter, let us consider the diffusion of a pure liquid through a polymer. To quantitatively describe this phenomenon, it is necessary to define a frame of reference. Two frames of reference can be used, namely fixed or moving (Paul, 1973; Kamaruddin and Koros, 1997; Galizia et al., 2016). In the moving framework, the diffusional flux is defined with respect to the center of mass of the polymer-penetrant system, which, in turn, moves with its own bulk velocity. Within this framework, the diffusional velocity relative to the bulk velocity causes the penetrant flux through the membrane. In the fixed or stationary frame of reference, the membrane itself is used as the frame of reference. The penetrant mass flux through the membrane,  $n_1$ , with respect to the fixed frame is expressed as follows (Paul, 1973; Kamaruddin and Koros, 1997; Galizia et al., 2016):

$$n_1 = n_1^{diff} + n_1^{conv} = j_1 + \omega_1 (n_1 + n_2) \quad (2)$$

where  $j_1$  is the diffusive mass flux, i.e., the mass flux of species 1 relative to the center of mass of the polymer-penetrant system,  $\omega_1$  is the penetrant mass fraction in the membrane, and  $n_2$  is the membrane flux (cf. **Figure 1**). This result can be extended to multicomponent permeation, so that, with respect to the fixed frame of reference, the mass flux of each permeating species is given by the convective flux resulting from the bulk motion of the permeating mixture (second term at the right-hand side in Equation 2), plus the diffusive flux (first term at the right-hand side in Equation 2).

In case of Fickian diffusion,  $j_1$  is expressed as follows:

$$j_1 = -\rho D_1 \frac{d\omega_1}{dx} \quad (3)$$

where  $D_1$  is the effective, concentration averaged penetrant diffusion coefficient through the membrane,  $\rho$  is the density of polymer-penetrant mixture, and  $x$  is the generic abscissa through the membrane thickness. Combining Equations 2, 3 and remembering that at steady state the polymer flux,  $n_2$ , is zero,

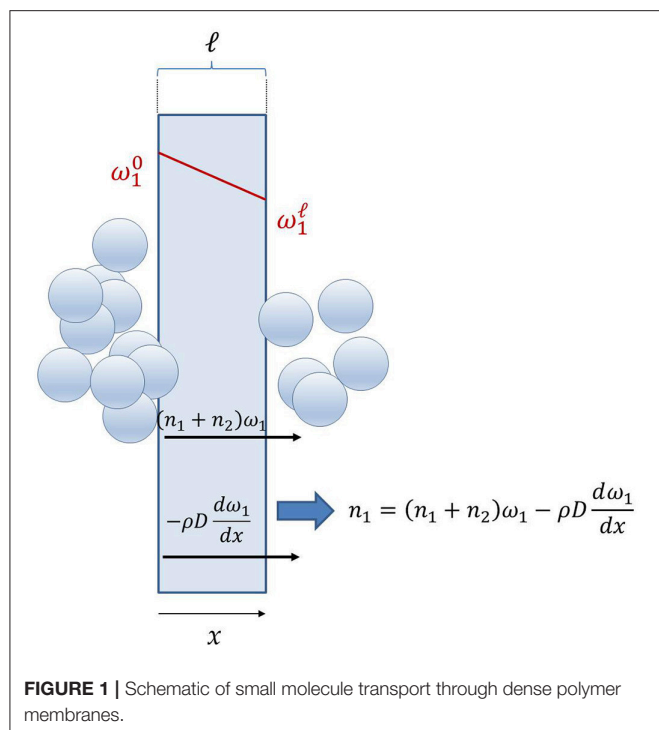


**FIGURE 1** | Schematic of small molecule transport through dense polymer membranes.

leads to the following expression for the penetrant mass flux with respect to the fixed frame of reference:

$$n_1 = - \left( \frac{\rho D_1}{1 - \omega_1} \right) \frac{d\omega_1}{dx} \quad (4)$$

During a permeation experiment, penetrant flux is measured with respect to the membrane, i.e., the experimentally measured flux is  $n_1$  (Paul, 1973). However, when considering gas and vapor transport in polymers,  $\omega_1$  is vanishing, so that  $1 - \omega_1 \cong 1$ . In this situation, the experimentally measured flux,  $n_1$ , is essentially equal to the diffusive flux,  $j_1$ . In contrast, liquid solvent uptake by polymers may be significant, so  $1 - \omega_1 \ll 1$ , which means that  $n_1$  significantly departs from  $j_1$ . In the latter situation, neglecting the factor  $1/(1 - \omega_1)$  in Equation 4 would cause significant errors in the estimation of the diffusion coefficient (Paul, 1973).

As the approach presented above can be generalized to the diffusion of multicomponent mixtures, Equation 4 should be used to describe solvent and solute transport in OSN membranes. Interestingly, such approach can be further generalized to account for the effects of osmotic pressure and concentration polarization (Peeva et al., 2004). Details about integration of Equation 4 were reported by Dinh (Dinh et al., 1992) and Paul (Paul, 1973). Integration of Equation 4 requires that the penetrant concentration profile in the membrane is known. As reported in previous studies (Paul, 2004; Galizia et al., 2016), the  $\omega_1$  profile can be considered linear, so that  $\omega_1 = \omega_1^0 (1 - \frac{x}{l})$ , where  $\omega_1^0$  is the penetrant concentration in the upstream face of the membrane, which can be estimated from liquid sorption experiments.

Correcting the Fick's law for the frame of reference is not sufficient. When considering a membrane separating two

solutions with different compositions, the chemical potential gradient across the membrane is the driving force for penetrant diffusion (Bird et al., 1960). However, as concentration is much easier to measure than chemical potential, often the concentration gradient across the membrane is assumed as the actual driving force for penetrant transport. Indeed, in writing Equation 4, we followed the latter approach. When the driving force is expressed in terms of concentration gradient, the diffusion coefficient appearing in Equation 4,  $D_1$ , is the product of a purely kinetic quantity, i.e., the mobility coefficient,  $L_1$ , which accounts for the frictional resistance offered by the polymer matrix to penetrant diffusion, and the thermodynamic factor,  $\frac{1}{RT} \frac{d\mu_1}{d\ln\omega_1}$ , related to polymer-penetrant interactions (Doghieri and Sarti, 1997; Galizia et al., 2011):

$$D_1 = L_1 \left( \frac{1}{RT} \frac{d\mu_1}{d\ln\omega_1} \right) \quad (5)$$

In Equation 5,  $\mu_1$  is the penetrant chemical potential in the polymer-penetrant mixture and  $\omega_1$  is the penetrant mass fraction in the polymer. When polymer-penetrant mixing is ideal (i.e., no special interactions take place), the factor  $\left( \frac{1}{RT} \frac{d\mu_1}{d\ln\omega_1} \right)$  is equal to one. Conversely, when polymer-penetrant mixing is non-ideal, which happens frequently, the thermodynamic factor deviates from one. Specifically, when the polymer and penetrant exhibit like physical-chemical properties and their mutual interactions are thermodynamically favorable,  $\left( \frac{1}{RT} \frac{d\mu_1}{d\ln\omega_1} \right) > 1$ . Conversely, when polymer-penetrant interactions are thermodynamically unfavorable,  $\left( \frac{1}{RT} \frac{d\mu_1}{d\ln\omega_1} \right) < 1$  (Doghieri and Sarti, 1997; Galizia et al., 2011). This aspect complicates significantly the analysis of diffusion coefficients, which need to be corrected also for thermodynamic non-idealities. While the latter issue has been addressed by Paul for rubbery membranes, based on the Flory-Huggins theory (Paul, 1973), no general solution has been proposed so far for glassy membranes. Such aspect represents a potential research topic *per se*, since polymers used for OSN are typically glassy. A very simple method to correct diffusion coefficients in glassy polymer for thermodynamic non-idealities relies on vapor sorption data. Gas and vapor sorption isotherms in glassy polymers can be described using the dual mode sorption model (Koros et al., 1976), which provides the following analytic expression for the thermodynamic factor (Merkel et al., 2000):

$$\frac{1}{RT} \frac{d\mu_1}{d\ln\omega_1} = \frac{k_D + \frac{C_H' b}{1 + b p}}{k_D + \frac{C_H' b}{(1 + b p)^2}} \left[ 1 + \frac{M_w}{22414 \rho_p} \left( k_D p + \frac{C_H' b p}{1 + b p} \right) \right] \quad (6)$$

where  $k_D$ ,  $C_H'$  and  $b$  are the three dual mode parameters, which can be estimated by fitting vapor sorption isotherms,  $p$  is the vapor partial pressure,  $M_w$  is the penetrant molecular mass and  $\rho_p$  is the polymer density. If vapor sorption data are available, the thermodynamic factor can be calculated as a function of activity using Equation 6, and then it can be extrapolated at activity 1, i.e., to the case of liquid sorption. However, such very simple method does not always work. For example, lower alcohols

(e.g., methanol and ethanol) sorption in some glassy polymers, such as polyacetylenes, cannot be described by the dual mode model, due to the occurrence of significant penetrant clustering (Galizia et al., 2011, 2012). For this reason, advanced methods based on more fundamental models are under development. For example, the non-equilibrium lattice fluid model provides a general, analytic expression for the penetrant chemical potential in mixture with a glassy polymer (Doghieri and Sarti, 1996), from which the derivative appearing in Equation 5 can be calculated analytically.

For rubbery polymers, the diffusion coefficient corrected for the frame of reference and thermodynamic non-idealities is given by (Paul, 1973):

$$L_1 = D_1 (1 - \phi_1)^2 (1 - 2\chi_1 \phi_1) \quad (7)$$

where  $D_1$  is the experimentally determined diffusion coefficient,  $\phi_1$  is the penetrant volume fraction in the membrane, and  $\chi_1$  is the polymer-penetrant Flory-Huggins interaction parameter (Flory, 1942).

Paul (1973) successfully used this approach to describe a set of experimental diffusion data presented by White (1960). White measured pure liquid water transport through rubbery polyacrylamide membranes whose water content was about 70% vol. Interestingly, water diffusion coefficient through the membrane, calculated as the ratio of permeability to sorption coefficients, resulted one order of magnitude larger than water self-diffusion coefficient (i.e.,  $2.8 \times 10^{-5} \text{ cm}^2/\text{s}$ ). To explain this unexpected result, White speculated that, for such highly swollen membrane, water transport occurs by pore flow. Paul demonstrated that the results presented by White could be rationalized using Equations 4 and 7 (Paul, 1973). Indeed, since the polyacrylamide membrane was highly swollen, neglecting the term  $1/(1 - \omega_1)$  in Equation 4, as well as thermodynamic non-idealities, led White to overestimate the diffusion coefficient by orders of magnitude. After correction for the effect of the frame of reference and thermodynamic non-ideality, water diffusion coefficients in polyacrylamide were far below the liquid water self-diffusion coefficient. So, invoking pore flow to describe water transport in polyacrylamide membranes was inappropriate.

In recent years, similar conclusions were drawn by Volkov et al. (1996) when assessing the suitability of glassy poly(trimethylsilyl propyne) (PTMSP) for OSN application. They observed that liquid ethanol diffusion coefficient in PTMSP (i.e.,  $1.27 \times 10^{-8} \text{ cm}^2/\text{s}$ ) was larger than ethanol self-diffusion coefficient (i.e.,  $1.10 \times 10^{-9} \text{ cm}^2/\text{s}$ ) and speculated occurrence of pore flow transport. This conclusion is dramatically altered if the experimental data are analyzed using the Paul's approach. From swelling experiments, ethanol volume fraction in PTMSP at room temperature resulted 0.46. If one assumes, in first approximation, the Flory-Huggins theory to account for thermodynamic non-ideality, the  $\chi$  parameter can be estimated from liquid ethanol sorption data. Doing so, gives  $\chi = 0.813$ . Finally, from Equation 7, the ethanol diffusion coefficient in PTMSP corrected for the frame of reference and thermodynamic non-idealities is  $9.30 \times 10^{-10} \text{ cm}^2/\text{s}$ , which is below the ethanol self-diffusion coefficient and fifteen times smaller relative to the

value calculated by Volkov. The dual mode approach, although more appropriate for glassy PTMSP, cannot be used to correct ethanol diffusion coefficient for thermodynamic non-idealities, since ethanol sorption in PTMSP is not dual-mode type (Doghieri and Sarti, 1997).

The examples discussed above show how poor has been, so far, the fundamental analysis of transport phenomena in OSN membranes, and how this issue continues to generate misleading interpretations of experimental data.

The solution-diffusion model links penetrant permeability, solubility and diffusion coefficients in the membrane as follows (Wijmans and Baker, 1995):

$$P_1 = D_1 \times S_1 \quad (8)$$

When considering the permeation of a binary mixture through a membrane, the selectivity for the component  $i$  vs. the component  $j$  is defined as follows (Wijmans and Baker, 1995):

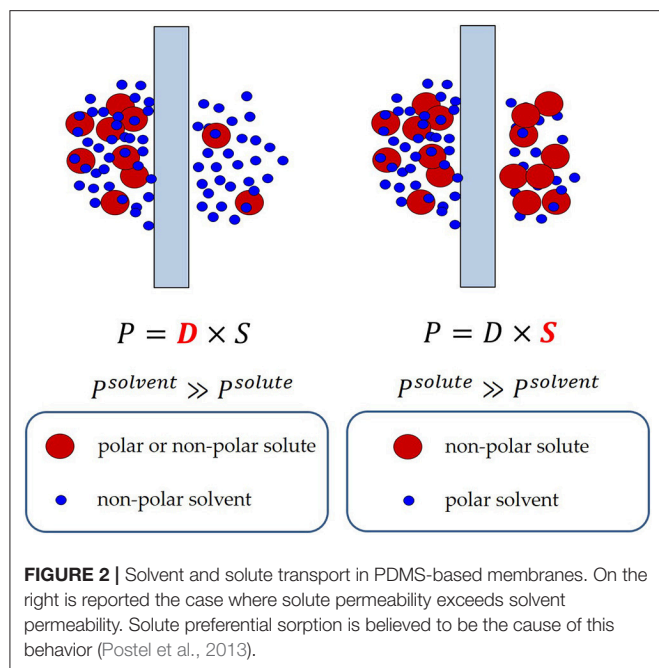
$$\alpha_{ij} = \frac{P_i}{P_j} = \frac{D_i}{D_j} \times \frac{S_i}{S_j} = \alpha_D \times \alpha_S \quad (9)$$

where  $\alpha_D$  and  $\alpha_S$  are the diffusivity-selectivity and the solubility-selectivity, respectively. The diffusivity-selectivity is believed to control the selective permeation of solvent over solute through OSN membranes. Indeed, since diffusivity decreases markedly with increasing penetrant size, solute molecules are expected to be rejected by the membrane due to their very slow diffusion in the membrane material. However, deviations from this rule of thumb have been observed. For example, Postel reported that during removal of non-polar hydrocarbon solutes (e.g., alkanes) from polar solvents (e.g., isopropanol) using rubbery PDMS membranes, solute permeability through the membrane largely exceeds solvent permeability (Postel et al., 2013). As a consequence, the solute is enriched in the permeate side relative to the feed side (i.e., the membrane is solute-selective instead of solvent-selective, cf. **Figure 2**). Postel hypothesized that preferential solute sorption in PDMS, caused by its higher thermodynamic affinity with the polymer, is responsible for this phenomenon, even though no direct proof of this hypothesis has been provided (Postel et al., 2013).

As we will see in the forthcoming sections, often commercial membranes are made by a thin active layer, which actually performs the separation, cast onto a porous support. Since the thickness of the active layer cannot be measured accurately, application of Equation 1 to calculate permeability is not straightforward. So, the performance of these composite membranes is expressed in terms of permeance instead permeability. Permeance is the thickness normalized permeability and, as such, it is not an intrinsic property of the membrane, since it depends on its geometry. Likewise, in practical applications, rejection is used instead selectivity. Rejection of species  $i$  is defined as follows (Marchetti et al., 2014, 2017):

$$R_i = 1 - \frac{C_i^p}{C_i^f} \quad (10)$$





where  $C_i^p$  and  $C_i^f$  are the concentrations of species  $i$  in the permeate and feed, respectively. Rejection is related to selectivity as follows:

$$\alpha_{ij} = \frac{1 - R_i}{1 - R_j} \quad (11)$$

## Plasticization

Membrane plasticization indicates an increase in chain mobility caused by penetrant sorption (Chiou et al., 1985). Such improved chain mobility reduces the energy penalty required to open gaps between polymer chains, thus enhancing penetrant diffusivity and permeability. However, such an increase in permeability is accompanied by a loss in membrane selectivity. OSN membranes must exhibit adequate resistance to plasticization, as they face directly organic liquids during their operation. Methods to mitigate membrane plasticization rely essentially on polymer chemistry: covalent or ionic cross-linking, as well as use of rigid monomers with limited rotation freedom are some relevant examples (Vanherck et al., 2013; Valtcheva et al., 2014, 2015).

## Physical Aging

Rigid materials, such as glassy polymers, are sought in OSN applications. Glassy polymers contain an excess free volume trapped in their structure and, as such, they are non-equilibrium materials. Excess free volume is *per se* unstable and tends to be relaxed over time, producing a progressive densification of the polymer matrix. This process is referred to as physical aging (Huang and Paul, 2004, 2006). Loss of free volume significantly affects transport properties of glassy membranes, as it reduces small molecule permeability and enhances selectivity. Paul and co-workers demonstrated that the physical aging rate of glassy polymer films is inversely proportional to their square thickness, which justifies the accelerated aging exhibited by thin films

typically used in membrane applications (Huang and Paul, 2004, 2006). Membranes 1  $\mu\text{m}$  thick or less lose 25% of their permeability within a few days after manufacturing. Another 25% of their permeability is lost in the following 15 days (Galizia et al., 2017a). For example, asymmetric membranes based on cross-linked Lenzing P84 polyimide, the current standard material for OSN, exhibit solvent permeance ranging from 1 to 2  $\text{L}/(\text{m}^2 \text{ h bar})$ . Thermal annealing at 200°C decreases solvent permeance to zero, due to polymer densification (See See-Toh et al., 2007a). The issue of physical aging becomes dramatic during operation at medium-high temperatures, as polymer chains motion, who is ultimately responsible for physical aging of glassy polymers, becomes faster with increasing temperature.

Strategies to mitigate this issue have been devised, which rely on covalent cross-linking and use of rigid monomers with frustrated rotation freedom. While the former strategy was sometimes successful, the latter did not always guarantee good results, as rigid polymers, such as PIMs (Bernardo et al., 2017) and thermally rearranged (TR) polymers (Wang et al., 2014) also exhibit physical aging when manufactured as thin films.

Recently, Livingston and co-workers reported negligible aging in poly(ether ether ketone) (PEEK) membranes for OSN (Da Silva Bursal et al., 2015, 2017). PEEK is a fully aromatic, semi-crystalline polymer made by hydroquinone and benzophenone segments. Physical aging of bulky membranes (10–50  $\mu\text{m}$ ) typically used in the academia is a slow process and its effects do not show up within experimentally accessible timescales (Galizia et al., 2017a). To accelerate physical aging, Da Silva Bursal annealed thick films made by PEEK, Lenzing P84 polyimide and polybenzimidazole at 120°C for 48 h (Da Silva Bursal et al., 2017). Polyimide and PBI samples became very brittle after thermal annealing, due to the accelerated free volume relaxation, which reduced polymer chain mobility. Their Young's modulus could not be measured after annealing. In contrast, PEEK didn't show any brittleness and its Young's modulus increased from 61 MPa to 108 MPa after annealing at 120°C. The unusual stability exhibited by PEEK is likely due to the presence of ultra-rigid crystalline domains, which freeze polymer chains in the amorphous domain in their original position (Da Silva Bursal et al., 2017).

Three dimethylformamide (DMF) filtration experiments were run with PEEK, polyimide P84 and PBI membranes at 30, 85, and 140°C, respectively, followed by a fourth run at 30°C. Permeance of P84 decreased by a factor 6 from 30 to 85°C. At 140°C, cross-linking thermal scission caused the membrane failure. PEEK and PBI permeance increased by a factor 20 and 2.5, respectively, from 30 to 140°C. Interestingly, during the fourth filtration cycle, when temperature was returned to 30°C, PEEK exhibited the same permeance as in the first run, and PBI lost 25% of its original permeance (cf. Figure 3). This result was justified by invoking negligible aging in PEEK (Da Silva Bursal et al., 2017).

## Permeability-Selectivity Trade-Off

The existence of a trade-off between permeability and selectivity in polymer membranes for gas separation was reported on empirical bases by Robeson (Robeson, 1991, 2008), and it was explained theoretically by Freeman (1999). Generally, highly permeable membranes exhibit poor selectivity, and vice-versa. As a consequence, the performance of polymer membranes is

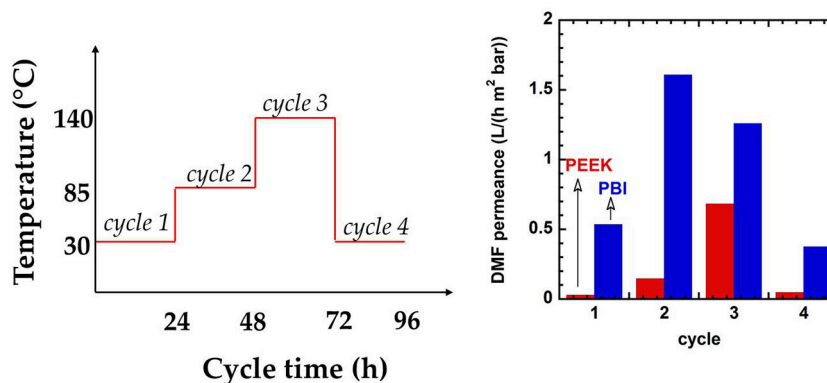


**FIGURE 3 |** Effect of physical aging on poly(ether ether ketone) and polybenzimidazole membranes. Adapted from Da Silva Bursal et al. (2017), with permission of Elsevier.

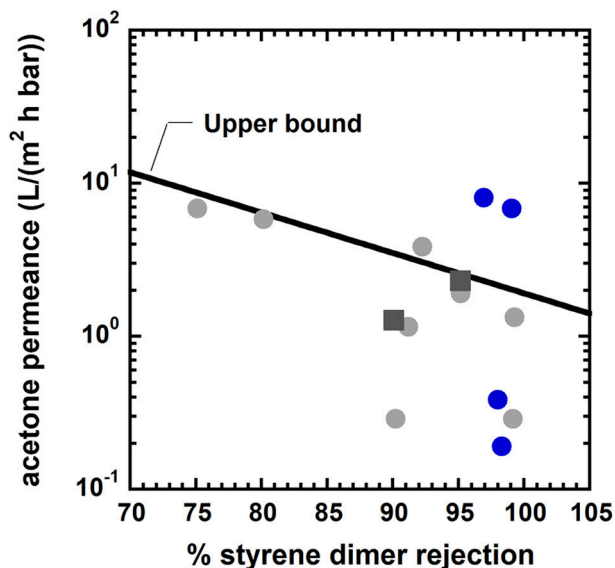


**FIGURE 4 |** Upper bound diagram for styrene dimers (molecular mass 236 g/mol) separation from acetone at room temperature. Solid gray circles: conventional asymmetric membranes. Solid black square: conventional composite membranes. Solid blue circles: nanoporous polyarylates synthesized by Jimenez-Salomon et al. (2016). Blue circles above the upper bound refer to polyarylates obtained using contorted, non-planar monomers [i.e., 9,9-bis(4-hydroxyphenyl)fluorene]. Blue circles below the upper bound refer to polyarylates obtained using planar, non-contorted monomers [i.e., dihydroxyanthraquinone]. Adapted from Jimenez-Salomon et al. (2016), with permission of NatureResearch.

limited to stay below the upper bound defined by the best performing materials. Conversely, inorganic materials, such as zeolites, often surpass the upper bound, as they exhibit high levels of permeability and selectivity. Recently, a permeability-selectivity trade-off for OSN membranes was reported by Marchetti (Marchetti et al., 2017). Such finding strongly supports the idea that the solution-diffusion mechanism rules solute and solvent transport in OSN membranes. An example of

permeance/rejection upper bound for OSN is reported in Figure 4.

### Effect of Pressure on Solvent Flux

One of the most controversial aspects in OSN is the dependence of solvent flux on the upstream pressure. Several authors observed that flux is linear with  $\Delta p$  (i.e., the pressure difference across the membrane), and it declines at high pressures. Membrane compaction caused by the upstream pressure has been invoked to explain this behavior (Machado et al., 1999; Grekhov et al., 2012; Ben Soltane et al., 2013). However, while this explanation could be physically sound for soft, rubbery membranes, such as PDMS (elastic modulus < 4 MPa), it seems unrealistic for rigid glassy polymers typically used in OSN (elastic modulus  $\cong$  4 GPa), especially if we consider that flux decline often starts at relatively low pressures, such as 10–12 bar. We believe the right explanation of this phenomenon should be found in the pioneering studies from Paul and co-workers (Paul and Ebra-Lima, 1970, 1971; Paul, 1973). Paul demonstrated that the driving force for liquid transport through a swollen membrane is the swelling gradient between the upstream and the downstream face of the membrane,  $\phi_1^0 - \phi_1^l$ , where  $\phi$  is the liquid volume fraction in the membrane material (Paul, 1973). While  $\phi_1^0$  (i.e., the liquid volume fraction in the upstream face) is constant, as it does not depend on the applied pressure,  $\phi_1^l$  (i.e., the liquid volume fraction in the downstream face) decreases with increasing upstream pressure. When the upstream pressure is high enough,  $\phi_1^l$  can become zero. In this situation, the maximum driving force is available, which means that flux cannot further increase with increasing pressure (cf. Figure 5). Paul derived the following expression for solvent mass flux as a function of applied  $\Delta p$  (Paul, 1976, 2004):

$$n_1 = \frac{C_1^0 D_1}{l(1-\omega_1^0)} \left[ 1 - \exp\left(-\frac{\tilde{V}_1 \Delta p}{RT}\right) \right] \quad (12)$$

where  $C_1^0$  and  $\omega_1^0$  are the solvent concentration and mass fraction at the upstream face of the membrane, respectively,  $\tilde{V}_1$  is

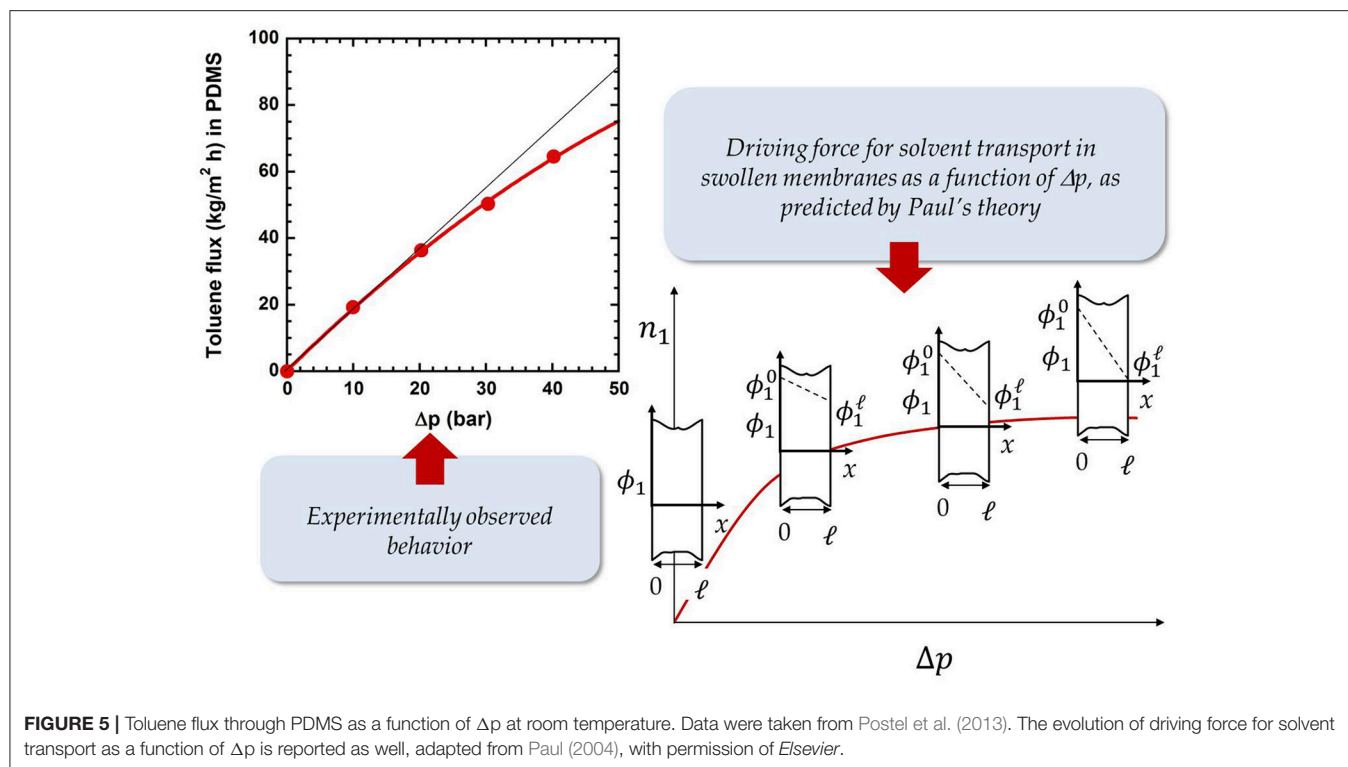


**FIGURE 5 |** Toluene flux through PDMS as a function of  $\Delta p$  at room temperature. Data were taken from Postel et al. (2013). The evolution of driving force for solvent transport as a function of  $\Delta p$  is reported as well, adapted from Paul (2004), with permission of Elsevier.

the solvent molar volume and  $\Delta p$  is the pressure difference across the membrane. Equation 12 states that the ceiling flux is attained more rapidly with increasing permeant molar volume.

Machado and co-workers (Machado et al., 1999) measured the permeability of pure liquid alcohols and hydrocarbons as a function of applied pressure in MPF-50, a commercial membrane made by cross-linked silicon rubber. They observed, especially for higher alcohols (i.e., isopropanol, butanol, and pentanol) and large hydrocarbons (n-pentane), a severe flux decline starting at 15 atm. For methanol such decline was less pronounced. To justify this behavior, Machado and co-workers invoked membrane compaction. However, in doing so, the authors recognized that flux decline at high pressures was significant especially for bulky solvents, i.e., solvent endowed with large molecular size. We believe their conclusions are somehow misleading, since membrane compaction is a purely mechanical effect that should take place regardless of penetrant size. Machado used the following empirical expression to fit flux vs. pressure curves:

$$n_1 = n_1^0 \exp(-\alpha_p \Delta p) \quad (13)$$

where  $n_1^0$  is a pre-exponential factor and  $\alpha_p$  is an empirical parameter that measures membrane compaction: the higher the membrane compaction, the higher  $\alpha_p$ . So, flux decline becomes faster with increasing  $\alpha_p$  (that is, flux decline starts at lower pressures with increasing  $\alpha_p$ ). Paul's theory can be used to rationalize this behavior, without invoking membrane compaction. Indeed, Equation 12 states that (i) at low  $\Delta p$  flux is linear, as it can be demonstrated by replacing the

exponential term with a first order Taylor expansion (i.e.,  $1 - \exp\left(-\frac{\tilde{V}_1 \Delta p}{RT}\right) \cong \frac{\tilde{V}_1 \Delta p}{RT}$  when  $\Delta p$  is small), and (ii) at sufficient high  $\Delta p$ , the downward curvature of the flux-pressure curve becomes more pronounced as the solvent molar volume increases. **Figure 6A** shows the dimensionless flux,  $n_1^{dim}$ , (i.e.,  $n_1^{dim} = \left[1 - \exp\left(-\frac{\tilde{V}_1 \Delta p}{RT}\right)\right]$ ) as a function of  $\Delta p$ , for different values of  $\tilde{V}_1$ . The downward curvature of the flux-pressure curves becomes more pronounced with increasing permeant molecular size, as observed by Machado.

Interestingly, for any given couple of solvents,  $i$  and  $j$ , the  $\alpha_p^i/\alpha_p^j$  ratio matches very well with the molar volumes ratio,  $\tilde{V}_1^i/\tilde{V}_1^j$  (cf. **Figure 6B**). This analysis points out that the parameter  $\alpha_p$  in the empirical Machado's model does not account for membrane compaction, as the authors state. According to Paul's theory,  $\alpha_p$  is a measure of penetrant molecular size. So, occurrence of flux decline is not sign of membrane compaction, as commonly believed in the literature. Flux decline simply indicates that the system is approaching a condition where the driving force for solvent transport is maximum. When this maximum is reached, the flux attains its ceiling value. Moreover, the magnitude of flux decline increases with increasing permeant molecular size. So, the empirical Machado's model, if interpreted correctly, coincides with the rigorous Paul's model.

## CURRENT OSN MATERIALS

OSN is a relatively young process, but with enormous potential for growth. Small scale applications of OSN are today in the

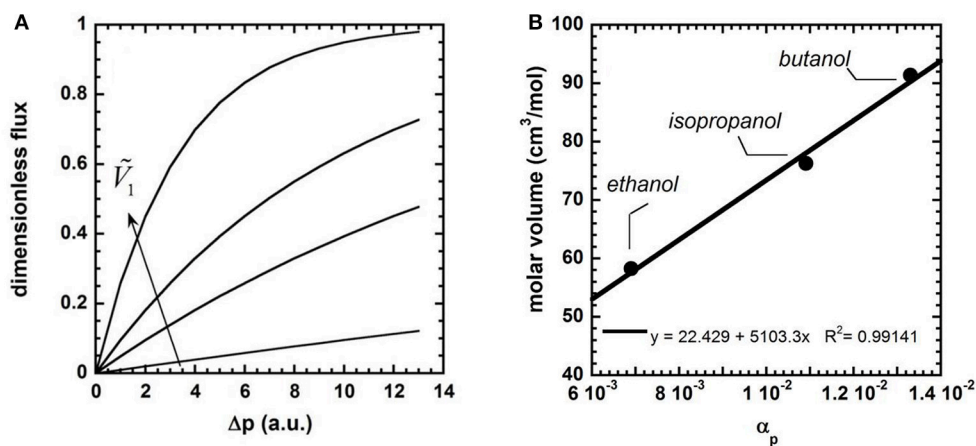


**FIGURE 6 | (A)** Solvent dimensionless flux vs.  $\Delta p$  at various solvent molar volumes, as predicted by the Paul theory (Paul, 1973). **(B)** Solvent molar volume,  $\tilde{V}_1$ , vs.  $\alpha_p$  in silicone rubber MPF-50 (Machado et al., 1999).

pharmaceutical and cosmetic industry, as well as in refinery (dewaxing of lube oil) (Marchetti et al., 2014, 2017; Buonomenna and Bae, 2015). Composite membranes, consisting of a very thin ( $<1 \mu\text{m}$  thick) active layer supported onto a porous backing, are often considered in the academic research and industrial practice (cf., Figure 7). The active layer and the backing support are made by different materials and have different structures and properties. They are combined together exploiting interfacial polymerization, as well as well-established spin coating or dip coating techniques. The support is generally made by polysulfone, polypropylene, polyimide or polybenzimidazole, depending on the environment the membrane has to face with. The active layer, which performs the separation, is generally made by cross-linked Lenzing P84 polyimide or cross-linked silicon rubber (PDMS) (Marchetti et al., 2014). The chemical structure of P84 polyimide and PDMS and their relevant chemical-physical properties are reported in Table 1. Alternatively, asymmetric membranes can be used (cf., Figure 7). Asymmetric membranes exhibit a dense skin, which performs the separation, supported onto a porous medium, made of the same material as the skin itself. They are prepared via phase-inversion, a process originally developed by Loeb and Sourirajan (Loeb and Sourirajan, 1963). A dilute solution of the membrane material in an appropriate solvent is cast onto a fabric backing. Then, the freshly cast membrane is soaked in a non-solvent bath where phase separation occurs. The polymer-rich phase generates the dense active layer, and the polymer-poor phase generates the porous support. Compared to composite membranes, asymmetric membranes exhibit lower resistance to physical aging and less stable properties during operation.

Standard membrane materials for OSN are polyimides (White, 2002) and cross-linked silicone rubber (Postel et al., 2013), even though new materials, such as polybenzimidazole and PIMs, are emerging as promising candidates (Valtcheva et al., 2014, 2015). Unlike gas separation, OSN currently relies on a limited number of membrane materials, since polymers capable to withstand organic environments are rare.

Since the pioneering studies conducted by White in the early 2000's (White, 2001, 2002), Lenzing P84, a polyimide obtained by the condensation of 2,4-diisocyanato-1-methylbenzene and 1,1'-methylenebis(4-isocyanatobenzene) with 5,5'-carbonylbis(1,3-isobenzofurandione), is currently the standard membrane material for OSN (Silva et al., 2005; See-Toh et al., 2007a, 2008). Lenzing P84 films can be fabricated via solution casting from DMF, NMP, DMSO and DMAc solutions. Due to its fully aromatic, rigid structure, Lenzing P84 exhibits long lasting resistance to several solvents, such as hydrocarbons, toluene, alcohols and ketones. White prepared asymmetric membranes based on Lenzing P84 to separate linear from branched alkanes in toluene solutions. He showed that pristane, a saturated hydrocarbon bearing 19 carbon atoms, exhibited lower flux through Lenzing P84 relative to n-docosane, a linear saturated hydrocarbon bearing 22 carbon atom. This behavior is interesting, since pristane has lower molecular weight and molar volume relative to docosane. White attributed this behavior to the larger cross-section area of pristane, which increases the frictional resistance offered by the polymer to molecular diffusion. Based on this picture, pristane is better rejected than docosane due to its slower diffusion through the membrane material (White, 2002).

Afterwards, White used Lenzing P84 to separate aromatic from aliphatic aromas: interestingly, aromatic compounds exhibited higher fluxed than aliphatic ones. This behavior was attributed to the sorption contribution. Indeed, aromatic compounds interact more favorably with the aromatic polymer backbone than aliphatic species do. Such favorable thermodynamic interaction enhances the solubility of aromatic over aliphatic species in the membrane, which, based on the solution-diffusion model, justifies the experimental findings (White, 2002).

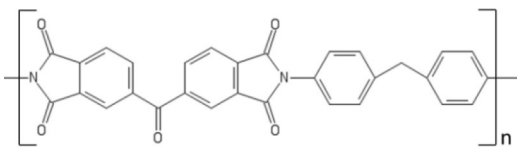
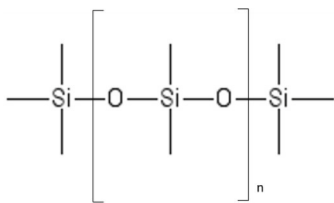
To improve the stability in aggressive aprotic solvents (e.g., THF, DMF and NMP), in which polyimides are soluble, Livingston and co-workers crosslinked Lenzing P84 using aliphatic diamines (ethylenediamine, propanediamine,





**FIGURE 7 |** Structure of composite **(A)** and asymmetric **(B)** membranes for OSN.

**TABLE 1 |** Current standard materials for OSN: Lenzing P84 polyimide and PDMS.

	P84 polyimide	PDMS
		
Glass transition temperature (°C)	329	−123
Young's modulus (GPa)	2.50	0.004
Methanol permeance* [L/(h m <sup>2</sup> bar)]	5.48	0.619
Source	(P84 product data, <a href="http://www.hppolymer.com/pdfs/Diamond%20wheel%20brochure.pdf">http://www.hppolymer.com/pdfs/Diamond%20wheel%20brochure.pdf</a> ; Darvishmanesh et al., 2010)	Lotters et al., 1997; Postel et al., 2013

\*At room temperature.

hexanediamine, and octanediamine) in methanol solution. The cross-linking mechanism was described in detail by Liu et al. (2001). Specifically, the amino groups available on the cross-linker react with the imide groups on the polymer backbone to form amide moieties. The matrix swelling induced by methanol sorption is an essential pre-requisite for the formation of cross-linking. Indeed, if the polymer is not swollen enough, the reaction between the amino and the imide groups can be very slow. The method devised by Livingston produces uniform cross-linking throughout the whole membrane thickness. Other methods based on the radical-initiated cross-linking cannot be exploited, since they would effectively cross-link just the membrane surface, thus causing the membrane failure in aprotic acids. Cross-linked Lenzing P84 exhibited excellent stability in tetrahydrofuran (THF), N-methyl pyrrolidone (NMP), and dimethylformamide (DMF). FTIR analysis demonstrated that no morphological changes occurred in the membrane after soaking in these solvents for 120 h (See-Toh et al., 2007b). Obviously, the gain in stability upon cross-linking is accompanied by a decrease in permeability, caused by the enhanced chain packing.

Cross-linked PDMS has been tested to concentrate dyes from organic solutions and remove solvents from vegetable oils

(Subramanian et al., 2001, 2003; Koike et al., 2002; de Moraes Coutinho et al., 2009). The main drawback for using PDMS is its poor resistance to aggressive solvents. Indeed, due to the high chain flexibility and weak rigidity, PDMS sorbs a significant amount of solvent (Favre et al., 1994; Whu et al., 2000; Sheth et al., 2003; Vankelecom et al., 2004), which prejudices the membrane stability.

Both Lenzing polyimide and PDMS suffer of several limitations. Lenzing PI exhibits, indeed, modest fluxes but high resistance to aggressive environments. In contrast, PDMS exhibits high fluxes but poor chemical resistance. So, new materials are sought to overcome such limitations.

In recent years, polybenzimidazole (PBI), commercially available under the trade name of Celazole<sup>®</sup>, emerged as a promising material for OSN. PBI, first synthesized by Vogel and Marvel (Vogel and Marvel, 1961), is prepared from isophthalic acid and 3,3'-diaminobenzidine. It exhibits a rigid, aromatic structure with frustrated chain mobility. Moreover, intermolecular hydrogen bonding acts as a cross-link and contributes to mitigate swelling and plasticization in the presence of organic liquids. PBI exhibits also unusual thermal stability, with a negligible mass loss (< 5%) upon exposure to 570°C. Such

unique combination of rigidity, high glass transition temperature and unprecedented chemical and thermal resistance, makes PBI suitable for separations in chemically challenging environments (Borjigin et al., 2015). However, the lack of solubility in most of organic solvents makes it difficult manufacturing thin membranes based on PBI. This polymer is only soluble in aggressive solvents, such as dimethylacetamide (DMAc). To further improve solubility in DMAc, LiCl is added to the dope solution, which complicates the post-processing treatment of the membranes as, after fabrication, LiCl has to be removed. These issues hamper the use of PBI in the industrial practice.

Livingston and co-workers developed cross-linked asymmetric membranes based on PBI with superior resistance in acid environments (Valtcheva et al., 2014). PBI was cast from a DMAc solution onto a non-woven polypropylene support. The nascent membrane was then soaked in water to generate phase separation and induce the asymmetric structure. Following this protocol, membranes were cross-linked upon immersion in a hot solution of dibromobenzene in acetonitrile (cf., Figure 8). Interestingly, the resulting cross-linked membranes exhibited good separation performance for several PEG markers in acetonitrile and dimethylformamide, as well as excellent dimensional stability even in hydrochloric acid solutions.

Since the pioneering work by Sourirajan in the early 60s, cellulose acetate and its derivatives have been, for at least two decades, the most studied materials for OSN applications. However, due to its poor resistance to aggressive solvents, cellulose acetate could only be used to separate a limited number of mixtures, such as water/alcohol. Moreover, due to the presence of crystalline domains, solvent flux through cellulose acetate membranes is relatively low. Recently, Vanherck et al. developed a new strategy to enhance the permeability of cellulose acetate OSN membranes without sacrificing the selectivity (Vanherck et al., 2011). They exploited the principle of photothermal heating by embedding gold nanoparticles (GNPs) into a cellulose acetate membrane. In this way it is possible to increase the local temperature in the membrane during operation by light irradiation, which, in turn, significantly enhances solvent flux. Such increase in solvent transport rate is essentially ascribable to an increase in diffusion coefficient. Indeed, solvent mobility coefficient through the membrane increases exponentially with increasing temperatures, due to the reduction of frictional resistance offered by polymer chains to penetrant diffusion. In contrast, the effect of temperature on the sorption coefficient is much weaker. The same principle was exploited by Nakai to improve by 37% CO<sub>2</sub> permeability through cellulose acetate (Nakai et al., 2002).

The method proposed by Vanherck leverages on the gold nanoparticles ability to absorb light and convert it into heat (Daniel and Astruc, 2004). Such an effect becomes especially efficient at specific wavelengths, where surface plasmon resonance occurs. Golden nanoparticles were generated directly into a pre-made cellulose acetate membrane using the protocol reported by Huang (Huang et al., 2005). The amount of nanoparticles in the membrane was varied between 0 and 2% wt. To run nanofiltration experiments, Vanherck modified a dead-end filtration cell by building a glass window on top of it, to allow

an argon-ion laser beam (wavelength = 514 nm) to irradiate the active membrane area (Vanherck et al., 2011).

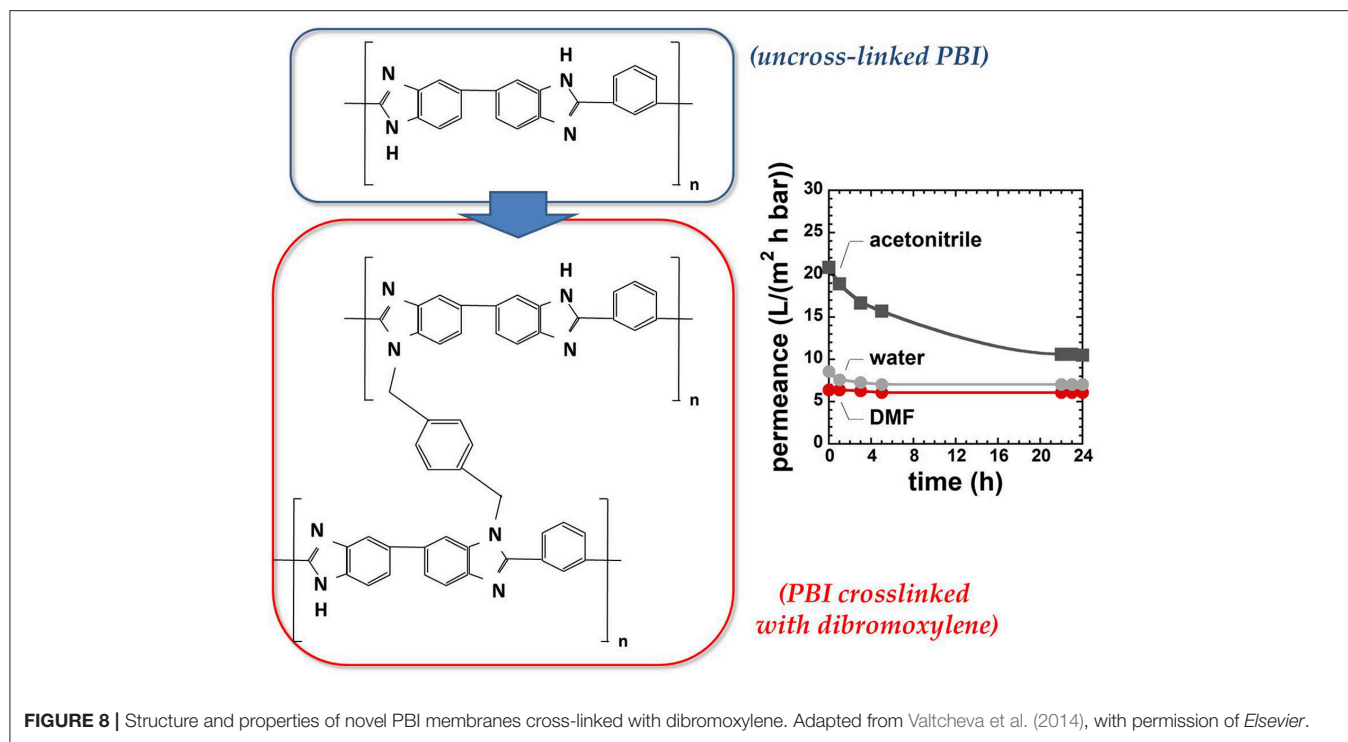
Interestingly, water and alcohol permeability increased up to 15 and 400%, respectively, upon laser irradiation, with no detectable effects on solute (bromothymol blue) rejection. Moreover, solvent permeability returned to its original value after the laser was turned off, indicating that the observed change in transport properties was only due to the reversible membrane heating and not to permanent structural modifications. The much larger permeability improvement observed for alcohols was attributed to the lower specific heat of alcohols relative to water, which permits a more rapid heating of the swollen membrane. Likewise, alcohols exhibit lower thermal conductivity relative to water, so, while flowing through the membrane, they remove less heat.

## MOLECULAR FACTORS AFFECTING SOLUTE AND SOLVENT TRANSPORT IN OSN MEMBRANES

The vast majority of research efforts on OSN focused, so far, on applications: commercially available or newly synthesized materials were used to measure solvent flux and solute rejection and such measurements helped to assess the suitability of those materials for specific applications. However, little information is available about molecular factors affecting solute and solvent transport in OSN membranes. The transport mechanism itself is object of discussion, as some researchers assume a solution-diffusion mechanism, others a pore-flow mechanism (Marchetti and Livingston, 2015; Ben Soltane et al., 2016). However, many factors, above all the existence of a permeability-selectivity trade-off, suggest that OSN membranes work based on the solution-diffusion mechanism. This conclusion was confirmed unequivocally by a series of simple but effective experiments performed by Paul in the early 70s. Specifically, Paul measured solvent permeability through a stack of several membranes. After reaching steady-state, the membranes were rapidly removed from the permeation cell and weighed. The experimental solvent concentration profile in the stack was in excellent agreement with that predicted assuming a solution-diffusion transport mechanism (cf. Figure 5, Paul and Ebra-Lima, 1971).

Fundamental structure-property correlations are available for gas separation membranes, which makes it possible to design polymers with pre-assigned transport properties. For example, use of polyethers for CO<sub>2</sub> separation leverages on the high thermodynamic affinity between CO<sub>2</sub> molecules and polar ether groups, which enhances CO<sub>2</sub> sorption and, according to Equation 8, CO<sub>2</sub> selective permeability (Bondar et al., 1999). So, membranes for gas separation are engineered by properly tuning solubility and diffusivity of the target penetrant in the membrane material. This goal is achieved, in turn, by tuning the polymer chemistry, that is, using monomers bearing specific functional groups.

The lack of information about the role of sorption and diffusion coefficients on solvent and solute transport is actually a roadblock toward the rational design of smart OSN membranes.



Nevertheless, in this section we identify, based on the few data available, the main molecular factors that influence solute and solvent transport in OSN membranes.

From a theoretical standpoint, small molecule sorption in polymers is a phase equilibrium problem (Galizia et al., 2012). Sorption equilibrium is reached when penetrant chemical potential in the external fluid phase equates that in the polymer mixture. As chemical potential contains, by its definition, an enthalpic (i.e., energetic) and an entropic contribution, small molecules sorption in polymers is influenced by these two effects (Galizia et al., 2012). Enthalpic effects are related to polymer-penetrant interactions and, as a rule of thumb, favorable interactions translate in high penetrant solubility in the membrane material. Entropic effects are related to penetrant size. As general rule, sorption decreases with increasing penetrant size. Indeed, absent specific interactions, it is less and less likely to accommodate bulkier penetrant molecules in the polymer matrix than smaller penetrant molecules.

Vankelecom et al. (1997) and Cocchi et al. (2015a) reported sorption and diffusion coefficients of several liquids in rubbery PDMS. Alkanes solubility in PDMS decreases linearly with the number of carbon atoms, indicating that sorption is affected essentially by entropic factors. In contrast, solubility of polar alcohols in PDMS follows a non-monotonous trend with the number of carbon atoms, as it increases moving from ethanol to 1-butanol, and then decreases linearly going from 1-butanol to higher alcohols, following the same trend observed for alkanes. This phenomenon was justified based on the interplay between enthalpic and entropic effects. Indeed, PDMS exhibits poor thermodynamic affinity with lower polar alcohols. The strong

repulsive interactions between –OH polar groups and the non-polar PDMS backbone strongly oppose to alcohol dissolution in the polymer. When the length of the alkyl tail increases, the affinity between alcohols and PDMS increases, which justifies the increase in solubility observed going from methanol to 1-butanol. When the alkyl tail is long enough, the polar –OH group is sterically shielded, so alcohols start to behave as alkanes and their solubility in PDMS decreases with increasing penetrant size. So, the increase in solubility from methanol to 1-butanol is driven by enthalpic (i.e., energetic) effects, and the subsequent decrease is driven by entropic effects.

Vankelecom demonstrated that the solubility of organic liquids in PDMS decreases linearly with increasing the difference between the penetrant and polymer Hildebrandt solubility parameter,  $\delta - \delta_{PDMS}$  (Vankelecom et al., 1997). Afterwards, Cocchi showed that a better linear correlation is obtained if penetrant solubility in PDMS is plotted against  $M_w^{0.75} (\delta - \delta_{PDMS})^2$ , where  $M_w$  is the penetrant molecular weight (Cocchi et al., 2015a). Indeed, while the correlation reported by Vankelecom accounts just for energetic factors, that reported by Cocchi accounts for both energetic (through  $\delta$ ) and entropic (through  $M_w$ ) factors. Doing so, sorption data for hydrocarbons, alcohols and several other organic liquids fall on a master curve. Unfortunately, such analysis is fairly absent in the literature for glassy polymers. Cocchi et al. (2015b) also reported mixed solvent-solute solubility data in PDMS. In mixed conditions, solute solubility in the membrane is greatly enhanced, up to 25 times, compared to pure solute solubility, which indicates that real solvent-to-solute solubility-selectivity is lower than that predicted on the basis of pure component sorption data. The

large enhancement in solute sorption in mixed conditions was justified based on the high degree of membrane swelling induced by the solvent.

Diffusivity-selectivity data for solute-solvent mixtures are virtually absent in the literature. Small molecules diffusion coefficients in polymers generally decrease with increasing penetrant size (Galizia et al., 2017b). The critical volume, as well as the kinetic diameter or squared kinetic diameter have been used as a measure of penetrant size. Interestingly, diffusion coefficients of liquid penetrants in PDMS do not always correlate to penetrant size. For example, as reported by Cocchi et al. (2015a), acetone diffusivity in PDMS is larger than water diffusivity, despite water (kinetic diameter = 0.265 nm) is a smaller molecule than acetone (kinetic diameter = 0.50 nm). This behavior was explained considering that acetone is sorbed to a greater extent than water by PDMS, so acetone diffusion occurs in a much more swollen membrane, which offers a lower frictional resistance to penetrant transport. However, subtle interactional effects influence penetrant diffusion in polymers. As discussed above, penetrants diffusion coefficient in polymers is the product of a purely kinetic quantity, i.e., the mobility coefficient,  $L_1$ , which quantifies the frictional resistance offered by the polymer matrix to penetrant diffusion, and a thermodynamic factor, related to polymer-penetrant interactions. The thermodynamic factor is higher than one when polymer-penetrant interactions are thermodynamically favorable, and less than one when such interactions are thermodynamically unfavorable. Due to the strong hydrophobicity of PDMS, acetone-PDMS affinity is much higher than water-PDMS affinity, so the thermodynamic contribution to acetone diffusion in PDMS is expected to largely exceed that of water (Favre et al., 1994; Singh et al., 1998), which would justify the experimental findings reported by Cocchi.

## RECENT ADVANCES AND FUTURE DIRECTIONS IN OSN

### Polybenzimidazoles

In this section, we identify new generation materials for OSN and outline applications that will likely drive OSN research in the next decades. As mentioned in section Current OSN Materials, polybenzimidazole exhibits unprecedented thermal, mechanical and chemical stability, however, some drawbacks limit its use in the industrial practice. Above all, the poor chain mobility caused by the rigid diaminobenzidine segments, combined with the efficient chain packing produced by intermolecular hydrogen bonds, reduces small molecule permeability in PBI. As a matter of fact, PBI exhibits quite low fluxes (i.e., low productivity), which makes it unappealing for practical applications. To circumvent these issues, Riffle and coworkers synthesized a substituted PBI with improved processability and higher permeability relative to commercial PBI (Borjigin et al., 2015). They replaced the linear, rigid diaminobenzidine monomer with 3,3', 4,4' tetraaminodiphenylsulfone (TADPS). Such monomer exhibits higher flexibility relative to diaminobenzidine, due to the presence of the sulfonyl linkage between diaminophenyl groups (cf. Table 2). Moreover, the kinked structure of TADPS-PBI induced by sulfonyl groups frustrates chain packing and

enhances small molecules sorption and transport. Interestingly, substituted PBI exhibits improved solubility in solvents (DMAc, DMSO, NMP), while maintaining chemical, mechanical and thermal stability comparable to those exhibited by commercial PBI.  $H_2$  and  $CO_2$  permeability coefficients in TADPS-PBI and in commercial PBI were fairly similar, but TADPS-PBI exhibited higher  $H_2/CO_2$  selectivity. This fact is significant, since the improved flexibility induced by sulfonyl groups did not sacrifice the membrane performance. Investigation of substituted PBI for OSN application is underway.

### Polymers of Intrinsic Microporosity (PIMs)

The most known member of this family of polymers, PIM-1, first synthesized by Budd and McKeown in 2004, is prepared by the nucleophilic substitution reaction of tetrafluoro-phthalonitrile with 5,5,6,6-tetrahydroxy-3,3,3,3-tetramethyl-1,1'-spirobisindane. The spiro-center of 5,5,6,6-tetrahydroxy-3,3,3,3-tetramethyl-1,1'-spirobisindane is responsible for the contorted structure exhibited by this polymer. PIM-1 exhibits a glass transition temperature above 450°C and a three-dimensional ladder structure, which frustrates chain packing and produces interconnected free volume cavities whose dimension is < 2 nm. Consistently, the BET surface area is very high, up to 800 m<sup>2</sup>/g. Due to this ladder-type, rigid structure, PIMs are poorly soluble in solvents, except THF and chloroform (Budd et al., 2004).

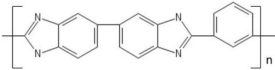
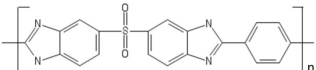
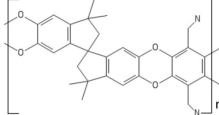
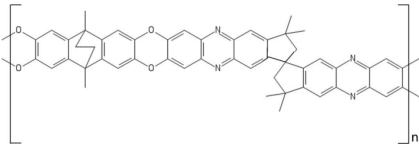
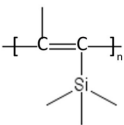
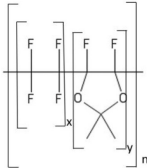
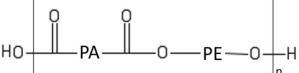
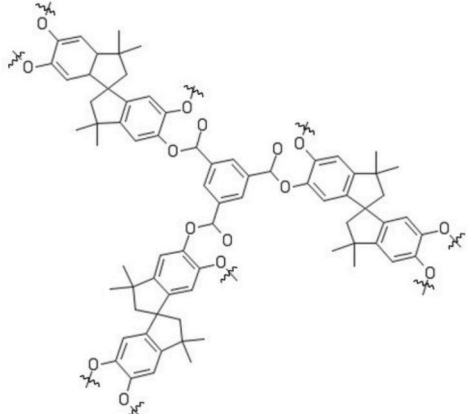
A drawback for using PIMs in OSN is their tendency to swell in the presence of solvents (Ogieglo et al., 2017), such as acetone and toluene, which produces very high flux but poor solute rejection. Several attempts have been made to synthesize alternative PIMs, but only a limited number of monomers is able to give polymers with a sufficiently high molecular weight (Sanders et al., 2013). Combining PIM-1 with other polymers could be, in principle, another route to improve its properties, but serious compatibility issues were reported. Gao et al. coated a PVDF support with a thin PIM-1 layer, but the adhesion of the active layer to the substrate was poor (Gao et al., 2017).

Currently, research efforts are underway to improve PIMs resistance to solvents by cross-linking or chemical modification. Fritsch (Fritsch et al., 2012) blended PIM-1 with polyethyleneimine (PEIm) in THF solution. Then, poly(ethylene glycol diglycidyl ether) (PEGDEG) was added to the solution. PEGDEG cross-linked the blend by reacting with the PEIm amino groups. Cross-linked PIM-1-PEIm membranes exhibited much better dimensional stability in solvents. Moreover, blending with rubbery PEIm reduced significantly the PIM-1 brittleness.

Livingston and coworkers developed composite membranes made of a 140 nm thick PIM-1 layer supported on PAN or alumina, which exhibited excellent resistance to physical aging after annealing for several hours at 150°C (Gorgojo et al., 2014). Remarkably, solvent permeability was almost 2 orders of magnitude higher than in commercial membranes based on Lenzing P84 polyimide. Unexpectedly, solvent permeance decreased with decreasing the active layer thickness below 140 nm. Indeed, as demonstrated by light interferometry, chain packing is enhanced in ultrathin films.



**TABLE 2** | New materials for OSN application.

Material	Structure
PBI	
TADPS-PBI	
PIM-1	
PIM-8	
PTMSP	
Teflon® AF	
Pebax	
Polyarylates	

Very recently, PIMs emerged as promising materials for isomer separation. The latter is among the most challenging separations, as isomers exhibit like size and very similar chemical-physical properties, which makes it difficult developing membranes with adequate levels of selectivity. Such separations are highly demanded in the pharmaceutical industry, where isomers of a given compound often exhibit different therapeutic properties. Intrinsically chiral materials exhibited high selectivity for chiral separations. Weng and coworkers (Weng et al., 2015) synthesized intrinsically chiral PIMs with spectacular selectivity for several isomers of practical deal. Chiral ladder (+)PIM-CN was prepared by condensation reaction between enantiomerically pure 5,5',6,6'-tetrahydroxy-3,3,3',3'-tetramethyl-1,1'-spirobisindane and 2,3,5,6-tetrafluorophthalonitrile in DMF, in the presence of K<sub>2</sub>CO<sub>3</sub>. Selectivities as high as 14 were observed for some chiral separations (e.g., the resolution of R,S mandelic acid and R,S-binol). Interestingly, sorption experiments revealed that solubility-selectivity is equal to one, so the selective permeation of isomers through this material is solely driven by the diffusion contribution. However, the fundamental origin of this behavior is still unknown.

Future research efforts will likely focus on PIMs different than PIM-1. For example, PIM-8 was synthesized by Ghanem et al. by polymerization of 2,3,6,7-tetrahydroxy-9,10-dimethyl-9,10-ethanoanthracene (Ghanem et al., 2008). PIM-8 exhibited a 50% higher selectivity for linear vs. branched alkanes relative to PIM-1. Cook and coworker attributed this behavior to a narrower and much regular size distribution of free volume cavities in PIM-8 (Cook et al., 2018).

## Perfluorinated Glassy Polymers

Perfluorinated polymers are soluble in a limited number of fluorinated liquids and exhibit excellent resistance to the vast majority of organic solvents. Recently, Chau reported solvent permeability and solute rejection data for a series of perfluorodioxole copolymers, such as Hyflon® AD and Cytop® (Chau et al., 2018). Solvent (methanol, hydrocarbons, aromatics, THF) sorption in perfluorodioxole copolymers is about 1% wt, which is much lower than in other glassy polymers. Interestingly, n-heptane sorption in perfluorodioxole copolymers is much larger, 2.5% wt, which enhances n-heptane flux far above that of other organic solvents and reduces substantially solute rejection. The molecular origin of this behavior was tentatively attributed to the higher matrix dilation induced by bulky n-heptane molecules. This explanation, however, appears not convincing on the basis of the relatively low n-heptane sorption level. This example demonstrates the urgent need of fundamental transport studies in glassy OSN membranes.

## Block Copolymers With Hard and Soft Segments

Poly(ether block amide), commercially available under the trade name Pebax®, is a thermoplastic block copolymer made by rigid polyamide segments, which provide mechanical rigidity, interspaced with highly permeable, rubbery polyether segments.

Pebax<sup>®</sup> has shown superior performance in gas separation (Bondar et al., 2000), and recently it raised attention in OSN (Aburabie and Peinemann, 2017). The relative amount of glassy and rubbery segments can be tuned, resulting in different Pebax<sup>®</sup> grades exhibiting different transport and mechanical properties (Bondar et al., 1999, 2000). The role of the glassy segments consists in providing mechanical strength, reducing the swelling of the highly permeable rubbery blocks and maintaining good levels of dimensional stability and selectivity. Pebax<sup>®</sup> can be cross-linked upon immersion in toluene diisocyanate (TDI) solutions, which promotes the formation of urethane linkages between the hydroxyl groups on the polyether segments and the carbonyl groups of TDI (Aburabie and Peinemann, 2017). The cross-linking mechanism proposed by Aburabie was confirmed via DSC analysis. Compared to the pristine, uncross-linked sample, the endothermic peak attributed to the fusion of polyether blocks in the cross-linked sample shifted from 50 to 80°C, whereas the peak assigned to the polyamide blocks did not show any change. This result confirms that the cross-linking is produced by the reaction of TDI with the polyether blocks, as explained above (Aburabie and Peinemann, 2017).

Aburabie showed that ethanol permeance of composite membranes fabricated by coating a PAN support with Pebax<sup>®</sup> was 8 times reduced relative to the PAN support alone (Aburabie and Peinemann, 2017). Moreover, the Pebax<sup>®</sup> active layer was not able to reject brilliant blue in ethanol solution, due to the excessive membrane swelling. A significant enhancement in separation performance was observed after cross-linking. The best results were obtained using a 2% wt cross-linker concentration and a reaction time of 30 min. In this condition, rejection of brilliant blue was about 95% and ethanol permeance was 0.1 L/(m<sup>2</sup> h bar). When the reaction time was larger than 30 min, the membrane assumed a strongly packed structure, likely due to a very high degree of cross-linking. In this condition, ethanol flux was fairly zero even at pressures of 20 bar.

Interestingly, Pebax<sup>®</sup>/PAN membranes cross-linked with 2% TDI for 30 min exhibit 100% rejection of olive oil from a 10% wt olive oil solution in acetone (Aburabie and Peinemann, 2017). Thus, Pebax<sup>®</sup> appears suitable for application in the food industry, where organic solvents are often used to extract vegetable oils from seeds. Currently, solvent recovery from edible oils is performed by distillation, which can alter the organoleptic properties of oils.

The main drawback for using Pebax<sup>®</sup> in OSN is its tendency to swell in water and alcohols, which leads to lower selectivities. Water flux through uncross-linked Pebax<sup>®</sup> membranes increases by almost 50% after 20 h of soaking in water. In contrast, membranes cross-linked with TDI do not exhibit any increase in water flux after swelling in water for 20 h (Aburabie and Peinemann, 2017). So, cross-linking with TDI appears a viable route to produce stable Pebax<sup>®</sup> membranes for OSN applications.

## High Free Volume Polyacetylenes

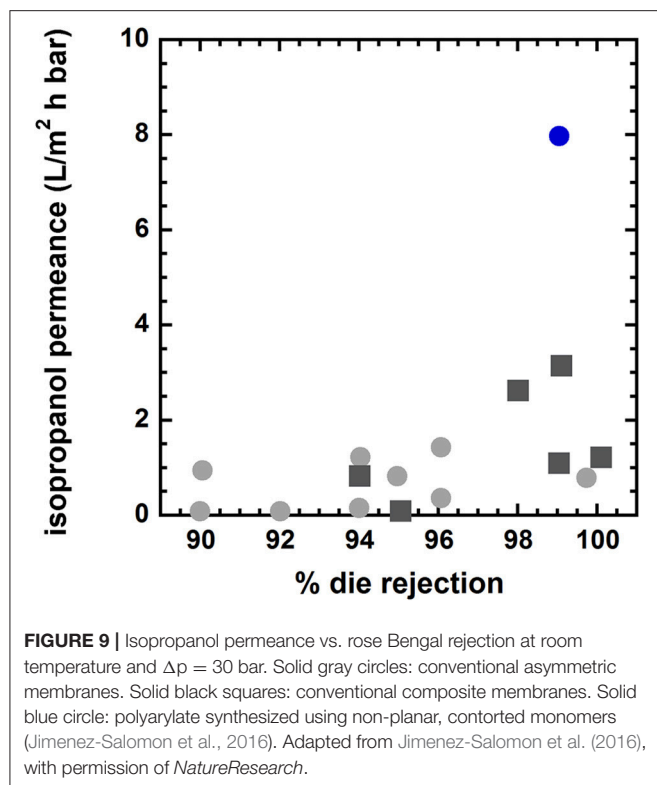
Substituted polyacetylenes, such as poly(trimethylsilyl propyne) (PTMSP) and poly(methylpentyne) (PMP), exhibit a rigid,

glassy structure and bulky functional groups that produce inefficient chain packing, with fractional free volume levels up to 30% (Tanaka et al., 1985; Merkel et al., 2000; Galizia et al., 2014). Composite PTMSP membranes exhibited ethanol permeances as high as 17 L/(m<sup>2</sup> h bar), which is one of the highest values reported in the literature so far (Grekhov et al., 2012; Volkov et al., 2013). However, freshly cast PTMSP membranes exhibit an accelerated physical aging even when they are fabricated as bulky films (Nagai et al., 2000). This behavior is due to the strong departure of this material from equilibrium conditions, as witnessed by the high free volume level. Recently, Lau and co-workers discovered that physical aging of PTMSP and PMP can be stopped upon addition of microporous PAFs (Porous Aromatic Frameworks) (Lau et al., 2014). Specifically, microporous PAFs exert a chain threading effect by partially sorbing the polymer in their pores, which freezes the polymer structure and keeps the polymer chains in their original position. Such beneficial effect completely stops compaction and densification of high free volume polyacetylenes. This result represents a breakthrough and could bring the scientific community to reconsider application of polyacetylenes in OSN. In principle, to further improve its stability in chemically aggressive environments and delay physical aging, PTMSP can be cross-linked with 3,3'-diazidodiphenylsulfone. However, as noted by Kelman et al., chemical cross-linking reduces gas permeability by 70% relative to uncross-linked PTMSP, which makes this material no longer attractive for industrial applications (Kelman et al., 2007). As a matter of fact, no systematic study about the use of cross-linked PTMSP in OSN is available in the literature.

## Isoporous Membranes

Developing isoporous membranes for OSN, i.e., membranes with a very uniform size and distribution of free volume cavities (improperly defined "pores"), will be an important goal over the next years (Yu et al., 2014). While this approach is under investigation for gas separation membranes (Abetz, 2014), a few authors attempted to exploit it for OSN. The actual challenge is that free volume architecture can be disrupted upon exposure to aggressive solvents, thus thwarting the efforts made to synthesize materials with specifically-sized free volume cavities.

Recently, Jimenez-Salomon exploited interfacial polymerization to fabricate highly permeable and selective polyarylate nanofilms, <20 nm thick, onto cross-linked polyimide nanofiltration membranes (Jimenez-Salomon et al., 2016). They used contorted monomers, such as 5,5',6,6'-tetrahydroxy-3,3',3'-tetramethylspirobisindane (TTSBI) and 9,9-bis(4-hydroxyphenyl)fluorene (BHPS) to prepare polyarylates with controlled and specifically-sized free volume elements. During polymerization, TTSBI units acquire a non-coplanar orientation, which leads to polymers having three-dimensional structures and interconnected free volume elements. This picture was confirmed by molecular simulations. For comparison, they also synthesized polyarylates with planar, non-contorted monomers, such as dihydroxyanthraquinone and 1,3-benzenediol, which exhibited much lower permeance but similar selectivity relative to materials containing contorted



monomers. Interestingly, isoporous polyarylates surpass abundantly the upper bound in several applications. As shown in **Figure 9**, isopropanol permeance exhibited by polyarylates is twice that of conventional asymmetric and composite membranes for OSN, and dye (rose Bengal) rejection is over 99%.

Another possible approach for the design of polymers with controlled free volume architecture relies on using monomers bearing triptycene moieties. Recently, this approach has been successfully used to design gas separation membranes (Luo et al., 2016, 2018; Weidman and Guo, 2017; Weidman et al., 2017) endowed with unprecedented levels of permeability and selectivity. Triptycenes are three-dimensional, paddlewheel-like structures formed by three aromatic rings arranged at  $120^\circ$  on three different planes. Once incorporated into the polymer backbone, triptycenes disrupt chain packing and introduce an ultra-fine microporosity which enables for superior size-sieving ability. Specifically, the microporosity is provided via the internal free volume associated to each triptycene moiety. Moreover, unlike ordinary glassy polymers, whose free volume is purely conformational, the internal free volume of triptycene units is configurational and, as such, it is not collapsible. According to this physical picture, triptycene-based polymers exhibit uncommon resistance to physical aging (Luo et al., 2016, 2018; Weidman and Guo, 2017; Weidman et al., 2017). Potential use of such materials in OSN is fairly unexplored. The advantages for using triptycene-based polymers in OSN could be twofold. First, the fine and homogeneous internal free volume provided by triptycenes is inaccessible to solute molecules, but it is potentially

accessible to solvent molecules whose diameter is  $<4\text{\AA}$ , which should guarantee high solvent flux and high solute rejection. Moreover, tough glassy polymers, such as polybenzoxazoles modified introducing triptycene moieties, would also guarantee outstanding resistance in harsh environments, which is an essential condition for applications in OSN.

## Hybrid Materials

The most revolutionary application of OSN in the future will likely be the separation of isomeric solutes from organic solutions. This application is relevant in the pharmaceutical and petrochemical industry. For example, separation of hexane isomers is crucial to enhance gasoline octane number. Mixed matrices formed by selective fillers embedded in polymer membranes could make this application a reality. For example, ZIF-77 has been identified as a good candidate for isomer separations (Dubbeldam et al., 2012; Krishna and van Baten, 2017), but, surprisingly, no publication dealing with mixed matrix membranes containing ZIF-77 is available in the literature.

Recently, a new MOF with hydrophobic quadrilateral channels was synthesized via a solvothermal process from  $[\text{Fe}_3(\mu_3\text{-O})(\text{COO})_6]$  and 2,2-bis(4-carboxyphenyl)-hexafluoropropane (6FDA) and tested for separation of hexane isomers (Lv et al., 2018). The successful separation of n-hexane from its branched isomers relies essentially on solubility-selectivity, as linear n-hexane can be selectively sorbed by the  $[\text{Fe}_3(\mu_3\text{-O})(\text{COO})_6]$ -6FDA MOF, while sorption of branched isomers is sterically hindered. The sorption selectivity exhibited by the  $[\text{Fe}_3(\mu_3\text{-O})(\text{COO})_6]$ -6FDA MOF is 20 times higher than that of other sorbents, such as ZIF-8, zeolite 5A and zeolite  $\beta$  (Luna-Triguero et al., 2017). Moreover, this smart MOF exhibits very stable sorption capacity and selectivity after several sorption-desorption cycles.

Significant research efforts are being devoted to the fabrication of hybrid materials that surpass the permeability-selectivity upper bound. For example, Wu and coworkers incorporated MXenes nanosheets in hydrophilic poly(ethyleneimine) (PEIm) and hydrophobic silicon rubber (PDMS) (Wu et al., 2016). MXenes, first reported by Naguib et al. in 2014, are 2-D inorganic structures consisting of a thin layer of transition metals (Naguib et al., 2014). The resulting membranes were mechanically robust and exhibited higher alcohol permeability and much higher alcohol selectivity relative to neat polymers, thus surpassing the permeability-selectivity upper bound. Specifically, MXenes nanosheets contain polar -OH groups which enhance alcohol sorption and, based on the solution-diffusion model, alcohol permeability (Wu et al., 2016). For example, isopropanol permeability in PDMS-MXenes membranes is 162% higher than in neat PDMS. Moreover, the MXenes nanosheets block solute (e.g., PEG oligomers whose molecular weight ranged from 200 to 1000 Da) transport through the membrane, by making their diffusional pathway more tortuous, which produces a significant increase in solute rejection.

The isopropanol flux and PEG1000 rejection of the PEIm-MXenes membrane at room temperature and 10 bar was tracked for 12 h (cf. **Figure 10**). Isopropanol flux declined by 20% (i.e.,

from 33.5 to 28 L/m<sup>2</sup> h) in the first 4 h and then reached a pseudo-steady state value for the following 8 h. PEG1000 rejection changed from 98.8 to 99.2% within the same time frame. The flux decline was explained invoking membrane compaction and pore blockage by solvent molecules (Wu et al., 2016).

## Membranes Based on Preassembled Nanoparticles

The phase separation process leads to membranes exhibiting a relatively broad distribution of free volume size. The possibility of tailoring the membrane microstructure so as to impart a well-defined free volume architecture has been explored in several ways. As discussed above, one possibility consists in using isoporous membranes. An alternative route to control the free volume architecture and create “manipulated” permeation pathways consists in preparing membranes based on preassembled nanoparticles. Several attempts have been made to deposit polymer nanoparticles on porous supports (Siddique et al., 2011). Nanoparticles can assemble in regular arrays, whose geometry influences the final transport properties of the membrane. Interstitial space between nanoparticles provides preferential permeation pathways. The “pore” size of these membranes can be controlled by tuning the nanoparticles size: if the nanoparticles size distribution is very uniform, the size of the interstitial channels is also uniformly distributed, which is an essential prerequisite to fabricate highly selective membranes (Siddique et al., 2011).

Siddique et al. deposited several layers of NIPAM (N-isopropylacrylamide)-HEMA(2-hydroxyethyl methacrylate) nanoparticles, whose diameter was 120 or 300 nm, onto a porous support via spin coating (Siddique et al., 2011). NIPAM-HEMA nanoparticles were first modified with acryloyl chloride to create polymerizable vinyl groups on their surface. The coating was then stabilized by UV cross-linking via radical polymerization. The support was prepared by casting a P84 polyimide solution onto a non-woven polyester backing. Phase separation of P84 was then induced upon immersion in a water bath. Following this step, the polyimide support was cross-linked upon soaking into a 1,6-hexanediamine-isopropanol solution. Finally, spin coating from methanol solutions was exploited to deposit a nanoparticle layer whose thickness ranged from 1 to 23 μm.

TEM micrographs show that moderate nanoparticle deformation takes place after deposition and UV cross-linking. Moreover, nanoparticles partially occupy the pores of the support membrane. Such observations are crucial to explain the results of nanofiltration experiments. Indeed, based on geometrical considerations, the theoretical pore size should be in the range 9–23 nm, so membranes coated with nanoparticles should not be able to separate molecules in the nanofiltration range (Siddique et al., 2011). However, rejection of styrene oligomers from toluene and acetone solutions was close to 100%, indicating that molecular separation in the nanofiltration range took place. The authors speculated that nanoparticle deformation is responsible for this behavior. As mentioned above, TEM analysis confirms

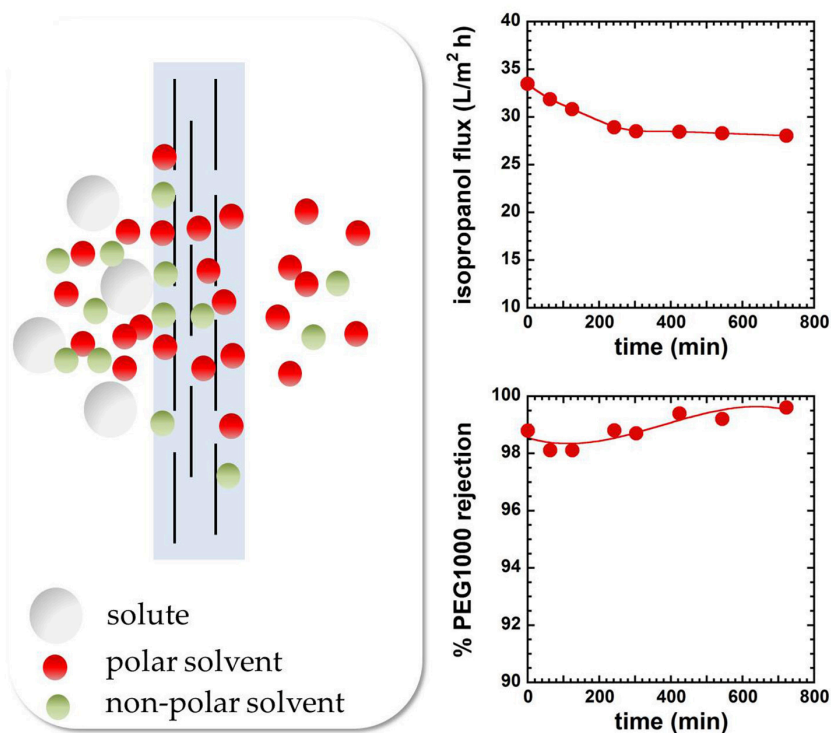


**FIGURE 10 |** Structure and properties of mixed matrix membranes based on PEIm and MXenes (Wu et al., 2016). OSN experiments were run at room temperature and 10 bar using an isopropanol/PEG1000 solution. Adapted from Wu et al. (2016), with permission of Elsevier.



this hypothesis. Interesting, solvent fluxes as high as 55 L/(m<sup>2</sup> h) were measured, which led the authors to hypothesize that polystyrenes transport occurs in the interstitial spaces only, while solvent permeates through both the interstitial spaces and the nanoparticles (Siddique et al., 2011). Such hypothesis is consistent with the typical behavior exhibited by swollen NIPAM nanogels, which are highly permeable to small molecules, and practically impermeable to bulky solutes (Schild, 1992).

Interestingly, polystyrenes rejection increases with increasing the thickness of the nanoparticle layer, due to the narrower pore size distribution, and decreases with increasing nanoparticle diameter, due to the formation of larger interstitial spaces. So, the best membranes are obtained upon deposition of a relatively thick layer of small nanoparticles (Siddique et al., 2011). Deposition of nanoparticles exhibiting different sizes further improves solute rejection. Specifically, the mean pore size can be decreases by coating the support with larger nanoparticles first, and then with smaller nanoparticles.

## Nanopapers

Manufacturing of polymer nanofiltration membranes often requires the use of large amounts of toxic solvents and chemicals. Use of membranes made of cellulose or nanocellulose would provide a solution to the above mentioned issue, as these materials can be processed in aqueous solution (Mautner et al., 2014; Sukma and Culfaz-Emecen, 2018). Nanofibrillated cellulose in the paper form, also called nanopaper, exhibits outstanding mechanical properties and thermal stability, other than good barrier properties (Klemm et al., 2011; Mautner et al., 2014). Moreover, nanopapers exhibit nanopores whose size is comparable to that of a single molecule and, for this reason, they would be ideal candidates for OSN applications (Mautner et al., 2014). Recently, Mautner et al. prepared solvent stable OSN membranes from aqueous suspension of (2,2,6,6-tetramethylpiperidin-1-yl)oxy (TEMPO) oxidized nanofibrillated cellulose (Mautner et al., 2014). Addition of trivalent salts, such as AlCl<sub>3</sub>, to the aqueous suspension induces the flocculation of nanofibrils by changing their surface charge. Specifically, trivalent cations are sorbed on the negatively charged nanofibrils surface, causing a decrease of the  $\zeta$ -potential (Mautner et al., 2014). Nanofibrils compaction leads to the formation of self-standing membranes that have shown organic solvents permeances up to 100 L/(h m<sup>2</sup> MPa) and retention of polystyrene close to 100%.

Interestingly, organic liquids (n-hexane, tetrahydrofuran) permeance was larger than that of water, irrespective of the hydrophilic behavior of nanocellulose (Mautner et al., 2014). The molecular origin of this behavior is still unknown, since permeability coefficients were not deconvoluted into their elemental sorption and diffusion contributions. Moreover, water permeance decreased from 47 to 5 L/(h m<sup>2</sup> MPa) after 1 h of operation (Mautner et al., 2014). The authors attributed this behavior to membrane compaction under pressure.

Interestingly, the average pore size is equal to the nanofibrils diameter, so the porosity of these membranes can be finely tuned

by changing the size of the cellulose nanofibrils (Mautner et al., 2014).

## CONCLUSIONS

Organic solvent nanofiltration is a new paradigm in the chemical industry. Despite it is intrinsically safe, energy efficient and scalable, OSN is today one of the most poorly understood processes at a fundamental level. Factors that limit its exploitation in the industry are:

- i) The lack of fundamental knowledge about solute and solvent transport mechanism. Moreover, the few elemental transport data available are often interpreted in a too simplistic way, which contributes to the spread of misleading conclusions in the literature.
- ii) The lack of materials capable to tolerate chemically challenging environments.

While recent research efforts contributed to address the latter point, fundamental understanding of OSN remains poor and incomplete. For example, diffusion coefficients in solvent swollen membranes have to be estimated carefully, by accounting for the effects of the frame of reference and thermodynamic non-idealities. Not taking into account these effects, hampers the possibility of developing structure-property correlations to be used for the rational design of OSN membranes.

The most important recent advances in OSN are the introduction of polymers and hybrid materials with improved permeability, selectivity, and long term stability. Polybenzimidazoles, PIMs, block copolymers with hard and soft segments, hybrid materials containing MOFs and ZIFs and membranes based on pre-assembled nanoparticles appear as the best candidates for future developments.

The most challenging application in the next decades will likely be the separation of isomers. Solving this problem will open a new era in chemical, petrochemical, food, and pharmaceutical industry. Joined efforts from polymer chemistry (to synthesize and modify materials) and physical chemistry (to understand and define optimal transport properties) are necessary to make such new era a reality.

## AUTHOR CONTRIBUTIONS

MG conceived and wrote the manuscript. KB contributed to select the contents, prepared the figures and run calculations.

## FUNDING

Financial support from the UROP Program sponsored by the University of Oklahoma is gratefully acknowledged.

## ACKNOWLEDGMENTS

MG wishes to dedicate this work to his mentor and friend, Prof. Donald R. Paul, with whom he worked for some years. His brilliant scholar inspired some of the ideas discussed in this paper.

## REFERENCES

- Abetz, V. (2014). Isoporous block copolymer membranes. *Macrom. Rapid Comm.* 36, 10–22. doi: 10.1002/marc.201400556
- Aburabie, J., and Peinemann, K. V. (2017). Crosslinked poly(ether block amide) composite membranes for organic solvent nanofiltration applications. *J. Membr. Sci.* 523, 264–272. doi: 10.1016/j.memsci.2016.09.027
- Ben Soltane, H., Roizard, D., and Favre, E. (2013). Effect of pressure on the swelling and fluxes of dense PDMS membranes in nanofiltration: an experimental study. *J. Membr. Sci.* 435, 110–119. doi: 10.1016/j.memsci.2013.01.053
- Ben Soltane, H., Roizard, D., and Favre, E. (2016). Study of the rejection of various solutes in OSN by a composite polydimethylsiloxane membrane: investigation of the role of the solute affinity. *Sep. Purif. Tech.* 161, 193–201. doi: 10.1016/j.seppur.2016.01.035
- Bernardo, P., Bazzarelli, F., Tasselli, F., Clarizia, G., Mason, C. R., Maynard-Atem, L., et al. (2017). Effect of physical aging on the gas transport and sorption in PIM-1 membranes. *Polymer* 113, 283–294. doi: 10.1016/j.polymer.2016.10.040
- Bird, R. B., Stewart, W. E., and Lightfoot, E. N. (1960). *Transport Phenomena*. New York, NY: John Wiley & Sons.
- Bondar, V. I., Freeman, B. D., and Pinnau, I. (1999). Gas sorption and characterization of poly(ether-b-amide) segmented block copolymers. *J. Polym. Sci. B* 37, 2463–2475.
- Bondar, V. I., Freeman, B. D., and Pinnau, I. (2000). Gas transport properties of poly(ether-b-amide) segmented block copolymers. *J. Polym. Sci. B38*, 2051–2062. doi: 10.1002/1099-0488(20000801)38:15<2051::AID-POLB100>3.0.CO;2-D
- Borjigin, H., Stevens, K. A., Liu, R., Moon, J. D., Shaver, A. T., Swinnea, S., et al. (2015). Synthesis and characterization of polybenzimidazoles derived from tetraaminodiphenylsulfone for high temperature gas separation membranes. *Polymer* 71, 135–142. doi: 10.1016/j.polymer.2015.06.021
- Budd, P. M., Ghanem, B. S., Makhseed, S., McKeown, N. B., Msayib, K. J., and Tattershall, C. E. (2004). Polymers of intrinsic microporosity (PIMs): robust, solution-processable, organic nanoporous materials. *Chem. Commun.* 230–231. doi: 10.1039/b311764b
- Buonomenna, M. G., and Bae, J. (2015). Organic solvent nanofiltration in pharmaceutical industry. *Sep. Purif. Rev.* 44, 157–182. doi: 10.1080/15422119.2014.918884
- Chau, J., Basak, P., Kaur, J., Hu, Y., and Sirkar, K. K. (2018). Performance of a composite membrane of a perfluorodioxole copolymer in organic solvent nanofiltration. *Sep. Purif. Tech.* 199, 233–241. doi: 10.1016/j.seppur.2018.01.054
- Chiou, J. S., Barlow, J. W., and Paul, D. R. (1985). Plasticization of glassy polymers by CO<sub>2</sub>. *J. Appl. Polym. Sci.* 30, 2633–2342. doi: 10.1002/app.1985.070300626
- Cocchi, G., De Angelis, M. G., and Doghieri, F. (2015a). Solubility and diffusivity of liquids for food and pharmaceutical applications in crosslinked polydimethylsiloxane (PDMS) films: I. Experimental data on pure organic components and vegetable oil. *J. Membr. Sci.* 492, 600–611. doi: 10.1016/j.memsci.2015.04.063
- Cocchi, G., De Angelis, M. G., and Doghieri, F. (2015b). Solubility and diffusivity of liquids for food and pharmaceutical applications in crosslinked polydimethylsiloxane (PDMS) films: I. Experimental data on mixtures. *J. Membr. Sci.* 492, 612–619. doi: 10.1016/j.memsci.2015.04.062
- Cook, M., Gaffney, P. R. J., Peeva, L. G., and Livingston, A. G. (2018). Roll-to-roll dip coating of three different PIMs for organic solvent nanofiltration. *J. Membr. Sci.* 558, 52–63. doi: 10.1016/j.memsci.2018.04.046
- Da Silva Bural, J., Peeva, L., Kumbharkar, S., and Livingston, A. G. (2015). Organic solvent resistant poly(ether-ether-ketone) nanofiltration membranes. *J. Membr. Sci.* 479, 105–116. doi: 10.1016/j.memsci.2014.12.035
- Da Silva Bural, J., Peeva, L., and Livingston, A. G. (2017). Negligible ageing in poly(ether-ether-ketone) membranes widens application range for solvent processing. *J. Membr. Sci.* 525, 48–56. doi: 10.1016/j.memsci.2016.10.015
- Daniel, M. C., and Astruc, D. (2004). Gold nanoparticles: assembly, supramolecular chemistry, quantum-size-related properties, and applications toward biology, catalysis, and nanotechnology. *Chem. Rev.* 104, 293–346. doi: 10.1021/cr030698+
- Darvishmanesh, S., Degreve, J., and Van der Bruggen, B. (2010). Mechanisms of solute rejection in solvent resistant nanofiltration: the effect of solvent on solute rejection. *Phys. Chem. Chem. Phys.* 12, 13333–13342. doi: 10.1039/c0cp00230e
- de Morais Coutinho, C., Chiu, M. C., Correa Basso, R., Badan Ribeiro, A. P., Guaraldo Gonçalves, L. A., and Viotto, L. A. (2009). State of art of the application of membrane technology to vegetable oils: a review. *Food Res. Int.* 42, 536–550. doi: 10.1016/j.foodres.2009.02.010
- Dinh, S. M., Berner, B., Sun, Y. M., and Lee, P. I. (1992). Sorption and transport of ethanol and water in poly(ethylene-co-vinyl-acetate) membranes. *J. Membr. Sci.* 69, 223–234. doi: 10.1016/0376-7388(92)80041-H
- Doghieri, F., and Sarti, G. C. (1996). Nonequilibrium lattice fluids: a predictive model for the solubility in glassy polymers. *Macromolecules* 29, 7885–7896.
- Doghieri, F., and Sarti, G. C. (1997). Solubility, diffusivity, and mobility of n-pentane and ethanol in poly(1-trimethylsilyl-1-propyne). *J. Polym. Sci. B* 35, 2245–2258.
- Dubbeldam, D., Krishna, R., Calero, S., and Yazydin, A. O. (2012). Computer-assisted screening of ordered crystalline nanoporous adsorbents for separation of alkane isomers. *Angew. Chem. Int. Ed.* 51, 11867–11871. doi: 10.1002/anie.201205040
- Fang, Y., Sourirajan, S., and Matsuura, T. (1992). Reverse osmosis separation of binary organic mixtures using cellulose acetate butyrate and aromatic polyamide membranes. *J. Appl. Polym. Sci.* 44, 1959–1969. doi: 10.1002/app.1992.070441111
- Favre, E., Schaezel, P., Nguyen, Q. T., Clement, R., and Neel, J. (1994). Sorption, diffusion and vapor permeation of various penetrants through dense poly(dimethylsiloxane) membranes: a transport analysis. *J. Membr. Sci.* 92, 169–184. doi: 10.1016/0376-7388(94)00060-3
- Flory, P. J. (1942). Thermodynamics of high polymer solutions. *J. Chem. Phys.* 10, 51–61. doi: 10.1063/1.1723621
- Freeman, B. D. (1999). Basis of Permeability/Selectivity Tradeoff Relations in Polymeric Gas Separation Membranes. *Macromolecules* 32, 375–380. doi: 10.1021/ma9814548
- Fritsch, D., Merten, P., Heinrich, K., Lazar, M., and Priske, M. (2012). High performance organic solvent nanofiltration membranes: development and thorough testing of thin film composite membranes made of polymers of intrinsic microporosity (PIMs). *J. Membr. Sci.* 401–402, 222–231. doi: 10.1016/j.memsci.2012.02.008
- Galizia, M., Chi, W. S., Smith, Z. P., Merkel, T. C., Baker, R. W., and Freeman, B. D. (2017a). 50th Anniversary perspective: polymers and mixed matrix membranes for gas and vapor separation: a review and prospective opportunities. *Macromolecules* 50, 7809–7843. doi: 10.1021/acs.macromol.7b01718
- Galizia, M., De Angelis, M. G., Messori, M., and Sarti, G. C. (2014). Mass transport in hybrid PTMSP/silica membranes. *Ind. Eng. Chem. Res.* 53, 9243–9255. doi: 10.1021/ie4035225
- Galizia, M., De Angelis, M. G., and Sarti, G. C. (2011). Sorption and transport of hydrocarbons and alcohols in addition-type poly(trimethyl silyl norbornene). I: Experimental data. *J. Membr. Sci.* 385–386, 141–153. doi: 10.1016/j.memsci.2011.09.032
- Galizia, M., De Angelis, M. G., and Sarti, G. C. (2012). Sorption of hydrocarbons and alcohols in addition-type poly(trimethyl silyl norbornene) and other high free volume glassy polymers. II: NELF model predictions. *J. Membr. Sci.* 405–406, 201–211. doi: 10.1016/j.memsci.2012.03.009
- Galizia, M., Paul, D. R., and Freeman, B. D. (2016). Liquid methanol sorption, diffusion and permeation in charged and uncharged polymers. *Polymer* 102, 281–291. doi: 10.1016/j.polymer.2016.09.010
- Galizia, M., Stevens, K. A., Paul, D. R., and Freeman, B. D. (2017b). Modeling gas permeability and diffusivity in HAB-6FDA polyimide and its thermally rearranged analogs. *J. Membr. Sci.* 537, 83–92. doi: 10.1016/j.memsci.2017.05.015
- Gao, L., Alberto, M., Gorgojo, P., Szekeley, G., and Budd, P. M. (2017). High flux PIM-1/PVDF thin film composite membranes for 1-butanol/water pervaporation. *J. Membr. Sci.* 529, 207–214. doi: 10.1016/j.memsci.2017.02.008
- Ghanem, B. S., McKeown, N. B., Budd, P. M., and Fritsch, D. (2008). Polymers of intrinsic microporosity derived from bis(phenazyl) monomers. *Macromolecules* 41, 1640–1646. doi: 10.1021/ma071846r
- Gorgojo, P., Karan, S., Wong, H. C., Jimenez-Salomon, M. F., Cabral, J. T., and Livingston, A. G. (2014). Ultrathin polymer films with intrinsic microporosity: anomalous solvent permeation and high flux membranes. *Adv. Func. Mater.* 24, 4729–4737. doi: 10.1002/adfm.201400400
- Grekhov, A., Belogorlov, A., Yushkin, A., and Volkov, A. (2012). New express dynamic technique for liquid permeation measurement in a wide

- range of transe-membrane pressures. *J. Membr. Sci.* 390–391, 160–163. doi: 10.1016/j.memsci.2011.11.038
- Haupt, K., and Mosbach, K. (2000). Molecularly imprinted polymers and their use in biomimetic sensors. *Chem. Rev.* 100, 2495–2504. doi: 10.1021/cr990099w
- Huang, Y., and Paul, D. R. (2004). Physical aging of thin glassy polymer films monitored by gas permeability. *Polymer* 45, 8377–8393. doi: 10.1016/j.polymer.2004.10.019
- Huang, Y., and Paul, D. R. (2006). Physical aging of thin glassy polymer films: free volume interpretation. *J. Membr. Sci.* 277, 219–229. doi: 10.1016/j.memsci.2005.10.032
- Huang, Y. J., Li, D., He, P., Sun, C. Y., Wang, M. J., and Li, J. H. (2005). Semipermeable membrane embodying noble metal nanoparticles and its electrochemical behaviors. *J. Electroanal. Chem.* 579, 277–282. doi: 10.1016/j.jelechem.2005.02.020
- Jimenez-Salomon, M. F., Song, Q., Jelfs, K. E., Munoz-Ibanes, M., and Livingston, A. G. (2016). Polymer nanofilms with enhanced microporosity by interfacial polymerization. *Nat. Mater.* 15, 760–767. doi: 10.1038/nmat4638
- Kamaruddin, H. D., and Koros, W. J. (1997). Some observations about the application of the Fick's first law for membrane separation of multicomponent mixtures. *J. Membr. Sci.* 135, 147–159.
- Kelman, S. D., Matteucci, S., Bielawski, C. W., and Freeman, B. D. (2007). Crosslinking poly(1-trimethylsilyl-1-propyne) and its effect on solvent resistance and transport properties. *Polymer* 48, 6881–6892. doi: 10.1016/j.polymer.2007.08.063
- Kim, J. F., Gaffney, P. R. J., Valtcheva, I. B., Williams, G., Buswell, A. M., Anson, M. S., et al. (2016). Organic solvent nanofiltration (OSN): a new technology platform for liquid-phase oligonucleotide synthesis (LPOS). *Org. Proc. Res. Dev.* 20, 1439–1452. doi: 10.1021/acs.oprd.6b00139
- Klemm, D., Kramer, F., Moritz, S., Lindstroem, T., Ankerfors, M., Gray, D., et al. (2011). Nanocelluloses: a new family of nature-based materials. *Angew. Chem. Int. Ed.* 50, 5438–5466. doi: 10.1002/anie.201001273
- Koh, D. Y., McCool, B. A., Deckman, H. W., and Lively, R. P. (2016). Reverse osmosis molecular differentiation of organic liquids using carbon molecular sieve membranes. *Science* 353, 804–807. doi: 10.1126/science.aaf1343
- Koike, S., Subramanian, R., Nabetani, H., and Nakajima, M. (2002). Separation of oil constituents in organic solvents using polymeric membranes. *J. Am. Oil Chem. Soc.* 79, 937–942. doi: 10.1007/s11746-002-0582-7
- Kopecek, J. (1970). Performance of porous cellulose acetate membranes for the reverse osmosis separation of mixtures of organic liquids. *Ind. Eng. Chem. Proc. Des. Dev.* 9, 5–12. doi: 10.1021/i260033a002
- Koros, W. J., Paul, D. R., and Rocha, A. A. (1976). Carbon dioxide sorption and transport in polycarbonate. *J. Polym. Sci.: Polym. Phys. Ed.* 14, 687–702. doi: 10.1002/pol.1976.180140410
- Koros, W. J., and Zhang, C. (2017). Materials for next generation molecularly selective synthetic membranes. *Nature Mat.* 16, 289–297. doi: 10.1038/nmat4805
- Krishna, R., and van Baten, J. M. (2017). Screening metal-organic frameworks for separation of pentane isomers. *Phys. Chem. Chem. Phys.* 19, 8380–8387. doi: 10.1039/C7CP00586E
- Lau, C. H., Nguyen, P. T., Hill, M. R., Thornton, A. W., Konstant, K., Doherty, C. M., et al. (2014). Ending aging in super glassy polymer membranes. *Angew. Chem.* 53, 5322–5326. doi: 10.1002/anie.201402234
- Li, K. (2007). *Ceramic Membranes for Separation and Reaction*. Chichester: John Wiley & Sons.
- Liang, P., Xu, J., and Li, Q. (2008). Application of dispersive liquid-liquid microextraction and high performance liquid chromatography for the determination of three phthalate esters in water samples. *Anal. Chim. Acta* 609, 53–58. doi: 10.1016/j.aca.2007.12.025
- Liu, Y., Wang, R., and Chung, T. S. (2001). Chemical cross-linking modification of polyimide membranes for gas separation. *J. Membr. Sci.* 189, 231–239. doi: 10.1016/S0376-7388(01)00415-X
- Lively, R. P., and Sholl, D. S. (2017). From water to organics on membrane separations. *Nature Mat.* 16, 276–279. doi: 10.1038/nmat4860
- Loeb, S., and Sourirajan, S. (1963). "Sea water demineralization by means of an osmotic membrane," in *Advances in Chemistry Series*, ed R. F. Gould (Washington, DC: ACS), 117–132.
- Lotters, J. C., Olthuis, W., Veltink, P. H., and Bergveld, P. (1997). The mechanical properties of the rubber elastic polymer polydimethylsiloxane for sensor applications. *J. Micromech. Microeng.* 7, 145–147. doi: 10.1088/0960-1317/7/3/017
- Luna-Triguero, A., Gomez-Alvarez, P., and Calero, S. (2017). Adsorptive process design for the separation of hexane isomers using zeolites. *Phys. Chem. Chem. Phys.* 19, 5037–5042. doi: 10.1039/C6CP08025A
- Luo, S., Wiegand, J. R., Kazanowska, B., Doherty, C. M., Konstant, K., Hill, A. J., et al. (2016). Finely tuning the free volume architecture in iptycene-containing polyimides for highly selective and fast hydrogen transport. *Macromolecules* 49, 3395–3405. doi: 10.1021/acs.macromol.6b00485
- Luo, S., Zhang, Q., Zhu, L., Lin, H., Kazanowska, B. A., Doherty, C. M., et al. (2018). Highly selective and permeable microporous polymer membranes for hydrogen purification and CO<sub>2</sub> removal from natural gas. *Chem. Mater.* 30, 5322–5332. doi: 10.1021/acs.chemmater.8b02102
- Lv, D., Wang, H., Chen, Y., Xu, F., Shi, R., Liu, Z., et al. (2018). Iron-based metal-organic framework with hydrophobic quadrilateral channels for highly selective separation of hexane isomers. *ACS Appl. Mater. Interfaces* 10, 6031–6038. doi: 10.1021/acsami.7b18620
- Ma, H., Jen, A. K. Y., and Dalton, L. R. (2002). Polymer-based optical waveguides: materials, processing, and devices. *Adv. Mater.* 14, 1339–1365. doi: 10.1002/1521-4095(20021002)14:19<1339::AID-ADMA1339>3.0.CO;2-O
- Machado, D. R., Hasson, D., and Semiat, R. (1999). Effect of solvent properties on permeate flow through nanofiltration membranes. Part I: investigation of parameters affecting solvent flux. *J. Membr. Sci.* 163, 93–102. doi: 10.1016/S0376-7388(99)00158-1
- Marchetti, P., Jimenez Salomon, M. F., Szekeley, G., and Livingston, A. G. (2014). Molecular separation with organic solvent nanofiltration: a critical review. *Chem. Rev.* 114, 10735–10806. doi: 10.1021/cr500006j
- Marchetti, P., and Livingston, A. G. (2015). Predictive membrane transport models for organic solvent nanofiltration: how complex do we need to be? *J. Membr. Sci.* 476, 530–553. doi: 10.1016/j.memsci.2014.10.030
- Marchetti, P., Peeva, L., and Livingston, A. G. (2017). The selectivity challenge in organic solvent nanofiltration: membrane and process solutions. *Ann. Rev. Chem. Biomol. Eng.* 8, 473–497. doi: 10.1146/annurev-chembioeng-060816-101325
- Mautner, A., Lee, K. Y., Lahtinen, P., Hakalahti, M., Tammelin, T., Li, K., et al. (2014). Nanopapers for organic solvent nanofiltration. *Chem. Comm.* 50, 5778–5781. doi: 10.1039/C4CC00467A
- Merkel, T. C., Bondar, V., Nagai, K., and Freeman, B. D. (2000). Sorption and transport of hydrocarbon and perfluorocarbon gases in poly(1-trimethylsilyl-1-propyne). *J. Polym. Sci. B: Polym. Phys.* 38, 273–296. doi: 10.1002/(SICI)1099-0488(20000115)38:2<273::AID-POLB1>3.0.CO;2-X
- Nagai, K., Freeman, B. D., and Hill, A. J. (2000). Effect of physical aging of poly(1-trimethylsilyl-1-propyne) films synthesized with TaCl<sub>5</sub> and NbCl<sub>5</sub> on gas permeability, fractional free volume, and positron annihilation lifetime spectroscopy parameters. *J. Polym. Sci. B: Polym. Phys.* 38, 1222–1239. doi: 10.1002/(SICI)1099-0488(20000501)38:9<1222::AID-POLB14>3.0.CO;2-P
- Naguib, M., Mochalin, V. M., Barsoum, M. W., and Gogotsi, Y. (2014). 25th anniversary article: MXenes: a new family of two-dimensional materials. *Adv. Mater.* 26, 992–1005. doi: 10.1002/adma.201304138
- Nakai, Y., Tsujita, Y., and Yoshimizu, H. (2002). Control of gas permeability for cellulose acetate membrane by microwave irradiation. *Desalination* 145, 375–377. doi: 10.1016/S0011-9164(02)00439-3
- Ogieglo, W., Rahimi, K., Rauer, S. B., Ghanem, B., Ma, H., Pinnau, I., et al. (2017). How do organic vapors swell ultrathin films of polymer of intrinsic microporosity PIM-1? *J. Phys. Chem. B* 121, 7210–7220. doi: 10.1021/acs.jpcc.7b03891
- Paul, D. R. (1973). Relation between hydraulic permeability and diffusion in homogeneous swollen membranes. *J. Polym. Sci.* 2, 289–296.
- Paul, D. R. (1976). The solution-diffusion model for swollen membranes. *Sep. Purif. Methods* 5, 33–50. doi: 10.1080/03602547608066047
- Paul, D. R. (2004). Reformulation of the solution-diffusion theory of reverse osmosis. *J. Membr. Sci.* 241, 371–386. doi: 10.1016/j.memsci.2004.05.026
- Paul, D. R., and Ebra-Lima, O. M. (1970). Pressure-induced diffusion of organic liquids through highly swollen polymer membranes. *J. Appl. Polym. Sci.* 14, 2201–2224. doi: 10.1002/app.1970.070140903
- Paul, D. R., and Ebra-Lima, O. M. (1971). The mechanism of liquid transport through swollen polymer membranes. *J. Appl. Polym. Sci.* 15, 2199–2210. doi: 10.1002/app.1971.070150912



- Peeva, L. G., Gibbins, E., Luthra, S. S., White, L. S., Stateva, R. P., and Livingston, A. G. (2004). Effects of concentration polarization and osmotic pressure on flux in organic solvent nanofiltration. *J. Membr. Sci.* 236, 121–136. doi: 10.1016/j.memsci.2004.03.004
- Postel, S., Spalding, G., Chirnside, M., and Wessling, M. (2013). On negative retentions in organic solvent nanofiltration. *J. Membr. Sci.* 447, 57–65. doi: 10.1016/j.memsci.2013.06.009
- Priske, M., Lazar, M., Schnitzer, C., and Baumgarten, G. (2016). Recent applications of organic solvent nanofiltration. *Chem. Ing. Tech.* 88, 39–49. doi: 10.1002/cite.201500084
- Robeson, L. M. (1991). Correlation of separation factor versus permeability for polymeric membranes. *J. Membr. Sci.* 62, 165–185. doi: 10.1016/0376-7388(91)80060-J
- Robeson, L. M. (2008). The upper bound revisited. *J. Membr. Sci.* 320, 390–400. doi: 10.1016/j.memsci.2008.04.030
- Sanders, D. F., Smith, Z. P., Guo, R., Robeson, L. M., McGrath, J. E., Paul, D. R., et al. (2013). Energy-efficient polymeric gas separation membranes for a sustainable future: a review. *Polymer* 54, 4729–4761. doi: 10.1016/j.polymer.2013.05.075
- Schild, H. G. (1992). Poly (N-isopropylacrylamide): experiments, theory and application. *Progr. Polym. Sci.* 17, 163–249. doi: 10.1016/0079-6700(92)90023-R
- See-Toh, Y. H., Ferreira, F. C., and Livingston, A. G. (2007a). The influence of membrane formation parameters on the functional performance of organic solvent nanofiltration membranes. *J. Membr. Sci.* 299, 236–250. doi: 10.1016/j.memsci.2007.04.047
- See-Toh, Y. H., Lim, F. W., and Livingston, A. G. (2007b). Polymeric membranes for nanofiltration in polar aprotic solvents. *J. Membr. Sci.* 301, 3–10. doi: 10.1016/j.memsci.2007.06.034
- See-Toh, Y. H., Silva, M., and Livingston, A. G. (2008). Controlling molecular weight cut off curves for highly solvent stable organic solvent nanofiltration (OSN) membranes. *J. Membr. Sci.* 324, 220–232. doi: 10.1016/j.memsci.2008.07.023
- Sheth, J. P., Qin, Y., Sirkar, K. K., and Baltzis, B. C. (2003). Nanofiltration-based diafiltration process for solvent exchange in pharmaceutical manufacturing. *J. Membr. Sci.* 211, 251–261. doi: 10.1016/S0376-7388(02)00423-4
- Siddique, H., Peeva, L. G., Stoikos, K., Pasparkis, G., Vamvakaki, M., and Livingston, A. G. (2011). Membranes for organic solvent nanofiltration based on preassembled nanoparticles. *Ind. Eng. Chem. Res.* 52, 1109–1121. doi: 10.1021/ie202999b
- Silva, P., Han, S., and Livingston, A. G. (2005). Solvent transport in organic solvent nanofiltration membranes. *J. Membr. Sci.* 262, 49–59. doi: 10.1016/j.memsci.2005.03.052
- Singh, A., Freeman, B. D., and Pinnau, I. (1998). Pure and mixed gas acetone/nitrogen permeation properties of polydimethylsiloxane [PDMS]. *J. Polym. Sci. B* 36, 289–301. doi: 10.1002/(SICI)1099-0488(19980130)36:2<289::AID-POLB8>3.0.CO;2-M
- Singh, A., and Koros, W. J. (1996). Significance of entropic selectivity for advanced gas separation membranes. *Ind. Eng. Chem. Res.* 35, 1231–1234. doi: 10.1021/ie950559l
- Sourirajan, S. (1964). Separation of hydrocarbon liquids by flow under pressure through porous membranes. *Nature* 203, 1348–1349. doi: 10.1038/2031348a0
- Subramanian, R., Raghavarao, K. S. M. S., Nabetani, H., Nagajima, M., Kimura, T., and Maekawa, T. (2001). Differential permeation of oil constituents in nonporous denser polymeric membranes. *J. Membr. Sci.* 187, 59–69. doi: 10.1016/S0376-7388(00)00673-6
- Subramanian, R., Raghavarao, K. S. M. S., Nakajima, M., Nabetani, H., Yamaguchi, T., and Kimura, T. (2003). Application of dense membrane theory for differential permeation of vegetable oil constituents. *J. Food Eng.* 60, 249–256. doi: 10.1016/S0260-8774(03)00045-1
- Sukma, F. M., and Culfaz-Emecen, P. Z. (2018). Cellulose membranes for organic solvent nanofiltration. *J. Membr. Sci.* 545, 329–336. doi: 10.1016/j.memsci.2017.09.080
- Szekely, G., Jimenez-Salomon, M. F., Marchetti, P., Kim, J. F., and Livingston, A. G. (2014). Sustainability assessment of organic solvent nanofiltration: from fabrication to application. *Green Chem.* 16, 4440–4473. doi: 10.1039/C4GC00701H
- Tanaka, K., Matsuya, H., Masuda, T., and Higashimura, T. (1985). Gas permeability of polyacetylenes carrying substituents. *J. Appl. Polym. Sci.* 30, 1605–1616. doi: 10.1002/app.1985.070300426
- Tsarkov, S., Khotimskiy, V., Budd, P. M., Volkov, V., Kukushkina, J., and Volkov, A. (2012). Solvent nanofiltration through high permeability glassy polymers: effect of polymer and solute nature. *J. Membr. Sci.* 423–424, 65–72. doi: 10.1016/j.memsci.2012.07.026
- Ulbricht, M. (2006). Advanced functional polymer membranes. *Polymer* 47, 2217–2262. doi: 10.1016/j.polymer.2006.01.084
- Valtcheva, I. B., Kumbharkar, S. C., Kim, J. F., Bhole, Y., and Livingston, A. G. (2014). Beyond polyimide: crosslinked polybenzimidazole membranes for organic solvent nanofiltration (OSN) in harsh environments. *J. Membr. Sci.* 457, 62–72. doi: 10.1016/j.memsci.2013.12.069
- Valtcheva, I. B., Marchetti, P., and Livingston, A. G. (2015). Crosslinked polybenzimidazole membranes for organic solvent nanofiltration (OSN): Analysis of crosslinking reaction mechanism and effects of reaction parameters. *J. Membr. Sci.* 493, 568–579. doi: 10.1016/j.memsci.2015.06.056
- Van der Bruggen, B. (2013). Integrated membrane separation processes for recycling of valuable wastewater streams: nanofiltration, membrane distillation, and membrane crystallizers revisited. *Ind. Eng. Chem. Res.* 52, 10335–10341. doi: 10.1021/ie302880a
- Vanherck, K., Hermans, S., Verbiest, T., and Vankelecom, I. (2011). Using the photothermal effect to improve membrane separations via localized heating. *J. Mater. Chem.* 21, 6079–6087. doi: 10.1039/c0jm03932b
- Vanherck, K., Koeckelberghs, G., and Vankelecom, I. F. J. (2013). Crosslinking polyimides for membrane application: a review. *Progr. Polym. Sci.* 38, 874–896. doi: 10.1016/j.progpolymsci.2012.11.001
- Vankelecom, I. F. J., De Beukelaer, S., and Uytterhoeven, J. B. (1997). Sorption and pervaporation of aroma compounds using zeolite-filled PDMS membranes. *J. Phys. Chem. B* 101, 5186–5190. doi: 10.1021/jp962273f
- Vankelecom, I. F. J., De Smet, K., Gevers, L. E. M., Livingston, A. G., Nair, D., Aerts, S., et al. (2004). Physio-chemical interpretation of the SRNF transport mechanism for solvents through dense silicone membranes. *J. Membr. Sci.* 231, 99–108. doi: 10.1016/j.memsci.2003.11.007
- Vogel, H., and Marvel, C. S. (1961). Polybenzimidazoles, new thermally stable polymers. *J. Polym. Sci.* 50, 511–539. doi: 10.1002/pol.1961.1205015419
- Volkov, A., Yushkin, A., Grekhov, A., Shutova, A., Bazhenov, S., Tsarkov, S., et al. (2013). Liquid permeation through PTMSP: One polymer for two different membrane applications. *J. Membr. Sci.* 440, 98–107. doi: 10.1016/j.memsci.2013.03.067
- Volkov, A., Yushkin, A., Kachula, Y., Khotimskiy, V., and Volkov, V. (2014). Application of negative retention in organic solvent nanofiltration for solutes fractionation. *Sep. Purif. Tech.* 124, 43–48. doi: 10.1016/j.seppur.2013.12.044
- Volkov, A. V., Stamatiadis, D. F., Khotimsky, V. S., Volkov, V. V., Wessling, M., and Plate, N. A. (1996). Poly[1-(trimethylsilyl)-1-propyne] as a solvent resistance nanofiltration membrane material. *J. Membr. Sci.* 281, 351–357. doi: 10.1016/j.memsci.2006.04.004
- Volkov, A. V., Tsarkov, S. E., Gilman, A. B., Khotimskiy, S. V., Roldughin, V., and Volkov, V. V. (2015). Surface modification of PTMSP membranes by plasma treatment: asymmetry of transport in organic solvent nanofiltration. *Adv. Coll. Interf. Sci.* 222, 716–727. doi: 10.1016/j.cis.2014.11.005
- Wang, H., Chung, T. S., and Paul, D. R. (2014). Physical aging and plasticization of thick and thin films of the thermally rearranged ortho-functional polyimide 6FDA-HAB. *J. Membr. Sci.* 458, 27–35. doi: 10.1016/j.memsci.2014.01.066
- Weidman, J. R., and Guo, R. (2017). The use of iptycenes in rational macromolecular design for gas separation membrane applications. *Ind. Eng. Chem. Res.* 56, 4220–4236. doi: 10.1021/acs.iecr.7b00540
- Weidman, J. R., Luo, S., Zhang, Q., and Guo, R. (2017). Structure manipulation in triptycene-based polyimides through main chain geometry variation and its effect on gas transport properties. *Ind. Eng. Chem. Res.* 56, 1868–1879. doi: 10.1021/acs.iecr.6b04946
- Weng, X., Baez, J. E., Khiterer, M., Hoe, M. Y., Bao, Z., and Shea, K. J. (2015). Chiral polymers of intrinsic microporosity: selective membrane permeation of enantiomers. *Angew. Chem. Int. Ed.* 54, 11214–11218. doi: 10.1002/anie.201504934
- White, L. S. (2001). *Polyimide Membranes for Hyperfiltration Recovery of Aromatic Solvents*. US patent 6.180.008.
- White, L. S. (2002). Transport properties of a polyimide solvent resistant nanofiltration membrane. *J. Membr. Sci.* 205, 191–202. doi: 10.1016/S0376-7388(02)00115-1



- White, L. S. (2006). Development of large-scale applications in organic solvent nanofiltration and pervaporation for chemical and refining processes. *J. Membr. Sci.* 286, 26–35. doi: 10.1016/j.memsci.2006.09.006
- White, M. L. (1960). The permeability of an acrylamide polymer gel. *J. Phys. Chem.* 64, 1563–1565. doi: 10.1021/j100839a055
- Whu, J. A., Baltzis, B. C., and Sirkar, K. K. (2000). Nanofiltration studies of larger organic microsolute in methanol solutions. *J. Membr. Sci.* 170, 159–172. doi: 10.1016/S0376-7388(99)00374-9
- Wijmans, J. G., and Baker, R. W. (1995). The solution-diffusion model: a review. *J. Membr. Sci.* 107, 1–21. doi: 10.1016/0376-7388(95)00102-I
- Wu, X., Hao, L., Zhang, J., Zhang, X., Wang, J., and Liu, J. (2016). Polymer-Ti<sub>3</sub>C<sub>2</sub>T<sub>x</sub> composite membranes to overcome the trade-off in solvent resistant nanofiltration for alcohol-based system. *J. Membr. Sci.* 515, 175–188. doi: 10.1016/j.memsci.2016.05.048
- Yu, H., Qiu, X., Nunes, S. P., and Peinemann, K. V. (2014). Self-assembled isoporous block copolymer membranes with tuned pore sizes. *Angew. Chem. Int. Ed.* 53, 10072–10076. doi: 10.1002/anie.20140449

**Conflict of Interest Statement:** The authors declare that the research was conducted in the absence of any commercial or financial relationships that could be construed as a potential conflict of interest.

Copyright © 2018 Galizia and Bye. This is an open-access article distributed under the terms of the Creative Commons Attribution License (CC BY). The use, distribution or reproduction in other forums is permitted, provided the original author(s) and the copyright owner(s) are credited and that the original publication in this journal is cited, in accordance with accepted academic practice. No use, distribution or reproduction is permitted which does not comply with these terms.



# Chitosan Grafted With $\beta$ -Cyclodextrin: Synthesis, Characterization, Antimicrobial Activity, and Role as Absorbefacient and Solubilizer

Wen-Ya Ding<sup>1,2,3†</sup>, Si-Di Zheng<sup>1,2†</sup>, Yue Qin<sup>1,2</sup>, Fei Yu<sup>1,2</sup>, Jing-Wen Bai<sup>4</sup>, Wen-Qiang Cui<sup>1,2</sup>, Tao Yu<sup>1,2</sup>, Xing-Ru Chen<sup>1,2</sup>, God'spower Bello-Onaghise<sup>1,2</sup> and Yan-Hua Li<sup>1,2\*</sup>

<sup>1</sup> College of Veterinary Medicine, Northeast Agricultural University, Harbin, China, <sup>2</sup> Heilongjiang Key Laboratory for Animal Disease Control and Pharmaceutical Development, Harbin, China, <sup>3</sup> Northeastern Science Inspection Station, China Ministry of Agriculture Key Laboratory of Animal Pathogen Biology, Northeast Agricultural University, Harbin, China, <sup>4</sup> College of Science, Northeast Agricultural University, Harbin, China

## OPEN ACCESS

### Edited by:

Nikhil Kumar Singha,  
Indian Institute of Technology  
Kharagpur, India

### Reviewed by:

Yasuhiro Matsuda,  
Shizuoka University, Japan  
Erathimanna Bhoje Gowd,  
National Institute for Interdisciplinary  
Science and Technology (CSIR), India

### \*Correspondence:

Yan-Hua Li  
liyanhua1970@163.com

<sup>†</sup>These authors have contributed  
equally to this work and share first  
authorship

### Specialty section:

This article was submitted to  
Polymer Chemistry,  
a section of the journal  
Frontiers in Chemistry

Received: 01 August 2018

Accepted: 18 December 2018

Published: 10 January 2019

### Citation:

Ding W-Y, Zheng S-D, Qin Y, Yu F,  
Bai J-W, Cui W-Q, Yu T, Chen X-R,  
Bello-Onaghise G and Li Y-H (2019)  
Chitosan Grafted With  $\beta$ -Cyclodextrin:  
Synthesis, Characterization,  
Antimicrobial Activity, and Role as  
Absorbefacient and Solubilizer.  
Front. Chem. 6:657.  
doi: 10.3389/fchem.2018.00657

We synthesized chitosan grafted with  $\beta$ -cyclodextrin (CD-g-CS) from mono-6-deoxy-6-(p-toluenesulfonyl)- $\beta$ -cyclodextrin and chitosan. Two different amounts of immobilized  $\beta$ -cyclodextrin ( $\beta$ -CD) on CD-g-CS ( $Q_{CD}$ :  $0.643 \times 10^3$  and  $0.6 \times 10^2$   $\mu\text{mol/g}$ ) were investigated. The results showed that the amino contents of CD-g-CS with  $Q_{CD} = 0.643 \times 10^3$  and  $0.6 \times 10^2$   $\mu\text{mol/g}$  were  $6.34 \pm 0.072$  and  $9.41 \pm 0.055\%$ , respectively. Agar diffusion bioassay revealed that CD-g-CS ( $Q_{CD} = 0.6 \times 10^2$   $\mu\text{mol/g}$ ) was more active against *Staphylococcus xylosus* and *Escherichia coli* than CD-g-CS ( $Q_{CD} = 0.643 \times 10^3$   $\mu\text{mol/g}$ ). Cell membrane integrity tests and scanning electron microscopy observation revealed that the antimicrobial activity of CD-g-CS was attributed to membrane disruption and cell lysis. Uptake tests showed that CD-g-CS promoted the uptake of doxorubicin hydrochloride by *S. xylosus*, particularly for CD-g-CS with  $Q_{CD} = 0.6 \times 10^2$   $\mu\text{mol/g}$ , and the effect was concentration dependent. CD-g-CS ( $Q_{CD} = 0.6 \times 10^2$  and  $0.643 \times 10^3$   $\mu\text{mol/g}$ ) also improved the aqueous solubilities of sulfadiazine, sulfamonomethoxine, and sulfamethoxazole. These findings provide a clear understanding of CD-g-CS and are of great importance for reducing the dosage of antibiotics and antibiotic residues in animal-derived foods. The results also provide a reliable, direct, and scientific theoretical basis for its wide application in the livestock industry.

**Keywords:** chitosan grafted with  $\beta$ -cyclodextrin, antimicrobial activity, membrane integrity, uptake, solubility

## INTRODUCTION

As a natural weak cationic polysaccharide, chitosan (CS) is made up of randomly distributed  $\beta$ -1,4-linked D-glucosamine and N-acetyl-D-glucosamine (Song et al., 2017). The ubiquity, non-toxicity and biodegradability of CS (Li et al., 2016) has made it useful in various scientific fields for many years (Guo et al., 2016). The unique characteristics of CS have prompted investigators (Castro Domingues et al., 2012) to propose CS as an alternative adsorbent. CS is also reported to have some anti-inflammatory activity (Maeda and Kimura, 2004). As a slow-release drug carrier, CS

nanoparticles enhance the intestinal absorption of insulin (Pan et al., 2002). In addition, CS can inhibit the growth of pathogens as an antimicrobial agent (Badawy et al., 2014). CS was previously reported to significantly inhibit the growth of bacteria (No et al., 2002). CS and its derivatives have also been extensively studied as absorption enhancers. N-trimethyl CS chloride was reported to significantly increase the oral absorption of buserelin and octreotide (van der Merwe et al., 2004).

Cyclodextrins are cyclic oligosaccharides made up of different numbers of glucose molecules that are joined together by  $\alpha$ -1,4 bonds. Cyclodextrins are grouped into  $\alpha$ -,  $\beta$ -, and  $\gamma$ -cyclodextrins. The most popular and widely studied member of the group is the  $\beta$ -cyclodextrin ( $\beta$ -CD) because it is a common host molecule for a variety of aqueous species due its availability and ideal molecular size (Cho et al., 2014). Furthermore, the outer layer of  $\beta$ -CD is hydrophilic in nature, while the center cavity is hydrophobic. The hollow part of the central cavity is lipophilic in nature and can contain many hydrophobic guest molecules based on hydrophobic interactions. According to Szejtli (2004), the formation of inclusion complexes with cyclodextrins can significantly increase the aqueous solubility of poorly soluble drugs. A good example is the formation of cyclodextrin inclusion complexes with natamycin (Koontz and Marcy, 2003).

Bacterial infection is a major challenge in the livestock industry. Farmers depend on antibiotics to prevent and control bacteria-related infections, and antibiotics have thus played a major role in the development of the industry (Long et al., 1990). However, many factors limit the clinical application of antibiotics. For instance, the long-term or heavy use of antibiotics frequently causes bacterial resistance and results in antibiotic residues in animal-derived foods, which can harm human health (de Jong et al., 2018; Todorovic et al., 2018; Yan et al., 2018). In addition, some antibiotics that are difficult to dissolve in water cannot be used in practical applications because the most important physicochemical property of a drug is its ability to be dissolved in water, thus, compounds that are not soluble in water are hardly used as drugs (Hanaee et al., 2005). To improve the efficacy of antibiotics, reduce the antibiotic dosage, overcome bacterial resistance and increase the solubility of antibiotics, it is of great importance to develop an excipient that can inhibit bacteria, reduce antibiotic use, and increase the solubility of antibiotics in water. CS can be used as antimicrobial agent to inhibit bacterial growth (Badawy et al., 2014) and as an absorption enhancer to promote drug oral absorption (van der Merwe et al., 2004).  $\beta$ -CD can increase the aqueous solubility of poorly soluble drugs (Szejtli, 2004). Based on this, we hypothesize that chitosan grafted with  $\beta$ -cyclodextrin (CD-g-CS) will function as a unique excipient with double potency. However, there are few reports on the antibacterial activity of CD-g-CS. In addition, no one has reported the mechanism of the antibacterial activity of CD-g-CS or the effects of CD-g-CS on drug uptake and the solubilization of insoluble drugs. Most existing studies focused on the application of CD-g-CS as an adsorption agent (Sajomsang et al., 2012), scaffold for tissue engineering applications (Prabaharan and Jayakumar, 2009), and compound for controlled drug release (Chen et al., 2017).

Thus, the above properties of CD-g-CS were studied in this paper.

In this study, we used Fourier transform infrared spectroscopy (FT-IR) and  $^1\text{H}$  nuclear magnetic resonance spectroscopy ( $^1\text{H}$  NMR) to characterize the structure of CD-g-CS. Acid-base titration was used to determine the amino content of CD-g-CS. Thereafter, the antimicrobial activity of CD-g-CS was evaluated. At the same time, ultrastructural analysis and cell membrane integrity tests revealed the complex mechanism of CD-g-CS activity against *Escherichia coli* and *Staphylococcus xylosus*. To demonstrate the ability of CD-g-CS to promote drug uptake, an uptake test was conducted. We also investigated the effect of CD-g-CS on the solubilization of antibiotics that are difficult to dissolve in water. This study is of great importance for improving the efficacy of antibiotics, reducing the dosage of antibiotics, and reducing antibiotic residues in animal-derived foods. The findings related to CD-g-CS also provide new ideas for addressing bacterial resistance in the cultivation industry.

## MATERIALS AND METHODS

### Materials

Chitosan, having a molar mass of 150 kDa and a deacetylation degree (DD) of over 90%, was purchased from Beijing Biotopped Science & Technology Co. Ltd (China) while Sinopharm Chemical Reagent Co. Ltd (China) supplied the  $\beta$ -Cyclodextrin ( $\beta$ -CD). P-Toluenesulfonyl chloride was purchased from Shanghai Macklin Biochemical Co. Ltd (China). Sulfadiazine, sulfamonomethoxine, sulfamethoxazole, and doxorubicin hydrochloride were purchased from Shanghai Yuan Ye Biochemical Co. Ltd (China). Acetic acid, calcium, dimethyl sulfoxide (DMSO), acetone, methyl orange, and sulfuric acid were purchased from Tianjin Kermel Analytical Reagent Co. Ltd (China). Trypticase Soy broth (TSB) was purchased from Summus Ltd (China). Super Optimal broth with Catabolite repression (Soc Medium) was purchased from Sijiqing Ltd., (China).

### Preparation of Mono-6-Deoxy-6-(p-Toluenesulfonyl)- $\beta$ -Cyclodextrin (6-OTs- $\beta$ -CD)

$\beta$ -CD (2.5 g) was suspended in 6.5 mL of DMSO, and 3.75 g of p-toluenesulfonyl chloride in 6 mL of DMSO was added dropwise. The solution was stirred for 24 h at 45°C, and 30 mL of acetone was added by gradual droppings. The solution immediately crystallized, and a white precipitate was observed. This white precipitate was filtered, rinsed with precooled acetone. This procedure was repeated three times.

### Preparation of CD-g-CS

CD-g-CS was synthesized using a modified procedure derived from Gonil (Gonil et al., 2011). CS (0.25 g) was dissolved in 1% (v/v) acetic acid. The 6-OTs- $\beta$ -CD produced above was added into the CS/acetic acid solution. The set up was then stirred for 48 h at 45°C, and the solution was dialyzed for 7 d using deionized water. Finally, the solution was freeze-dried.

## Characterization of CD-g-CS

This procedure followed that of Gonil et al. (2011). The  $^1\text{H}$  NMR readings of the samples were recorded on a Bruker DPX300 spectrometer using tetramethylsilane as an internal standard and 1% DCl as a solvent at 25°C.

This procedure followed that of Zhu et al. (2006). The FT-IR scores of the products were recorded on a double-beam Mattson Galaxy Series FTIR-3000 spectrometer in the range of 4,000–600  $\text{cm}^{-1}$  using KBr pellets.

## Measurement of the Apparent Amount of $\beta$ -CD Immobilized Onto CS

The apparent amount of  $\beta$ -CDs immobilized on CS was determined using Yi's method (Yi et al., 2006) with slight modification. A standard curve was plotted in line with that of Yi et al. (2006) using the following procedure. We hydrolyzed 10 mg of CD-g-CS in 30 mL of sulfuric acid (0.5 mol/L) and stirred the solution for 10 h at 100°C. The resultant solution was poured into a measuring flask and diluted to 50 mL. A photospectrometer was used to determine the glucose content of the solution at a wavelength of 490 nm. The apparent amount of immobilized  $\beta$ -CD ( $Q_{\text{CD}}$ ) was calculated using Equation (1):

$$Q_{\text{CD}} = \frac{C \times 50 \times 1000}{180 \times 7 \times W} \quad (1)$$

where  $C$  is the concentration of glucose ( $\mu\text{g/mL}$ ),  $W$  is the weight of CD-g-CS (mg), 50 is the final volume of CD-g-CS hydrolysate, 1,000 is the conversion factor that is used to convert CD-g-CS from mg to g ( $1 \text{ mg} = 10^{-3} \text{ g}$ ), 180 is the molecular weight of glucose, and 7 is the number of units containing glucose groups in  $\beta$ -CD.

## Determination of the Amino Content of CD-g-CS

The amino content of CD-g-CS was determined as described by Hamdi et al. (2018) with a few modifications. CD-g-CS (30 mg) was dissolved in 5 mL of HCl (0.1 mol/L). The dissolution time was 1 h, and the setup was kept at room temperature. Methyl orange served as an indicator for the titration experiment. The acid was titrated against NaOH (0.1 mol/L). A sharp change in color change (from red to yellow) indicated the end point of the titration. This color change was followed by the appearance of suspended solutes in the solution. The volume of NaOH used and recorded. The amino content of CD-g-CS was calculated using the following Equation (2):

$$\text{NH}_2\% = \frac{(C_1 V_1 - C_2 V_2) \times 0.016}{G} \times 100\% \quad (2)$$

where 0.016 is the amount of amino acid equivalent to 1 mol/L HCl,  $V_1$  and  $V_2$  are the volumes (mL) of HCl and NaOH solutions used, respectively;  $C_1$  and  $C_2$  are the concentrations (mol/L) of HCl and NaOH, respectively; and  $G$  is the weight of CD-g-CS (g).

## Antimicrobial Assessments

### Bacterial Strains and Growth Conditions

The culturing of bacteria was done in line with the procedure described in Yang et al. (2015) with a few modifications. *S. xyloso* ATCC 700404 and *E. coli* ATCC 25922 were grown in TSB and SOC, respectively. All strains were subjected to aerobic incubation at 37°C for 16 h. The incubated strains were again subcultured under the same conditions. Cultured *S. xyloso* and *E. coli* were grown on TSB and SOC agar, respectively, and incubated at 37°C. Overnight cultures of *S. xyloso* and *E. coli* were diluted in sterile saline to produce a solution with a concentration of  $1 \times 10^8$  CFU/mL. The cultures of *S. xyloso* and *E. coli* were then diluted to a ratio of 1:1,000 in a TSB and SOC agar, respectively, at 48°C and used as inoculated layers.

### Agar Diffusion Bioassay

Agar diffusion bioassay was performed according to Schmidt's method (Schmidt et al., 2009). For the base layer agar, 20 mL of TSB or SOC agar culture medium was poured into microbiological plates. After solidification, 5 mL of inoculated TSB or SOC agar medium was added to the base layer. In each plate, six stainless-steel cylinders were placed on the surface of the inoculated medium. Subsequently, 240  $\mu\text{L}$  of 10, 5, or 2.5 mg/mL CD-g-CS was poured into each cylinder and filled to the mark. The plates were incubated for 16 h at 37°C. Finally, an electronic caliper was used to measure the diameters of the inhibition zones.

## Effect of CD-g-CS on Bacterial Membrane Integrity

Experiments were conducted as stated in Lou et al. (2011) with a few modifications. The cultured *S. xyloso* and *E. coli* were harvested at their logarithmic phase, washed and re-suspended in a sterile 0.9% saline solution. The bacterial suspensions were adjusted to an optical density (OD) at 630 nm of  $0.5 \pm 0.02$ . CD-g-CS solution was mixed with the bacterial suspension to give a final CD-g-CS concentration of 10 mg/mL. The mixture was then incubated at 37°C for 0, 60, 120, 240, 360, or 480 min. The mixture was centrifuged, and the supernatant was filtrated using a 0.22- $\mu\text{m}$  filter membrane. The filtrates were analyzed using a microplate reader at 260 nm.

## Effect of CD-g-CS on Microcosmic Morphology of Bacteria

Acetic acid [1% (v/v)] was used to dissolve the CD-g-CS. The dissolved CD-g-CS solution was then adjusted to a pH of 5 using NaOH (8 mol/L). *S. xyloso* and *E. coli* in their logarithmic phase were harvested and re-suspended in solutions with and without 10 mg/mL CD-g-CS. Subsequently, the mixtures were incubated at 37°C for 1.5 h. Then the mixtures were incubated in fixation buffer [2.5 % (w/v) glutaraldehyde, pH 7.2] for 1.5 h at 4°C, and washed three times with 0.1 M cacodylate buffer (pH 7.0) for 20 min each time. The samples were dehydrated using a graded series of ethanol (50, 70, 95, and 100%). After the dehydrated samples were subjected to critical point drying and gold sputtering, they were examined by scanning electron microscopy (SEM) (Yang et al., 2015).



## Study on the Uptake of Drugs Promoted by CD-g-CS in *S. xylosus*

The cultured *S. xylosus* in the logarithmic phase were mixed with CD-g-CS (5, 2, or 0.5 mg/mL) containing 50  $\mu\text{mol/L}$  doxorubicin hydrochloride. The mixtures were incubated at 37°C for 1 h. Subsequently, the *S. xylosus* solutions were centrifuged, washed three times with PBS (pH = 7.2), and resuspended in 500  $\mu\text{L}$  PBS. For each sample, *S. xylosus* was sorted using a Flow Cytometry System (FCS). *S. xylosus* treated with only doxorubicin hydrochloride served as a control.

Cultured *S. xylosus* in the logarithmic phase was mixed with 2 mg/mL CD-g-CS containing 50  $\mu\text{mol/L}$  doxorubicin hydrochloride. The mixtures were incubated at 37°C for 30 min, 1 or 3 h. The mixtures of *S. xylosus* were then centrifuged, washed three times, and re-suspended in 500  $\mu\text{L}$  PBS (pH = 7.2). Each sample with *S. xylosus* was placed on a glass slide and observed by confocal laser scanning microscopy (CLSM). *S. xylosus* treated with only doxorubicin hydrochloride for 30 min, 1 or 3 h served as the control.

## The Effect of CD-g-CS on the Solubilization of Sulfonamides

### Measurement of the Aqueous Solubility of Sulfadiazine, Sulfamonomethoxine, and Sulfamethoxazole

Aqueous solubility measurements were conducted according to the method of Wang and Wang (2000). Large amounts of sulfadiazine, sulfamonomethoxine, and sulfamethoxazole were added to distilled water in an equilibrium cell. The mixture was agitated until reaching equilibrium with water in the equilibrium cell and then kept for 30 min. A known amount of the upper layer of the mixture was removed from the equilibrium cell and diluted with distilled water. The calibration curve established by ultraviolet-visible spectrophotometry (UV-Vis) was used to determine the concentration of the solution.

## Solubilization of Sulfadiazine, Sulfamonomethoxine, and Sulfamethoxazole With CD-g-CS

Solubilization was evaluated using the method described by Furuishi et al. (2017) with a few modifications. Acetic acid [1 mL, 1 % (v/v)] was used to dissolve 10 mg of CD-g-CS, and the pH of the solution was adjusted to be similar to that of the distilled water. Aliquots of sulfadiazine, sulfamonomethoxine, and sulfamethoxazole were separately added to 1 mL of 10 mg/mL CD-g-CS. A vortex mixer was used to mix the suspension followed by sonication for 20 min. The mixture was then stirred for 2 h at 25°C followed by the centrifugation of the suspension at 8,000 r/min for 10 min. The supernatant was filtered using a membrane with 0.45- $\mu\text{m}$  pore size. The sulfadiazine, sulfamonomethoxine, and sulfamethoxazole concentrations were determined by UV-Vis.

## Statistical Analysis

Statistical analyses were conducted using Microcal Origin v. 7.5 (OriginLab Corp). The data obtained were analyzed for significant means using a one-way analysis of variance (ANOVA). Values were reported as means  $\pm$  standard deviations, and statistical means were compared by *t*-test with  $p < 0.05$ .

## RESULTS AND DISCUSSION

### Synthesis and Characterization of CD-g-CS

Generally, 6-OTs- $\beta$ -CD is considered as the most widely used intermediate for changing the primary hydroxyl moiety of  $\beta$ -CD into other functional groups such as amino groups (Melton and Slessor, 1971). The resultant compound, 6-OTs- $\beta$ -CD so formed is then grafted with the amino group in CS under acidic conditions (Figure 1). CD-g-CS is therefore the product of the reaction between 6-OTs- $\beta$ -CD and CS in an acid-controlled environment. Thus, CS was protonated under this environment.

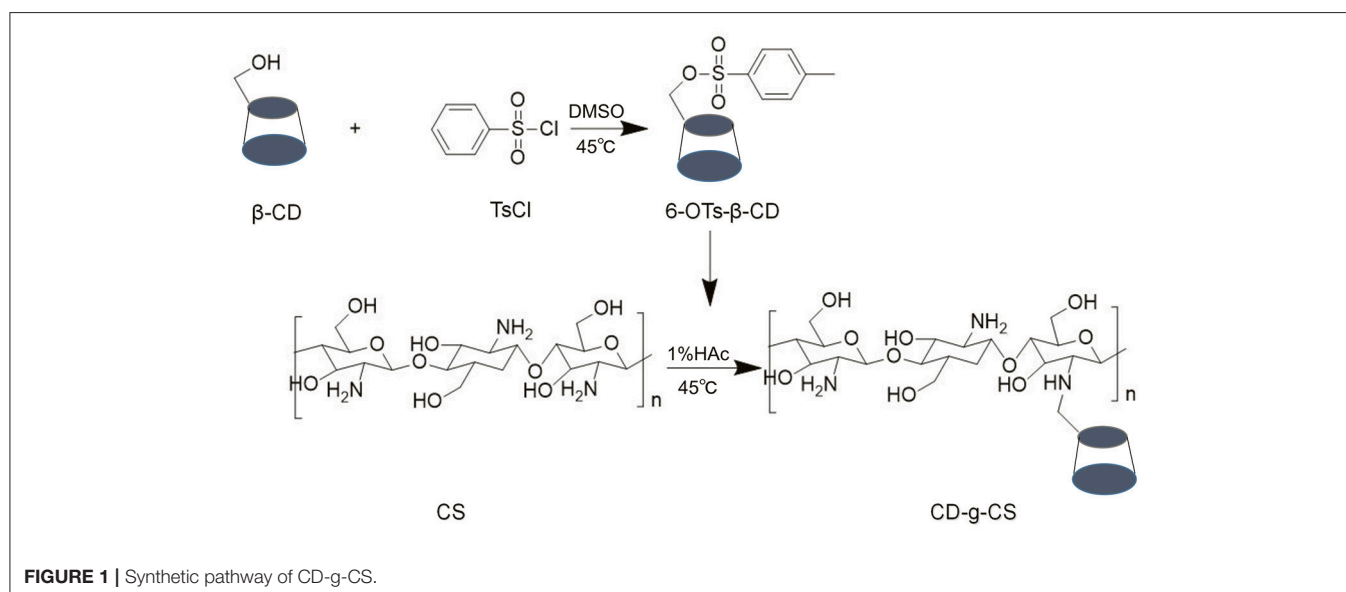
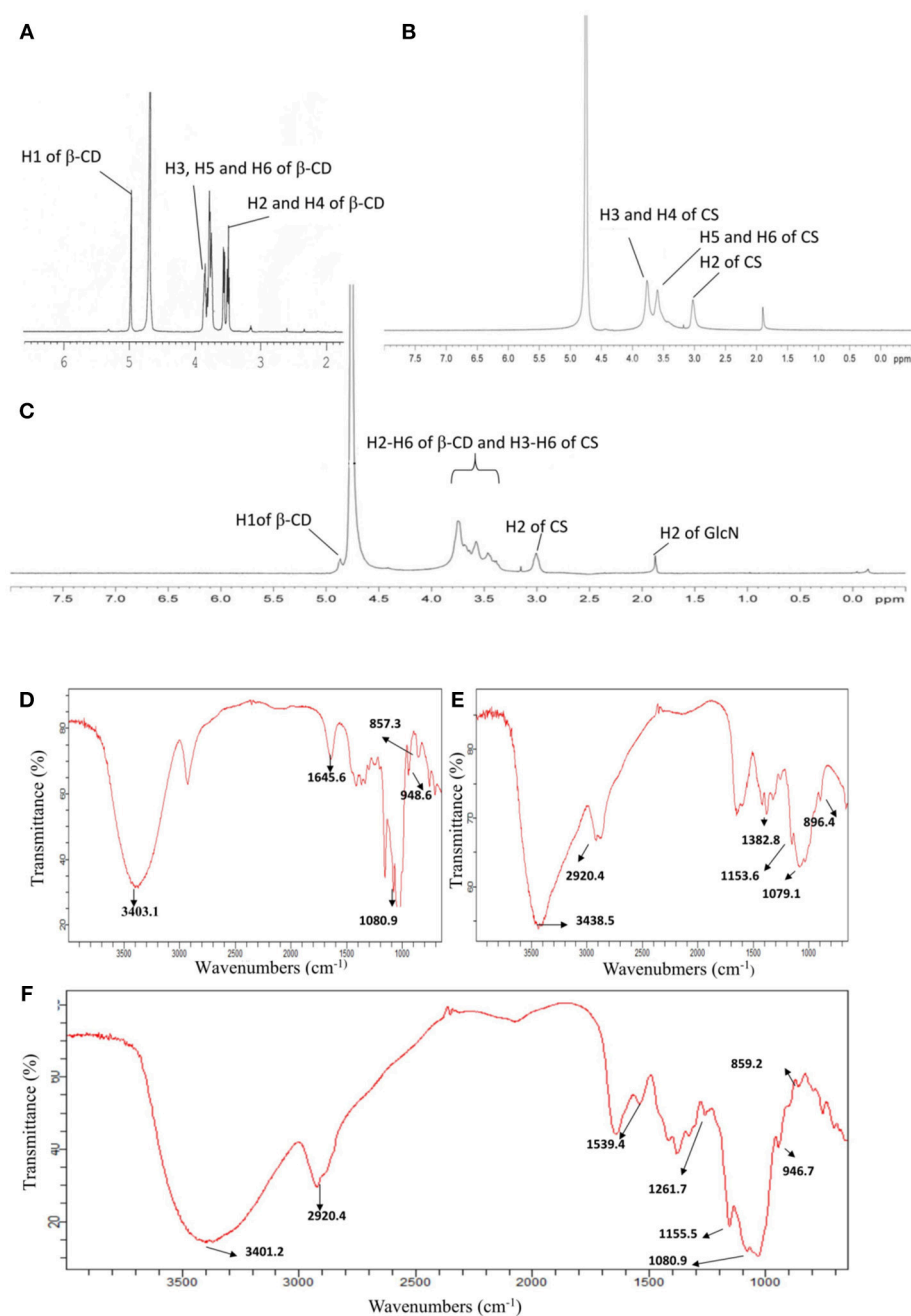


FIGURE 1 | Synthetic pathway of CD-g-CS.

The chemical structures of CS,  $\beta$ -CD and CD-g-CS were characterized by  $^1\text{H}$  NMR and FT-IR (see **Figure 2**). The  $^1\text{H}$  NMR spectrum of CS and  $\beta$ -CD is assigned in the **Supplementary Material**. In the  $^1\text{H}$  NMR spectrum of CD-g-CS (**Figure 2C**), the multiplet proton signals at  $\delta = 5.0$ – $3.0$  ppm are attributed to the H2–H6 protons of  $\beta$ -CD and H3–H6 of CS. The complex multiplet proton signals is because the D-galactopyranose and  $\beta$ -(1,4)-2-amino-2-deoxy-D-glucopyranose structural units of  $\beta$ -CD and CS are very similar (Sajomsang et al.,

2012), this similarities cause the peaks of  $\beta$ -CD and CS to overlaps each other. Moreover, singlet at  $\delta = 1.875$  ppm is attributed to the H2 proton of the glucosamine (GlcN). The signals at  $\delta = 4.864$  and  $3.003$  ppm result from the H1 proton of  $\beta$ -CD and H2 of CS, respectively (Gonil et al., 2011; Sajomsang et al., 2012; Yuan et al., 2013). These results conflict with the observation of Gonil et al. (2011), who did not observe an aromatic proton signal at around  $\delta = 7$  ppm. This signifies that the tosyl group present in the CD-g-CS structure was removed.



**FIGURE 2** |  $^1\text{H}$  NMR spectra of  $\beta$ -CD (A), CS (B), and CD-g-CS (C). FT-IR spectra of  $\beta$ -CD (D), CS (E), and CD-g-CS (F).

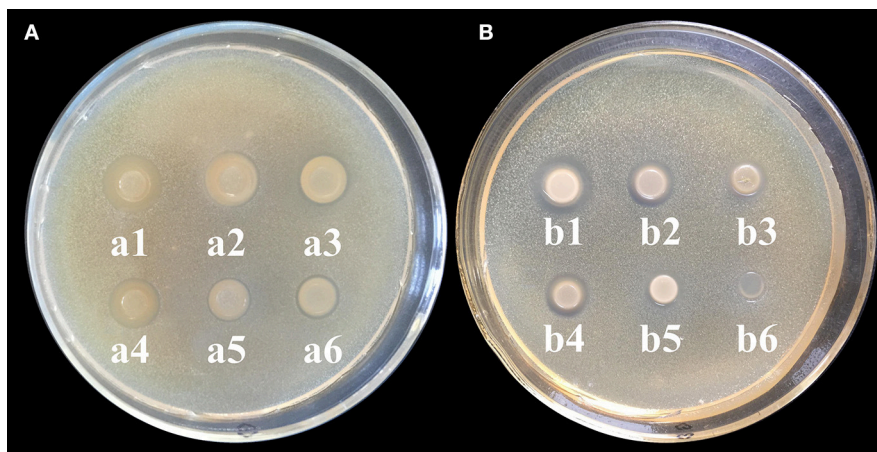


**FIGURE 3 | (A,B)** Agar diffusion results for *S. xylosois* and *E. coli*, respectively. **a1 (b1)**, **a2 (b2)**, and **a3 (b3)** show the inhibition zones for 10, 5, and 2.5 mg/mL CD-g-CS ( $Q_{CD} = 0.6 \times 10^2 \mu\text{mol/g}$ ), respectively. **a4 (b4)**, **a5 (b5)**, and **a6 (b6)** show the inhibition zones for 10, 5, and 2.5 mg/mL CD-g-CS ( $Q_{CD} = 0.643 \times 10^3 \mu\text{mol/g}$ ), respectively.

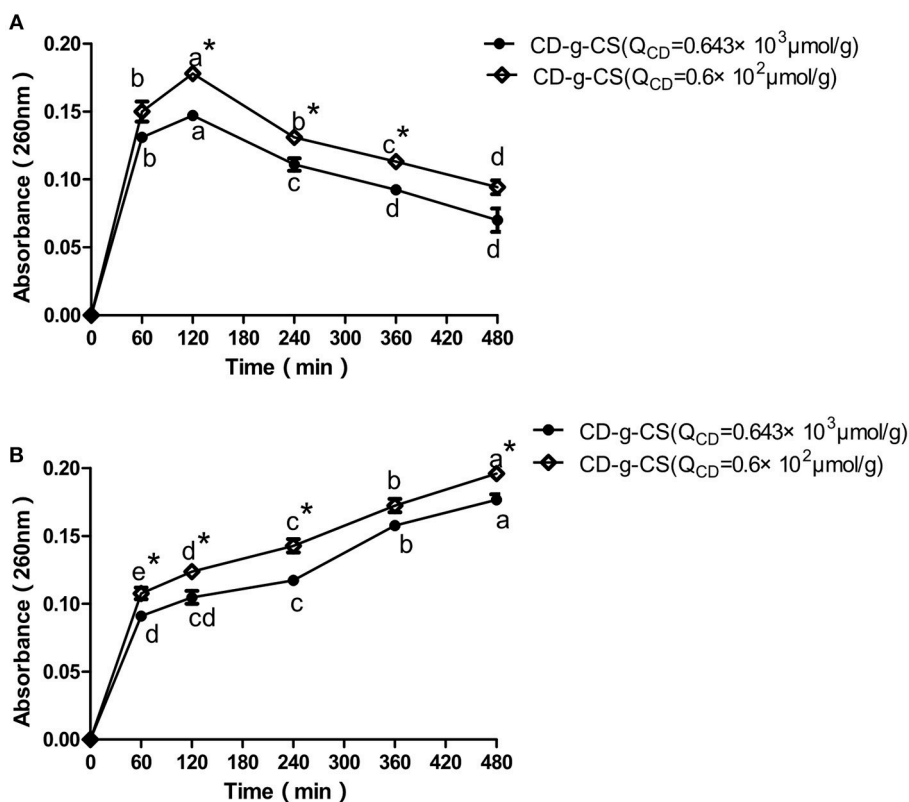


**FIGURE 4 |** Release of intracellular components of *E. coli* (A) and *S. xylosois* (B) suspensions treated with 10 mg/mL of CD-g-CS ( $Q_{CD} = 0.643 \times 10^3 \mu\text{mol/g}$ ) and CD-g-CS ( $Q_{CD} = 0.6 \times 10^2 \mu\text{mol/g}$ ). Different letters indicate a significant difference within groups at  $p \leq 0.05$ . \*Indicates a significant difference between the control and CD-g-CS ( $Q_{CD} = 0.643 \times 10^3 \mu\text{mol/g}$ ) at  $p \leq 0.05$ . Data are expressed as mean  $\pm$  standard deviation ( $n = 3$ ).

The FT-IR spectrum of CS is shown in the **Supplementary Material** (Brugnerotto et al., 2001). In the FT-IR spectrum of CD-g-CS (**Figure 2F**), the dominant peaks at

wavenumbers 3401.2 and 1384.7  $\text{cm}^{-1}$  are attributed to the  $-\text{OH}$  stretching and  $-\text{C}-\text{O}$  stretching of the CS backbone, respectively. Comparing the spectra of  $\beta$ -CD and CD-g-CS, the peak of

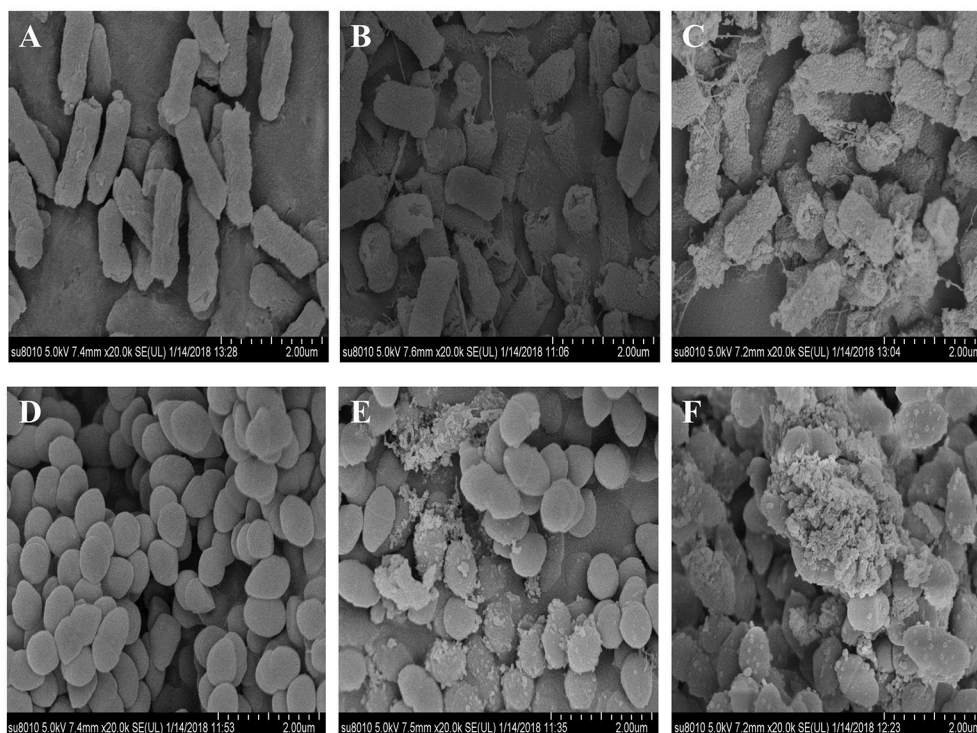


**FIGURE 5 |** SEM micrographs of *E. coli* and *S. xylosus* untreated (**A,D**), treated with 10 mg/mL CD-g-CS ( $Q_{CD} = 0.643 \times 10^3 \mu\text{mol/g}$ ) (**B,E**), and treated with 10 mg/mL CD-g-CS ( $Q_{CD} = 0.6 \times 10^2 \mu\text{mol/g}$ ) (**C,F**), respectively.

C–O– at  $1080.9 \text{ cm}^{-1}$  is blurred in the spectrum of CD-g-CS. Furthermore, the dominant peak of  $\alpha$ -(1,4) glucopyranose in  $\beta$ -CD at  $859.2 \text{ cm}^{-1}$  and the peak corresponding to the  $\alpha$ -pyranil vibration of  $\beta$ -CD at  $946.7 \text{ cm}^{-1}$  are also observed. These findings are in agreement with the report of Wang et al. (2007). The  $^1\text{H}$  NMR and FT-IR results suggest the formation of CD-g-CS.

$Q_{CD}$  was measured by the phenol-sulfuric acid method according to the number of 6-OTs- $\beta$ -CD groups in each primary amino group of CS. The phenol-sulfuric acid method can be used for the quantitative colorimetric microdetermination of oligosaccharides and polysaccharides. The method is simple and sensitive (Dubois et al., 1956). We found that the system formed by CS, phenol and concentrated sulfuric acid was not absorbed at 490 nm after the above treatment. Therefore, it does not interfere with the determination of  $\beta$ -CD by this method. Good linearity was achieved in the hydrolysate of  $\beta$ -CD (**Figure S1**). The results revealed that the CD-g-CS with two different  $Q_{CD}$  ( $0.643 \times 10^3$  and  $0.6 \times 10^2 \mu\text{mol/g}$ ) were successfully prepared. The higher molar ratio of 6-OTs- $\beta$ -CD to primary amino groups of CS resulted in the higher  $Q_{CD}$ .

### Amino Content of CD-g-CS

According to Kasaai (2009), DD can be obtained as the actual amino content of CS divided by the ideal amino content. DD is a key structural characteristic of CS on which other biological, physico-chemical, and mechanical properties depend. Hence, the

amino content of CD-g-CS was determined by the acid-base titration method (Yi et al., 2006). The results revealed that the amino contents of CD-g-CS with  $Q_{CD} = 0.643 \times 10^3$  and  $0.6 \times 10^2 \mu\text{mol/g}$  were  $6.34 \pm 0.072$  and  $9.41 \pm 0.055\%$ , respectively. The ideal amino content is 9.94% when DD is 100% (Yi et al., 2006). The amino content of CD-g-CS decreased to some extent as the amino groups on CS reacted with  $\beta$ -CD to form CD-g-CS. Thus, the higher amino content of CD-g-CS ( $Q_{CD} = 0.6 \times 10^2 \mu\text{mol/g}$ ) compared to CD-g-CS ( $Q_{CD} = 0.643 \times 10^3 \mu\text{mol/g}$ ) was related to CS being linked to less  $\beta$ -CD.

### Antimicrobial Assessments

CS and its derivatives have been reported to show some antimicrobial activity against microbial pathogens (Rabea et al., 2003). Thus, we investigated the antimicrobial activity of CD-g-CS to evaluate its potency as an antimicrobial excipient. In the present study, Gram-negative and Gram-positive bacteria were used to investigate of the antimicrobial activity of CD-g-CS. As shown in **Figure 3A**, the inhibition zone diameters for *S. xylosus* corresponding to 10, 5, and 2.5 mg/mL CD-g-CS ( $Q_{CD} = 0.6 \times 10^2 \mu\text{mol/g}$ ) were 14.5 mm (**a1**), 13.5 mm (**a2**), and 12 mm (**a3**), respectively, and those for 10, 5, and 2.5 mg/mL CD-g-CS ( $Q_{CD} = 0.643 \times 10^3 \mu\text{mol/g}$ ) were 12.5 mm (**a4**), 10 mm (**a5**), and 10 mm (**a6**), respectively. For *E. coli* (**Figure 3B**), the inhibition zone diameters corresponding to 10, 5, and 2.5 mg/mL of CD-g-CS ( $Q_{CD} = 0.6 \times 10^2 \mu\text{mol/g}$ ) and CD-g-CS ( $Q_{CD} = 0.643 \times 10^3 \mu\text{mol/g}$ ) were 13.5 mm (**b1**), 11.5 mm (**b2**), and 9.5 mm (**b3**),



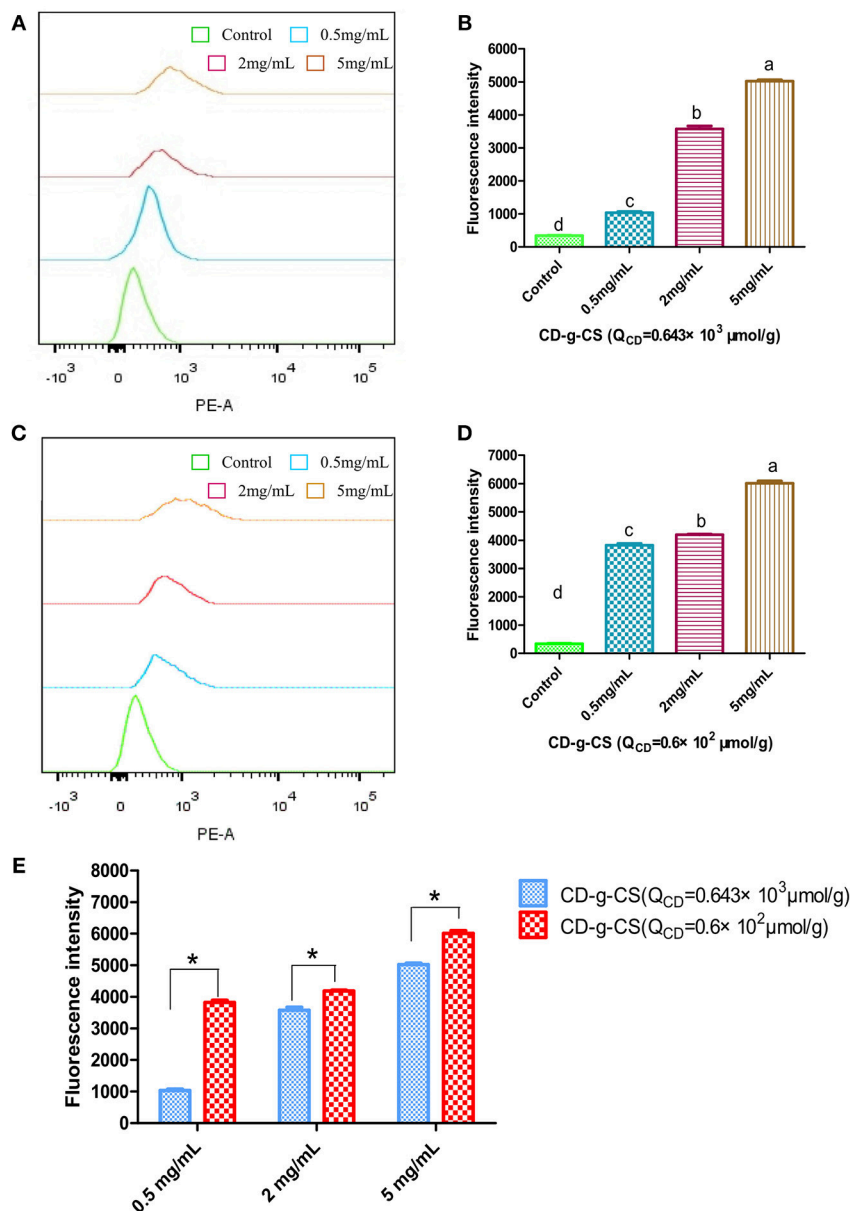


**FIGURE 6 |** Quantitative *S. xylosus* uptake of doxorubicin hydrochloride by FCS. (A,C) Fluorescence intensity measured after *S. xylosus* was incubated with different concentrations of CD-g-CS ( $Q_{CD} = 0.643 \times 10^3 \mu\text{mol/g}$ ) and CD-g-CS ( $Q_{CD} = 0.6 \times 10^2 \mu\text{mol/g}$ ) (0.5, 2, and 5 mg/mL) for 1 h, respectively. (B,D,E) Fluorescence intensity measured at 0.5, 2, and 5 mg/mL, of CD-g-CS ( $Q_{CD} = 0.643 \times 10^3 \mu\text{mol/g}$ ) and CD-g-CS ( $Q_{CD} = 0.6 \times 10^2 \mu\text{mol/g}$ ), respectively (mean  $\pm$  S.D.,  $n = 3$ ). Different letters indicate a significant difference within groups at  $p \leq 0.05$ . \*Indicates a significant difference between CD-g-CS ( $Q_{CD} = 0.643 \times 10^3 \mu\text{mol/g}$ ) and CD-g-CS ( $Q_{CD} = 0.6 \times 10^2 \mu\text{mol/g}$ ) at  $p \leq 0.05$ .

11 mm (b4), 9 mm (b5), and 8 mm, and no inhibition zone (b6), respectively.

CD-g-CS exhibited antimicrobial activity against *S. xylosus* and *E. coli* as a result of the prominent antimicrobial properties of CS, as reported by Chen et al. (2017). Previous studies have also reported the antimicrobial activity of CS against bacteria (Hamdi et al., 2018). The difference in the antibacterial ability of CD-g-CS with  $Q_{CD} = 0.643 \times 10^3$  and  $0.6 \times 10^2 \mu\text{mol/g}$  may be attributed to the amount of CS. Studies have shown that sterilization with

CS results in the elimination of pathogens. The concentration of CS and antibacterial activity are positively related (i.e., a higher CS concentration results in a stronger antimicrobial effect). The mechanism behind this effect can be explained as follows. As the concentration of CS increases, there is a resultant increase in the amount of free amino groups, leading to more positive charges under acidic conditions (Chen et al., 2002). The antimicrobial activity of the CS is based on the idea that the positive charge density of CS absorbed onto the negatively charged cell surfaces

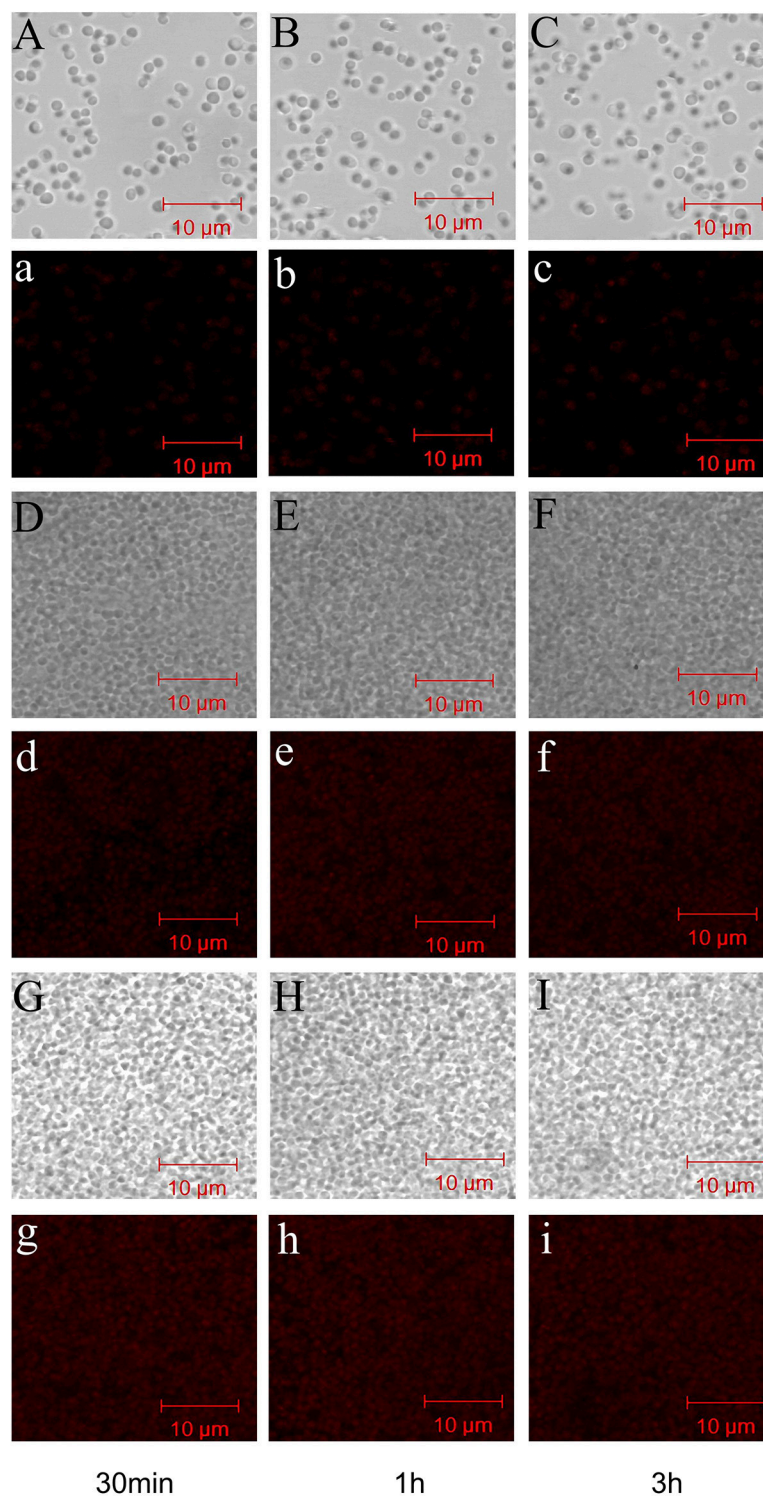


**FIGURE 7 |** CLSM images showing the uptake of doxorubicin hydrochloride in *S. xylosus*. **(A–C)** Images of *S. xylosus* treated with only doxorubicin hydrochloride for 30 min, 1 and 3 h, respectively. **(D–I)** *S. xylosus* treated with CD-g-CS ( $Q_{CD} = 0.643 \times 10^3 \mu\text{mol/g}$ ) and CD-g-CS ( $Q_{CD} = 0.6 \times 10^2 \mu\text{mol/g}$ ) containing doxorubicin hydrochloride for 30 min, 1 and 3 h, respectively. **(a–i)** Bright-field CLSM images.

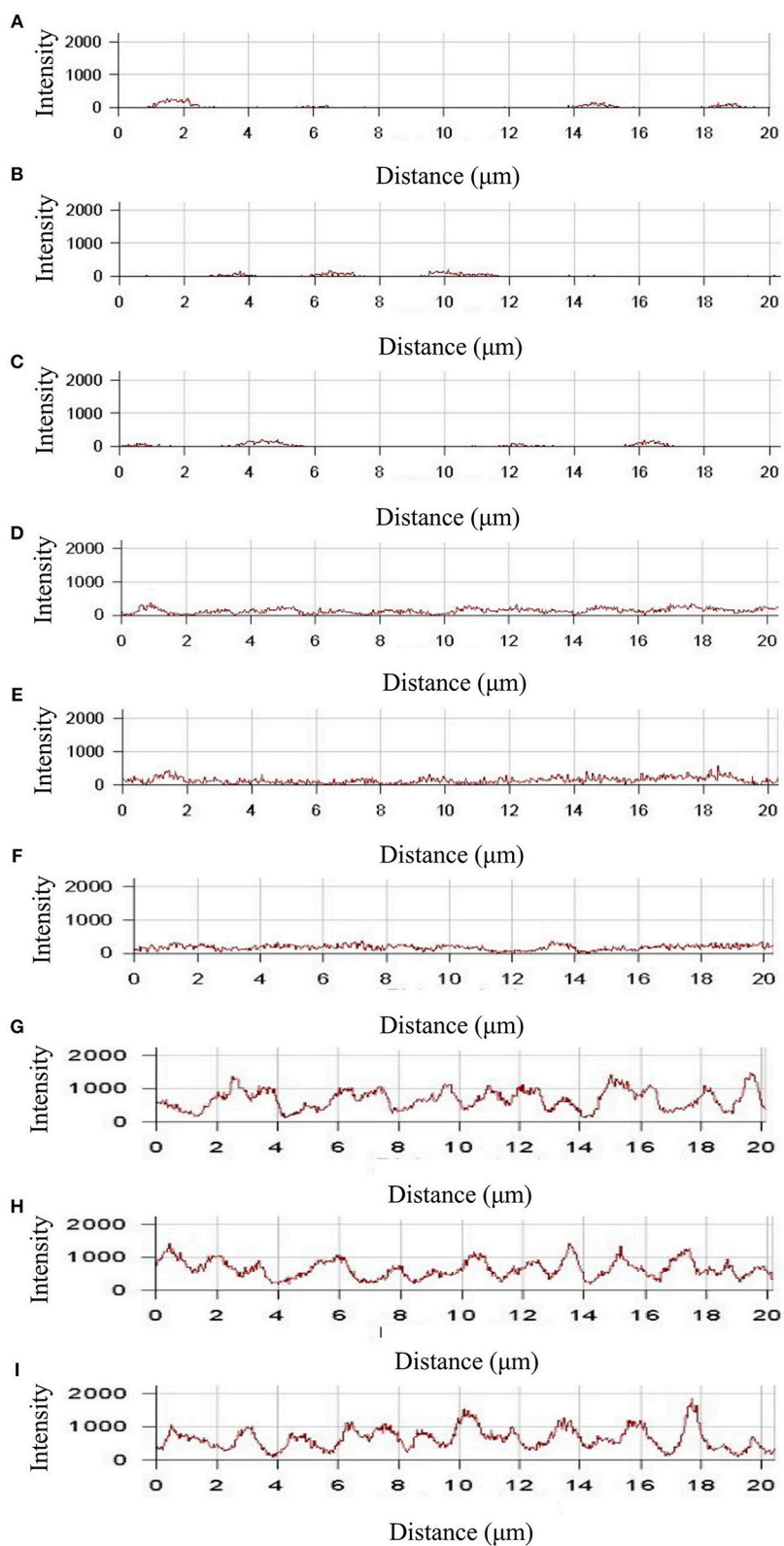


**FIGURE 8 |** The fluorescence intensity was obtained by CLSM in *S. xylosus* uptake doxorubicin hydrochloride. **(A–C)** The fluorescence intensity of *S. xylosus* was treated with only doxorubicin hydrochloride for 30 min, 1 and 3 h, respectively. **(D–I)** *S. xylosus* was treated with CD-g-CS ( $Q_{CD} = 0.643 \times 10^3 \mu\text{mol/g}$ ) and CD-g-CS ( $Q_{CD} = 0.6 \times 10^2 \mu\text{mol/g}$ ) that contained doxorubicin hydrochloride for 30 min, 1 and 3 h, respectively.

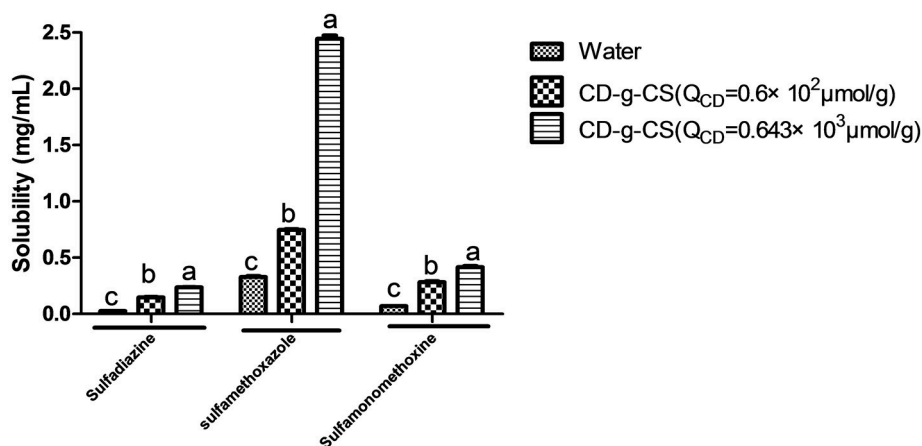


**FIGURE 9 |** Effect of CD-g-CS on the solubility of sulfadiazine, sulfamonomethoxine and sulfamethoxazole. Different letters indicate a significant difference at  $p \leq 0.05$ . Data are expressed as mean  $\pm$  standard deviation ( $n = 3$ ).

of bacteria leads to the leakage of proteinaceous and other intracellular constituents, causing cell death (Gonil et al., 2011). In this study, the amino content of CD-g-CS with  $Q_{CD} = 0.6 \times 10^2 \mu\text{mol/g}$  was greater than that of CD-g-CS with  $Q_{CD} = 0.643 \times 10^3 \mu\text{mol/g}$ , and the positive charge density was higher in determination of amino content of CD-g-CS. Thus, CD-g-CS with  $Q_{CD} = 0.6 \times 10^2 \mu\text{mol/g}$  showed better antibacterial activity.

### Effect of CD-g-CS on Bacterial Membrane Integrity

The intracellular components of cells are protected by cell membranes. Thus, the release of the intracellular components of bacterial cells can be used to monitor the membrane integrity (Denyer and Hugo, 1991). The detection of DNA and RNA from the protoplasm of bacterial cells signifies that the cell membrane has been ruptured (Chen and Cooper, 2002). Thus, the amount of DNA and RNA detected reveals the extent of damage done to the bacterial cell. **Figure 4** shows the amount of DNA and RNA released from *S. xylosus* and *E. coli* cells in suspensions treated with CD-g-CS. Initially, a rapid increase in the  $OD_{260\text{nm}}$  of *E. coli* was observed at 60 and 120 min followed by a gentle decrease for CD-g-CS ( $Q_{CD} = 0.643 \times 10^3 \mu\text{mol/g}$ ) and CD-g-CS ( $Q_{CD} = 0.6 \times 10^2 \mu\text{mol/g}$ ), respectively. This is because CS can combine with teichoic acid (Gram-positive bacteria) on the cell wall and also through the interaction with the cell membrane, thereby leading to the leakage of some intracellular substances (Tokura et al., 1997; Tsai and Su, 1999). Moreover, the thin and loosed crosslinking nature of the cell wall of Gram-negative bacteria may allow CD-g-CS to cause more damage to their cell walls. Thus, there was a rapid increase in the  $OD_{260\text{nm}}$  of *E. coli* up to 120 min. After that, the absorbance decreases may be adduced from the fact that the damage caused by CD-g-CS on *E. coli* reached its maximum value at 120 min. This was followed by the release of proteins or DNA gradually interacted CD-g-CS with the extension of time, resulting in the decrease of absorbance. Similar results were also reported for *Burkholderia*

*seminalis* strain treated with CS. The result showed that the  $OD_{260\text{nm}}$  decreased with time after 60 min due to the interaction between CS and protein or DNA (Lou et al., 2011). For *S. xylosus* suspensions, the absorbance at 260 nm increased with time and depended on the amount of CD-g-CS. The release of intracellular components of *S. xylosus* and *E. coli* was greater for treatment with CD-g-CS ( $Q_{CD} = 0.6 \times 10^2 \mu\text{mol/g}$ ) compared to CD-g-CS ( $Q_{CD} = 0.643 \times 10^3 \mu\text{mol/g}$ ). This finding might be related to the fact that CS in CD-g-CS ( $Q_{CD} = 0.6 \times 10^2 \mu\text{mol/g}$ ) was linked to a lower concentration of  $\beta$ -CD than in CD-g-CS ( $Q_{CD} = 0.643 \times 10^3 \mu\text{mol/g}$ ), and the positive charge density of CD-g-CS ( $Q_{CD} = 0.6 \times 10^2 \mu\text{mol/g}$ ) was higher. The CD-g-CS with high positive charge density absorbed onto the negatively charged cell surfaces of bacteria, leading to the leakage of intracellular constituents (Gonil et al., 2011). This is in line with the antimicrobial assessment tests. The results of this study indicate that CD-g-CS is bactericidal in nature and acts by rupturing the cell membranes of *S. xylosus* and *E. coli*, thereby causing the leakage of the DNA and RNA from the cells.

### The Effect of CD-g-CS on Microcosmic Morphology of Bacteria

*E. coli* and *S. xylosus* untreated or treated with 10 mg/mL CD-g-CS were examined by SEM. **Figures 5A,D** show that in the controls *E. coli* and *S. xylosus* cells had intact cell membranes with electron-dense lines. On the other hand, *E. coli* treated with CD-g-CS showed disrupted and altered cell membrane after 1.5 h, especially in the groups treated with CD-g-CS ( $Q_{CD} = 0.6 \times 10^2 \mu\text{mol/g}$ ). **Figures 5B,C** show that the CD-g-CS treated *E. coli* cells exhibited extracellular and intracellular changes compared to untreated cells. These changes included the following: the disruption of outer membrane structures with membrane sloughing and breaching; formation of irregular cell shapes and morphologies; degradation of bacilliform cells into short rods; formation of irregular condensed masses with bleb-like shapes; the development of faint bacterial profiles as a result of the loss of cell contents; blurring of the cell surface; and the



development of dim, hollow and even crushed structures. The micrographs in **Figure 5** showed that CD-g-CS damaged the cell membranes. Similar findings were reported by Helander et al. (2001) and Liu et al. (2004).

The micrographs of *S. xylosus* treated with CD-g-CS revealed severely damaged, atrophied, sunken and disrupted cell membranes after 1.5 h, especially the cells treated with CD-g-CS ( $Q_{CD} = 0.6 \times 10^2 \mu\text{mol/g}$ ). *S. xylosus* cells were irregularly shaped, and the cell contents were lacking. In addition, the profiles of the bacteria became faint. Morphs of the bacteria were multiplied, and a small amount of cells were markedly elongated from the initial spherical shape. The results show that CD-g-CS affected the microcosmic morphology of *S. xylosus* (**Figures 5D–F**), as previously reported in an earlier study (Liu et al., 2004). **Figure 5** shows that CD-g-CS ( $Q_{CD} = 0.6 \times 10^2 \mu\text{mol/g}$ ) had a greater effect on the microcosmic morphology of bacteria than CD-g-CS ( $Q_{CD} = 0.643 \times 10^3 \mu\text{mol/g}$ ). The result is in tandem with the effect of CD-g-CS on bacterial membrane integrity. The cell membrane integrity tests and SEM observation revealed that the antimicrobial mechanism of CD-g-CS was related to membrane disruption and cell lysis. The discovery of this antibacterial mechanism provides a scientific basis for the application of CD-g-CS as an antibacterial agent.

## Study of Drug Uptake Promoted by CD-g-CS in Bacteria

CS has previously been used to effectively enhance the absorption of hydrophilic drugs (Schipper et al., 1996). Nevertheless, the effect of CD-g-CS on drug uptake has not been reported. Thus, we used doxorubicin hydrochloride as a model drug to study the effect of CD-g-CS on drug uptake by *S. xylosus*. Doxorubicin hydrochloride exhibits red fluorescence under 480-nm excitation. After the bacterial uptake of doxorubicin hydrochloride, the amount of drug in the bacteria was indirectly reflected by the intensity of fluorescence.

The uptake of doxorubicin hydrochloride was investigated using FCS, as shown in **Figure 6**. The uptake of doxorubicin hydrochloride by *S. xylosus* was very low. However, with the extension of concentration, *S. xylosus* treated with CD-g-CS ( $Q_{CD} = 0.643 \times 10^3 \mu\text{mol/g}$ ) and CD-g-CS ( $Q_{CD} = 0.6 \times 10^2 \mu\text{mol/g}$ ). It was observed that the peak of fluorescence intensity shifted to the right compared to the control, and the concentration dependency was as pronounced as observed for the result, respectively. Namely, the fluorescence intensity of doxorubicin hydrochloride in *S. xylosus* increased significantly, especially for *S. xylosus* treated with CD-g-CS ( $Q_{CD} = 0.6 \times 10^2 \mu\text{mol/g}$ ). The results demonstrate that CD-g-CS can promote the uptake of doxorubicin hydrochloride by *S. xylosus*. CD-g-CS ( $Q_{CD} = 0.6 \times 10^2 \mu\text{mol/g}$ ) promoted uptake to a greater extent than CD-g-CS ( $Q_{CD} = 0.643 \times 10^3 \mu\text{mol/g}$ ), and the uptake was concentration dependent.

To study the time dependence of drug uptake by bacteria treated with CD-g-CS, CLSM was used to observe the fluorescence intensity of bacteria. The results are presented in **Figures 7, 8**. In the CLSM images of the controls (**Figures 7A–C, 8A–C**), the fluorescence intensities of *S. xylosus* treated with only doxorubicin hydrochloride for 30 min, 1 and 3 h were very weak, and no significant differences

were observed. With increasing incubation time for the same concentration of CD-g-CS, the fluorescence of *S. xylosus* was enhanced (**Figures 7D–I**). However, the fluorescence intensity was similar after *S. xylosus* treated with CD-g-CS ( $Q_{CD} = 0.643 \times 10^3 \mu\text{mol/g}$ ) containing doxorubicin hydrochloride was incubated for 30 min, 1 and 3 h, respectively (**Figures 8D–F**). Similar results were found in the CD-g-CS ( $Q_{CD} = 0.6 \times 10^2 \mu\text{mol/g}$ ) group (**Figures 8G–I**). Compared to the CD-g-CS ( $Q_{CD} = 0.643 \times 10^3 \mu\text{mol/g}$ ) groups, the fluorescence intensity was higher in the CD-g-CS ( $Q_{CD} = 0.6 \times 10^2 \mu\text{mol/g}$ ) groups, in agreement with the FCS results. Thus, we can conclude that CD-g-CS promotes the uptake of doxorubicin hydrochloride by *S. xylosus*, with CD-g-CS ( $Q_{CD} = 0.6 \times 10^2 \mu\text{mol/g}$ ) showing a better promotion effect than CD-g-CS ( $Q_{CD} = 0.643 \times 10^3 \mu\text{mol/g}$ ). However, the uptake was not time dependent.

CD-g-CS can promote the uptake of drugs by bacteria because it has the properties of CS (Chen et al., 2017). An earlier study by Illum et al. (1994) found that the absorption of peptides such as insulin and calcitonin across the nasal epithelium of rats and sheep was significantly enhanced by CS. Schipper investigated the effect of CS on poorly absorbable drugs across human epithelial cells and found that CS effectively enhanced the absorption of hydrophilic drugs such as peptides and proteins across nasal and intestinal epithelia (Schipper et al., 1996). Therefore, the mechanisms by which CD-g-CS and CS derivatives promote drug uptake may be the same because CS derivatives can increase membrane permeability (Je and Kim, 2006). The discovery that CD-g-CS can promote the uptake of drugs by bacteria is of great importance for improving the efficacy of antibiotics, reducing antibiotic dosage, and reducing antibiotic residues in animal-derived foods.

## The Solubilization Effect of CD-g-CS on Sulfonamides

The inclusion complexes of poorly water-soluble drugs with CD-g-CS were investigated using sulfadiazine, sulfamonomethoxine, and sulfamethoxazole as model drugs. The methodological verification of sulfamethoxazole, sulfadiazine and sulfamonomethoxine was implemented by UV-Vis, such as linear, precision, stability, and recovery in **Supplementary Material**. The solubilities of sulfadiazine, sulfamonomethoxine, and sulfamethoxazole with CD-g-CS in water were studied, as shown **Figure 9**. The solubilities of sulfadiazine, sulfamonomethoxine, and sulfamethoxazole in water were  $0.026 \pm 0.00168$ ,  $0.069 \pm 0.00159$ , and  $0.329 \pm 0.01157 \text{ mg/mL}$ , respectively. However, the solubilities of sulfadiazine, sulfamonomethoxine and sulfamethoxazole with 10 mg/mL CD-g-CS ( $Q_{CD} = 0.6 \times 10^2 \mu\text{mol/g}$ ) were  $0.147 \pm 0.00705$ ,  $0.283 \pm 0.013$ , and  $0.747 \pm 0.00985 \text{ mg/mL}$ , respectively, representing solubility enhancements of approximately 5.6, 4.1, and 2.3 times, respectively, compared to the aqueous solutions.

The respective solubilities of sulfadiazine, sulfamonomethoxine, and sulfamethoxazole with 10 mg/mL CD-g-CS ( $Q_{CD} = 0.643 \times 10^3 \mu\text{mol/g}$ ) were  $0.236 \pm 0.00425$ ,  $0.416 \pm 0.019$ , and  $2.444 \pm 0.05012 \text{ mg/mL}$ , corresponding to enhancements of 9.1, 6.7, and 7.3 times, respectively. These results suggest that CD-g-CS increased the solubilities of sulfadiazine, sulfamonomethoxine, and sulfamethoxazole. This

effect is attributed to the structure of the  $\beta$ -CD molecules of CD-g-CS. These molecules have a truncated cone structure with the ring having an interior hydrophobic cavity and an outer hydrophilic character. The hydrophobic interior and hydrophilic exterior allow  $\beta$ -CD to serve as a carrier to enhance the solubility of drugs that are poorly soluble in water. The addition of drug molecules into the hydrophobic cavity of  $\beta$ -CD improves the aqueous solubility, dissolution rate, bioavailability and stability of the drug (Szejtli, 1988). CD-g-CS can increase the solubility of sulfonamides, providing a new strategy for increasing the solubility of insoluble antibiotics. This finding is expected to facilitate the application of insoluble antibiotics in clinical treatment.

## CONCLUSIONS

CD-g-CS with two different  $Q_{CD}$  was successfully synthesized. CD-g-CS showed antimicrobial activity against *E. coli* and *S. xylosus*, and the antimicrobial activity of CD-g-CS was higher for the lower  $Q_{CD}$ . Furthermore, the antimicrobial mechanism of CD-g-CS was due to membrane disruption and cell lysis based on cell membrane integrity tests and SEM observation. The uptake of doxorubicin hydrochloride in *S. xylosus* was significantly increased by CD-g-CS, demonstrating that CD-g-CS can promote the uptake of drugs by bacteria. In addition, CD-g-CS can enhance the solubility of sulfadiazine, sulfamonomethoxine, and sulfamethoxazole. The findings of this study can help reduce the use of antibiotics and suggest new ways to solve

the problems caused by antibiotics in clinical application (e.g., bacterial resistance and antibiotic residues in animal-derived foods).

## AUTHOR CONTRIBUTIONS

The experiment was designed by Y-HL and directed by W-YD and S-DZ. YQ, FY, J-WB, W-QC, TY, X-RC, and GB-O were supportive during the experiment.

## ACKNOWLEDGMENTS

This work was supported by the National Natural Science Foundation of China (No.31802228), the University of Nursing Programs for Young Scholars with Creative Talents in Heilongjiang Province (UNPYSCT-2016133), the Northeastern Science Inspection Station and China Ministry of Agriculture Key Laboratory of Animal Pathogen Biology (DY201702), the earmarked fund for China Agriculture Research System—35 and Program for Science and Technology Research of China (2015BAD11B03-07).

## SUPPLEMENTARY MATERIAL

The Supplementary Material for this article can be found online at: <https://www.frontiersin.org/articles/10.3389/fchem.2018.00657/full#supplementary-material>

## REFERENCES

- Badawy, M. E. I., Rabea, E. I., and Taktak, N. E.M. (2014). Antimicrobial and inhibitory enzyme activity of N-(benzyl) and quaternary N-(benzyl) chitosan derivatives on plant pathogens. *Carbohydr. Polym.* 111, 670–682. doi: 10.1016/j.carbpol.2014.04.098
- Brunerotto, J., Lizardi, J., Goycoolea, F. M., Argüelles-Monal, W., Desbrières, J., and Rinaudo, M. (2001). An infrared investigation in relation with chitin and chitosan characterization. *Polymer* 42, 3569–3580. doi: 10.1016/S0032-3861(00)00713-8
- Castro Domingues, R. C., Faria Junior, S. B., Silva, R. B., Cardoso, V. L., and Miranda Reis, M. H. (2012). Clarification of passion fruit juice with chitosan: effects of coagulation process variables and comparison with centrifugation and enzymatic treatments. *Process Biochem.* 47, 467–471. doi: 10.1016/j.procbio.2011.12.002
- Chen, C. Z., and Cooper, S. L. (2002). Interactions between dendrimer biocides and bacterial membranes. *Biomaterials* 23, 3359–3368. doi: 10.1016/S0142-9612(02)00036-4
- Chen, P., Song, H., Yao, S., Tu, X., Su, M., and Zhou, L. (2017). Magnetic targeted nanoparticles based on beta-cyclodextrin and chitosan for hydrophobic drug delivery and a study of their mechanism. *RSC Adv.* 7, 29025–29034. doi: 10.1039/C7RA02398G
- Chen, Y.-M., Chung, Y.-C., Wang, L.-W., Chen, K.-T., and Li, S.-Y. (2002). Antibacterial properties of chitosan in waterborne pathogen. *J. Environ. Sci. Health. Part A* 37, 1379–1390. doi: 10.1081/ESE-120005993
- Cho, E., Jeong, D., Paik, H.-D., and Jung, S. (2014). solubility enhancement of flavonols in the inclusion complex with thioether-bridged dimeric  $\beta$ -cyclodextrins. *Bull. Korean Chem. Soc.* 35, 2487–2493. doi: 10.5012/bkcs.2014.35.8.2487
- de Jong, A., El Garch, F., Simjee, S., Moyaert, H., Rose, M., Youala, M., et al. (2018). Monitoring of antimicrobial susceptibility of udder pathogens recovered from cases of clinical mastitis in dairy cows across Europe: vetPath results. *Vet. Microbiol.* 213, 73–81. doi: 10.1016/j.vetmic.2017.11.021
- Denyer, S. P., and Hugo, W. B. (1991). *Mechanisms of Action of Chemical Biocides. Their Study and Exploitation*. Oxford: Blackwell Scientific.
- Dubois, M., Gilles, K. A., Hamilton, J. K., Rebers, P. A., and Smith, F. (1956). Colorimetric method for determination of sugars and related substances. *Anal. Chem.* 28, 350–356. doi: 10.1021/ac60111a017
- Furuishi, T., Takahashi, S., Ogawa, N., Gunji, M., Nagase, H., Suzuki, T., et al. (2017). Enhanced dissolution and skin permeation profiles of epalrestat with  $\beta$ -cyclodextrin derivatives using a cogrinding method. *Eur. J. Pharm. Sci.* 106, 79–86. doi: 10.1016/j.ejps.2017.05.047
- Gonil, P., Sajomsang, W., Ruktanonchai, U. R., Pimpha, N., Sramala, I., Nuchuchua, O., et al. (2011). Novel quaternized chitosan containing  $\beta$ -cyclodextrin moiety Synthesis, characterization and antimicrobial activity. *Carbohydr. Polym.* 83, 905–913. doi: 10.1016/j.carbpol.2010.08.080
- Guo, P., Anderson, J. D., Bozell, J. J., and Zivanovic, S. (2016). The effect of solvent composition on grafting gallic acid onto chitosan via carbodiimide. *Carbohydr. Polym.* 140, 171–180. doi: 10.1016/j.carbpol.2015.12.015
- Hamdi, M., Hajji, S., Affes, S., Taktak, W., Maalej, H., Nasri, M., et al. (2018). Development of a controlled bioconversion process for the recovery of chitosan from blue crab (*Portunus segnis*) exoskeleton. *Food Hydrocoll.* 77, 534–548. doi: 10.1016/j.foodhyd.2017.10.031
- Hanaee, J., Jouyban, A., Dastmalchi, S., and Adibkia, K. (2005). Solubility prediction of sulfonamides at various temperatures using a single determination. *Daru J. Pharm. Sci.* 13, 1604–1608.

- Helander, I. M., Nurmiaho-Lassila, E. L., Ahvenainen, R., Rhoades, J., and Roller, S. (2001). Chitosan disrupts the barrier properties of the outer membrane of gram-negative bacteria. *Int. J. Food Microbiol.* 71, 235–244. doi: 10.1016/S0168-1605(01)00609-2
- Illum, L., Farrar, N. F., and Davis, S. S. (1994). Chitosan as a novel nasal delivery system for peptide drugs. *Pharm. Res.* 11, 1186–1189. doi: 10.1023/A:1018901302450
- Je, J.-Y., and Kim, S.-K. (2006). Chitosan derivatives killed bacteria by disrupting the outer and inner membrane. *J. Agric. Food Chem.* 54, 6629–6633. doi: 10.1021/jf061310p
- Kasaai, M. R. (2009). Various methods for determination of the degree of N-acetylation of chitin and chitosan: a review. *J. Agric. Food Chem.* 57, 1667–1676. doi: 10.1021/jf803001m
- Koontz, J. L., and Marcy, J. E. (2003). Formation of natamycin: cyclodextrin inclusion complexes and their characterization. *J. Agric. Food Chem.* 51, 7106–7110. doi: 10.1021/jf030332y
- Li, R., Li, P., Cai, J., Xiao, S., Yang, H., and Li, A. (2016). Efficient adsorption of both methyl orange and chromium from their aqueous mixtures using a quaternary ammonium salt modified chitosan magnetic composite adsorbent. *Chemosphere* 154, 310–318. doi: 10.1016/j.chemosphere.2016.03.100
- Liu, H., Du, Y. M., Wang, X. H., and Sun, L. P. (2004). Chitosan kills bacteria through cell membrane damage. *Int. J. Food Microbiol.* 95, 147–155. doi: 10.1016/j.ijfoodmicro.2004.01.022
- Long, A. R., Hsieh, L. C., Malbrough, M. S., Short, C. R., and Barker, S. A. (1990). Multiresidue method for the determination of sulfonamides in pork tissue. *J. Agric. Food Chem.* 38, 423–426. doi: 10.1021/jf00092a018
- Lou, M.-M., Zhu, B., Muhammad, I., Li, B., Xie, G.-L., Wang, Y.-L., et al. (2011). Antibacterial activity and mechanism of action of chitosan solutions against apricot fruit rot pathogen *Burkholderia seminalis*. *Carbohydr. Res.* 346, 1294–1301. doi: 10.1016/j.carres.2011.04.042
- Maeda, Y., and Kimura, Y. (2004). Antitumor effects of various low-molecular-weight chitosans are due to increased natural killer activity of intestinal intraepithelial lymphocytes in sarcoma 180-bearing mice. *J. Nutr.* 134, 945–950. doi: 10.1093/jn/134.4.945
- Melton, L. D., and Slessor, K. N. (1971). Synthesis of monosubstituted cyclohexaamyloses. *Carbohydr. Res.* 18, 29–37. doi: 10.1016/S0008-6215(00)80256-6
- No, H. K., Park, N. Y., Lee, S. H., and Meyers, S. P. (2002). Antibacterial activity of chitosans and chitosan oligomers with different molecular weights. *Int. J. Food Microbiol.* 74, 65–72. doi: 10.1016/S0168-1605(01)00717-6
- Pan, Y., Li, Y.-J., Zhao, H.-Y., Zheng, J.-M., Xu, H., Wei, G., et al. (2002). Bioadhesive polysaccharide in protein delivery system: chitosan nanoparticles improve the intestinal absorption of insulin *in vivo*. *Int. J. Pharm.* 249, 139–147. doi: 10.1016/S0378-5173(02)00486-6
- Prabaharan, M., and Jayakumar, R. (2009). Chitosan-graft-beta-cyclodextrin scaffolds with controlled drug release capability for tissue engineering applications. *Int. J. Biol. Macromol.* 44, 320–325. doi: 10.1016/j.ijbiomac.2009.01.005
- Rabea, E. I., Badawy, M. E. T., Stevens, C. V., Smagghe, G., and Steurbaut, W. (2003). Chitosan as antimicrobial agent: applications and mode of action. *Biomacromolecules* 4, 1457–1465. doi: 10.1021/bm034130m
- Sajomsang, W., Nuchuchua, O., Gonil, P., Saesoo, S., Sramala, I., Soottitawat, A., et al. (2012). Water-soluble beta-cyclodextrin grafted with chitosan and its inclusion complex as a mucoadhesive eugenol carrier. *Carbohydr. Polym.* 89, 623–631. doi: 10.1016/j.carbpol.2012.03.060
- Schipper, N. G., Varum, K. M., and Artursson, P. (1996). Chitosans as absorption enhancers for poorly absorbable drugs. I: Influence of molecular weight and degree of acetylation on drug transport across human intestinal epithelial (Caco-2) cells. *Pharm. Res.* 13, 1686–1692. doi: 10.1023/A:1016444808000
- Schmidt, C. A., Agarraya, D. A., Laporta, L. V., Machado, J. C., Manfio, M. L., and Bittencourt, C. F. (2009). Development and validation of a microbiological agar assay for determination of cefuroxime sodium in pharmaceutical preparations. *J. Microbiol. Methods* 77, 308–315. doi: 10.1016/j.mimet.2009.03.012
- Song, M., Li, L., Zhang, Y., Chen, K., Wang, H., and Gong, R. (2017). Carboxymethyl-beta-cyclodextrin grafted chitosan nanoparticles as oral delivery carrier of protein drugs. *React. Funct. Polym.* 117, 10–15. doi: 10.1016/j.reactfunctpolym.2017.05.008
- Szejtli, J. (1988). *Cyclodextrin Technology. Topics in Inclusion Science*. Budapest; Dordrecht: Springer.
- Szejtli, J. (2004). Past, present, and future of cyclodextrin research. *Pure Appl. Chem.* 76, 1825–1845. doi: 10.1351/pac200476101825
- Todorovic, D., Velhner, M., Grego, E., Vidanovic, D., Milanov, D., Krnjaic, D., et al. (2018). Molecular characterization of multidrug-resistant *Escherichia coli* Isolates from bovine clinical mastitis and pigs in the Vojvodina Province, Serbia. *Microb. Drug Resist.* 24, 95–103. doi: 10.1089/mdr.2017.0016
- Tokura, S., Ueno, K., Miyazaki, S., and Nishi, N. (1997). Molecular weight dependent antimicrobial activity by Chitosan. *Macromol. Symp.* 120, 1–9. doi: 10.1002/masy.19971200103
- Tsai, G. J., and Su, W. H. (1999). Antibacterial activity of shrimp chitosan against *Escherichia coli*. *J. Food Prot.* 62, 239–243. doi: 10.4315/0362-028X-62.3.239
- van der Merwe, S. M., Verhoef, J. C., Verheijden, J. H. M., Kotze, A. F., and Junginger, H. E. (2004). Trimethylated chitosan as polymeric absorption enhancer for improved peroral delivery of peptide drugs. *Eur. J. Pharm. Biopharm.* 58, 225–235. doi: 10.1016/j.ejpb.2004.03.023
- Wang, H.-D., Chu, L.-Y., Song, H., Yang, J.-P., Xie, R., and Yang, M. (2007). Preparation and enantiomer separation characteristics of chitosan/ $\beta$ -cyclodextrin composite membranes. *J. Memb. Sci.* 297, 262–270. doi: 10.1016/j.memsci.2007.03.055
- Wang, L. S., and Wang, X. L. (2000). Solubilities of dichlorophenylphosphine sulfide and Bis(4-carboxyphenyl)phenylphosphine oxide in water. *J. Chem. Eng. Data* 45, 743–745. doi: 10.1021/je9903303
- Yan, S., Lai, X. X., Du, G. R., and Xiang, Y. H. (2018). Identification of aminoglycoside antibiotics in milk matrix with a colorimetric sensor array and pattern recognition methods. *Anal. Chim. Acta* 1034, 153–160. doi: 10.1016/j.aca.2018.06.004
- Yang, Y.-B., Wang, S., Wang, C., Huang, Q.-Y., Bai, J.-W., Chen, J.-Q., et al. (2015). Emodin affects biofilm formation and expression of virulence factors in *Streptococcus suis* ATCC700794. *Arch. Microbiol.* 197, 1173–1180. doi: 10.1007/s00203-015-1158-4
- Yi, Y., Wang, Y. T., and Zhang, W. (2006). Synthesis of a new chitosan immobilized with beta-cyclodextrins and its adsorption properties for bilirubin. *J. Appl. Polym. Sci.* 99, 1264–1268. doi: 10.1002/app.22652
- Yuan, Z., Ye, Y., Gao, F., Yuan, H., Lan, M., Lou, K., et al. (2013). Chitosan-graft- $\beta$ -cyclodextrin nanoparticles as a carrier for controlled drug release. *Int. J. Pharm.* 446, 191–198. doi: 10.1016/j.ijpharm.2013.02.024
- Zhu, A., Chen, T., Yuan, L., Wu, H., and Lu, P. (2006). Synthesis and characterization of N-succinyl-chitosan and its self-assembly of nanospheres. *Carbohydr. Polym.* 66, 274–279. doi: 10.1016/j.carbpol.2006.03.014

**Conflict of Interest Statement:** The authors declare that the research was conducted in the absence of any commercial or financial relationships that could be construed as a potential conflict of interest.

Copyright © 2019 Ding, Zheng, Qin, Yu, Bai, Cui, Yu, Chen, Bello-Onaghise and Li. This is an open-access article distributed under the terms of the Creative Commons Attribution License (CC BY). The use, distribution or reproduction in other forums is permitted, provided the original author(s) and the copyright owner(s) are credited and that the original publication in this journal is cited, in accordance with accepted academic practice. No use, distribution or reproduction is permitted which does not comply with these terms.



# Thermo-Responsive Molecularly Imprinted Hydrogels for Selective Adsorption and Controlled Release of Phenol From Aqueous Solution

Zhenhui Si<sup>1,2</sup>, Ping Yu<sup>1,2\*</sup>, Yanying Dong<sup>1,2</sup>, Yang Lu<sup>1,2</sup>, Zhenjiang Tan<sup>1,2</sup>, Xiaopeng Yu<sup>1,2</sup>, Rui Zhao<sup>1,2</sup> and Yongsheng Yan<sup>3</sup>

<sup>1</sup> School of Computer Science, Jilin Normal University, Siping, China, <sup>2</sup> Key Laboratory of Numerical Simulation of Jilin Province, Jilin Normal University, Siping, China, <sup>3</sup> School of Chemistry and Chemical Engineering, Jiangsu University, Zhenjiang, China

## OPEN ACCESS

### Edited by:

Giuseppe Mensitieri,  
University of Naples Federico II, Italy

### Reviewed by:

Artur J. M. Valente,  
University of Coimbra, Portugal  
Christophe Daniel,  
University of Salerno, Italy

### \*Correspondence:

Ping Yu  
jlsdyp@126.com

### Specialty section:

This article was submitted to  
Polymer Chemistry,  
a section of the journal  
Frontiers in Chemistry

**Received:** 18 May 2018

**Accepted:** 24 December 2018

**Published:** 24 January 2019

### Citation:

Si Z, Yu P, Dong Y, Lu Y, Tan Z, Yu X,  
Zhao R and Yan Y (2019)  
Thermo-Responsive Molecularly  
Imprinted Hydrogels for Selective  
Adsorption and Controlled Release of  
Phenol From Aqueous Solution.  
Front. Chem. 6:674.  
doi: 10.3389/fchem.2018.00674

In this study, thermo-responsive molecularly imprinted hydrogels (T-MIHs) were developed as an effective potential adsorbent for selectively adsorption phenol from wastewater. During the process, N-isopropyl acrylamide (NIPAm) was used as thermal responsive monomer. The obtained materials were characterized in detail by fourier transform infrared (FT-IR) spectrometer, scanning electron microscope (SEM), and thermo gravimetric analysis (TGA). A series of static adsorption studies were performed to investigate the kinetics, specific adsorption equilibrium, and selective recognition ability of phenol. Reversible adsorption and release of phenol were realized by changing temperatures. Three type of phenols, namely 3-chlorophenols (3-CP), 2,4-dichlorophenol (2,4-DCP), and 2,4,6-trichlorophenol (2,4,6-TCP) were selected as model analytes to evaluate the selective recognition performance of T-MIHs. The T-MIHs have good selectivity, temperature response, and reusability, making them ideal in applying in the controlled separation and release of phenol pollutants.

**Keywords:** thermo-responsive, molecularly imprinted hydrogels, N-isopropyl acrylamide, recognition, phenol

## INTRODUCTION

Molecular imprinted technique (MIT) was acknowledged as a simple and convenient method for synthesizing molecularly imprinted polymers (MIPs), which provided artificial receptor-like recognition sites for target molecule (Wang Y. X. et al., 2011; Xu et al., 2011). It generates a specific binding site by polymerizing functional monomers and template molecule in the presence of cross-linking monomers. Subsequently, template molecules are eluted from the polymers with a certain physical or chemical method, leaving a specific recognition site for template molecules in the polymer (Zayats et al., 2011). MIPs have the advantages of specific recognition, low cost, and excellent chemical, thermal, and mechanical stability (Urraca et al., 2007). Nowadays, MIPs have been applied in more and more fields, such as separation, chiral chromatographic column, solid-phase extraction, chemosensor, enzyme mimic catalysis (Li et al., 2007; Díaz-Díaz et al., 2011; Valero-Navarro et al., 2011; Liang et al., 2012; Plewa et al., 2012; Herrero-Hernández et al., 2013), and so on.



In recent years, intelligent materials with thermal, magnetic or pH sensitivity have been introduced into the preparation of MIPs (Zhang et al., 2009; Wang et al., 2010; Fang et al., 2011; Liu et al., 2011). When thermal susceptible materials are introduced into MIPs, thermo-responsive molecularly imprinted polymers (TRMIPs) not only have high selective adsorption capacity, but can also sense temperature change and provide an appropriate response. N-isopropylacrylamide (PNIPAm) is a kind of typical thermoresponsive polymer monomer, which possesses amphiphilic properties. Above the lower critical solution temperature (LCST), which is about 32°C (Li et al., 2011), the hydrogen bond becomes weaker, forming a hydrophobic layer between molecules, resulting in a phase separation from hydrophilic state to hydrophobic state in water (Wang et al., 2015). The expansion or contraction of TRMIPs can be controlled by changing the ambient temperature. This characteristic has been utilized in applications of controlled drugs release, biological separation technology and catalysis. Wang et al. carried out a study about selective adsorption and controlled release of 2,4,5-trichlorophenol from aqueous solutions by thermo-responsive molecularly imprinted  $\text{Fe}_3\text{O}_4$ @carbon nanospheres (Wang et al., 2015). Xu et al. investigated the adsorption and recognizing ability of thermal-responsive molecularly imprinted polymers toward antibiotics from aqueous solutions (Xu et al., 2012).

Phenol compounds are widely used in chemicals, plastic, rubber, tanning and wood preservatives (Pan et al., 2016). The release of phenolic compounds into the aqueous environment has attracted widespread attention due to its high carcinogenicity and toxicity, as phenol leads to long-term damage to biology and the environment. According to the Environmental Protection Agency (EPA) the permissible concentration of phenol in wastewater is 1 mg/L. Regulation by the World Health Organization for limiting phenol in drinking water is 1 µg/L (Asmaly et al., 2015). Therefore, it is crucial to find efficient methods to treat phenol pollutants in water environment. In recent years, MIPs have been applied to pollutant treatment and their excellent selective adsorption capacity makes them a very promising adsorbent material. Yu et al. selective adsorption of 2,4,6-trichlorophenol from wastewater using magnetic molecularly imprinted microspheres (Yu et al., 2015a). Wang et al. carried out a study about surface molecularly imprinted polymers for highly efficient separation of 3-chlorophenol (Wang X. et al., 2011). The above-mentioned polymers represented favorably selectivity for the phenol compounds. However, to the best of our knowledge, thermo-responsive molecularly imprinted polymers for selective adsorption and controlled release of phenol from aqueous solution have been rarely reported.

In this study, it should be noted that molecular imprinting and temperature-sensitive technologies are combined. Thermo-responsive molecularly imprinted hydrogels (T-MIHs) were developed as a possible effective adsorbent for selectively adsorption phenol existent in aquatic environments. During the process, N-isopropyl acrylamide (NIPAm) was used as the thermal responsive monomer, potassium persulfate as initiator, acrylamide as monomer, N,N-methylene double acrylamide as

crosslinking agent, Span-80 as surfactant, phenol as template molecule, and the obtained T-MIHs were characterized by FT-IR, SEM, and TGA. Then, T-MIHs were used as adsorbents for selective recognition phenol from wastewater. A batch mode of adsorption experiments were used to investigate the adsorption properties, such as equilibrium isotherm, kinetics, regeneration, and selectivity of T-MIHs. Moreover, the release of template molecules was realized by changing environmental temperatures.

## EXPERIMENTAL SECTION

### Materials

Cyclohexane, toluene, acrylamide (AM, 99.8%), potassium persulfate (KPS, 99%), methanol, hydrochloric acid (HCL), and ethanol were purchased from Sinopharm Chemical Reagent Co., Ltd. (Shanghai, China). Span-80, N-isopropyl acrylamide (NIPAm, 98%), and N,N'-methylene-bis-acrylamide (MBA, 99%) were purchased from Aladdin reagent Co., Ltd (Shanghai, China). 3-chlorophenols (3-CP), 2,4,6-trichlorophenol (2,4,6-TCP), 2,4-dichlorophenol (2,4-DCP) and phenol were purchased from Tianda Chemical Reagent Factory (Tianjin, China).

### Instrumentation

Infrared spectra (3,500–500  $\text{cm}^{-1}$ ) were recorded on a Nicolet NEXUS-470 FT-IR apparatus (USA). A field-emission scanning electron microscope (SEM, JEOL, JSM-7001F) was used to observe the morphologies of T-MIHs. Thermogravimetric analysis (TGA) of samples was carried out using a Diamond TG/DTA instrument (STA 449C Jupiter, Netzsch, Germany) under a nitrogen atmosphere of up to 900°C with a heating rate of 5.0°C  $\text{min}^{-1}$ . UV-vis adsorption spectra were measured using a UV-vis spectrophotometer (UV-2450, Shimadzu, Japan). HPLC analysis was performed on a Shimadzu LC-20A system (Shimadzu, Kyoto, Japan) equipped with a UV-vis detector. The pH of the solution was determined by PHS-2 acidimeter (The Second Analytical Instrument Factory of Shanghai, China) (Yu et al., 2015b).

### Preparation of Thermo-Responsive Molecularly Imprinted Hydrogels

The synthetic process of T-MIHs followed a literature procedure with a few modifications (Hao et al., 2012). Firstly, organic phase solutions were prepared by dissolving span-80 (0.5 g) and toluene (3.5 mL) into cyclohexane (136 mL) with vigorous stirring (360 rpm) under nitrogen at 35°C for 30 min. Then, NIPAm (3.0 g) was added to 40 mL deionized ultrapure water. After that, phenol (0.33 g), AM (1.0 g), KPS (0.4 g), and MBA (1.0 g) were successively added into the above solution. The mixture was stirred at 25°C for 30 min to form aqueous phase. Subsequently, aqueous phase was added to organic phase dropwisely during vigorous stirring (360 rpm) for 60 min. For the next step, the reaction maintained 4.0 h with vigorous stirring (360 rpm) under nitrogen at 68°C. After sufficient polymerization, the thermo-responsive molecularly imprinted hydrogels were collected and washed alternatively with deionized ultrapure water and ethanol for several times. Soxhlet extraction with a mixture of acetic acid/methanol (10:90 v/v) was used to elute template molecules

from polymers, until no template molecules could be detected in the eluent. The resulting T-MIHs were finally washed several times with deionized ultrapure water and freeze-dried for 96 h. In comparison, the non-imprinted hydrogels (T-NIHs) were prepared by parallel method but with the phenol omitting.

## Procedures for Adsorption and Release of Template Phenol

The adsorption and release of phenol were studied by changing the experimental parameters (pH, temperature, initial concentration, reaction time). In adsorption isotherm studies, 10 mL of different initial concentration (from 10 to 300 mg L<sup>-1</sup>)

of phenol solutions (pH = 6.0) were mixed with 10 mg T-MIHs or T-NIHs. The studies were carried out on a thermostatic water bath at 308.5 K until the equilibrium was established. After that, the mixture was separated and the concentration of free phenol in the supernatant was measured. The adsorption capacity ( $Q$ , mg g<sup>-1</sup>) of T-MIHs/T-NIHs was calculated according to Equation (1).

$$Q = \frac{(C_0 - C)}{m} V \quad (1)$$

Where  $C$  (mg L<sup>-1</sup>) and  $C_0$  (mg L<sup>-1</sup>) represent the equilibrium and initial phenol concentrations in the supernatant, respectively.  $V$  (mL) is the solution volume,  $m$  (mg) is the dry weight of T-MIHs or T-NIHs.

The imprinting factor (IF) was used to evaluate the specific property of the prepared T-MIHs, calculated from the following equation (Li et al., 2014).

$$IF = \frac{Q_{MIHs}}{Q_{NIHs}} \quad (2)$$

Where  $Q_{MIHs}$  and  $Q_{NIHs}$  are adsorption capacity of T-MIHs and T-NIHs for template phenol, respectively.

The release property of phenol from the T-MIHs and T-NIHs was carried out as follows: 10 mg of the T-MIHs or T-NIHs was placed into 10 mL of phenol solutions (pH = 6.0) with an initial concentration of 100 mg L<sup>-1</sup> to capture phenol at 308.5 K for 12 h and then collected from the solution by centrifugation. In order to reduce non-specific adsorption, the T-MIHs or T-NIHs were then washed with 5.0 mL of deionized ultrapure water twice. Subsequently, 10 mL of deionized ultrapure water was mixed with T-MIHs or T-NIHs, and the reaction temperatures ranged from 25 to 55°C. The release kinetics is shown in Figure S1. After 12 h of reaction, the amount of phenol released from adsorbents was determined with a UV-vis spectrophotometer.

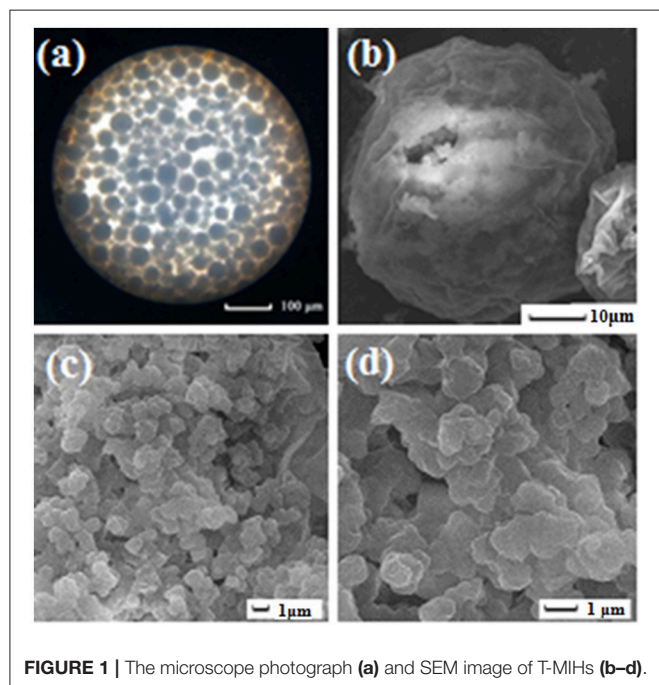


FIGURE 1 | The microscope photograph (a) and SEM image of T-MIHs (b-d).

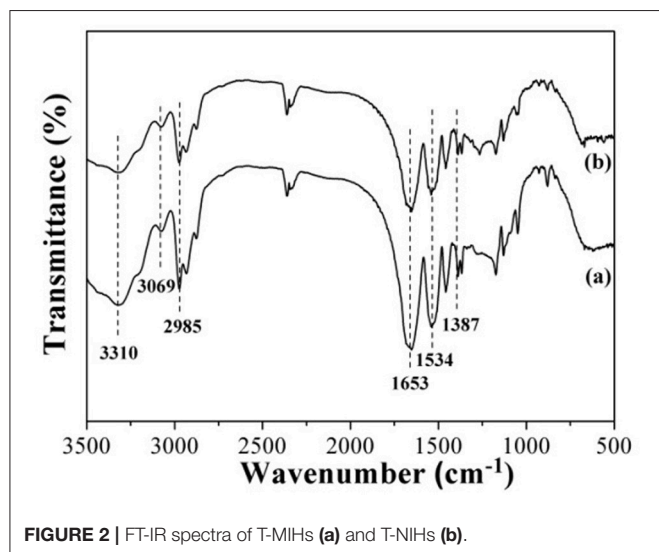


FIGURE 2 | FT-IR spectra of T-MIHs (a) and T-NIHs (b).

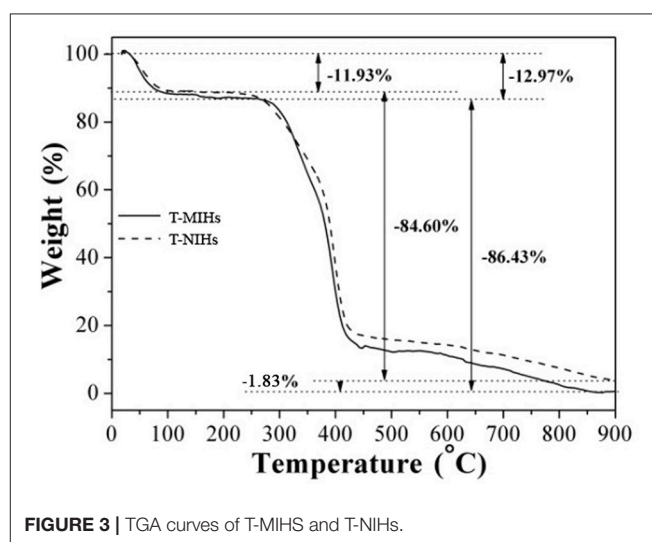


FIGURE 3 | TGA curves of T-MIHs and T-NIHs.

## Procedure for Selective Binding Experiments

Ten milligram of T-MIHs or T-NIHs were mixed with 10.0 mL solution ( $\text{pH} = 6.0$ ) in turn, which contained  $100 \text{ mg L}^{-1}$  of 3-CP, phenol, 2,4,6-TCP and 2,4-DCP. In comparison, the competitive adsorption of T-MIHs or T-NIHs for phenol at the presence of  $100 \text{ mg L}^{-1}$  of 2,4,6-TCP, 2,4-DCP and 3-CP were also studied. The competitive adsorption lasted 12 h in a thermostatic water bath at 308.5 K. The remnant concentration of phenol in the solution was detected using high performance liquid chromatography (HPLC). The mobile phase was consisted of deionized ultrapure water/methanol (20:80 v/v), the injection loop volume was  $20 \mu\text{L}$ , and the flow rate of the mobile phase was  $1.0 \text{ mL min}^{-1}$ .

## RESULTS AND DISCUSSION

### Morphological Characterization

The surface morphology of T-MIHs was observed by microscope photograph and scanning electron micrograph, respectively, which are shown in **Figure 1**. Through the lens of the microscope, **Figure 1a** showed that T-MIHs possessed spherical structure and the average size distribution of T-MIHs was about  $46 \pm 2 \mu\text{m}$  tested by the statistical calculation of 200 particles. From **Figure 1b**, it is clear that the T-MIHs particle was spherical and the surface rough, which consisted of many small-sized particles. At the high magnification in **Figures 1c,d** it can be seen that rough imprinted polymers with an average size of about one micron are deposited randomly on the surface of the polymer. A large number of identification sites existed between the imprinted particles, which were benefit for selective adsorption target molecular from water environment. Meanwhile, the surface morphology of T-NIHs was also observed in Figure S2, which also showed the spherical microparticles with the same size as T-MIHs, and rough surface structure.

### Infrared Spectroscopic Characterization

The FT-IR spectrometer was used to test the surface groups of the as-obtained T-MIHs and T-NIHs gel microsphere using the KBr pellet technique, which was recorded (32 scans) at room

temperature between the wave number  $4,000$  and  $400 \text{ cm}^{-1}$ . FT-IR spectra of the T-MIHs (a) and T-NIHs (b) were measured and shown in **Figure 2**. The contrast showed that the infrared spectra of T-MIHs and T-NIHs were similar in shape. A strong peak at

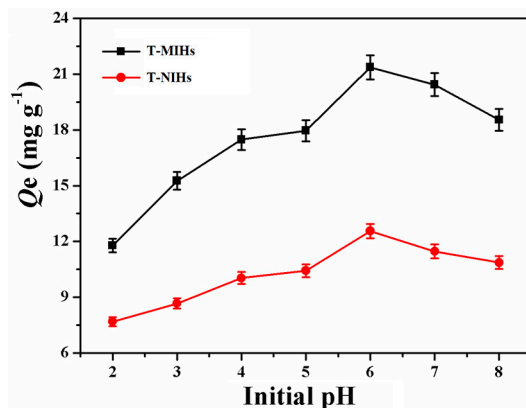


**FIGURE 5** | Effect of pH on adsorption of phenol.

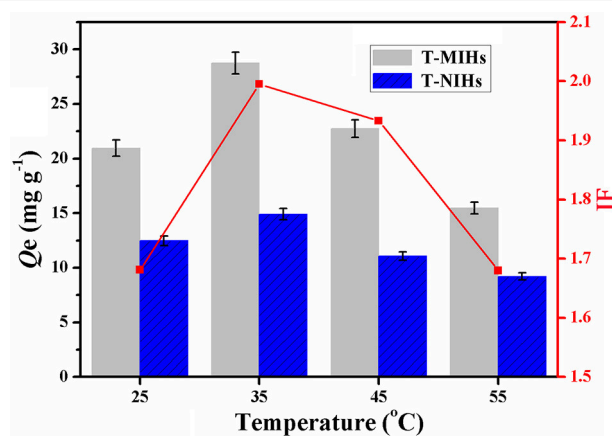


**FIGURE 6** | Effect of the temperature on adsorption capacity and the change curve of imprinting factor.

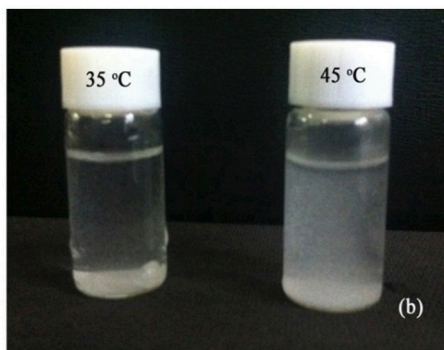
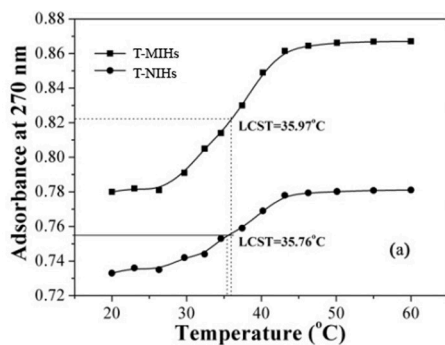


**FIGURE 4** | Absorbance change curve of T-MIHs and T-NIHs aqueous solution at various temperatures (a), dispersion photographs under 35 and  $45^{\circ}\text{C}$  (b).

$3,310\text{ cm}^{-1}$  could be attributed to the N-H stretching vibration of amide group (Pan et al., 2011b). Several vibration peaks were recorded at around  $1,653$ ,  $1,534$ , and  $1,387\text{ cm}^{-1}$ , which might attributed to amide C=O stretching and deformation of methyl groups on  $-\text{C}(\text{CH}_3)_2$ , all characteristic of peaks of NIPAm (Tian and Yang, 2009). A strong adsorption band appeared at  $2,985\text{ cm}^{-1}$  assigned to N-H stretching vibration of MBA. Moreover, **Figure 2** exhibited a broad adsorption band during  $3,100\text{--}3,000\text{ cm}^{-1}$ , which was assigned to the C-H stretching vibration of AM (Xin et al., 2008).

## Thermo-Gravimetric Analysis

The thermo-gravimetric analysis (TGA) curves of T-MIHs and T-NIHs are shown in **Figure 3**. When temperature is lower than  $300^\circ\text{C}$ , TGA curves showed a slight mass loss, which was due to the evaporation of residual water. Subsequently, accompanied by the temperature increase to  $850^\circ\text{C}$ , both curves showed significant mass loss, which was  $86.43$  and  $84.60\%$  for T-MIHs and T-NIHs, respectively. At this stage, the mass loss is mainly due to the decomposition of polymers. There is a difference of  $1.83\%$  in the residual quality of T-MIHs and T-NIHs, which may because of the residual template molecules in T-MIHs. When the temperature exceeds  $850^\circ\text{C}$ , T-MIHs and T-NIHs residues quality had no obvious change. Thus, both T-MIHs and T-NIHs exhibited good thermal stability and could meet the need for practical application in water environment.

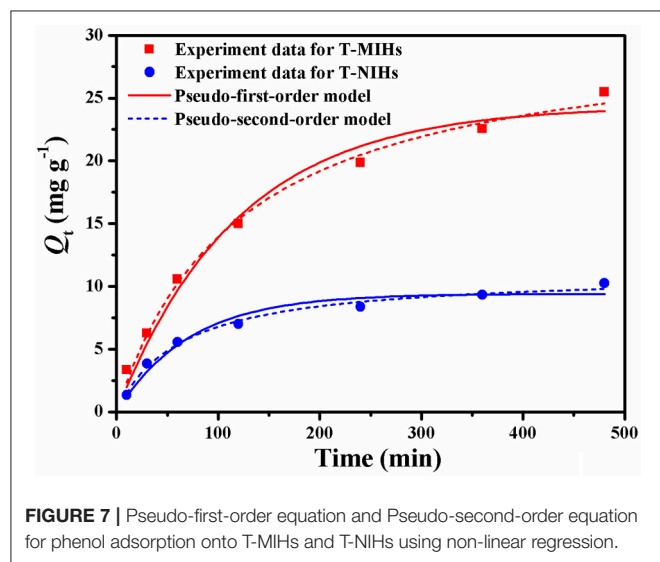


**FIGURE 7** | Pseudo-first-order equation and Pseudo-second-order equation for phenol adsorption onto T-MIHs and T-NIHs using non-linear regression.

## Thermoresponsive Property of Molecularly Imprinted Hydrogels

In order to test the temperature responsive effect, the LCST values were determined by monitoring the absorbance change of aqueous polymer solutions (Chang et al., 2009; Pan et al., 2011a). As shown in **Figure 4a**, the two curves showed similar trends, the LCST values were  $35.97$  and  $35.76^\circ\text{C}$ , respectively, and the results indicated that T-MIHs and T-NIHs have remarkable temperature responsive effect. Two types of functional groups, hydrophilic and hydrophobic, existed in PNIPAm at the same time. When the temperature is lower than LCST, water molecules interact with amide groups on the molecular chain of PNIPAm to form hydrogen bonds, under the action of hydrogen bonding, PNIPAm dissolved in the water. When the temperature is higher than LCST, the hydrogen bond is weakened and the

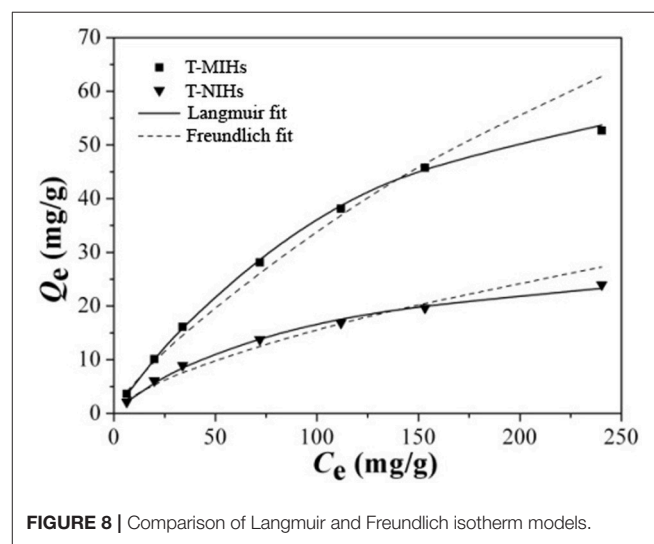


**FIGURE 8** | Comparison of Langmuir and Freundlich isotherm models.

**TABLE 2** | Adsorption isotherm constants at  $35^\circ\text{C}$ .

Isotherm models		T-MIHs	T-NIHs
Langmuir equation	$R^2$	0.993	0.991
	$Q_{m,c}$ (mg/g)	77.09	32.89
	$K_L$ (L/mg)	0.006	0.009
	$R_L$	0.38	0.28
Freundlich equation	$R^2$	0.984	0.977
	$K_F ((\text{mg g}^{-1})(1\text{ mg}^{-1})^{1/n})$	0.97	0.66
	$n$	1.30	1.51

**TABLE 1** | Kinetic constants for the Pseudo first-order equation and Pseudo second-order equation at  $35^\circ\text{C}$ .

Samples	Pseudo-first-order model				Pseudo-second-order model					
	$Q_{e,c1}$	$k_1$	$R^2$	$AIC$	$Q_{e,c2}$	$k_2$	$R^2$	$AIC$	$h$	$t_{1/2}$
	(mg/g)	(L/min)			(mg/g)	(g/mg/min)			(mg/g/min)	(min)
T-MIHs	24.39	$8.42 \times 10^{-3}$	0.977	26.83	30.73	$2.70 \times 10^{-4}$	0.992	19.08	0.27	110.7
T-NIHs	9.403	$1.29 \times 10^{-2}$	0.957	17.59	11.07	$1.43 \times 10^{-3}$	0.988	8.742	0.20	56.44



hydrophobic functional group of PNIPAm is strengthened, resulting in the two-phase separation between PNIPAm polymer and water molecule (Xu et al., 2012). **Figure 4b** showed that when the temperature reached 35°C, we found that hydrogels were uniformly dispersed in the solution. The shape of the template molecular was well-consistent with that of imprinted cavity and, in this condition, the best adsorption effect will be achieved. As the temperature increased, the polymer showed a certain degree of shrinkage and aggregation (Wei et al., 2008).

### Effect of pH Value on Adsorption of Phenol

As the key factor in the adsorption study, pH can affect the performance of adsorption. The pH of the solution

affects the degree of ionization, and subsequently brings about a change in kinetics and equilibrium characteristics during the adsorption process (Yu et al., 2015b). In the experiment, 10 mg T-MIHs or T-NIHs was dispersed in 10 mL of solution which contains 100 mg L<sup>-1</sup> phenol. 1.0 mol L<sup>-1</sup> NH<sub>3</sub>·H<sub>2</sub>O and HCl solutions were used to adjust the initial pH value of solution, which was varied from 2.0 to 8.0. The studies were carried out on a thermostatic water bath at 25°C for 12 h. Then, the mixture was separated and the concentration of phenol in the supernatant was measured. The result was listed in **Figure 5**. As pH increased from 2.0 to 6.0, the adsorption capacity for T-MIHs and T-NIHs also increased significantly, and then declined in the pH range 6.0–8.0. Therefore, a pH of 6.0 was selected for further experiments.

### Thermally Modulated Adsorption of Phenol

The thermoresponsive character was demonstrated through static adsorption experiment. In temperature impact studies, 10 mg T-MIHs or T-NIHs was dispersed in 10 mL of solution which contains 100 mg L<sup>-1</sup> phenol (pH = 6.0). The reaction temperatures were controlled from 25 to 55°C. The studies were conducted in a thermostatic water bath at different temperatures for 12 h. The results were listed in **Figure 6**. As shown in **Figure 6**, the Q value reached the maximum value at 35°C. Such thermally modulated adsorption of phenol was closely related to thermoresponsive behavior of the imprinted hydrogels. When the temperatures reaches 35°C, as shown in **Figure 4b**, we found that hydrogel was uniformly dispersed in the solution. In this condition, the shape of the template phenol was well-consistent with that of the imprinted cavity, resulting in the best adsorption performance. Further increasing the temperature leads to some degrees of shrinkage and aggregation

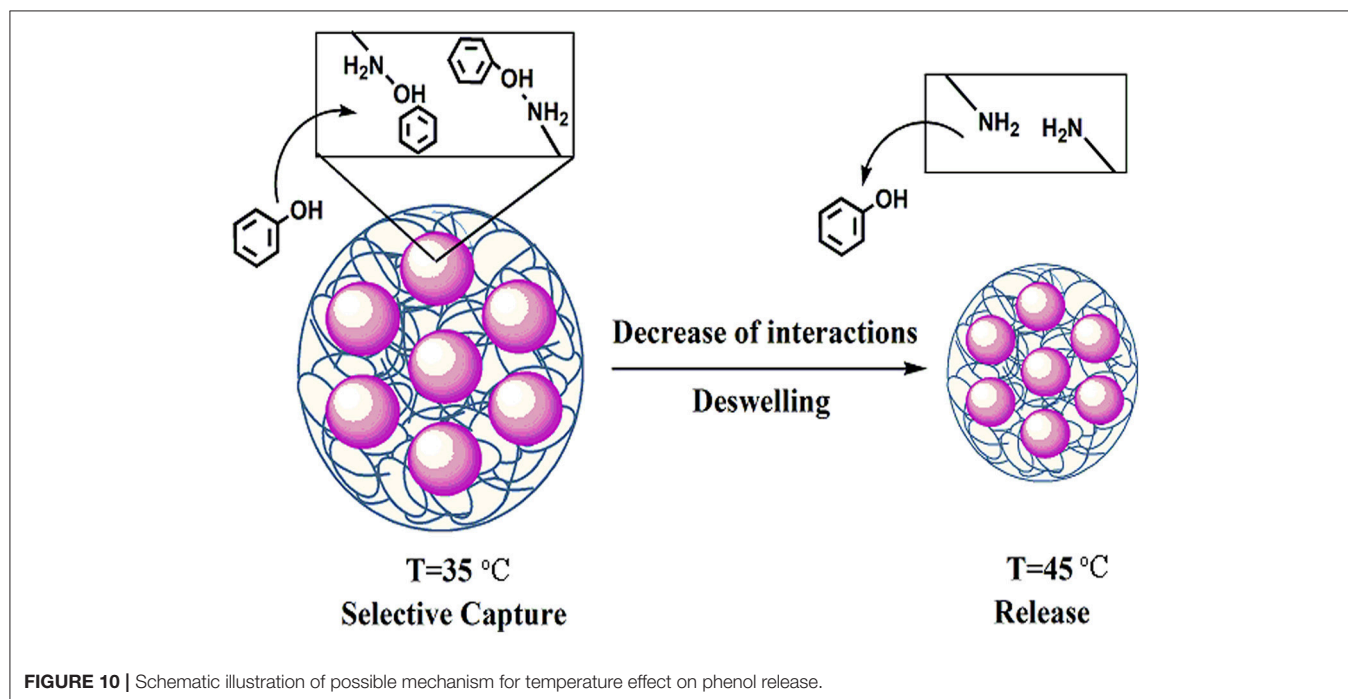
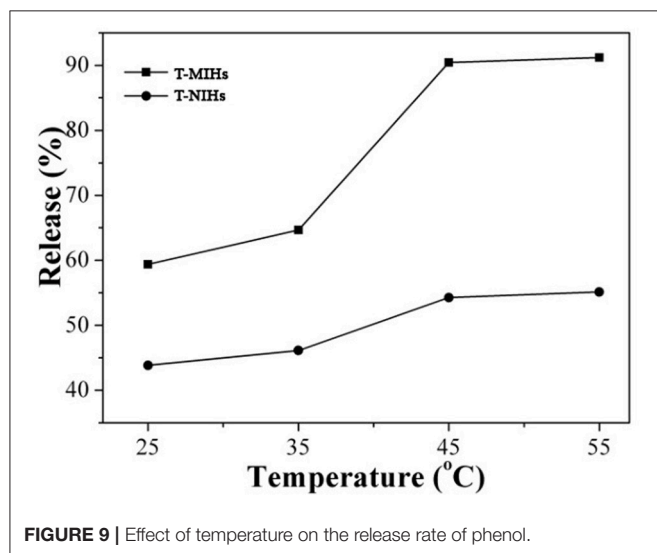


(Figure 4b), which reduced the accessibility of the active sites and further reduced the  $Q$ -value. For T-NIHs, the trend of the  $Q$ -value variation was same with the T-MIHs, but the adsorption ability was lower than that of T-MIHs. In addition, the IF value reached the maximum value at 35°C, which further demonstrated that the optimum temperature for phenol adsorption was 35°C.

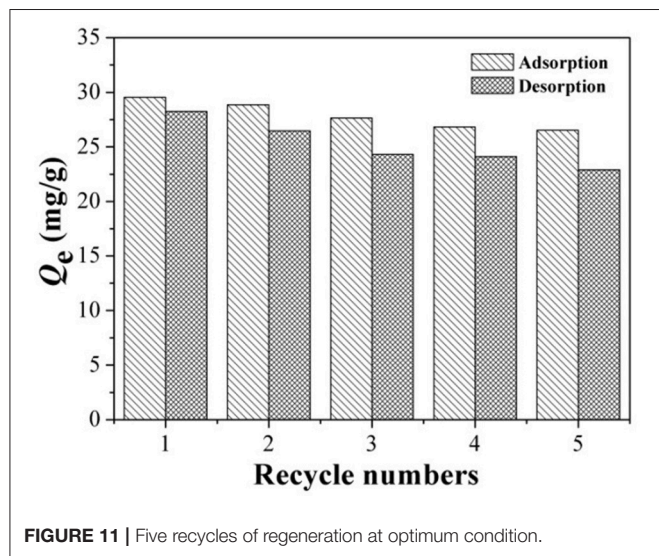
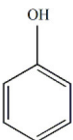
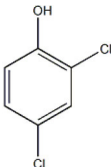
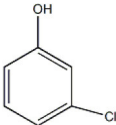
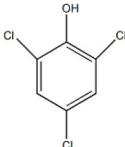


FIGURE 11 | Five recycles of regeneration at optimum condition.

TABLE 3 | Molar mass and molecular structures of the phenolic compounds.

Phenolic compounds	Molar mass (g/mol)	Structure
Phenol (template molecule)	94.11	
2,4-DCP (competition content)	163	
3-CP (competition content)	128.56	
2,4,6-TCP (competition content)	197.44	

## Adsorption and Release Properties of T-MIHs and T-NIHs

At the optimum adsorption temperature, the adsorption properties of T-MIHs and T-NIHs were investigated. Adsorption kinetics showed that, compared with T-NIHs, T-MIHs absorbed more phenol because of the stronger specific adsorption (Figure 7). For both T-MIHs and T-NIHs, the  $Q$  value increased significantly in the first 60 min and then reached equilibrium within 480 min. Aiming at the examination of the adsorption mechanism such as chemical reaction and mass transfer, pseudo first-order rate equation and pseudo second-order rate equation (Supporting Information, SI) were used to analyze the kinetic data, which were obtained from experiments.

According to Equations (3–8), the values of  $R^2$ ,  $k_1$ ,  $k_2$ ,  $h$ ,  $t_{1/2}$ , and  $Q_e$  were calculated and listed in Table 1. Based on data listed in Table 1, the adsorption of T-MIHs and T-NIHs followed pseudo second-order kinetics because of the favorable fit between calculated and experimental values of  $Q_e$  with the lower values of Akaike Information Criterion (AIC) for Pseudo-second-order kinetic model, suggesting that the former one was more reliable. Whereas, the experimental data was not well-fit for the pseudo first-order. This showed that chemical adsorption might be the rate limiting step in the adsorption process for phenol (Mazzotti, 2006).

A batch mode of static adsorption experiments were carried out to investigate the binding properties of phenol onto T-MIHs and T-NIHs. Adsorption equilibrium data obtained by experiments was fitted to the Langmuir and Freundlich isotherm models (SI). The two adsorption isotherm models are used to describe the equilibrium distribution of adsorbent between solution and adsorbent. Langmuir isotherm model is often used for the adsorption of monomolecular layer, while Freundlich isotherm model is often used for the adsorption of multi-molecular layer (Li et al., 2012a). The applicability of isotherm models to adsorption behavior is expressed by the correlation coefficient ( $R^2$ ). Table 2 lists the adsorption isotherm constants for T-MIHs and T-NIHs at optimum reaction temperature. Moreover, the regression curves of Langmuir and Freundlich isotherm models for phenol adsorption onto T-MIHs and T-NIHs are illustrated in Figure 8.

As it can be seen from the adsorption isotherms in Figure 8, with the concentration of phenol increasing from 10 to 240 mg mL<sup>-1</sup>, the  $Q$ -value for T-MIHs and T-NIHs increased significantly. Moreover, the  $Q$ -values of T-NIHs were all lower than those of T-MIHs due to the imprinted effect. The adsorption isotherm constants for T-MIHs and T-NIHs are shown in Table 2. Obviously, compared with Freundlich isotherm model, the correlation coefficient was more suitable for the Langmuir isotherm model. Moreover, T-MIHs/T-NIHs had good applicability for the Langmuir isotherm model, indicating monolayer molecular adsorption for T-MIHs/T-NIHs (Lin et al., 2014).

T-MIHs and T-NIHs with captured phenol were applied in subsequent release experiments. Figure 9 shows the released amounts of phenol after its release at different temperatures for 12 h. It can be seen that the release percentage of

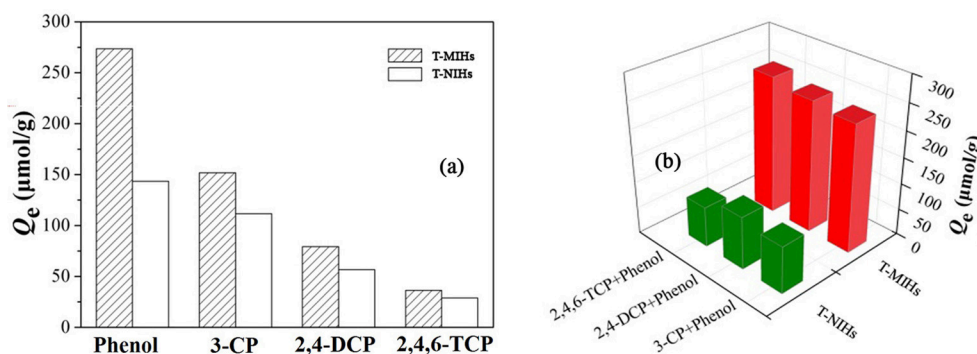


**FIGURE 12 |** Adsorption selectivity of phenol onto T-MIHs and T-NIHs in single (a) and dual (b) solute.

phenol gradually increased with the increasing temperature. For example, considering T-MIHs, the release rates of phenol at four temperatures are 59.37, 64.67, 90.45, and 91.21%, respectively. When the temperature exceeded  $45^{\circ}\text{C}$ , the release rate of absorbed phenol could reach 90%. The reason for this phenomenon could be that increased temperature made the T-MIHs/T-NIHs more hydrophobic and caused deswelling, resulting in the interactions between the hydrogels and phenol weakened, and the sites were too small to capture the template molecular, triggering the release of phenol, as shown in **Figure 10**. The results showed that the temperature sensitive property could be effectively applied in the treatment of pollutants, in which the target molecular could effectively switch adsorption and release by changing temperatures.

## Reusability

In order to verify the recycle and stability of the T-MIHs, five regeneration cycles were carried out under the same experiment conditions. Firstly, isothermal adsorption at 308 K was performed on T-MIHs. Subsequently, the mixture of acetic acid and methanol was used to elute the adsorbed phenol at 318 K. Ultimately, deionized ultrapure water washed the T-MIHs to neutral conditions for the next adsorption-desorption cycle. **Figure 11** shows the final results of five cycles of adsorption. After five regenerations, the loss of adsorption percentage for T-MIHs toward target molecular was around 6.78%, and the TGA curve of cycled sample was matched with that of fresh T-MIHs (as shown in Figure S3), demonstrating remarkable chemical and structure stability of T-MIHs.

## Selectivity Analysis of the T-MIHs

To measure the selectivity of T-MIHs, the recognition of phenol was compared with 2,4,6-TCP, 2,4-DCP and 3-CP, respectively. The molar mass and molecular structures of phenolic compounds are shown in **Table 3**. A series of static adsorption experiments were carried out in single and binary aqueous solutions, respectively. The initial solution concentration was  $100\text{ mg L}^{-1}$  and pH value was 6.0. Adsorption capacity of T-MIHs and T-NIHs for phenol in single and binary aqueous solutions is shown in **Figure 12**. As is shown in **Figure 12**, T-MIHs

possessed the best adsorption capacity to target molecular among the four adsorbents. The results further proved that T-MIHs possessed specific recognition for phenol. In binary aqueous solutions, due to the influence of competitive compounds, the adsorption capacity of T-MIHs and T-NIHs decreased slightly and, even so, T-MIHs still showed the specific adsorption for the target phenol. The two results above indicated that the selectivity of T-MIHs for phenol was still obvious. Here, acrylamide, N-isopropyl acrylamide and N,N-methylene double acrylamide were used as functional monomer, thermo-responsive monomer and cross-linker, respectively, to prepare imprinted polymers. Thus, the hydrogen-bonding interaction can be formed between phenolic hydroxyl groups of template molecule phenol and amino- (amide) groups from imprinted sites, the energy of which is between 25 and  $40\text{ kJ mol}^{-1}$ . Phenol, 2,4,6-TCP, 2,4-DCP and 3-CP are different in structure, size and functional groups, resulting in the different conformation memory of specific binding sites (Pan et al., 2013). Also, the size, sharpness and structure of imprinted sites provided a strong interaction.

## CONCLUSION

In this study, combining an imprinted technique and temperature response, molecularly imprinted hydrogels were successfully synthesized by suspension polymerization. A series of adsorption experiments indicated that T-MIHs performed well, for instance in selective recognition, excellent adsorption capacity and fast adsorption kinetics, and the target molecular could effectively switch adsorption and release by changing temperatures. We believe that the smart imprinting systems should be promoted at the forefront of MIHs, which possessed the stimulus-responsive recognition. This kind of material has great application potential for drug release, separation, protein recognition and so on.

## AUTHOR CONTRIBUTIONS

ZS: the complementary adsorption experiments and article revision. PY: study of adsorption mechanism. YD: material

preparation. YL: kinetic analysis. ZT: thermodynamic analysis. XY and RZ: characterization. YY: adsorption experiment.

## FUNDING

This work was financially supported by the National Natural Science Foundation of China (No. 21606099, No. 21878120, No. 21607013), Science and Technology Research Foundation of Jilin Province Department of

Education (No. JJKH20180782KJ, No. JJKH20180761KJ, No. JJKH20180785KJ, No. JJKH20170376KJ), Natural Science Foundation of Jilin Province (No. 20180623042TC).

## SUPPLEMENTARY MATERIAL

The Supplementary Material for this article can be found online at: <https://www.frontiersin.org/articles/10.3389/fchem.2018.00674/full#supplementary-material>

## REFERENCES

- Asmaly, H. A., Abussaud, B., Saleh, T. A., Laoui, T., Gupta, V. K., and Atieh, M. A. (2015). Adsorption of phenol on aluminum oxide impregnated fly ash. *Desalin. Water Treat.* 57, 6801–6808. doi: 10.1080/19443994.2015.1010238
- Chang, C., Wei, H., Feng, J., Wang, Z. C., Wu, X. J., Wu, D. Q., et al. (2009). Temperature and pH double responsive hybrid cross-linked micelles based on P (NIPAAm-co-MPMA) -b-P(DEA): RAFT synthesis and schizoprenic micellization. *Macromolecules* 42, 838–844. doi: 10.1021/ma900492v
- Díaz-Díaz, G., Diñeiro, Y., and Menéndez, M. I. (2011). Molecularly imprinted catalytic polymers with biomimetic chloroperoxidase activity. *Polymer* 52, 2468–2473. doi: 10.1016/j.polymer.2011.04.004
- Fang, L. J., Chen, S. J., Zhang, Y., and Zhang, H. Q. (2011). Azobenzene-containing molecularly imprinted polymer microspheres with photoresponsive template binding properties. *J. Mater. Chem.* 21, 2320–2329. doi: 10.1039/c0jm02898c
- Hao, L., Yang, H., and Lei, Z. L. (2012). Synthesis and properties of thermo-responsive macroporous PAM-co-PNIPAM microspheres. *Mater. Lett.* 70, 83–85. doi: 10.1016/j.matlet.2011.11.112
- Herrero-Hernández, E., Rodríguez-Gonzalo, E., Andrades, M. S., Sánchez-González, S., Carabias-Martínez, R. (2013). Occurrence of phenols and phenoxyacid herbicides in environmental waters using an imprinted polymer as a selective sorbent. *Sci. Total Environ.* 454, 299–306. doi: 10.1016/j.scitotenv.2013.03.029
- Li, N., Qi, L., Shen, Y., Qiao, J., and Chen, Y. (2014). Novel oligo(ethylene glycol)-based molecularly imprinted magnetic nanoparticles for thermally modulated capture and release of lysozyme. *ACS Appl. Mater. Interfaces* 6, 17289–17295. doi: 10.1021/am505427
- Li, S. J., Ge, Y., and Turner, A. P. F. (2011). A catalytic and positively thermosensitive molecularly imprinted polymer. *Adv. Funct. Mater.* 21, 1194–1200. doi: 10.1002/adfm.201002099
- Li, X., Pan, J., Dai, J., Dai, X., Ou, H., Xu, L., et al. (2012b). Removal of cefalexin using yeast surface-imprinted polymer prepared by atom transfer radical polymerization. *J. Sep. Sci.* 35, 2787–2795. doi: 10.1002/jssc.201200397
- Li, X. X., Pan, J. M., Dai, J. D., Dai, X. H., Xu, L. C., Wei, X., et al. (2012a). Surface molecular imprinting onto magnetic yeast composites via atom transfer radical polymerization for selective recognition of cefalexin. *Chem. Eng. J.* 198–199, 503–511. doi: 10.1016/j.cej.2012.05.106
- Li, Z. Y., Liu, Z. S., Zhang, Q. W., and Duan, H. Q. (2007). Chiral separation by (S)-naproxen imprinted monolithic column with mixed functional monomers. *Chinese Chem. Lett.* 18, 322–324. doi: 10.1016/j.ccl.2007.01.037
- Liang, R. N., Gao, Q., and Qin, W. (2012). Potentiometric sensor based on molecularly imprinted polymers for rapid determination of clenbuterol in pig urine. *Chinese J. Anal. Chem.* 40, 354–358. doi: 10.1016/S1872-2040(11)60535-5
- Lin, S., Song, Z. L., Che, G. B., Ren, A., Li, P., Liu, C. B., et al. (2014). Adsorption behavior of metal-organic frameworks for methylene blue from aqueous solution. *Micropor. Mesopor. Mat.* 193, 27–34. doi: 10.1016/j.micromeso.2014.03.004
- Liu, X. Y., Zhou, T., Du, Z. W., Wei, Z., and Zhang, J. H. (2011). Responsive wetting transition on superhydrophobic surfaces with sparsely grafted polymer brushes. *Soft Matter* 7, 1986–1993. doi: 10.1039/c0sm00682c
- Mazzotti, M. (2006). Equilibrium theory based design of simulated moving bed processes for a generalized Langmuir isotherm. *J. Chromatogr. A* 1126, 311–322. doi: 10.1016/j.chroma.2006.06.022
- Pan, J. M., Li, L. Z., Hang, H., Ou, H. X., Zhang, L., and Yan, Y. S. (2013). Study on the nonylphenol removal from aqueous solution using magnetic molecularly imprinted polymers based on fly-ash-cenospheres. *Chem. Eng. J.* 223, 824–832. doi: 10.1016/j.cej.2013.02.004
- Pan, J. M., Wang, B., Dai, J. D., Dai, J. D., Hang, H., Ou, H. X., et al. (2011a). Selective recognition of 2,4,5-trichlorophenol by temperature responsive and magnetic molecularly imprinted polymers based on halloysite nanotubes. *J. Mater. Chem.* 22, 3360–3369. doi: 10.1039/c1jm14825g
- Pan, J. M., Yao, H., Xu, L. C., Ou, H. X., and Yan, Y. S. (2011b). Selective recognition of 2,4,6-trichlorophenol by molecularly imprinted polymers based on magnetic halloysite nanotubes composites. *J. Phys. Chem. C* 115, 5440–5449. doi: 10.1021/jp111120x
- Pan, Y., Li, Z., Zhang, Z., Tong, X. S., and Li, H. (2016). Adsorptive removal of phenol from aqueous solution with zeolitic imidazolate framework-67. *J. Environ. Manage.* 169, 167–173. doi: 10.1016/j.jenvman.2015.12.030
- Plewa, A., Yusa, S., Szuwarzynski, M., Szczubialka, K., Morishima, Y., and Nowakowska, M. (2012). Molecularly imprinted hybrid adsorbents for adenine and adenosine-5'-triphosphate. *J. Med. Chem.* 55, 8712–8720. doi: 10.1021/jm300934v
- Tian, B. S., and Yang, C. (2009). Temperature-responsive nanocomposites based on mesoporous SBA-15 silica and PNIPAAm: synthesis and characterization. *J. Phys. Chem. C* 113, 4925–4931. doi: 10.1021/jp808534q
- Urraca, J. L., Moreno-Bondi, M. C., Hall, A. J., and Sellergren, B. (2007). Direct extraction of Penicillin G and derivatives from aqueous samples using a stoichiometrically imprinted polymer. *Anal. Chem.* 79, 695–701. doi: 10.1021/ac061622r
- Valero-Navarro, A., Gómez-Romero, M., Fernández-Sánchez, J. F., Cormack, P. A. G., Segura-Carretero, A., and Fernández-Gutiérrez, A. (2011). Synthesis of caffeic acid molecularly imprinted polymer microspheres and high-performance liquid chromatography evaluation of their sorption properties. *J. Chromatogr. A* 1218, 7289–7296. doi: 10.1016/j.jlchroma.2011.08.043
- Wang, C., Javadi, A., Ghaffari, M., and Gong, S. Q. (2010). A pH-sensitive molecularly imprinted nanospheres/hydrogel composite as a coating for implantable biosensors. *Biomaterials* 31, 4944–4951. doi: 10.1016/j.biomaterials.2010.02.073
- Wang, J. X., Pan, J. M., Yin, Y. J., Wu, R. R., Dai, X. H., Dai, J. D., et al. (2015). Thermo-responsive and magnetic molecularly imprinted Fe<sub>3</sub>O<sub>4</sub>@carbon nanospheres for selective adsorption and controlled release of 2,4,5-trichlorophenol. *J. Ind. Eng. Chem.* 25, 321–328. doi: 10.1016/j.jiec.2014.11.011
- Wang, X., Pan, J. M., Guan, W., Dai, J. D., Zou, H., Yan, Y. S., et al. (2011). Selective removal of 3-chlorophenol from aqueous solution using surface molecularly imprinted microspheres. *J. Chem. Eng. Data* 56, 2793–2801. doi: 10.1021/je101275e
- Wang, Y. X., Liu, Q. M., Rong, F., Fu, D. G., Wang, Y. X., Liu, Q. M., et al. (2011). A facile method for grafting of bisphenol A imprinted polymer shells onto poly(divinylbenzene) microspheres through precipitation polymerization. *Appl. Surf. Sci.* 257, 6704–6710. doi: 10.1016/j.apsusc.2011.02.105
- Wei, H., Cheng, C., Chang, C., Chen, W. Q., Cheng, S. X., Zhang, X. Z., et al. (2008). Synthesis and applications of shell cross-linked thermoresponsive



- hybrid micelles based on poly (N-isopropylacrylamide-co-3-(trimethoxysilyl) propyl methacrylate)-b-poly(methyl methacrylate). *Langmuir* 24, 4564–4570. doi: 10.1021/la703320h
- Xin, Z., Yang, R., Tang, X., and Zheng, L. Y. (2008). Part 1: characterization of solid dispersions of nimodipine prepared by hot-melt extrusion. *Drug Dev. Ind. Pharm.* 26, 791–802. doi: 10.1080/03639040601050213
- Xu, L., Pan, J., Dai, J., Li, X., Hang, H., Cao, Z., et al. (2012). Preparation of thermal-responsive magnetic molecularly imprinted polymers for selective removal of antibiotics from aqueous solution. *J. Hazard. Mater.* 233–234, 48–56. doi: 10.1016/j.jhazmat.2012.06.056
- Xu, S. F., Li, J. H., and Chen, L. X. (2011). Molecularly imprinted core-shell nanoparticles for determination of trace atrazine by reversible addition-fragmentation chain transfer surface imprinting. *J. Mater. Chem.* 21, 4346–4351. doi: 10.1039/C0JM03593A
- Yu, P., Sun, Q. L., Li, J. F., Tan, Z. J., Pan, J. M., and Yan, Y. S. (2015a). Preparation and characterization of magnetic molecularly imprinted microspheres for highly effective adsorption of 2,4,6-trichlorophenol from aqueous solutions. *Korean J. Chem. Eng.* 32, 767–776. doi: 10.1007/s11814-014-0251-8
- Yu, P., Sun, Q. L., Li, J. F., Tan, Z. J., Yan, Y. S., and Li, C. X. (2015b). Magnetic imprinted nanomicrosphere attached to the surface of bacillus using Miniemulsion polymerization for selective recognition of 2,4,6-trichlorophenol from aqueous solutions. *J. Ind. Eng. Chem.* 29, 349–358. doi: 10.1016/j.jiec.2015.04.014
- Yu, P., Sun, Q. L., Li, J. F., Tan, Z. J., Yan, Y. S., and Li, C. X. (2015c). Selective removal of 2,4-dichlorophenol in aqueous solutions by nanoparticles modified yeast using miniemulsion imprinting polymerization. *J. Environ. Chem. Eng.* 3, 797–806. doi: 10.1016/j.jece.2015.03.029
- Zayats, M., Kanwar, M., Ostermeier, M., and Searson, P. C. (2011). Molecular imprinting of maltose binding protein: tuning protein recognition at the molecular level. *Macromolecules* 44, 3966–3972. doi: 10.1021/ma200355j
- Zhang, Y., Liu, R., Hu, Y., and Li, G. (2009). Microwave heating in preparation of magnetic molecularly imprinted polymer beads for trace triazines analysis in complicated samples. *Anal. Chem.* 81, 967–976. doi: 10.1021/ac8018262

**Conflict of Interest Statement:** The authors declare that the research was conducted in the absence of any commercial or financial relationships that could be construed as a potential conflict of interest.

Copyright © 2019 Si, Yu, Dong, Lu, Tan, Yu, Zhao and Yan. This is an open-access article distributed under the terms of the Creative Commons Attribution License (CC BY). The use, distribution or reproduction in other forums is permitted, provided the original author(s) and the copyright owner(s) are credited and that the original publication in this journal is cited, in accordance with accepted academic practice. No use, distribution or reproduction is permitted which does not comply with these terms.



# Porous Surface Films With Tunable Morphologies and Hydrophobic Properties Based on Block Copolymer Under the Effects of Thermal Annealing

Guadalupe del C. Pizarro<sup>1\*</sup>, Oscar G. Marambio<sup>1</sup>, Manuel Jeria-Orell<sup>1</sup>, Diego P. Oyarzún<sup>2</sup>, Rudy Martín-Trasanco<sup>2</sup> and Julio Sánchez<sup>3</sup>

<sup>1</sup> Departamento de Química, Universidad Tecnológica Metropolitana, Santiago, Chile, <sup>2</sup> Facultad de Ciencias Exactas, Center of Applied Nanosciences, Universidad Andrés Bello, Santiago, Chile, <sup>3</sup> Departamento de Ciencias del Ambiente, Facultad de Química y Biología, Universidad de Santiago de Chile, Santiago, Chile

## OPEN ACCESS

### Edited by:

Giuseppe Mensitieri,  
University of Naples Federico II, Italy

### Reviewed by:

Arnab Rudra,  
Koch Institute for Integrative Cancer  
Research at MIT, United States  
Ioannis A. Kartsonakis,  
National Technical University of  
Athens, Greece

### \*Correspondence:

Guadalupe del C. Pizarro  
gpizarro@utem.cl

### Specialty section:

This article was submitted to  
Polymer Chemistry,  
a section of the journal  
Frontiers in Chemistry

**Received:** 13 September 2018

**Accepted:** 07 March 2019

**Published:** 28 March 2019

### Citation:

Pizarro GdC, Marambio OG,  
Jeria-Orell M, Oyarzún DP,  
Martín-Trasanco R and Sánchez J  
(2019) Porous Surface Films With  
Tunable Morphologies and  
Hydrophobic Properties Based on  
Block Copolymer Under the Effects of  
Thermal Annealing.  
Front. Chem. 7:181.  
doi: 10.3389/fchem.2019.00181

The fabrication of porous-structured polymer films with patterned surface structures has recently attracted increased interest within the material science field. In this work, a series of microstructure scale patterned polymer films were obtained via breath figure methods (BF) with hydrophobic surface films based on self-assembled diblock copolymers by atom-transfer radical polymerization (ATRP). The surface characteristics and morphological properties, pore size, roughness, thickness, and wettability of the block copolymer films was studied in response to variation of the hydrophilic co-monomer structures. A significant improvement of the quality and order of the hydrophobic films was observed in response to thermal annealing and a consequent optimization of the assembly process.

**Keywords:** controlled radical polymerization, self-assembly diblock copolymers, thermal behavior, morphological surface characteristic, hydrophobic surfaces, self-assembled copolymers, porous films, surface morphology

## INTRODUCTION

Block copolymers provide the perfect platform for fabricating novel microstructured materials for advanced technologies, for example bio-related materials (Lai et al., 2011; Pizarro et al., 2016). Additionally, these materials are considered very attractive for use in the synthesis of functional microstructures (Kim et al., 2007; Oz et al., 2008; Wen et al., 2008; Tobis et al., 2010; Zhang et al., 2010; Yao et al., 2011). Within such fields, polymer domain size, separation, and degree of order are used to identify the impact of the different process parameters in order to achieve optimization of the self-assembly process (Guarini et al., 2002). The morphology and domain size are generally controlled by adjusting individual block lengths, while copolymer molecular weights define the absolute template dimensions (Shirtcliffe et al., 2011; Cardoso et al., 2015; Hong et al., 2016). Moreover, recent studies have demonstrated that it is possible to obtain superhydrophobic surfaces by tuning the roughness and morphology of the co-polymer block surface (Wu et al., 2016). Several superhydrophobic surfaces have been obtained on hydrophilic materials by inducing an adequate

roughness (Hosono et al., 2005; Zhu et al., 2006; Cao et al., 2007; Karlsson et al., 2010; Celia et al., 2013). The literature reveals the great interest for fundamental research and practical applications in these topics (Lai et al., 2011; Shirtcliffe et al., 2011; Yao et al., 2011; Kumar et al., 2015).

In this work we report the preparation of block copolymer films with varying structures. This was achieved by inducing changes to the structure and morphology of hydrophilic co-monomers via template processing and thermal annealing processes. It is well known that the properties of film surfaces strongly depend on uniformity at the micro/nanometer-scale (i.e., the structural domains) and on the hierarchical structures constituted by these domains. Both factors often play the main role within the desired application. The micro-structured porous films prepared herein may constitute new materials for potential application in biomedicine; for example as support for cell growth with biological purposes. Additionally, the hydrophilic domains composed by carboxylic acid groups should serve as 3D-scaffolds for further chemical modifications which would hold further potential within such fields as catalysis and gas/chemical sensors (Phillip et al., 2010; Nunes et al., 2011; Hilke et al., 2013; Baettig et al., 2017).

In this article, we specifically report a series of experiments in which we systematically varied template processing parameters in order to understand their influence on the self-assembly process. Additionally, we investigate the effect of thermal annealing on the control the uniformity of the films, maintaining the thickness of the films and molecular weight practically constant. The block copolymers containing different block units are expected to produce self-assembled microstructures with tunable morphology giving porous and rough surface films. Subsequently, the wettability of the porous polymer films was also investigated.

The control over the copolymer structure is crucially important to the preparation of porous structured films. For this reason, atom-transfer radical polymerization (ATRP) was used. The ATRP technique is more versatile than other polymerization methods such as synthetic route based on anionic and cationic polymerizations. For the latter, rigorous operation conditions are required and the reaction is limited to certain types of monomers. On the other hand, ATRP is very attractive because of its tolerance to impurities, compatibility with a wide range of monomers, and relatively mild polymerization conditions (Wang and Matyjaszewski, 1995; Coca et al., 1998; Huang et al., 2012).

The block copolymers were prepared using a ATRP technique based on polystyrene (PS) (first block) and the hydrophilic co-monomers dimethyl allylmalonate (DMM), dimethyl itaconate (DMI), and tert-butyl acrylate (tBA) forming the second block. The block copolymers were characterized using size exclusion chromatography (SEC), FT-IR, Raman, and  $^1\text{H}$ -NMR spectroscopy. Thermal analyses were conducted by TGA and DSC. Subsequently, the porous polymer films were prepared on glass substrates under controlled experimental conditions. The surface morphologies of the polymer porous films were characterized with scanning electron microscopy (SEM) and atomic force microscopy (AFM), the hydrophilicity of the surface was observed via static water

contact angle (WCA). Finally, the film thickness was obtained via ellipsometry.

## EXPERIMENTAL DETAILS

### Materials

Copper(I) bromide (CuBr, 98%) was supplied by Sigma-Aldrich and was further purified with repeated stirring overnight in acetone at room temperature. The solid was washed with ethanol and diethylether prior to drying at 50°C under vacuum for 24 h. Benzoyl peroxide (BPO, 75% remainder water), 2,2-bipyridine (BPY, 99%) and tetrabutylammonium fluoride (1.0 N in THF) were purchased from Sigma-Aldrich and were used as received. Styrene (Sigma-Aldrich Chemicals) was washed with 5% NaOH aqueous solution and was then distilled under reduced pressure prior to use. All other reagents and solvents were analytical grade and were utilized as received: Dimethyl allylmalonate (DMM), dimethyl itaconate (DMI), and tert-butyl acrylate (tBA) (Sigma-Aldrich, 99%).

### Instrumentation and Equipments

$^1\text{H}$ -NMR spectra were recorded in solution using a Bruker AC 250 (Bruker, Karlsruhe, Germany) spectrometer at room temperature with deuterated dimethylsulfoxide ( $\text{DMSO}-d_6$ , 99.8%) and deuterated chloroform ( $\text{CDCl}_3$ ), as solvent. FT-IR spectra were performed using a Bruker Vector 22 (Bruker Optics GmbH, Inc., Ettlingen, Germany). The molecular weights [number average ( $M_n$ ) and weight average ( $M_w$ )], and the molecular weight distribution (polydispersity,  $M_w/M_n$ ) of the polymers were determined by size exclusion chromatography (SEC) using a Shimadzu LC 20 instrument equipped with RI detectors with DMF as the solvent (flow rate: 1.0 mL/min). The structural and vibrational properties of the copolymer films were characterized using Raman spectroscopy with a LabRam 010 instrument from ISA equipped with a 5.5 mW, 632.8 nm He-Ne laser without a filter. The Raman microscope used back-scattering geometry, where the incident beam is linearly polarized at a 500:1 ratio. The objective of the microscope lens was an Olympus Mplan 100x (numerical aperture 0.9). The optical properties were examined by UV-Vis absorption and fluorescence emission spectra. The absorption spectra of the films were recorded at 25°C between 250 and 700 nm using a Perkin Elmer Lambda 35 spectrophotometer. Thermal studies were recorded using a Star System 1 thermogravimetric analyzer (TGA) at a heating rate of 10°C/min. The morphological properties of the self-assembled block copolymers were examined by SEM, and AFM. The SEM was a model LEO 1420VP with a 100  $\mu\text{A}$  beam current and a working distance of 12–14 mm. The microscope was operated at high vacuum (system vacuum  $\sim 10^{-6}$  mbar and chamber  $10^{-3}$  mbar). The surface morphology of the copolymer porous films was characterized by AFM using Nanonics MultiView MV1000. In AFM measurements, n-type silicon cantilevers ( $f_{1/4}$  37.2 kHz;  $k_{1/4}$  0.01–0.60 N/m; tip radius 10 nm) in contact mode or optical fiber cantilevers were employed. Statistical analysis of the images obtained was performed using image processing software Gwyddion 2.37. The powder polymer was dissolved in THF and cast on glass slides

**TABLE 1** | Experimental conditions and results of amphiphilic block copolymers.

Samples	$Mn^a$ (theo)/10 <sup>3</sup> g mol <sup>-1</sup>	$Mn^b$ (SEC)/10 <sup>3</sup> g mol <sup>-1</sup>	$\bar{D} = Mw/Mn$
PS	10.4	11.7	1.13
PS- <i>b</i> -PAA	13.9	14.8	1.20
PS- <i>b</i> -PIA	14.9	16.3	1.10
PS- <i>b</i> -PAMA	14.0	14.1	1.22

<sup>a</sup>Theoretical number average molar mass.<sup>b</sup> $Mn$  was determined from SEC in THF.

using a spin coating technique with rotation velocity ramps of 500 rpm for approximately 10 s and 1,600 rpm for ~10 s. A KW-4A spin coater (Chemat Scientific), coupled with an oil free vacuum pump (Rocker Chemker 410), was utilized for deposit of the copolymer solutions on glass substrate. Contact angle measurements were performed in a Ramé-hart model 250 (p/n 250-U1) standard goniometer/tensiometer using a sessile drop on drop method over the solid substrate. A Multi-angle laser ellipsometer model SE 400adv (SENTECH Instrument GmbH) was used to perform optical measurements; He-Ne laser ( $\lambda = 633$  nm) in PCSA null configuration which was used to determine the film thickness. The angle of incidence of the laser beam was 60.5° with respect to the normal sample.

## Synthesis and Characterization of Macroinitiator

The synthesis of the PS was carried out according to the literature (Beers et al., 1999; Teodorescu et al., 2000; Min et al., 2005). The styrene and the catalyst system [BPO]:[CuBr]:[BPy] at a mole ratio of 100:1:1/2 were added into a polymerization flask under nitrogen gas. The resulting polymer was precipitated into methanol, and then the product was dried at 60°C under vacuum to a constant weight (yield: ~80%). The macroinitiator was obtained with a narrow polydispersity index ( $\bar{D} = 1.13$ ). Experimental data of the PS-Br is presented in **Table 1**. The <sup>1</sup>H-NMR spectra ( $\delta$  ppm) of PS showed the signals at 1.42 [2H, -CH<sub>2</sub> from the backbone]; 1.86-1H, >CH-Ar side chain, respectively, from S] and 6.60 [2H, m, H-Ar], at 7.34 [3H, s, H-Ar]. The FT-IR spectra exhibited characteristic absorption bands at 3,026 cm<sup>-1</sup> [ $\nu$ (CH, CH<sub>2</sub> and CH aromatic)]; 2,921 cm<sup>-1</sup> [ $\nu$ (CH, CH<sub>2</sub>)]; 1,943-1,721 cm<sup>-1</sup> [ $\nu$ (aromatic overtone)]; 1,600 cm<sup>-1</sup> (tension C-C, aromatic ring) and 1,448 cm<sup>-1</sup> [ $\nu$ (flexion -C-H, CH<sub>2</sub>)]; 756 and 697 cm<sup>-1</sup> [ $\nu$ (flexion mono substitute aromatic ring)].

## Synthesis of the Block Copolymers

The amphiphilic block copolymers based on PS with the acrylic acid (AA), itaconic acid (IA), and allylmalonic acid (AMA) blocks were obtained via ATRP using CuBr/BPy as the catalyst system with the co-monomers DMM/DMI/tBA in a molar ratio of 1/1/2/100 forming first the precursors poly(styrene-*b*-tert-butylmethacrylate) PS-*b*-PtBA; poly(styrene-*b*-dimethylallylmalonate) PS-*b*-PDMM and poly(styrene-*b*-dimethylitaconate) PS-*b*-PDMI and then the amphiphilic block copolymers PS-*b*-PAA, PS-*b*-PIA. Subsequently PS-*b*-PAMA

were obtained, with a molecular weight approximately between 14,000 and 16,500 Da, see **Table 1** and **Scheme 1**. This was performed in accordance with similar reported procedures (Coca et al., 1998; Hamley, 1998; Beers et al., 1999; Teodorescu et al., 2000; Min et al., 2005; Pizarro et al., 2013, 2015).

## Procedure

The synthesis of PS-*b*-PDMM block copolymer was carried out with the PS-Br/CuBr/BPy/co-monomers in a mole ratio of 1/1/2/100 (Coca et al., 1998; Pizarro et al., 2013). First, 0.1581 mmol of macroinitiator, assuming the molar mass of PS is  $Mn = 11,701$  Da, was added to a polymerization flask and dissolved in 3 mL of THF. Subsequently, 15.81 mmol of DMM monomer and 0.3162 mmol of ligand BPy were then added under vigorous stirring at room temperature. Then, the mixture was purged with liquid nitrogen. While stirring at 25°C for 20 min, 0.158 mmol of CuBr was added to the system and placed in an oil bath at 85°C for 4 h. After reaction, the resulting PS-*b*-PDMM, was dissolved in THF and repeatedly precipitated into methanol and then dried at 60°C under vacuum up to constant weight to obtain the final product (yield: ~60%). Similar procedures were carried out for the PS-*b*-PtBA and PS-*b*-PDMI. A series of block copolymers, with narrow dispersity ( $\bar{D} = 1.11$ -1.23), were obtained by acidic hydrolysis of the alkyl ester linkages, obtaining the block copolymers with assembling behavior, see **Table 1** and **Scheme 1**. Similar polydispersity indexes were reported elsewhere (Ashford et al., 1999; Davis et al., 2000; Wang et al., 2000; Ke et al., 2010).

## Preparation of the Samples for Morphological Study

Approximately 3 mg of polymer was stirred in 1 mL of solvent (THF). The resultant solution was cast onto a glass substrate. The porous films were usually obtained within 30 min due to the high solvent volatility. Subsequently, the samples were heated at 120°C for 2 h.

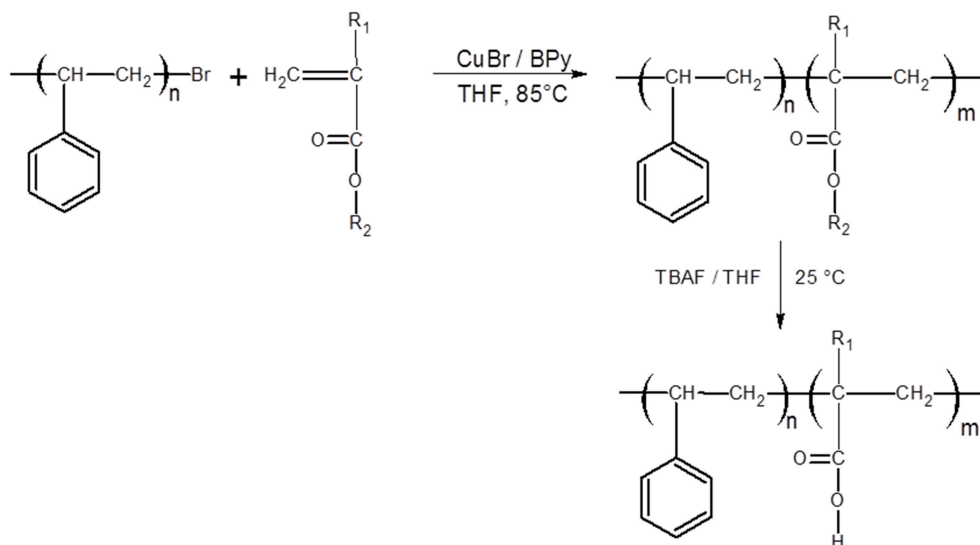
## RESULTS AND DISCUSSION

The block copolymerization based on polystyrene with tert-butyl acrylate (tBA), has been reported previously (Coca et al., 1998; Beers et al., 1999; Teodorescu et al., 2000; Min et al., 2005; Pizarro et al., 2013, 2015; Yu et al., 2016), however block copolymers with dimethyl allylmalonate (DMM), and dimethyl itaconate (DMI) as specific monomers were used. To the best of our knowledge, block copolymers with DMM and DMI monomers have not yet been reported. The PS-*b*-PtBA was taken as comparative model.

## Characterization of the Block Copolymers

The block copolymers were soluble in chloroform, acetone, DMF, and DMSO. The <sup>1</sup>H NMR spectra (400 Hz, CDCl<sub>3</sub>,  $\delta$  ppm) for PS-*b*-PDMM block copolymer (as an example), clearly shows resonance signals at ( $\delta$ , ppm): **7.20** [3H, s (wide), H-Ar]; **6.60** [2H, m, H-Ar]; **3.75** [6H, s, -O-CH<sub>3</sub>]; **3.60** [1H, s, >CH-]; **2.60** [2H, s, -CH<sub>2</sub>-]; **1.90** [1H, s (wide), >CH-Ar]; **1.42** [5H, s (wide), >CH-, -CH<sub>2</sub>-], see **Figure 1**. The <sup>1</sup>H NMR spectra (400 Hz, CDCl<sub>3</sub>,  $\delta$  ppm) for the PS-*b*-PAMA block copolymer





**SCHEME 1** | Structures of the self-assembled block copolymers: PS-*b*-PAA; PS-*b*-PIA; and PS-*b*-PAMA were obtained from its precursors by hydrolysis procedure, respectively.

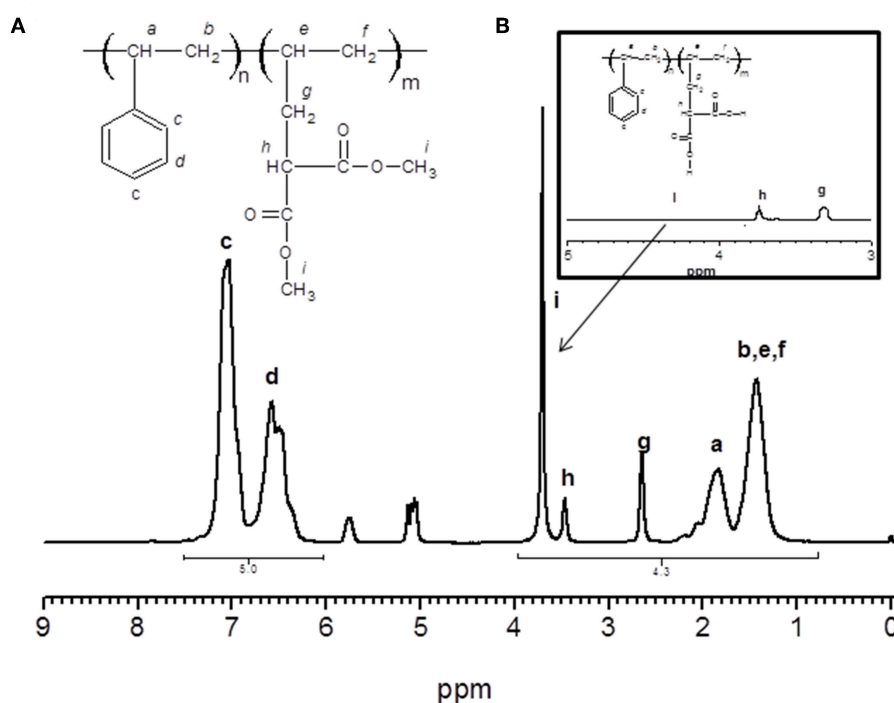


**FIGURE 1** | (A,B)  $^1\text{H}$ -NMR spectra of PS-*b*-DMM and PS-*b*-PAMA ( $\text{CDCl}_3$ ).

(as an example), shows the same signals, except the signal of the hydrolyzed block copolymer which shows a decrease in signal intensity at 3.5–3.6 ppm which corresponds to the percent hydrolysis of the alkyl ester—indicating the formation of -COOH groups. The hydrolysis procedure was realized by treatment with tetrabutylammonium fluoride [TBAF,  $(\text{C}_4\text{H}_9)_4\text{NF}$ ] as described in the literature (Hamley, 1998), yield in weight, ~80%.

## Raman Analysis of the Copolymers

Raman spectra (see **Figure 2**) exhibited a strong peak at 2,910–3,050  $\text{cm}^{-1}$  assigned to the aromatic protons (C–H stretching in plane bending), and a band of low intensity at 1,721  $\text{cm}^{-1}$  assigned to C=O (stretching). The band at 1,451  $\text{cm}^{-1}$  was assigned to alkenes (–CH bending). The band at 1,189  $\text{cm}^{-1}$  was assigned to C–O stretching of ester groups. A strong signal at 998

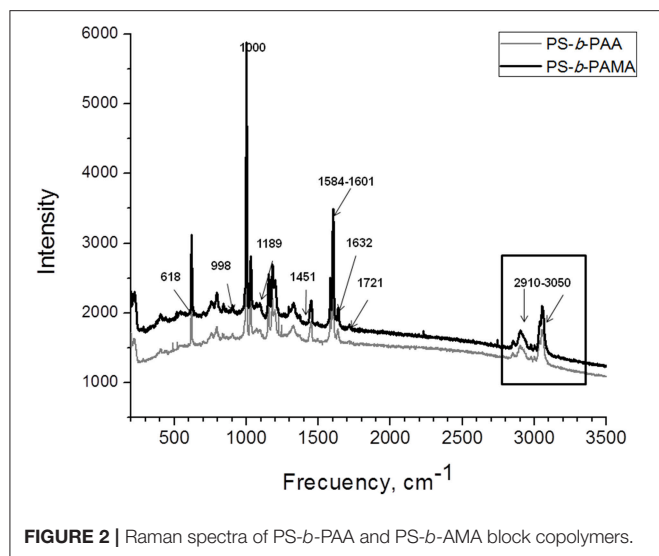


**FIGURE 2 |** Raman spectra of PS-*b*-PAA and PS-*b*-PAMA block copolymers.

$\text{cm}^{-1}$  was assigned to C–C aromatic (stretching), and the band at  $618\text{ cm}^{-1}$  was assigned to C–H aromatic (stretching out of plane in opposite direction).

## Thermal Studies and Optical Properties

TGA was employed to evaluate the effect of hydrophilic block on the thermal decomposition temperature (TDT) of the diblock copolymers. The TGA curves in the **Figure 3A** exhibit three decomposition curves in one-step; for PS-*b*-PAA and PS-*b*-PIA. The resulting block copolymers have an extrapolated thermal decomposition temperature (TDT) from 380 to  $388^\circ\text{C}$ , when decomposition of the backbone chain occurs; except for the case of the PS-*b*-PAMA block copolymers which exhibit a weight loss approximately of 10% at  $400^\circ\text{C}$ , see **Figure 3A**.

The optical properties of the material exhibited one characteristic band at 260 nm (see **Figure 3B**). This intense absorption band was attributed to the  $\pi$ - $\pi^*$  transition due to electron delocalization in the aromatic ring (inter-molecular transfer change) of the first block (PS). The fluorescence emission spectra of the PS-*b*-PAMA block copolymers exhibited a weak band at 525 nm (green luminescence emission). The  $\pi$ - $\pi^*$  transition is assigned to the interactions between neighboring –COOH functional groups in these polar co-monomers and also the distance between –COOH groups. Transparent materials with high UV absorption can be prepared using these block copolymer as polymeric matrices.

## Morphological Characterization of the Film

In this work, all samples were compared considering similar molecular weight (14,000–16,500 Da) and similar film thicknesses. The morphological images were obtained by SEM and AFM using the constant force method (see **Figures 4a–f**). The films showed a large distribution of elongated pore sizes with varying pore spacing. The PS-*b*-AA block copolymer samples displayed smaller pore diameter size (from  $\sim 1.0$  to  $2.5\text{ }\mu\text{m}$ ) than the PS-*b*-PIA samples which exhibited pore diameter size

**TABLE 2 |** Thickness and pore diameter and pore depth of thin porous polymer films.

Samples	Thickness of the films(nm)	Pore diameter (nm)	Pore depth (nm)
PS- <i>b</i> -PAA*	$2,391 \pm 20$	$1,236 \pm 55$	$2,210 \pm 61$
PS- <i>b</i> -PIA*	$2,362 \pm 16$	$2,849 \pm 50$	$2,050 \pm 40$
PS- <i>b</i> -PAMA*	$2,224 \pm 25$	$4,100 \pm 140$	$2,150 \pm 50$

\*C = 3 mg/mL (THF); thickness of the films was obtained using ellipsometry, pore depth, and pore diameter size (maximum values) were obtained by AFM.

ranging between  $\sim 2.5$  and  $4.0\text{ }\mu\text{m}$ . In addition, the PS-*b*-PAMA block copolymer exhibited a differing surface morphology; a rough structure with straight cylinder-like morphology was observed for this case (see **Figures 4a,c,e**). This different behavior was attributed mainly to the choice of monomer, where the phase separation can occur at slower rates for PS-*b*-AMA and PS-*b*-PIA block copolymer systems. The AFM images showed that the block copolymers tend to self-assemble due to their amphiphilic characteristics, displaying a rough surface with a pore diameter size ranging from  $\sim 1.0$  to  $4.0\text{ }\mu\text{m}$  and depth from  $\sim 2.1$  to  $2.2\text{ }\mu\text{m}$ . The difference in the morphologies is attributed to several factors that affect the phase separation such as the nature of monomers, copolymer composition, molecular size, and molecular configuration (Hamley, 1998). The results of the film thickness and depth were obtained by ellipsometry, see **Table 2**.

## Morphological Properties Under Annealing Process

Subsequently, for the PS-*b*-PIA and PS-*b*-PAMA films, the effect of thermal annealing on the self-assembly process was explored due to its low degree of porous uniformity encountered. The film thickness for the block copolymers was controlled by maintaining constant spin speeds and solution concentrations. The block copolymer films were annealed at  $120^\circ\text{C}$  for 2 h. An important effect on the resulting morphological quality was thus observed which resulted in a high degree of uniformity of the pores (see **Figure 4**). This change was attributed to the experimental procedure being performed at temperatures above the glass-transition temperature ( $T_g = 98.3^\circ\text{C}$  and  $94.3^\circ\text{C}$ ), which favored the speed of spontaneous self-assembly for PS-*b*-PIA and PS-*b*-PAMA block copolymers which improved the quality and order in the films. These results indicate that porous-film quality was improved under the described thermal annealing process (see **Figures 4b,d,f**). The pore size diameter values were from 1.0 to  $4.0\text{ }\mu\text{m}$ . It also was possible to observe smaller pore sizes ( $1\text{ }\mu\text{m}$ ) for PS-*b*-PAA block copolymer samples compared to the PS-*b*-PIA samples which exhibited pore diameter size (approximately from 1.0 to  $1.5\text{ }\mu\text{m}$ ). In contrast, the PS-*b*-PAMA block copolymer, which exhibited a different behavior under these experimental conditions; showed a porous structured morphology but with dispersed pore sizes (approx. from 1.5 to  $4.0\text{ }\mu\text{m}$ ). Hence, the porous films with thermal annealing process possess smaller pore diameter size than the films without

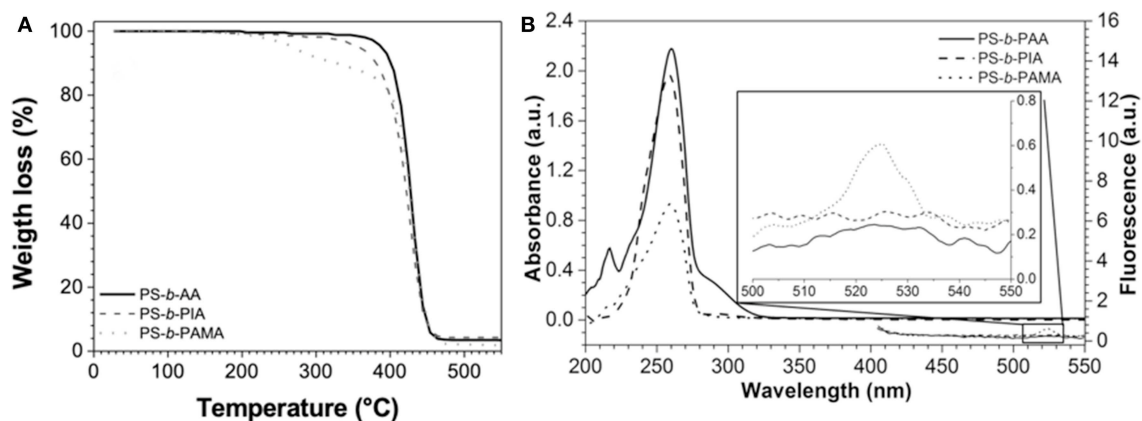


**FIGURE 3 | (A)** TGA thermograms of PS-*b*-PAA, and PS-*b*-PIA and PS-*b*-PAMA block copolymers; **(B)** Optical properties of PS-*b*-PAA, PS-*b*-PIA and PS-*b*-PAMA block copolymers.

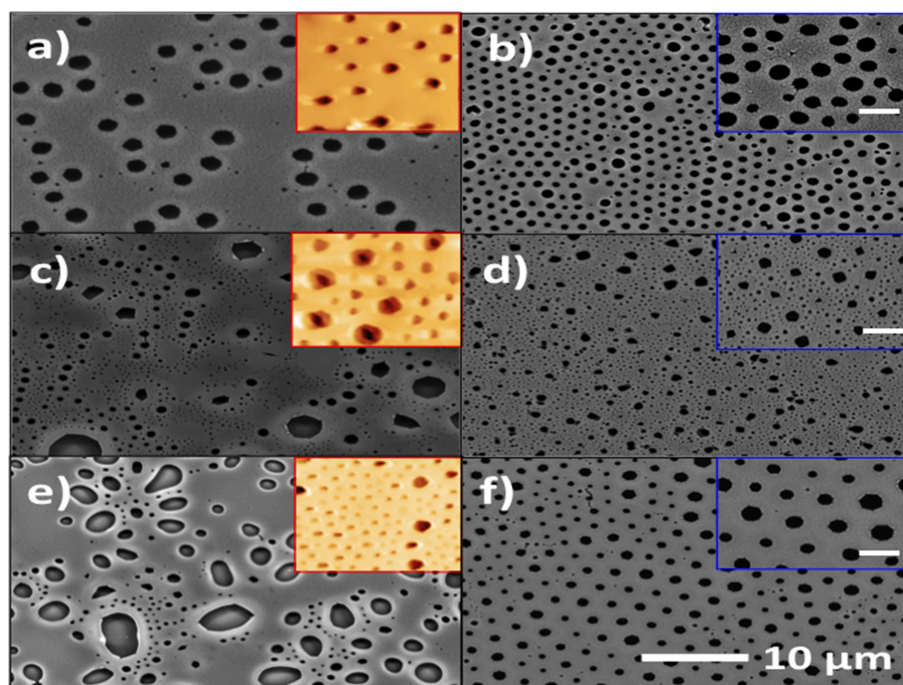


**FIGURE 4 |** SEM micrographs of the surfaces of PS-*b*-PAA (a), PS-*b*-PIA (c), PS-*b*-PAMA (e) before annealing, and PS-*b*-PAA (b), PS-*b*-PIA (d), PS-*b*-PAMA (f) after annealing. Inset of (a,c,e) are the corresponding AFM micrographs. Inset of (b,d,f) are the corresponding magnified micrographs (scale bar = 2 μm).

annealing. This outcome contrasts results previously reported from Pizarro et al. (2013).

### Contact Angle on the Polymeric Film With and Without Annealing Process

The surface wettability surface of materials is known to be mainly dependent on the geometrical structure and the chemical composition, with consequent practical applications (Wan et al., 2012; Sasmal et al., 2014; Cheng et al., 2015; Yu et al., 2016). A direct expression of the wettability of a surface is the water contact angle (WCA), which a water drop is placed on the film

surface for WCA measurements. The roughness and porosity of the surface films observed using SEM are expected to affect the contact angle values.

In this case, when the films were annealed at 120°C (for 2 h) [above the glass transition temperature (92–98°C)], the water droplet, can penetrate into the cavities of surface (pore depth approximately of 230 nm). It is the high roughness which increases the contact area which then increases the liquid–solid interaction. For contact angles <90°, the surface is conventionally described as hydrophilic, if the contact angle varies between 90° and 150°, the surface is hydrophobic, and

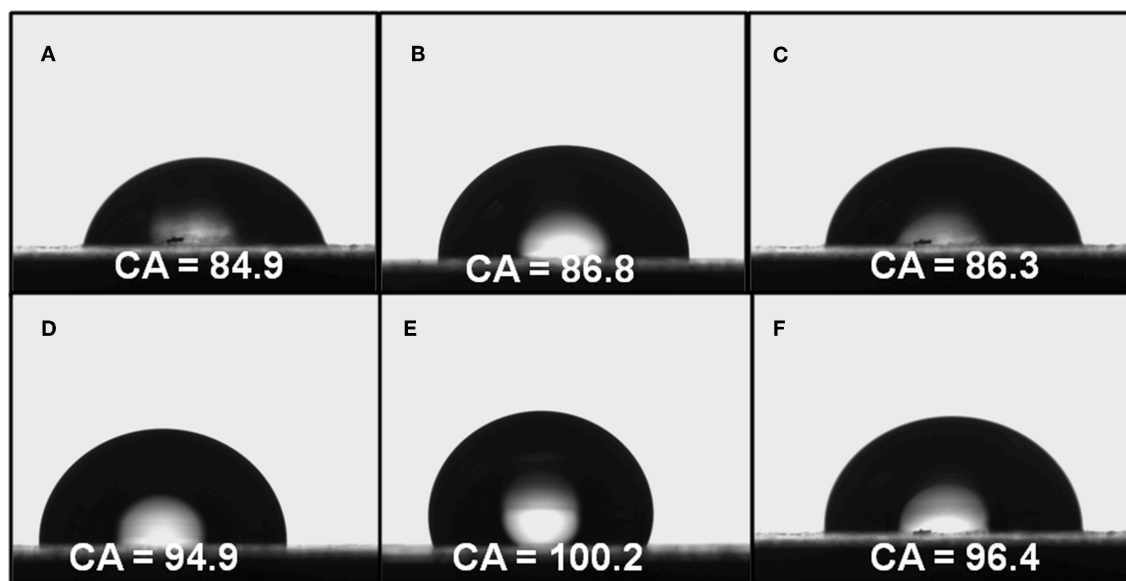


**FIGURE 5 |** Water contact angle (WCA) images of the surfaces of without and with annealing (A,D) PS-*b*-PAA, (B,E) PS-*b*-PIA, (C,F) PS-*b*-PAMA.

if WAC is  $>150^\circ$ , the surface is conventionally described as a superhydrophobic surface. Before thermal annealing, the PS-*b*-PAA film showed the lower WCA whilst PS-*b*-PIA and PS-*b*-PAMA showed similar values. The WCA values of the polymer's films submitted to the annealing process, increases, except for PS that remains constant. It is expected that the thermal annealing provokes a partial rearrangement of the polymer chains and therefore the probability of self-assembling of copolymers carrying  $-\text{COOH}$  groups. This self-assembling leads to an increase of the hydrophobicity since the no longer availability of this carboxylic acid groups to interact with water. Based on this WCA values range, the values varied from  $96.4^\circ$  to  $103.2^\circ$  for the polymer films, according with these results is possible to conclude that the films exhibited good hydrophobicity properties (see **Figure 5** and **Table 3**). This behavior was attributed to the annealing process that produces a change in the self-assembly of the films and in the order and formation of the pores. These changes promote hydrophobicity on the surface by reducing the surface tension, while its carboxylic acid functions is anchored the polymer film onto glass substrate and probably also into cavities of the pores. The increases in the contact angle value suggest additional hydrogen bonding interactions between the majority carboxylic acid groups on the surface and into the pores that influence the wettability of the films pre-annealing. These porous films exhibited a WAC  $>90^\circ$ , which indicates its hydrophobic characteristics (see **Table 3**).

## CONCLUSIONS

This work has presented the synthesis of a series of diblock copolymers which were used for the preparation of hydrophobic structured polymer films. The films displayed surface structures

**TABLE 3 |** Water contact angle (WCA) values of the porous polymer films without and with annealing(\*).

Films	Left	Right	Mean
PS	104.6°	106.5°	105.6°
PS*	<b>106.1°</b>	<b>108.5°</b>	<b>107.3°</b>
PS- <i>b</i> -PAA	84.9°	82.8°	83.6°
PS- <i>b</i> -PAA*	<b>94.9°</b>	<b>97.8°</b>	<b>96.4°</b>
PS- <i>b</i> -PIA	86.8°	90.1°	89.1°
PS- <i>b</i> -PIA*	<b>100.2</b>	<b>106.9</b>	<b>103.5</b>
PS- <i>b</i> -PAMA	86.3°	90.8°	87.3°
PS- <i>b</i> -PAMA*	<b>96.4°</b>	<b>98.5°</b>	<b>97.5°</b>

Contact angle of the glass substrate =  $51.9^\circ$ .

patterned at microstructure scale. The block copolymers showed high thermal stability temperatures (TDT) of approximately  $380^\circ\text{C}$ . The optical properties of the material exhibited one characteristic absorption band at 260 nm. This intense absorption band was attributed to the  $\pi-\pi^*$  transition due to electron delocalization in the aromatic ring (inter-molecular transfer change) of the first block (PS). The SEM and AFM images showed the block copolymers tended to form a rough and porous surface films with a pore size diameter ranging between  $\sim 1.0$  and  $4.0\ \mu\text{m}$ . This variation was due to their amphiphilic characteristics under experimental annealing conditions. Post annealing procedures demonstrated that the quality, porous uniformity and degree of order were improved; due to the spontaneously self-assembled diblock copolymers being favored. This suggests that the variation of the hydrophilic block (the number of  $-\text{COOH}$  in the polar co-monomers) can produce these differences in the surface films, moreover increasing or decreasing the intermolecular



interactions of the functional groups of the matrices (-COOH groups) due to mutual orientation and distance between -COOH groups. The results indicate that the phase behavior of the block copolymers is predominately determined by the PS block with hydrophobic characteristics, which was predominant in the formation of the films.

## AUTHOR CONTRIBUTIONS

GP: design, synthesis and characterization of monomers, discussion of experiments, and paper writing; OM: contribution in FT-IR and NMR spectroscopy analysis and discussion of the corresponding results; MJ-O: analysis and discussion of

fluorescence results; DO: TGA analysis; RM-T: analysis of SEM Micrographs and paper writing; JS: analysis and discussion on films wettability and paper writing.

## ACKNOWLEDGMENTS

The authors acknowledge the financial assistance of this work by VRAC, Grant Number L217-15 and L217-21 of Universidad Tecnológica Metropolitana (UTEM), Initiative funded by the Initiation R&D Program. DICY 021741SP, and Basal USA 1555-Vridei 021741SP\_PUBLIC Universidad de Santiago de Chile. DO thank to project DI-15-18/RG of Universidad Andrés Bello.

## REFERENCES

- Ashford, E. J., Naldi, V., O'Dell, R., Billingham, N. C., and Armes, S. P. (1999). First example of the atom transfer radical polymerisation of an acidic monomer: direct synthesis of methacrylic acid copolymers in aqueous media. *Chem. Commun.* 33, 1285–1286. doi: 10.1039/a903773j
- Baettig, J., Oh, J., Bang, J., and Khan, A. (2017). Sequential coating of nanopores with charged polymers: a general approach for controlling pore properties of self-assembled block copolymer membranes. *Macromol. Res.* 25, 1091–1099. doi: 10.1007/s13233-017-5142-5
- Beers, K. L., Boo, S., Gaynor, S. G., and Matyjaszewski, K. (1999). Atom transfer radical polymerization of 2-hydroxyethyl methacrylate. *Macromolecules* 32, 5772–5776. doi: 10.1021/ma990176p
- Cao, L., Hu, H. A., and Gao, D. (2007). Design and fabrication of micro-textures for inducing a superhydrophobic behavior on hydrophilic materials. *Langmuir* 23, 4310–4314. doi: 10.1021/la063572r
- Cardoso, V. F., Botelho, G., and Lanceros-Méndez, S. (2015). Nonsolvent induced phase separation preparation of poly(vinylidene fluoride-co-chlorotrifluoroethylene) membranes with tailored morphology, piezoelectric phase content and mechanical properties. *Mater. Des.* 88, 390–397. doi: 10.1016/j.matdes.2015.09.018
- Celia, E., Darmanin, T., Taffin de Givenchy, E., Amigoni, S., and Guittard, F. (2013). Recent advances in designing superhydrophobic surfaces. *J. Colloid Interface Sci.* 402, 1–18. doi: 10.1016/j.jcis.2013.03.041
- Cheng, Z., Wang, J., Lai, H., Du, Y., Hou, R., Li, C., et al. (2015). PH-controllable on-demand oil/water separation on the switchable superhydrophobic/superhydrophilic and underwater low-adhesive superoleophobic copper mesh film. *Langmuir* 31, 1393–1399. doi: 10.1021/la503676a
- Coca, S., Jasieczek, C. B., Beers, K. L., and Matyjaszewski, K. (1998). Polymerization of acrylates by atom transfer radical polymerization. Homopolymerization of 2-hydroxyethyl acrylate. *J. Polym. Sci. Part A Polym. Chem.* 36, 1417–1424.
- Davis, K. A., Charleux, B., and Matyjaszewski, K. (2000). Preparation of block copolymers of polystyrene and poly (t-butyl acrylate) of various molecular weights and architectures by atom transfer radical polymerization. *J. Polym. Sci. Part A Polym. Chem.* 38, 2274–2283. doi: 10.1002/(SICI)1099-0518(20000615)38:12<2274::AID-POLA170>3.0.CO;2-I
- Guarini, K. W., Black, C. T., and Yeung, S. H. I. (2002). Optimization of diblock copolymer thin film self assembly. *Adv. Mater.* 14, 1290–1294. doi: 10.1002/1521-4095(20020916)14:18<1290::AID-ADMA1290>3.0.CO;2-N
- Hamley, I. W. (1998). *The Physics of Block Copolymers*. Oxford: Oxford University.
- Hilke, R., Pradeep, N., Madhavan, P., Vainio, U., Behzad, A. R., Sougrat, R., et al. (2013). Block copolymer hollow fiber membranes with catalytic activity and pH-response. *ACS Appl. Mater. Interfaces* 5, 7001–7006. doi: 10.1021/am401163h
- Hong, Q., Ma, X., Li, Z., Chen, F., and Zhang, Q. (2016). Tuning the surface hydrophobicity of honeycomb porous films fabricated by star-shaped POSS-fluorinated acrylates polymer via breath-figure-templated self-assembly. *Mater. Des.* 96, 1–9. doi: 10.1016/j.matdes.2016.01.137
- Hosono, E., Fujihara, S., Honma, I., and Zhou, H. (2005). Superhydrophobic perpendicular nanopin film by the bottom-up process. *J. Am. Chem. Soc.* 127, 13458–13459. doi: 10.1021/ja053745j
- Huang, B., Fan, X., Wang, G., Zhang, Y., and Huang, J. (2012). Synthesis of twin-tail tadpole-shaped (cyclic polystyrene)- block-[linear poly (tert-butyl acrylate)]2 by combination of glaser coupling reaction with living anionic polymerization and atom transfer radical polymerization. *J. Polym. Sci. Part A Polym. Chem.* 50, 2444–2451. doi: 10.1002/pola.26021
- Karlsson, M., Forsberg, P., and Nikolajeff, F. (2010). From hydrophilic to superhydrophobic: Fabrication of micrometer-sized nail-head-shaped pillars in diamond. *Langmuir* 26, 889–893. doi: 10.1021/la902361c
- Ke, B.-B., Wan, L.-S., Zhang, W.-X., and Xu, Z.-K. (2010). Controlled synthesis of linear and comb-like glycopolymers for preparation of honeycomb-patterned films. *Polymer* 51, 2168–2176. doi: 10.1016/j.polymer.2010.03.021
- Kim, S. G., Lim, J. Y., Sung, J. H., Choi, H. J., and Seo, Y. (2007). Emulsion polymerized polyaniline synthesized with dodecylbenzene-sulfonic acid and its electrorheological characteristics: temperature effect. *Polymer* 48, 6622–6631. doi: 10.1016/j.polymer.2007.09.013
- Kumar, D., Wu, X., Fu, Q., Ho, J. W. C., Kanhere, P. D., Li, L., et al. (2015). Hydrophobic sol-gel coatings based on polydimethylsiloxane for self-cleaning applications. *Mater. Des.* 86, 855–862. doi: 10.1016/j.matdes.2015.07.174
- Lai, Y.-K., Chen, Z., and Lin, C.-J. (2011). Recent progress on the superhydrophobic surfaces with special adhesion: from natural to biomimetic to functional. *J. Nanoeng. Nanomanufactur.* 1, 18–34. doi: 10.1166/jnan.2011.1007
- Min, K., Gao, H., and Matyjaszewski, K. (2005). Preparation of homopolymers and block copolymers in miniemulsion by ATRP Using Activators Generated by Electron Transfer (AGET). *J. Am. Chem. Soc.* 127, 3825–3830. doi: 10.1021/ja042936a
- Nunes, S. P., Karunakaran, M., Pradeep, N., Behzad, A. R., Hooghan, B., Sougrat, R., et al. (2011). From micelle supramolecular assemblies in selective solvents to isoporous membranes. *Langmuir* 27, 10184–10190. doi: 10.1021/la201439p
- Oz, K., Yavuz, M., Yilmaz, H., Unal, H. I., and Sari, B. (2008). Electrorheological properties and creep behavior of polyindole/poly(vinyl acetate) composite suspensions. *J. Mater. Sci.* 43, 1451–1459. doi: 10.1007/s10853-007-2319-x
- Phillip, W. A., O'Neill, B., Rodwogin, M., Hillmyer, M. A., and Cussler, E. L. (2010). Self-assembled block copolymer thin films as water filtration membranes. *ACS Appl. Mater. Interfaces* 2, 847–853. doi: 10.1021/am900882t
- Pizarro, G. d. C., Jeria-Orell, M., Marambio, O. G., Olea, A. F., Valdés, D. T., and Geckeler, K. E. (2013). Synthesis of functional poly(styrene)-block-(methyl methacrylate/methacrylic acid) by homogeneous reverse atom transfer radical polymerization: spherical nanoparticles, thermal behavior, self-aggregation, and morphological properties. *J. Appl. Polym. Sci.* 129, 2076–2085. doi: 10.1002/app.38923
- Pizarro, G. d. C., Marambio, O. G., Jeria-Orell, M., González-Henríquez, C. M., Sarabia-Vallejos, M., and Geckeler, K. E. (2015). Effect of

- annealing and UV-radiation time over micropore architecture of self-assembled block copolymer thin film. *Express Polym. Lett.* 9, 525–535. doi: 10.3144/expresspolymlett.2015.50
- Pizarro, G. del C., Marambio, O. G., Jeria-Orell, M., Oyarzún, D. P., and Geckeler, K. E. (2016). Size, morphology and optical properties of ZnO nanoparticles prepared under the influence of honeycomb-porous poly[(2-hydroxyethylmethacrylate)-*m*-block-poly(N-phenyl maleimide)] copolymer films. *Mater. Des.* 111, 513–521. doi: 10.1016/j.matdes.2016.09.036
- Sasmal, A. K., Mondal, C., Sinha, A. K., Gauri, S. S., Pal, J., Aditya, T., et al. (2014). Fabrication of superhydrophobic copper surface on various substrates for roll-off, self-cleaning, and water/oil separation. *ACS Appl. Mater. Interfaces* 6, 22034–22043. doi: 10.1021/am5072892
- Shirtcliffe, N. J., McHale, G., and Newton, M. I. (2011). The superhydrophobicity of polymer surfaces: Recent developments. *J. Polym. Sci. Part B Polym. Phys.* 49, 1203–1217. doi: 10.1002/polb.22286
- Teodorescu, M., Gaynor, S. G., and Matyjaszewski, K. (2000). Halide anions as ligands in iron-mediated atom transfer radical polymerization. *Macromolecules* 33, 2335–2339. doi: 10.1021/ma991652e
- Tobis, J., Thomann, Y., and Tiller, J. C. (2010). Synthesis and characterization of chiral and thermo responsive amphiphilic conetworks. *Polymer* 51, 35–45. doi: 10.1016/j.polymer.2009.10.055
- Wan, L. S., Li, J. W., Ke, B. B., and Xu, Z. K. (2012). Ordered microporous membranes templated by breath figures for size-selective separation. *J. Am. Chem. Soc.* 134, 95–98. doi: 10.1021/ja2092745
- Wang, J.-S., and Matyjaszewski, K. (1995). Controlled/"living" radical polymerization. atom transfer radical polymerization in the presence of transition-metal complexes. *J. Am. Chem. Soc.* 117, 5614–5615. doi: 10.1021/ja00125a035
- Wang, X. S., Jackson, R. A., and Armes, S. P. (2000). Facile synthesis of acidic copolymers via atom transfer radical polymerization in aqueous media at ambient temperature. *Macromolecules* 33, 255–257. doi: 10.1021/ma000671h
- Wen, W., Huang, X., and Sheng, P. (2008). Electrorheological fluids: structures and mechanisms. *Soft Matter* 4, 200–210. doi: 10.1039/B710948M
- Wu, X., Fu, Q., Kumar, D., Ho, J. W. C., Kanhere, P., Zhou, H., et al. (2016). Mechanically robust superhydrophobic and superoleophobic coatings derived by sol-gel method. *Mater. Des.* 89, 1302–1309. doi: 10.1016/j.matdes.2015.10.053
- Yao, X., Song, Y., and Jiang, L. (2011). Applications of bio-inspired special wettable surfaces. *Adv. Mater.* 23, 719–734. doi: 10.1002/adma.201002689
- Yu, H., Liu, J., Fan, X., Yan, W., Han, L., Han, J., et al. (2016). Bionic micro-nano-bump-structures with a good self-cleaning property: the growth of ZnO nanoarrays modified by polystyrene spheres. *Mater. Chem. Phys.* 170, 52–61. doi: 10.1016/j.matchemphys.2015.12.018
- Zhang, W., He, J., Liu, Z., Ni, P., and Zhu, X. (2010). Biocompatible and pH-responsive triblock copolymer mPEG-*b*-PCL-*b*-PDMAEMA: Synthesis, self-assembly, and application. *J. Polym. Sci. Part A Polym. Chem.* 48, 1079–1091. doi: 10.1002/pola.23863
- Zhu, M., Zuo, W., Yu, H., Yang, W., and Chen, Y. (2006). Superhydrophobic surface directly created by electrospinning based on hydrophilic material. *J. Mater. Sci.* 41, 3793–3797. doi: 10.1007/s10853-005-5910-z

**Conflict of Interest Statement:** The authors declare that the research was conducted in the absence of any commercial or financial relationships that could be construed as a potential conflict of interest.

Copyright © 2019 Pizarro, Marambio, Jeria-Orell, Oyarzún, Martín-Trasanco and Sánchez. This is an open-access article distributed under the terms of the Creative Commons Attribution License (CC BY). The use, distribution or reproduction in other forums is permitted, provided the original author(s) and the copyright owner(s) are credited and that the original publication in this journal is cited, in accordance with accepted academic practice. No use, distribution or reproduction is permitted which does not comply with these terms.



# Review on Polymer-Based Composite Electrolytes for Lithium Batteries

Penghui Yao<sup>††</sup>, Haobin Yu<sup>††</sup>, Zhiyu Ding<sup>1</sup>, Yanchen Liu<sup>1</sup>, Juan Lu<sup>1</sup>, Marino Lavorgna<sup>2</sup>, Junwei Wu<sup>1\*</sup> and Xingjun Liu<sup>1</sup>

<sup>1</sup> Shenzhen Key Laboratory of Advanced Materials, Department of Materials Science and Engineering, Harbin Institute of Technology, Shenzhen, China, <sup>2</sup> Institute of Polymers, Composite, and Biomaterials, National Research Council, Portici, Italy

## OPEN ACCESS

### Edited by:

Pellegrino Musto,  
Italian National Research Council  
(CNR), Italy

### Reviewed by:

Helinando Pequeno De Oliveira,  
Universidade Federal do Vale do São  
Francisco, Brazil  
Giuseppe Scherillo,  
University of Naples Federico II, Italy

### \*Correspondence:

Junwei Wu  
junwei.wu@hit.edu.cn

<sup>††</sup>These authors have contributed  
equally to this work

### Specialty section:

This article was submitted to  
Polymer Chemistry,  
a section of the journal  
Frontiers in Chemistry

**Received:** 29 January 2019

**Accepted:** 08 July 2019

**Published:** 08 August 2019

### Citation:

Yao P, Yu H, Ding Z, Liu Y, Lu J,  
Lavorgna M, Wu J and Liu X (2019)  
Review on Polymer-Based Composite  
Electrolytes for Lithium Batteries.  
Front. Chem. 7:522.  
doi: 10.3389/fchem.2019.00522

Lithium-ion batteries have dominated the high performance and mobile market for last decade. Despite their dominance in many areas, the development of current commercial lithium-ion batteries is experiencing bottlenecks, limited by safety risks such as: leakage, burning, and even explosions due to the low-boiling point organic liquid electrolytes. Solid electrolyte is a promising option to solve or mitigate those issues. Among all solid electrolytes, polymer based solid electrolytes have the advantages of low flammability, good flexibility, excellent thermal stability, and high safety. Numerous researchers have focused on implementing solid polymer based Li-ion batteries with high performance. Nevertheless, low Li-ion conductivity and poor mechanical properties are still the main challenges in its commercial development. In order to tackle the issues and improve the overall performance, composites with external particles are widely investigated to form a polymer-based composite electrolyte. In light of their work, this review discusses the progress of polymer-based composite lithium ion's solid electrolytes. In particular, the structures, ionic conductivities, electrochemical/chemical stabilities, and fabrications of solid polymer electrolytes are introduced in the text and summarized at the end. On the basis of previous work, the perspectives of solid polymer electrolytes are provided especially toward the future of lithium ion batteries.

**Keywords:** polymer solid electrolytes, polymer, lithium-ion batteries, Li-ion conductivity, composite

## INTRODUCTION

From the moment in 1991 when the SONY corporation launched the commercialization of lithium-ion batteries, lithium-ion batteries have thrived significantly and dominated in many different applications, such as electric vehicles, portable devices (Scrosati and Garche, 2010; Verma et al., 2010; Manthiram et al., 2017). Although lithium-ion batteries have many advantages such as high energy density and long cycle life, the potential safety issues and saturated high energy density have become bottlenecks which impedes further development.

Current commercial lithium-ion batteries use liquid organic electrolytes, which have significant advantages of high conductivity and excellent wettability on electrode surfaces. However, the obvious and inevitable drawbacks of liquid electrolytes are electrochemical instabilities and potential risks, plus low ion selectivity. Compared with liquid electrolytes, solid electrolytes have higher safety and thermal stability, since it can provide a physical barrier layer to separate positive

and negative electrodes and prevent thermal runaway under high temperature or impact. In addition, solid electrolyte makes it possible to use a lithium metal anode, due to its effective suppression of Li dendrite formation. Despite the significant advantages, some weaknesses still remain to be improved, such as low ionic conductivity and insufficient interface contact. Plenty of research is being conducted to conquer the weakness and develop new generation of solid lithium batteries (Tang et al., 2007; Zhao et al., 2012; Liu et al., 2013; Zhang Q. Q. et al., 2017). To meet the commercial requirements, high ionic conductivity, favorable mechanical properties, and outstanding interfacial stability with the electrodes are the most fundamental requirements for solid electrolytes (Fergus, 2010).

Inorganic solid electrolyte (ISE), solid polymer electrolyte (SPE), and composite electrolyte (CSE) are widely studied in lithium-ion batteries. Oxide group and sulfide group are two types widely used in ISE. Some of them [such as sulfide-based  $\text{Li}_{10}\text{GeP}_2\text{S}_{12}$  (Kamaya et al., 2011)] exhibit high conductivity equivalent to that of organic liquid electrolytes, but the issues of high processing difficulty, high cost, and large interface impedance restricts its wide application (Knauth, 2009; Fergus, 2010). SPEs not only have excellent electrochemical performance and high safety, but are also good in flexibility and process ability, which has high possibilities for use in next-generation high-energy batteries (Dias et al., 2000; Stephan and Nahm, 2006; Yarmolenko et al., 2018). In the meantime, it avoids the danger of Li metal dendrite growth (Meyer, 1998; Agrawal and Pandey, 2008; Tikekar et al., 2016). SPEs, including polyethylene oxide (PEO) (Farrington and Briant, 1979; Watanabe et al., 1999; Siqueira and Ribeiro, 2006), polycarbonate (Forsyth et al., 1997; Sun et al., 2014; Liu et al., 2015), and polysiloxane (Sun et al., 1996; Fonseca and Neves, 2002) have been extensively investigated. However, the ionic conductivity and mechanical strength of SPEs are still not ideal, which is the major obstacle to hamper their wide applications (Chen et al., 2016).

Different methods are adopted for improving the polymer electrolyte system. Typically, they can be categorized into two approaches: (1) Polymer/polymer coordination and (2) Composite polymer electrolyte.

Copolymerization, crosslinking, interpenetration, and blending are widely used as polymer/polymer coordination; however, it does not significantly increase the mechanical properties of the electrolyte. Various composites had been mixed into polymers, as shown in **Figure 1**, including inert ceramic fillers (Agrawal and Pandey, 2008; Lin et al., 2016), fast-ion conductive ceramics (Aliahmad et al., 2016; Keller et al., 2017; Ling et al., 2018), lithium salts (Do et al., 1996), ionic liquid (Subianto et al., 2009), etc. With the synergistic effect of polymer and inorganic filler, the room temperature conductivity and mechanical strength of composite polymer electrolyte can be greatly improved, as well as the interface stability with the electrode. In my group, similar synergistic effects on composite electrolyte had been reported in inorganic fillers composite with Nafion membrane for direct methanol fuel cell applications (Cui et al., 2015, 2018), the corresponding mechanism is similar with the composite electrolyte with organic fillers. The used polymer matrices and properties for SPE are summarized in **Table 1**.

Solid polymer electrolytes (SPEs) currently have great application prospects in lithium batteries fabrication, numerous researchers also take great efforts to develop innovative SPEs and the successful applications will play a key role in developing lithium battery with excellent performance. **Figure 2** shows that the number of published sci-tech articles in the polymer-based solid electrolyte over a period of 19 years from 2000 to 2018. The trend shows the steady increase from about 750 in 2000 to the largest point around 2,400 in 2017. From the year of 2010, the number of essays in this field keep steady over 2000, which is the fact that polymer-based solid electrolyte will have excellent application prospects. A large number of reviews have summarized the research and development history of polymer electrolytes (Qiu et al., 2004; Dong and Wang, 2005; Srivastava and Tiwari, 2009; Fergus, 2010; Liu et al., 2013; Osada et al., 2016; Zhang Q. Q. et al., 2017). However, there is relatively few reviews on polymer-based solid electrolytes.

This review article highlights recent researches on SPEs for solid state lithium-ion batteries, in particular about the effects of composition with various filler materials. In this review, polymer based composite electrolytes, including polymer/inert ceramics, polymer/fast-ion conductive, polymer/ionic liquid, polymer/MOFs, and polymer/cellulose composite electrolytes. Furthermore, a perspective on the future research direction for developing safety, stable, and high energy density composite polymer electrolytes for solid-state batteries will be provided.

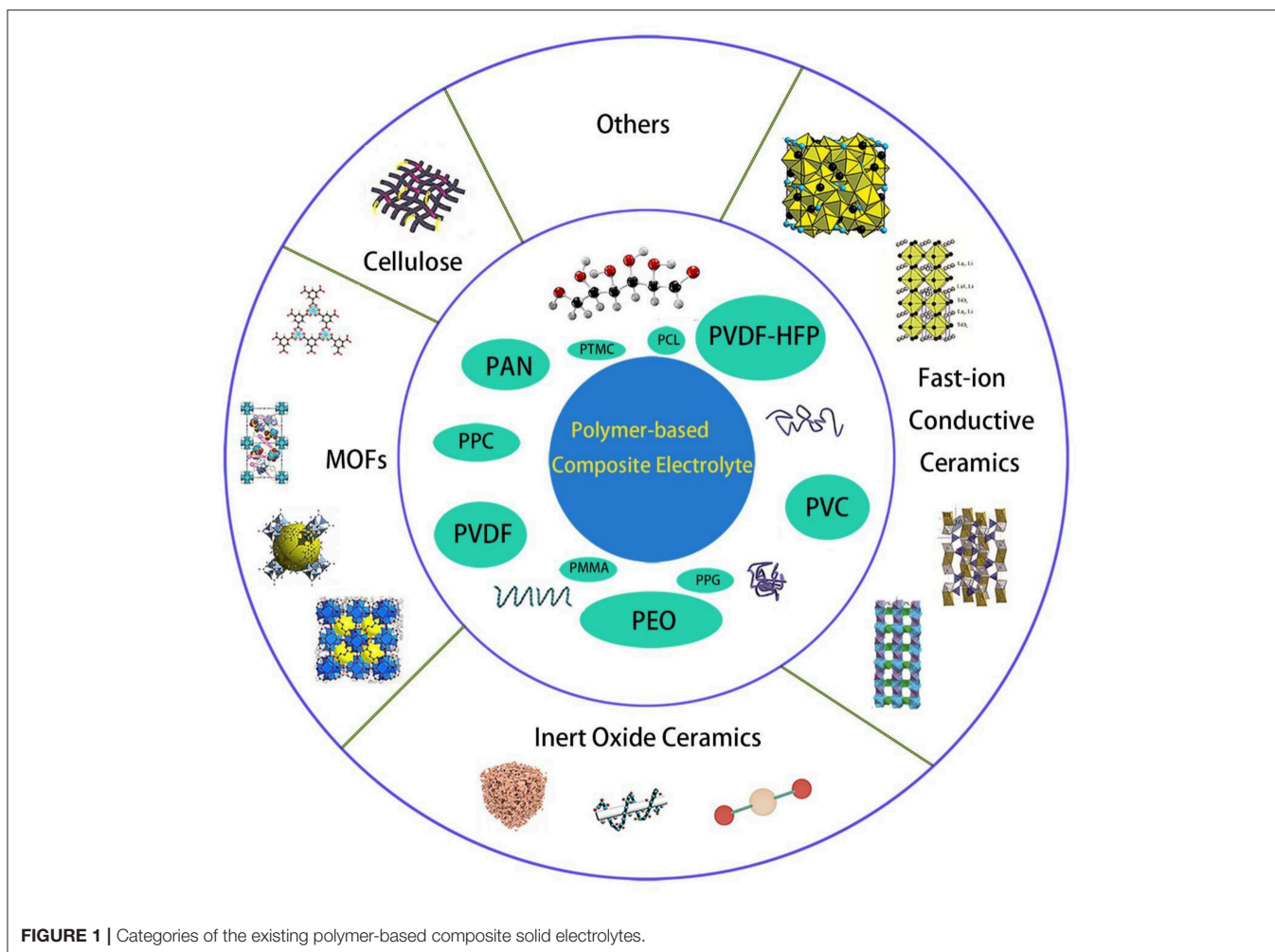
## IONIC CONDUCTIVITY AND INTERFACE

### Ionic Conductivity Mechanism

In order to develop SPEs with high lithium ion conductivity, the polymer should not only dissolve lithium salt, but also be able to couple with lithium ions. The polar groups in the polymer ( $-\text{O}-$ ,  $-\text{S}-$ , etc.) are effective building blocks for dissolving lithium salts. Most of the research on all-SPEs is focused on polyethylene oxide (PEO) and its derivatives. The lone pair of oxygens on the PEO segment is coordinated to the lithium ion by Coulombic interaction, causing the anion and cation of the lithium salt to dissociate. In the process, PEO acts as solvent, and the lithium salt dissolves into the PEO matrix. In addition to the oxygen atom ( $-\text{O}-$ ) on the PEO chain, other atoms such as the nitrogen in the imide ( $-\text{NH}-$ ) and the sulfur in the thiol ( $-\text{S}-$ ) also play a similar role. Under the electric field, the migration movement of  $\text{Li}^+$  cations are from one coordination point to another along the polymer segment, or jump from one segment to another. The ion transport mechanism of polymer electrolytes such as PEO is shown in **Figure 3** (Xu, 2004).

In the polymer-lithium salt composite system, the ions are not free to move due to the huge size of the polymer chain plus the boundary effect of crystalline domains. The factors affecting the ionic conductivity are the number of lithium ions and the mobility of the polymer chain. The amount of ions that can be migrated depends on the ability of the polymer to dissociate the lithium salt, and thus the lithium salt of low lattice energy and the polymer of high dielectric constant can promote this dissociation (Young et al., 2014). Under steady state conditions, the ionic conductivity can be expressed by the





following equation (Wei-Min, 2012):

$$\sigma = F \sum n_i q_i \mu_i \quad (1)$$

Here,  $F$  is the Faraday constant;  $n_i$  represents the number of free ions;  $q_i$  represents the number of charges, and  $\mu_i$  is the mobility. Therefore, it can be seen that in the polymer electrolyte, the increase of the concentration of the movable ions and the migration speed of the ions can increase the conductivity of the ions.

In SPEs, the most commonly used theory to explain the migration of ions in polymers includes Arrhenius theory, Vogel-Tammann-Fulcher (VTF) theory, William-Landel-Ferry (WLF) theory, and the combinations of above theories (Ratner et al., 2000; Quartarone and Mustarelli, 2011).

The classical Arrhenius theory explains the temperature relationship of ion migration caused by polymer segment motion, expressed as (Zhang Q. Q. et al., 2017):

$$\sigma = \sigma_0 \exp\left(\frac{-E_a}{KT}\right) \quad (2)$$

Here,  $E_a$  represents the activation energy for single molecules or groups of ions to migrate,  $\sigma_0$  represents the pre-exponential factor, while  $T$  represents thermodynamic temperature.

Generally, ion jump motion and polymer chain relaxation and/or segmental motion together affect conductivity, so the vs.  $1/T$  curve is generally non-linear (Agrawal and Pandey, 2008). The typical  $\lg-1/T$  in polymers is usually based on the  $T_g$ -based equation, so VTF mainly describes the relationship between polymer electrolyte conductivity and temperature (Zhang Q. Q. et al., 2017):

$$\sigma = \sigma_0 T^{-\frac{1}{2}} \exp\left(-\frac{B}{T - T_0}\right) \quad (3)$$

Here,  $\sigma_0$  is a pre-exponential factor,  $B$  is an action factor with dimension as the energy dimension, and  $T_0$  is the reference temperature, which can be expressed in  $T_g$ , normally 10–50 K below the experimental glass transition temperature. At room temperature, if only the effect of the polymer segment on conductivity is considered, low glass transition temperature can play a positive role in the improvement of the conductivity.

Based on the study of PEO and PPO salt complexes, the ionic conductivity can be related to frequency and temperature

**TABLE 1** | Common polymer matrix.

Polymer matrix	Molecular formula	Glass transition temperature $T_g/^\circ\text{C}$	Melting point $T_m/^\circ\text{C}$
PEO	$\left[ \text{O}-\text{CH}_2-\text{CH}_2 \right]_n$	-64	65
PVC	$\left[ \text{CH}_2-\underset{\text{Cl}}{\text{CH}} \right]_n$	80	220
PAN	$\left[ \text{CH}_2-\underset{\text{CN}}{\text{CH}} \right]_n$	125	317
PMMA	$\left[ \text{CH}_2-\underset{\text{COOCH}_3}{\overset{\text{CH}_3}{\text{C}}} \right]_n$	105	Amorphous
PVDF	$\left[ \underset{\text{H}}{\overset{\text{H}}{\text{C}}}-\underset{\text{F}}{\overset{\text{F}}{\text{C}}} \right]_n$	-40	171
PVDF-HFP	$\left[ \text{CH}_2-\text{CF}_2 \right]_x \left[ \text{CF}_2-\underset{\text{CH}_3}{\text{CF}} \right]_y$	-90	135
PPG	$\left[ \text{O}-\text{CH}_2-\underset{\text{CH}_3}{\text{CH}} \right]_n$	-60	Amorphous
PDMS	$\left[ \underset{\text{CH}_3}{\overset{\text{CH}_3}{\text{Si}}}-\text{O} \right]_n$	-127	-40
PEC	$\left[ \text{O}-\text{C}(=\text{O})-\text{O}-\text{CH}_2-\text{CH}_2-\text{CH}_2-\text{CH}_2 \right]_n$	5	Amorphous
PPC	$\left[ \text{CH}_2-\underset{\text{R}}{\text{CH}}-\text{O}-\text{C}(=\text{O})-\text{O} \right]_n$	35	Amorphous
PCL	$\left[ \text{O}-\text{CH}_2-\text{CH}_2-\text{CH}_2-\text{CH}_2-\text{CH}_2-\text{C}(=\text{O}) \right]_n$	-60	Amorphous
PTMC	$\left[ \text{O}-\text{C}(=\text{O})-\text{O}-\text{CH}_2-\text{CH}_2-\text{CH}_2-\text{CH}_2 \right]_n$	-15	Amorphous

by using the William-Landel-Ferry (WLF) equation, considering the relaxation process of polymer molecular chain motion in an amorphous system. The expression is:

$$\lg \frac{\sigma(T)}{\sigma(T_g)} = \frac{C_1(T - T_g)}{C_2 + (T - T_g)} \quad (4)$$

Here,  $\sigma(T_g)$  is the conductivity of the relevant ions at glass transition temperature  $T_g$ , and  $C_1$  and  $C_2$  are the WLF parameters in the free volume equation of ion migration, respectively.

$T_g$  is one of the most critical parameter of polymer electrolyte. The conductivity is very low as the temperature below  $T_g$ , and it

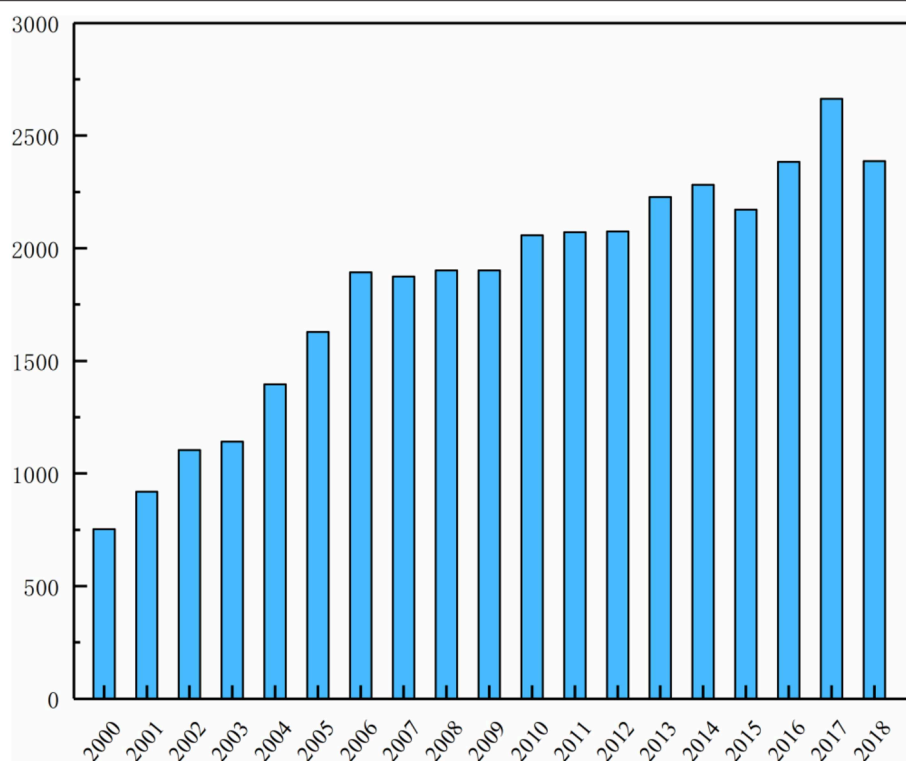


**FIGURE 2** | The number of published sci-tech articles in the polymer-based solid electrolyte over a period of 19 years from 2000 to 2019.

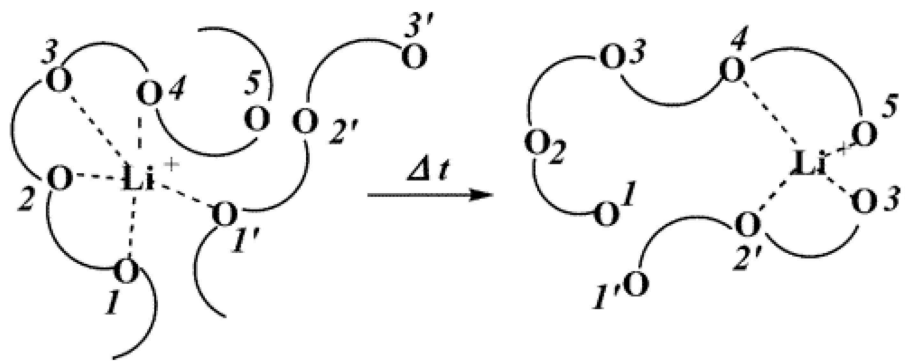


**FIGURE 3** | Schematic diagram of lithium ion conduction mechanism of PEO-based polymer electrolyte. [Reproduction with permission from Xu (2004), Copyright 2004, American Chemical Society].

will be obviously improved above  $T_g$ . Therefore, to reduce  $T_g$  is beneficial to the improvement of conductivity.

The above three theories well-explain the conductive mechanism of the PEO-based electrolyte. The amorphous phase of the polymer is mainly effective for the migration of ions. The theory can also be applied to other polymer electrolytes.

## Interface

In the solid lithium-metal battery, the cathode is typically  $\text{LiFePO}_4$  or  $\text{LiCoO}_2$ . Metallic lithium is used as a negative electrode. The cathode/electrolyte interface requires a solid

electrolyte with excellent flexibility to ensure low interface resistance, while the anode/electrolyte interface requires a strong solid electrolyte to withstand the puncture of the metal lithium dendrites (Camacho-Forero and Balbuena, 2018; Wang L. P. et al., 2018; Zhang et al., 2018). The good flexibility of the SPE makes the lower interface resistance possible, but the low mechanical properties are difficult to withstand the puncture of the metal lithium dendrites. In contrast, a rigid inorganic ceramic electrolyte can withstand the metallic lithium dendrites, but has a large interfacial resistance due to insufficient contact with the electrodes (Xu et al., 2018). Therefore, the flexible polymer

electrolyte or the rigid inorganic ceramic electrolyte has difficulty used in solid metal lithium battery separately. In order to take full advantage of polymer and inorganic ceramic electrolyte, polymer composite inorganic ceramic electrolyte offers an option. It is expected that the obtained solid metal lithium battery has both low interface resistance and the ability to inhibit lithium dendrite formation. In addition, the electrochemical instability of the interface easily leads to the occurrence of side reactions and thus the cover of the electrodes form a solid electrolyte interface (SEI), which may lead to a shortened cycle life of the cell (Xu et al., 2018).

## SOLID POLYMER ELECTROLYTES WITH INERT OXIDE CERAMICS

In recent years, many studies have been addressed to incorporate inert oxide ceramics particles into polymer electrolyte, in order to improve the mechanical properties, reduce polymer crystallinity, and thus solve the problem of low ionic conductivity of SPE. Different types of inert ceramics had been incorporated into the polymer, such as SiO<sub>2</sub> (Nan et al., 2003; Ketabi and Lian, 2013), Al<sub>2</sub>O<sub>3</sub> (Weston and Steele, 1982; Capuano et al., 1991; Tambelli et al., 2002; Liang et al., 2015), TiO<sub>2</sub> (Pal and Ghosh, 2018), zeolite, etc. The ionic conductivities of solid polymer composite electrolyte containing inert ceramic filler are showed in **Table 2**. In 1982, Weston and Steele (1982) mixed PEO with Al<sub>2</sub>O<sub>3</sub> to form a composite. It was firstly proved that PEO doped with inert material particles exhibited an improvement of mechanical properties and ionic conductivity. Subsequently, Capuano et al. (1991) explored the contribution of the doping amount and particle size of LiAlO<sub>2</sub> powder on the conductivity of solid electrolyte. It was found that the conductivity reached the highest as the doping amount of LiAlO<sub>2</sub> was around 10 wt.%. It is also worth noting that particle size of the inert ceramic material affected the conductivity of the SPE, which increases with particle sizes as the size is <10 μm. Tambelli et al. (2002) reported that Al<sub>2</sub>O<sub>3</sub> can effectively reduce the crystallinity and glass transition temperature of PEO. This confirms that the decrease of polymer crystallinity promotes the improvement of ionic conductivity. The decrease in crystallinity can enlarge the number of free segments of the polymer and accelerate the movement of the segments, which can effectively promote the migration of lithium ions. Similar results were reported on PEO-PMMA-LiTFSI-Al<sub>2</sub>O<sub>3</sub> composite electrolytes. They were prepared based on PEO-PMMA as a host matrix and nano Al<sub>2</sub>O<sub>3</sub> as filler by solution casting technique (Liang et al., 2015). The composite electrolytes doped with Al<sub>2</sub>O<sub>3</sub> exhibited an improvement of the ionic conductivity from  $6.71 \times 10^{-7}$  to  $9.39 \times 10^{-7}$  S/cm.

SiO<sub>2</sub> is also a common inert ceramic filler material used in the preparation of SPE. Lee et al. reported a composite of a PEO matrix and SiO<sub>2</sub> fillers containing ethylene carbonate (EC)/propylene carbonate (PC). The composite had an ionic conductivity of  $2 \times 10^{-4}$  S/cm at ambient temperature (Nan et al., 2003) with 2.5 wt.% filler loadings. In addition to powder, SiO<sub>2</sub> is also designed as a three-dimensional framework doped into the polymer. Lin et al. (2018) prepared a composite of

PEO-Silica aerogel which exhibited high ionic conductivity  $6 \times 10^{-4}$  S/cm and high modulus 0.43 GPa. This study effectively solves the issue of poor mechanical properties and ionic conductivity of composite by controlling powder dispersion. SiO<sub>2</sub> aerogel skeleton has a good acidic surface. It can interact with lithium cations extensively and form a continuous channel in the composite material, beneficial to salt dissociation and improvement of ionic conductivity. Ion pairs are difficult to form because of the strong Lewis acid-base interaction of doped TiO<sub>2</sub> and the anion of lithium salt, resulting in more mobile charge carriers (Pal and Ghosh, 2018). Croce et al. (1998) studied a solid polymer electrode consisting of a nanosized TiO<sub>2</sub> particles, PEO, and LiClO<sub>4</sub>. This hybrid exhibits a higher ionic conductivity of  $10^{-5}$  S/cm. Pal and co-workers fabricated SPEs comprising of PMMA, LiClO<sub>4</sub>, and TiO<sub>2</sub>, by standard solution cast technique (Pal and Ghosh, 2018). The results showed that by composite nanosized-TiO<sub>2</sub> to the polymer electrolytes, the thermal stability can be improved as well. The conductivity reached  $3 \times 10^{-4}$  S/cm at 303 K. Moreover, specific capacity of such polymer electrolyte-based LiCoO<sub>2</sub>/graphite at 30°C exhibited 30 mAh/g at room temperature in twelfth cycle. In addition, some studies have incorporated a variety of inorganic ceramics into the polymer, and the ionic conductivity has also been improved. For example, nanosized SiO<sub>2</sub>, and nanoporous Al<sub>2</sub>O<sub>3</sub> were combined with PVDF-HFP to obtain composite electrolytes that delivered moderate conductivity of  $10^{-3}$  S/cm with 2.5 wt.% of fillers (Aravindan and Vickraman, 2008).

Liu et al. (2016) has the designed and fabricated a SPE comprising Y<sub>2</sub>O<sub>3</sub> nanoparticle, ZrO<sub>2</sub> nanowire fillers, and PAN by electrospinning (**Figure 4A**). Y<sub>2</sub>O<sub>3</sub>-stabilized ZrO<sub>2</sub>(YSZ) nanowire in PAN have a lot of positively charged oxygen vacancies with Lewis acid character, which may attract the anion of lithium salt and thus promote the dissociation of salts. The addition of YSZ nanoparticles or YSZ nanowires has a different degree of improvement in ionic conductivity compared to the absence of YSZ. The improvement effect of YSZ nanowires is better, and 7YSZ (7 mol% of Y<sub>2</sub>O<sub>3</sub>-doped ZrO<sub>2</sub> nanowires) had a high room-temperature ionic conductivity of  $1.07 \times 10^{-5}$  S/cm at 30°C with an enhancement of two orders of magnitude compared with pristine PAN electrolyte (**Figure 4B**). Recently, Tao et al. (Sheng et al., 2018) incorporated Mg<sub>2</sub>B<sub>2</sub>O<sub>5</sub> nanowires into PEO-LiTFSI-based solid electrolyte. The composite electrolytes exhibit good mechanical properties, outstanding electrochemical stability, and ionic conductivity, because of the fast ion motion on the surfaces of Mg<sub>2</sub>B<sub>2</sub>O<sub>5</sub> and interactions between the Mg<sub>2</sub>B<sub>2</sub>O<sub>5</sub> and TFSI<sup>-</sup> (**Figure 4C**). In addition, other inert oxide ceramics have also been reported to improve the SPE performance, such as LiAlO<sub>2</sub> (Gang et al., 1992; Hu et al., 2007), ZnO (Xiong et al., 2006), Fe<sub>3</sub>O<sub>4</sub> (Reddy et al., 2006), and BaTiO<sub>3</sub> (Itoh et al., 2003a,b).

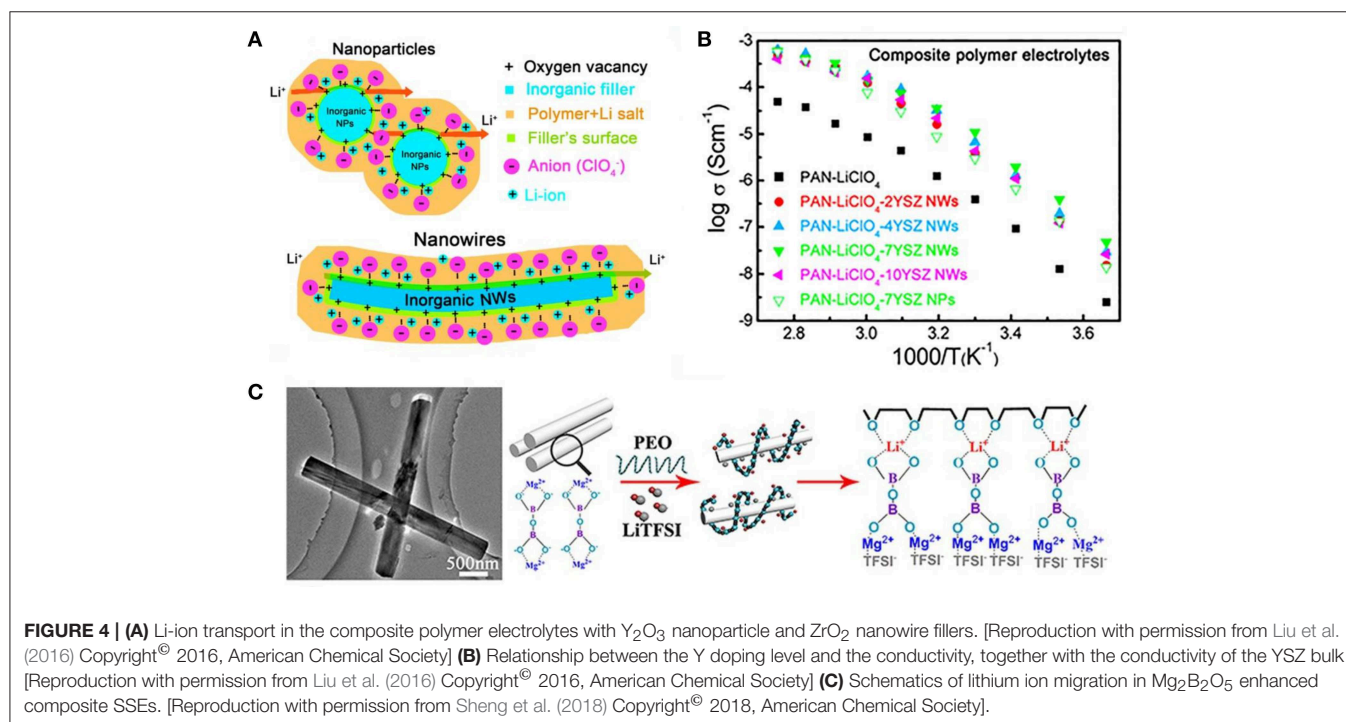
## SOLID POLYMER ELECTROLYTES WITH FAST-ION CONDUCTIVE CERAMICS

Fast ion conductor ceramics, also known as active inorganic electrolytes, exhibit a high ionic conductivity of up to  $10^{-2}$  S/cm



**TABLE 2** | Summary of inert oxide Ceramics/polymer solid electrolytes.

Year	Polymer electrolyte ingredients	Ionic conductivity (S/cm)	References
1991	LiAlO <sub>2</sub> -PEO-LiClO <sub>4</sub>	10 <sup>-4</sup> (60°C)	Liu et al., 2013
1998	TiO <sub>2</sub> -PEO-LiClO <sub>4</sub>	10 <sup>-5</sup> (30°C)	Manthiram et al., 2017
2002	Al <sub>2</sub> O <sub>3</sub> -PEO-LiClO <sub>4</sub>	10 <sup>-2</sup> (60°C)	Liu et al., 2017
2003	SiO <sub>2</sub> -PEO-LiClO <sub>4</sub> -EC/PC	2 × 10 <sup>-4</sup> (25°C)	Lin et al., 2016
2015	Al <sub>2</sub> O <sub>3</sub> -PEO-PMMA-LiTFSI	9.39 × 10 <sup>-7</sup> (25°C)	Liu et al., 2016
2016	SiO <sub>2</sub> -Al <sub>2</sub> O <sub>3</sub> -PVDF-HFP-LiPF <sub>6</sub> (CF <sub>3</sub> CF <sub>2</sub> ) <sub>3</sub>	10 <sup>-3</sup> (25°C)	Meyer, 1998
2016	Y <sub>2</sub> O <sub>3</sub> -doped ZrO <sub>2</sub> nanowire (YSZ)–PAN–LiClO <sub>4</sub>	1.07 × 10 <sup>-5</sup> (30°C)	Mueller et al., 2006
2018	TiO <sub>2</sub> -PMMA-LiClO <sub>4</sub>	3 × 10 <sup>-4</sup> (30°C)	Liu et al., 2015
2018	Silica aerogel-PEO-LiTFSI	6 × 10 <sup>-4</sup> (30°C)	Liu et al., 2015
2018	Mg <sub>2</sub> B <sub>2</sub> O <sub>5</sub> Nanowire-PEO-LiTFSI	1.53 × 10 <sup>-4</sup> (40°C)	Nair et al., 2009



at 25°C. Four structures of fast ion conductors are displayed in **Figure 5**.

However, the poor interfacial contact restricts their direct use as solid electrolytes. Thus, composite of fast ion conductor ceramics with polymer can take full advantages of both parts. Fast ionic conductors commonly have garnet-type, NASICON-type and LISICON-type ceramics etc. **Table 3** gives a summary of fast-ion conductive ceramics/polymer solid electrolytes.

## Garnet-Type Composite Polymer Electrolytes

From the moment in 2007 when Li<sub>7</sub>La<sub>3</sub>Zr<sub>2</sub>O<sub>12</sub> (LLZO) was first found, garnet-type Li solid-state electrolyte generates great interest in recent years. Li<sub>7</sub>La<sub>3</sub>Zr<sub>2</sub>O<sub>12</sub> (LLZO), garnet-type Li solid-state electrolyte, has attracted much attention since it was first reported in 2007 (Xie H. et al., 2018). Li<sub>5</sub>La<sub>3</sub>M<sub>2</sub>O<sub>12</sub> (M = Nb, Ta) is the first reported lithium ion conductor with a garnet structure (**Figure 5A**; Thangadurai et al., 2003; O'Callaghan et al.,

2008). The traditional garnet chemical formula is A<sub>3</sub>B<sub>2</sub>(XO<sub>4</sub>)<sub>3</sub> (A = Ca, Mg, Y, La or rare-earth elements; B = Al, Fe, Ga, Ge, Mn, Ni, or V). Garnet-type Li solid-state electrolyte has high ionic conductivity and wide electrochemical window (Wu et al., 2017). At room temperature, the ionic conductivity of Li<sub>5</sub>La<sub>3</sub>M<sub>2</sub>O<sub>12</sub> (M = Nb, Ta) reached 10<sup>-3</sup> S/cm and exhibits outstanding chemical stability over a wide temperature range. However, when the all-solid-state battery is assembled using garnet-type ceramics, the electrode/electrolyte interface always shows poor conductivity, resulting in deteriorated battery performance, as well as increased interface resistance and decreased ionic conductivity (Chen et al., 2018). Polymer/Garnet composite electrolytes offer an option of improving the overall electrochemical performances.

With a large specific surface area, nanoscale garnet ceramic fillers improve the transition rate of ions (Kumar and Scanlon, 2000). A composite electrolyte composed of PEO containing 52.5 wt.% Li<sub>7</sub>La<sub>3</sub>Zr<sub>2</sub>O<sub>12</sub> (LLZO) particles displays a conductivity

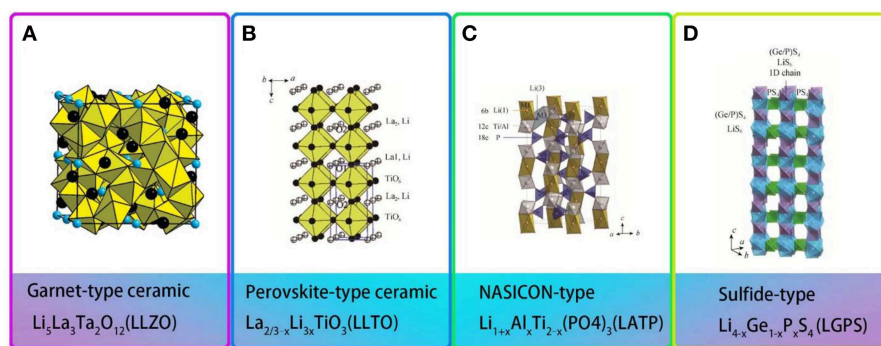


**FIGURE 5 |** Structures of different types of fast ion conductors **(A)** Framework of garnet-type ceramic [Reproduction with permission from O'Callaghan et al. (2008) Copyright© 2008, American Chemical Society] **(B)** Crystal structure of perovskite-type ceramic. [Reproduction with permission from Stramare et al. (2003) Copyright© 2003, American Chemical Society] **(C)** Crystal structure of NASICON-type ceramic. [Reproduction with permission from Perez-Estebanez et al. (2014) Copyright© 2015, The Royal Society of Chemistry] **(D)** Crystal structure of Sulfide-type ceramic. [Reproduction with permission from Kamaya et al. (2011) Copyright© 2011, nature].

**TABLE 3 |** Summary of fast-ion conductive ceramics/polymer solid electrolytes.

Year	Polymer electrolyte ingredients	Ionic conductivity (S/cm)	References
2003	Li <sub>5</sub> La <sub>3</sub> M <sub>2</sub> O <sub>12</sub> (M = Nb, Ta)-PEO-LiPF <sub>6</sub>	10 <sup>-6</sup> (25°C)	Ratner et al., 2000
2015	Li <sub>7</sub> La <sub>3</sub> Zr <sub>2</sub> O <sub>12</sub> (LLZO)-PEO-LiClO <sub>4</sub>	4.42 × 10 <sup>-4</sup> (55°C)	Shi et al., 2017
2015	Li <sub>0.33</sub> La <sub>0.557</sub> TiO <sub>3</sub> (LLTO) random nanowire-PAN-LiClO <sub>4</sub>	2.4 × 10 <sup>-4</sup> (25°C)	Subianto et al., 2009
2015	Li <sub>2.5</sub> Al <sub>0.5</sub> Ge <sub>1.5</sub> (PO <sub>4</sub> ) <sub>3</sub> (LAGP)-PEO-LiClO <sub>4</sub>	2.6 × 10 <sup>-4</sup> (55°C)	Tikekar et al., 2016
2015	Li <sub>7</sub> La <sub>3</sub> Zr <sub>2</sub> O <sub>12</sub> (LLZO)-PEO-LiClO <sub>4</sub>	4.42 × 10 <sup>-4</sup> (55°C)	Shi et al., 2017
2016	Li <sub>6.4</sub> La <sub>3</sub> Zr <sub>2</sub> Al <sub>0.2</sub> O <sub>12</sub> (LLZO)-PEO-LiTFSI	2.5 × 10 <sup>-4</sup> (25°C)	Stavila et al., 2014
2016	Li <sub>1.5</sub> Al <sub>0.5</sub> Ge <sub>1.5</sub> (PO <sub>4</sub> ) <sub>3</sub> (LAGP)-PEO-LiTFSI	6.76 × 10 <sup>-4</sup> (60°C)	Thokchom et al., 2008
2016	Li <sub>10</sub> GeP <sub>2</sub> S <sub>12</sub> -PEO-LiTFSI	10 <sup>-5</sup> (25°C)	Verma et al., 2010
2017	Li <sub>6.20</sub> Ga <sub>0.30</sub> La <sub>2.95</sub> Rb <sub>0.05</sub> Zr <sub>2</sub> O <sub>12</sub> -PVDF-LiTFSI	1.62 × 10 <sup>-3</sup> (25°C)	Scrosati and Garche, 2010
2017	Li <sub>6.75</sub> La <sub>3</sub> Zr <sub>1.75</sub> Ta <sub>0.25</sub> O <sub>12</sub> -PVDF-LiClO <sub>4</sub>	5 × 10 <sup>-4</sup> (25°C)	Siqueira and Ribeiro, 2006
2017	Li <sub>0.33</sub> La <sub>0.557</sub> TiO <sub>3</sub> (LLTO) aligned nanowire-PAN-LiClO <sub>4</sub>	6.05 × 10 <sup>-5</sup> (30°C)	Srivastava and Tiwari, 2009
2017	Li <sub>1.3</sub> Al <sub>0.3</sub> Ti <sub>1.7</sub> (PO <sub>4</sub> ) <sub>3</sub> (LATP)-PEO-BPEG-LiTFSI	2.5 × 10 <sup>-4</sup> (60°C)	Thangadurai et al., 2003
2018	Li <sub>7</sub> La <sub>3</sub> Zr <sub>2</sub> O <sub>12</sub> (LLZO)-PEO-LiTFSI	1.12 × 10 <sup>-4</sup> (25°C)	Quartarone and Mustarelli, 2011
2018	Li <sub>6.4</sub> La <sub>3</sub> Zr <sub>1.4</sub> Ta <sub>0.6</sub> O <sub>12</sub> (LLZTO)-PEO-LiTFSI	10 <sup>-4</sup> (55°C)	Sheng et al., 2017
2018	Li <sub>0.33</sub> La <sub>0.557</sub> TiO <sub>3</sub> -PEO-LiClO <sub>4</sub>	2.4 × 10 <sup>-4</sup> (25°C)	Stramare et al., 2003
2018	3D-Li <sub>0.35</sub> La <sub>0.55</sub> TiO <sub>3</sub> (LLTO)-PEO-LiTFSI	8.8 × 10 <sup>-5</sup> (25°C)	Sun et al., 2014

which reaches  $4.42 \times 10^{-4}$  S/cm at 55°C (Thokchom et al., 2008). Li<sub>6.75</sub>La<sub>3</sub>Zr<sub>1.75</sub>Ta<sub>0.25</sub>O<sub>12</sub> (LLZTO) is selected as an active filler and dispersed into PVDF matrix to fabricate PVDF/LLZTO hybrid electrolytes (Zhang X. et al., 2017). The hybrid electrolyte with 10 wt.% LLZTO loadings exhibited the highest ionic conductivity ( $5 \times 10^{-4}$  S/cm), about seven times more than none LLZTO. It is attributed to that LLZTO particles react with Li<sup>+</sup> via acid-base interaction. Dissociation of the lithium salt will raise the carrier density for conduction. Furthermore, the garnet ceramic filler contributes to reduce the crystallinity of polymer and so to increase the ionic conductivity. Instead of simply mixing active ceramic particles into polymers, Goodenough et al. (Chen et al., 2018) introduced a novel approach of composite polymer into ceramic.

As a consequence, high ionic conductivity ( $10^{-4}$  S/cm at 55°C) were gained and the electrochemical window of 0–5.0 V. As used in the all-solid-state

Li/LiFePO<sub>4</sub> cells, both “ceramic-in-polymer” and “polymer-in-ceramic” with a LiTFSI salt display remarkable cycling stability. The systems, “polymer-in-ceramic” provide higher mechanical strength and safety than “ceramic-in-polymer.”

Morphologies of ceramics fillers such as particles, distribution of nanowire and 3D framework may affect the ionic conductivity of polymer composite electrolytes. Unlike particles and random nanowires, aligned nanowires combined with polymers can provide continuous transport pathways for Li<sup>+</sup> (Figure 6). Cui et al. (Liu et al., 2017) compares the different morphologies of LLZO to evaluate their benefits for ionic transport. They found that a composite polymer electrolyte with well-aligned inorganic nanowires (LLZO) shows an ionic conductivity of  $6.05 \times 10^{-5}$  S/cm at 30°C, which was increased by almost one order of magnitude than the composite with randomly aligned nanowires or nanoparticles. The appreciable conductivity

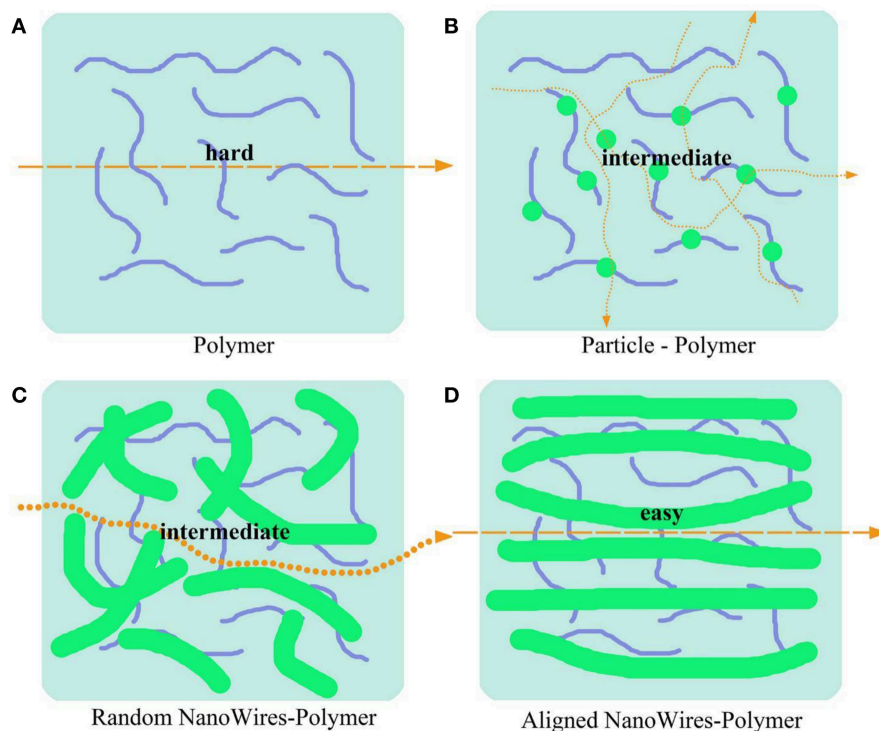


**FIGURE 6 |** Schematic of conduction mechanism in three kinds of morphologies solid polymer electrolytes. **(A)** Ionic transport path in pure polymer electrolytes. **(B–D)** Ionic transport path in polymer-based composite electrolytes with nanoparticles **(B)**, random nanowires **(C)** and aligned nanowires **(D)**.

improvement is due to  $\text{Li}^+$  migration without crossing junctions on the nanowire surfaces.

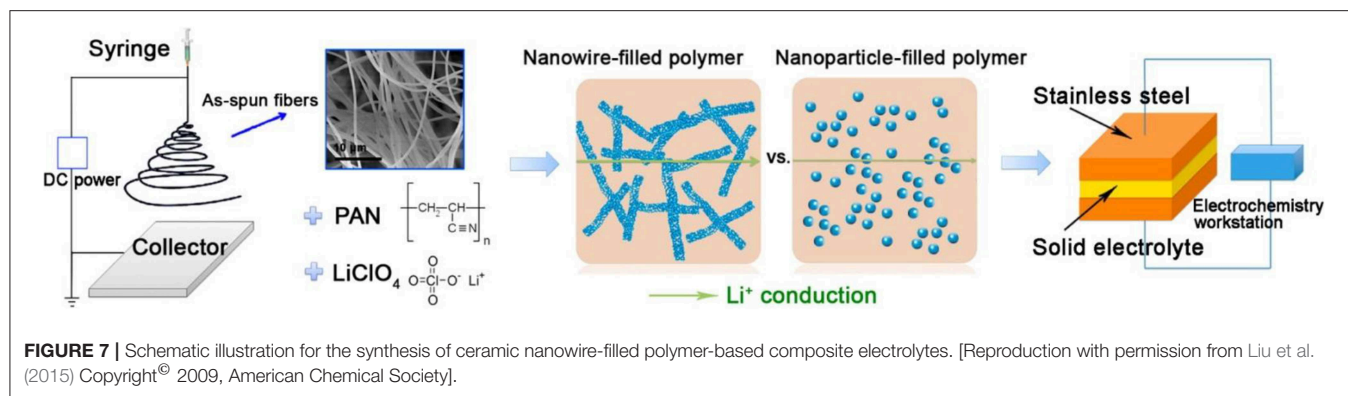
In addition to 1D nanowires (Bae et al., 2018), prepared 3D ceramic  $\text{Li}_{6.28}\text{La}_3\text{Zr}_2\text{Al}_{0.24}\text{O}_{12}$  networks by using hydrogel and mixed it into polymer solution to attain solid electrolyte. The designed structure is believed to have high conductivity ( $8.5 \times 10^{-5}$  S/cm at  $25^\circ\text{C}$ ) and good interfacial compatibility with electrodes. The integrated structure of 3D LLZO structure provides continuous 3D network of conduction pathways leading to highly improved ionic conductivity and mechanical properties. Similarly, 3D garnet nanofiber networks-polymer composite was also prepared (Fu et al., 2016). In this approach, the LLZO porous structure, composed of casually distributed and interconnected nanofibers, forms a continuous transport network for  $\text{Li}^+$ . The LiTFSI-PEO polymer is then filled into the porous 3D LLZO ceramic networks, forming the 3D garnet-polymer composite films. Then LiTFSI-PEO polymer and porous 3D Inorganic structure are combined to synthesize a 3D LLZO-polymer composite membrane which exhibited a high ionic conductivity of  $2.5 \times 10^{-4}$  S/cm at  $25^\circ\text{C}$ . The three-dimensional ion transport network offers a new option of designing composite electrolytes.

## Perovskite-Type Composite Polymer Electrolytes

Perovskite-type solid electrolytes  $\text{Li}_{3-x}\text{La}_{2/3-x}\text{TiO}_3$  (LLTO) has a cubic structure with space group of P4/mmm and Cmmm (Figure 5B; Stramare et al., 2003). LLTO is well-known for its stable at high voltages. However, its preparation conditions are

very strict and the ionic conductivity is also low. Recently, a polymer-ceramic composite electrolyte PEO/ $\text{LiClO}_4$  has been studied by composite PEO with  $\text{Li}_{0.33}\text{La}_{0.557}\text{TiO}_3$  nanowires. It exhibited extreme lithium-ion conductivity of  $2.4 \times 10^{-4}$  S/cm at  $25^\circ\text{C}$  (Zhu et al., 2018). Cui et al. (Liu et al., 2015) studied the effect of two different morphological LLTO materials on the ionic conductivity of polymer electrolytes, which are nanoscale particles and nanowire LLTO, respectively (Figure 7). The introduction of LLTO nanowire into PAN achieved higher ionic conductivity  $2.4 \times 10^{-4}$  S/cm at room temperature as compared to pristine PAN film. The composite electrolyte offers a 3D long distance Lithium-ion transmission network, which reduce the negative effect of agglomeration of inorganic ceramics in polymers relative to nanoparticles. This work opened a new way to develop one-dimensional fast ion conductive ceramic materials in solid electrolytes for lithium batteries.

The ionic conductivity has a strong relationship with the ceramic component loadings in the composite electrolyte. Generally, the higher the content, the lower the ionic conductivity will be, because nano-sized ceramic fillers are agglomerated and may block the percolation network around the phase interface. Meanwhile, in order to achieve high security of the composite electrolyte, it is necessary to reduce the proportion of combustible organic polymer content and increase the flame-retardant inorganic ceramic portion. Goodenough et al. (Bae et al., 2018) constructed a 3D-LLTO/PEO composite electrolyte using a hydrogel-derived method. The LLTO was incorporated into the hydrogel template, then it was cast with



PEO after removing the template. This artificial 3D infiltration network naturally avoids the agglomeration of nanofillers compared to the traditional simple dispersion process, and its ultra-high specific surface area provides a continuous phase interface network as lithium ion transport channel. Therefore, this composite electrolyte displayed a high ionic conductivity of  $8.8 \times 10^{-5} \text{ S cm}^{-1}$  at room temperature.

## NASICON-Type Composite Polymer Electrolytes

NASICON-type ceramics (aka “sodium super ion conductor”) were firstly discovered in 1968 with composition of  $\text{NaM}_2(\text{PO}_4)_3$  ( $\text{M} = \text{Ge}, \text{Ti}, \text{Zr}$ ) (Epp et al., 2015). Surdrear et al. firstly reported NASICON-type solid electrolyte  $\text{LiZr}_2(\text{PO}_4)_3$  at 1989. For formula  $\text{LiM}_2(\text{XO}_4)_3$ ,  $[\text{M}_2(\text{XO}_4)_3]$  constitutes the basic structure of NASICON. The  $\text{MO}_6$  octahedron and the  $\text{XO}_4$  tetrahedron are connected in a common angle to form Li-ion transmission channel. Aono et al. (1990) first reported doped trivalent ions into  $\text{LiTi}_2(\text{PO}_4)_3$  and found that the ionic conductivity was improved. In 2014, Perez-Estebanez et al. (2014) achieved high conductivity in the  $\text{Li}_{1+x}\text{Al}_x\text{Ti}_{2-x}(\text{PO}_4)_3$  (LATP) of  $6.76 \times 10^{-4} \text{ S/cm}$  at  $60^\circ\text{C}$  (Figure 5C). After that, research on NASICON-type electrolyte experienced fast growth because of its high ionic conductivity (over  $10^{-3} \text{ S/cm}$ ) at ambient temperature and stable in the ambient atmosphere.

Pan group (Yang et al., 2017) fabricated  $\text{Li}_{1.3}\text{Al}_{0.3}\text{Ti}_{1.7}(\text{PO}_4)_3$ -PEO polymer electrolyte. The discharge specific capacity of  $\text{LiFePO}_4/\text{Li}$  using this polymer electrolyte was 158.2 and 94.2 mAh/g at 0.1 and 2 C, respectively. LATP can not only form pathways for lithium transportation in the interphase, leading to improved ionic conductivity, but also physically resist lithium dendrite growth. Lithium aluminum germanium phosphate (LAGP) is also a kind of NASICON-type fast ion conductor ceramic with relative high ionic conductivity ( $>10^{-4} \text{ S/cm}$ ). Zhao et al. (2016a) similarly incorporated NASICON-type  $\text{Li}_{1.5}\text{Al}_{0.5}\text{Ge}_{1.5}(\text{PO}_4)_3$  (LAGP) as  $\text{Li}^+$  conductors into PEO matrix. The resultant polymer electrolyte displayed a wide electrochemical window of 0–5.3 V and an ion-conductivity of  $6.76 \times 10^{-4} \text{ S/cm}$  at  $60^\circ\text{C}$ . More intriguingly, such polymer electrolyte based  $\text{LiFePO}_4/\text{Li}$  battery showed prominent cycling stability (90% after 50 cycles). Jung et al. (2015) designed a stretchable ceramic-polymer composite electrolyte

membrane where NASICON-type LAGP were incorporated into a polymer-Li salt  $\text{LiClO}_4$  matrix, to synthesize a polyethylene oxide solid electrolyte membrane (Figure 8A). The PEO- $\text{LiClO}_4$ -LAGP composite electrolyte with 60–80 wt.% LAGP is still capable of providing enough mechanical modulus and good electrochemical performance.  $\text{Li}/\text{LiFePO}_4$  cells initial discharge capacities reach 138.5 mAh/g and deliver good capacity retention.

## Sulfide-Type Polymer Electrolytes

Sulfide-type electrolytes show supreme ion-conductivities in the magnitude of  $10^{-2} \text{ S/cm}$  at room temperature (Kamaya et al., 2011). However, they demonstrate instability due to reaction with water vapor in air. Sulfide-type ceramics can be divided into three categories: glasses, glass-ceramic, and ceramic. The entire types ion-conductivity can near or exceed liquid electrolyte. Glass/glass-ceramic  $\text{Li}_2\text{S-P}_2\text{S}_5$  and ceramic thio-LISICON  $\text{Li}_{4-x}\text{Ge}_{1-x}\text{P}_x\text{S}_4$  ( $0 < x < 1$ ) are the most promising ones.  $\text{Li}_{10}\text{GeP}_2\text{S}_{12}$  and PEO has been composited to prepare solid electrolyte membrane (Zhao et al., 2016b). The conductivity at room temperature reaches  $10^{-5} \text{ S/cm}$ , which is higher than other conventional PEO electrolyte at least one order of magnitude, and the electrochemical window spans between 0 and 5.7 V. It greatly expands the selection range of positive electrode materials and presents improved stability to lithium metal. The solid polymer batteries show capacity retentions approaching 92.5% after 50 cycles. Villaluenga et al. (2016) prepared a non-flammable composite electrolytes by fully mechanochemical reaction between hydroxy-terminated perfluoropolyether (PFPE-diol), LiTFSI and  $75\text{Li}_2\text{S-}25\text{P}_2\text{S}_5$  by ball milling for 2 h. The electrolyte containing 77 wt.% ( $75\text{Li}_2\text{S-}25\text{P}_2\text{S}_5$ ) and 23 wt.% PFPE-diol/LiTFSI displays a conductivity of  $10^{-4} \text{ S/cm}$  at room temperature (Figure 8B).

## Solid Polymer Electrolytes With Ionic Liquid

An ionic liquid (IL) is a molten salt at low temperatures and generally consist of organic cations and inorganic anions (Zhao et al., 2016b). Due to the special state, ionic liquids have the characteristics of vapor pressure free, high electrochemical stability, and good thermal stability (Armand et al., 2009).



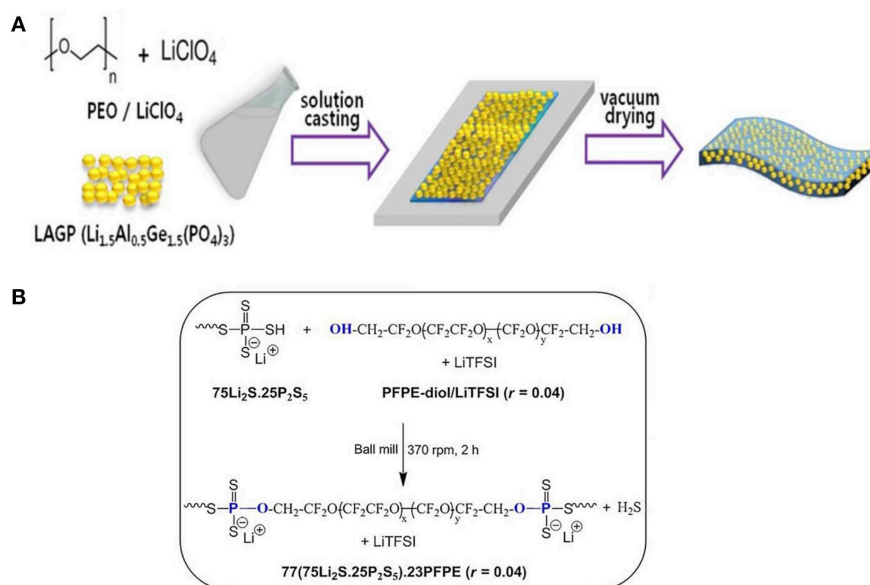


**FIGURE 8 | (A)** Schematic presentation of preparation for PEO-LiClO<sub>4</sub>-LAGP hybrid solid electrolyte. [Reproduction with permission from Jung et al. (2015) Copyright 2017, The Electrochemical Society.] **(B)** Synthesis of the hybrid electrolyte 77(75Li<sub>2</sub>S.25P<sub>2</sub>S<sub>5</sub>).23PFPE ( $r = 0.04$ ) by mechanochemical reaction. [Reproduction with permission from Villaluenga et al. (2016). Copyright 2016, National Academy of Sciences].

Although ionic liquids have high ionic conductivity, they are not suitable for direct use as electrolytes because of low viscosity. The combination of ionic liquid and polymer offers an option as solid electrolyte for lithium ion batteries.

The introduction of IL into the polymer results in higher ionic conductivity, but it is usually accompanied by a decrease in mechanical strength, especially at high temperature. Lower IL concentration leads to higher mechanical strength, and a smoother continuous electrolyte surface, which is more favorable for ion transport. Therefore, the amount of IL plays an important influence on the ionic conductivity and mechanical properties. Moreover, battery cycling at high temperatures usually causes decomposition of IL components, resulting in degraded performances. It added one more requirement of the polymer components to retain high IL contents.

IL-based polymer electrolytes are mainly classified into three categories. (1) polymer doped IL; (2) ILs/polymerizable monomers crosslinks; (3) polymeric ionic liquids (PILs). The first one is just IL added to the polymer solution or infused in the polymer film directly. For example, Subianto et al. (2009) prepared an electrolyte consisting of IL, silica nano-particles, and Nafion by using sulfonated polyhedral oligomeric silsesquioxane (S-POSS) modified Nafion membranes soaking with 1-butyl-3-methylimidazolium bis-(trifluoromethylsulfonyl)imide (BMI-BTFSI) (**Figure 9**). The thermal stability of Nafion films was improved after ionic liquid infiltration. More importantly, the conductivity of the infiltrated films is increased by one to two orders of magnitude than that of the unmodified one. ILs/polymer monomer cross-linking is the mixing of ILs and polymerizable monomers to obtain electrolytes by means of thermal or photo polymerization. Polymeric ionic

liquids (PILs) can be designed by the direct polymerization of polymerizable IL-based monomer or polymerizing a modified polymer and an IL monomer. By taking full advantages of the specific properties of ionic liquids and polymers, PIL membrane has generated great interest in recent years. By adopting solution cast technique, Karuppasamy et al. (2016) designed PIL synthesized solid electrolytes by preparing ionic liquids of lithium N, N-bis(trifluoromethanesulfonyl)imide (LiTFSI) in N-ethyl-N-methylimidazolium-bis(trifluoromethanesulfonyl)imide (EMImTFSI) IL with incorporated organic solvent and nanoparticle into PEO. The prepared PIL electrolyte exhibits high ionic conductivity of  $10^{-2}$  S/cm and high electrochemical stability. Yang et al. (Li et al., 2011) designed a solid electrolyte by combining PIL with different anions such as BF<sub>4</sub><sup>-</sup>, PF<sub>6</sub><sup>-</sup>, ClO<sub>4</sub><sup>-</sup>, and N(CF<sub>3</sub>SO<sub>2</sub>)<sub>2</sub><sup>-</sup>. PILs electrolyte with 1g2-MA-BF<sub>4</sub>/LiBF<sub>4</sub> exhibited ionic conductivity as high as  $1.35 \times 10^{-4}$  S/cm at 30°C. Starting from PEO, modified sepiolite (TPGS-S), LiTFSI, and 1-Butyl-1-methylpyrrolidinium bis(trifluoromethanesulfonyl)imide (PYR14TFSI) ionic liquid, electrolytes was synthesized via solvent free extrusion method (Gonzalez et al., 2018). The resultant polymer electrolyte displayed wide electrochemical window of 4.2 V and ion-conductivity of  $5 \times 10^{-4}$  S/cm at 60°C.

## SOLID POLYMER ELECTROLYTES WITH MOFs

Metal-organic frameworks (MOFs) are a new kind of porous material, which are composed of metal ions and bridging organic ligands (Stavila et al., 2014; Indra et al., 2018; Xie X. C. et al.,

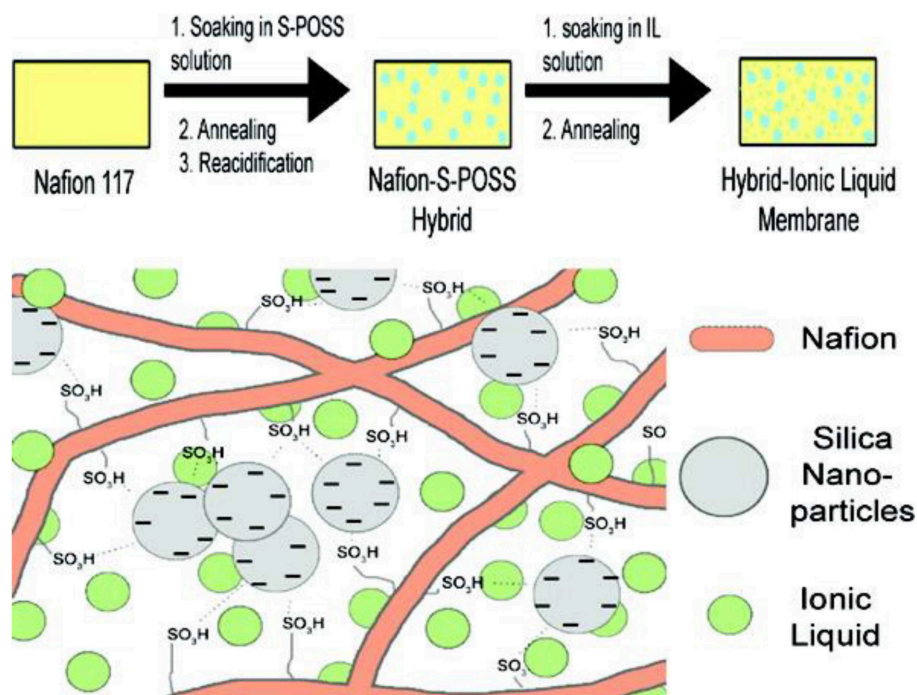


**FIGURE 9** | Schematic illustration of the overall procedure for the preparation of Hybrid-Ionic liquid electrolyte. [Reproduction with permission from Subianto et al. (2009). Copyright© 2009, American Chemical Society].

2018). MOFs have many properties such as porosity, large specific surface area, and polymetallic sites (Yuan et al., 2013), so they are widely used in many fields including gas adsorption, molecular separation, drug delivery (Mueller et al., 2006; Kuppler et al., 2009; Li et al., 2009). Many investigations have indicated that MOFs also has positive effect on increased ionic conductivity due to high specific surface and the good adsorption property. Yuan et al. (2013) prepared a new SPE by the addition of Zn-based MOF-5 into PEO polymer electrolyte. The combination of MOFs and polymer showed positive effect on the mechanical and electrochemical properties as solid electrolyte. The ionic conductivity of these membrane can reach  $3.16 \times 10^{-5}$  S/cm at ambient temperature, which is attributed to two parts. Firstly, the interaction of the Lewis acidic sites on the MOF-5 with the PEO chain and the lithium salt hinder the crystallization of the PEO, and facilitate the formation of Li<sup>+</sup> conductive channels. Secondly, the isotropic open MOF-5 can adsorb solvent to accelerate the transport of ions. Gerbaldi et al. (2014) proposed a new filler material (aluminum-based MOF) (**Figure 10A**), which was successfully prepared and incorporated in a PEO-based polymer matrix. Ionic conductivity of the composite membrane is two orders of magnitude greater than that without mixed MOFs. lithium batteries (Li/LiFePO<sub>4</sub>) with the electrolyte showed distinguished charge-discharge performance and high specific capacity. At 1 C rate, the battery can still cycle stably at 50°C, and the decay of specific capacity is not obvious when restored to 70°C. After 500 cycles, the capacity is almost maintained as the initial, and the Coulombic efficiency is only slightly decreased. This shows an excellent capacity retention

capability and good cycle stability (**Figure 10B**). Recently, Wang Z. et al. (2018) synthesized a new chemically linked composite MOF-polymer electrolyte. The film was prepared by photopolymerization with post-synthetic modification of the MOF (M-UiO-66-NH<sub>2</sub>), poly(ethylene glycol) diacrylate and LITFSI (**Figure 11**). The interface between MOF and polymer provides a fast channel for lithium-ion transport, accordingly the conductivity of the composite electrolyte (HSPE-1-8) is  $4.31 \times 10^{-5}$  S/cm at 30°C that is up to five times more than that of no composite MOF. The solid Li/LiFePO<sub>4</sub> cells assembled with these SPEs cycled at 60°C demonstrated excellent coulombic efficiencies.

## SOLID POLYMER ELECTROLYTES WITH CELLULOSE

Cellulose is a non-toxic harmless, inexpensive, and natural eco-friendly materials with high mechanical strength and a large specific surface area (Baxter et al., 2009; Sheng et al., 2017) Due to the unique properties, cellulose can not only enhance the mechanical properties of polymers in electrolytes, but hinder the growth of lithium dendrites effectively acting as a physical barrier. The interface between cellulose and polymer behaves as a channel for ion transport, facilitating ion transport. In addition, polar groups in cellulose can improve salt dissociation (Shi et al., 2017). Nair et al. (2009) reported a polymer composite electrolyte with cellulose reinforcement. The reinforced electrolyte exhibited a high ionic conductivity ( $2.0 \times 10^{-4}$  S/cm at 25°C) and

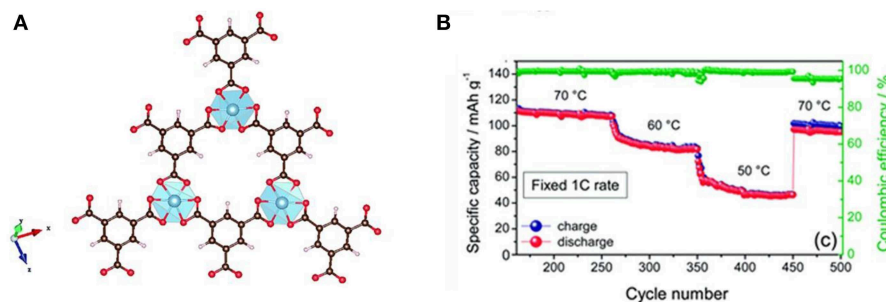


**FIGURE 10 | (A)** Schematic diagram of the ideal network structure of an aluminum(III)-1,3,5-benzenetricarboxylate (Al-BTC) metal organic framework. **(B)** Electrochemical characteristics of the  $\text{LiFePO}_4/\text{S4-NCPE}/\text{Li}$  cell at different temperatures and current regimes. [Reproduction with permission from Gerbaldi et al. (2014). Copyright© 2014, The Royal Society of Chemistry].

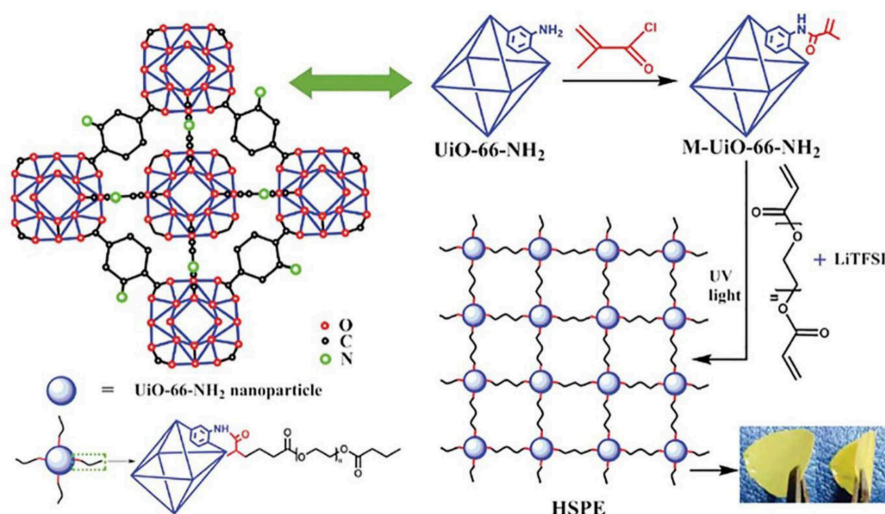


**FIGURE 11 |** Synthetic route of the hybrid covalently linked MOF-PEGDA-based all-solid-state electrolyte. [Reproduction with permission from Wang Z. et al. (2018). Copyright© 2018, The Royal Society of Chemistry].

an exceptional mechanical property, which is expected for flexible electronic devices applications. Furthermore, ionic liquid compounded with cellulose can solve the issues of IL leakage in the composite electrolyte. Shi et al. (2017) designed a new type of 3D self-assembled polymeric ionic liquid (PIL)-nanocellulose to form polymer electrolyte. The structure not only enhances the mechanical properties of the SPE, but also forms strong lithium coordination to promote lithium salt dissolution. The dissolved lithium salt can combine with IL to form an ion-conducting domain, thereby promoting ion transport. Asghar et al. (2012) adequately utilizes the characteristics of networked cellulose (NC), with mechanical strength and adopted it to design quasi-solid PEG- $\text{LiClO}_4$ -NC polymer electrolyte. The resultant composite electrolyte with a 12.8 wt.% NC resulted in the highest ion conductivity ( $10^{-4}$  S/cm at  $25^\circ\text{C}$ ) and is electrochemically stable up to 4.7 V. Similarly, Zhang et al. (2014) combined cellulose non-woven with PCA-PEO to fabricate a rigid-flexible coupling SPE, upgrading their comprehensive properties of the composite electrolyte significantly.

## SUMMARY AND OUTLOOK

Although lithium-ion batteries have long been commercialized, the use of liquid electrolytes has some disadvantages such as poor safety and unstable electrochemical performance, which greatly limits its further development and wider applications. Solid composite polymer electrolyte in lithium-ion batteries has received a lot of attention lately because of its low flammability, good flexibility, excellent thermal stability, and high safety. In this review, we have provided fundamental understandings of the ionic conductivity mechanisms and interfaces for solid composite electrolytes, in the meantime, recent progresses on polymer-based composite electrolytes were summarized, including polymer/inert ceramics, polymer/fast-ion conductive, polymer/ionic liquid, polymer/MOFs, and polymer/cellulose composite electrolytes.

Although substantial researches have been dedicated to the polymer-based composite electrolytes, some fundamental issues still need to be solved urgently before commercialization. For

example, ionic conductivity of the composite solid electrolyte still differs by several orders of magnitude from the liquid counterpart; many polymer-based solid electrolytes exhibit high ionic conductivity at high temperatures, while it drops dramatically at lower temperatures; the conductivity mechanism and interfacial interaction need to be further clarified not accelerate further studies.

At present, the polymer/ionic liquid solid electrolyte inevitably causes a decrease in mechanical properties when obtaining high ionic conductivity, which has great safety hazards. The difficulty in polymer/inert ceramic solid electrolytes is how to construct a good dispersion and strengthen the interaction between the filler and the polymer, which restricts the further improvement of ionic conductivity. In comparison, polymer/fast ion conductors composite electrolytes have both high ionic conductivity at room temperature and good mechanical properties. The future development direction of polymer-based solid electrolytes is likely to be the combination of fast ion conductors and polymers, which can combine the advantages of high ion conductivity of fast ion conductors and solve the problem of poor interface contact. Of all the types of polymer-based composite solid electrolytes, SPEs with fast ion conductors have gained all the advantages and are the direction of development of commercial solid electrolytes.

The following aspects were recommended of focusing on solid electrolyte in future developments. Firstly, using materials genome database to analyze, guide, and design composite material can promote efficiency and cost savings. Material calculations facilitate an in-depth understanding of the material. The corresponding ionic mechanism can be simulated

and interpreted by material calculations. Secondly, most of battery materials, such as electrodes, electrolytes, and SEI films, are sensitive to electron beams and difficult to observe under conventional transmission electron microscopy (TEM). Advanced characterization techniques can facilitate analysis of material mechanisms. For example, using cryo-electron microscopy, Zachman et al. (2018) reveals atomic structure of sensitive battery materials and interfaces. Similarly, Meng et al. (Wang et al., 2017) studied the interface of solid electrolytes via Cryogenic TEM, which has greatly promoted further research on the interface. Finally, struggling to find suitable composite electrolytes with high conductivities at low temperature always deserves more study. Commercial solid electrolytes require high ionic conductivity at room temperature, safety and easy processing to compete with the liquid counterpart.

## AUTHOR CONTRIBUTIONS

PY, JW, and HY collected the data, performed the statistical analysis, interpretation of the results, and wrote the manuscript. ZD, YL, and JL carried out the bibliographical research and performed the inferential analyses together with other authors. ML and XL offered Suggestions and revisions in English for the article.

## FUNDING

This work was financially supported by the Shenzhen International Collaboration project (GJHZ20180923193456903), and Shenzhen Fundamental Research Program of Subject Layout (JCYJ20170413102735544).

## REFERENCES

- Agrawal, R. C., and Pandey, G. P. (2008). Solid polymer electrolytes: materials designing and all-solid-state battery applications: an overview. *J Phys D Appl Phys.* 41:223001. doi: 10.1088/0022-3727/41/22/223001
- Aliahmad, N., Shrestha, S., Varshamyan, K., and Agarwal, M. (2016). Poly(vinylidene fluoride-hexafluoropropylene) polymer electrolyte for paper-based and flexible battery applications. *AIP Adv.* 6:065206. doi: 10.1063/1.4953811
- Aono, H., Sugimoto, E., Sadaoka, Y., Imanaka, N., and Adachi, G. (1990). Ionic-conductivity of solid electrolytes based on lithium titanium phosphate. *J. Electrochem. Soc.* 137, 1023–1027. doi: 10.1149/1.2086597
- Aravindan, V., and Vickraman, P. (2008). Characterization of SiO<sub>2</sub> and Al<sub>2</sub>O<sub>3</sub> incorporated PVdF-HFP based composite polymer electrolytes with LiPF<sub>6</sub>(CF<sub>3</sub>CF<sub>2</sub>)(3). *J. Appl. Polym. Sci.* 108, 1314–1322. doi: 10.1002/app.27824
- Armand, M., Endres, F., MacFarlane, D. R., Ohno, H., and Scrosati, B. (2009). Ionic-liquid materials for the electrochemical challenges of the future. *Nat. Mater.* 8, 621–629. doi: 10.1038/Nmat2448
- Asghar, A., Samad, Y. A., Lalia, B. S., and Hashaikh, R. (2012). PEG based quasi-solid polymer electrolyte: mechanically supported by networked cellulose. *J. Memb. Sci.* 421, 85–90. doi: 10.1016/j.memsci.2012.06.037
- Bae, J., Li, Y., Zhang, J., Zhou, X., Zhao, F., Shi, Y., et al. (2018). A 3D nanostructured hydrogel-framework-derived high-performance composite polymer Lithium-ion electrolyte. *Angew. Chem. Int. Ed.* 57, 2096–2100. doi: 10.1002/anie.201710841
- Baxter, J., Bian, Z., Chen, G., Danielson, D., Dresselhaus, M. S., Fedorov, A. G., et al. (2009). Nanoscale design to enable the revolution in renewable energy. *Energy Environ. Sci.* 2, 559–588. doi: 10.1039/b821698c
- Camacho-Forero, L. E., and Balbuena, P. B. (2018). Exploring interfacial stability of solid-state electrolytes at the lithium-metal anode surface. *J. Power Sources* 396, 782–790. doi: 10.1016/j.jpowsour.2018.06.092
- Capuano, F., Croce, F., and Scrosati, B. (1991). Composite polymer electrolytes. *J. Electrochem. Soc.* 138, 1918–1922. doi: 10.1149/1.2085900
- Chen, L., Li, Y., Li, S.-P., Fan, L.-Z., Nan, C.-W., and Goodenough, J. B. (2018). PEO/garnet composite electrolytes for solid-state lithium batteries: from “ceramic-in-polymer” to “polymer-in-ceramic”. *Nano Energy* 46, 176–184. doi: 10.1016/j.nanoen.2017.12.037
- Chen, R. J., Qu, W. J., Guo, X., Li, L., and Wu, F. (2016). The pursuit of solid-state electrolytes for lithium batteries: from comprehensive insight to emerging horizons. *Mater. Horizon.* 3, 487–516. doi: 10.1039/c6mh00218h
- Croce, F., Appetecchi, G. B., Persi, L., and Scrosati, B. (1998). Nanocomposite polymer electrolytes for lithium batteries. *Nature* 394, 456–458.
- Cui, Y., Baker, A. P., Xu, X., Xiang, Y., Wang, L., Lavorgna, M., et al. (2015). Enhancement of Nafion based membranes for direct methanol fuel cell applications through the inclusion of ammonium-X zeolite fillers. *J. Power Sources* 294, 369–376. doi: 10.1016/j.jpowsour.2015.06.078
- Cui, Y., Liu, Y., Wu, J., Zhang, F., Baker, A. P., Lavorgna, M., et al. (2018). Porous silicon-aluminum oxide particles functionalized with acid moieties: an innovative filler for enhanced Nafion-based membranes of direct methanol fuel cell. *J. Power Sources* 403, 118–126. doi: 10.1016/j.jpowsour.2018.09.090



- Dias, F. B., Plomp, L., and Veldhuis, J. B. J. (2000). Trends in polymer electrolytes for secondary lithium batteries. *J. Power Sources* 88, 169–191. doi: 10.1016/s0378-7753(99)00529-7
- Do, J. S., Chang, C. P., and Lee, T. J. (1996). Electrochemical properties of lithium salt-poly(ethylene oxide)ethylene carbonate polymer electrolyte and discharge characteristics of Li/MnO<sub>2</sub>. *Solid State Ionics* 89, 291–298. doi: 10.1016/0167-2738(96)00343-8
- Dong, X. C., and Wang, L. (2005). Compositions, structures and properties of polymer electrolytes for lithium ion battery. *Progr. Chem.* 17, 248–253.
- Epp, V., Ma, Q., Hammer, E.-M., Tietz, F., and Wilkening, M. (2015). Very fast bulk Li ion diffusivity in crystalline Li<sub>1.5</sub>Al<sub>0.5</sub>Ti<sub>1.5</sub>(PO<sub>4</sub>)(3) as seen using NMR relaxometry. *Phys. Chem. Chem. Phys.* 17, 32115–32121. doi: 10.1039/c5cp05337d
- Farrington, G. C., and Briant, J. L. (1979). Fast ionic transport in solids. *Science* 204, 1371–1379. doi: 10.1126/science.204.4400.1371
- Fergus, J. W. (2010). Ceramic and polymeric solid electrolytes for lithium-ion batteries. *J. Power Sources* 195, 4554–4569. doi: 10.1016/j.jpowsour.2010.01.076
- Fonseca, C. P., and Neves, S. (2002). Characterization of polymer electrolytes based on poly(dimethyl siloxane-co-ethylene oxide). *J. Power Sources* 104, 85–89. doi: 10.1016/s0378-7753(01)00902-8
- Forsyth, M., Tipton, A. L., Shriver, D. F., Ratner, M. A., and MacFarlane, D. R. (1997). Ionic conductivity in poly(diethylene glycol-carbonate)/sodium triflate complexes. *Solid State Ionics* 99, 257–261. doi: 10.1016/s0167-2738(97)00115-x
- Fu, K. K., Gong, Y., Dai, J., Gong, A., Han, X., Yao, Y., et al. (2016). Flexible, solid-state, ion-conducting membrane with 3D garnet nanofiber networks for lithium batteries. *Proc. Natl. Acad. Sci. USA* 113, 7094–7099. doi: 10.1073/pnas.1600422113
- Gang, W., Roos, J., Brinkmann, D., Capuano, F., Croce, F., and Scrosati, B. (1992). Comparison of NMR and conductivity in (PEO)(8)LiClO<sub>4</sub>+GAMMA-LiAlO<sub>2</sub>. *Solid State Ionics* 53, 1102–1105. doi: 10.1016/0167-2738(92)90297-3
- Gerbaldi, C., Nair, J. R., Kulandainathan, M. A., Kumar, R. S., Ferrara, C., Mustarelli, P., et al. (2014). Innovative high performing metal organic framework (MOF)-laden nanocomposite polymer electrolytes for all-solid-state lithium batteries. *J. Mater. Chem. A* 2, 9948–9954. doi: 10.1039/c4ta01856g
- Gonzalez, F., Tiemblo, P., Garcia, N., Garcia-Calvo, O., Fedeli, E., Kvasha, A., et al. (2018). High performance polymer/ionic liquid thermoplastic solid electrolyte prepared by solvent free processing for solid state lithium metal batteries. *Membranes* 8:55. doi: 10.3390/membranes8030055
- Hu, L., Tang, Z., and Zhang, Z. (2007). New composite polymer electrolyte comprising mesoporous lithium aluminate nanosheets and PEO/LiClO<sub>4</sub>. *J. Power Sources* 166, 226–232. doi: 10.1016/j.jpowsour.2007.01.028
- Indra, A., Song, T., and Paik, U. (2018). Metal organic framework derived materials: progress and prospects for the energy conversion and storage. *Adv. Mater.* 30:1705146. doi: 10.1002/adma.201705146
- Itoh, T., Ichikawa, Y., Uno, T., Kubo, M., and Yamamoto, O. (2003a). Composite polymer electrolytes based on poly(ethylene oxide), hyperbranched polymer, BaTiO<sub>3</sub> and LiN(CF<sub>3</sub>SO<sub>2</sub>)(2). *Solid State Ionics* 156, 393–399. doi: 10.1016/s0167-2738(02)00682-3
- Itoh, T., Miyamura, Y., Ichikawa, Y., Uno, T., Kubo, M., and Yamamoto, O. (2003b). Composite polymer electrolytes of poly(ethylene oxide)/BaTiO<sub>3</sub>/Li salt with hyperbranched polymer. *J. Power Sources* 119, 403–408. doi: 10.1016/s0378-7753(03)00261-1
- Jung, Y.-C., Lee, S.-M., Choi, J.-H., Jang, S. S., and Kim, D.-W. (2015). All solid-state lithium batteries assembled with hybrid solid electrolytes. *J. Electrochem. Soc.* 162, A704–A710. doi: 10.1149/2.0731504jes
- Kamaya, N., Homma, K., Yamakawa, Y., Hirayama, M., Kanno, R., Yonemura, M., et al. (2011). A lithium superionic conductor. *Nat. Mater.* 10, 682–686. doi: 10.1038/nmat3066
- Karuppasamy, K., Rhee, H. W., Reddy, P. A., Gupta, D., Mitu, L., Polu, A. R., et al. (2016). Ionic liquid incorporated nanocomposite polymer electrolytes for rechargeable lithium ion battery: a way to achieve improved electrochemical and interfacial properties. *J. Ind. Eng. Chem.* 40, 168–176. doi: 10.1016/j.jiec.2016.06.020
- Keller, M., Appetecchi, G. B., Kim, G.-T., Sharova, V., Schneider, M., Schuhmacher, J., et al. (2017). Electrochemical performance of a solvent-free hybrid ceramic-polymer electrolyte based on Li<sub>7</sub>La<sub>3</sub>Zr<sub>2</sub>O<sub>12</sub> in P(EO)(15)LiTFSI. *J. Power Sources* 353, 287–297. doi: 10.1016/j.jpowsour.2017.04.014
- Ketabi, S., and Lian, K. (2013). Effect of SiO<sub>2</sub> on conductivity and structural properties of PEO-EMIHSO<sub>4</sub> polymer electrolyte and enabled solid electrochemical capacitors. *Electrochim. Acta* 103, 174–178. doi: 10.1016/j.electacta.2013.04.053
- Knauth, P. (2009). Inorganic solid Li ion conductors: An overview. *Solid State Ionics* 180, 911–916. doi: 10.1016/j.ssi.2009.03.022
- Kumar, B., and Scanlon, L. G. (2000). Composite electrolytes for lithium rechargeable batteries. *J. Electroceramics* 5, 127–139. doi: 10.1023/a:1009958118260
- Kuppler, R. J., Timmons, D. J., Fang, Q.-R., Li, J.-R., Makal, T. A., Young, M. D., et al. (2009). Potential applications of metal-organic frameworks. *Coord. Chem. Rev.* 253, 3042–3066. doi: 10.1016/j.ccr.2009.05.019
- Li, J.-R., Kuppler, R. J., and Zhou, H.-C. (2009). Selective gas adsorption and separation in metal-organic frameworks. *Chem. Soc. Rev.* 38, 1477–1504. doi: 10.1039/b802426j
- Li, M., Yang, L., Fang, S., and Dong, S. (2011). Novel polymeric ionic liquid membranes as solid polymer electrolytes with high ionic conductivity at moderate temperature. *J. Memb. Sci.* 366, 245–250. doi: 10.1016/j.memsci.2010.10.004
- Liang, B., Tang, S., Jiang, Q., Chen, C., Chen, X., Li, S., et al. (2015). Preparation and characterization of PEO-PMMA polymer composite electrolytes doped with nano-Al<sub>2</sub>O<sub>3</sub>. *Electrochim. Acta* 169, 334–341. doi: 10.1016/j.electacta.2015.04.039
- Lin, D., Liu, W., Liu, Y., Lee, H. R., Hsu, P.-C., Liu, K., et al. (2016). High ionic conductivity of composite solid polymer electrolyte via *in situ* synthesis of monodispersed SiO<sub>2</sub> nanospheres in poly(ethylene oxide). *Nano Lett.* 16, 459–465. doi: 10.1021/acs.nanolett.5b04117
- Lin, D., Yuen, P. Y., Liu, Y., Liu, W., Liu, N., Dauskardt, R. H., et al. (2018). A silica-aerogel-reinforced composite polymer electrolyte with high ionic conductivity and high modulus. *Adv. Mater.* 30:e1802661. doi: 10.1002/adma.201802661
- Ling, S.-G., Peng, J.-Y., Yang, Q., Qiu, J.-L., Lu, J.-Z., and Li, H. (2018). Enhanced ionic conductivity in LAGP/LATP composite electrolyte. *Chin. Phys. B* 27:038201. doi: 10.1088/1674-1056/27/3/038201
- Liu, J., Xu, J. Y., Lin, Y., Li, J., Lai, Y. Q., Yuan, C. F., et al. (2013). All-solid-state lithium ion battery: research and industrial prospects. *Acta Chim. Sin.* 71, 869–878. doi: 10.6023/a13020170
- Liu, W., Lee, S. W., Lin, D., Shi, F., Wang, S., Sendek, A. D., et al. (2017). Enhancing ionic conductivity in composite polymer electrolytes with well-aligned ceramic nanowires. *Nat. Energy* 2:17035. doi: 10.1038/nenergy.2017.35
- Liu, W., Lin, D., Sun, J., Zhou, G., and Cui, Y. (2016). Improved lithium ionic conductivity in composite polymer electrolytes with oxide-ion conducting nanowires. *ACS Nano* 10, 11407–11413. doi: 10.1021/acs.nano.6b06797
- Liu, W., Liu, N., Sun, J., Hsu, P. C., Li, Y. Z., Lee, H. W., et al. (2015). Ionic conductivity enhancement of polymer electrolytes with ceramic nanowire fillers. *Nano Lett.* 15, 2740–2745. doi: 10.1021/acs.nanolett.5b00600
- Manthiram, A., Yu, X. W., and Wang, S. F. (2017). Lithium battery chemistries enabled by solid-state electrolytes. *Nat. Rev. Mater.* 2:16103. doi: 10.1038/natrevmats.2016.103
- Meyer, W. H. (1998). Polymer electrolytes for lithium-ion batteries. *Adv. Mater.* 10, 439–+. doi: 10.1002/(sici)1521-4095(199804)10:6<439::Aid-adma439>3.0.Co;2-i
- Mueller, U., Schubert, M., Teich, F., Puetter, H., Schierle-Arndt, K., and Pastre, J. (2006). Metal-organic frameworks—prospective industrial applications. *J. Mater. Chem.* 16, 626–636. doi: 10.1039/b511962f
- Nair, J. R., Gerbaldi, C., Chiappone, A., Zeno, E., Bongiovanni, R., Bodoardo, S., et al. (2009). UV-cured polymer electrolyte membranes for Li-cells: Improved mechanical properties by a novel cellulose reinforcement. *Electrochem. Commun.* 11, 1796–1798. doi: 10.1016/j.elecom.2009.07.021
- Nan, C. W., Fan, L. Z., Lin, Y. H., and Cai, Q. (2003). Enhanced ionic conductivity of polymer electrolytes containing nanocomposite SiO<sub>2</sub> particles. *Phys. Rev. Lett.* 91:4. doi: 10.1103/PhysRevLett.91.266104
- O'Callaghan, M. P., Powell, A. S., Titman, J. J., Chen, G. Z., and Cussen, E. J. (2008). Switching on fast lithium ion conductivity in garnets: The structure and transport properties of Li(3+x)Nd(3)Te(2-x)Sb(x)O(12). *Chem. Mater.* 20, 2360–2369. doi: 10.1021/cm703677q

- Osada, I., de Vries, H., Scrosati, B., and Passerini, S. (2016). Ionic-liquid-based polymer electrolytes for battery applications. *Ange. Chem. Int. Ed.* 55, 500–513. doi: 10.1002/anie.201504971
- Pal, P., and Ghosh, A. (2018). Influence of TiO<sub>2</sub> nano-particles on charge carrier transport and cell performance of PMMA-LiClO<sub>4</sub> based nano-composite electrolytes. *Electrochim. Acta* 260, 157–167. doi: 10.1016/j.electacta.2017.11.070
- Perez-Estebanez, M., Isasi-Marin, J., Toebe, D. M., Rivera-Calzada, A., and Leon, C. (2014). A systematic study of Nasicon-type Li-i + XMXTi<sub>2</sub> - x(PO<sub>4</sub>)(3) (M: Cr, Al, Fe) by neutron diffraction and impedance spectroscopy. *Solid State Ionics* 266, 1–8. doi: 10.1016/j.ssi.2014.07.018
- Qiu, W.-L., Yang, Q.-H., Ma, X.-h., Fu, Y.-B., and Zong, X.-F. (2004). Research on PEO-based dry solid polymer electrolytes for rechargeable lithium batteries. *Chin. J. Power Sources* 28, 440–448, 457.
- Quartarone, E., and Mustarelli, P. (2011). Electrolytes for solid-state lithium rechargeable batteries: recent advances and perspectives. *Chem. Soc. Rev.* 40, 2525–2540. doi: 10.1039/c0cs00081g
- Ratner, M. A., Johansson, P., and Shriver, D. F. (2000). Polymer electrolytes: ionic transport mechanisms and relaxation coupling. *Mrs. Bull.* 25, 31–37. doi: 10.1557/mrs2000.16
- Reddy, M. J., Chu, P. P., Kumar, J. S., and Rao, U. V. S. (2006). Inhibited crystallization and its effect on conductivity in a nano-sized Fe oxide composite PEO solid electrolyte. *J. Power Sources*, 161, 535–540. doi: 10.1016/j.jpowsour.2006.02.104
- Scrosati, B., and Garche, J. (2010). Lithium batteries: status, prospects and future. *J. Power Sources*, 195, 2419–2430. doi: 10.1016/j.jpowsour.2009.11.048
- Sheng, J., Tong, S., He, Z., and Yang, R. (2017). Recent developments of cellulose materials for lithium-ion battery separators. *Cellulose* 24, 4103–4122. doi: 10.1007/s10570-017-1421-8
- Sheng, O., Jin, C., Luo, J., Yuan, H., Huang, H., Gan, Y., et al. (2018). Mg<sub>2</sub>B<sub>2</sub>O<sub>5</sub> Nanowire enabled multifunctional solid-state electrolytes with high ionic conductivity, excellent mechanical properties, and flame-retardant performance. *Nano Lett.* 18, 3104–3112. doi: 10.1021/acs.nanolett.8b00659
- Shi, Q. X., Xia, Q., Xiang, X., Ye, Y. S., Hai Yan, P., Xue, Z. G., et al. (2017). Self-assembled polymeric ionic liquid-functionalized cellulose nanocrystals: constructing 3D ion-conducting channels within ionic liquid-based composite polymer electrolytes. *Chem. Euro. J.* 23, 11881–11890. doi: 10.1002/chem.201702079
- Siqueira, L. J. A., and Ribeiro, M. C. C. (2006). Molecular dynamics simulation of the polymer electrolyte poly(ethylene oxide)/LiClO<sub>4</sub>. II. Dynamical properties. *J. Chem. Phys.* 125:214903. doi: 10.1063/1.2400221
- Srivastava, N., and Tiwari, T. (2009). New trends in polymer electrolytes: a review. *E-Polymers* 146, 1–17. doi: 10.1515/epoly.2009.9.1.1738
- Stavila, V., Talin, A. A., and Allendorf, M. D. (2014). MOF-based electronic and optoelectronic devices. *Chem. Soc. Rev.* 43, 5994–6010. doi: 10.1039/c4cs00096j
- Stephan, A. M., and Nahm, K. S. (2006). Review on composite polymer electrolytes for lithium batteries. *Polymer* 47, 5952–5964. doi: 10.1016/j.polymer.2006.05.069
- Stramare, S., Thangadurai, V., and Weppner, W. (2003). Lithium lanthanum titanates: A review. *Chem. Mater.* 15, 3974–3990. doi: 10.1021/cm0300516
- Subianto, S., Mistry, M. K., Choudhury, N. R., Dutta, N. K., and Knout, R. (2009). Composite polymer electrolyte containing ionic liquid and functionalized polyhedral oligomeric silsesquioxanes for anhydrous PEM applications. *ACS Appl. Mater. Interfaces* 1, 1173–1182. doi: 10.1021/am900020w
- Sun, B., Mindemark, J., Edstrom, K., and Brandell, D. (2014). Polycarbonate-based solid polymer electrolytes for Li-ion batteries. *Solid State Ionics* 262, 738–742. doi: 10.1016/j.ssi.2013.08.014
- Sun, J. Z., MacFarlane, D. R., and Forsyth, M. (1996). Ion conductive poly(ethylene oxide dimethyl siloxane) copolymers. *J. Polymer Sci. Polymer Chem.* 34, 3465–3470.
- Tambelli, C. C., Bloise, A. C., Rosario, A., Pereira, E. C., Magon, C. J., and Donoso, J. P. (2002). Characterisation of PEO-Al<sub>2</sub>O<sub>3</sub> composite polymer electrolytes. *Electrochim. Acta* 47, 1677–1682. doi: 10.1016/s0013-4686(01)00900-8
- Tang, Z., Hu, L., Zhang, Z., and Su, F. (2007). Research progress of solid polymer electrolytes for lithium ion batteries. *J. Chin. Ceramic Soc.* 35, 123–128.
- Thangadurai, V., Kaack, H., and Weppner, W. J. F. (2003). Novel fast lithium ion conduction in garnet-type Li<sub>5</sub>La<sub>3</sub>M<sub>2</sub>O<sub>12</sub> (M = Nb, Ta). *J. Am. Ceramic Soc.* 86, 437–440. doi: 10.1111/j.1151-2916.2003.tb03318.x
- Thokchom, J. S., Gupta, N., and Kumar, B. (2008). Superionic conductivity in a lithium aluminum germanium phosphate glass-ceramic. *J. Electrochem. Soc.* 155, A915–A920. doi: 10.1149/1.2988731
- Tikekar, M. D., Choudhury, S., Tu, Z., and Archer, L. A. (2016). Design principles for electrolytes and interfaces for stable lithium-metal batteries. *Nat. Energy* 1, 1–7. doi: 10.1038/nenergy.2016.114
- Verma, P., Maire, P., and Novak, P. (2010). A review of the features and analyses of the solid electrolyte interphase in Li-ion batteries. *Electrochim. Acta* 55, 6332–6341. doi: 10.1016/j.electacta.2010.05.072
- Villaluenga, I., Wujcik, K. H., Tong, W., Devaux, D., Wong, D. H. C., DeSimone, J. M., et al. (2016). Compliant glass-polymer hybrid single ion-conducting electrolytes for lithium batteries. *Proc. Natl. Acad. Sci. USA* 113, 52–57. doi: 10.1073/pnas.1520394112
- Wang, L.-P., Zhang, X.-D., Wang, T.-S., Yin, Y.-X., Shi, J.-L., Wang, C.-R., et al. (2018). Ameliorating the interfacial problems of cathode and solid-state electrolytes by interface modification of functional polymers. *Adv. Energy Mater.* 8:1801528. doi: 10.1002/aenm.201801528
- Wang, X., Zhang, M., Alvarado, J., Wang, S., Sina, M., Lu, B., et al. (2017). new insights on the structure of electrochemically deposited lithium metal and its solid electrolyte interphases via cryogenic TEM. *Nano Lett.* 17, 7606–7612. doi: 10.1021/acs.nanolett.7b03606
- Wang, Z., Wang, S., Wang, A., Liu, X., Chen, J., Zeng, Q., et al. (2018). Covalently linked metal-organic framework (MOF)-polymer all-solid-state electrolyte membranes for room temperature high performance lithium batteries. *J. Mater. Chem. A* 6, 17227–17234. doi: 10.1039/c8ta05642k
- Watanabe, M., Endo, T., Nishimoto, A., Miura, K., and Yanagida, M. (1999). High ionic conductivity and electrode interface properties of polymer electrolytes based on high molecular weight branched polyether. *J. Power Sources* 81, 786–789. doi: 10.1016/s0378-7753(99)00250-5
- Wei-Min, W. (2012). Study on all solid-state composite polymer electrolyte. *Adv. Mat. Res.* 571, 13–16. doi: 10.4028/www.scientific.net/AMR.571.13
- Weston, J. E., and Steele, B. C. H. (1982). Effects of inert fillers on the mechanical and electrochemical properties of lithium salt poly (ethylene-oxide) polymer electrolytes. *Solid State Ionics* 7, 75–79. doi: 10.1016/0167-2738(82)90072-8
- Wu, J.-F., Pang, W. K., Peterson, V. K., Wei, L., and Guo, X. (2017). Garnet-type fast Li-ion conductors with high ionic conductivities for all-solid-state batteries. *ACS Appl. Mater. Interfaces* 9, 12461–12468. doi: 10.1021/acsami.7b00614
- Xie, H., Yang, C., Fu, K., Yao, Y., Jiang, F., Hitz, E., et al. (2018). Flexible, scalable, and highly conductive garnet-polymer solid electrolyte templated by bacterial cellulose. *Adv. Energy Mater.* 8:1703474. doi: 10.1002/aenm.201703474
- Xie, X.-C., Huang, K.-J., and Wu, X. (2018). Metal-organic framework derived hollow materials for electrochemical energy storage. *J. Mater. Chem. A* 6, 6754–6771. doi: 10.1039/c8ta00612a
- Xiong, H. M., Wang, Z. D., Xie, D. P., Cheng, L., and Xia, Y. Y. (2006). Stable polymer electrolytes based on polyether-grafted ZnO nanoparticles for all-solid-state lithium batteries. *J. Mater. Chem.* 16, 1345–1349. doi: 10.1039/b514346b
- Xu, K. (2004). Nonaqueous liquid electrolytes for lithium-based rechargeable batteries. *Chem. Rev.* 104, 4303–4417. doi: 10.1021/cr030203g
- Xu, R. C., Xia, X. H., Zhang, S. Z., Xie, D., Wang, X. L., and Tu, J. P. (2018). Interfacial challenges and progress for inorganic all-solid-state lithium batteries. *Electrochim. Acta* 284, 177–187. doi: 10.1016/j.electacta.2018.07.191
- Yang, L., Wang, Z., Feng, Y., Tan, R., Zuo, Y., Gao, R., et al. (2017). Flexible composite solid electrolyte facilitating highly stable “soft contacting” Li-electrolyte interface for solid state lithium-ion batteries. *Adv. Energy Mater.* 7:1701437. doi: 10.1002/aenm.201701437
- Yarmolenko, O. V., Yudin, A. V., and Khatmullina, K. G. (2018). Nanocomposite polymer electrolytes for the lithium power sources (a Review). *Rus. J. Electrochem.* 54, 325–343. doi: 10.1134/s1023193518040092
- Young, W. S., Kuan, W. F., and Epps, T. H. (2014). Block copolymer electrolytes for rechargeable lithium batteries. *J. Polymer Sci. B Polymer Phys.* 52, 1–16. doi: 10.1002/polb.23404
- Yuan, C., Li, J., Han, P., Lai, Y., Zhang, Z., and Liu, J. (2013). Enhanced electrochemical performance of poly(ethylene oxide) based composite polymer electrolyte by incorporation of nano-sized metal-organic framework. *J. Power Sources* 240, 653–658. doi: 10.1016/j.jpowsour.2013.05.030
- Zachman, M. J., Tu, Z., Choudhury, S., Archer, L. A., and Kourkoutis, L. F. (2018). Cryo-STEM mapping of solid-liquid interfaces and dendrites

- in lithium-metal batteries. *Nature* 560, 345–349. doi: 10.1038/s41586-018-0397-3
- Zhang, J., Yue, L., Hu, P., Liu, Z., Qin, B., Zhang, B., et al. (2014). Taichi-inspired rigid-flexible coupling cellulose-supported solid polymer electrolyte for high-performance lithium batteries. *Sci. Rep.* 4:6272. doi: 10.1038/srep06272
- Zhang, Q. Q., Liu, K., Ding, F., and Liu, X. J. (2017). Recent advances in solid polymer electrolytes for lithium batteries. *Nano Res.* 10, 4139–4174. doi: 10.1007/s12274-017-1763-4
- Zhang, X., Liu, T., Zhang, S., Huang, X., Xu, B., Lin, Y., et al. (2017). Synergistic Coupling between  $\text{Li}_{6.75}\text{La}_3\text{Zr}_{1.75}\text{Ta}_{0.25}\text{O}_{12}$  and Poly(vinylidene fluoride) induces high ionic conductivity, mechanical strength, and thermal stability of solid composite electrolytes. *J. Am. Chem. Soc.* 139, 13779–13785. doi: 10.1021/jacs.7b06364
- Zhang, X.-Q., Cheng, X.-B., and Zhang, Q. (2018). Advances in interfaces between Li metal anode and electrolyte. *Adv. Mater. Interfaces* 5:1701097. doi: 10.1002/admi.201701097
- Zhao, Y., Huang, Z., Chen, S., Chen, B., Yang, J., Zhang, Q., et al. (2016a). A promising PEO/LAGP hybrid electrolyte prepared by a simple method for all-solid-state lithium batteries. *Solid State Ionics* 295, 65–71. doi: 10.1016/j.ssi.2016.07.013
- Zhao, Y., Wu, C., Peng, G., Chen, X., Yao, X., Bai, Y., et al. (2016b). A new solid polymer electrolyte incorporating  $\text{Li}_{10}\text{GeP}_2\text{S}_{12}$  into a polyethylene oxide matrix for all-solid-state lithium batteries. *J. Power Sources* 301, 47–53. doi: 10.1016/j.jpowsour.2015.09.111
- Zhao, Y., Zhang, Y., Gosselink, D., Doan, T. N. L., Sadhu, M., Cheang, H.-J., et al. (2012). Polymer electrolytes for lithium/sulfur batteries. *Membranes* 2, 553–564. doi: 10.3390/membranes2030553
- Zhu, P., Yan, C., Dirican, M., Zhu, J., Zang, J., Selvan, R. K., et al. (2018).  $\text{Li}_{0.33}\text{La}_{0.557}\text{TiO}_3$  ceramic nanofiber-enhanced polyethylene oxide-based composite polymer electrolytes for all-solid-state lithium batteries. *J. Mater. Chem. A* 6, 4279–4285. doi: 10.1039/c7ta10517g

**Conflict of Interest Statement:** The authors declare that the research was conducted in the absence of any commercial or financial relationships that could be construed as a potential conflict of interest.

Copyright © 2019 Yao, Yu, Ding, Liu, Lu, Lavorgna, Wu and Liu. This is an open-access article distributed under the terms of the Creative Commons Attribution License (CC BY). The use, distribution or reproduction in other forums is permitted, provided the original author(s) and the copyright owner(s) are credited and that the original publication in this journal is cited, in accordance with accepted academic practice. No use, distribution or reproduction is permitted which does not comply with these terms.



# Fabrication, Investigation, and Application of Light-Responsive Self-Assembled Nanoparticles

Juan Pang<sup>1†</sup>, Ziyu Gao<sup>1†</sup>, Huaping Tan<sup>2</sup>, Xincheng Mao<sup>1</sup>, Jialing Xu<sup>1</sup>, Jingyang Kong<sup>1</sup> and Xiaohong Hu<sup>1\*</sup>

<sup>1</sup> School of Material Engineering, Jinling Institute of Technology, Nanjing, China, <sup>2</sup> Biomaterials for Organogenesis Laboratory, School of Materials Science & Engineering, Nanjing University of Science & Technology, Nanjing, China

## OPEN ACCESS

### Edited by:

Clemens Kilian Weiss,  
Fachhochschule Bingen, Germany

### Reviewed by:

Si Wu,  
University of Science and Technology  
of China, China  
Jiefei Wang,  
Henan University, China

### \*Correspondence:

Xiaohong Hu  
huxiaohong07@163.com

<sup>†</sup>These authors have contributed  
equally to this work as co-first authors

### Specialty section:

This article was submitted to  
Polymer Chemistry,  
a section of the journal  
Frontiers in Chemistry

Received: 19 July 2019

Accepted: 28 August 2019

Published: 12 September 2019

### Citation:

Pang J, Gao Z, Tan H, Mao X, Xu J,  
Kong J and Hu X (2019) Fabrication,  
Investigation, and Application of  
Light-Responsive Self-Assembled  
Nanoparticles. *Front. Chem.* 7:620.  
doi: 10.3389/fchem.2019.00620

Light-responsive materials have attracted increasing interest in recent years on account of their adjustable on-off properties upon specific light. In consideration of reversible isomerization transition for azobenzene (AZO), it was designed as a light-responsive domain for nanoparticles in this research. At the same time, the interaction between AZO domain and  $\beta$ -cyclodextrin ( $\beta$ -CD) domain was designed as a driving force to assemble nanoparticles, which was fabricated by two polymers containing AZO domain and  $\beta$ -CD domain, respectively. The formed nanoparticles were confirmed by Dynamic Light Scattering (DLS) results and Transmission Electron Microscope (TEM) images. An obvious two-phase structure was formed in which the outer layer of nanoparticles was composed of PCD polymer, as verified by <sup>1</sup>HNMR spectroscopy. The efficient and effective light response of the nanoparticles, including quick responsive time, controllable and gradual recovered process and good fatigue resistance, was confirmed by UV-Vis spectroscopy. The size of the nanoparticle could be adjusted by polymer ratio and light irradiation, which was ascribed to its light-response property. Nanoparticles had irreversibly pH dependent characteristics. In order to explore its application as a nanocarrier, drug loading and *in vitro* release profile in different environment were investigated through control of stimuli including light or pH value. Folic acid (FA), as a kind of target fluorescent molecule with specific protein-binding property, was functionalized onto nanoparticles for precise delivery for anticancer drugs. Preliminary *in vitro* cell culture results confirmed efficient and effective curative effect for the nanocarrier on MCF-7 cells.

**Keywords:** nanoparticle, self-assemble, light-responsive property, nanocarrier, drug delivery

## INTRODUCTION

As a fundamental backbone, materials play an irreplaceable role in the development of science and technology in all fields, especially in fast-growing current functional and intelligent research fields. Stimuli-responsive materials have attracted great interest due to their adjustable properties in response to external stimuli (Guragain et al., 2015; Lorenzo et al., 2015; Cao and Wang, 2016; Lu et al., 2016; Mao et al., 2016; Ahmed et al., 2017; Huang et al., 2018; Kydd et al., 2018). From commonly used external stimuli sources including photo, heat, solution pH value, electric signal and magnetic signal, photo-responsive materials are commonly employed in bio-related fields and information-related fields on account of convenient control, high efficiency and low cost



(Guragain et al., 2015; Lorenzo et al., 2015; Cao and Wang, 2016; Lu et al., 2016; Mao et al., 2016; Ahmed et al., 2017; Huang et al., 2018; Kydd et al., 2018). Photo molecular switch offered precise photo response upon specific light source enabling a material response (Beharry and Woolley, 2011; Sun et al., 2012; Pang et al., 2015; Bian et al., 2016; Ye et al., 2016; Kathan and Hecht, 2017). Currently, many molecules with precise alterable spatiotemporal structures, such as chiral helicene, azobenzene, diarylethene, spiropyran, and binaphthyl compounds, have been explored for application as photo switches (Sun et al., 2012; Yuan et al., 2014; Kim et al., 2015; Lin et al., 2016). Generally, these molecules possess conjugated structures, which influence their compatibility to aqueous environment and future application in that environment (Sun et al., 2012; Yuan et al., 2014; Kim et al., 2015; Lin et al., 2016). Moreover, photo switch cytotoxicity may restrict application in bio-related fields (Pang et al., 2018). In order to improve the performance of photo switches in aqueous environments, and decrease photo switch cytotoxicity, copolymer and polysaccharide derivatives with azobenzene pendent groups were designed, respectively, in our previous work. The former showed a more controllable light-response and light-recovery performance in an aqueous environment (Pang et al., 2018, 2019).

Although the emergence of macromolecule photo switches broaden their potential application, especially in biomedical fields, a suitable carrier is needed to realize the actual application of the functional material. Films, particles, fibers and 3D scaffolds are main forms of carriers, while nanoparticles are effective for their application in the drug delivery field (Bhosale et al., 2018; Intasa-Rad and Ogawa, 2018; Zhang et al., 2018; Ma et al., 2019). Therefore, a light responsive nanoparticle based on previous synthesized azobenzene copolymer was designed in this research.

As a drug carrier, biocompatibility and drug encapsulated capacity are two primary requirements of carrier materials (Wang et al., 2017, 2018). In consideration of the two requests,  $\beta$ -cyclodextrin ( $\beta$ -CD) possesses good biocompatibility and hydrophobic cavity, which can form an inclusion complex with small molecules (Wang et al., 2015; Zhou et al., 2015; Wang and Wu, 2016). The hydrophobic cavity of  $\beta$ -CD could include an azobenzene group to form a super molecular link as an effective and efficient method to prepare carriers like hydrogels and nanoparticles (Hu and Gong, 2016; Hu et al., 2017; Malik et al., 2017; Song et al., 2017). Therefore, the self-assembly technique based on interactions between  $\beta$ -CD group and azobenzene group was used to prepare nanoparticles in this work. Since more than one functional group per molecule is a premise of super molecular self-assemble, polymerization or crosslinking of  $\beta$ -CD should be obtained before fabrication of nanoparticles.

Targeted delivery is a requirement of drug delivery vehicles in order to realize effective and efficient drug delivery (Huang et al., 2017; Merzel et al., 2017). Folic acid can be recognized and integrated by a folic acid receptor, which exists in both normal tissue and tumors (Huang et al., 2017; Merzel et al., 2017). Nevertheless, either the number or activity of folic acid receptors in tumors is higher than that in normal tissue (Huang et al., 2017; Merzel et al., 2017). Thus, folic acid was used to functionalize the surface of nanoparticles during the fabrication process for

the preliminary application evaluation of a nanoparticle as a drug carrier in the research. In order to realize the object, we synthesized FA functional poly( $\beta$ -cyclodextrin) (PCD) through the chemical coupling method, which was assembled with copolymer and azobenzene pendent (HANN copolymer). The final functional nanoparticle was preliminarily evaluated by the cytotoxicity of cancer cells in order to explore its application in the anticancer drug delivery field.

In summary, aiming at responsive nanoparticles for the drug delivery field, we designed a light-responsive azobenzene (AZO) domain for copolymers as a stimuli-responsive unit and a self-assemble unit simultaneously. Poly( $\beta$ -CD) was used to construct a nanoparticle by a driving force coming from the interaction between AZO domain and domain considering its good biocompatibility and drug controllable performance in the research. Finally, FA functionalization broadened the application of the nanoparticle in the biomedical field.

## EXPERIMENT SECTION

### Materials

Folic acid (FA),  $\beta$ -cyclodextrin ( $\beta$ -CD), sodium periodate, dichloromethane (DCM), diethyl ether, tetrahydrofuran (THF), dioxane, benzoyl peroxide (BPO), triethylamine (TEA), and dimethylsulfone (DMSO) were obtained from Sinopharm Chemical Reagent Co., Ltd, China. N-hydroxysuccinimide (NHS), acryloyl chloride and p-aminoazobenzene (AZO) were purchased from Aladdin. Trypsin, Dulbecco's modified Eagle's medium (DMEM), Camptothecin (CPT) and 3-(4, 5-dimethyl) thiazol-2,5-dimethyl tetrazolium bromide (MTT) were obtained from Sigma. Fetal bovine serum (FBS) was purchased from Sijiqing biotech. Co., China. All other reagents and solvents were of analytical grade and used as received.

### Synthesis of HANN Copolymer and PCDs

HANN copolymer was synthesized by copolymerization of functional monomers including HEMA, double carbon modified NHS (NAS), NVP and double carbon modified AZO, the structure of HANN was characterized in detail in our previous work (Pang et al., 2019). Briefly, AZO and NAS monomer was synthesized by acylchlorination. Then 10 mmol monomers were dissolved by 30 ml dioxane containing 0.5 mmol BPO under nitrogen atmosphere. The sealed solution was reacted at 70°C for 24 h. Final product was precipitated by diethyl ether/THF ( $\times 3$ ) and obtained by freeze-drying ( $-50^\circ\text{C}$ , 7–8 Pa), which was denoted with HANN copolymer.

PCD was synthesized by epichlorohydrin crosslinking according to the previous method (Chen et al., 2015). Briefly, epichlorohydrin (4 ml) was slowly added into  $\beta$ -CD (2 g)/30% NaOH (10 ml) solution at 40°C. Furthermore, the mixture was heated to 60°C. After the solution became viscous, HCl was added to adjust the pH value to 7. The resultant product was dialyzed for 3 days (MW: 8 kDa) and finally obtained by freeze-drying.

Poly( $\beta$ -CD)-CHO (PCD-CHO) was synthesized by the oxidation method (Ye et al., 2019). Briefly, sodium periodate solution (0.6 M, 2 ml) was added dropwise into 100 ml 1.4% w/v

PCD solution (pH = 2). After a 2 h reaction at room temperature in the dark, 0.3 ml ethylene glycol was then added to inactivate any unreacted periodate. The solution was purified by dialyzing (MW: 8 kDa) and then freeze-dried to get PCD-CHO.

Poly( $\beta$ -CD)-CHO-FA (PCD-CHO-FA) was synthesized by the reaction between the aldehyde group and amino group. FA was dissolved in DMSO with a final concentration of 1% w/v, into which  $\beta$ -CD-CHO was added with a final concentration of 1% w/v. The reaction was kept at 40°C for 24 h, and PCD-CHO-FA was also obtained by dialyzing and freeze-drying. The product was characterized by proton nuclear magnetic resonance spectrum ( $^1\text{H}$  NMR, Bruker AV-300).

## Self-Assemble of Light Response Nanoparticle

HANN was dissolved in DMSO to obtain a HANN/DMSO solution with certain concentration. Simultaneously, PCD was dissolved in water to obtain PCD solution with 10 mg/ml. Forty microliter HANN solution and 4 ml PCD solution was mixed to obtain nanoparticle, which was further dialyzed to remove DMSO. The obtained nanoparticle was characterized by dynamic light scattering (DLS, nano ZS) and transmission electron microscope (TEM, Philips, Tecnai 12). The nanoparticle was further characterized by  $^1\text{H}$  NMR (Bruker AV-500).

Nanoparticle for *in vitro* evaluation was formed by HANN copolymer and Poly( $\beta$ -CD)-CHO-FA using the same method, which was denoted as Nano-FA 33.

## Photo Response and pH Dependent Properties of Nanoparticle

Nano 33 aqueous solution was tracked by UV spectroscopy (Cary 50). A UV lamp (10 W) with light density of 5 mW/cm<sup>2</sup> was used as a photo source to induce trans-to-cis transition of AZO domain. After UV irradiation, white light of 260  $\mu\text{W}/\text{cm}^2$  was used to induce cis-to-trans recovery at room temperature. To track structural change of molecules, real-time UV spectra as a function of irradiation time and recovery time was recorded. Repeated irradiation and recovery method were applied to demonstrate fatigue resistance of the material.

Furthermore, the effective diameter of nanoparticle in suspension as a function of time in one response-recovery circle was tracked by DLS (nano ZS).

Additionally, effective diameter of nano 33 aqueous solution as a function of pH value was recorded by DLS (nano ZS). Transparency of nano 33 aqueous solution as a function of pH value was tracked by UV spectroscopy (Cary 50). TEM images of nano 33 dried from pH 3 solution was characterized by TEM (Philips, Tecnai 12).

## Simulation and Computational Details

Molecular dynamics (MD) simulations were carried out with the forcite module in MS8.0 package.

The torsion force field function form of  $^*\text{-N=N}^*$  was  $E = \frac{1}{2} \sum_j \{B_j (1 - d_j \cos[n_j \phi])\}$ . However, for simulation the trans-to-cis isomerization of AZO, modified PCFF parameters of  $B_j = 25$ ,  $d_j = 1$ , and  $n_j = 1$  were adopted. NVT ensemble was used,

and the temperature of 298 K was controlled by Nose thermostat. Moreover, velocity Verlet algorithm was applied by a time step of 1 fs.

The clusters of AZO and  $\beta$ -CD also optimized using G09 programs at cam-b3lyp/6-31g(d) level (Trucks et al., 2009). The interaction energies ( $\Delta E$ ) between AZO and  $\beta$ -CD were calculated, and the basis set superposition error (BSSE) was corrected by counterpoise method.

## In vitro Evaluation for Nanocarrier

An anticancer drug (CPT) was chosen as the model drug to be encapsulated into the above-mentioned nanoparticle during the process of nanoparticle fabrication. Briefly, CPT was dissolved in HANN copolymer/DMSO solution with a different final concentration, which was further mixed with poly( $\beta$ -CD) aqueous solution, as mentioned above. The final drug encapsulated nanoparticles were obtained using this method. The encapsulated CPT amount was obtained by the difference between the added amount and precipitation amount in solution. The precipitation was collected, dissolved with certain volume DMSO and quantified by the ultraviolet spectrophotometric method using UV spectroscopy (Cary 50) at 360 nm according to the standard curve. For CPT release assay, nanoparticle suspension was dialyzed in 15 ml water solution with PBS. At appropriate intervals, 3 ml released dialysis solution was withdrawn and the absorbance at 360 nm was recorded to calculate the cumulate CPT release. Simultaneously, 3 ml fresh solution was supplemented into dialysis solution.

Besides *in vitro* drug release profiles, effects of drug encapsulated nanoparticles on viability of MCF7 cells were evaluated by MTT assay. Briefly, nanoparticles DMEM solution with different nanoparticle concentration was added into the 96-well culture plate with 80 to 90% cell confluence. At different intervals, after being supplemented with 20  $\mu\text{L}$  MTT, the cells were continually cultured for another 4 h. After cell was stained by MTT, they are observed by optical microscope (IX73). At the same time, 200  $\mu\text{L}$  of DMSO was added to dissolve the formed formazan pigment. The absorbance of 150  $\mu\text{L}$  above solution at 570 nm was recorded by a microplate reader (Tecan M200 Pro).

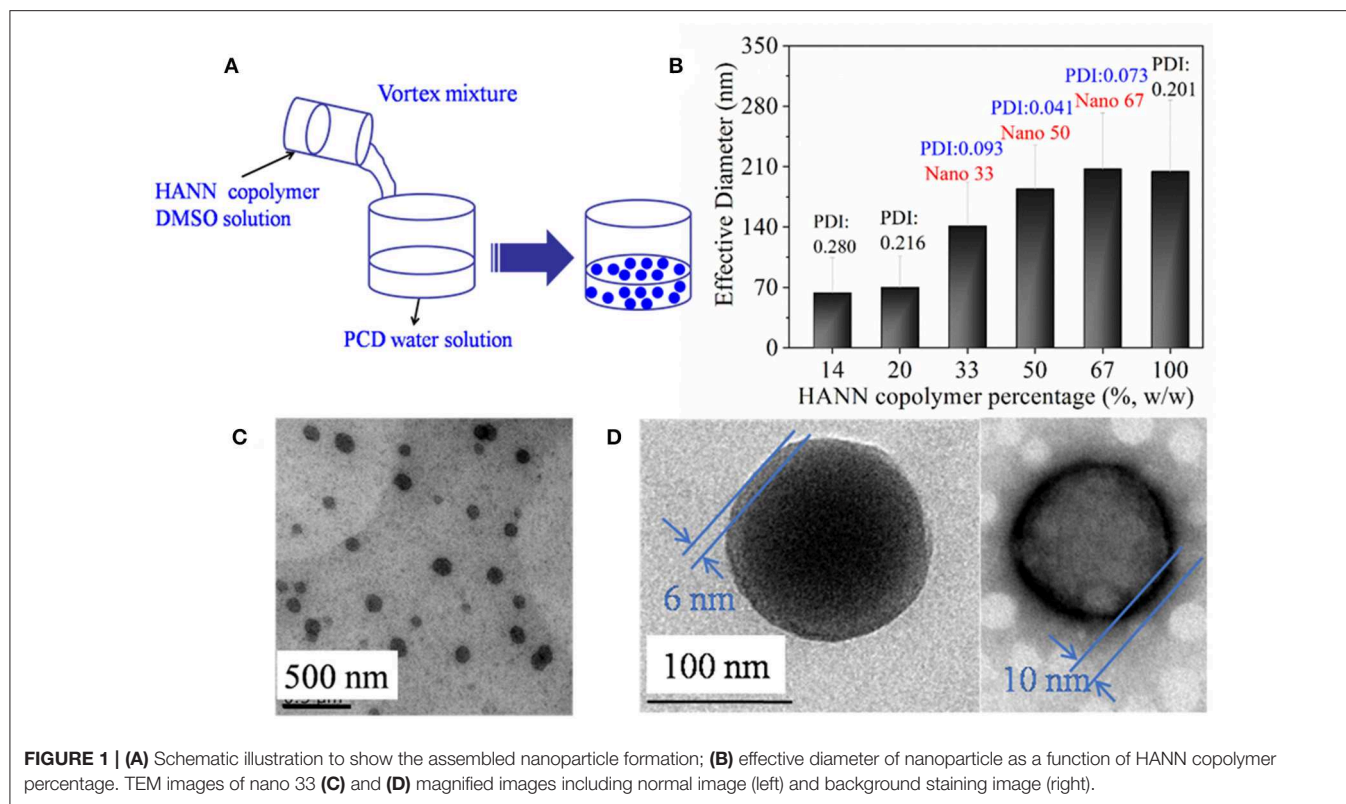
## Statistical Analysis

Data were analyzed using the *t*-test for differences. Results were reported as means  $\pm$  standard deviation. The significant level was set at  $p < 0.05$ .

## RESULTS AND DISCUSSION

### Self-Assemble of Light Response Nanoparticle

Since HANN copolymer had little solubility in water, nanoparticles were self-assembled under the help of DMSO cosolvent in water (Figure 1A). The formed nanoparticles were characterized by DLS and TEM in Figures 1B–D. In order to optimize two polymer ratio, effective diameter as a function of HANN copolymer concentration was recorded by DLS (Figure 1B). It was found that the effective nanoparticle diameter increased until the nanoparticles consisted of 67%



HANN copolymer. The PDI value of effective nanoparticle diameter increased when HANN copolymer concentration was either higher than 67% or lower than 33%, which indicated the correlation between results and actual diameter became worse. Since small diameter and narrow dispersity of nanoparticles were preferred to obtain homogeneous dispersion as nanocarrier, nano 33 was chosen for further investigation. Well-dispersed nanoparticles with diameters of about 100 nm were observed by TEM analysis (Figure 1C) for nano 33, which confirmed the formation of nanoparticles by self-assembly. The diameters from the TEM image were smaller than effective diameter of 140 nm from the DLS result, which might be attributed to nanoparticle hydration in solution. In addition, distinctive light and dark color with an obvious boundary was found in a magnified unstained TEM image (Figure 1D). A dark ring with thickness of about 10 nm was witnessed in magnified background staining TEM image, which was considered as the border of nano 33. In the polysaccharide component, the samples need to be negatively stained in the process of TEM so can the morphology of PCD can be observed in white color. In this case, the dark ring was considered as the edge of nano 33 and the white surface was PCD. Combining the normal and background staining TEM images, the structure nano 33 we could refer to was a two-phase structure with PCD as the outside layer.

From these results, it was inferred that HANN copolymer was embedded inside the nanoparticle and PCD was assembled outside the nanoparticle, which might be ascribed to the enhanced hydrophilicity or PCD rather than HANN copolymer (Figure 2A). For further structure confirmation,  $^1\text{H}$  NMR

analysis of nanoparticles was performed (Figure 2B). The chemical shifts from 3.5 to 4.0 ppm are attributed to the protons of pyranose ring of  $\beta$ -CD. Simultaneously, the typical chemical shifts of 7.4 to 8.5 ppm are ascribed to the AZO domain, 2.7 ppm to the NAS domain, 1.2 to 2.3 ppm to the NVP domain and 0.5 to 1.2 ppm to the HEMA domain. These specific peaks from HANN copolymer decreased significantly, compared to the  $^1\text{H}$  NMR spectra of pure HANN copolymer, which was available in our previous work (Pang et al., 2019). This obvious change was attributed to the hydrophilic PCD component, which was cycled around the outer layer of nanoparticles and illustrated the inter-mechanism in the nanoparticles. The result of  $^1\text{H}$  NMR spectrum for nanoparticles further verified our proposed mechanism.

## Photo Response and pH Dependent Properties of Nanoparticle

Firstly, UV-Vis spectra of assembled nanoparticle aqueous solution as a function of irradiation time and recovery time were obtained in order to investigate their light response process (Figures 3A,B). Before UV irradiation, a maximum absorption peak at 353 nm and a small flat absorption peak at 450 nm emerged in the UV spectrum of nanoparticle solution (Figure 3A), which was consistent with the UV spectrum of HANN copolymer from our previous research (Pang et al., 2019). Upon UV irradiation, the maximum absorbance at 353 nm decreased significantly and shifted to 328 nm and the absorbance at 450 nm increased slightly with irradiation time until 120 s on account of trans-to-cis transformation (Figure 3A). The phenomenon was similar to

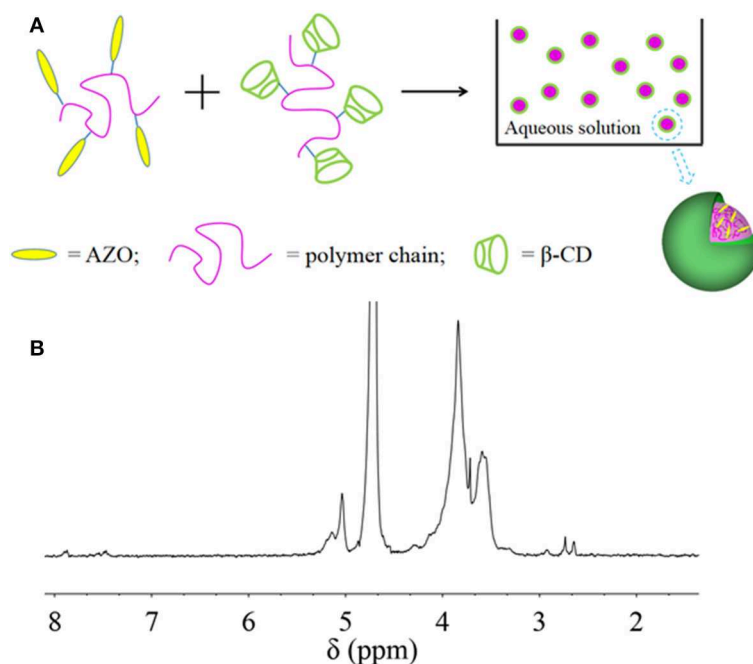


**FIGURE 2 |** (A) Proposed mechanism for nanoparticle self-assembly; (B)  $^1\text{H}$  NMR spectrum of Nano 33.

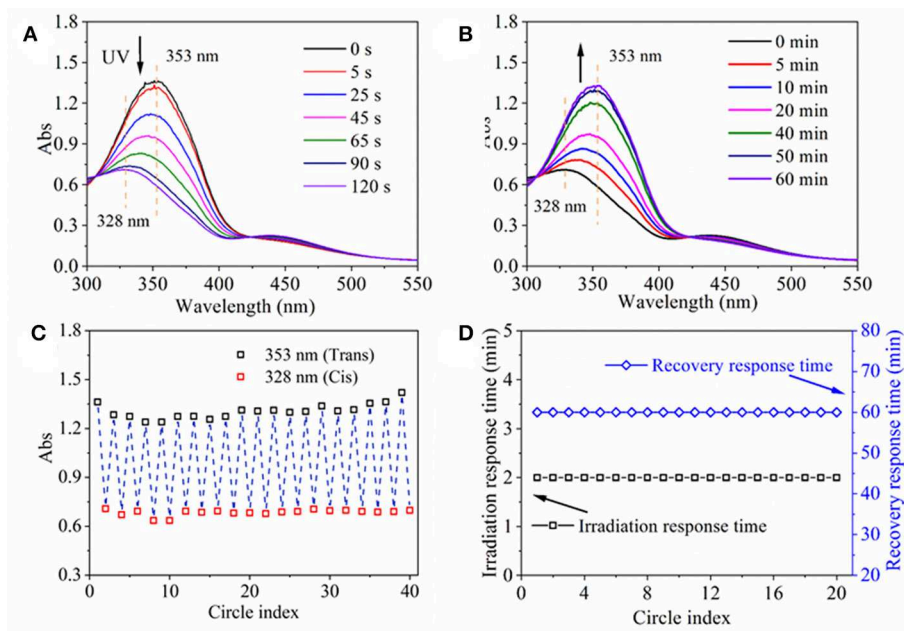


**FIGURE 3 |** UV spectra of assembled nanoparticle aqueous solution as a function of irradiation time (A) and recovery time (B). (C) Absorbance at 353 nm/328 nm of assembled nanoparticle aqueous solution, and (D) irradiation response time under UV irradiation and recovery response time under  $260 \mu\text{W}/\text{cm}^2$  white light at room temperature as a function of circle index.

that of HANN copolymer except prolonged response time from 60 s to 120 s, which might be a result of confined molecular movement. Upon white light irradiation, two peaks were gradually recovered to their respective original absorbance

value, in 1 h on account of cis-to-trans recovery (Figure 3B). Upon repeated UV/white light irradiation, the absorbance at 353 nm/328 nm of the nanoparticle solution as a function of cycle number was recorded to characterize fatigue resistance of



nanoparticle, which was shown in **Figure 3C**. Simultaneously, maximum absorbance at 353 nm was stabilized at 1.2 to 1.5 regardless and minimum absorbance at 328 nm was stabilized at 0.6 to 0.8 regardless of cycle number (**Figure 3C**). At the same time, irradiation response time and recovery response time was stable at 2 and 60 min, respectively, regardless of cycle number (**Figure 3D**). These properties, including quick response time, controllable and gradual recovered process and good fatigue resistance, ensured that efficient and effective light response property are highly desirable for the nanoparticles.

Next, the effective nanoparticle diameter as a function of irradiation and recovery time was monitored by DLS (**Figure 4A**). Considering that the homogeneity and dispersion of nanoparticles may affect the self-assemble behavior, in this period the time-dependent tracking was carried on the same sample every time point to observe the influence of UV-light in dynamic diameters. The effective diameter decreased to < 138 nm from 141 nm after UV irradiation and then the effective diameter was gradually increased to 141 nm after white light irradiation, as opposed to UV irradiation. From these results, it was inferred that the nanoparticles could form a tighter structure after UV irradiation and reversibly recover to their original state, which might be ascribed to an inter-molecular structure change between  $\beta$ -CD domain and AZO domain upon

UV/white light. In order to clarify the light response mechanism for the nanoparticle, the trans  $\rightarrow$  cis process was modeled by MD simulation and modified PCFF parameters in **Figure 4B**. Before simulation, the initial structure of trans-AZO and  $\beta$ -CD cluster (A cluster) was optimized by G09 and used as a starting point for the MD simulations. In simulation, the angle of the C-N=N-C torsion decreased to a low value after time evolution of 10 ps, which indicated that trans-AZO changed to its cis form since the angle is a direct indicator for trans or cis structure of AZO domain. Simultaneously, the final structure of cis-AZO and  $\beta$ -CD cluster (B cluster) was obtained by simulation, which was a tighter cluster evolved by  $\beta$ -CD ring sliding from pendant AZO group to inner polymer domain on the foundation of A cluster. After simulation, B cluster was further optimized by G09 to form C cluster. Subsequently, the interaction energies ( $\Delta E$ ) of A cluster and C cluster calculated to  $-10.45$  kcal/mol for the former and  $-16.68$  kcal/mol for the latter by quantum chemistry, while also confirmed that the cluster of cis-AZO and  $\beta$ -CD was more stable than the cluster of trans-AZO and  $\beta$ -CD. Therefore, we proposed a UV/white light response mechanism in **Figure 4**. In their natural state, nanoparticles were assembled by inclusion interaction between AZO pendant group and hydrophobic cavity of  $\beta$ -CD domain. Upon UV light irradiation, the AZO pendant group stretched out of hydrophobic cavity so that the whole nanoparticle became

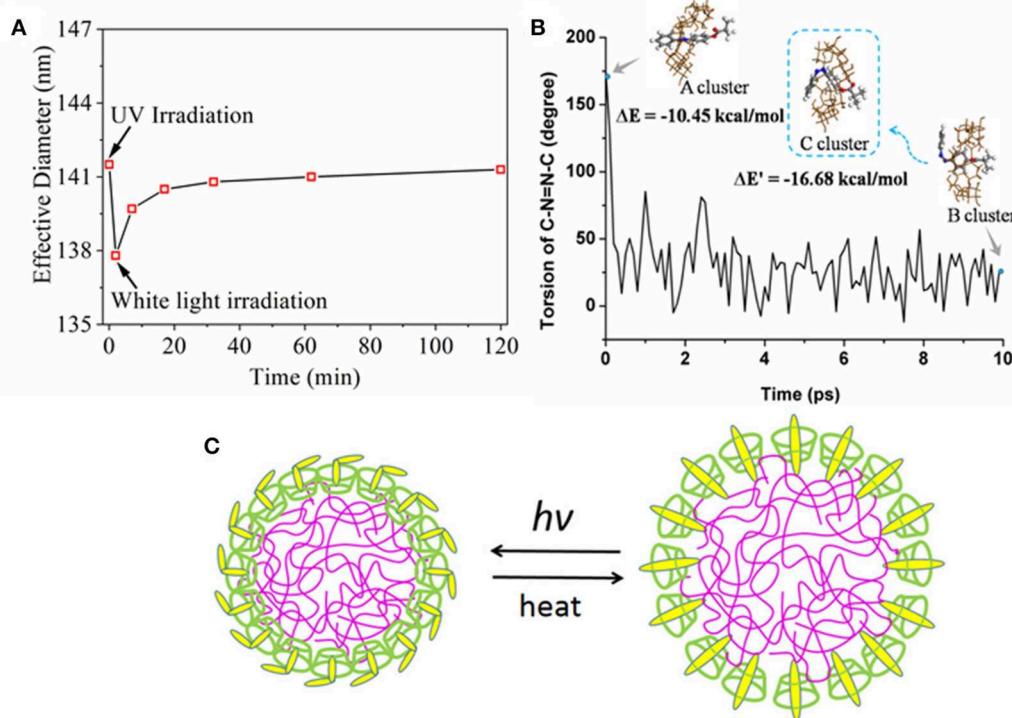


**FIGURE 4 | (A)** Effective diameter as a function of irradiation time and recovery time; **(B)** Torsion of C-N=N-C (degree) of AZO evolved by dynamics time (ps) carried out by MD simulation. The insets of A cluster was the optimized structure of trans-AZO and  $\beta$ -CD by G09 package, meanwhile the initial structure of our simulation; B cluster was the final structure of the simulation; and C cluster was the optimized structure of cis-AZO and  $\beta$ -CD cluster from B cluster; **(C)** Proposed UV response mechanism for assembled nanoparticle.

more tightly bond. The mechanism was supported by both experimental and theoretical results.

Beside the UV response, the nanoparticles pH response was also studied in **Figure 5**. Effective nanoparticle diameter increased a from 140 nm to 7  $\mu\text{m}$  when the pH value of environment was  $< 6$  according to **Figure 5a**. The effective nanoparticle diameter exhibited no dependent relationship on the solution pH value when the pH value was lower than 5.5 or higher than 6.5. Similar phenomenon of critical pH point for solution transparency existed in **Figure 5b**. At the same

time, nano 33 solution was clear when pH value was higher than 6.5 or it was turbid when pH value was lower than 5.5 either from eyesight or from transparency of **Figure 5b**. Not surprisingly, enlarged nanoparticle size impeded light transmission so that the solution became turbid even sediment, which was assumed to be a result of nanoparticle aggregation or nanoparticle coalescence. In order to clarify the actual status of nanoparticle in acid solution, nanoparticles dried from acid solution were characterized by TEM in **Figures 5c,d**. On the TEM image, aggregated nanoparticles were dispersed homogeneously,

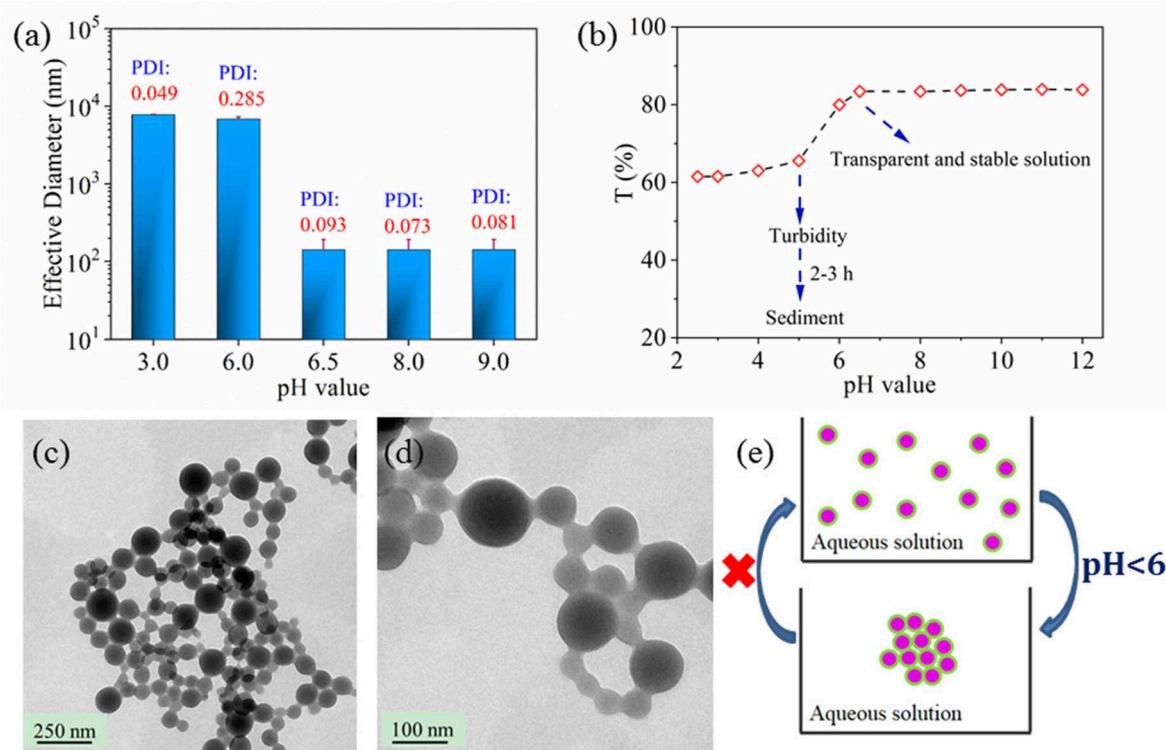


**FIGURE 5 |** Effective diameter **(a)** and transparency **(b)** of nano 33 aqueous solution as a function of pH value. TEM images of nano 33 dried from pH 3 solution, scale bar 250 nm **(c)**, 100 nm **(d)**. Proposed pH dependent behavior for nanoparticle **(e)**.

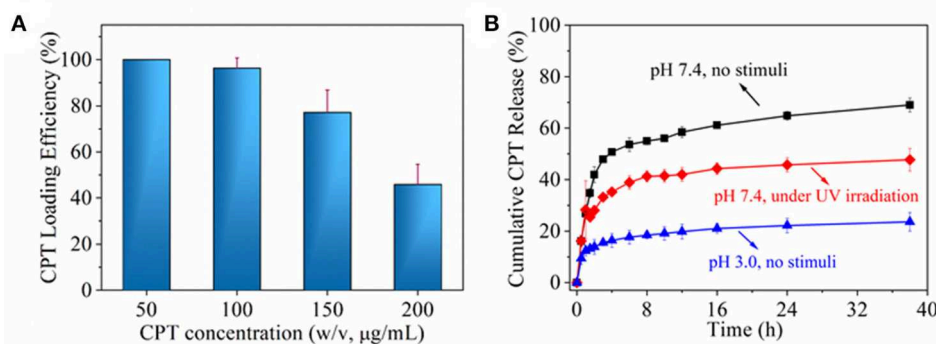
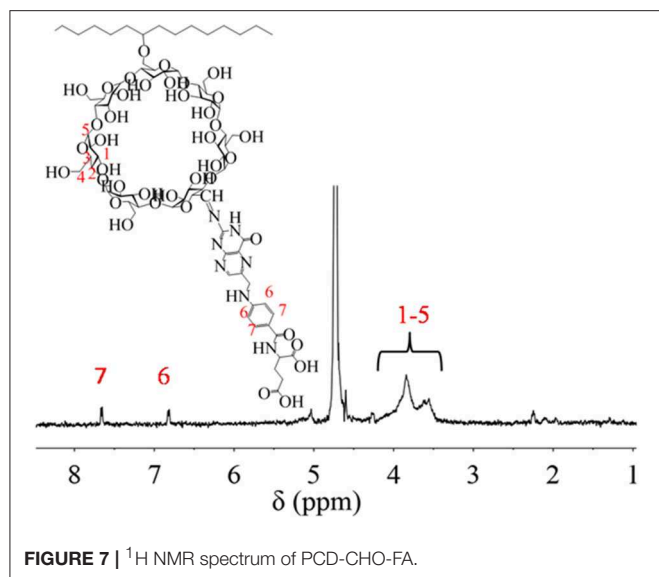


**FIGURE 6 | (A)** CPT loading efficiency as a function of CPT concentration. **(B)** cumulative CPT release under different environment.



which verified that pH dependent properties were due to nanoparticle aggregation. However, effective diameter kept to  $7\ \mu\text{m}$  and the nanoparticle solution kept turbid when the nanoparticle solution was adjusted to neutral or alkaline value again from original acid value, which indicated that nanoparticle aggregation was irreversible. Therefore, the pH dependent behavior was proposed in **Figure 5E**. The aggregation for nanoparticles respond in an acid environment, while their reversible process could not be realized. The pH dependent aggregation could ensure the nanoparticle staying in low pH area to play their therapeutic and responsive role, which is important for their application especially in the drug delivery field.

### In vitro Evaluation for Nanocarrier

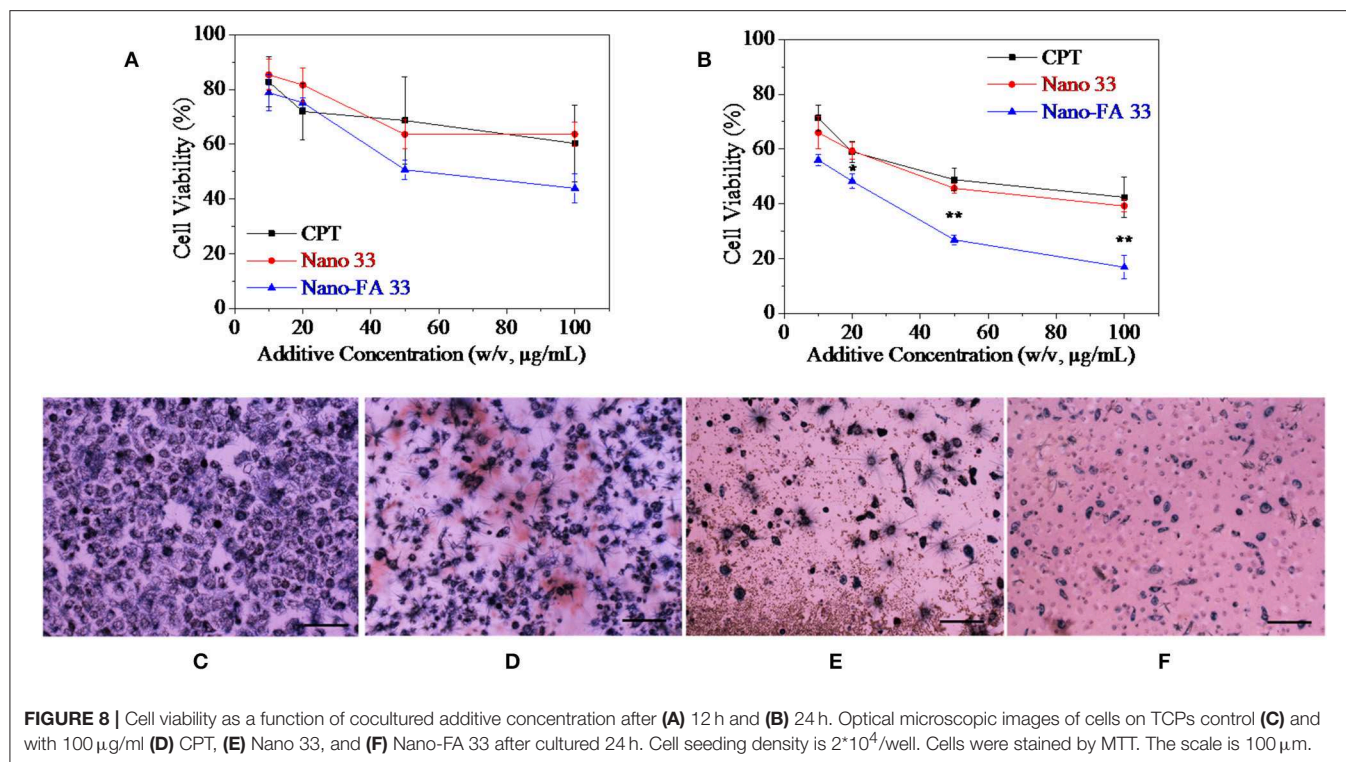
Next, the chemotherapeutic CPT was loaded into nanoparticles through the *in situ* fabrication method (Hu et al., 2016). It was found that CPT loading efficiency decreased with the increase of CPT concentration, especially when  $>100\ \mu\text{g/ml}$ , which was shown in **Figure 6A**. Actually, since the loaded CPT amount was due to definite free volume of inner nanoparticle, saturated CPT loading amount made its loading efficiency decrease for its higher loading concentration. According to the result of **Figure 6A**, CPT loading concentration of  $100\ \mu\text{g/ml}$  was chosen for further drug release behavior investigation (**Figure 6B**). CPT molecules in nanoparticle might exist in two statuses. One is a free molecule status; the other is a combined molecule status by interaction with nanoparticle. The free molecule could be easily released from nanoparticle by diffusion mechanism; while combined molecule should be exchanged to release medium by stronger interaction from molecules, ions or even groups. In PBS without any stimuli, about 50% CPT was quickly released from nanoparticles in 1 h and another 20% CPT was gradually released within 36 h. In PBS with UV irradiation, about 30% CPT was quickly released from nanoparticle in 1 h and another 20% CPT was gradually released within 36 h. In

medium of pH 3 without any stimuli,  $<20\%$  CPT was gradually released from nanoparticle within 36 h. The initial burst release might be attributed to the diffusion of free CPT molecule and further gradual release might be interactions between CPT and polymer domains including  $\beta$ -CD domain. In PBS without any stimuli, incompact structure of nanoparticle permitted more free volume that accommodate a freer CPT molecule. Upon UV irradiation, firmer nanoparticle structure reduced free volume, which decreased free CPT molecule. While in acid medium, CPT diffusion became very slow on account of small surface area induced by aggregation of nanoparticle. To sum up, the results indicated that drug could be hold or controlled to stay a specific place through the control of stimuli light or pH value.

In order to increase the recognition of nanoparticle, FA was grafted onto PCD through the two-step method of oxidation and covalent crosslinking. After functionalization, PCD-CHO-FA was characterized by  $^1\text{H}$  NMR spectrum in **Figure 7**. The details of chemical shift are listed as follows: chemical shifts from 3.5 to 4.2 ppm are attributed to the protons of pyranose ring on  $\beta$ -CD domain at 1-5 position, chemical shifts at 6.8 ppm and 7.7 ppm are attributed to the protons of benzene ring on new modified FA domain at 6 and 7 positions.

Then nanoparticles fabricated by self-assemble of HANN copolymer and PCD-CHO-FA functional polymer for further *in vitro* evaluation. Two kinds of nanocarriers with or without FA targeted domain were evaluated by *in vitro* cancer cell culture along with pure CPT group and TCPs control group, and the 3 results are shown in **Figure 8**. After coculture for 12 h, cytoviability decreased to 70% of original value with the increase of CPT concentration, and cytoviability decreased to 70% of original value with the increase of Nano 33 concentration, while cytoviability decreased to lower than 50% of original value with the increase of Nano-FA 33 concentration (**Figure 8A**). Although no significant difference was found between the three groups, the group for Nano-FA 33 exhibited relatively good effects to inhibit cell growth. After coculture for 24 h, cytoviability decreased to lower than 50% of original value with the increase of CPT concentration, and cytoviability decreased to 45% of original value with the increase of Nano 33 concentration, while cytoviability decreased to only 10% of original value with the increase of Nano-FA 33 concentration (**Figure 8B**). Cell growth was nearly completely inhibited by the Nano-FA 33 nanocarrier when its concentration reached  $100\ \mu\text{g/ml}$  after coculture for 24 h, which showed a significant difference between the Nano-FA 33 group and other two groups. These results were further supported by MTT stained optical microscopic cell images after coculture for 24 h. On TCPs control, homogenous dispersed cells were intact with fewer cell debris (**Figure 8C**). On CPT group, less intact cells and more cell debris were found, which indicated more dead cells (**Figure 8D**). On Nano 33 group, a small number of cells were witnessed to anchor on the culture plate, which was fewer than two above-mentioned groups (**Figure 8E**). On Nano 33-FA group, only limited several cells were observed with a large amount of cell debris (**Figure 8F**). In a word, many dead cells





confirmed the effectiveness and efficiency of nanocarriers on cancer cells.

## CONCLUSION

Nanoparticles were successfully self-assembled by HANN copolymer and PCD polymer. The effective diameter was influenced by the HANN/PCD ratio. Optimal HANN copolymer concentration was from 33 to 67%. Homogeneous dispersed nanoparticle with two-phase structure was also confirmed by TEM images. <sup>1</sup>HNMR spectroscopy confirmed the outer layer of nanoparticle to be composed of PCD polymer. UV spectrum verified the efficient and effective light response property for the nanoparticle, for example quick responsive time, controllable and gradual recovered process and good fatigue resistance, which were induced by the structural change for AZO domain. Upon UV irradiation, the self-assembled nanoparticles became more compact. MD simulations found that the β-CD slides toward the HANN copolymer main chain and quantum chemistry calculated that the cluster with cis-form had even larger interaction energy than that with trans-form. MD and quantum chemistry gave a reasonable explanation of the diameter response of nanoparticles upon UV light. Nanoparticles could irreversibly aggregate in acid medium (pH < 6.0), which indicated the pH dependent characteristic for nanoparticles. The *in vitro* drug release profile confirmed that the drug could be held or controlled to stay a specific site through the control of stimuli

including light or pH value. FA functionalized nanoparticles were successfully prepared for their application as a drug carrier. Preliminary *in vitro* cell culture results confirmed efficient and effective curative effect for the nanocarrier on MCF-7 cells.

## DATA AVAILABILITY

All datasets generated for this study are included in the manuscript/supplementary files.

## AUTHOR CONTRIBUTIONS

JP designed macromolecule and finished the calculation part. ZG prepared and characterized the self-assembled nanoparticles. HT helped with characterization and suggested potential application for this nanoparticle. XM, JX, and JK worked for the UV light responsive behavior. XH gave the ideas and designed the whole research. All the authors were involved in the data analysis.

## ACKNOWLEDGMENTS

This study was financially supported by Natural Science Foundation of China (21702082), Natural Science Foundation of Jiangsu Province (BK20171113), Qing Lan Project, Six talent peaks project in Jiangsu Province (JY-071).



## REFERENCES

- Ahmed, T., Walia, S., Kim, J., Nili, H., Ramanathan, R., Mayes, E. L. H., et al. (2017). Transparent amorphous strontium titanate resistive memories with transient photo-response. *Nanoscale* 9, 14690–14702. doi: 10.1039/C7NR04372D
- Beharry, A. A., and Woolley, G. A. (2011). Azobenzene photoswitches for biomolecules. *Chem. Soc. Rev.* 40, 4422–4437. doi: 10.1039/c1cs15023e
- Bhosale, R. R., Gangadharappa, H. V., Gowda, D. V., Osmani, R., Vaghela, R., Kulkarni, P. K., et al. (2018). Current perspectives on novel drug carrier systems and therapies for management of pancreatic cancer: an updated inclusive review. *Crit. Rev. Therapeut. Drug Carrier Syst.* 35, 195–292. doi: 10.1615/CritRevTherDrugCarrierSyst.2018019429
- Bian, Q., Wang, W., Han, G., Chen, Y., Wang, S., and Wang, G. (2016). Photoswitched cell adhesion on azobenzene-containing self-assembled films. *Chemphyschem* 17, 2503. doi: 10.1002/cphc.201600362
- Cao, Z. Q., and Wang, G. J. (2016). Multi-stimuli-responsive polymer materials: particles, films, and bulk gels. *Chem. Rec.* 16, 1398–1435. doi: 10.1002/tcr.201500281
- Chen, P., Wang, X., Dong, Y., and Hu, X. H. (2015). Development of a layer-by-layer assembled film on hydrogel for ocular drug delivery. *Int. J. Poly. Sci.* 2015:535092. doi: 10.1155/2015/535092
- Guragain, S., Bastakoti, B. P., Malgras, V., Nakashima, K., and Yamauchi, Y. (2015). Multi-stimuli-responsive polymeric materials. *Chemistry* 21, 13164–13174. doi: 10.1002/chem.201501101
- Hu, X., Gong, X. (2016). A new route to fabricate biocompatible hydrogels with controlled drug delivery behavior. *J. Colloid Interf. Sci.* 470, 62–70. doi: 10.1016/j.jcis.2016.02.037
- Hu, X., Tan, H., Chen, P., Wang, X., and Pang, J. (2016). Polymer micelles laden hydrogel contact lenses for ophthalmic drug delivery. *J. Nanosci. Nanotechnol.* 16, 5480–5488. doi: 10.1166/jnn.2016.11733
- Hu, X. H., Chen, S. N., Gong, X., Gao, Z. Y., Wang, X., Chen, P. (2017). Synthesis and preparation of biocompatible and pH-responsive cyclodextrin-based nanoparticle. *J. Nanoparticle Res.* 19:109. doi: 10.1007/s11051-017-3819-5
- Huang, C. Y., Chen, M. L., Yu, C. W., Wan, T. C., Chen, S. H., Chang, C. Y., et al. (2018). Dual functional photo-response for p-Si/SiO<sub>2</sub>/n-InGaZnO graphene nanocomposites photodiodes. *Nanotechnology* 29:505202. doi: 10.1088/1361-6528/aae474
- Huang, Y., Mao, K., Zhang, B., and Zhao, Y. (2017). Superparamagnetic iron oxide nanoparticles conjugated with folic acid for dual target-specific drug delivery and MRI in cancer theranostics. *Mater Sci Eng C Mater Biol Appl.* 70, 763–771. doi: 10.1016/j.msec.2016.09.052
- Intasa-Rad, S. G., and Ogawa, M. (2018). Layered silicates as a possible drug carrier. *Enzymes* 44, 117–136. doi: 10.1016/bs.enz.2018.08.003
- Kathan, M., and Hecht, S. (2017). Photoswitchable molecules as key ingredients to drive systems away from the global thermodynamic minimum. *Chem. Soc. Rev.* 46, 5536–5550. doi: 10.1039/C7CS00112F
- Kim, D. Y., Lee, S. A., Park, M., Choi, Y. J., Kang, S. W., and Jeong, K. U. (2015). Multi-responsive chameleon molecule with chiral naphthyl and azobenzene moieties. *Soft Matter* 11, 2924–2933. doi: 10.1039/C5SM00073D
- Kydd, J., Jadia, R., and Rai, P. (2018). Co-administered polymeric nano-antidotes for improved photo-triggered response in glioblastoma. *Pharmaceutics* 10:226. doi: 10.3390/pharmaceutics10040226
- Lin, L. R., Wang, X., Wei, G. N., Tang, H. H., Zhang, H., and Ma, L. H. (2016). Azobenzene-derived tris- $\beta$ -diketonate lanthanide complexes: reversible *trans*-to-*cis* photoisomerization in solution and solid state. *Dalton Transac.* 45, 14954–14964. doi: 10.1039/C6DT01310D
- Lorenzo, R. A., Carro, A. M., Concheiro, A., and Alvarez-Lorenzo, C. (2015). Stimuli-responsive materials in analytical separation. *Anal. Bioanal. Chem.* 407, 4927–4948. doi: 10.1007/s00216-015-8679-1
- Lu, T., Zhu, S., Chen, Z., Wang, W., Zhang, W., and Zhang, D. (2016). Hierarchical photonic structured stimuli-responsive materials as high-performance colorimetric sensors. *Nanoscale* 8, 10316–10322. doi: 10.1039/C6NR01875K
- Ma, K., Xia, H., and Ni, Q. Q. (2019). Drug carrier three-layer nanofibrous tube for vascular graft engineering. *J. Biomater. Sci.* 30, 501–507. doi: 10.1080/09205063.2018.1493670
- Malik, N. S., Ahmad, M., and Minhas, M. U. (2017). Cross-linked  $\beta$ -cyclodextrin and carboxymethyl cellulose hydrogels for controlled drug delivery of acyclovir. *PLoS ONE* 12:0172727. doi: 10.1371/journal.pone.0172727
- Mao, Y., Ding, Z., Yuan, C., Ai, S., Isakov, M., Wu, J., et al. (2016). 3D printed reversible shape changing components with stimuli responsive materials. *Sci. Rep.* 6:24761. doi: 10.1038/srep24761
- Merzel, R. L., Frey, C., Chen, J., Garn, R., van Dongen, M., Dougherty, C. A., et al. (2017). Conjugation dependent interaction of folic acid with folate binding protein. *Bioconjugate Chem.* 28, 2350–2360. doi: 10.1021/acs.bioconjchem.7b00373
- Pang, J., Gao, Z., Tan, H., Mao, X., Wang, H., Hu, X. (2019). Design, synthesis, investigation, and application of a macromolecule photoswitch. *Front. Chem.* 7:86. doi: 10.3389/fchem.2019.00086
- Pang, J., Gao, Z., Zhang, L., Wang, H., and Hu, X. (2018). Synthesis and characterization of photoresponsive macromolecule for biomedical application. *Front. Chem.* 6:217. doi: 10.3389/fchem.2018.00217
- Pang, J., Ye, Y. F., Tian, Z. Q., Pang, X. Y., Wu, Y. (2015). Theoretical insight into azobis-(benzo-18-crown-6) ether combined with the alkaline earth metal cations. *Computat. Theoret. Chem.* 1066, 28–33. doi: 10.1016/j.comptc.2015.04.012
- Song, X., Zhu, J. L., Wen, Y., Zhao, F., Zhang, Z. X., and Li, J. (2017). Thermoresponsive supramolecular micellar drug delivery system based on star-linear pseudo-block polymer consisting of  $\beta$ -cyclodextrin-poly(N-isopropylacrylamide) and adamantyl-poly(ethylene glycol). *J. Colloid Interf. Sci.* 490, 372–379. doi: 10.1016/j.jcis.2016.11.056
- Sun, Y., Yu, C., Liu, Z., Huang, C., Hao, Q., and Xu, L. (2012). Synthesis, structure, photo-responsive properties of 4-(2-fluorobenzyldeneamino)antipyrine: a combined experimental and theoretical study. *Spectrochim. Acta. Part A Mol Biomol Spectrosc.* 97, 1013–1022. doi: 10.1016/j.saa.2012.07.117
- Trucks, G. W., Frisch, M. J., Schlegel, H. B., Scuseria, G. E., Robb, M. A., Cheeseman, J. R., et al. (2009). *Gaussian 09, Revision A.02*. Wallingford, CT: Gaussian Inc.
- Wang, D., Schellenberger, F., Pham, J. T., Butt, H. J., and Wu, S. (2018). Orthogonal photo-switching of supramolecular patterned surfaces. *Chem. Commun.* 54, 3403–3406. doi: 10.1039/C8CC00770E
- Wang, D., Wagner, M., Butt, H., and Wu, S. (2015). Supramolecular hydrogels constructed by red-light-responsive host-guest interactions for photo-controlled protein release in deep tissue. *Soft Matter* 11: 7656–7662. doi: 10.1039/C5SM01888A
- Wang, D., Wagner, M., Saydjari, A. K., Mueller, J., Winzen, Butt, H. J., and Wu, S. (2017). A Photoresponsive orthogonal supramolecular complex based on host-guest interactions. *Chemistry* 23, 2628–2634. doi: 10.1002/chem.201604634
- Wang, D., and Wu, S. (2016). Red-light-responsive supramolecular valves for photocontrolled drug release from mesoporous nanoparticles. *Langmuir* 32, 632–636. doi: 10.1021/acs.langmuir.5b04399
- Ye, Y. F., Mao, X. M., Xu, J. L., Kong, J., and Hu, H. (2019). Functional graphene oxide nanocarriers for drug delivery. *Int. J. Poly. Sci.* 57:8453493. doi: 10.1155/2019/8453493
- Ye, Y. F., Pang, J., Zhou, X. J., and Huang, J. W. (2016). Understanding the torsion effects on optical properties of azobenzene derivatives. *Comput. Theoret. Chem.* 1076, 17–22. doi: 10.1016/j.comptc.2015.11.022
- Yuan, K., Guo, Y. J., and Zhao, X. (2014). A novel photo-responsive azobenzene-containing nanoring host for fullerene-guest facile encapsulation and release. *Phys. Chem. Chem. Phys.* 16, 27053–27064. doi: 10.1039/C4CP03687E
- Zhang, X., Huang, G., and Huang, H. (2018). The glyconanoparticle as carrier for drug delivery. *Drug Deliv.* 25, 1840–1845. doi: 10.1080/10717544.2018.1519001
- Zhou, Y., Wang, D., Huang, S., Auernhammer, G., He, Y., Butt, H., et al. (2015). Reversible Janus particle assembly via responsive host-guest interactions. *Chem. Commun.* 51, 2725–2727. doi: 10.1039/C4CC09672J

**Conflict of Interest Statement:** The authors declare that the research was conducted in the absence of any commercial or financial relationships that could be construed as a potential conflict of interest.

Copyright © 2019 Pang, Gao, Tan, Mao, Xu, Kong and Hu. This is an open-access article distributed under the terms of the Creative Commons Attribution License (CC BY). The use, distribution or reproduction in other forums is permitted, provided the original author(s) and the copyright owner(s) are credited and that the original publication in this journal is cited, in accordance with accepted academic practice. No use, distribution or reproduction is permitted which does not comply with these terms.



# Modeling the Kinetics, Curing Depth, and Efficacy of Radical-Mediated Photopolymerization: The Role of Oxygen Inhibition, Viscosity, and Dynamic Light Intensity

Jui-Teng Lin<sup>1†</sup>, Hsia-Wei Liu<sup>2†</sup>, Kuo-Ti Chen<sup>3</sup> and Da-Chuan Cheng<sup>4\*</sup>

<sup>1</sup> New Vision, Inc., Taipei City, Taiwan, <sup>2</sup> Department of Life Science, Fu Jen Catholic University, New Taipei City, Taiwan, <sup>3</sup> Graduate Institute of Applied Science and Engineering, Fu Jen Catholic University, New Taipei City, Taiwan, <sup>4</sup> Department of Biomedical Imaging and Radiological Science, China Medical University, Taichung, Taiwan

## OPEN ACCESS

### Edited by:

Pellegrino Musto,  
Italian National Research Council  
(CNR), Italy

### Reviewed by:

Jiefei Wang,  
Henan University, China  
Marco Gigliotti,  
École Nationale Supérieure de  
Mécanique et  
d'Aérotechnique, France

### \*Correspondence:

Da-Chuan Cheng  
freiburg226@gmail.com

<sup>†</sup>These authors have contributed  
equally to this work

### Specialty section:

This article was submitted to  
Polymer Chemistry,  
a section of the journal  
Frontiers in Chemistry

**Received:** 12 September 2019

**Accepted:** 23 October 2019

**Published:** 13 November 2019

### Citation:

Lin J-T, Liu H-W, Chen K-T and  
Cheng D-C (2019) Modeling the  
Kinetics, Curing Depth, and Efficacy of  
Radical-Mediated  
Photopolymerization: The Role of  
Oxygen Inhibition, Viscosity, and  
Dynamic Light Intensity.  
Front. Chem. 7:760.  
doi: 10.3389/fchem.2019.00760

Kinetic equations for a modeling system with type-I radical-mediated and type-II oxygen-mediated pathways are derived and numerically solved for the photopolymerization efficacy and curing depth, under the quasi-steady state assumption, and bimolecular termination. We show that photopolymerization efficacy is an increasing function of photosensitizer (PS) concentration ( $C_0$ ) and the light dose at transient state, but it is a decreasing function of the light intensity, scaled by  $[C_0/I_0]^{0.5}$  at steady state. The curing (or cross-link) depth is an increasing function of  $C_0$  and light dose (time  $\times$  intensity), but it is a decreasing function of the oxygen concentration, viscosity effect, and oxygen external supply rate. Higher intensity results in a faster depletion of PS and oxygen. For optically thick polymers ( $>100$   $\mu\text{m}$ ), light intensity is an increasing function of time due to PS depletion, which cannot be neglected. With oxygen inhibition effect, the efficacy temporal profile has an induction time defined by the oxygen depletion rate. Efficacy is also an increasing function of the effective rate constant,  $K = k'/k_T^{0.5}$ , defined by the radical producing rate ( $k'$ ) and the bimolecular termination rate ( $k_T$ ). In conclusion, the curing depth has a non-linear dependence on the PS concentration, light intensity, and dose and a decreasing function of the oxygen inhibition effect. Efficacy is scaled by  $[C_0/I_0]^{0.5}$  at steady state. Analytic formulas for the efficacy and curing depth are derived, for the first time, and utilized to analyze the measured pillar height in microfabrication. Finally, various strategies for improved efficacy and curing depth are discussed.

**Keywords:** cross-link, curing, efficacy, kinetic modeling, oxygen, ultraviolet light

## INTRODUCTION

Photoinitiated (photosensitized) polymerization and cross-linking provide advantageous means over thermal-initiated polymerization, including fast and controllable reaction rates, and spatial and temporal control over the formation of the material, without the need for high temperatures or harsh conditions (Fouassier, 1995; Odian, 2006). Tissue engineering using scaffold-based procedures for chemical modification of polymers has been reported to improve its mechanical

properties by cross-linking or polymerization with ultraviolet (UV) or visible light to produce gels or high-molecular-weight polymers (Chen and Shi, 2014; Kotisch et al., 2017). The progress of light-responsive smart nanomaterials was recently review by Yang et al. (2018).

Industrial applications include developing materials for applications such as thin films, coatings, printing, graphic work, dentistry, contact lenses, and electronics. It is a noncontact, low-energy, and rapid process with capabilities of spatially specifying the reaction via photomasks (photolithography) (Cabral et al., 2004; O'Brien and Bowman, 2006; Cramer et al., 2008; Dendukuri et al., 2008; Alvankarian and Majlis, 2015; Wohlers and Caffrey, 2016; Chen et al., 2017; Wu et al., 2018). The polymerization rate is inhibited by air due to oxygen inhibition, which scavenges the radical species needed for cross-linking initialization. Diffusion of oxygen from a high-concentration zone into a prepolymer resin during UV curing requires an additional amount of photoinitiator and UV energy to consume the dissolved and diffused oxygen (O'Brien and Bowman, 2006; Cramer et al., 2008; Dendukuri et al., 2008; Alvankarian and Majlis, 2015).

Cabral et al. (2004) investigated the concept of frontal photopolymerization, in which the position of the frontal border can be controlled by adjusting UV power and the available atmospheric air. The utilization of microfabrication to reduce the deposition steps and to obtain a monolithic product was reported by Alvankarian and Majlis (2015). Chen et al. (2017) proposed a kinetic model for pillar growth that includes free-radical generation and oxygen inhibition in thick films of photoinitiated media and have demonstrated control over the pillar spacing and pillar height with the irradiation intensity, film thickness, and the size and spacing of the optical beams. In microfabrication system, the formation of radical decreases over depth due to the reduction in light intensity and photosensitizer (PS) concentration and increase in oxygen inhibition. Oxygen diffuses into the film and consumes radicals. The balance of radical production and oxygen inhibition gives rise to the inhibition zone, where the polymerization is completely suppressed (Wu et al., 2018).

The kinetics of polymerization has been extensively studied (Cabral et al., 2004; O'Brien and Bowman, 2006; Cramer et al., 2008; Dendukuri et al., 2008; Alvankarian and Majlis, 2015; Semchishen et al., 2015; Lin and Wang, 2016; Chen et al., 2017; Lin and Cheng, 2017; Lin, 2018, 2019; Wu et al., 2018; Lin et al., 2019). However, most of the previous models (Cabral et al., 2004; O'Brien and Bowman, 2006; Cramer et al., 2008; Dendukuri et al., 2008; Alvankarian and Majlis, 2015; Chen et al., 2017; Wu et al., 2018) are based on oversimplified assumptions of constant PS concentration (without depletion), and the light intensity in the polymer following a conventional Beer–Lambert law (BLL), with neglected PS depletion, which is only valid for optically thin polymers (Lin and Cheng, 2017).

This study will present a more general kinetic model with coupled equations for the PS and oxygen concentration and monomer, which will be numerically solved for various conditions. Analytic formulas for the efficacy and curing depth will be derived and utilized to analyze the measured pillar height in microfabrication reported by Chen et al. (2017). Various

scaling laws for the efficacy and curing depth, in both transient and steady state, will be derived, for the first time. The importance of PS depletion and dynamic light intensity in an optically thick polymer, based on a revised BLL, will be shown numerically (Lin and Cheng, 2017). Finally, various strategy for improved efficacy and curing depth, by reducing oxygen inhibition effect, will be discussed.

## METHODS

### Kinetic Equations

Photopolymerization in general includes radical-mediated, cationic, and anionic catalyzed, and atom transfer radical polymerization. In a radical-mediated photopolymerization, the monomer is converted to polymer after the light irradiation of the photosensitizer (PS) or photoinitiator. The UV (or visible) light-produced triplet state ( $T^*$ ) is coupled to the substrate monomer [A] and the oxygen to produce radicals. Each radical becomes the center of origin of a polymer chain. The chain growth of a polymer radical with  $m$ -links stops as a result of chain termination reactions. Kinetic equations of an  $m$ -component radical photopolymerization process (with a triplet excited state as the catalyst) may be described as follows: (Semchishen et al., 2015; Lin, 2019)

$$\frac{\partial T(z, t)}{\partial t} = bIC - (k_5 + k_3[O_2] + k_7[A])T \quad (1)$$

$$\frac{\partial [O_2]}{\partial t} = P - k_3 T[O_2] + \sum_{m=1}^{\infty} k_m R_m [O_2] \quad (2)$$

$$\frac{\partial R_1}{\partial t} = k_8[A]T - k'_1 R_1 [A] - R_1 \sum_{m=1}^{\infty} k_m R_m \quad (3)$$

$$\frac{\partial R_{n+1}}{\partial t} = k'_1 (R_n - R_{n+1}) [A] - R_{n+1} \sum_{m=1}^{\infty} k_m R_m \quad (4)$$

$$\frac{\partial [A]}{\partial t} = -k_7 [A] T - \sum_{m=1}^{\infty} k_m R_m [A] \quad (5)$$

As shown in **Figure 1**, for a one-component monomer A, with three-radical system consisting of two PS radicals ( $R'$  and  $R$ ) and one singlet oxygen, the pathways are described as follows. The ground-state PS molecules are excited by the UV light to its singlet excited state ( $S_1$ ), which could be relaxed to its ground state or to a triplet excited state ( $T^*$ ). In type-I process,  $T^*$  could interact directly with the substrate [A] and produces the first-radical ( $R'$ ), which could produce (by chain reaction) a second radical ( $R$ ) which could interact with the ground state oxygen or the first radical. For type-II process, ( $T_3$ ) interacts with  $[O_2]$  to form oxygen singlet [ $^1O_2$ ]. These reactive radicals,  $R$ ,  $R'$ , and [ $^1O_2$ ], could be relaxed to its ground states or interacts with the substrate [A]. This article will focus on the one-monomer system, and the two-monomer and two-initiator systems will be shown elsewhere (Chen et al., 2019b; Lin, 2019).

For a one-monomer system, using the short-hand notations, the concentration of various components:  $C(z, t)$  and  $T$  for the PS ground and triplet state, respectively;  $[O_2]$  and  $X$  for the oxygen ground and singlet state;  $R$  and  $R'$  for the first and intermediate free radical; and  $[A]$  for the available extracellular

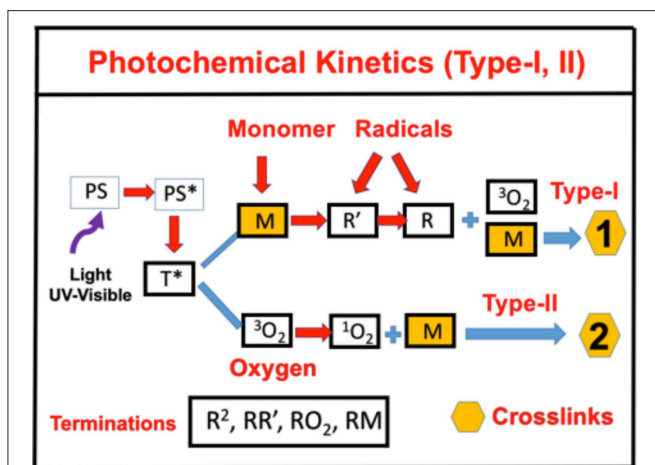


**FIGURE 1 |** Schematics of photochemical pathways. Pathway of one-monomer system, for radical-mediated pathway-1 and oxygen-mediated pathway-2; where  $P$  is the ground-state photosensitizer, having an excited and triplet state  $PS^*$  and  $T^*$ , which interacts with the substrate  $A$  to form radicals  $R'$  and  $R$ .

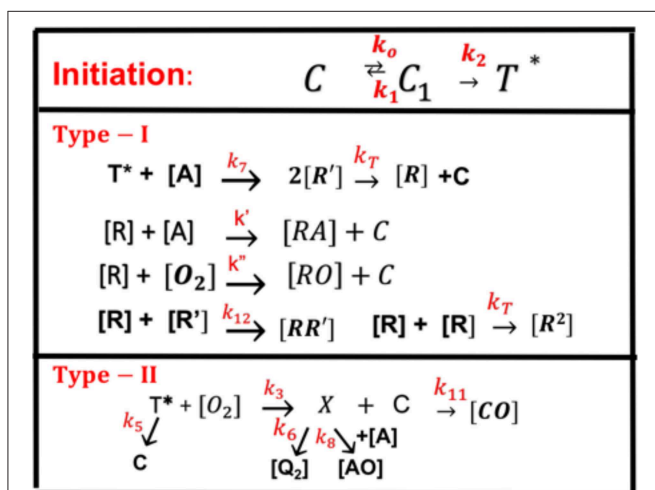


**FIGURE 2 |** The ground-state photosensitizer (PS) ( $C$ ) is excited by a UV light to its singlet excited state ( $C_1$ ), which could be relaxed to its ground state or to a triplet excited state ( $T^*$ ). In type-I process,  $T^*$  could interact directly with the monomer  $[A]$  to generate free radical ( $R'$ ) by recombination. The radical  $R$  could interact with  $[A]$  for cross-linking, or oxygen  $[O_2]$ , or terminated by coupling with  $R'$ , or bimolecular recombination ( $2R^2$ ). For type-II process,  $T^*$  interacts with  $[O_2]$  to form oxygen singlet ( $^1O_2$ ) ( $X$ ), which could relax to its oxygen  $[O_2]$ , or interacts with  $[A]$  for cross-linking, or coupling with  $C$ . All rate constants are shown in red next to arrows.

matrix substrate; and the kinetic equations for a three-radical system becomes

$$\frac{\partial C(z, t)}{\partial t} = -bI(z, t)C - k_{11}XC + (k_5 + k_3[O_2])T + R_E \quad (6)$$

$$\frac{\partial T}{\partial t} = bI(z, t)C - (k_5 + k_3[O_2] + k_7[A])T \quad (7)$$

$$\frac{\partial R'}{\partial t} = 2k_7T[A] - k_{12}RR' - 2k_TR'^2 \quad (8)$$

$$\frac{\partial R}{\partial t} = 2k_TR'^2 - k'R[A] - k_{12}RR' - 2k_TR'^2 - k''R[O_2] \quad (9)$$

$$\frac{\partial X}{\partial t} = k_3[O_2]T - (k_6 + k_{11}C + k_8[A])X \quad (10)$$

$$\frac{\partial [O_2]}{\partial t} = P - k_3[O_2]T + k_6X - k''R[O_2] \quad (11)$$

$$\frac{\partial [A]}{\partial t} = -(k_7T + k_8X + k'R)[A] \quad (12)$$

where  $b = 83.6a'qw$ ,  $w$  being the UV light wavelength (in cm) and light intensity  $I(z, t)$  in  $mW/cm^2$ ;  $q$  is the quantum yield of the PS triplet state; Equation (11) also includes an oxygen source term given by Semchishen et al. (2015),  $P = (1 - [O_2]/O_0)P'$ , with a maximum rate constant  $P'$ , with a maximum rate constant  $P_0$  and initial oxygen concentration  $Y_0$ . This term may be also given by the oxygen diffusion  $P = D_0 \nabla^2 [O]$ . In Equation (1), the regeneration term is given by  $R_E = k'R[O_2] + 2k_TR^2 + R'^2$ .

All the reaction rate constants are defined by the associated coupling terms, as shown by Figure 2. For examples, in Equation (9),  $k_7$  is for the coupling rate of  $[A]$  and  $T$ , which has a ground-state relaxation rate  $k_5$ ; in Equation (11),  $k'$  is for  $[A]$  and  $R$ , which is coupled with  $R'$  by  $k_{12}$  and a bimolecular termination rate of  $k_T$ ; in Equation (12),  $k'$  is for the reaction of  $[A]$  and  $R$ , which is coupled with oxygen by  $k''$  and a bimolecular termination rate  $k_T$ . Figure 2 also shows the rate constants for type-II process:  $k_3$  for singlet-oxygen ( $X$ ) production;  $k_8$  for cross-link of  $X$  with  $[A]$  and having a relaxation rate of  $k_6$ ; and a reduction rate  $k_{11}$ , by coupling to  $C$ .

The dynamic light intensity is given by (Lin and Wang, 2016; Lin and Cheng, 2017)

$$\frac{\partial I(z, t)}{\partial z} = -A'(z, t)I(z, t) \quad (13)$$

$$A'(z, t) = 2.3[(a' - b')C(z, t) + b'C_0 + Q] \quad (14)$$

where  $a'$  and  $b'$  are the extinction coefficients of PS and the photolysis product, respectively;  $Q$  is the absorption coefficient of the monomer at the UV wavelength. Most previous modeling (O'Brien and Bowman, 2006; Cramer et al., 2008; Dendukuri et al., 2008; Alvankarian and Majlis, 2015; Chen et al., 2017; Wu et al., 2018) assumed a constant  $C(z, t)$  in Equation (14). Our analytic formulas in this article will use a time average of  $A(z, t)$  to count for the dynamic of light intensity due to PS depletion.

The kinetic Equations (6)–(12) may be numerically calculated to find the conversion efficacy, which, however, is too complex for us to analyze the roles of each of the parameters. For comprehensive modeling, we will use the so-called quasi-steady-state assumption (Lin, 2018; Lin et al., 2019). The life time of the singlet and triplet states of photosensitizer, the radicals ( $R$  and  $R'$ ), and the singlet oxygen ( $X$ ) are very short (nanosecond to microsecond time scale) since they either decay or react with cellular matrix immediately after they are created. Thus, one may set  $dT/dt = dR/dt = dR'/dt = dX/dt = 0$ , which give the quasi-steady-state solutions:  $T = bIgC$ ,  $X = bIg'[O_2]/k_8$ ,  $g = k_8/(k_3[O_2] + k_8[A] + k_5)$ ;  $g' = k_3/(k_6 + k_{11}C + k_7[A])$ ;  $k =$



$(k_{11}/k_8)$ . The kinetic Equations (8)–(12) become,

$$\frac{\partial[A]}{\partial t} = -[bIgC(1 + g'[O_2]) + k' R] [A] \quad (17)$$

$$\frac{\partial C(z, t)}{\partial t} = -bI(g[A] + kgg'C[O_2])C + R_E \quad (15)$$

$$\frac{\partial[O_2]}{\partial t} = -(bICg + k''R)[O_2] + P \quad (16)$$

where the PS regeneration term  $R_E = k_9R[O_2] + 2k_T R^2$ . The radicals,  $R$  and  $R'$ , are given by the solution of the following

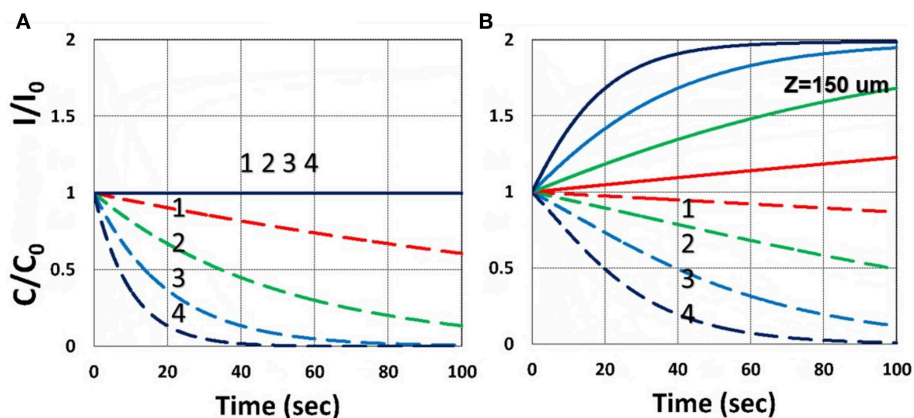


**FIGURE 3 |** Dynamic profiles of the PS concentration (blue curves) and light intensity increase ratio (red curves) at various light intensity  $I_0 = (0.5, 2, 5, 10)$  mW/cm<sup>2</sup>, at  $z = 0$  (A) and  $150 \mu m$  (B).

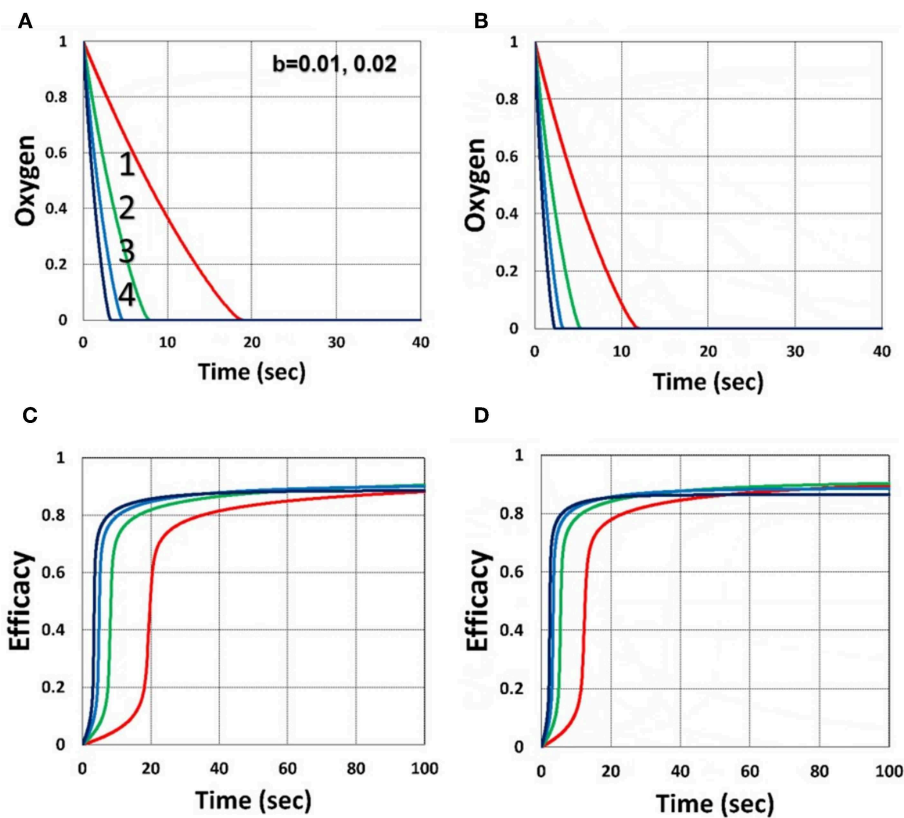


**FIGURE 4 |** Dynamic profiles. Efficacy and oxygen profiles for various light intensity  $I_0 = (0.5, 2, 5, 10)$  mW/cm<sup>2</sup>, for curves (1, 2, 3, 4), for  $b = 0.02$ , shown by (A,C); and  $b = 0.04$ , shown by (B,D); for  $C_0 = 0.01$  mM, and without viscosity effect (or  $\nu = 0$ ), and without external oxygen supply (with  $P' = 0$ ).

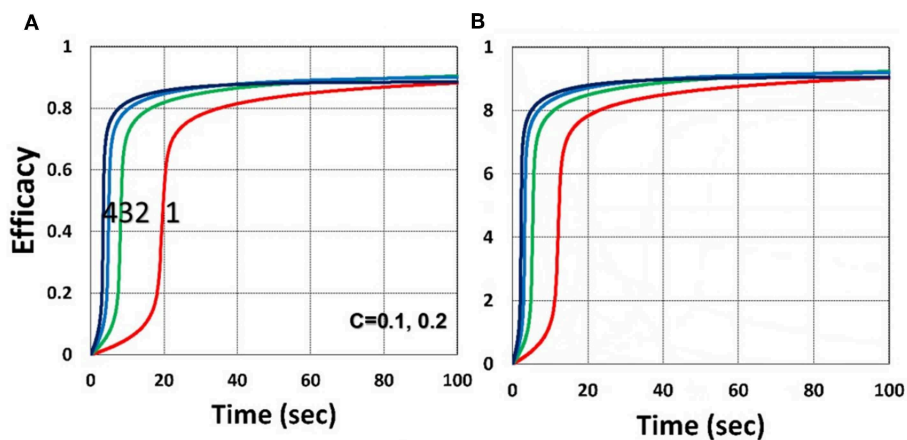


**FIGURE 5 |** Dynamic profiles. Same as **Figure 4**, but for (A)  $C_0 = 0.1\%$  and (B)  $C_0 = 0.2\%$ ; for  $b = 0.02$ .

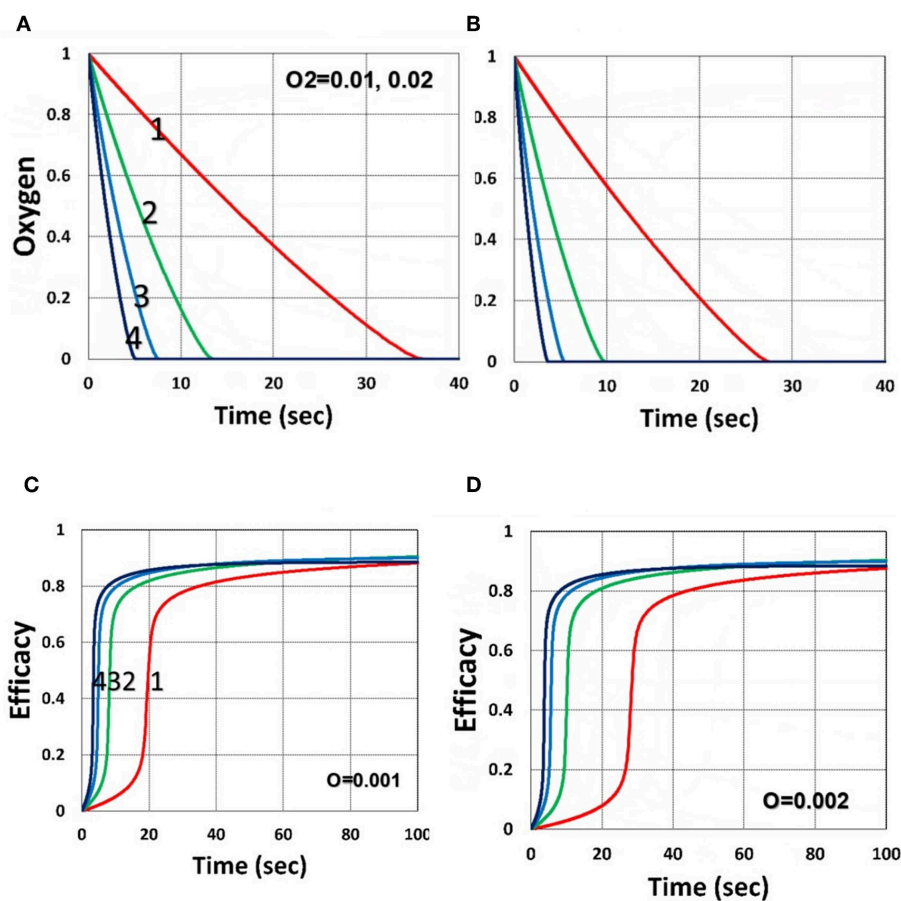


**FIGURE 6 |** Dynamic profiles. Same as **Figure 4**, but for oxygen initial value of 0.001 mM shown by (A,C); and 0.002 mM shown by (B,D); for  $b = 0.02$  and  $C_0 = 0.01$  mM.

steady-state of Equations (8) and (9):

$$2bIgC[A] - k_{12}RR' - 2k_T R'^2 = 0 \quad (18)$$

$$2k_T R'^2 - k'R[A] - k_{12}RR' - 2k_T R^2 - k''R[O_2] = 0 \quad (19)$$

Numerical solutions are required for  $R$  and  $R'$ . However, analytic formulas are available for the case that coupling of  $R'$  and

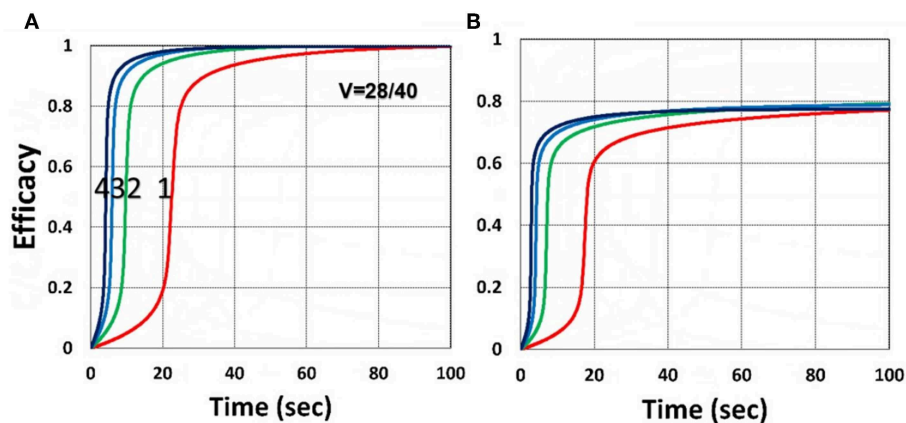


**FIGURE 7 |** Dynamic profiles. Same as **Figure 4**, but for viscosity factor  $v = 28$  (A); and  $v = 40$  (B); for  $b = 0.02$  and  $C_0 = 0.01$  mM.

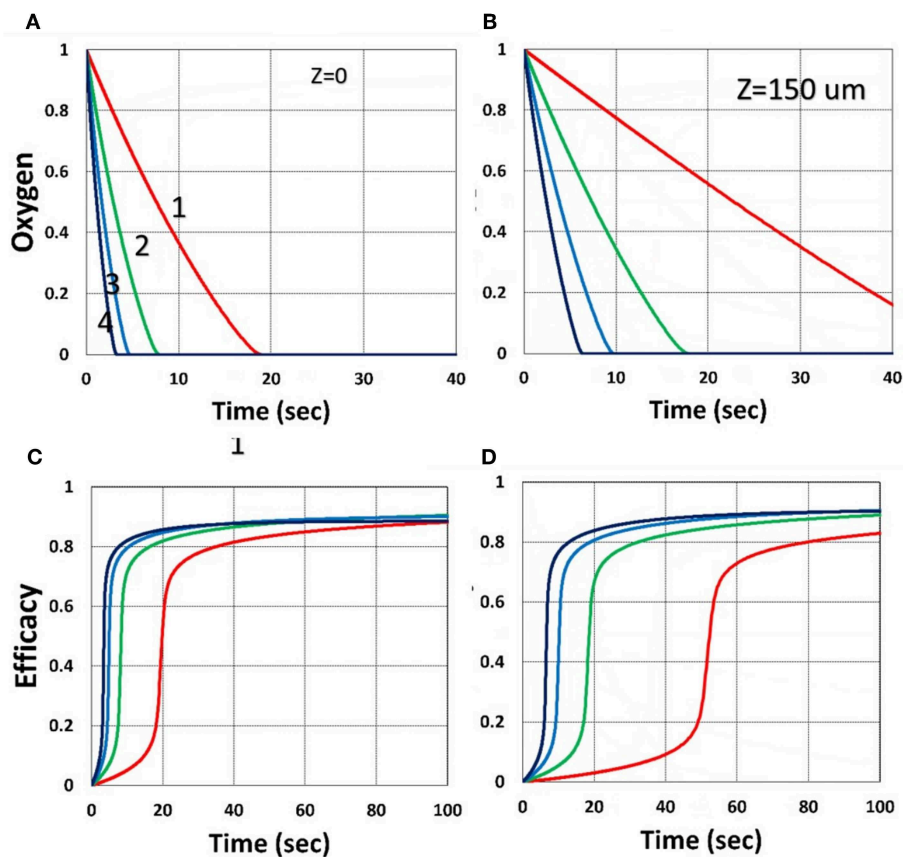


**FIGURE 8 |** Dynamic profiles. Same as **Figure 3**, but for  $z = 0$  (on surface), shown by (A,C); and  $z = 150 \mu\text{m}$ , shown by (B,D); for  $b = 0.02$  and  $C_0 = 0.01$  mM.

$R$  is weaker than the bimolecular recombination, i.e.,  $2k_T R'^2 \gg k_{12} R R'$  in Equation (18), we obtain  $R' = (bI_g C[A]/k_T)^{0.5}$ . Substituting this steady-state  $R'$  into Equation (19), we obtain

$$R(z, t) = \left( \frac{1}{4k_T} \right) [-G + \sqrt{G^2 + 16k_T B(z, t)}] \quad (20)$$

where  $B = bI_g C[A]$ , and  $G = k'' [O_2] + 2k_{12} R' + k'[A]$ . For  $G^2 \ll 8k_T B$ , Equation (20) is further reduced to  $R = (B/k_T)^{0.5} - k'' [O_2] (1 - B') / (4k_T)$ , with  $B' = 0.5k'' [O_2] / (8Bk_T)^{0.5}$ , which shows that  $R$ , and efficacy, are decreasing functions of  $k'' [O_2]$ , referred as the oxygen inhibition effect.

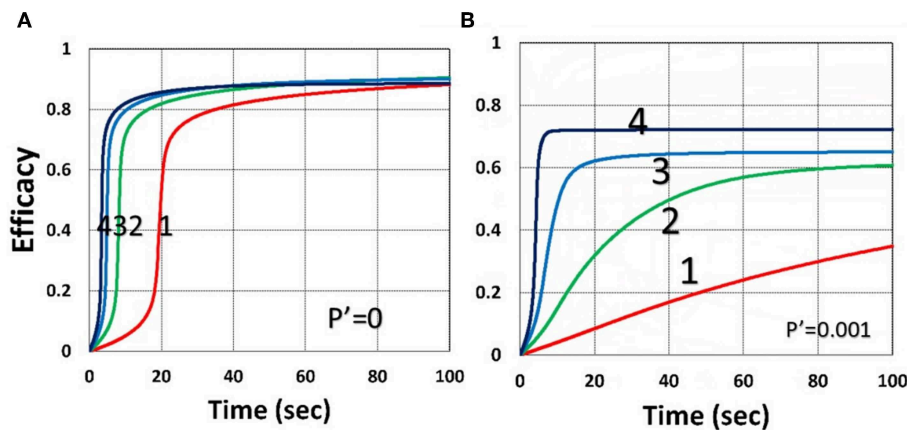


**FIGURE 9** | Dynamic profiles. Same as **Figure 4**, but for without ( $P' = 0$ ) and with ( $P' = 0.001$ ) external oxygen supply, shown by **(A,B)**, respectively; for  $b = 0.02$  and  $C_0 = 0.01$  mM.

Equations (15)–(17) may be numerically solved. However, it requires all the rate constants ( $k_j$ ) to be given for specific materials. Without knowing these parameters, we will further simplify Equations (15)–(17) as follows. In most situations, the monomer concentration ( $[A]$ ) is much larger than the oxygen, which is also depleted faster than PS (or  $C$ ), or  $k_8[A] \gg (k_3[O_2] + k_5)$ , such that  $g = 1/[A]$ ,  $k''[O_2]C/A^2 \ll 1$ , and  $bIC/A \ll k'R$ . These conditions were also reported by Dendukuri et al. (2008), Alvankarian and Majlis (2015), and Chen et al. (2017) in their modeling. Therefore, the depletion of  $C$  of Equation (15) is mainly due to type-I mechanism, whereas oxygen depletion is mainly due to the coupling term of  $k'R[O_2]$  in Equation (16). Equations (15)–(17) reduce to the following

$$\frac{\partial C}{\partial t} = -bI(z, t)C(z, t) \quad (21)$$

$$\frac{\partial [O]}{\partial t} = -k'R(z, t)[O_2] + P \quad (22)$$

$$\frac{\partial [A]}{\partial t} = -k'R(z, t)[A] \quad (23)$$

The above simplified kinetic equations reduce to that of Dendukuri et al. (2008) for the special situations (or assumptions): the PS concentration,  $C(z, t)$ , is a constant, or Equation (21)  $dC/dt = 0$  (or  $bIt \ll 1$ , for small dose), and light intensity is also a constant, or Equation (13),  $dI/dz = 0$ , which, however, is valid only for a short exposure time, or an optically thin polymer (with  $Az \ll 0.1$ ). Wu et al. (2018) included the light intensity reduction in their thick polymer system. However, they have ignored the PS depletion, or  $dC/dt = 0$ . Furthermore, the rate constants,  $k'$  and  $k''$ , in general, are reduction function of the monomer conversion efficacy due to the viscosity effects, which were also ignored by Dendukuri et al. (2008) and Alvankarian and Majlis (2015). They also used a simplified format of Equation (16) for the oxygen inhibition effect. Our Equations (15)–(17), to be numerically solved later, are more accurate than previous model (Dendukuri et al., 2008; Alvankarian and Majlis, 2015; Semchishen et al., 2015; Chen

et al., 2017; Wu et al., 2018), which used our simplified Equations (22) and (23), with  $I(z, t)$  and  $C(z, t)$  are constants.

Accurate solutions of Equations (21)–(23) require numerical simulations (to be shown later). For analytic formulas, we will use approximated analytic formulas for the light intensity and the PS concentration, such that we do not need to solve for Equation (13), and the expressive closed forms of  $I(z, t)$  and  $C(z, t)$  allow us to solve for the first- and second-order solutions of  $[O_2]$ ,  $[A]$ , and the conversion efficacy.

## Analytic Formulas for Efficacy

The monomer conversion efficacy for a bimolecular termination process is given by  $C_{\text{EFF}} = 1 - [A]/[A]_0 = 1 - \exp(-S)$ , with  $[A]_0$  being the initial monomer concentration, and the  $S$ -function is given by the time integral of  $k'R$ . Without the oxygen diffusion (with  $P' = 0$ ), the first-order solution of Equation (22), with  $R = (0.5B/k_T)^{0.5}$  is given by,  $[O]^{(1)} = Y_0 \exp(-S)$ ,  $Y_0$  is the initial oxygen, which gives the second-order solution of Equation (6),  $R(2) = B/k_T^{0.5} - k''[O_2](1 - B')/(4k_T)$ , with  $B = bIC$ ,  $B' = 0.5k''[O_2]/(Bk_T)^{0.5}$ , for  $B \ll 1$ .  $R'(2)$  may be used to find the second-order solution of oxygen concentration (for  $P' = 0$ ) given by

$$[O_2] = Y_0 \exp(-S') \quad (24)$$

$$S' = k' \int_0^t R'(2) dt \quad (25)$$

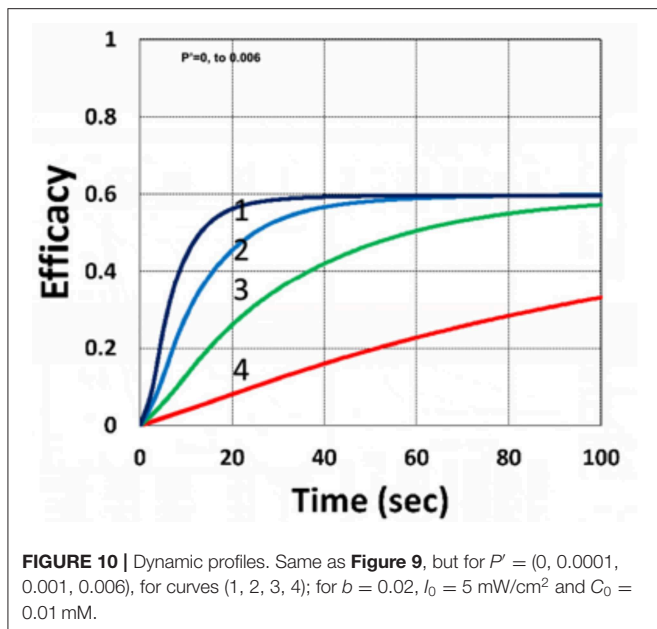
To include the oxygen diffusion effect, for small time when oxygen is present, the approximate solution of Equation (22) is given by (Dendukuri et al., 2008)

$$[O_2] = Y_0 - 4k'Bt/(\pi k) \quad (26)$$

The induction time ( $T_{ID}$ ) is defined by when  $[O_2] = 0$ . We obtain

$$T_{ID} = \pi k Y_0 / (4k'B) \quad (27)$$





During the induction time (with  $t < T_{ID}$ ), the solution of Equation (23) is given by

$$[A] = A_0 \exp(-S') \quad (28)$$

$$S' = k' \int_{T_{ID}}^t (B/G') dt' \quad (29)$$

where  $G' = D_0 Y_0 (1 - 4k' B t / (\pi k))$ .

For large time when oxygen is largely depleted, the radical concentration is given by  $R = (B/k_T)^{0.5} - K_{12}[O_2]$ , with  $K_{12} = k'(1 - B')/(4k_T)$ , with  $[O_2]$  given by Equation (24), which gives the solution of Equation (23),

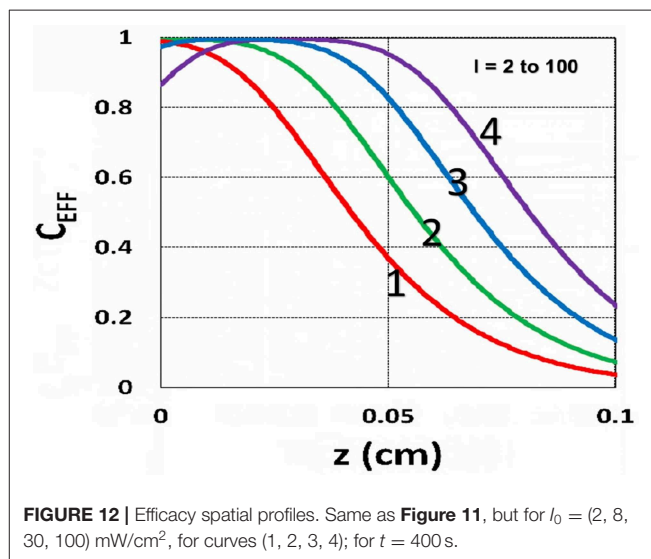
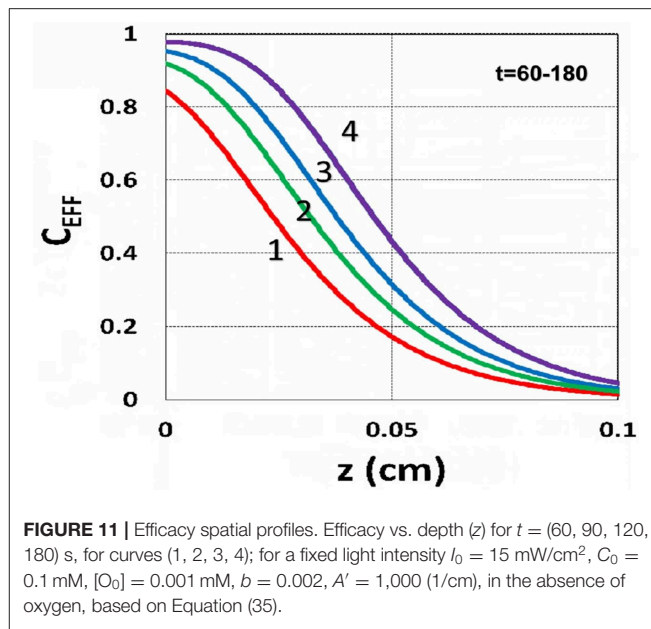
$$[A] = A_0 \exp(-S) \quad (30)$$

$$S = k' \int_0^t (\sqrt{0.5 B(z, t) / k_T} - K_{12}[O_2]) dt' \quad (31)$$

where  $[O_2]$  may be analytically given by Equations (24) or (26). Equation (30) was also presented by Alvankarian and Majlis (2015). However, they assumed a constant PS concentration, or  $B$  is time independent. When the diffusion and consumption of oxygen inside the photo resin, or  $d[O_2]/dt = 0$ , the closed form solution is available. For the case that oxygen diffusion is stopped, or  $d[O_2]/dz = 0$ , the closed form solution of Equation (22) and the conversion efficacy. We note that, during the induction time (with  $t < T_{ID}$ ),  $S'$  of Equation (29) is much smaller than  $S$  of Equation (31); therefore, the conversion efficacy is a fast-rising function of time after  $t > T_{ID}$ . We will show the numerical results later.

## The Dynamic Light Intensity

Solving Equations (13) and (14) for the light intensity,  $I(z, t)$  and PS concentration  $C(z, t)$  concentration, we may numerically find



$S'$  and then the conversion efficacy. We may further derive the analytic form of conversion efficacy which requires a closed form of  $I(z, t)$  and  $C(z, t)$  as follows. Using our previously developed approximated analytic formulas (Lin and Wang, 2016; Lin and Cheng, 2017)

$$I(z, t) = I_0 \exp[-A'z] \quad (32)$$

$$C'(z, t) = C_0 \exp[-B't] \quad (33)$$

$$A'(z, t) = 2.3(a'C_0 + Q) - A_1 t \quad (34)$$

where  $B' = bI_0 \exp(-A''z)$ ,  $A_1 = 2.3(a' - b')C_0 I_0 b z$ , with  $A''$  being the averaged absorption given by  $A'' = 0.5 \times 2.3(a' + b') + 2.3Q$ . We note that the  $-A_1 t$  term represents the decrease in  $A'$  or increase in light intensity due to PS depletion. Using Equations

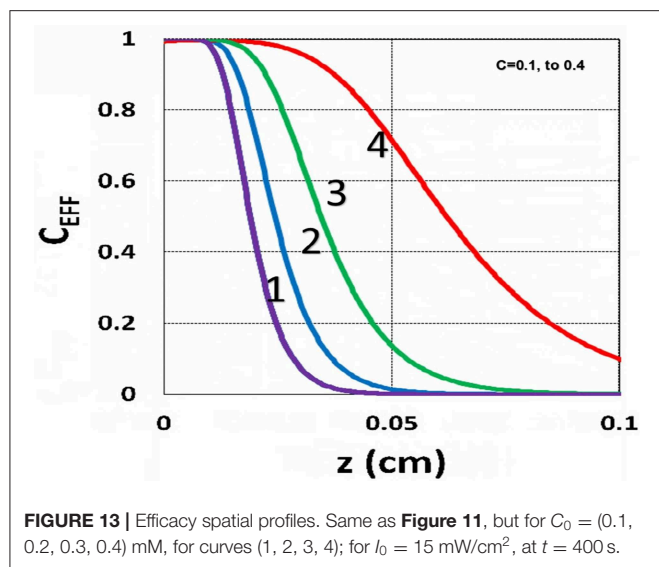


**FIGURE 13** | Efficacy spatial profiles. Same as **Figure 11**, but for  $C_0 = (0.1, 0.2, 0.3, 0.4)$  mM, for curves (1, 2, 3, 4); for  $I_0 = 15 \text{ mW/cm}^2$ , at  $t = 400 \text{ s}$ .

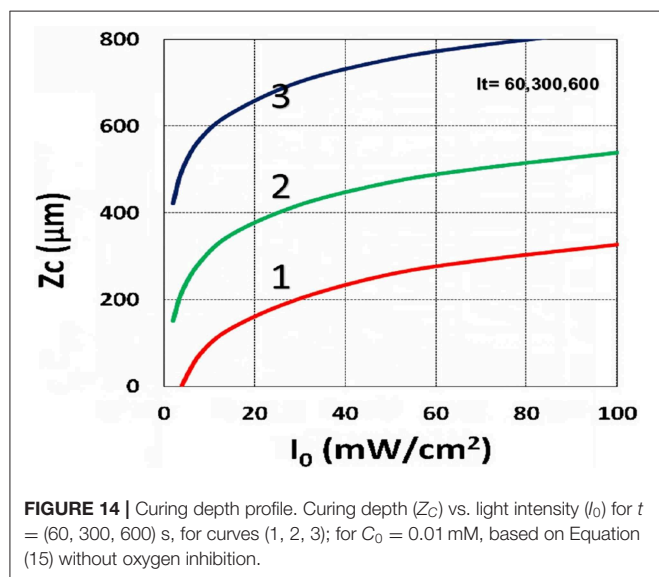


**FIGURE 14** | Curing depth profile. Curing depth ( $Z_c$ ) vs. light intensity ( $I_0$ ) for  $t = (60, 300, 600) \text{ s}$ , for curves (1, 2, 3); for  $C_0 = 0.01 \text{ mM}$ , based on Equation (15) without oxygen inhibition.

(32)–(34), we obtain analytic solution of Equation (30), when  $K_{12}[\text{O}_2]$  is ignored in Equation (31) for a type-I predominated mechanism, as follows.

$$S = KG(z, t) \sqrt{0.5bXI_0C_0} \quad (35)$$

$$G(z, t) = [1 - \exp[-B''t'']]/B'' \quad (36)$$

where  $K = k'/k_T^{0.5}$ ,  $t'' = t - T_{ID}$ ,  $B'' = 0.5(B' - 0.5A_1t)$ ,  $X = \exp[-A_2z]$ , with  $A_2 = 2.3(a'C_0 + Q)$ . We note that Equation (34) defines the dynamic feature of the light intensity which is an increasing function of time due to the depletion of the PS concentration. It also provides the non-linear dynamic dependence of  $A'(z, t)$ , given by  $A_1t$ , which is important for optical-thick polymer and for high light dose. Greater detail analysis will be given later. The above analytic formulas provide useful information to analyze and predict critical roles of each of

the influencing factors without numerically solving the coupled equations. Equation (35) will also be used to analyze the numerical results and the experimental data later.

## The Effects of Viscosity

To include the viscosity effects, the free-volume is reduced when cross-link efficacy increases. As proposed by Wu et al. (2018), the rate parameters  $k'$  and  $k_T$ , are decreasing function of the efficacy ( $C_{\text{EFF}}$ ) given by (in CGS units,  $\text{cm}^3/\text{mM/s}$ ):  $k' = 1,865/(1 + 2E' \times 10^{-9})$ ,  $k_T = 10^7/(2.3 + E') + k'(1 - C_{\text{EFF}})$ ; with  $E' = \exp(\nu C_{\text{EFF}})$ , where  $\nu$  is a constant ranging 25–40 defining the viscosity strength. High viscosity effect leads to a lower conversion efficacy. To include the viscosity effect, the effective rate constant,  $K = k'/k_T^{0.5}$ , of Equation (14) may be revised to a smaller value as:  $1 - m [1 - \exp(-S)]$ , with  $S$  is the first-order solution (with no revision), where  $m = 0.1$ – $0.3$  is a fit parameter to measured data. The revised  $K$  leads to a smaller efficacy due to the less free volume of cross-link resulted by the increase in viscosity when efficacy increases. Numerical results will be shown later.

## Curing Depth and Inhibition Zone

A curing depth ( $Z_C$ ) is defined by when the conversion efficacy is higher than a critical value,  $C_{\text{EFF}} > C_T$ , or when  $S > S_T$ , with  $S_T = \ln [1/(1 - C_T)]$ . Using Equation (35), and let  $S = S_T = 2$  (or  $C_T = 0.86$ ),  $Z_C$  is related to the cross-link time ( $T_C$ ) by, for the case that  $K_{12}[\text{O}_2]$  is ignored in Equation (31),

$$T_C = \left( \frac{1}{B''} \right) \ln [2B''/(K' \sqrt{0.5bXI_0C_0}) - 1] \quad (37)$$

where  $K' = k'/k_T^{0.5}$ ,  $X' = \exp(-A''Z_C)$  defines the curing depth ( $Z_C$ ). We plot the curve of  $T_C$  vs.  $Z_C$ , then rotate the axis to show curve of  $Z_C$  vs.  $T_C$ . The above curing depth ( $Z_C$ ) is proportional to the pillar height measured by Chen et al. (2017) where their measured data of **Figure 4** will be analyzed by Equation (37) later. For a given photo resin thickness of  $H$ , Chen et al. (2017) also defined an inhibition zone ( $Z_D$ ) given by  $Z_D = H - Z_C$ . When the oxygen inhibition effect, or  $k[\text{O}_2]$  is included in Equation (31), the analytic formula of Equation (37) is not available and  $Z_C$  needs a numerical solution to be shown later.

## RESULTS AND DISCUSSION

In the following numerical solutions of Equations (21)–(23), we will also use the radical  $R$  given by Equation (20) and light intensity given by Equation (32). The roles of key parameters of  $b$ ,  $k'$ ,  $I_0$ , and the initial PS and oxygen concentrations, polymer thickness, and the viscosity effect will be analyzed.

## Dynamic Concentration and Light Intensity

**Figure 3** shows the dynamic profiles of the PS concentration and light intensity obtained by the numerical solution of Equations (21)–(23), using light intensity given by Equation (32). Depending on the coupling parameter  $b$  and  $I(z, t)$ , as shown by Equation (32), the depletion of  $C(z, t)$  causes the increasing

profile of  $I(z,t)$ , defined by a ratio  $R_Z' = I(z,t)/I(z,t=0)$ , which is also a decreasing function of the depth ( $z$ ) per BLL. **Figure 3** shows the ratio  $R_Z$ , at  $z = 150\ \mu\text{m}$ , for  $b = 0.01\text{--}0.02$ ,  $a' = 458$  (1/mM),  $b' = Q = 0$ . **Figure 2** shows that higher intensity results a faster PS depletion and hence larger light intensity increase. For thick polymers ( $>100\ \mu\text{m}$ ). Therefore, the assumption of time-independent light intensity and PS concentration is valid only for optically thin (with  $A'z < 0.2$ ) polymers and under a small dose, i.e., under the condition that the time-dependent term  $A_1t$  of Equation (34) is neglected. For optically thick polymers under a larger dose, with  $bI_0tz > 0.2$ , the thin-polymer assumption (O'Brien and Bowman, 2006; Cramer et al., 2008; Dendukuri et al., 2008; Alvankarian and Majlis, 2015; Chen et al., 2017; Wu et al., 2018) will cause an error of 10–30%, depending on the value of  $A'$  in Equation (34). **Figure 3B** shows the dynamic feature of  $I(z,t)/I_0$  due to PS depletion for  $z > 0$ .

### Efficacy Temporal Profiles

We will now show the numerical results of the efficacy by solving Equations (21)–(23) using light intensity given by Equation (32). We will also show the dynamic profiles of oxygen. Roles of key parameters of  $b$ ,  $k''$ , and  $I_0$  and the initial PS and oxygen concentrations, polymer thickness, and the viscosity effect will be analyzed.

As shown by **Figure 4**, higher light intensity ( $I_0$ ) and coupling factor ( $b$ ) cause faster oxygen depletion (and shorter induction time) leading to higher conversion efficacy, as also predicted by Equations (24)–(35). **Figure 5** shows that higher PS initial concentration ( $C_0$ ) leads to higher efficacy, as predicted by our analytic Equation (35).

**Figure 6** shows that larger initial oxygen concentration causes higher inhibition effects and leads to lower efficacy, as predicted by Equation (31). It also shows longer induction time for lower light intensity and/or higher oxygen initial concentration. The induction time is defined by when oxygen is depleted.

**Figure 7** shows that larger viscosity factor ( $\nu$ ) causes smaller free volume and thus smaller radical coupling rate ( $k'$ ) and leads to a lower efficacy, as predicted by the effective rate constant,

$K = k'/k_T^{0.5}$ , in Equation (35). **Figure 8** shows that, inside the polymer (with  $z = 150\ \mu\text{m}$ ), both light intensity and PS concentration are reduced; thus, conversion is less, although oxygen is depleted slower inside the polymer, as predicted by the  $z$ -dependent  $X = \exp[-A_2z]$  in Equation (31).

**Figure 9** shows that external oxygen supply cause increased radical inhibition and thus smaller conversion, as predicted by Equation (34). **Figure 10** shows the efficacy profiles for various external oxygen supply ( $P' > 0$ ) that larger  $P'$  causes higher oxygen inhibition effect and leads to smaller efficacy, as predicted by Equation (31).

### Efficacy Spatial Profiles

The efficacy spatial profiles will be shown based on the analytic formula of Equation (35), with ignored oxygen effects, in Equation (31). **Figure 11** shows that efficacy is a decreasing

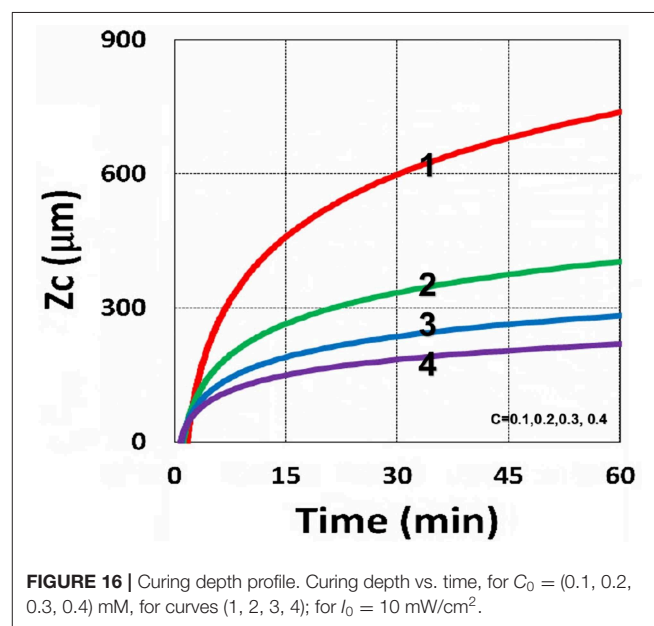


**FIGURE 16 |** Curing depth profile. Curing depth vs. time, for  $C_0 = (0.1, 0.2, 0.3, 0.4)$  mM, for curves (1, 2, 3, 4); for  $I_0 = 10\ \text{mW/cm}^2$ .

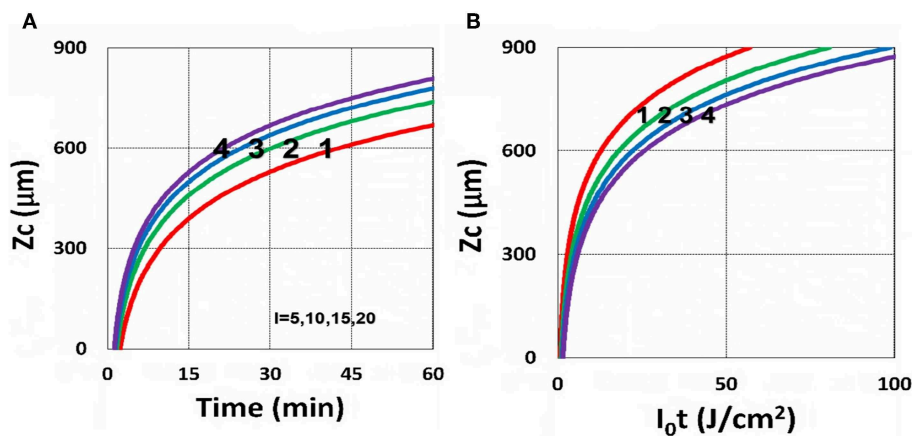


**FIGURE 15 |** Curing depth profile. Curing depth for  $I_0 = (5, 10, 15, 20)$  mW/cm<sup>2</sup>, for curves (1, 2, 3, 4); for (A)  $Z_c$  vs. time and (B)  $Z_c$  vs. light dose.

function of  $z$ , but it is an increasing function of light exposure time, as predicted by Equation (35). **Figure 12** shows that efficacy is an increasing function of light intensity. The efficacy is also an increasing function of PS concentration ( $C_0$ ), as shown by **Figure 13**. When the oxygen inhibition effect is included, as shown by Equation (31), the above analytic formulas produced efficacy will be reduced. However, only numerical data are available. The modeling curves of Alvankarian and Majlis (2015) shown by their Figures 3F,G are not accurate because their Equation (5) for the conversion have over simplified the oxygen inhibition effect, shown by our Equation (17) by a reduction factor of  $(1 - [O_2]) C_{EFF}$ , and also assumed a constant PS concentration throughout the resin thickness. Therefore, their

efficacy curves in their Figure 7G are overestimated, compared to our **Figure 10**, which includes the PS depletion.

## Curing Depth Profile

In microfabrication system, formation of radical ( $R'$ ) decreases over depth ( $z$ ) due to the reduction in light intensity and PS concentration and increase in oxygen inhibition. When oxygen diffuses into the film and consumes radicals, the balance of radical production and oxygen inhibition gives rise to the inhibition zone, where the polymerization is completely suppressed, as presented by kinetic Equation (37).

Using the analytic formula, Equation (37), we are able to investigate the roles of PS and oxygen concentration, light intensity, and exposure time in curing depth. **Figure 13** shows that curing depth ( $Z_C$ ) is an increasing function of light intensity and exposure time. **Figure 15** shows curing depth profiles vs. time and light dose, in which the intensity dependence is reversed in **Figures 15A,B**. This unexpected feature also shown in the efficacy profile, shown by Equation (35), that smaller light intensity achieves higher steady-state efficacy (for a fixed light dose). **Figure 16** shows that curing depth is an increasing function of the PS concentration ( $C_0$ ), as also predicted by Equation (35) that efficacy has a scaling law of  $C_0^{0.5}$ , and so does  $Z_C$ . The effect of time-dependent absorption factor  $A'$  shown in Equation (35) on the curing depth is shown in **Figure 17** that assumption of a constant PS concentration, or  $A_1 t = 0$  in Equation (34), will underestimate the cross-link depth 1–12%, especially for high dose and optically thick polymer. **Figure 17** shows the viscosity effect on the efficacy. The effective rate constant ( $K$ ) of Equation (35) is revised to a smaller value as:  $1 - m [1 - \exp(-S)]$ , with  $S$  is the first-order solution (with no revision), where  $m = 0.1$ – $0.3$  is a fit parameter to measured data. The revised  $K$  leads to a smaller efficacy due to the less free volume of cross-link resulted by the increase of viscosity when efficacy increases.

It is important to note that the  $S$ -function is scaled by  $[C_0 I_0 t^2]^{0.5}$  for transient state (with  $B't \ll 1$ ), and scaled by  $[C_0 / I_0]^{0.5}$  for steady state. Therefore, the dose-dependence Bunsen Roscoe law, scaled by a light dose  $E_0 = I_0 t$ , failed in a bimolecular termination system, with radical ( $R'$ ) scaled by  $[C_0 I_0 \exp(-B't)]^{0.5}$ , as shown by Equation (35). These features also apply to the curing depth shown by **Figure 13** that it is a non-linear function of time ( $t$ ) and light intensity. The simple dose-dependence law does not apply to  $Z_C$ . **Figure 13** also shows that for a given light dose, higher light intensity achieves a lower depth, for large exposure time, with  $B't \gg 1$ . This leads to a strategy to use a higher light intensity for faster curing but an extended exposure time ( $\sim 30\%$ ) than what is predicted by BBL is required to achieve the same curing depth as that of lower intensity. This strategy has been clinically demonstrated in corneal cross-link (Lin and Wang, 2016), but not yet in curing of other biomaterials.

The analytic formula of Equation (37) is available only when the oxygen effect is neglected, or  $K_{12}[O_2] = 0$  in Equation (31). The oxygen inhibition effect on  $Z_C$  is further investigated by the numerical solutions of Equation (37), including  $K_{12}[O_2]$ , where  $Z_C$  is graphically found by the crossing points of  $C_{EFF} = C_T$  (a

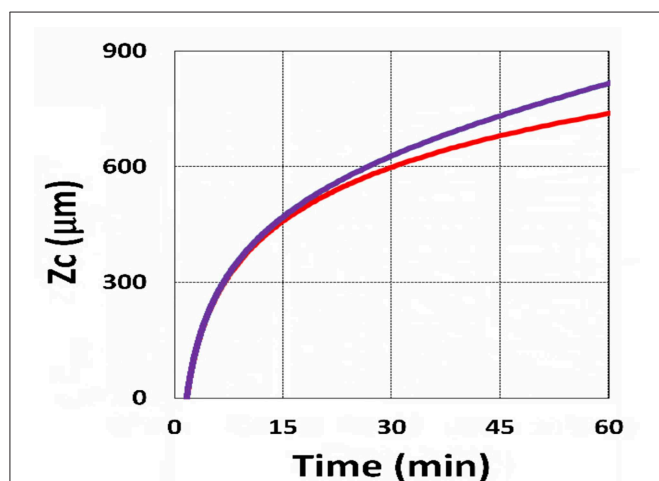


**FIGURE 17** | Curing depth profile. Curing depth vs. time, with (blue) and without (red) the correction of time-dependent absorption factor  $A'$  shown in Equations (13) and (14) for  $C_0 = 0.1$  mM,  $I_0 = 10$  mW/cm<sup>2</sup>.

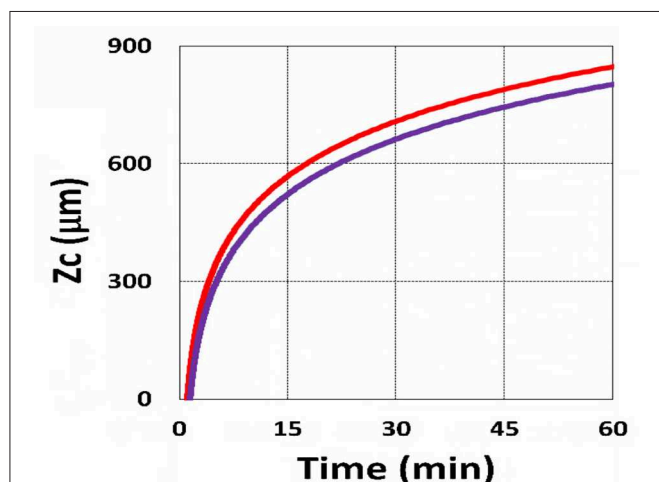


**FIGURE 18** | Curing depth profile. Curing depth vs. time, with (blue) and without (red) the correction of viscosity effect.



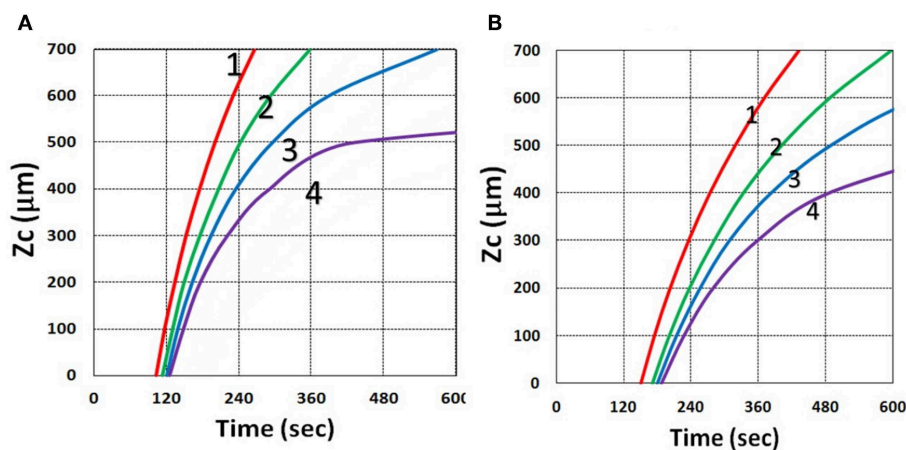


**FIGURE 19 |** Curing depth profile. Curing depth vs. time, for various oxygen external supply rates,  $P' = (0, 3.0, 5.0, 7.0) \times 10^{-6}$  (mM/s), for curves (1, 2, 3, 4); for oxygen initial concentration **(A)**  $[O_0] = 0.001$  mM and **(B)**  $[O_0] = 0.002$  mM, for  $b = 0.0001$ ,  $C_0 = 0.02$  mM and  $I_0 = 10$  mW/cm<sup>2</sup>.

threshold value, 0.8) and the curves of  $C_{\text{EFF}}$  vs. time for various  $z$ . **Figure 19** shows that  $Z_C$  is a decreasing function of external oxygen supply rate ( $P'$ ) and the initial oxygen concentration,  $[O_0]$ , where larger  $[O_0]$  or  $P'$  lead to smaller efficacy, thus smaller  $Z_C$  due to larger oxygen inhibition effect, as also predicted by Equation (31).

## Analysis of Measured Data

Utilization of microfabrication to reduce the deposition steps and to obtain a monolithic product was reported by Alvankarian and Majlis (2015) and Chen et al. (2017), and Wu et al. (2018) in which structures of arrays of pillars in photo-cross-linkable films were measured by irradiation with a periodic array of microscale optical beams under ambient conditions. The optical beams experience a self-focusing non-linearity owing to the photopolymerization-induced changes in refractive index, thereby concentrating light and driving the concurrent, parallel growth of microscale pillars along their path length (Wu et al., 2018). In microfabrication system, formation of radical decreases over depth due to the reduction in light intensity and PS concentration and increase in oxygen inhibition. Under ambient conditions, oxygen diffuses into the film and consumes radicals. The balance of radical production and oxygen inhibition gives rise to the inhibition zone, where the polymerization is completely suppressed.

The curing depth ( $Z_C$ ) given by the solution of Equation (37) is proportional to the pillar height defined by Chen et al. (2017) where their measured data of their Figure 4 are analyzed as follows. Our **Figure 13** shows  $Z_C$  vs. time based on Equation (37) that  $Z_C$  is proportional to  $\ln(t^2 I_0)$ , for small  $t$ , and reaches its steady-state time ( $T_S$ ) (when  $Z_C = 0.9$  h), which is scaled by  $I_0^{-0.5}$ . For example, our calculated  $T_S = (1,050, 735, 609)$  s, for  $I_0 = (5, 10, 15)$  mW/cm<sup>2</sup>, which shows the similar trend of the measured data of Chen et al. (2017)  $T_S = (1,050, 600, 480)$  s. Furthermore, their measured pillar heights ranging 300–600 μm (at  $t = 600$  s), for  $I_0 = 5$ –15 mW/cm<sup>2</sup> are consistent with our

**Figure 13.** Figure 7 of Chen et al. (2017) also showed the similar trend as our scaling law of  $Z_C$  vs. light intensity given by Equation (35) that  $Z_C$  is scaled by  $(1/A')\ln(I_0)$ .

Curing depth control is one of the key factors for microfabrication, in which the influencing factors of curing depth include light intensity and exposure time (or dose), the initial concentration of PS and oxygen, and the external supply of oxygen, as shown by **Figures 13–19**. For a given photo resin thickness of  $H$ , Chen et al. (2017) also defined an inhibition zone ( $Z_N$ ) given by  $Z_N = H - Z_C$ . Therefore, a better understanding and manipulation of  $Z_C$  (and  $Z_N$ ) will enable a strong bias differential in the growth between bright (irradiated) and dark regions. The balance of radical production and oxygen inhibition gives rise to the inhibition zone. Figure 8 of Chen et al. (2017) showed a similar trend as our scaling law, in which the log-log plots of inhibition zone vs. light intensity show a linear relationship having slopes depended by various mask spacing ratios.

The above described experimental works have validated certain features of our modeling and the analytic formulas. However, further studies are required to validation other features presented by our modeling, such as (i) the role of PS concentration ( $C_0$ ) in thick polymers ( $>1.0$  mm), which was assumed as a constant for optically thin polymers ( $<0.2$  mm); (ii) the curing depth at various  $C_0$ , as shown by our **Figure 16**; (iii) dynamic measurement of the light intensity in a strongly depleted PS system, which was assumed as time independent and follows the conventional BLL; however our theory presented a non-BLL; (iv) as shown by **Figure 18**, the viscosity effect on the reduction in curing depth; and (v) the role of oxygen external supply rate on the reduction of curing depth, as shown by **Figure 19**.

## Strategy for Improved Efficacy and Depth

As discussed earlier, a higher light intensity will accelerate the curing speed but suffers a smaller curing depth and efficacy (at steady state). This also indicates that there is

a limitation of maximum light intensity and the associate minimum exposure time. Higher PS initial concentration will improve the efficacy, but there is an optimal value (Lin et al., 2019). There are many conventional strategies to reduce oxygen inhibition in photoinduced polymerization: working in an inert or closed environment, increasing the photoinitiator concentration, increasing the light dose or light intensity (for reduced induction time), use of multiple photoinitiators with different rate of initiation, or addition of oxygen scavengers. Chemical mechanisms incorporate additives or suitably functionalized monomers which are insensitive to oxygen, such as the thiol-ene and thiol-acrylate-Michael additive systems (Claudino et al., 2016; Chen et al., 2019a,b). Additive enhancer monomer was proposed to improve the curing (cross-link) efficacy by either reducing the oxygen inhibition effect by stable monomer or increase the lifetime of radicals in clinical applications (Chen et al., 2019b; Wertheimer et al., 2019). The multimonomer system may be applied to industrial materials as an alternative to manipulate the microfabrication. Dual-wavelength (red and UV) photopolymerization was also reported, in which preirradiation of the red light eliminated the oxygen inhibition effect and thus enhanced the conversion efficacy of the UV light (Childress et al., 2019).

## CONCLUSION

Photopolymerization efficacy ( $C_{\text{EFF}}$ ) is an increasing function of PS concentration ( $C_0$ ) and the light dose at transient state, but it is a decreasing function of the light intensity, scaled by  $[C_0/I_0]^{0.5}$  at steady state. The curing depth is an increasing function of  $C_0$

and light dose (time  $\times$  intensity), but it is a decreasing function of the oxygen concentration, viscosity effect, and oxygen external supply rate. For optically thick polymers, light intensity is an increasing function of time due to PS concentration depletion, which cannot be neglected. Saturation of efficacy profile is governed by the PS depletion rate and light dose. Efficacy is also an increasing function of the effective rate constant,  $K = k'/k_t^{0.5}$ , defined by the radical producing rate ( $k'$ ) and the bimolecular termination rate. The curing depth is a decreasing function of the oxygen inhibition effect.

## DATA AVAILABILITY STATEMENT

The datasets generated for this study are available on request to the corresponding author.

## AUTHOR CONTRIBUTIONS

J-TL: concept. D-CC and K-TC: software and data. J-TL and H-WL: supervision. D-CC: financial. J-TL, H-WL, and D-CC: writing and editing. All authors listed have made a substantial, direct and intellectual contribution to the work, and approved it for publication.

## ACKNOWLEDGMENTS

D-CC thanks the financial support from the Ministry of Science and Technology (MOST), under grant number MOST108-2221-E-039-003 and China Medical University under grant number CMU 108-MF-98.

## REFERENCES

- Alvankarian, J., and Majlis, B. Y. (2015). Exploiting the oxygen inhibitory effect on UV curing in microfabrication: a modified lithography technique. *PLoS ONE* 10:e0119658. doi: 10.1371/journal.pone.0119658
- Cabral, J. T., Hudson, S. D., Harrison, C., and Douglas, J. F. (2004). Frontal photopolymerization for microfluidic applications. *Langmuir* 20, 10020–10029. doi: 10.1021/la049501e
- Chen, F. H., Pathreker, S. B., and Hosein, I. D. (2017). Synthesis of micropillar arrays via photopolymerization: an *in situ* study of light-induced formation, growth kinetics, and the influence of oxygen inhibition. *Macromolecules* 50, 5767–5778. doi: 10.1021/acs.macromol.7b01274
- Chen, F. M., and Shi, S. (2014). *Principles of Tissue Engineering, 4th Edn.* New York, NY: Elsevier. doi: 10.1016/B978-0-12-398358-9.00072-0
- Chen, K. T., Cheng, D. C., Lin, J. T., and Liu, H. W. (2019a). Thiol-ene photopolymerization in thick polymers: kinetics and analytic formulas for the efficacy and crosslink depth. *Polymers* 11:1640. doi: 10.3390/polym11101640
- Chen, K. T., Lin, J. T., and Liu, H. W. (2019b). Enhancing radical-mediated photopolymerization efficacy and crosslink depth: kinetic and model of a two-monomer system. *Res. Med. Eng. Sci.* 8, 853–860. doi: 10.31031/RMES.2019.08.000682
- Childress, K. K., Kim, K., Glugla, D. J., Musgrave, C. B., and Bowman, C. N. (2019). Independent control of singlet oxygen and radical generation via Irradiation of a two-color photosensitive molecule. *Macromolecules* 52, 4968–4978. doi: 10.1021/acs.macromol.9b00424
- Claudino, M., Zhang, X., Alim, M. D., Podgórski, M., and Bowman, C. N. (2016). Mechanistic kinetic modeling of Thiol-Michael addition photopolymerizations via photocaged “superbase” generators: an analytical approach. *Macromolecules* 49, 8061–8074. doi: 10.1021/acs.macromol.6b01605
- Cramer, N. B., O'Brien, C. P., and Bowman, C. N. (2008). Mechanisms, polymerization rate scaling, and oxygen inhibition with an ultra-rapid monovinyl urethane acrylate. *Polymer* 49, 4756–4761. doi: 10.1016/j.polymer.2008.08.051
- Dendukuri, D., Panda, P., Haghgoie, R., Kim, J. M., Hatton, T. A., and Doyle, P. S. (2008). Modeling of oxygen-inhibited free radical photopolymerization in a PDMS microfluidic device. *Macromolecules* 41, 8547–8556. doi: 10.1021/ma801219w
- Fouassier, J. P. (1995). *Photoinitiation, Photo-Polymerization, and Photocuring: Fundamentals and Applications*; Hanser Gardner Publications. Munich.
- Kotisch, V., Michaudel, Q., and Fors, B. P. (2017). Photocontrolled interconversion of cationic and radical polymerizations. *J. Am. Chem. Soc.* 139:10665. doi: 10.1021/jacs.7b06661
- Lin, J. T. (2018). Efficacy S-formula and kinetics of oxygen-mediated (type-II) and non-oxygen-mediated (type-I) corneal cross-linking. *Ophthalmol. Res.* 8, 1–11. doi: 10.9734/OR/2018/39089
- Lin, J. T. (2019). Kinetics of enhancer-monomer for corneal cross-linking: two-initiator system. *Ophthalmol. Res.* 10, 1–6. doi: 10.9734/or/2019/v10i3 30109
- Lin, J. T., and Cheng, D. C. (2017). Modeling the efficacy profiles of UV-light activated corneal collagen crosslinking. *PLoS ONE* 12:e0175002. doi: 10.1371/journal.pone.0175002
- Lin, J. T., Liu, H. W., Chen, K. T., and Cheng, D. C. (2019). Modeling the optimal conditions for improved efficacy and crosslink depth of photo-initiated polymerization. *Polymers* 11:217. doi: 10.3390/polym110 20217

- Lin, J. T., and Wang, K. C. (2016). Analytic formulas and numerical simulations for the dynamics of thick and non-uniform polymerization by a UV light. *J. Polym. Res.* 23:53. doi: 10.1007/s10965-016-0934-4
- O'Brien, A. K., and Bowman, C. N. (2006). Modeling the effect of oxygen on photopolymerization kinetics. *Macromol. Theory Simul.* 15,176–182. doi: 10.1021/ma051863l
- Odian, G. (2006). *Principles of Polymerization, 4th Edn.* New York, NY: John Wiley & Sons, Inc.
- Semchishen, A., Mrochen, A., and Semchishen, V. (2015). Model for optimization of the UV-A/Riboflavin strengthening (cross-linking) of the cornea: percolation threshold. *Photochem. Photobiol.* 91, 1403–1411. doi: 10.1111/php.12498
- Wertheimer, C. M., Elhardt, C., Kaminsky, S. M., Pham, L., Pei, Q., Menders, B., et al. (2019). Enhancing rose Bengal photosensitized protein crosslinking in the cornea. *Invest. Ophthalmol. Vis. Sci.* 60, 1845–1852. doi: 10.1167/iops.19-26604
- Wohlers, T., and Caffrey, T. (2016). *3D Printing and Additive Manufacturing State of the Industry*. Annual Worldwide Progress Report, Wohlers Report, Wohlers Associates, Inc.
- Wu, J., Zhao, Z., Hamel, C. M., Mu, X., Kuang, X., Guo, Z., et al. (2018). Evolution of material properties during free radical photopolymerization. *J. Mech. Phys. Solid* 112, 25–49. doi: 10.1016/j.jmps.2017.11.018
- Yang, L., Tang, H., and Sun, H. (2018). Progress in photo-responsive polypeptide derived nano-assemblies. *Micromachines* 9, 296–313. doi: 10.3390/mi9060296

**Conflict of Interest:** J-TL was CEO of New Vision Inc.

The remaining authors declare that the research was conducted in the absence of any commercial or financial relationships that could be construed as a potential conflict of interest.

Copyright © 2019 Lin, Liu, Chen and Cheng. This is an open-access article distributed under the terms of the Creative Commons Attribution License (CC BY). The use, distribution or reproduction in other forums is permitted, provided the original author(s) and the copyright owner(s) are credited and that the original publication in this journal is cited, in accordance with accepted academic practice. No use, distribution or reproduction is permitted which does not comply with these terms.



# Preparation of Covalent-Ionically Cross-Linked UiO-66-NH<sub>2</sub>/Sulfonated Aromatic Composite Proton Exchange Membranes With Excellent Performance

Penglun Zheng<sup>1</sup>, Quanyi Liu<sup>1\*</sup>, Donghui Wang<sup>1</sup>, Zekun Li<sup>1</sup>, Yawei Meng<sup>1</sup> and Yun Zheng<sup>2\*</sup>

<sup>1</sup> College of Civil Aviation Safety Engineering, Civil Aviation Flight University of China, Guanghan, China, <sup>2</sup> Key Laboratory of Optoelectronic Chemical Materials and Devices, Ministry of Education, Jiangnan University, Wuhan, China

## OPEN ACCESS

### Edited by:

Giuseppe Mensitieri,  
University of Naples Federico II, Italy

### Reviewed by:

Ali Sekizkardes,  
National Energy Technology  
Laboratory (DOE), United States  
YuanQiao Rao,  
Dow Chemical Company,  
United States

### \*Correspondence:

Quanyi Liu  
quanyiliu2005@126.com  
Yun Zheng  
yunzheng\_0824@163.com

### Specialty section:

This article was submitted to  
Polymer Chemistry,  
a section of the journal  
Frontiers in Chemistry

Received: 12 September 2019

Accepted: 17 January 2020

Published: 18 February 2020

### Citation:

Zheng P, Liu Q, Wang D, Li Z, Meng Y  
and Zheng Y (2020) Preparation of  
Covalent-Ionically Cross-Linked  
UiO-66-NH<sub>2</sub>/Sulfonated Aromatic  
Composite Proton Exchange  
Membranes With Excellent  
Performance. *Front. Chem.* 8:56.  
doi: 10.3389/fchem.2020.00056

Metal-organic frameworks (MOFs), as newly emerging filler materials for polyelectrolytes, show many compelling intrinsic features, such as variable structural designability and modifiability of proton conductivity. In this manuscript, UiO-66-NH<sub>2</sub>, a stable MOF with -NH<sub>2</sub> functional groups in its ligands, was selected to achieve a high-performance sulfonated poly(arylene ether nitrile)s (SPENs)/UiO-66-NH<sub>2</sub>-x covalent-ionically cross-linked composite membrane. Simultaneously, the obtained composite membranes displayed excellent thermal stability and dimensional stability. The as-prepared SPEN/UiO-66-NH<sub>2</sub>-x cross-linked membranes exhibited higher proton conductivity than recast SPENs, which can be attributed to the construction of ionic clusters and well-connected ionic nanochannels along the interface between UiO-66-NH<sub>2</sub>-x and SPEN matrix via molecular interactions. Meanwhile, the methanol permeability of the SPEN/UiO-66-NH<sub>2</sub>-x composite membrane had been effectively reduced due to the barrier effect of cross-linking and the addition of UiO-66-NH<sub>2</sub>-x. The SPEN/UiO-66-NH<sub>2</sub>-5 composite membrane had the highest selectivity of  $6.42 \times 10^5$  S·s·cm<sup>-3</sup>: 14.3-times higher than that of Nafion 117. The preparation of cross-linked UiO-66-NH<sub>2</sub>/SPEN composite was facile, which provides a new strategy for preparing high performance proton exchange membrane.

**Keywords:** metal-organic frameworks, sulfonated poly(arylene ether nitrile)s, proton conductivity, selectivity, methanol permeability

## INTRODUCTION

Direct methanol fuel cell (DMFC) is one of the most eco-friendly power sources because of its relatively high efficiency, clean and low carbon technology, and renewable methanol compared with traditional fossil fuels (Antolini, 2018; Eris et al., 2018; Li et al., 2018a,b; Yilmaz and Can, 2018). Proton exchange membranes (PEMs) have attracted substantial attention as the core components of DMFC for ion conduction. Perfluorosulfonic acid (PFSA) polymer membranes are the most widely commercialized proton exchange membrane, due to their high proton conductivity ( $10^{-2}$ – $10^{-1}$  S·cm<sup>-1</sup>) and excellent chemical stability (Chang et al., 2013; Kuo et al., 2018; Yan et al., 2018; Ling et al., 2019). Among all kinds of proton exchange membranes, Nafion membranes, typically made



by DuPont™, has been extensively used owing to their high proton conductivity and good chemical stability. However, Nafion has its disadvantages, such as high cost, low thermal stability, low proton conductivity under high temperature (>80°C), and hazardous manufacturing processes, which restrict its commercial application (Wang et al., 2015a; Zakil et al., 2016; Ressam et al., 2018). In this regard, numerous efforts have been paid to solve these problems. Alternatives or modifications and inorganic–organic composite membranes have been prepared to replace Nafion for exploring new types of PEMs. With this development trend, large quantities of sulfonated aromatic polymers have been explored as alternative PEMs to Nafion, such as sulfonated poly(arylene ether nitrile)s (Zheng et al., 2017a,b, 2018; Feng et al., 2018), sulfonated polyimides (Perrot et al., 2011; Yin et al., 2011; Yao et al., 2015; Zhang et al., 2017), sulfonated poly(benzimidazole)s (Li et al., 2009; Yue et al., 2015, 2016; Singha et al., 2016), sulfonated poly(arylene ether ketone)s (Pang et al., 2015; Xu et al., 2015; Nguyen et al., 2016; Oh et al., 2016), and sulfonated poly(arylene ether sulfone)s (Ko et al., 2015; Kim et al., 2017a,b; Ahn et al., 2018).

Among all the mentioned sulfonated polymers, SPENs possess great potential as excellent PEMs because of the following striking features (Zheng et al., 2015; Wan et al., 2017; Zhan et al., 2018, 2019): (1) The strong polar nitrile group can promote the adhesion of SPEN to many substrates through strong polar nitrile group interactions with other polar chemical groups; (2) the strong dipole interaction between the copolymer chains leads to good water retention and dimensional stability of SPEN; (3) the excellent chemical and thermal stability and high mechanical strength; and (4) lower cost and the variable structural designability of SPENs. However, for such sulfonated polyaromatic ethers, their dimensional stability, methanol crossover resistance, tensile strength, and thermal stability tend to decrease as the sulfonation degree reaches a high level. The shortcoming of the SPENs might restrict its commercial applications. Cross-linking is recognized as the most efficient method to overcome the aforementioned shortcomings of the SPENs (Zheng et al., 2017c). Unfortunately, cross-linked membranes normally exhibit low proton conductivity due to two factors: (1) Sulfonic acid groups participating in the cross-linked reactions results in the elimination of sulfonic acid groups; (2) the sulfonic acid groups may be diluted by introducing cross-linker. Therefore, besides the cross-linking of the membranes, it is necessary to add proper functional particles to improve the conductivity that can enhance the comprehensive properties of proton exchange membranes.

Metal organic frameworks (MOFs), as newly emerging materials, have attracted great attention in many fields due to their compelling intrinsic structural features, such as large porosity, high crystallinity, tremendous structural flexibility, and pore size tenability as well as tailorable functionality (Wu et al., 2015; Zhang et al., 2015; Zhao et al., 2016; Kahn et al., 2017). In recent years, more and more attention has been paid to the study of proton conduction in MOFs (Gil-Hernández et al., 2015; Liu et al., 2016; Xu et al., 2016; Joarder et al., 2017; Yang et al., 2017). The high crystallinity of MOFs can bring specified proton conduction pathway, such that protons can

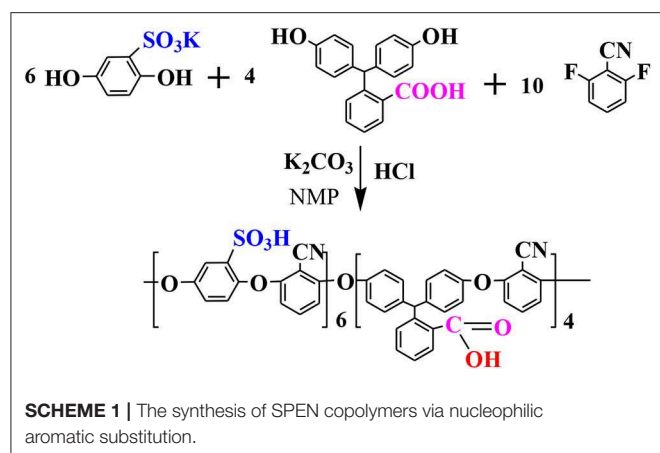
be transferred through hydrogen bond networks or functional sites loaded in holes. Among them, Zr-MOFs have attracted considerable interests, owing to their high robustness and easy tunable structure. Despite that diverse Zr-MOFs with different structures and porosities have been reported recently (Jiang et al., 2013; Furukawa et al., 2014; Wang et al., 2015b), only the benchmark compound, Zr-terephthalate MOF UiO-66, displays the best performances and the lowest cost of synthesis and scale-up (Cavka et al., 2008; Taddei et al., 2015; DeStefano et al., 2017). Specifically, the metal-ligand bond strength of UiO-66-NH<sub>2</sub> is stronger than those of MIL-53-NH<sub>2</sub> and MIL-101-NH<sub>2</sub> (two other kinds of MOFs with high stability). Thus, to some extent, UiO-66-NH<sub>2</sub> is relatively more stable compared to MIL-53-NH<sub>2</sub> and MIL-101-NH<sub>2</sub> (Bai et al., 2016). However, their proton conduction channels are not consecutive enough and the fabrication of MOFs into the form of membranes is still immature, which restricts their proton conductivity and limits their practical application. The fabrication of MOFs into sulfonated polymer matrix is a significant step for their practical application (Patel et al., 2016; Dong et al., 2017). Sulfonated polymers are not only easy-to-prepare membranes, but also act as a good medium to form continuous and effective channels for proton conduction.

In this manuscript, an amino-functionalized UiO-66 (UiO-66-NH<sub>2</sub>), a well-known Zr-based MOF, was synthesized and *in situ* incorporated with SPENs to form UiO-66-NH<sub>2</sub>/SPENs covalent-ionically cross-linked composite membranes in combination with the high proton conductivity and surface amino reaction activity of UiO-66-NH<sub>2</sub>. The preparation of the cross-linked UiO-66-NH<sub>2</sub>/SPENs composite was facile, which provides a new strategy for preparing high-performance proton exchange membrane. The results showed that the methanol permeability, water uptake, and swelling ratio of the cross-linked UiO-66-NH<sub>2</sub>/SPENs composite membranes decreased with the introduction of functional nanoparticles, which indicates that the covalent-ionically cross-linking between -NH<sub>2</sub> and carboxyl/sulfonic acid can effectively improve the methanol resistance and dimensional stability of the composite membranes. At the same time, because the -NH<sub>2</sub> in UiO-66-NH<sub>2</sub> is a very good proton acceptor/donor, it provides a new way for proton transfer in SPENs membranes, thus significantly improving the proton conductivity of composite membranes. All the results showed that the cross-linked UiO-66-NH<sub>2</sub>/SPENs composite membranes prepared by covalent-ionically cross-linking have excellent comprehensive properties.

## EXPERIMENT

### Materials

Hydroquinone sulfonic acid potassium salt (SHQ), hydrochloric acid, zinc powder, 2, 6-difluorobenzonitrile (DFBN) and phenolphthalin (PPL), sodium hydroxide (NaOH, AR), N,N-dimethylacetamide (DMAc, AR), sodium chloride (NaCl, AR), zirconium tetrachloride (ZrCl<sub>4</sub>, AR) 2-aminotropic acid (BDC-NH<sub>2</sub>, AR), acetone (AR), NMP (AR), and K<sub>2</sub>CO<sub>3</sub> (AR) were



supplied by KeLong. All the materials were used without further purification.

## SPEN Synthesis

In a typical reaction (**Scheme 1**), 0.06 mol of SHQ, 0.10 mol of DFBN, 0.2 mol of K<sub>2</sub>CO<sub>3</sub>, 0.04 mol of PPL, 25 mL toluene, and 75 mL NMP were poured into a three-necked flask equipped with a condenser and a mechanical stirrer. The reactants were first heated to 150°C and maintained for 2 h at this temperature. Secondly, it was gradually heated up to 185°C and maintained at this temperature until the copolymers achieve a high viscosity. Finally, the copolymers were precipitated by pouring the mixture into alcohol. The copolymers were thoroughly washed several times for purification, and the collected copolymers were treated at 120°C in vacuum overnight.

## Preparation of UiO-66-NH<sub>2</sub>

Rapid and large-scale synthesis of UiO-66-NH<sub>2</sub>: First, 1L DMF was added into the three-necked bottle equipped with an oil bath, overhead mechanical stirrer, and condenser. The oil bath was raised to 120°C and maintained at this temperature. Then, 15.0 g (64.4 mmol) ZrCl<sub>4</sub>, 11.7 g (64.4 mmol) 2-amino terephthalic acid (BDC-NH<sub>2</sub>), and 440 mL (7.73 mol) acetic acid were added sequentially and stirred to dissolve evenly. The mixture was stirred and maintained at 120°C for 15 min, then naturally cooled to room temperature. The mixture was immersed in DMF for 12 h to remove the unreacted substances, and then immersed in ethanol for 48 h and replaced with ethanol every 6 h. The final product was obtained by drying in a vacuum oven at 120°C.

## Preparation of SPEN/UiO-66-NH<sub>2</sub>-x Covalent-Ionically Cross-Linked Composite Membrane

The SPEN/UiO-66-NH<sub>2</sub>-x covalent-ionically cross-linked composite membranes were obtained as follows: Firstly, a certain amount of SPENs was dissolved in 15 mL DMAc to obtain a clear and transparent solution, which was recorded as solution A. At the same time, a certain amount of UiO-66-NH<sub>2</sub> was added to the 5 mL DMAc and put into the ultrasonic bath to make it dispersed uniformly, which was recorded as solution B. Then,

solution B was poured into solution A, which were sonicated and stirred for several hours at room temperature. The mixed solution then was cast onto clean glass plates and then cured in an oven with the consecutive temperature profiles of 80, 100, 120, 140, and 160°C (2 h each step) to remove the solvent. At the end of the heating procedure, the oven was naturally cooled to room temperature. Then the composite membrane was taken out and immersed in 1 M sulfuric acid solution for 24 h. After that, the membrane was washed repeatedly with DI water to neutralize the residual acid. The composite membranes were then placed in a vacuum oven and treated at 160°C for 12 h to obtain SPEN/UiO-66-NH<sub>2</sub> covalent-ionically cross-linked composite membranes, named as SPEN/UiO-66-NH<sub>2</sub>-x (x = 0, 1, 3, 5, 7, and 9).

## Characterization

Fourier Transform Infrared (FTIR) spectra were performed by a Shimadzu FTIR8400S spectrometer between 4,000 and 400 cm<sup>-1</sup> in air. The cross-sectional morphologies of the membranes were observed by scanning electron microscope (SEM, JEOL, JSM-5900 LV). The microstructure, particle size, and element distributions of UiO-66-NH<sub>2</sub> were characterized by JEM2100F field emission transmission electron microscope (TEM). Before TEM observation, the membranes were brittle fractured in liquid nitrogen and then coated with gold. The thermal degradation processes of the membranes were evaluated by thermal gravimetric analysis (TGA, TA, Q50) with a heating rate of 20°C/min under 40 mL/min N<sub>2</sub> flow. The sample loading for TGA was around 6–10 mg. The membranes were first heated to 160°C and dwelled for 5 min to remove the remaining water and solvent. They were then reheated from room temperature to 600°C with a heating rate of 20°C min<sup>-1</sup>. The tensile strength and Young's modulus were measured on a SANS CMT6104 series desktop electromechanical universal testing machine at room temperature. The crosshead speed was fixed at 5 mm min<sup>-1</sup>. At least five membrane samples were prepared for the mechanical test.

## Ion Exchange Capacity (IEC)

Weight-based IEC (IEC<sub>w</sub>) was determined by the titration method. All the membranes were immersed in 2.0 M NaCl solution for 48 h to liberate the H<sup>+</sup> ions. Then, the H<sup>+</sup> ions were titrated with 0.01 M NaOH solution using phenolphthalein as indicator. The titrated IEC was calculated from the following formula:

$$\text{IEC (mmol/g)} = \frac{V_{\text{NaOH}}^* M_{\text{NaOH}}}{W_{\text{dry}}}$$

where M<sub>NaOH</sub> (mol/L) and V<sub>NaOH</sub> (L) are the concentration and volume of NaOH solution, respectively, and W<sub>dry</sub> (g) is the mass of membrane.

## Methanol Permeability and Proton Conductivity

The methanol permeability of samples was tested by using a diffusion cell. The cell consists of two diffusion cells (20 mL

each) and was separated by the as-prepared membranes. The membranes were hydrated in deionized water for 24 h. Initially, 10 M methanol solution (20 mL) was added in one side of the diffusion cell (cell A), and ultrapure water (20 mL) was added in the other side (cell B). The methanol concentration in the cell B was tested by using a HIMADZU GC-8A chromatograph. The methanol diffusion coefficient was calculated by the following formula:

$$C_B(t) = \frac{A}{V_B} \frac{DK}{L} C_A(t - t_0)$$

where  $L$ ,  $A$ , and  $V_B$  are the thickness of membrane, the effective area, and the volume of receptor reservoir, respectively.  $C_A$  and  $C_B$  are the methanol concentrations in the donor and receptor reservoirs, respectively.  $DK$  (in  $\text{cm}^2 \text{s}^{-1}$ ) denotes the methanol permeability.

The proton conductivity of the membranes was tested from  $10^{-1}$  to  $10^6$  Hz. The membrane samples were hydrated in deionized water at different temperatures for 24 h. The membranes were infibulated between two pairs of stainless steel

electrodes. Conductivity measurements under fully hydrated conditions were carried out with the stainless steel electrodes immersed in deionized water. The proton conductivity ( $\sigma$ ) was calculated by the following formula:

$$\sigma = \frac{L}{SR}$$

where  $\sigma$  is the proton conductivity (S/cm),  $L$  is the distance between the electrodes (cm),  $R$  is the impedance of the membrane ( $\Omega$ ), and  $S$  is the surface area ( $\text{cm}^2$ ). Each sample was measured three times to ensure data reproducibility.

## Water Uptake and Swelling Ratio

Water uptake was determined by the weight differences between the full-dried and full-hydrated membranes. All membrane samples were immersed in deionized water at different temperatures for 24 h to ensure that the membranes were saturated with water. Subsequently, the water was wiped from the surface of the membranes quickly with blotting paper, and then the weight of wet membranes was measured. The swelling

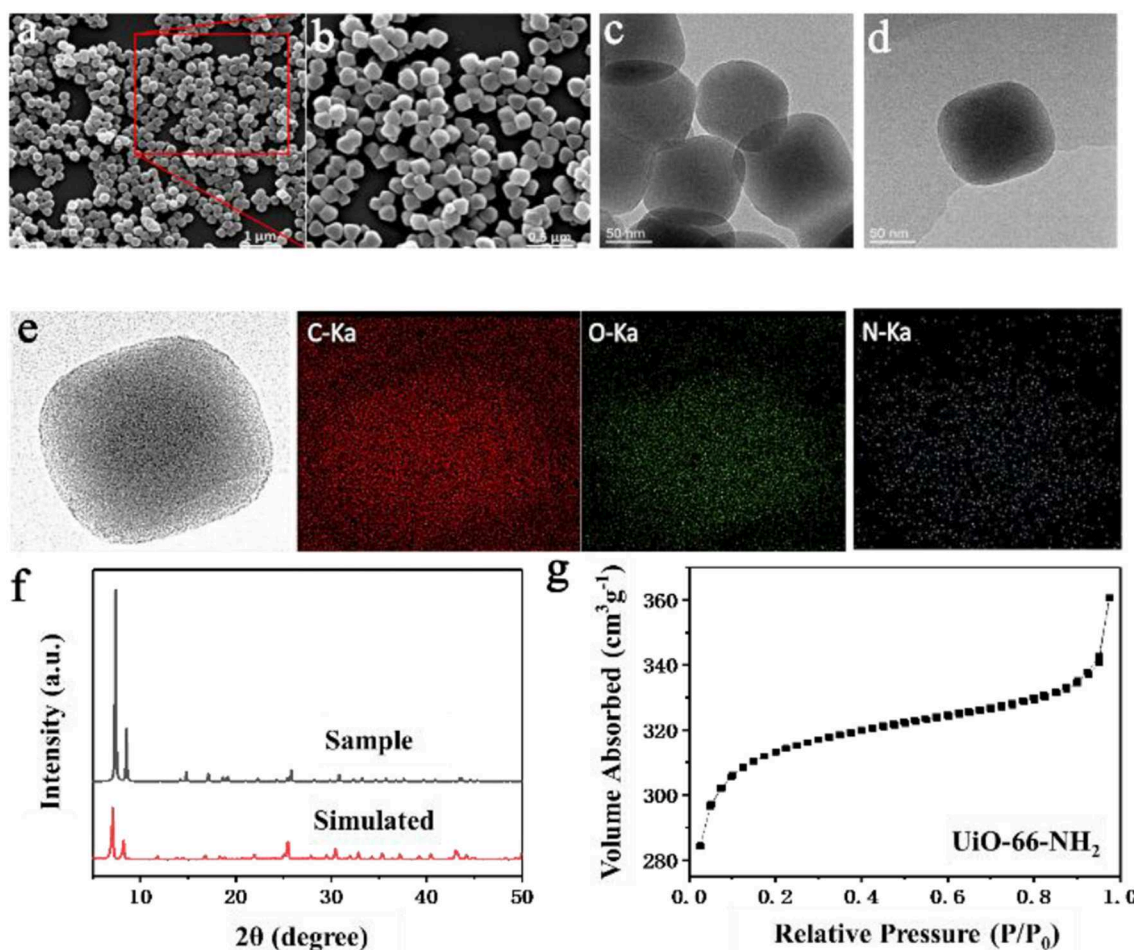


**FIGURE 1 |** (a,b) SEM, (c,d) TEM, (e) EDS mapping, (f) XRD curve, and (g) N<sub>2</sub> adsorption isotherm (77 K) of UiO-66-NH<sub>2</sub>.



ratio of the membrane sample was determined by immersing it in deionized water at certain temperatures for 24 h and measuring the change in length before and after the swelling process. The water uptake and swelling ratio of the membranes were calculated using the following equations:

$$\text{Water uptake} = \frac{W_{\text{wet}} - W_{\text{dry}}}{W_{\text{dry}}} \times 100\%$$

$$\text{Swelling ratio} = \frac{L_{\text{wet}} - L_{\text{dry}}}{L_{\text{dry}}} \times 100\%$$

where  $W_{\text{wet}}$  and  $W_{\text{dry}}$  are the mass of wet and dry membrane samples, respectively, and  $L_{\text{wet}}$  and  $L_{\text{dry}}$  are the length of wet and dry samples, respectively.

## DISCUSSION AND RESULT

### Characterization of UiO-66-NH<sub>2</sub>

The structure, morphology, composition, and porosity of synthesized UiO-66-NH<sub>2</sub> were studied by various characterization techniques. Firstly, the morphology of synthesized UiO-66-NH<sub>2</sub> was studied by SEM and TEM, as shown in **Figure 1**. The synthesized UiO-66-NH<sub>2</sub> has a highly uniform cubic state with an average diameter of about 135 nm, which can be inferred from **Figures 1a,b**. The TEM diagrams in **Figures 1c,d** further confirm the typical cube structure of UiO-66-NH<sub>2</sub> with smooth and flat surfaces. **Figure 1e** is the EDS element mapping of UiO-66-NH<sub>2</sub>, which can be used to evaluate the element distribution of synthesized UiO-66-NH<sub>2</sub> materials. As shown in **Figure 1e**, the elements of N and O are uniformly distributed in the cubic region corresponding to UiO-66-NH<sub>2</sub>. **Figure 1f** is the XRD pattern of UiO-66-NH<sub>2</sub>, which is very similar to the simulated curve, indicating the successful synthesis of UiO-66-NH<sub>2</sub>. At the same time, the narrow and sharp diffraction peaks show the high crystallinity of the synthesized UiO-66-NH<sub>2</sub>. The N<sub>2</sub> adsorption-desorption isotherms of UiO-66-NH<sub>2</sub> at 77 K are shown in **Figure 1g**. It is noteworthy that the specific surface area of UiO-66-NH<sub>2</sub> reaches 1,253.97 m<sup>2</sup>·g<sup>-1</sup>. The large specific surface area can provide enough proton-hopping sites to UiO-66-NH<sub>2</sub> and enhance the proton transfer in the membrane, which is also conducive to the adsorption of methanol molecules.

### FTIR of SPEN/UiO-66-NH<sub>2</sub>-x Covalent-Ionically Cross-Linked Composite Membrane

The characteristic functional groups in SPEN/UiO-66-NH<sub>2</sub>-x covalent-ionically cross-linked composite membrane were characterized by FTIR. From **Figure 2**, it can be observed that there is a significant ether bond characteristic absorption at 1,243 cm<sup>-1</sup> in the composite membranes, which indicates that the sulfonated poly(arylene ether nitrile)s were formed by condensation polymerization. In addition, there is a characteristic absorption band at 2,230 cm<sup>-1</sup> in all the SPEN/UiO-66-NH<sub>2</sub>-x composite membranes, which is unique to

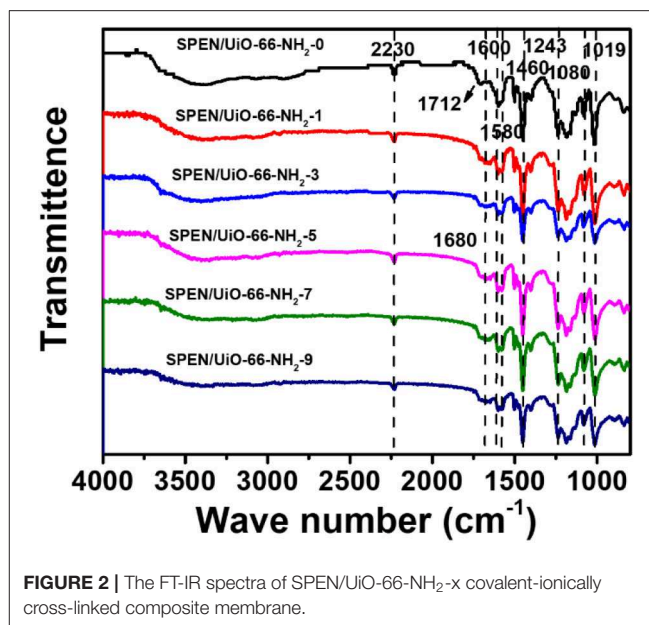


**FIGURE 2 |** The FT-IR spectra of SPEN/UiO-66-NH<sub>2</sub>-x covalent-ionically cross-linked composite membrane.

the nitrile group on the main chain of SPEN. The characteristic absorption bands at 1,018 and 1,080 cm<sup>-1</sup> correspond to the symmetrical and asymmetrical stretching vibration absorption of the sulfonic group (–SO<sub>3</sub>H), which indicates that the –SO<sub>3</sub>H has been successfully introduced into the SPEN. The obvious absorption bands at 1,460, 1,580, and 1,600 cm<sup>-1</sup> can be attributed to the vibration absorption of benzene ring skeleton. It is also observed that before the addition of UiO-66-NH<sub>2</sub>, there was a distinct characteristic absorption band at 1,712 cm<sup>-1</sup> for pure SPEN. However, the characteristic absorption band disappeared gradually with the doping of UiO-66-NH<sub>2</sub>, and appeared gradually at 1,680 cm<sup>-1</sup> which belonged to the characteristic absorption band of carbonyl group, indicating that the –NH<sub>2</sub> of UiO-66-NH<sub>2</sub> reacted with the carboxyl groups of SPEN in the SPEN/UiO-66-NH<sub>2</sub>-x composite membranes.

### SEM of SPEN/UiO-66-NH<sub>2</sub>-x Covalent-Ionically Cross-Linked Composite Membrane

The performance of composite membranes is closely related to the dispersion, interface connectivity, and compatibility of functional nanoparticles in the matrix. SEM was used to observe the internal microstructures of the SPEN/UiO-66-NH<sub>2</sub>-x composite membranes and the dispersion of UiO-66-NH<sub>2</sub> in the membranes. **Figure 3** is the SEM image of the cross section of SPEN/UiO-66-NH<sub>2</sub>-x covalent-ionically cross-linked composite membrane. As can be seen in the **Figure 3**, the SPEN/UiO-66-NH<sub>2</sub>-0 membrane showed a smooth cross section. With the increasing UiO-66-NH<sub>2</sub> content, the cross section of SPEN/UiO-66-NH<sub>2</sub>-x covalent-ionically cross-linked composite membrane becomes rough. Particularly, some holes appeared in the cross section of SPEN/UiO-66-NH<sub>2</sub>-9 composite membrane. When the doping amount of UiO-66-NH<sub>2</sub> is no more than 5 wt% (**Figures 3b–d**), it can be uniformly dispersed in the composite



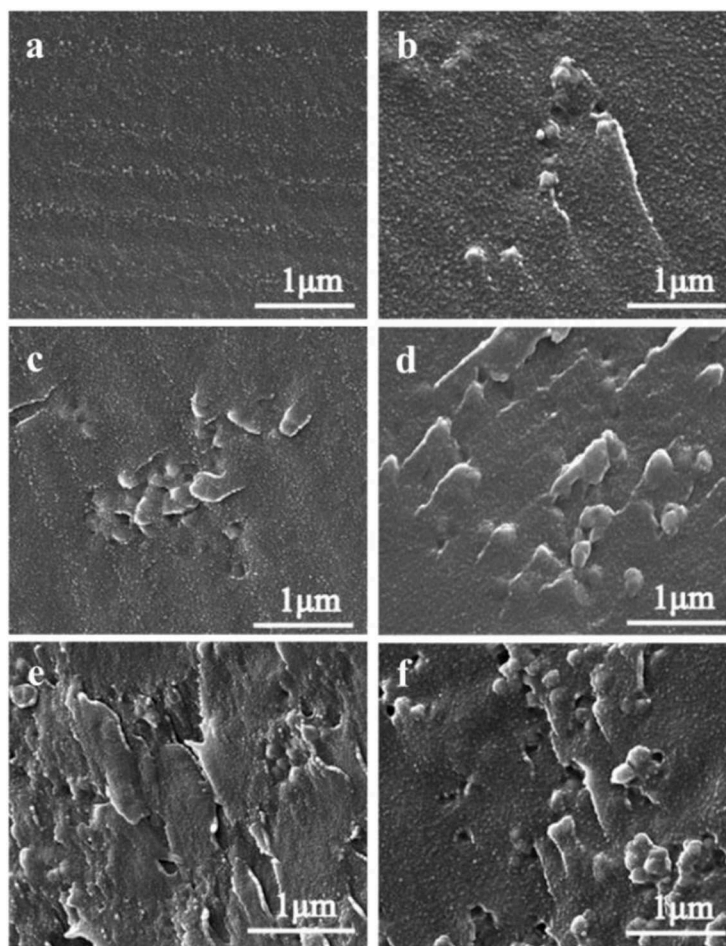


**FIGURE 3 |** The SEM images of SPEN/UiO-66-NH<sub>2</sub>-x covalent-ionically cross-linked composite membrane with (a) x = 0 wt%; (b) x = 1 wt%; (c) x = 3 wt%; (d) x = 5 wt%; (e) x = 7 wt%; and (f) x = 9 wt%.

membrane. Moreover, the interface between UiO-66-NH<sub>2</sub> and SPEN is relatively close, and no phase separation is observed. This can be attributed to the good compatibility of UiO-66-NH<sub>2</sub> and polymers, and the amino group easily interacts with sulfonic group/nitrile group in SPEN matrix, which greatly increases the compatibility of inorganic function in matrix. However, the agglomeration trend began to appear when the content of UiO-66-NH<sub>2</sub> further increased, which is well-illustrated in **Figures 3e,f**. As shown in **Figure 3f**, when the UiO-66-NH<sub>2</sub> content reaches 9 wt%, obvious agglomeration was observed. And, some holes begin to appear in the composite membrane.

## Thermal Properties

The thermal stability of the prepared SPEN/UiO-66-NH<sub>2</sub>-x covalent-ionically cross-linked composite membrane was studied by TGA in nitrogen atmosphere, as shown in **Figure 4**. The TGA curves of all SPEN/UiO-66-NH<sub>2</sub>-x composite membranes show two decomposition patterns. The first decomposition range can be attributed to the thermal decomposition of sulfonic groups, and the second decomposition range can be attributed to the degradation of the main chain of SPEN. Furthermore, the initial decomposition temperature of SPEN/UiO-66-NH<sub>2</sub>-0

composite membrane is about 260°C, which is much higher than that of Nafion 117. With the addition of UiO-66-NH<sub>2</sub>, the thermal decomposition temperature of the SPEN/UiO-66-NH<sub>2</sub>-x composite membranes increases greatly, and the initial decomposition temperature of all the composite membranes is higher than 290°C. It can be attributed that: (1) After the formation of covalent-ionically cross-linking between UiO-66-NH<sub>2</sub> and SPEN, the movement of molecular chains and sulfonic acid groups was limited, thus the thermal stability of the SPEN/UiO-66-NH<sub>2</sub>-x composite membranes could be improved accordingly; (2) as a kind of functional nanoparticles, the interaction between UiO-66-NH<sub>2</sub> and molecular chains hinders the mobilities of the chains, and delays the degradation of SPEN molecular chains, thus improving the thermal stability of the SPEN/UiO-66-NH<sub>2</sub>-x composite membranes.

## Mechanical Properties

The mechanical properties of proton exchange membranes (PEMs) directly determines whether the PEMs can be used for long-term operation in fuel cells. The mechanical properties of SPEN/UiO-66-NH<sub>2</sub>-x composite membranes in wet state are listed in **Figure 5**. The tensile strength and Young's modulus

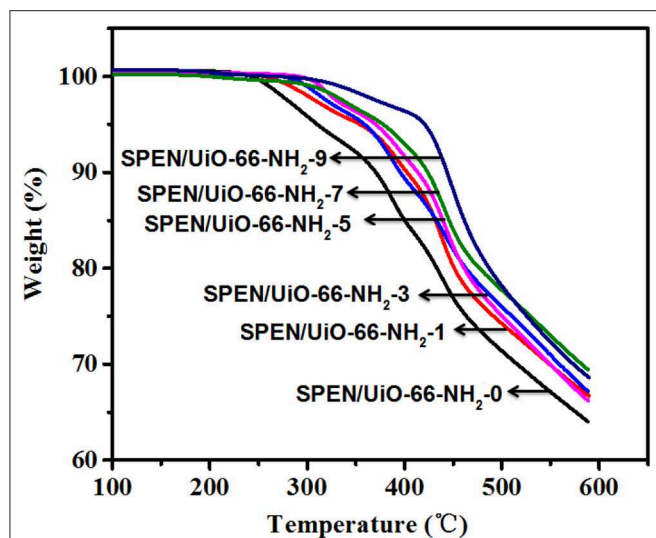


**FIGURE 4** | The thermal degradation (TGA) curve of SPEN/UiO-66-NH<sub>2</sub>-x covalent-ionically cross-linked composite membrane.

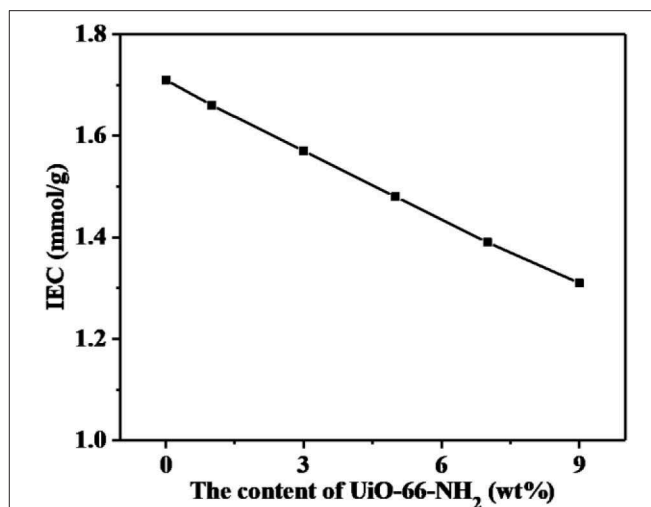


**FIGURE 6** | The ion exchange capacity (IEC) values of SPEN/UiO-66-NH<sub>2</sub>-x covalent-ionically cross-linked composite membrane.

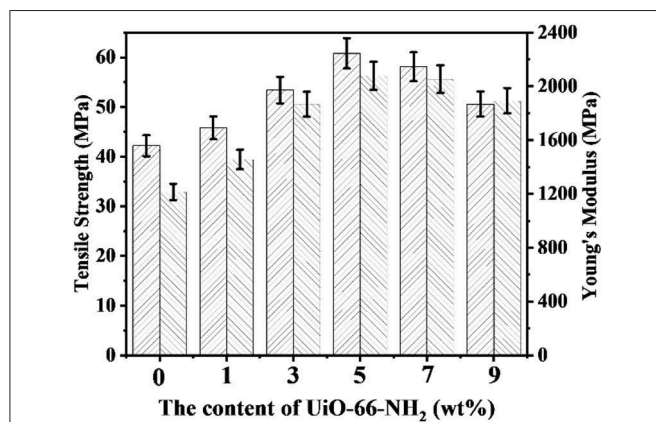


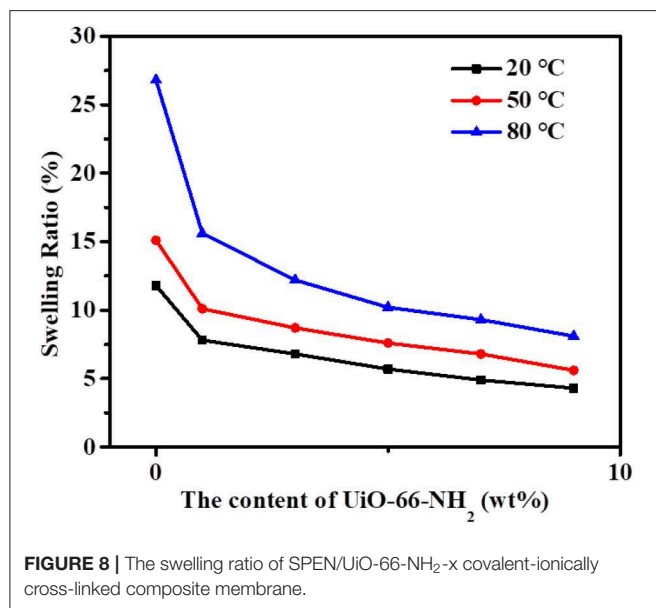
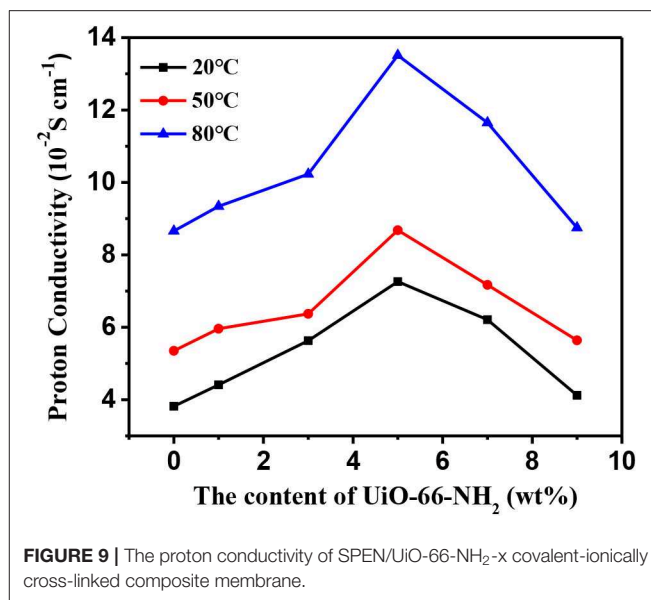
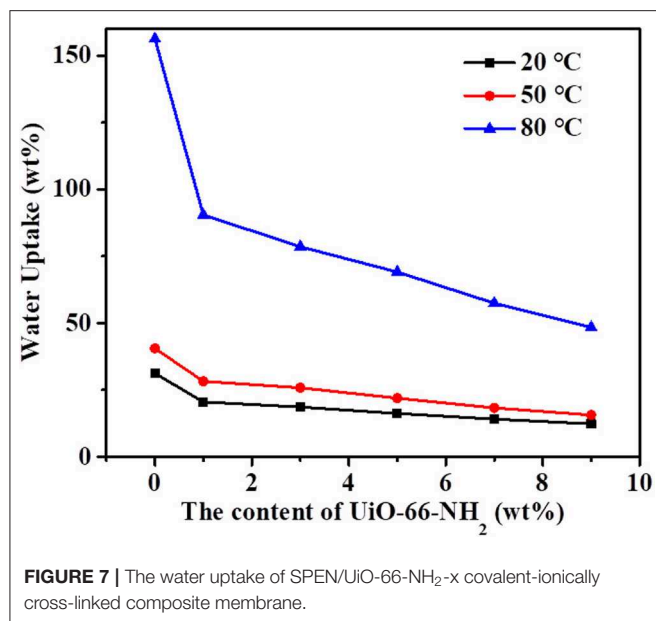
**FIGURE 5** | The mechanical properties of SPEN/UiO-66-NH<sub>2</sub>-x covalent-ionically cross-linked composite membrane.

of SPEN/UiO-66-NH<sub>2</sub>-x composite membranes are 42.2–60.8 MPa and 1,215–2,078 MPa, respectively. With the addition of UiO-66-NH<sub>2</sub>, all composite membranes demonstrated enhanced mechanical properties. This is mainly due to the covalent-ionically cross-linking between UiO-66-NH<sub>2</sub> and SPEN, which results in the lower mobility of SPEN molecular chains in a certain range. Both the tensile strength and Young's modulus of SPEN/UiO-66-NH<sub>2</sub>-x composite membranes show an increasing trend with the addition of UiO-66-NH<sub>2</sub> <5 wt%. However, while the content exceeds 5 wt%, the mechanical properties begin to decrease, which is determined by the dispersion of UiO-66-NH<sub>2</sub>. As mentioned above by SEM, UiO-66-NH<sub>2</sub> has good compatibility and good dispersion with the SPEN matrix as the content of UiO-66-NH<sub>2</sub> below 5 wt%, which can enhance the mechanical properties of the SPEN/UiO-66-NH<sub>2</sub>-x composite membranes. While the addition exceeds 5 wt%, UiO-66-NH<sub>2</sub> is prone to agglomeration, which resulting in defects in the SPEN/UiO-66-NH<sub>2</sub>-x composite membranes.

## Ion Exchange Capacity, Water Uptake, and Swelling Ratio

The ion exchange capacity (IEC) values represent the amount of hydrogen ions that can be replaced in proton exchange membranes, which plays an important role to the water uptake, proton conductive, and dimensional stability of membranes. As shown in **Figure 6**, with the increase of UiO-66-NH<sub>2</sub> addition, the IEC value of SPEN/UiO-66-NH<sub>2</sub>-x composite membranes decreased from 1.71 to 1.31 mmol/g. The main reasons are as follows: (1) The addition of UiO-66-NH<sub>2</sub> to the SPEN matrix diluted the concentration of sulfonic groups in the composite membranes to a certain extent. (2) The addition of UiO-66-NH<sub>2</sub> can cause covalent-ionically cross-linking reaction with carboxyl and sulfonic groups under certain heat treatment, which consumes the carboxyl and sulfonic groups, and the cross-linking network limits the replacement of H<sup>+</sup> by Na<sup>+</sup>, thus leading to the decrease of IEC value of the composite membrane.

The water uptake of the PEMs has an important influence on the proton transport mechanism and methanol permeability. It is also closely related to the dimensional stability and mechanical properties of the proton exchange membrane. Therefore, the proton exchange membrane must have a proper water uptake. The water uptake of SPEN/UiO-66-NH<sub>2</sub>-x composite membrane at corresponding temperatures is shown in **Figure 7**. The water uptake of SPEN/UiO-66-NH<sub>2</sub>-x composite membrane increases with the increasing temperature. For example, at room temperature, the water uptake of SPEN/UiO-66-NH<sub>2</sub>-0 composite membranes is 31.2 wt%, and at 80°C, the water uptake of SPEN/UiO-66-NH<sub>2</sub>-0 composite membranes is 156.2 wt%. It was also observed that the water uptake of the SPEN/UiO-66-NH<sub>2</sub>-x composite membranes decreased gradually with the increasing of UiO-66-NH<sub>2</sub> content. For example, at room temperature, the water uptake of SPEN/UiO-66-NH<sub>2</sub>-x composite membranes decreased from 31.2 to 12.3 wt% with the increase of UiO-66-NH<sub>2</sub> content from 0 to



9 wt%. The reasons for this phenomenon can be attributed to two aspects: (1) After the addition of UiO-66-NH<sub>2</sub>, the covalent-ionically cross-linking between UiO-66-NH<sub>2</sub> and SPEN was formed. In addition, UiO-66-NH<sub>2</sub> as a filler could also restrict the molecular chain movement of SPEN. These two effects synergistically reduced the free volume of the composite membrane, thus resulting in the water uptake of the composite membrane decreased correspondingly. (2) The UiO-66-NH<sub>2</sub> filler has lower IEC value than SPEN leads to the decreasing water uptake with the increasing of UiO-66-NH<sub>2</sub> content after covalent-ionically cross-linking with the matrix.

From **Figure 8**, it can be seen that the swelling ratio of SPEN/UiO-66-NH<sub>2</sub>-x composite membranes at different temperatures shows a similar trend to that of the

above-mentioned water uptake; that is, the swelling ratio increases with the increasing temperature and decreases with the increasing filler content. For example, at room temperature, the swelling rate of SPEN/UiO-66-NH<sub>2</sub>-0 composite membrane is 11.8%, while that of SPEN/UiO-66-NH<sub>2</sub>-9 composite membrane is 4.3%. When the temperature is raised from 20 to 80°C, the swelling ratio of SPEN/UiO-66-NH<sub>2</sub>-0 composite membrane is 26.8%, while that of SPEN/UiO-66-NH<sub>2</sub>-9 composite membrane is 8.1%. The above results show that the formation of covalent-ionically cross-linking can significantly improve the dimensional stability of SPEN.

## Proton Conductivity

The effects of temperature and UiO-66-NH<sub>2</sub> contents on the proton conductivity of SPEN/UiO-66-NH<sub>2</sub>-x covalent-ionically cross-linked composite membrane are shown in **Figure 9** and **Table 1**. Firstly, the proton conductivity of the SPEN/UiO-66-NH<sub>2</sub>-x composite membranes increases with the increasing temperature. For example, the proton conductivity of SPEN/UiO-66-NH<sub>2</sub>-5 composite membrane is  $7.26 \times 10^{-2} \text{ S} \cdot \text{cm}^{-1}$  at 20°C, while the proton conductivity of SPEN/UiO-66-NH<sub>2</sub>-5 composite membrane is  $13.51 \times 10^{-2} \text{ S} \cdot \text{cm}^{-1}$  at 80°C. This can be attributed to the fact that temperature increases can promote the mobility of water molecules and polymer chains, thus improving the migration rate of hydrated protons. At all temperatures, the proton conductivity of the SPEN/UiO-66-NH<sub>2</sub>-x composite membranes increased first and then decreased with the increasing UiO-66-NH<sub>2</sub> content. These phenomena can be explained by the illustration of **Figure 10**. When the UiO-66-NH<sub>2</sub> content is <5 wt%, the increase of proton conductivity can be attributed to the fact that the amino groups in the UiO-66-NH<sub>2</sub> framework are good proton acceptors/donors. When the content of UiO-66-NH<sub>2</sub> is  $\leq 5$  wt%, it can be uniformly dispersed and cause the change of sulfonic groups at the interface between UiO-66-NH<sub>2</sub> and SPEN matrix.



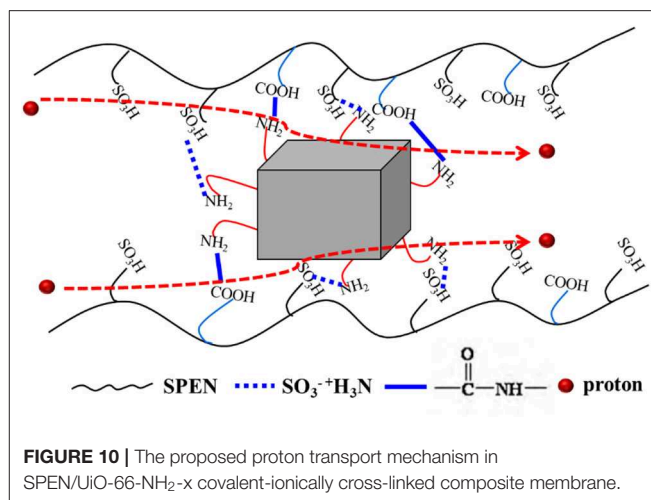
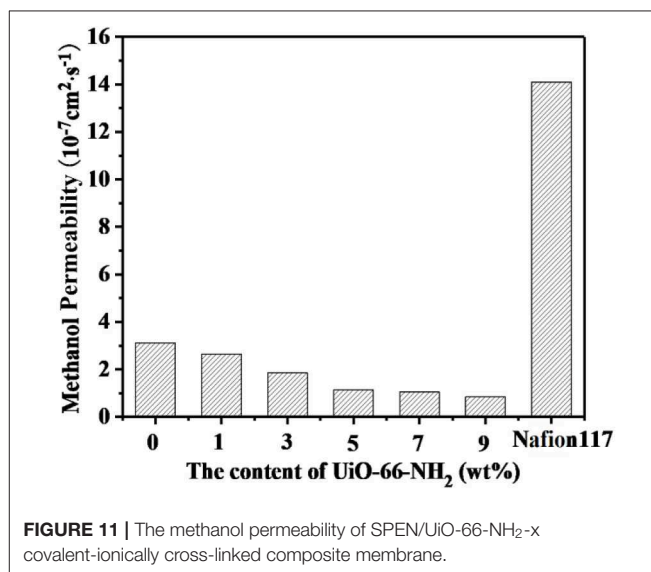
**TABLE 1** | The proton conductivity, methanol permeability, and selectivity of SPEN/UiO-66-NH<sub>2</sub>-x covalent-ionically cross-linked composite membrane.

Membranes	Proton conductivity (10 <sup>-2</sup> S·cm <sup>-1</sup> )			Methanol permeability (10 <sup>-7</sup> cm <sup>2</sup> ·s <sup>-1</sup> )	Selectivity (10 <sup>5</sup> S·s·cm <sup>-3</sup> )
	20°C	50°C	80°C		
SPEN/UiO-66-NH <sub>2</sub> -0	3.82	5.35	8.66	3.12	1.22
SPEN/UiO-66-NH <sub>2</sub> -1	4.41	5.96	9.34	2.65	1.66
SPEN/UiO-66-NH <sub>2</sub> -3	5.63	6.37	10.23	1.85	3.04
SPEN/UiO-66-NH <sub>2</sub> -5	7.26	8.68	13.51	1.13	6.42
SPEN/UiO-66-NH <sub>2</sub> -7	6.21	7.17	11.65	1.04	5.97
SPEN/UiO-66-NH <sub>2</sub> -9	4.12	5.64	8.75	0.85	4.84
Nafion117	6.4	—	—	14.1	0.45

The sulfonic groups interact with the basic amino group to form acid-base proton pairs, with the aid of water molecule, protons are continuously transferred between amino group and sulfonic groups in the membrane by acid-base interaction and Grotthuss mechanism. In this process, the formation and breakage of hydrogen bond network structure are alternately carried out. In conclusion, UiO-66-NH<sub>2</sub> can enhance the proton conduction of the composite membrane by increasing the density of proton conduction groups at the interface of UiO-66-NH<sub>2</sub>/SPEN under the condition of good rational dispersion; the other part of protons can combine with free water molecules to form hydrated protons (H<sub>3</sub>O<sup>+</sup>), which can transport through a continuous ion transport channel. Therefore, the addition of UiO-66-NH<sub>2</sub> into SPEN could significantly enhance proton transport. However, when the content of UiO-66-NH<sub>2</sub> continued to increase in the composite membrane, the proton conductivity of the composite membrane began to show a downward trend, especially that of SPEN/UiO-66-NH<sub>2</sub>-9 composite membrane, which decreased to  $4.12 \times 10^{-2}$  S·cm<sup>-1</sup> (at room temperature). This is mainly attributed to the aggregation of UiO-66-NH<sub>2</sub> when the content is too high, which makes its dispersion in composite membranes become worse. In addition, the high content of UiO-66-NH<sub>2</sub> leads to the decrease of IEC value of composite membranes. In summary, it is more appropriate to control the content of UiO-66-NH<sub>2</sub> at about 5 wt%.

## Methanol Permeability and Selectivity

Methanol permeability from anode to cathode can lead to fuel loss, polarization of fuel cell electrodes and significant reduction of fuel cell efficiency, and even catalyst poisoning. Therefore, in DMFCs, proton exchange membranes must possess both excellent proton conductivity and methanol resistance. The methanol permeability of SPEN/UiO-66-NH<sub>2</sub>-x composite membranes is listed in **Table 1** and **Figure 11**. The methanol permeability of the SPEN/UiO-66-NH<sub>2</sub>-x composite membranes decreased gradually with the increasing of UiO-66-NH<sub>2</sub> content. The methanol permeability of the SPEN/UiO-66-NH<sub>2</sub>-x composite membranes ranged from  $3.2 \times 10^{-7}$  S·cm<sup>2</sup>·s<sup>-1</sup> to  $0.85 \times 10^{-7}$  S·cm<sup>2</sup>·s<sup>-1</sup>, and the SPEN/UiO-66-NH<sub>2</sub>-9 composite membranes had the lowest methanol permeability.

**FIGURE 10** | The proposed proton transport mechanism in SPEN/UiO-66-NH<sub>2</sub>-x covalent-ionically cross-linked composite membrane.**FIGURE 11** | The methanol permeability of SPEN/UiO-66-NH<sub>2</sub>-x covalent-ionically cross-linked composite membrane.

This is mainly due to: (1) UiO-66-NH<sub>2</sub> covalent-ionically cross-linking with carboxyl and sulfonic groups will form a three-dimensional cross-linking network in the membranes. The cross-linking network restricts the movement of SPEN molecular chains, thus making the membranes more compact and the methanol permeability of the SPEN/UiO-66-NH<sub>2</sub>-x composite membranes significantly reduced. (2) The interaction between the nitrile group of SPEN and UiO-66-NH<sub>2</sub> further inhibits the mobility of the polymer chain and reduces the free volume of the composite membrane. (3) The transport of methanol in the membrane is similar to that of proton transport mechanism, which requires hydrophilic ion channels in the membrane. The barrier effect of UiO-66-NH<sub>2</sub> in the proton transport channel can increase the curvature of the transport channel, thus prolonging the methanol diffusion pathway and reducing the methanol permeability. (4) UiO-66-NH<sub>2</sub> can trap methanol in its pores, thus inhibiting the methanol permeability.



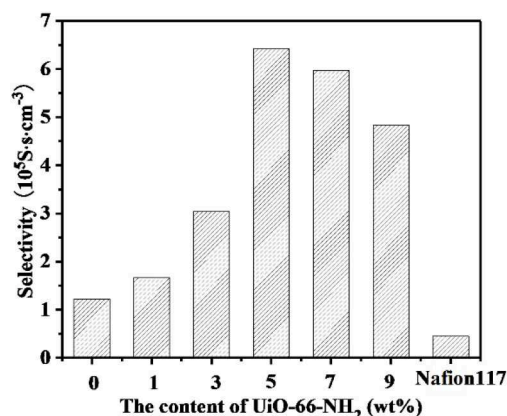


**FIGURE 12 |** The selectivity of SPEN/UiO-66-NH<sub>2</sub>-x covalent-ionically cross-linked composite membrane.

As shown in **Figure 12** and **Table 1**, with the increasing addition of UiO-66-NH<sub>2</sub>, the selectivity (which is calculated by the ratio of proton conductivity to methanol permeability) of all SPEN/UiO-66-NH<sub>2</sub>-x composite membranes are improved compared with pure SPEN membranes. This is mainly due to the increase of proton conductivity and methanol resistance of SPEN/UiO-66-NH<sub>2</sub>-x composite membranes. However, the selectivity of the SPEN/UiO-66-NH<sub>2</sub>-x composite membranes increased first and then decreased with the increasing of UiO-66-NH<sub>2</sub> content. This was mainly due to the dispersion, interface connectivity, and compatibility of UiO-66-NH<sub>2</sub> in the SPEN matrix. It is for the fact that when the UiO-66-NH<sub>2</sub> content is below 5 wt%, the methanol permeability and the proton conductivity of SPEN/UiO-66-NH<sub>2</sub>-x increase simultaneously. Thus, the selectivity of SPEN/UiO-66-NH<sub>2</sub>-x presents a growing trend with increasing x. However, when the content of UiO-66-NH<sub>2</sub> exceeds 5 wt%, the increased cross-linking structure makes the membrane highly dense, which results in more significant decrease of proton conductivity than that of methanol permeability. Thus, the selectivity of SPEN/UiO-66-NH<sub>2</sub>-x membranes presents a downward trend. The UiO-66-NH<sub>2</sub> addition can increase the proton conductivity and methanol resistance of SPEN/UiO-66-NH<sub>2</sub>-x; however, excessive UiO-66-NH<sub>2</sub> may lead to the agglomeration which decreases the proton conductivity in the SPEN/UiO-66-NH<sub>2</sub>-x membranes and leads to the reduction of overall performance. The SPEN/UiO-66-NH<sub>2</sub>-5 composite membrane has the highest selectivity, which is  $6.42 \times 10^5 \text{ S} \cdot \text{s} \cdot \text{cm}^{-3}$ , 14.3-times higher than that of Nafion 117.

## REFERENCES

- Ahn, M. K., Lee, B., Jang, J., Min, C. M., Lee, S. B., Pak, C., et al. (2018). Facile preparation of blend proton exchange membranes with highly sulfonated poly (arylene ether) and poly (arylene ether sulfone) bearing dense triazoles. *J. Membr. Sci.* 560, 58–66. doi: 10.1016/j.memsci.2018.05.011
- Antolini, E. (2018). Photo-assisted methanol oxidation on Pt-TiO<sub>2</sub> catalysts for direct methanol fuel cells: a short review. *Appl. Catal. B Environ.* 237, 491–503. doi: 10.1016/j.apcatb.2018.06.029

## CONCLUSION

In this manuscript, we have successfully achieved a high-performance SPEN/UiO-66-NH<sub>2</sub>-x covalent-ionically cross-linked composite membrane by doping UiO-66-NH<sub>2</sub> (a kind of newly emerging porous materials with solution processability) into SPEN. The structure and morphology of large-scale synthesized UiO-66-NH<sub>2</sub> were characterized by XRD, SEM, TEM, and BET. Simultaneously, the obtained SPEN/UiO-66-NH<sub>2</sub>-x covalent-ionically cross-linked composite membranes displays excellent thermal stability and dimensional stability. The as-prepared SPEN/UiO-66-NH<sub>2</sub>-x composite membranes display excellent proton conductivity compared with that of recast SPEN. The enhanced proton conductivity can be attributed to the construction of ionic clusters and well-connected ionic nanochannels along the interface between UiO-66-NH<sub>2</sub>-x and SPEN matrix via molecular interactions. Meanwhile, the methanol permeability of SPEN/UiO-66-NH<sub>2</sub>-x covalent-ionically cross-linked composite membrane is well-suppressed due to the barrier effect of cross-linking and UiO-66-NH<sub>2</sub>-x. At the same time, the selectivity of SPEN/UiO-66-NH<sub>2</sub>-x also increased significantly as the UiO-66-NH<sub>2</sub>-x was added. The SPEN/UiO-66-NH<sub>2</sub>-5 composite membrane exhibits the highest selectivity of  $6.42 \times 10^5 \text{ S} \cdot \text{s} \cdot \text{cm}^{-3}$ , 14.3-times higher than that of Nafion 117. All the above results indicate that preparation of SPEN/UiO-66-NH<sub>2</sub>-x covalent-ionically cross-linked composite membranes is an efficient method to modify PEMs with improved proton-transfer and methanol resistant properties.

## DATA AVAILABILITY STATEMENT

The datasets generated for this study are available on request to the corresponding author.

## AUTHOR CONTRIBUTIONS

PZ: writing—original draft preparation, conceptualization, methodology, investigation, and data curation. YZ: writing—review and editing. ZL, DW, and YM: data curation. QL: validation.

## ACKNOWLEDGMENTS

The authors gratefully thank the financial support from National Key R&D Program of China (No. 2018YFC0809500), the National Natural Science Foundation of China (Nos. U1633203, U1733126), and Sichuan Science and Technology Program (No. 2018GZYF0069).

- Bai, Y., Dou, Y., Xie, L. H., Rutledge, W., Li, J. R., and Zhou, H. C. (2016). Zr-based metal-organic frameworks: design, synthesis, structure, and applications. *Chem. Soc. Rev.* 45, 2327–2367. doi: 10.1039/C5CS00837A
- Cavka, J. H., Jakobsen, S., Olsbye, U., Guillo, N., Lamberti, C., Bordiga, S., et al. (2008). A new zirconium inorganic building brick forming metal organic frameworks with exceptional stability. *J. Am. Chem. Soc.* 130, 13850–13851. doi: 10.1021/ja8057953
- Chang, Y., Brunello, G. F., Fuller, J., Disabb-Miller, M. L., Hawley, M. E., and Kim, Y. S. (2013). Polymer electrolyte membranes based on poly (arylene

- ether sulfone) with pendant perfluorosulfonic acid. *Polym. Chem.* 4, 272–281. doi: 10.1039/C2PY20666H
- DeStefano, M. R., Islamoglu, T., Garibay, S. J., Hupp, J. T., and Farha, O. K. (2017). Room-temperature synthesis of UiO-66 and thermal modulation of densities of defect sites. *Chem. Mater.* 29, 1357–1361. doi: 10.1021/acs.chemmater.6b05115
- Dong, X. Y., Li, J. J., Han, Z., Duan, P. G., Li, L. K., and Zang, S. Q. (2017). Tuning the functional substituent group and guest of metal–organic frameworks in hybrid membranes for improved interface compatibility and proton conduction. *J. Mater. Chem. A* 5, 3464–3474. doi: 10.1039/C6TA07761G
- Eris, S., Daşdelen, Z., and Sen, F. (2018). Enhanced electrocatalytic activity and stability of monodisperse Pt nanocomposites for direct methanol fuel cells. *J. Colloid. Interf. Sci.* 513, 767–773. doi: 10.1016/j.jcis.2017.11.085
- Feng, M., Huang, Y., Wei, M., and Liu, X. (2018). Sulfonated poly(arylene ether nitrile)-based hybrid membranes containing amine-functionalized GO for constructing long-range ionic nanochannels. *Int. J. Hydrogen Energy* 43, 11214–11222. doi: 10.1016/j.ijhydene.2018.04.227
- Furukawa, H., Gándara, F., Zhang, Y. B., Jiang, J., Queen, W. L., Hudson, M. R., et al. (2014). Water adsorption in porous metal–organic frameworks and related materials. *J. Am. Chem. Soc.* 136, 4369–4381. doi: 10.1021/ja500330a
- Gil-Hernández, B., Savvin, S., Makhlofi, G., Núñez, P., Janiak, C., and Sanchiz, J. (2015). Proton conduction and long-range ferrimagnetic ordering in two isostructural copper (II) mesoxalate metal–organic frameworks. *Inorg. Chem.* 54, 1597–1605. doi: 10.1021/ic502586a
- Jiang, H. L., Feng, D., Wang, K., Gu, Z. Y., Wei, Z., Chen, Y. P., et al. (2013). An exceptionally stable, porphyrinic Zr metal–organic framework exhibiting pH-dependent fluorescence. *J. Am. Chem. Soc.* 135, 13934–13938. doi: 10.1021/ja406844r
- Joarder, B., Lin, J. B., Romero, Z., and Shimizu, G. K. (2017). Single crystal proton conduction study of a metal organic framework of modest water stability. *J. Am. Chem. Soc.* 139, 7176–7179. doi: 10.1021/jacs.7b03397
- Kahn, J. S., Freage, L., Enkin, N., Garcia, M. A. A., and Willner, I. (2017). Stimuli-responsive DNA-functionalized metal–organic frameworks (MOFs). *Adv. Mater.* 29:1602782. doi: 10.1002/adma.201602782
- Kim, K., Bae, J., Lim, M. Y., Heo, P., Choi, S. W., Kwon, H. H., et al. (2017a). Enhanced physical stability and chemical durability of sulfonated poly(arylene ether sulfone) composite membranes having antioxidant grafted graphene oxide for polymer electrolyte membrane fuel cell applications. *J. Membr. Sci.* 525, 125–134. doi: 10.1016/j.memsci.2016.10.038
- Kim, K., Kim, S. K., Park, J. O., Choi, S. W., Kim, K. H., Ko, T., et al. (2017b). Highly reinforced pore-filling membranes based on sulfonated poly(arylene ether sulfone)s for high-temperature/low-humidity polymer electrolyte membrane fuel cells. *J. Membr. Sci.* 537, 11–21. doi: 10.1016/j.memsci.2017.05.014
- Ko, T., Kim, K., Jung, B. K., Cha, S. H., Kim, S. K., and Lee, J. C. (2015). Cross-linked sulfonated poly(arylene ether sulfone) membranes formed by *in situ* casting and click reaction for applications in fuel cells. *Macromolecules* 48, 1104–1114. doi: 10.1021/ma5021616
- Kuo, A. T., Takeuchi, K., Tanaka, A., Urata, S., Okazaki, S., and Shinoda, W. (2018). Exploring the effect of pendent side chain length on the structural and mechanical properties of hydrated perfluorosulfonic acid polymer membranes by molecular dynamics simulation. *Polymer* 146, 53–62. doi: 10.1016/j.polymer.2018.05.033
- Li, J., Xu, G., Luo, X., Xiong, J., Liu, Z., and Cai, W. (2018a). Effect of nano-size of functionalized silica on overall performance of swelling-filling modified Nafion membrane for direct methanol fuel cell application. *Appl. Energy* 213, 408–414. doi: 10.1016/j.apenergy.2018.01.052
- Li, Q., Jensen, J. O., Savinell, R. F., and Bjerrum, N. J. (2009). High temperature proton exchange membranes based on polybenzimidazoles for fuel cells. *Prog. Polym. Sci.* 34, 449–477. doi: 10.1016/j.progpolymsci.2008.12.003
- Li, Y., Liang, L., Liu, C., Li, Y., Xing, W., and Sun, J. (2018b). Self-healing proton-exchange membranes composed of nafion–poly(vinyl alcohol) complexes for durable direct methanol fuel cells. *Adv. Mater.* 30:1707146. doi: 10.1002/adma.201707146
- Ling, X., Bonn, M., Domke, K. F., and Parekh, S. H. (2019). Correlated interfacial water transport and proton conductivity in perfluorosulfonic acid membranes. *Proc. Natl. Acad. Sci. U.S.A.* 116, 8715–8720. doi: 10.1073/pnas.1817401116
- Liu, S. J., Cao, C., Yang, F., Yu, M. H., Yao, S. L., and Zheng, T. F. (2016). High proton conduction in two CoII and MnII anionic metal–organic frameworks derived from 1, 3, 5-benzenetricarboxylic acid. *Cryst. Growth Des.* 16, 6776–6780. doi: 10.1021/acs.cgd.6b00776
- Nguyen, M. D. T., Yang, S., and Kim, D. (2016). Pendant dual sulfonated poly(arylene ether ketone) proton exchange membranes for fuel cell application. *J. Power Sources* 328, 355–363. doi: 10.1016/j.jpowsour.2016.08.041
- Oh, K., Ketpang, K., Kim, H., and Shanmugam, S. (2016). Synthesis of sulfonated poly(arylene ether ketone) block copolymers for proton exchange membrane fuel cells. *J. Membr. Sci.* 507, 135–142. doi: 10.1016/j.memsci.2016.02.027
- Pang, J., Jin, X., Wang, Y., Feng, S., Shen, K., and Wang, G. (2015). Fluorinated poly(arylene ether ketone) containing pendent hexasulfofenyl for proton exchange membrane. *J. Membr. Sci.* 492, 67–76. doi: 10.1016/j.memsci.2015.05.027
- Patel, H. A., Mansor, N., Gadipelli, S., Brett, D. J., and Guo, Z. (2016). Superacidity in Nafion/MOF hybrid membranes retains water at low humidity to enhance proton conduction for fuel cells. *ACS Appl. Mater. Inter.* 8, 30687–30691. doi: 10.1021/acsami.6b12240
- Perrot, C., Nonon, L., Marestin, C., and Gebel, G. (2011). Hydrolytic degradation of sulfonated polyimide membranes for fuel cells. *J. Membr. Sci.* 379, 207–214. doi: 10.1016/j.memsci.2011.05.063
- Ressam, I., El Kadib, A., Lahcini, M., Luinstra, G. A., Perrot, H., and Sel, O. (2018). Enhanced proton transport properties of Nafion via functionalized halloysite nanotubes. *Int. J. Hydrogen Energy* 43, 18578–18591. doi: 10.1016/j.ijhydene.2018.05.025
- Singha, S., Jana, T., Modestra, J. A., Kumar, A. N., and Mohan, S. V. (2016). Highly efficient sulfonated polybenzimidazole as a proton exchange membrane for microbial fuel cells. *J. Power Sources* 317, 143–152. doi: 10.1016/j.jpowsour.2016.03.103
- Taddei, M., Dau, P. V., Cohen, S. M., Ranocchiar, M., van Bokhoven, J. A., Costantino, F., et al. (2015). Efficient microwave assisted synthesis of metal–organic framework UiO-66: optimization and scale up. *Dalton Trans.* 44, 14019–14026. doi: 10.1039/C5DT01838B
- Wan, X., Zhan, Y., Zeng, G., and He, Y. (2017). Nitrile functionalized halloysite nanotubes/poly(arylene ether nitrile) nanocomposites: interface control, characterization, and improved properties. *Appl. Surf. Sci.* 393, 1–10. doi: 10.1016/j.apsusc.2016.09.148
- Wang, H., Zhuang, X., Tong, J., Li, X., Wang, W., Cheng, B., et al. (2015a). Solution-blown SPEEK/POSS nanofiber–nafion hybrid composite membranes for direct methanol fuel cells. *J. Appl. Polym. Sci.* 132, 42843–42850. doi: 10.1002/app.42843
- Wang, T. C., Bury, W., Gómez-Gualdrón, D. A., Vermeulen, N. A., Mondloch, J. E., Deria, P., et al. (2015b). Ultrahigh surface area zirconium MOFs and insights into the applicability of the BET theory. *J. Am. Chem. Soc.* 137, 3585–3591. doi: 10.1021/ja512973b
- Wu, H. B., Xia, B. Y., Yu, L., Yu, X. Y., and Lou, X. W. D. (2015). Porous molybdenum carbide nano-octahedrons synthesized via confined carburization in metal–organic frameworks for efficient hydrogen production. *Nat. Commun.* 6:6512. doi: 10.1038/ncomms7512
- Xu, H., Tao, S., and Jiang, D. (2016). Proton conduction in crystalline and porous covalent organic frameworks. *Nat. Mater.* 15:722. doi: 10.1038/nmat4611
- Xu, J., Ni, H., Wang, S., Wang, Z., and Zhang, H. (2015). Direct polymerization of a novel sulfonated poly(arylene ether ketone sulfone)/sulfonated poly(vinylalcohol) crosslinked membrane for direct methanol fuel cell applications. *J. Membr. Sci.* 492, 505–517. doi: 10.1016/j.memsci.2015.06.031
- Yan, Z. B., Young, A. P., and Goward, G. R. (2018). A magnetic resonance and electrochemical study of the role of polymer mobility in supporting hydrogen transport in perfluorosulfonic acid membranes. *Phys. Chem. Chem. Phys.* 20, 19098–19109. doi: 10.1039/C8CP02676A
- Yang, F., Xu, G., Dou, Y., Wang, B., Zhang, H., Wu, H., et al. (2017). A flexible metal–organic framework with a high density of sulfonic acid sites for proton conduction. *Nat. Energy* 2:877. doi: 10.1038/s41560-017-0018-7
- Yao, H., Zhang, Y., Liu, Y., You, K., Song, N., Liu, B., et al. (2015). Pendant-group cross-linked highly sulfonated co-polyimides for proton exchange membranes. *J. Membr. Sci.* 480, 83–92. doi: 10.1016/j.memsci.2014.12.014
- Yilmaz, E., and Can, E. (2018). Cross-linked poly(aryl ether sulfone) membranes for direct methanol fuel cell applications. *J. Polym. Sci. Polym. Phys. Ed.* 56, 558–575. doi: 10.1002/polb.24582

- Yin, Y., Du, Q., Qin, Y., Zhou, Y., and Okamoto, K. I. (2011). Sulfonated polyimides with flexible aliphatic side chains for polymer electrolyte fuel cells. *J. Membr. Sci.* 367, 211–219. doi: 10.1016/j.memsci.2010.10.054
- Yue, Z., Cai, Y. B., and Xu, S. (2015). Proton conducting sulfonated poly (imide-benzimidazole) with tunable density of covalent/ionic cross-linking for fuel cell membranes. *J. Power Sources* 286, 571–579. doi: 10.1016/j.jpowsour.2015.04.030
- Yue, Z., Cai, Y. B., and Xu, S. (2016). Phosphoric acid-doped cross-linked sulfonated poly (imide-benzimidazole) for proton exchange membrane fuel cell applications. *J. Membr. Sci.* 501, 220–227. doi: 10.1016/j.memsci.2015.11.045
- Zakil, F. A., Kamarudin, S. K., and Basri, S. (2016). Modified Nafion membranes for direct alcohol fuel cells: an overview. *Renew. Sust. Energy Rev.* 65, 841–852. doi: 10.1016/j.rser.2016.07.040
- Zhan, Y., He, S., Wan, X., Zhao, S., and Bai, Y. (2018). Thermally and chemically stable poly(arylene ether nitrile)/halloysite nanotubes intercalated graphene oxide nanofibrous composite membranes for highly efficient oil/water emulsion separation in harsh environment. *J. Membr. Sci.* 567, 76–88. doi: 10.1016/j.memsci.2018.09.037
- Zhan, Y., Zhang, J., He, S., Zhao, S., Bai, Y., and Liu, X. (2019). Thermally stable and dielectric nanocomposite based on poly(arylene ether nitrile) and BaTiO<sub>3</sub> functionalized by modified mussel-inspired route. *J. Polym. Res.* 26:77. doi: 10.1007/s10965-019-1740-6
- Zhang, B., Ni, J., Xiang, X., Wang, L., and Chen, Y. (2017). Synthesis and properties of reprocessable sulfonated polyimides cross-linked via acid stimulation for use as proton exchange membranes. *J. Power Sources* 337, 110–117. doi: 10.1016/j.jpowsour.2016.10.102
- Zhang, J., Zhao, Z., Xia, Z., and Dai, L. (2015). A metal-free bifunctional electrocatalyst for oxygen reduction and oxygen evolution reactions. *Nat. Nanotechnol.* 10:444. doi: 10.1038/nnano.2015.48
- Zhao, M., Yuan, K., Wang, Y., Li, G., Guo, J., Gu, L., et al. (2016). Metal-organic frameworks as selectivity regulators for hydrogenation reactions. *Nature* 539:76. doi: 10.1038/nature19763
- Zheng, P., Liu, J., Liu, X., and Jia, K. (2017a). Cross-linked sulfonated poly(arylene ether nitrile)s with high selectivity for proton exchange membranes. *Solid State Ionics* 303, 126–131. doi: 10.1016/j.ssi.2017.03.001
- Zheng, P., Tang, H., Jia, K., and Liu, X. (2015). Novel polyarylene ether nitrile nanofibrous mats with fluorescence and controllable surface morphology. *Mater. Lett.* 156, 32–35. doi: 10.1016/j.matlet.2015.04.117
- Zheng, P., Xu, M., and Liu, X. (2017b). Phthalonitrile-terminated sulfonated poly(arylene ether nitrile)s for direct methanol fuel cells (DMFCs) application. *Ionics* 23, 1035–1041. doi: 10.1007/s11581-016-1969-6
- Zheng, P., Xu, M., Liu, X., and Jia, K. (2017c). Novel cross-linked membrane for direct methanol fuel cell application: sulfonated poly (ether ether nitrile) s. *Ionics* 23, 87–94. doi: 10.1007/s11581-016-1805-z
- Zheng, P., Xu, M., Liu, X., and Jia, K. (2018). Sulfonated poly(arylene ether nitrile)s containing cross-linkable nitrile groups for proton exchange membranes. *Solid State Ionics* 316, 110–117. doi: 10.1016/j.ssi.2018.01.002

**Conflict of Interest:** The authors declare that the research was conducted in the absence of any commercial or financial relationships that could be construed as a potential conflict of interest.

Copyright © 2020 Zheng, Liu, Wang, Li, Meng and Zheng. This is an open-access article distributed under the terms of the Creative Commons Attribution License (CC BY). The use, distribution or reproduction in other forums is permitted, provided the original author(s) and the copyright owner(s) are credited and that the original publication in this journal is cited, in accordance with accepted academic practice. No use, distribution or reproduction is permitted which does not comply with these terms.



# Wet-Spun Trojan Horse Cell Constructs for Engineering Muscle

Anita F. Quigley<sup>1,2,3†</sup>, Rhys Cornock<sup>1†</sup>, Tharun Mysore<sup>4</sup>, Javad Foroughi<sup>1</sup>, Magdalena Kita<sup>1,2</sup>, Joselito M. Razal<sup>5</sup>, Jeremy Crook<sup>1,6,7</sup>, Simon E. Moulton<sup>8</sup>, Gordon G. Wallace<sup>1\*</sup> and Robert M. I. Kapsa<sup>1,2,3\*</sup>

<sup>1</sup> ARC Centre for Electromaterials Science, Intelligent Polymer Research Institute, University of Wollongong, Fairy Meadow, NSW, Australia, <sup>2</sup> Centre for Clinical Neurosciences and Neurological Research, St. Vincent's Hospital Melbourne, Fitzroy, VIC, Australia, <sup>3</sup> School of Engineering, Royal Melbourne Institute of Technology, Melbourne, VIC, Australia, <sup>4</sup> School of Medicine and Faculty of Health, Deakin University, Waurn Ponds, VIC, Australia, <sup>5</sup> Institute for Frontier Materials, Deakin University, Waurn Ponds, VIC, Australia, <sup>6</sup> Illawarra Health and Medical Research Institute, University of Wollongong, Wollongong, NSW, Australia, <sup>7</sup> Department of Surgery, St Vincent's Hospital, The University of Melbourne, Fitzroy, VIC, Australia, <sup>8</sup> Department of Biomedical Engineering, Faculty of Science, Engineering and Technology, Swinburne University of Technology, Hawthorn, VIC, Australia

## OPEN ACCESS

### Edited by:

Giuseppe Mensitieri,  
University of Naples Federico II, Italy

### Reviewed by:

Rui Miranda Guedes,  
University of Porto, Portugal  
Marino Lavorgna,  
Institute of Polymers, Composite and  
Biomaterials, Italian National Research  
Council, Italy

### \*Correspondence:

Robert M. I. Kapsa  
rmik@unimelb.edu.au  
Gordon G. Wallace  
gwallace@uow.edu.au

<sup>†</sup>These authors share first authorship

### Specialty section:

This article was submitted to  
Polymer Chemistry,  
a section of the journal  
Frontiers in Chemistry

Received: 01 March 2019

Accepted: 08 January 2020

Published: 20 February 2020

### Citation:

Quigley AF, Cornock R, Mysore T,  
Foroughi J, Kita M, Razal JM, Crook J,  
Moulton SE, Wallace GG and  
Kapsa RMI (2020) Wet-Spun Trojan  
Horse Cell Constructs for Engineering  
Muscle. *Front. Chem.* 8:18.  
doi: 10.3389/fchem.2020.00018

Engineering of 3D regenerative skeletal muscle tissue constructs (skMTCs) using hydrogels containing muscle precursor cells (MPCs) is of potential benefit for repairing Volumetric Muscle Loss (VML) arising from trauma (e.g., road/industrial accident, war injury) or for restoration of functional muscle mass in disease (e.g., Muscular Dystrophy, muscle atrophy). Additive Biofabrication (AdBiofab) technologies make possible fabrication of 3D regenerative skMTCs that can be tailored to specific delivery requirements of VML or functional muscle restoration. Whilst 3D printing is useful for printing constructs of many tissue types, the necessity of a balanced compromise between cell type, required construct size and material/fabrication process cyto-compatibility can make the choice of 3D printing a secondary alternative to other biofabrication methods such as wet-spinning. Alternatively, wet-spinning is more amenable to formation of fibers rather than (small) layered 3D-Printed constructs. This study describes the fabrication of biosynthetic alginate fibers containing MPCs and their use for delivery of dystrophin-expressing cells to dystrophic muscle in the *mdx* mouse model of Duchenne Muscular Dystrophy (DMD) compared to poly(DL-lactic-co-glycolic acid) copolymer (PLA:PLGA) topically-seeded with myoblasts. In addition, this study introduces a novel method by which to create 3D layered wet-spun alginate skMTCs for bulk mass delivery of MPCs to VML lesions. As such, this work introduces the concept of “Trojan Horse” Fiber MTCs (TH-fMTCs) and 3d Mesh-MTCs (TH-mMTCs) for delivery of regenerative MPCs to diseased and damaged muscle, respectively.

**Keywords:** alginate fibers, myoblasts, wet-spun, muscle engineering, biosynthetic muscle scaffold

## INTRODUCTION

In absence of effective pharmaceutical treatments for the long-term functional restoration of muscle tissue mass or function lost due to disease or trauma, numerous cell-based strategies have emerged to improve regenerative outcomes in damaged and dysfunctional skeletal muscle (Emery, 2002). These strategies include myoblast transfer therapies, growth factor delivery, stem cell delivery, gene therapy, and combinations of each (Emery, 2002; Mendell et al., 2010; Gombotz and Wee, 2012; Proto and Huard, 2013).



While skeletal muscle is a regenerative tissue by comparison with other soft tissues, regeneration is dependent on the activation of a pool of satellite cells (SCs) from their quiescent state, and in the case of larger traumas or degenerative disease, this process is hindered, and medical intervention is required. The function of the SCs is to initiate (in the response to major injury) cell-based myoregeneration by proliferative differentiation of muscle precursors that eventually fuse into multi-nucleated myotubes, forming functional myofibers whilst retaining a myoregenerative muscle precursor cell (MPC) niche (Proto and Huard, 2013).

In degenerative myopathies such as the muscular dystrophies, regenerative MPC loss occurs more rapidly than in non-dystrophic muscle due to progressive myofiber degeneration and removal from the functional niche. This places excessive demand on the regenerative MPC pool to replace the lost muscle fibers until the MPC pool is exhausted. This regenerative/functional niche dynamic underpins the progressive skeletal muscle weakness and volume loss characteristic to the disease. By example, the X-linked congenital Duchenne's Muscular Dystrophy (DMD), is caused by mutation of the gene encoding the cytoskeletal protein dystrophin results in a lack of functional dystrophin (Mendell et al., 2010), resulting in membrane destabilization and loss of muscle tissue (Blake et al., 2002). This dystrophic process can be ameliorated by implantation of dystrophin-expressing donor cells that fuse with the host muscle and provide functional dystrophin. However, past attempts at Myoblast Transplantation Therapy (MTT) have had mixed success in dystrophic *mdx* mice but failed in humans due to factors including (i) limited migration of the cells from the injection site, (ii) immune rejection of the cells by the host muscle, and (iii) general high-level post-implant cell death. Corrective gene editing (cGE) Strategies have been designed and successfully applied for editing out the dystrophin gene mutation *in vitro* and *in vivo* (Kapsa et al., 2001, 2003; Wong et al., 2005; Bengtsson et al., 2017). These facilitate the possibility of providing autologous myoregenerative cells with corrected dystrophin loci to restore non-dystrophic functional/myoregenerative niche dynamics in dystrophic muscle provided that cells can be effectively delivered to the dystrophic muscle. In the case of volumetric muscle loss (VML) injury, the situation is similarly dependent on cell delivery/matrix technology that allows for myoregenerative activity to be successfully localized to the VML lesion.

To be of clinical benefit, transplanted myoblasts must either fuse with the host myofibers to or form *de novo* skeletal muscle via fusion of the donor cells (Skuk et al., 2004, 2006, 2011). The current "gold-standard" methodology for introduction of regenerative cells to muscle involves Bolus injection. This is of limited efficacy due to failure of donor cells to engraft away from the injection site, as well as immune reaction toward the donor cells (Skuk et al., 2004, 2006, 2011). This technique has been attempted for the delivery of myoblast transfers and stem cell doses to diseased muscle, and in many cases, studies have used alginate as a protecting hydrogel for the donor cells (Borselli et al., 2011). Other studies have examined the use of thermoplastic implantable fiber structures which exploit their

linear nature in aiding the alignment of transplanted myoblasts to encourage myogenesis and eliminate difficulties with dystrophin localization (Razal et al., 2009).

Alginate is an abundant, naturally occurring anionic polysaccharide, harvested from marine brown algae or less commonly, from bacterial sources (Augst et al., 2006; Dragnet and Taylor, 2009; Lee and Mooney, 2012). It is a co-polymer consisting of (1-4)-linked  $\beta$ -D-mannuronate (M) and its C-5 epimer  $\alpha$ -L-guluronate (G) residues, covalently linked together in varying sequences or blocks, typically homopolymer blocks and poly-alternating sequence blocks (e.g., GGGG, MMMM, and GMGM). Due to its biocompatibility, low toxicity and almost temperature independent gelation in the presence of divalent cations, alginate has been the subject of extensive investigation in wound healing roles, in the transplantation of cells, and in the delivery of pharmaceuticals and immobilized bioactive agents (Gombotz and Wee, 2012; Lee and Mooney, 2012; Falzarano et al., 2013).

Current high-level complexity possible in material design of medical alginate structures has revived exploration into biofabrication techniques for implantable alginate/cell construct technologies. Several additive assembly techniques such as nanofibrous electrospinning, microbead encapsulation, wet-spinning, casting, and bioplotting or 3D printing have each been studied as a means of encapsulating cells within alginate constructs. Of these processes, wet-spinning is desirable due to its high throughput for fiber production and as the output mimics the linear geometric characteristics of native muscle. Furthermore, wet spinning allows for bio-functional components (including cells) to be deposited, woven or knitted into defined structures with minimal effect to biological function (Chen et al., 2009). In addition as with other additive biofabrication technologies such as 3D printing, wet spinning facilitates the precise placement within and release of bio-factors from fibers, enabling more effective and reproducible fabrication of functionally defined devices and structures (De Ruijter et al., 2006; Mironov et al., 2009). Control of the processing parameters during the fabrication of wet-spun fibers, such as (in the case of alginates) the coagulation or non-solvent bath concentration, the feedstock character and concentration and draw rate (injection speed/collection spindle speed), can be used to tune the throughput, porosity, and consistency of the generated fibers (Qin, 2008; Peng et al., 2012).

Earlier studies by others (Hill et al., 2006; Borselli et al., 2011), confirmed Alginate as being useful for delivery of regenerative cells to muscle injury sites through compliance with base requirements for successful re-engineering of damaged muscle (Lee and Mooney, 2012). However, these studies applied cell-laden alginate structures in "patch" formats covering VML injuries to replace bulk muscle, but did not apply Alginate as an intramuscular implant to restore dystrophin expression to dystrophin-negative muscle.

This study applies Cell-laden Alginate "Trojan Horse" structures implanted into dystrophic *mdx* mouse gastrocnemius muscles to evaluate their potential to remodel dystrophic muscle with dystrophin-expressing cells. In particular, this study presents an optimized alginate/myoblast wet-spinning protocol

alternative to 3D bioprinting. This protocol allows high-viability encapsulation of muscle precursor cells (MPCs) within well-characterized alginates as biocompatible fibers to form Trojan Horse fiber muscle tissue constructs (fMTC) that hide the introduced regenerative cells from host immune response. These Trojan Horse fMTCs (TH-fMTCs) containing transgenic wild type (i.e., non-dystrophic)  $\beta$ -Galactosidase-expressing mouse myoblasts encapsulated within alginate fiber carriers, were implanted into dystrophic (*mdx*) mouse muscle (mouse model of DMD). This method of cell encapsulation within an alginate hydrogel was compared to implantation of poly(DL-lactic-co-glycolic acid) copolymer (PLA:PLGA) topically-seeded with myoblasts or cells implanted by themselves as a cell bolus. Applicability of the TH-fMTCs to replacement of bulk muscle for VML injury was then further explored by in-process assembly of TH-fMTCs into 3D Trojan Horse Mesh-MTC (TH-mMTC) scaffolds using an additive wet-spinning approach.

## MATERIALS AND METHODS

### Materials

A buffer solution of 4-(2-hydroxyethyl)-1-piperazineethane sulfonic acid (HEPES, Biochemical, #L505388) was made up to a concentration of 308 mM in a 20 mM sodium chloride (NaCl) solution. Alginic acid with sodium salt (Sigma, #035K0205) was made to concentrations of 2 and 4% (wt/v) utilizing an appropriate volume of distilled and autoclaved water at 60°C with stirring. Primary myoblasts were grown to 80% confluence in a series of 30 T-75 flasks in 20 ml of Dulbecco's Modified Eagle's Medium (DMEM) at 37°C. The cells were then trypsinised and centrifuged at 280 g for 2 min to pellet the cells. The cells were then resuspended in HEPES solution to concentrations of 20, 40, and 60 million cells/ml. Mixing with corresponding alginate solutions resulted in cell concentrations of 10, 20, and 30 million cells/ml for both 1 and 2% (wt/v) alginate concentration.

### Feedstock (Spinning Dope) Preparation

Alginate feedstocks containing no cells were made for myoblast-loaded feedstocks: A buffer solution of 4-(2-hydroxyethyl)-1-piperazineethanesulfonic acid (HEPES, Biochemical, #L505388) was made up to a concentration of 308 in a 20 mM sodium chloride (NaCl) solution. Alginate solutions were made to concentrations of 2 and 4% (wt/v) utilizing an appropriate volume of deionized and autoclaved water at 60°C with stirring.

Cultured donor C57BL/10ScSn <sup>$\beta$ -Gal</sup>/SVHM (C57/BL10) <sup>$\beta$ -Gal</sup>; wild-type- $\beta$ Gal; *wt*- $\beta$ Gal) mouse myoblasts were grown to 80% confluence in 20 ml of Dulbecco's Modified Eagle's Medium (DMEM) at 37°C in a series of 30 T-75 flasks. The cells were then trypsinised and centrifuged at 2,200 rpm for 2 min to pellet the cells. The cells were then resuspended in HEPES solution to concentrations of 20, 40, and 60 million cells/ml. Mixing with corresponding alginate solutions resulted in cell concentrations of 10, 20, and 30 million cells/ml for both 1 and 2% (wt/v) alginate concentrations.

### Donor Myoblast Cell Preparation

Male C57BL/10ScSn <sup>$\beta$ -Gal</sup>/SVHM mice, 5–6 week of age were obtained (Bioresources Center, St. Vincent's Hospital,

Melbourne, Australia), exposed to a 12 h day/night cycle and fed *ad-libitum* until they were required for muscle culture. All animal handling aspects of this study were carried out in accordance with the recommendations of the Australian Code of Practice for the Care of Animals for Scientific Purposes (NHMRC) as outlined in protocol SVHM86/06 and approved by the St. Vincent's Hospital Animal Ethics Committee. After cervical dislocation, skeletal muscle was removed from the hind limbs of the mice and primary myoblast cultures prepared as described elsewhere (Todaro et al., 2007).

Briefly, the muscle tissue was finely minced using scissors and digested with 10 mg ml<sup>-1</sup> Collagenase D (Roche), 2.4 U ml<sup>-1</sup> Dispase II (Roche), and 2.5 mM CaCl<sub>2</sub> for 2 h. The muscle slurry was filtered through 70 and 40  $\mu$ m filters, respectively. Red blood cells were lysed by 5 min, room temperature incubation with 17 mM tris(hydroxymethyl)aminomethane and 144 mM ammonium chloride. The myoblast cultures were preplated once for 20 min, once for 40 min, once for 2 h, and then at 24 h intervals for the next 4 days in proliferation medium consisting of Hams/F10 (TRACE) supplemented with 20% fetal bovine serum (Invitrogen), 2.5 ng ml<sup>-1</sup> bFGF (PeproTech Asia), 2 mM L-glutamine (Invitrogen), 100 U ml<sup>-1</sup> of penicillin (Invitrogen), and 100 mg ml<sup>-1</sup> streptomycin (Invitrogen). Adherent myoblasts at preplate 9 were cultured in proliferation medium at 37°C and 5% CO<sub>2</sub> and passaged at >80% confluence.

### Wet Spinning

A wet spinning arrangement as shown in **Figures 1A,B** was used to fabricate cell-impregnated poly(DL-lactic-co-glycolic acid) copolymer (PLA:PLGA) (**Figures 1D,E**) and alginate (**Figure 1F**) Trojan Horse fibers. The unit consists of a digitally controlled, four-beam stainless steel spindle, with outermost diameter of 40 mm, and a second controller with a piston for directed fiber output along a single axis.

For wet spinning cell-containing Alginate fibers, an aqueous coagulation bath (L = 1 m) of 2% calcium chloride (Sigma, #48H0106) was used for cross-linking the fibers. Myoblasts were encapsulated in Pronova ultra-pure low viscosity, high guluronate sodium alginate (20–200 mPa.s for 2% w/w solution at 25°C, >60%G, *ca.* 75–200 kDa) obtained from Novamatrix for all *in vitro* and *in vivo* experiments.

Prior to encapsulation, myoblasts were suspended in 2 x cell buffer (300 mM NaCl, 20 mM HEPES) at a concentration of 60  $\times$  10<sup>6</sup>, 40  $\times$  10<sup>6</sup>, or 20  $\times$  10<sup>6</sup> cells/ml. Cells were then mixed with an equal volume of alginate solution (2 or 4% w/v in sterile RO H<sub>2</sub>O) resulting in final cell concentrations of 30, 20, and 10  $\times$  10<sup>6</sup> cells/ml in 1 or 2% alginate. The alginate/cell mixtures were extruded into a coagulation bath using a high precision KD Scientific KDS-410 constant volume syringe pump at a rate of 0.03 ml min<sup>-1</sup>. A 30G EFD Nordson A rotating drum was operated at a fixed velocity of 2 cm s<sup>-1</sup> for the collection of fibers following coagulation. The collected fibers were immediately transferred to a solution of 154 mM HEPES and 10 mM NaCl to avoid drying and cell damage.

For PLA:PLGA fibers, the same apparatus was used with the modification that 20 wt % 75:25 PLA:PLGA (110,000 MW; 0.71 i.v.) suspended in chloroform was coagulated (and washed) in isopropanol baths. The spinning solution

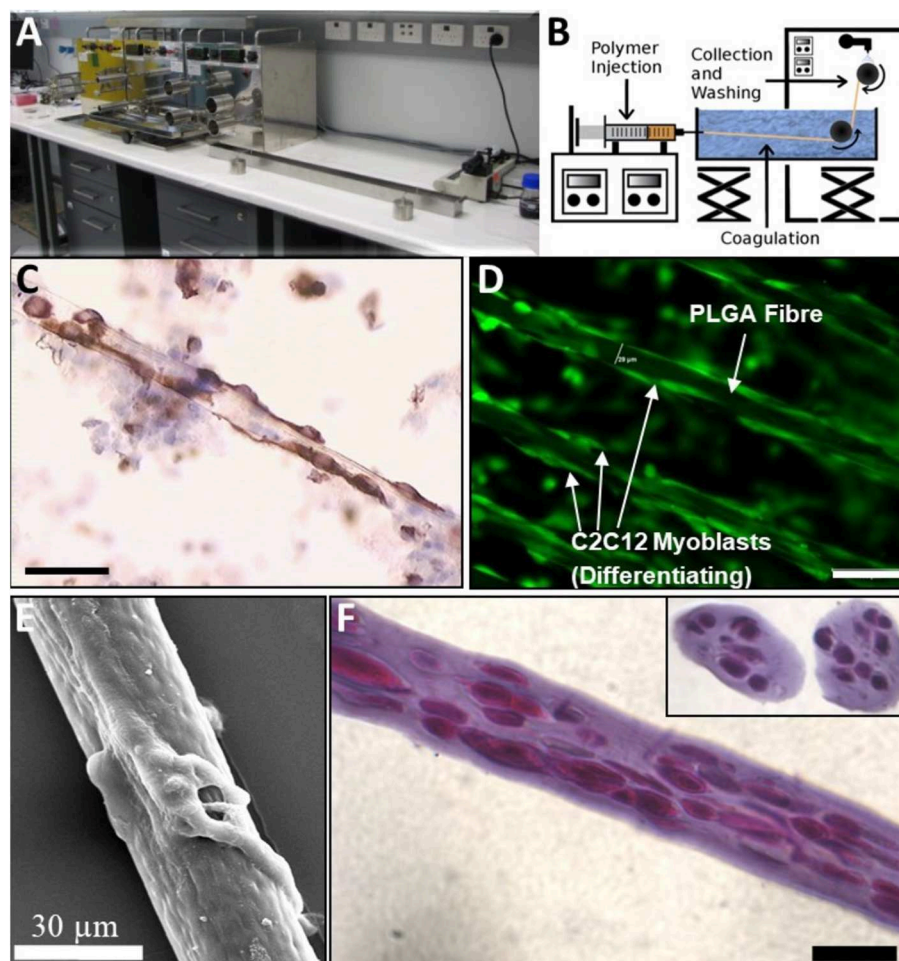


**FIGURE 1 |** Wet-Spinning BioSynthetic Myoblast Fibers (PLGA and Alginate): Comparison of native Muscle, PLGA and “Trojan Horse” Alginate Fibers. **(A)** Apparatus. **(B)** Line Schematic. **(C)** Native Muscle Fibers and myoblasts immunostained with Desmin: early culture. **(D)** PLGA Fibers with myoblasts and myotubes attached externally (immunostained with Desmin). **(E)** SEM of PLGA fiber with myotubes attached. Myoblasts on the PLGA fibers were seen to spread and differentiate longitudinally without evidence of retained proliferative capacity under differentiation conditions *in vitro*. **(F)** 1% Alg Trojan Horse Fibers with  $2 \times 10^7$  myoblasts/ml (longitudinal and cross sections inset, Hematoxylin and Eosin). Unless otherwise specified, size calibration markers are 100  $\mu\text{m}$ .

injection and fiber collection rates were held, respectively, to 1.8 ml/h and 8.5 m/min as described elsewhere (Razal et al., 2009). The resulting fibers were seeded with myoblasts 48 h in Hams/F10 (TRACE) supplemented with 20% fetal bovine serum (Invitrogen),  $2.5 \text{ ng ml}^{-1}$  bFGF (PeproTech Asia), 2 mM L-glutamine (Invitrogen),  $100 \text{ U ml}^{-1}$  of penicillin (Invitrogen), and  $100 \text{ mg ml}^{-1}$  streptomycin (Invitrogen) before they were implanted into mouse muscle.

To populate the PLGA fibers with cells, MPCs were grown *ex vivo* on the PLGA fibers as described elsewhere (Razal et al., 2009) for 7 days at which point they were detached from the substrate for implantation into recipient *mdx* and *wt* mouse muscle.

### Analysis of Biosynthetic Trojan Horse Fiber Muscle Tissue Constructs (TH-fMTCs)

For viability and characterization, cell-bearing alginate biofibres were collected into HEPES containing  $1 \mu\text{M}$  calcein AM in DMSO and  $1 \mu\text{g ml}^{-1}$  of propidium iodide (PI). An Olympus

IX70 fluorescence microscope was used at  $10\times$  magnification to visualize fibers with varying cell densities (Figures 2A–C) and to establish optimal Alginate concentration (Figure 2D) and cell density (Figure 2E) for the alginate-based TH-fMTCs.

For quantification of DNA content within the fibers, a PicoGreen assay was used. For each subgroup, five sets of twenty 10 mm fibers were added to a microfuge tube containing 100  $\mu\text{L}$  0.1% wt  $\text{v}^{-1}$  Triton-X in PBS solution. For cryo-sectioning, samples of fibers were embedded into Tissue-Tek Optimal Cutting Temperature Compound and placed into a slurry of dry ice and ethanol. These were stored at  $-70^\circ\text{C}$  before being sectioned using a LEICA CM1900 Rapid Sectioning Cryostat.

In all analyses, four independent synthesis experiments were evaluated to confirm/otherwise the repeatability of the fabrication process. Finally, several fibers were collected into both proliferation and differentiation media for visualization of cell placement within the fibers and to establish biomimetic support of key pro-myoregenerative behavior (proliferation,



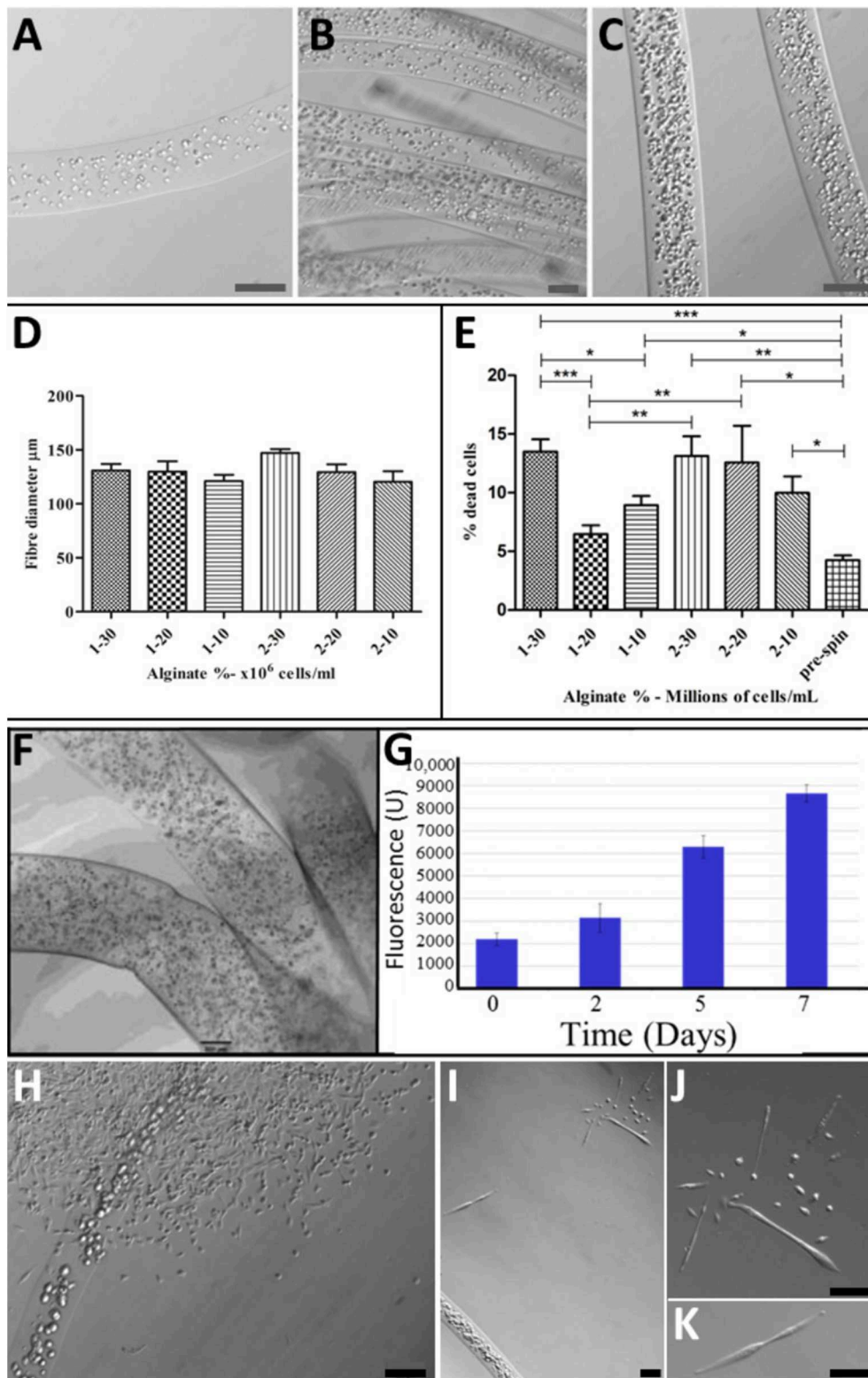


**FIGURE 2 |** Optimization of BioSynthetic Alginate/Myoblast Trojan Horse Constructs for Implantation: Alg Fibers with: (A)  $1 \times 10^7$  cells/ml; (B)  $2 \times 10^7$  Cells/ml; (C)  $3 \times 10^7$  Cells/ml; (D) Controlled and consistent fiber diameter regardless of cell numbers or alginate concentration was achieved, with no statistical differences evident between syntheses (*t*-test). (E) Cell Death (%Dead Cells) was evaluated in 1 and 2% alginate fibers loaded with 1, 2, and  $3 \times 10^7$  Cells/ml to establish optimal (Continued)



**FIGURE 2 |** alginate/cell combination as evident by post-spun cell viability. A maximum of ~15% of cells died as a result of wet-spinning in 1 and 2% alginate loaded with  $3 \times 10^7$  Cells/ml and in biosynthetic fiber constructs of 2% alginate loaded with  $2 \times 10^7$  Cells/ml. This evaluation showed that 1% Alg/2  $\times 10^7$  Cells/ml resulted in the least numbers of cells entering programmed cell death as a result of the wet-spinning process. Statistical-significance markers for student *t* statistics shown are as follows: \**p* < 0.05; \*\**p* < 0.01; \*\*\**p* < 0.005. (F) Cells disperse inside the BioSynthetic 1% Alginate/2  $\times 10^7$  myoblasts/ml Trojan Horse constructs *in vitro*, where they (G) Proliferate freely until they (H) Migrate from the constructs into the surrounding environment and (I–K) Differentiate normally according to biological cues within the environment. This biological behavior *in vitro* models the cell delivery dynamic expected when the cell-loaded alginate-based Trojan Horse constructs are implanted into muscle. Unless otherwise specified, size calibration bars are 100  $\mu$ m. Optimization of PLGA/Cell fibers was limited to seeding cells on fibers at optimal *ex vivo* cell plating density immediately prior to implantation. Unless otherwise specified, size calibration bars are 100  $\mu$ m.

differentiation and migratory capabilities) of the cells encapsulated within the alginate fMTCs (Figures 2G–K).

## Surgical Implantation of Trojan Horse Fibers and Cell Bolus Into *mdx* and *wt* Muscle

C57BL/10ScSn/Arc (wild-type; *wt*) and C57BL/10ScSn-Dmd<sup>mdx</sup>/Arc (X-Linked Muscular Dystrophy) male mice, 8–9 weeks of age were obtained from Animal Resources Center, WA, exposed to a 12h day/night cycle and fed *ad-libitum* until they were required for surgery. All animal handling was performed according to the St. Vincent's Hospital Animal Ethics Committee protocol 013/11, in accordance with the Australian Code of Practice for the Care of Animals for Scientific Purposes (NHMRC).

All surgical procedures were performed under anesthesia using inhaled isoflurane (1% v/v, 1 L min<sup>-1</sup> O<sub>2</sub>). The hind leg fur was removed by shaving and 10  $\mu$ l of 5  $\mu$ g/ml notexin (Sigma-Aldrich) was injected into the gastrocnemius muscle of both legs. The following day the gastrocnemius muscles were exposed by an incision through the skin. A 3–4 mm deep, 5 mm long incision was made in the muscle parallel to the muscle fibers with a scalpel blade. The incision was teased open with tweezers and 5 mm long cell-laden alginate or PLA:PLGA fibers ( $\sim 5 \times 10^5$  cells) were placed inside (Figure 3A). The muscle was closed by suturing the muscle fascia with a 6/0 silk suture (Dytek) and the skin closed with 9 mm wound clips (Becton Dickinson). All mice received subcutaneous injection of (Carprofen, 5 mg kg<sup>-1</sup>) analgesic post-surgery.

Cell Bolus groups were injected with  $1 \times 10^6$  cells suspended in mouse-tonicity saline after the notexin treatment.

At selected post implantation analysis times, mice were euthanized by cervical dislocation, and gastrocnemius muscles removed. The muscles were snap frozen in liquid nitrogen-cooled 2-methylbutane (Sigma-Aldrich) and stored at -70°C prior to analysis.

Muscles were cryosectioned by cutting 10  $\mu$ m serial cross-sections through the entire length of the specimen to find localization of donor ( $\beta$ Gal<sup>+</sup>) cells.

## Beta-Galactosidase ( $\beta$ Gal) Staining

Cryosections were equilibrated to room temperature and fixed in 0.5% glutaraldehyde in PBS (Sigma-Aldrich) for 5 min at room temperature. Sections were washed in three changes of PBS and staining solution (2.5 mM K<sub>3</sub>Fe(CN)<sub>6</sub>, 2.5 mM K<sub>4</sub>Fe(CN)<sub>6</sub>·3H<sub>2</sub>O, 2 mM MgCl<sub>2</sub>, 1 mg ml<sup>-1</sup> X-Gal, 1 $\times$  PBS pH 7.4) was applied. Sections were incubated overnight at 37°C

in a humidified chamber. At completion of staining sections were washed in two changes of distilled water and mounted in aqueous mounting medium. In some cases, sections were back-stained with Haematoxylin and Eosin as described below (Figures 3B,C,E,F). The specimens were visualized using an Olympus IX-70 fluorescent microscope, and images were taken using Spot Advanced 4.0.9 software.

## Dystrophin Immunofluorescence

Cryosections were equilibrated to room temperature and rinsed in phosphate buffered saline (PBS, pH 7.4). Sections were blocked in 10% v/v donkey serum in PBS for 60 min, then incubated with either rabbit anti-dystrophin antibody (Santa Cruz) at 1:100 dilution in blocking solution for 60 min at 37°C, followed by two washes with PBS. Secondary donkey anti-rabbit Alexa Fluor 488 (Molecular Probes) diluted 1:2,000 in blocking solution was incubated for 60 min at 37°C. After two washes in PBS, nuclei were stained with 1  $\mu$ g ml<sup>-1</sup> DAPI (4,6-diamidino-2-phenylindole dihydrochloride) (Sigma-Aldrich) for 5 min and the specimens mounted in Fluorescence Mounting Media (DAKO). The specimens were visualized using an Olympus IX-70 fluorescent microscope, and images were taken using Spot Advanced 4.0.9 software (Figure 3D). Dystrophin positive fibers were counted for PLGA (*n* = 5) and Alginate (*n* = 5) Trojan Horse constructs as well as for cells injected as a cell Bolus (*n* = 4) as shown in Figure 3G.

## Hematoxylin and Eosin Staining

Cryosections were equilibrated to room temperature and fixed in 10% Formalin (Sigma-Aldrich) for 5 min at room temperature. Sections were washed in tap water, stained with Gills' Hematoxylin (Sigma-Aldrich) for 30 s, rinsed in 30 immersions into tap water (water changes every 10 immersions), stained in Alcoholic Eosin Y (Sigma-Aldrich) with 2 immersions, rinsed in 30 immersions of tap water (3 water changes), dehydrated in three changes of 100% ethanol and cleared in xylene. Sections were mounted in DPX. The specimens were visualized using an Olympus IX-70 fluorescent microscope, and images were taken using Spot Advanced 4.0.9 software.

## RESULTS

The fabrication process (Figures 1A,B) of PLGA (Figures 1D,E) and alginate (Figure 1F) Trojan Horse fibers containing myoblasts and subsequent biological viability of these fibers were optimized *in vitro* by analysis of process parameters: PLGA fibers were maximally over-grown with myoblasts immediately prior

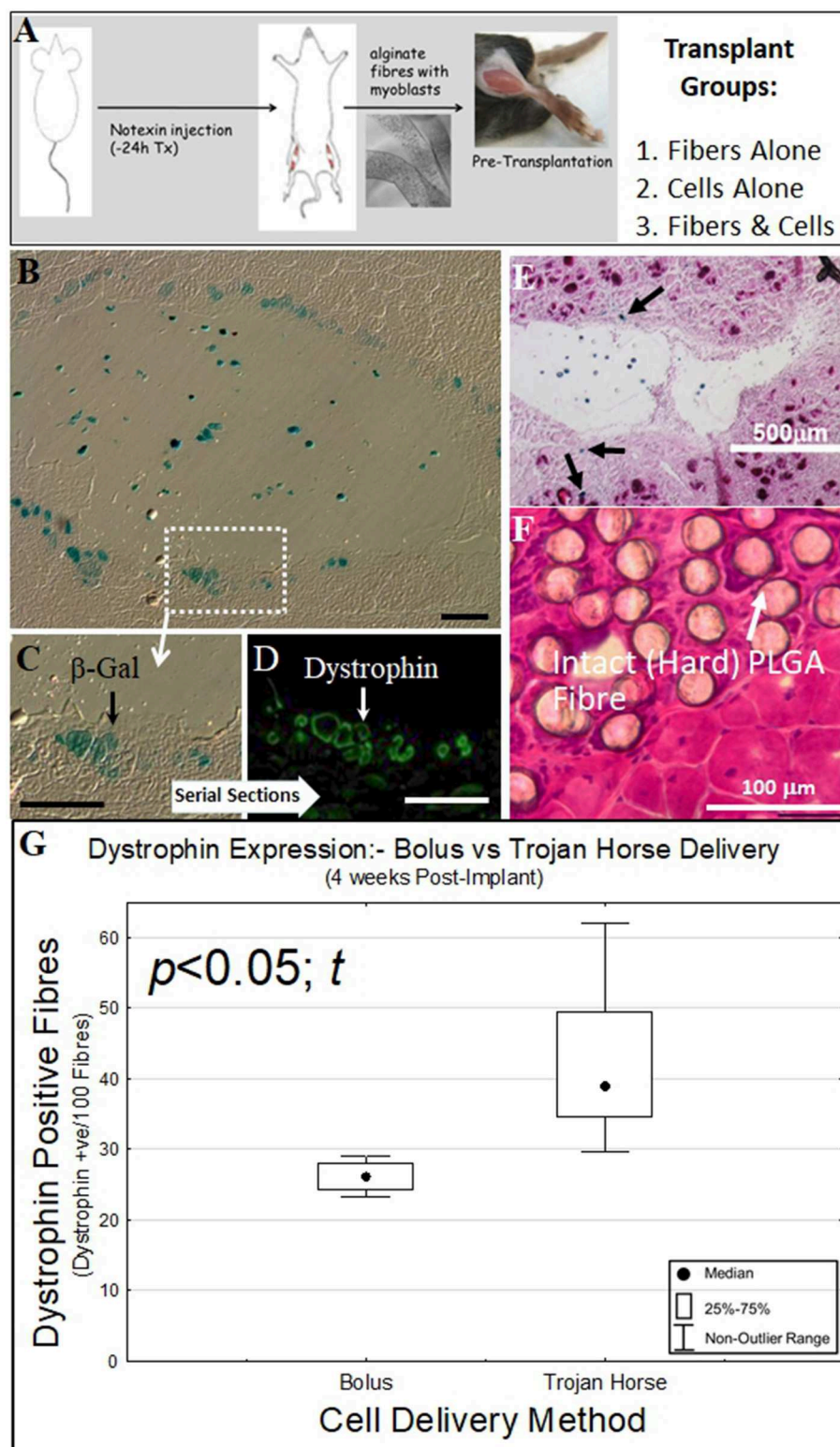


**FIGURE 3 |** Biosynthetic PLGA and alginate fiber and cell bolus implantation into dystrophic and damaged mouse muscle. **(A)** Experimental schematic for implantation of biosynthetic cell/fiber constructs containing dystrophin and  $\beta$ -Galactosidase-expressing C57BL10/ $\beta$ -Gal mouse myoblasts into *mdx* and C57BL10J mouse muscle. **(B)** Biosynthetic 1% Alginate Trojan Horse Fibers loaded with  $\beta$ -Gal transgenic C57BL10/ $\beta$ -Gal myoblasts ( $3 \times 10^6$  c/ml) were transplanted into dystrophic C57BL10-*mdx* mouse (muscular dystrophy) muscle showed that donor cells that migrated into the surrounding muscle expressed both (blue)  $\beta$ -Gal

(Continued)

**FIGURE 3 | (C)** As well as (green) dystrophin **(D)** in the dystrophic *mdx* host muscle. **(E)** This behavior also occurred in non-dystrophic muscle, with  $\beta$ -Gal-positive cells evident within the Trojan Horse construct and in fibers (Eosin/ $\beta$ -Gal-stained) of the surrounding muscle. **(F)** Myoblasts implanted on PLGA fibers did not survive and the PLGA fibers were still intact within the recipient muscle at 4 weeks post-implantation, with the PLGA fibers remaining hard (H&E stain). This was evident even at 3 months post implant. **(G)** Alginate Trojan Horse constructs yielded demonstrably more effective re-modeling of recipient dystrophic muscle with dystrophin-expressing cells ( $p < 0.05$ ;  $t$ ) than either cell bolus or cells implanted on PLGA fibers. PLGA fibers implanted with cells attached yielded no donor cells engrafted into the host muscle tissue at this timepoint (data not shown) and were discounted from further consideration as a cell delivery vehicle. Unless otherwise specified, size calibration bars are 100  $\mu$ m.

to further studies, whilst evaluation of alginate concentration and cell-loading parameters reproducibly yielded 1% and 2% alginate fibers containing large numbers of cells. PLGA/myoblast constructs required no further evaluation/optimization. Cell numbers in alginate Trojan Horse Fiber Mus were controlled by material feed rate and handling methods, reliably yielding fibers that contained between 1 and  $3 \times 10^7$  cells (**Figures 2A–C**). The fiber diameter was able to be controlled likewise via material feed rate, to between  $\sim 130$  and  $150 \mu$ m, with an average diameter of  $125 \mu$ m regardless of incorporated cell loading density or alginate (w/v) concentration (**Figure 2D**).

Cell loading density was evaluated by extraction of DNA from the synthetic bio-fibers and quantification using PicoGreen assay for nucleic acids and was shown to increase accordingly with cell numbers suspended within the originating alginate solution. Of the six configurations evaluated, cell viability (based on PI infiltration assay) with respect to cell loading and percentage (w/v) Alg, was highest in fiber configurations of 1% alginate containing 20 million cells/ml ( $96 \pm 1\%$ ) (**Figure 2E**). These fibers were taken as optimal synthetic bio-fibers for subsequent experiments. Fibers produced using 2% alginate as a matrix material, while displaying similar fiber diameters, demonstrated a lower cell viability and consistency compared to correspondingly cell-loaded 1% alginate fibers (**Figure 2E**).

The synthetic Trojan Horse bio-fibers were modeled in the first instance on native muscle fiber/myoblast structures observed in early primary culture stages (**Figure 1C**) and compared to PLGA/myoblast fiber constructs (**Figures 1D,E**) as possible structures for regenerative cell delivery into muscle. Histological evaluation of these cell-laden fibers showed that the myoblasts were evenly distributed longitudinally along and cross-dimensionally across the diameter of the alginate fibers (**Figure 1F**), whilst the PLA:PLGA fibers (**Figure 1D**) showed distinct similarity to native fiber explants (**Figure 1C**).

To see if these constructs could be used to deliver functional cells to muscle tissues, optimized biosynthetic fiber constructs containing transgenic C57BL10J- $\beta$ Gal mouse myoblasts in alginate or on PLA:PLGA fibers were prepared for implantation into mouse muscle (**Figure 3A**): Synthetic (alginate) bio-fibers of  $\sim 500 \mu$ m diameter were wet-spun using 1% alginate and myoblasts at a density of  $3 \times 10^5$  cells/ml derived from non-dystrophic,  $\beta$ -Gal-expressing C57BL10J-ScSn <sup>$\beta$ Gal</sup> mice (**Figure 2F**). Well below the  $20 \times 10^6$  cells/ml viability threshold for 1% alginate fibers (**Figure 2E**), this low cell density facilitated reliable inclusion of  $\sim 3,000$  cells per 5 mm fiber implant for (quantitative) tracking of post-transplantation cell fate within the recipient muscle tissue. The use of the C57BL10J- $\beta$ Gal mouse myoblasts provided an allogeneic donor cell source

that facilitated post-implantation tracking of implanted cells' localization via the  $\beta$ Gal transgene whilst the larger diameter facilitated manageability of handling during surgery.

PLA:PLGA fibers of  $\sim 130 \mu$ m diameter were likewise seeded with C57BL10J- $\beta$ Gal mouse myoblasts as previously described, for implantation into the recipient *mdx* mouse muscle.

Prior to implantation, the synthetic alginate bio-fibers' cell-loading and viability were confirmed by microscopy (**Figure 2E**) and the integrated cells' ability to proliferate within the fibers was confirmed over 7 days' culture *in vitro*. This established that myoblasts embedded in the alginate fibers could be expanded to at least four-fold the original cell numbers over 7 days (**Figure 2G**) to attain required cell numbers if necessary. The myoblasts displayed the ability to migrate from the alginate fibers and to proliferate (**Figure 2H**) and differentiate (**Figures 2I–K**) within the *in vitro* culture environment, a precursor indication of the fibers constructs' expected biological behavior when implanted into muscle. Likewise for the PLA:PLGA fibers (**Figure 1D**). Cells seeded on PLA:PLGA fibers likewise retained proliferative and migration abilities *in vitro* (data not shown).

The bio-synthetic constructs (5 mm in length) were surgically implanted into notexin myo-ablated gastrocnemius muscles of C57BL10J ScSn (*wt*) and C57BL10J ScSn<sup>*DMD*</sup> (*mdx*) mice. These fibers were left in the recipient mouse muscles for 1 and 2 weeks, respectively, after which the mice were euthanized and the tissues harvested for analysis of (i) cell survival within the constructs, (ii) cell migration from the constructs into the host muscle, and (iii) ability to remodel the host muscle with regenerative muscle fibers derived from the donor cells.

Donor cells implanted in alginate Trojan Horse fMTCs into both *mdx* (**Figure 3D**) and C57BL10J non-dystrophic (**Figure 3E**) mouse muscles survived within the host tissue 4 and 2 2 and 1 week post implantation, respectively. In both dystrophic and non-dystrophic environments, donor cells were evident both within the boundary of the alginate fiber component in which they had been implanted, as well as within the recipient mouse muscle tissue. Serial sections of the biosynthetic fiber construct-implanted *mdx* muscle showed that expression of the  $\beta$ Gal transgene from the non-dystrophic C57BL10J-ScSn <sup>$\beta$ Gal</sup> derived donor myoblasts (**Figures 3B,C**) corresponded with dystrophin expression from the donor myoblasts within the implanted *mdx* muscle (**Figure 3D**). In addition, there were clear signs that the alginate vehicle used to deliver the cells into the muscle environment had begun to undergo degradation even after 1 week, in stark contrast to PLA:PLGA/myoblast fibers, which were clearly evident as intact in recipient muscle after 12 weeks without cell survival and with significant foreign body response (**Figure 3F**). These results suggest that *in vitro* myoblast



proliferation in, and migration from a biosynthetic alginate/cell construct with subsequent differentiation to muscle fibers within the surrounding environment shown *in vitro* in **Figures 2I–K** translate to cell behavior from within such constructs when implanted into muscle tissue *in vivo*. On the other hand, the lack of cell engraftment into host *mdx* muscle by cells seeded on PLA:PLGA fMTCs indicates that this mode of delivery is unsuitable for delivery of cells to muscle tissues, whilst the alginate Trojan Horse-fMTC delivery method resulted in better engraftment of recipient muscle with donor cells that bolus injection of donor cell mass (**Figure 3G**).

## DISCUSSION

Additive fabrication and assembly of functionalized fibers produced by wet-spinning into implantable three dimensional constructs presents attractive prospects for the field of regenerative medical bionics (Wallace et al., 2012). In particular, the incorporation of biologically active agents including growth factors (Quigley et al., 2013a,b) and living cells (Chung et al., 2013) within biocompatible and macroporous fibers that allow for mass transfer and cell migration, is expected to deliver improvements to cell and drug delivery platforms, particularly in the area of tissue engineering biotechnology (Hong et al., 2006; Lee et al., 2011).

This study investigated application of wet-spinning as an alternative (to 3D printing) additive bio-fabrication technology for generating three-dimensional cell-bearing (encapsulated and topically-seeded) biosynthetic fibers containing live muscle precursor cells (myoblasts) for remodeling damaged and dystrophic muscle.

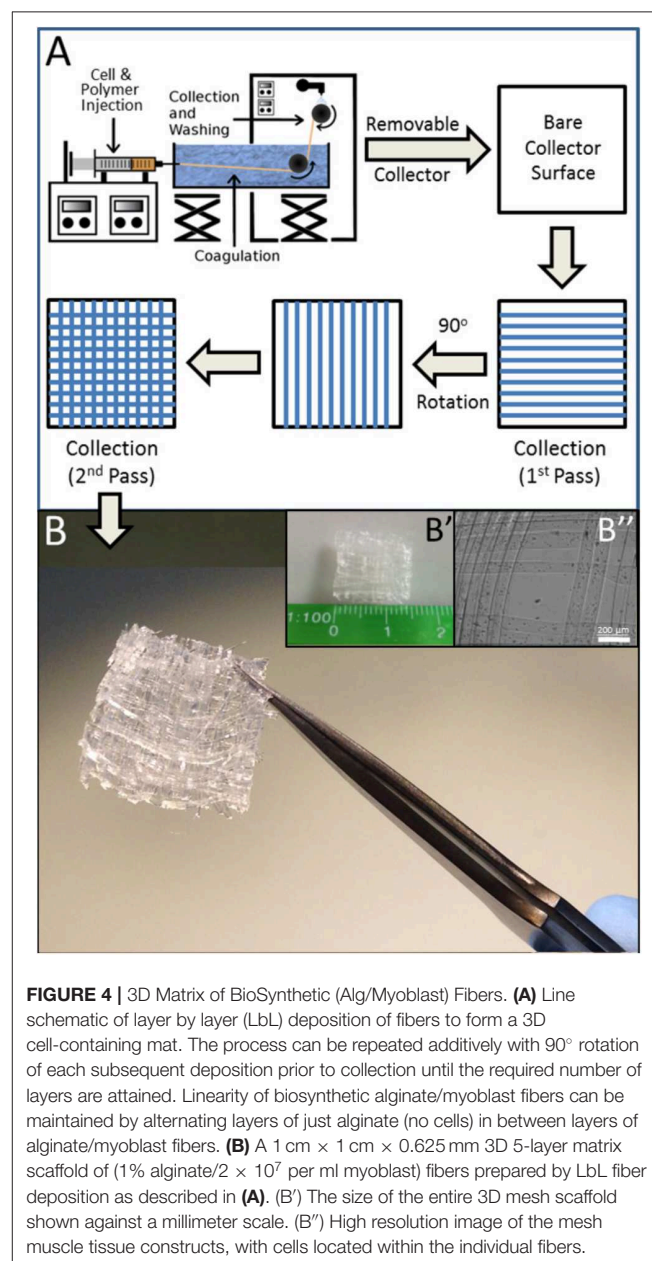
Our previous studies evaluated a cell transplantation approach in which cells can be grown onto wet-spun fibers *ex vivo* for subsequent implantation into muscle tissue as biosynthetic fiber/cell structures. Razal et al. (2009) The cell-bearing fibers from earlier applications using poly(DL-lactic-co-glycolic acid) copolymer (PLA:PLGA) were shown here to be unsuitable muscle remodeling due to prolonged hardness and subsequent stimulation of fibrosis within the implanted muscle.

Subsequently, our long-standing use of sodium alginate (Alg) hydrogel cross-linked with calcium for delivery of myotrophic growth factors (Austin et al., 2000), identified Alg as a suitable material for muscle (i.e., soft tissue) engineering applications. Alg owes its suitability for such applications to its general physical compliance with soft tissue target properties and its permissive degradation profile that elicits minimal inflammatory response and facilitates passive diffusion of oxygen and mass transport (Qin, 2004; Berthiaume and Morgan, 2010).

In contrast to 3D bioprinting, which is somewhat limited to short, usually hatch-like structures, the structural linearity of wet-spun fibers mimics the linear characteristics of native muscle structure. Furthermore, wet spinning allows functional materials to be deposited, woven or knitted into defined structures with minimal disruption of incorporated biological factors' or cells' functional integrity (Chen et al., 2009). Perhaps most importantly, wet spinning affords precise control of placement

and release of factors within and from the fibers, yielding more effective and reproducible fabrication of functionally defined devices and structures (De Ruijter et al., 2006; Mironov et al., 2009).

Further development of the wet-spun fiber/myoblast biosynthetic fiber system described here along these lines stands to deliver a highly defined regenerative cell construct for the repair and remodeling of damaged and diseased muscle that yields superior engraftment compared to bolus-injections of cell mass. In particular, refinement of the alginate component with biofactors (e.g., extracellular matrix and/or growth proteins) (Austin et al., 2000; Lee and Mooney, 2012) and possible pre-conditioning of the cells to specific defined sub-phenotypes will





potentiate the value of these biosynthetic constructs for muscle engineering and repair.

A further point of refinement that better facilitates this system's application to tissue engineering is its translation to a three-dimensional format. Toward this end, the linear collection system outlined in **Figure 1A** was modified to incorporate a layer by layer approach in which fiber collection was periodically discontinued and resumed after a 90° adjustment of the collection axis (**Figure 4A**). In this manner, a 5-layer mat of wet-spun fibers containing cells was readily obtained (**Figure 4B**), demonstrative of further applicability of wet spinning to the construction of 3D myo-regenerative implants for applications of volumetric muscle loss.

Collectively, the wet spinning of cells into biocompatible fibers and subsequent formation of 3D structures from these fibers as described in this study provides a new avenue by which 3D muscle microtissues can be engineered *ex-vivo* for *in vitro* experimentation modeling or for re-engineering injured or diseased muscle. This layer by layer wet-spinning approach mitigates some of the issues such as exposing cells to excessive nozzle pressures evident in formation of such structures using other additive fabrication technologies such as 3D bio-printing.

## CONCLUSION

This work communicates the successful wet spinning of biosynthetic alginate/myoblast Trojan Horse fiber muscle tissue constructs (TH-fMTCs) composed of 1% alginate fibers containing primary myoblasts at high cell concentrations. The cells remained highly viable post-fabrication and it was determined that the most efficient subgroup consisted of a 1% wt/v alginate matrix incorporating a cell concentration of  $2 \times 10^7$  cells  $\text{ml}^{-1}$ . The myoblasts embedded within the alginate fibers were shown to be proliferative *in vitro* and to migrate from the fibers into the surrounding environment, where they were able to undergo appropriate differentiation into myotubes. These regenerative biological behaviors were recapitulated *in vivo* by biosynthetic alginate/myoblast fiber constructs containing primary allogeneic C57BL10J-ScSn<sup>βGal</sup> myoblasts carrying a βGal reporter transgene, implanted into myo-ablated non-dystrophic C57BL10J ScSn (*wt*) and dystrophic C57BL10J ScSn<sup>DMD</sup> (*mdx*) mice. In these experiments, donor cell-derived βGal reporter transgene expression detected in muscle fibers outside of the alginate vehicle both in *mdx* and *wt* mouse muscle, confirmed that some of the donor myoblasts migrated from the biosynthetic fiber constructs, incorporated into the surrounding muscle tissue network and formed donor-derived muscle fibers. Importantly, co-expression of dystrophin (denoting functional, fully differentiated non-dystrophic muscle

fibers normally absent in *mdx* muscle) with βGal in serial sections of the implanted *mdx* muscle highlighted that the biosynthetic alginate/myoblast constructs could remodel dystrophin-negative *mdx* muscle tissue with dystrophin-producing fibers.

In considering the material/cell configuration to be used for remodeling muscle tissue, the biosynthetic alginate/myoblast system reported here resulted in more robust regenerative results than did myoblasts attached to PLA:PLGA fibers, which left intact PLA:PLGA fibers devoid of donor myoblasts even 3 months after implantation. Likewise, the alginate TH-fMTC configuration yielded better engraftment of donor cells than did bolus-injected MPCs. These results suggest that 3D “Trojan Horse” scaffolds composed of biosynthetic soft gel alginate/myoblast fibers present an attractive method by which to promote remodeling of diseased and/or damaged muscle.

## DATA AVAILABILITY STATEMENT

The datasets generated for this study are available on request to corresponding author RK.

## ETHICS STATEMENT

This study was approved by St. Vincent's Hospital Research Animal Ethics Committee Protocol 86/06.

## AUTHOR CONTRIBUTIONS

AQ, RC, TM, MK, and JR performed the experiments. JF, JC, SM, GW, and RK supervised bench experimentation and planned the study. All authors provided intellectual input and collaboratively wrote the manuscript. RK and GW conceived and coordinated the study.

## ACKNOWLEDGMENTS

Equal first co-authorship is acknowledged for AQ and RC, on their equal contribution to the publication of this work. The authors would also like to thank the Australian Research Council (CE140100012) the National Health and Medical Research Council (573430) and the Australian Nano-Fabrication Facility (ANFF) for supporting this work.

## DEDICATION

This work is dedicated to Professors Lawrie Austin and Leon Kane-Maguire, who would have greatly enjoyed working together and whose collective vision led to this work.

## REFERENCES

- Augst, A. D., Kong, H. J., and Mooney, D. J. (2006). Alginate hydrogels as biomaterials. *Macromol. Biosci.* 6:11. doi: 10.1002/mabi.200600069
- Austin, L., Bower, J. J., Bennett, T. M., Lynch, G. S., Kapsa, R., White, J. D., et al. (2000). Leukemia inhibitory factor ameliorates muscle fiber degeneration in the *mdx* mouse. *Muscle Nerve* 23, 1700–1705. doi: 10.1002/1097-4598(200011)23:11<1700::AID-MUS53.0.CO;2-W
- Bengtsson, N. E., Hall, J. K., Odom, G. L., Phelps, M. P., Andrus, C. R., Hawkins, R. D., et al. (2017). Muscle-specific CRISPR/Cas9 dystrophin gene editing ameliorates pathophysiology in a mouse model for Duchenne muscular dystrophy. *Nat. Commun.* 8:14454. doi: 10.1038/ncomms14454

- Berthiaume, F. M., and Morgan, J. (2010). *Methods in Bionengineering: 3D Tissue Engineering*. Norwood, MA: Artech House.
- Blake, D. J., Weir, A., Newey, S. E., and Davies, K. E. (2002). *Function and Genetics of Dystrophin and Dystrophin-Related Proteins in Muscle*. *Physiol Rev.* 82, 291–329.
- Borselli, C., Cezar, C. A., Shvartsman, D., Vandenburgh, H. H., and Mooney, D. J. (2011). The role of multifunctional delivery scaffold in the ability of cultured myoblasts to promote muscle regeneration. *Biomaterials* 32, 8905–8914. doi: 10.1016/j.biomaterials.2011.08.019
- Chen, Y. Y., Chiu, C. T., Chang, Y. P., and Wang, Y. J. (2009). Fabrication of porous gelatin microfibers using an aqueous wet spinning process. *Artificial Cells Blood Subst. Biotechnol.* 37:4. doi: 10.1080/10731190903041022
- Chung, J. H. Y., Naficy, S., Yue, Z., Kapsa, R., Quigley, A., Moulton, S. E., et al. (2013). Bio-ink properties and printability for extrusion printing living cells. *Biomater. Sci.* 1, 763–773. doi: 10.1039/c3bm00012e
- De Ruijter, C., Mendes, E., Boerstel, H., and Picken, S. J. (2006). Orientational order and mechanical properties of poly(amide-block-aramid) alternating block copolymer films and fibers. *Polymer* 47, 8517–8526. doi: 10.1016/j.polymer.2006.10.006
- Dragnet, K. I., and Taylor, C. (2009). Chemical, physical and biological properties of alginates and their biomedical implications. *Food Hydrocoll.* 25:6. doi: 10.1016/j.foodhyd.2009.10.007
- Emery, A. E. H. (2002). The muscular dystrophies. *Lancet* 359, 687–695. doi: 10.1016/S0140-6736(02)07815-7
- Falzarano, M. S., Passarelli, C., Bassi, E., Fabris, M., Perrone, D., Sabatelli, P., et al. (2013). Biodistribution and molecular studies on orally administered nanoparticle-AON complexes encapsulated with alginate aiming at inducing dystrophin rescue in *mdx* mice. *Biomed. Res. J.* 2013:13. doi: 10.1155/2013/527418
- Gombotz, W. R., and Wee, S. F. (2012). Protein release from alginate matrices. *Adv. Drug Deliv. Rev.* 64, 194–205. doi: 10.1016/j.addr.2012.09.007
- Hill, E., Boontheekul, T., and Mooney, D. J. (2006). Regulating activation of transplanted cells controls tissue regeneration. *Proc. Natl. Acad. Sci. U.S.A.* 103, 2494–2499. doi: 10.1073/pnas.0506004103
- Hong, Y., Song, H., Mao, Z., Gao, C., and Shen, J. (2006). Covalently crosslinked chitosan hydrogel: properties of in vitro degradation and chondrocyte encapsulation. *Acta Biomater.* 3, 23–31. doi: 10.1016/j.actbio.2006.06.007
- Kapsa, R., Kornberg, A. J., and Byrne, E. (2003). Novel therapies for Duchenne muscular dystrophy. *Lancet Neurol.* 2, 299–310. doi: 10.1016/S1474-4422(03)00382-X
- Kapsa, R., Quigley, A., Lynch, G. S., Steeper, K., Kornberg, A. J., Gregorevic, P., et al. (2001). In vivo and in vitro correction of the *mdx* dystrophin gene nonsense mutation by short-fragment homologous replacement. *Hum. Gene Ther.* 12, 629–642. doi: 10.1089/104303401300057324
- Lee, B. R., Lee, K. H., Kang, E., Kim, D. S., and Lee, S. H. (2011). Microfluidic wet spinning of chitosan-alginate microfibers and encapsulation of HepG2 Cells in fibers. *Biomicrofluidics* 5:022208. doi: 10.1063/1.3576903
- Lee, K. Y., and Mooney, D. J. (2012). Alginate: properties and biomedical applications. *Prog. Polym. Sci.* 37:21. doi: 10.1016/j.progpolymsci.2011.06.003
- Mendell, J. R., Campbell, K., Rodino-Klapac, L., Sahenk, Z., Shilling, C., Lewis, S., et al. (2010). Dystrophin immunity in duchenne's muscular dystrophy. *N. Engl. J. Med.* 363, 1429–1437. doi: 10.1056/NEJMoa1000228
- Mironov, V., Trusk, T., Kasyanov, V., Little, S., Swaja, R., and Markwald, R. (2009). Biofabrication: a 21st century manufacturing paradigm. *Biofabrication* 1:022001. doi: 10.1088/1758-5082/1/2/022001
- Peng, N., Widjojo, N., Sukitpaneinit, P., Teoh, M. M., Lipscomb, G. G., Chung, T.-S., et al. (2012). Evolution of polymeric hollow fibers as sustainable technologies: past, present, future. *Prog. Polym. Sci.* 37:24. doi: 10.1016/j.progpolymsci.2012.01.001
- Proto, J., and Huard, J. (2013). “Development of biological approaches to improve muscle healing after injury and disease,” in *Regenerative Medicine and Cell Therapy*, eds H. Baharvand and N. Aghdami (Totowa, NJ: Humana Press), 113–130. doi: 10.1007/978-1-62703-098-4\_6
- Qin, Y. (2004). A comparison of alginate and chitosan fibres. *Med. Device Technol.* 15, 34–37.
- Qin, Y. (2008). Alginate fibres: an overview of the production processes and applications in wound management. *Polym. Int.* 57:10. doi: 10.1002/pi.2296
- Quigley, A. F., Bulluss, K. J., Kyratzis, I. L., Gilmore, K., Mysore, T., Schirmer, K. S., et al. (2013a). Engineering a multimodal nerve conduit for repair of injured peripheral nerve. *J. Neural. Eng.* 10:016008. doi: 10.1088/1741-2560/10/1/016008
- Quigley, A. F., Wagner, K., Kita, M., Gilmore, K. J., Higgins, M. J., Breukers, R. D., et al. (2013b). *In vitro* growth and differentiation of primary myoblasts on thiophene based conducting polymers. *Biomater. Sci.* 1, 983–995. doi: 10.1039/c3bm60059a
- Razal, J. M., Kita, M., Quigley, A. F., Kennedy, E., Moulton, S. E., Kapsa, R. M. I., et al. (2009). Wet-spun biodegradable fibers on conducting platforms: novel architectures for muscle regeneration. *Adv. Funct. Mater.* 19, 3381–3388. doi: 10.1002/adfm.200900464
- Skuk, D., Goulet, M., Paradis, M., and Tremblay, J. P. (2011). “Myoblast transplantation: techniques in nonhuman primates as a bridge to clinical trials,” in *Methods in Bioengineering: Cell Transplantation*, eds S. Guiterrez, A. Navarro-Alvarez, N. Fox, and J. Ira (Norwood, MA: Artech House), 219–237.
- Skuk, D., Goulet, M., Roy, B., Chapdelaine, P., Bouchard, J.-P., Roy, R., et al. (2006). Dystrophin expression in muscles of duchenne muscular dystrophy patients after high-density injections of normal myogenic cells. *J. Neuropathol. Exp. Neurol.* 65:16. doi: 10.1097/01.jnen.0000218443.45782.81
- Skuk, D., Roy, B., Goulet, M., Chapdelaine, P., Bouchard, J.-P., Roy, R., et al. (2004). Dystrophin expression in myofibers of duchenne muscular dystrophy patients following intramuscular injections of normal myogenic cells. *Mol. Ther.* 9:8. doi: 10.1016/j.ymthe.2003.11.023
- Todaro, M., Quigley, A., Kita, M., Chin, J., Lowes, K., Kornberg, A. J., et al. (2007). Effective detection of corrected dystrophin loci in *mdx* mouse myogenic precursors. *Hum. Mutat.* 28, 816–823. doi: 10.1002/humu.20494
- Wallace, G. G., Moulton, S. E., Higgins, M. J., and Kapsa, R. M. I. (2012). *Organic Bionics*. Weinheim: Wiley-VCH Verlag & Co. KGaA.
- Wong, S. H., Lowes, K. N., Quigley, A. F., Marotta, R., Kita, M., Byrne, E., et al. (2005). DNA electroporation in vivo targets mature fibres in dystrophic *mdx* muscle. *Neuromuscul. Disord.* 15, 630–641. doi: 10.1016/j.nmd.2005.04.008

**Conflict of Interest:** The authors declare that the research was conducted in the absence of any commercial or financial relationships that could be construed as a potential conflict of interest.

Copyright © 2020 Quigley, Cornock, Mysore, Foroughi, Kita, Razal, Crook, Moulton, Wallace and Kapsa. This is an open-access article distributed under the terms of the Creative Commons Attribution License (CC BY). The use, distribution or reproduction in other forums is permitted, provided the original author(s) and the copyright owner(s) are credited and that the original publication in this journal is cited, in accordance with accepted academic practice. No use, distribution or reproduction is permitted which does not comply with these terms.



# Electrically Conducting Hydrogel Graphene Nanocomposite Biofibers for Biomedical Applications

Sepehr Talebian<sup>1,2</sup>, Mehdi Mehrali<sup>3</sup>, Raad Raad<sup>4</sup>, Farzad Safaei<sup>4</sup>, Jiangtao Xi<sup>4</sup>, Zhoufeng Liu<sup>5</sup> and Javad Foroughi<sup>1,2,4\*</sup>

<sup>1</sup> Intelligent Polymer Research Institute, University of Wollongong, Wollongong, NSW, Australia, <sup>2</sup> Illawarra Health and Medical Research Institute, University of Wollongong, Wollongong, NSW, Australia, <sup>3</sup> Department of Mechanical Engineering, Technical University of Denmark, Lyngby, Denmark, <sup>4</sup> School of Electrical, Computer and Telecommunications Engineering, Faculty of Engineering and Information Sciences, University of Wollongong, Wollongong, NSW, Australia, <sup>5</sup> School of Textile Engineering, Zhongyuan University of Technology, Zhengzhou, China

## OPEN ACCESS

### Edited by:

Clemens Kilian Weiss,  
Fachhochschule Bingen, Germany

### Reviewed by:

Baolin Guo,  
Xi'an Jiaotong University, China  
Jae Young Lee,  
Gwangju Institute of Science and  
Technology, South Korea  
Ashok Kumar,  
Indian Institute of Technology  
Kanpur, India

### \*Correspondence:

Javad Foroughi  
foroughi@uow.edu.au

### Specialty section:

This article was submitted to  
Polymer Chemistry,  
a section of the journal  
Frontiers in Chemistry

Received: 07 May 2019

Accepted: 27 January 2020

Published: 27 February 2020

### Citation:

Talebian S, Mehrali M, Raad R,  
Safaei F, Xi J, Liu Z and Foroughi J  
(2020) Electrically Conducting  
Hydrogel Graphene Nanocomposite  
Biofibers for Biomedical Applications.  
Front. Chem. 8:88.  
doi: 10.3389/fchem.2020.00088

Conductive biomaterials have recently gained much attention, specifically owing to their application for electrical stimulation of electrically excitable cells. Herein, flexible, electrically conducting, robust fibers composed of both an alginate biopolymer and graphene components have been produced using a wet-spinning process. These nanocomposite fibers showed better mechanical, electrical, and electrochemical properties than did single fibers that were made solely from alginate. Furthermore, with the aim of evaluating the response of biological entities to these novel nanocomposite biofibers, *in vitro* studies were carried out using C2C12 myoblast cell lines. The obtained results from *in vitro* studies indicated that the developed electrically conducting biofibers are biocompatible to living cells. The developed hybrid conductive biofibers are likely to find applications as 3D scaffolding materials for tissue engineering applications.

**Keywords:** biopolymer, hydrogel, electrically conductive hydrogel, graphene, wet spinning, nanocomposite, biofibers

## INTRODUCTION

Soft and flexible conductors are essential materials for bioelectronics that can be potentially implemented in a broad range of biomedical applications, ranging from cardiovascular (Shin et al., 2014, 2016; Navaei et al., 2016; Wang L. et al., 2017; Hu et al., 2019), muscle (Sasaki et al., 2014; Chen et al., 2015; Annabi et al., 2016; Jo et al., 2017; Guo et al., 2019), and nerve tissue engineering (Yang et al., 2016; Liu X. et al., 2017; Wang S. et al., 2017; Zhou et al., 2018) to implantable or wearable biosensors for human health monitoring (Mehrli et al., 2018; Kadumudi et al., 2019). In this context, conductive hydrogels are one of the most promising soft conductors owing to their high water content and molecular similarity to the natural soft tissues (Kim S. et al., 2015; Wu et al., 2016; Han et al., 2017; Qu et al., 2019). Conductive hydrogels are commonly composed of inherently conducting polymers such as polypyrrole (PPy) and polyaniline (PANI); however, these polymers often suffer from weak mechanical properties and poor biocompatibility and processability, which further hinder their biomedical application (Foroughi et al., 2009, 2011, 2015; Kaur et al., 2015; Mirabedini et al., 2016b). Thus, incorporation of conducting nanomaterials (such as

graphene, carbon nanotubes, and gold nanoparticles) into hydrogels has emerged as an alternative approach to yield mechanically robust conductive hydrogels with enhanced biocompatibility (Mirabedini et al., 2016a; Mehrali et al., 2017; Wu et al., 2017; Liang et al., 2019). Nevertheless, the electrical conductivity of nanocomposite hydrogels is hampered by factors such as random distribution of nanomaterials in the polymeric network, and consequently efforts have been made to address this issue by assembling the nanomaterials into a macroscopically ordered structures within the hydrogel network (Ahadian et al., 2014, 2017; Shin et al., 2015; Luo et al., 2018). In this direction, wet spinning has emerged as a simple yet high-throughput assembly technique to transform carbon-based nanomaterials into fibers with highly ordered structures (Foroughi et al., 2012, 2016; Xu and Gao, 2014; Apollo et al., 2015; Mirabedini et al., 2015; Lu et al., 2017). The distinguishing factor of these wet-spun fibers is their flexibility in design, as they can be applied to common textile manufacturing processes (braiding, weaving, and knitting) to fabricate 3D structures and scaffolds (Akbari et al., 2014; Wang et al., 2015).

Among various carbon-based nanomaterials, graphene is the most suitable for fabrication of wet-spun fibers, owing to its liquid crystalline behavior (Cong et al., 2012; Xu Z. et al., 2013). In addition, graphene offers an array of peculiar properties (such as extraordinary electronic transport properties, thermal conductivity, and mechanical stiffness), which make them a unique candidate for development of conductive platforms (Stankovich et al., 2006; Chen et al., 2008). Graphene also showed to have the ability to interface/interact with the biomolecules, cells, and tissues, which further expanded the application of this nanomaterial in various biomedical fields (Zhang et al., 2012; Liu et al., 2013), ranging from tissue engineering to drug delivery. For instance, Ku et al. studied the effect of graphene oxide (GO) on mouse myoblast C2C12 cells, and their results revealed that myogenic differentiation was markedly enhanced on GO, which resulted from serum protein adsorption and nanotopographical cues (Ku and Park, 2013). Nevertheless, the biocompatibility of graphene is still a subject of debate (Zhang et al., 2011; Kiew et al., 2016), and specifically, issues such as its hemocompatibility, inflammation responses, and clearance pathways are major obstacles in the way of transition of graphene from laboratory to clinic (Kurapati et al., 2016). In addition, wet-spun graphene fibers often suffer from low flexibility and weak mechanical properties, which further hinder their practical application in the engineering field (Dong et al., 2012; Xiang et al., 2013).

Consequently, in this study, with the aim of developing a bio-friendly, conductive, and robust platform, we have utilized graphene nanosheets alongside the highly biocompatible alginate to institute composite fibers *via* the well-established wet-spinning technique. The resulting composite biofibers showed to have great flexibility and mechanical properties. Most remarkably, these composite fibers possessed a high level of electrochemical properties and showed a good level of cellular biocompatibility when tested against myoblast cell lines. Given the favorable properties of these nanocomposite biofibers, they could be used as scaffolding materials for tissue engineering applications.

## EXPERIMENTAL

### Materials

Alginate sodium salt from brown algae (medium viscosity) and graphene nanosheets (with electrical conductivity of  $>10^3$  S/m) were purchased from Sigma-Aldrich. Calcium chloride ( $\text{CaCl}_2$ ) and ethanol were purchased from Chem-Supply.

### Preparation of Spinning Solution

To prepare alginate (Alg) fiber, a spinning solution containing 3% (w/v) alginate in distilled water was prepared. To produce hybrid alginate/graphene (Alg/G) nanocomposite fibers, 8% (wt%) of graphene nanosheets was added into the alginate solution (3% wt) under constant stirring and sonication. The mixture was further stirred and sonicated for 24 h to ensure homogeneous dispersion of graphene nanosheets into the polymer matrix.

### Fiber Spinning

Single alginate and nanocomposite Alg/G biofibers were fabricated using a coagulation bath of  $\text{H}_2\text{O}$ /ethanol (1:1) containing 3%  $\text{CaCl}_2$  (w/v). Both types of fibers were fabricated by simply extruding the corresponding spinning solutions (50 ml/h) into the coagulation bath using a blunt needle (gauge 19).

### Instrumentation

All rheology experiments were conducted on a Physica MCR 301 Rheometer (Anton Paar) in parallel plate geometry (50-mm disk, 0.097-mm measuring distance) and at room temperature ( $23^\circ\text{C}$ ). Flow experiment was performed to evaluate the viscosity of polymer solution (shear rate varying from 1 to  $100\text{ s}^{-1}$ ). Fourier transform infrared (FTIR) spectra were measured between 700 and  $4,000\text{ cm}^{-1}$  on a Shimadzu IRPrestige-21 infrared spectrometer with internal beam equipped with standard detector with mirror speed of 2.8. The spectra were obtained using attenuated total reflection (ATR) on the fibers with resolution of 8 and number of scans of 30, on a transmittance mode. Raman spectra were recorded on a Jobin

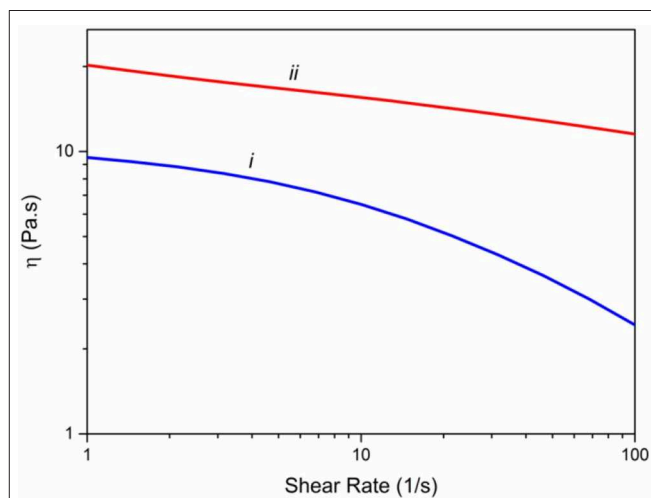


**FIGURE 1** | Viscometry of spinning solutions including (i) alginate 3% (w/v) and (ii) hybrid alginate-graphene (3 and 8% w/v, respectively).



Yvon Horiba HR800 Raman system using a 632-nm laser line and a 300-line grating. The weight loss of the biofibers was obtained by thermogravimetric analysis (TGA; Mettler Toledo-SDTA851) on 10 mg of samples with heating rate of 5°C/min under a nitrogen atmosphere, between temperatures of 30°C and 600°C. The morphology of fibers, and surface and cross-sectional structure were examined using a JSM-6490LV scanning electron microscope (SEM) and Leica M205A microscope. For SEM imaging, the fibers were cut into small pieces and inserted into holes that had been pre-drilled into a small brass block. The block containing the mounted fibers was then immersed into liquid nitrogen for about 45 s and a liquid nitrogen cooled razor blade was run across the surface of the block to fracture the

fibers. The block was then quickly transferred to the low-voltage SEM (LVSEM) for examination. SEM images were taken in high vacuum (HV) mode at 15-kV operating voltage and a spot size setting of 60. The mechanical properties of fibers were assessed using a dynamic mechanical tester (EZ-L tester from Shimadzu) at 10 mm/min *via* 50- and 10-N load cells for dry and wet fibers, respectively. The swelling properties of the hydrogel fibers were determined by examining their water uptake capacity. The hydrogel fibers were incubated in simulated body fluid (SBF) at 37°C and allowed to fully swell. The swelling ratio was calculated using the equation  $(W_s - W_d)/W_d$ , where  $W_s$  represents the weight of the swollen hydrogel fibers and  $W_d$  represents the weight of the dried hydrogel fibers at the beginning.

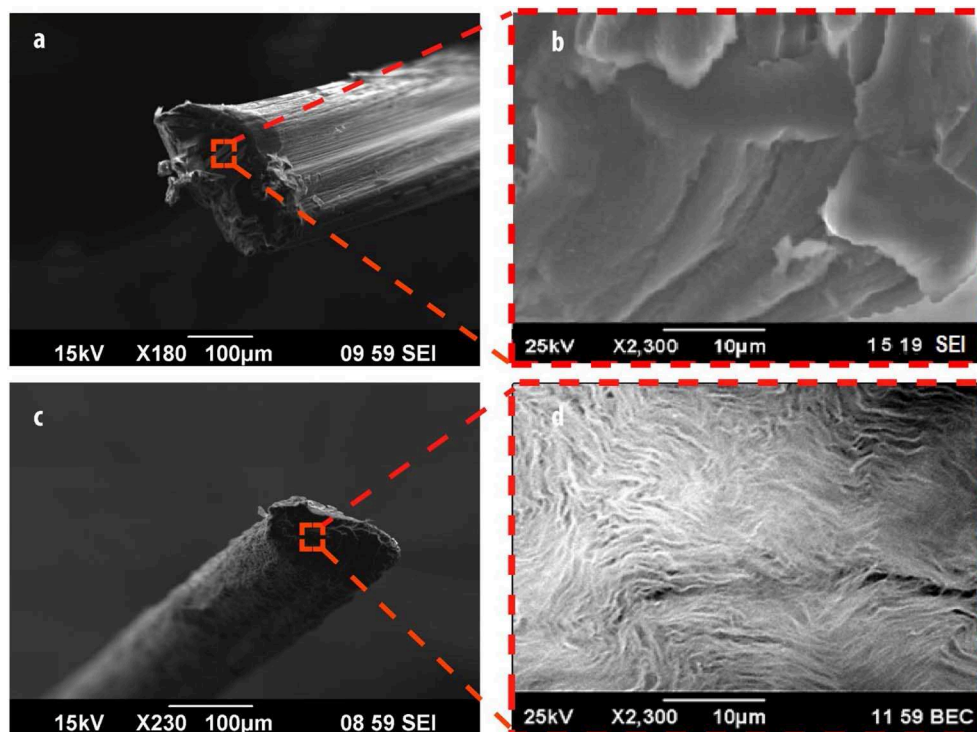


**FIGURE 2 |** Morphological analysis of fibers, including scanning electron microscope (SEM) images of alginate (a,b) and alginate/graphene (c,d) fibers.

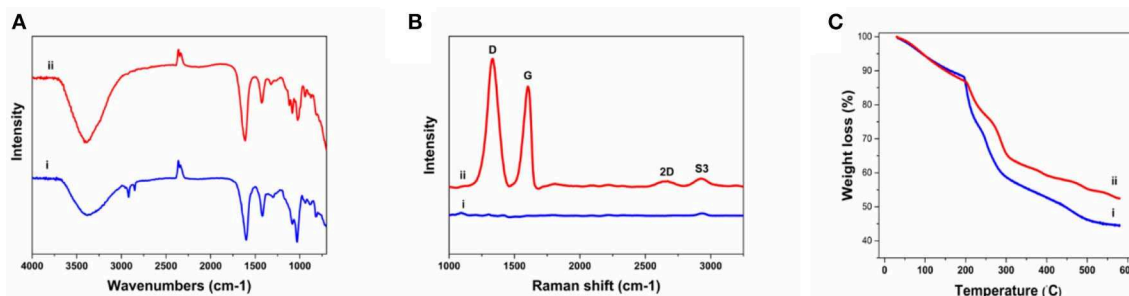


**FIGURE 3 |** Physiochemical characterization of as-prepared fibers including (A) Fourier transform infrared (FTIR) spectra of (i) alginate and (ii) alginate/graphene, (B) Raman spectra of (i) alginate and (ii) alginate/graphene fibers, (C) thermogravimetric analysis (TGA) of (i) alginate and (ii) alginate/graphene fibers.

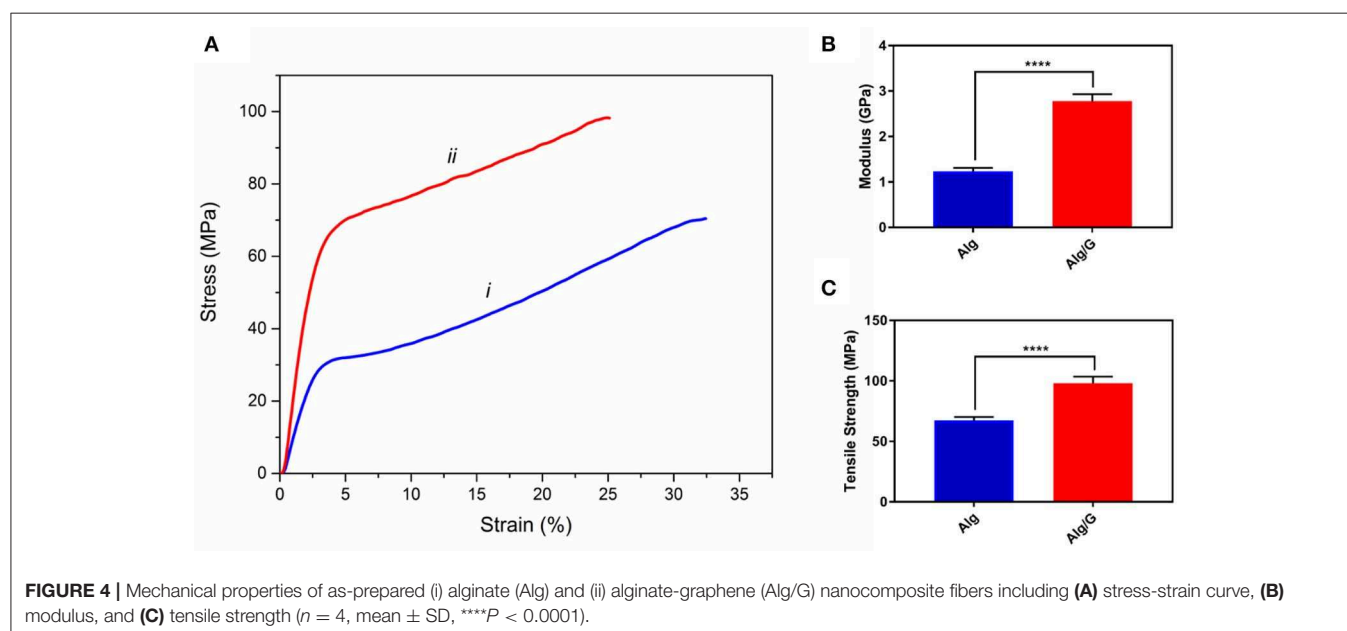
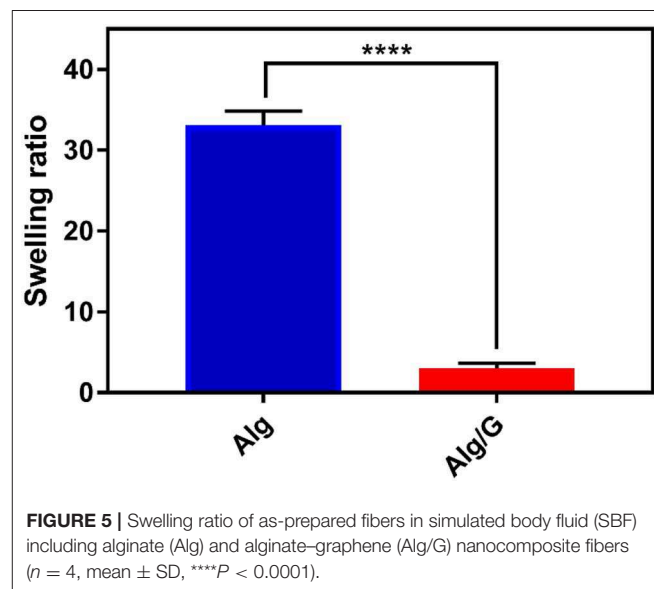
A three-electrode electrochemical cylindrical cell ( $15 \times 50$  mm) coupled to a Bioanalytical Systems (Model CV27) potentiostat was used for cyclic voltammetry. Dry Alg/G fibers at 20 mm were used as the working electrode with a Ag/AgCl reference electrode and a Pt mesh counter electrode. All cyclic voltammetric tests were performed in SBF. The electrical conductivity of the fibers was measured using an in-house built, four-point probe. The electrodes consisted of four parallel rods at a spacing of 0.33 cm; the fibers were connected to the parallel rods using silver paint (obtained from SPI). A constant current was applied between the two outer electrodes using a potentiostat/galvanostat (Princeton Applied Research Model 363). The potential difference between the inner electrodes was recorded using a digital multimeter 34401A (Agilent).

## Cytotoxicity and Cell Morphology Studies

Murine C2C12 myoblasts cells, purchased from the European Collection of Cell Cultures (ECACC; catalog no. 91031101), were cultured in Dulbecco's modified Eagle medium (DMEM; Sigma-Aldrich, St. Louis, MO, USA) supplemented with 10% (v/v) fetal bovine serum (FBS; Sigma-Aldrich, St. Louis, MO, USA) and penicillin-streptomycin (1% v/v) and maintained at 37°C in the presence of 5% CO<sub>2</sub> and 95% air. When ~70% confluency was reached, the cells were detached by using 0.25% (w/v) trypsin/0.1% (w/v) EDTA, and they were either subcultured or used to set up the experiments. The cytotoxicity and cell viability of fibers were evaluated by a colorimetric Cell Counting Kit-8 (CCK-8; Dojindo Laboratories Inc., Kumamoto, Japan). Briefly, cells (passage numbers between 4 and 6) were seeded in 96-well plates at a density of  $5 \times 10^3$  cells per well, to which 1 cm of fibers (either Alg or Alg/G) was added and subsequently allowed to culture for 1, 2, and 4 days. At each time point, fibers were taken out, and cells were washed twice with phosphate-buffered saline (PBS) and then incubated with Dulbecco's PBS (DPBS) solution,

and then 100  $\mu$ l of medium containing 10% CCK-8 solution was added to the cells and kept for a further 3 h. Then, the absorbance was read at the wavelength of 450 nm according to the manufacturer's instructions by a microplate spectrophotometer (Benchmark Plus, Tacoma, Washington, USA).

Fluorescent staining was employed to observe the cell morphology *via* confocal laser scanning microscopy (CLSM) (Zeiss LSM710, Carl Zeiss, Inc., Jena, Germany). Briefly, after day 4, the fibers were removed from the wells, and the cells were washed three times with DPBS. Then, the cells were incubated for 45 min incubation at 37°C with a solution of rhodamine phalloidin [1:40 dilution in 0.1% (w/v) bovine serum albumin (BSA)]. The cells were washed three times in DPBS, and then the nuclei of



the cells were stained with Hoechst (Thermo Fisher Scientific; 33342) and incubated for 15 min at 37°C. Then, cells were washed three times with DPBS before imaging. Furthermore, live staining, based on our previously published work, was implemented to evaluate the adhesion of cells to the surface of fibers (Mehrali et al., 2019). Briefly, the fibers were fixed in a 24-well plate using sterilized stainless steel rings. Next, cells (passage numbers between 4 and 6) were seeded on top of the fixed fibers in the 24-well plates at a density of  $10 \times 10^3$  cells per well and allowed to culture for 2 days. Next, the cells (on the fibers as well as cells growing on the tissue culture plastic underneath) were washed two times with DPBS and then stained with a calcein-AM (live cells) for 15 min at 37°C. The samples were washed twice with DPBS before the image is captured. Of note, to encourage the adhesion of cells to the fiber surface, we have coated the samples with a thin layer of collagen.

## Statistical Analysis

Statistical significance of treatment groups as compared with control groups was determined using a two-way ANOVA with a Bonferroni post-test or unpaired students multiple *t*-test (GraphPad Prism V 6.0; San Diego, CA, USA). *P* values < 0.05 were considered statistically significant. Values are reported as the average  $\pm$  standard deviation.

## RESULTS AND DISCUSSION

### Viscometry of Spinning Solution

Rheological properties of the spinning solutions are essential factors in determining the mechanical properties of the yielding fibers (Mirabedini et al., 2016a). Consequently, we have measured the viscosity of alginate solution (3%) and Alg/G solution (8% wt) in a ranges of  $1\text{--}100\text{ s}^{-1}$  of shear rate (Figure 1). Accordingly, both solutions showed a shear thinning behavior; however, graphene-containing alginate solution experienced a much lower drop in its viscosity, a phenomenon that was observed previously with Alg/G composites (Li et al., 2016). In addition, graphene-containing solution showed a higher level of viscosity over the entire shear rate range, which was reported to be a consequence of

attachment of alginate chains onto the surface of graphene sheets (Liu and Li, 2017).

### Morphology of As-Spun Fibers

SEM imaging was utilized to assess the surface morphology of alginate (Figures 2a,b) and Alg/G fibers (Figures 2c,d). As-spun fibers were cut in the middle, and their cross section was further analyzed. Accordingly, Alg fibers showed a smooth surface corresponding to soft polymeric nature of alginate, whereas Alg/G fibers showed a layered dense structure with rough surface as a result of graphene sheets (Li et al., 2014). In addition, Alg/G fibers possessed an average diameter of 186  $\mu\text{m}$ , whereas pure Alg fibers had an average diameter of 243  $\mu\text{m}$ . This difference in fiber diameter is a consequence of intermolecular interactions between graphene and alginate (in correspondence with viscometry data), which leads to formation of a more compact structure. The SEM images of Alg/G fibers also revealed the homogenous dispersion of graphene sheets throughout the alginate polymeric network.

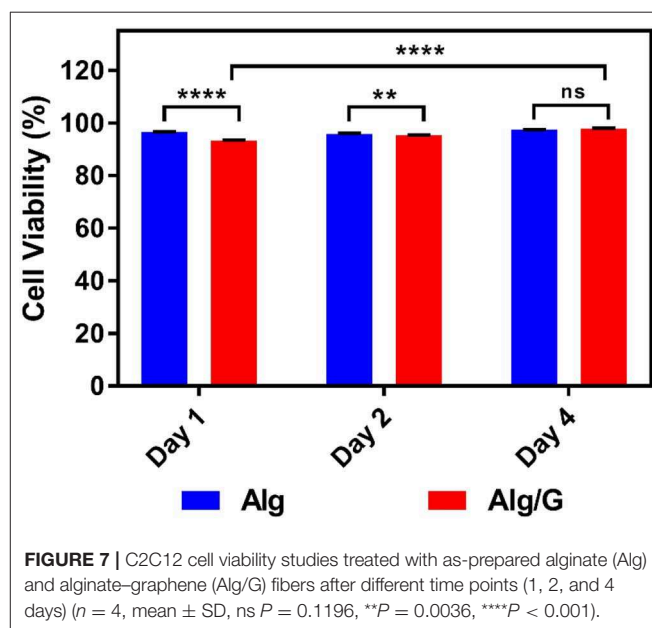


**FIGURE 7 |** C2C12 cell viability studies treated with as-prepared alginate (Alg) and alginate-graphene (Alg/G) fibers after different time points (1, 2, and 4 days) ( $n = 4$ , mean  $\pm$  SD, ns  $P = 0.1196$ , \*\* $P = 0.0036$ , \*\*\*\* $P < 0.001$ ).

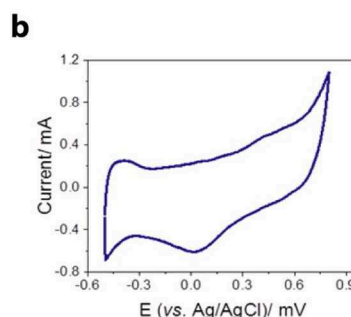


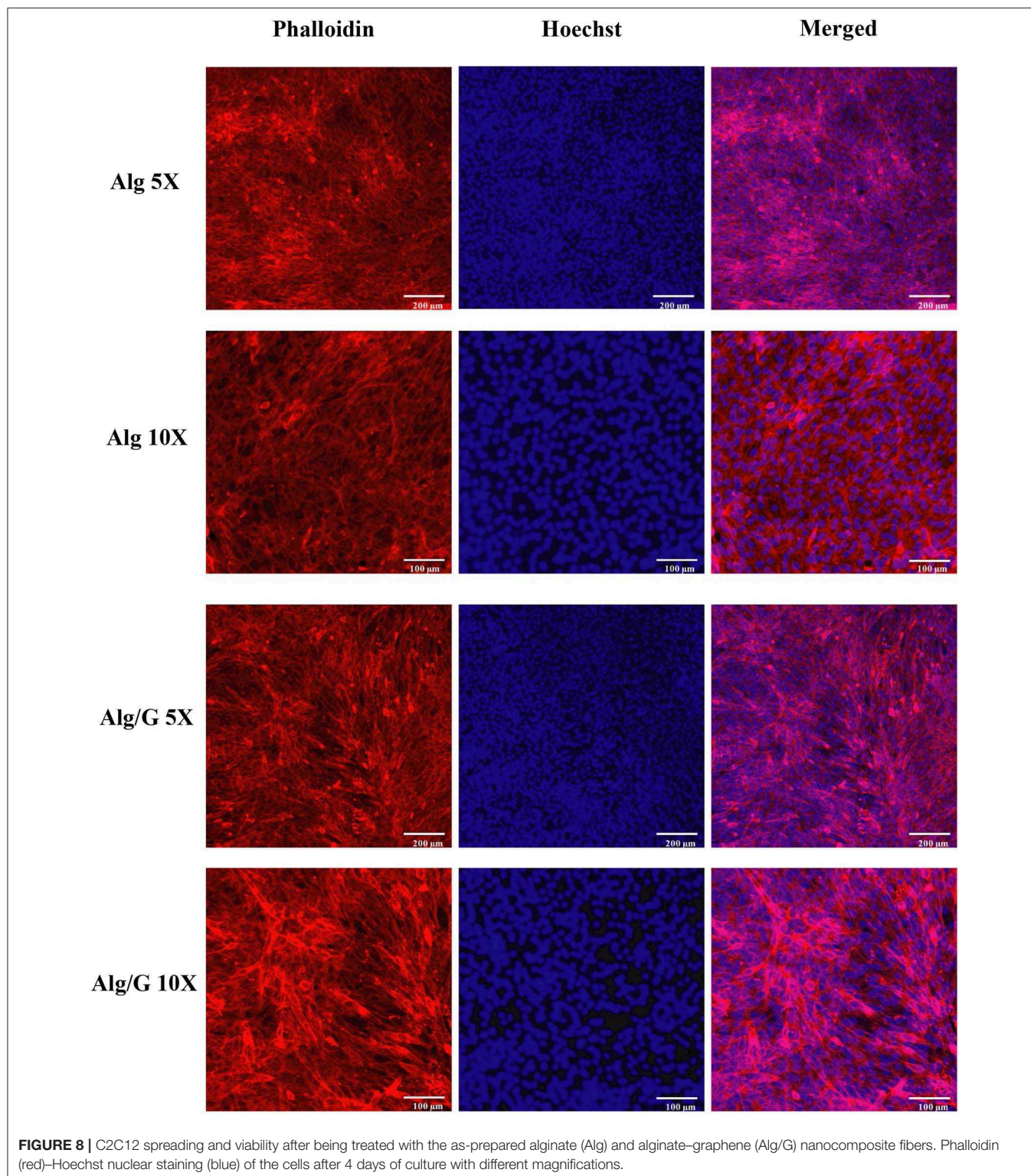
**FIGURE 6 |** Electrical conductivity of alginate-graphene fibers. (a) Light microscope image of the fiber used as the working electrode. (b) Cyclic voltammograms of alginate-graphene fibers. Potential was scanned between  $-0.5$  and  $+0.8\text{ V}$  (vs. Ag/AgCl) in simulated body fluid (SBF) at  $100\text{ mV/s}$ .



## Physiochemical Characterization of Fibers

The FTIR was implanted to further characterize the chemical composition of the fibers (**Figure 3A**). The Alg fibers showed the characteristic peaks of alginic acid at 3,380, 1,600, 1,418, and 1,028  $\text{cm}^{-1}$ , corresponding to OH stretching

vibration, symmetric, and asymmetric stretching vibration of carboxylate salt group, and stretching vibration of C–O–C groups, respectively (Zheng et al., 2016). The Alg/G fibers showed a similar absorption pattern to alginate, but the appearance of peaks between 1,050 and 1,250  $\text{cm}^{-1}$  (C–O–C stretching





vibration) and an increase in intensity of peak at  $3,380\text{ cm}^{-1}$  ( $-\text{OH}$  stretching vibration) were assigned to graphene functional groups (Li et al., 2018). To further investigate the state of graphene sheets in the Alg/G nanocomposite fibers, we have conducted Raman spectroscopy (**Figure 3B**). Accordingly, the Raman spectrum of Alg fibers did not show any peak, whereas the Alg/G nanocomposite fibers showed the characteristic peaks of graphene at  $1,332$ ,  $1,600$ ,  $2,655$  (2D band), and  $2,926\text{ cm}^{-1}$  (S3 band), corresponding to D vibration band arising from the breathing mode of j-point phonons of  $A_{1g}$  symmetry, G vibration band arising from the  $E_{2g}$  phonon of the  $sp^2$  C atoms, 2D band as an indicator of the number of graphene layers, and S3 band derived from the D–G peak combination, respectively (Johra et al., 2014; Mehrali et al., 2016). In addition, the D band to G band intensity ratio ( $I_D/I_G$ ) was measured to be 1.21, suggesting that graphene was partially reduced in the fabrication process, which led to a decrease in the average size of the  $sp^2$  domains (Stankovich et al., 2007).

We also compared the thermal properties of alginate and Alg/G fibers using TGA (**Figure 3C**). The results showed that both fibers undergo three-stage thermal degradation processes: (i) the loss of volatile products through dehydration (from

room temperature to  $200^\circ\text{C}$ ), (ii) the thermal degradation of the polymer ( $200$ – $300^\circ\text{C}$ ), and (iii) the carbonization process (above  $300^\circ\text{C}$ ). As-prepared Alg/G fibers indicated that the degradation and proceeding carbonization processes happened at slightly higher temperatures, when compared with that of Alg fibers, which showed that graphene nanosheets enhanced the thermal stability of alginate and retarded the pyrolysis of the composite fibers. This might be associated with the graphene layers restraining the movement of the alginate polymeric chains, impeding the thermal decomposition process, and increasing the needed energy of thermal decomposition (Li et al., 2018). Lastly, the mass fraction of the graphene in the composite fibers was evaluated by comparing the TGA graph of alginate and alginate–graphene at  $580^\circ\text{C}$ , which showed that about 8 wt% of the fibers was composed of graphene nanosheets.

The mechanical properties of soft conductors are one of the most essential traits of these systems, especially when it comes to practical applications such as tissue engineering or biosensors (Mehrili et al., 2018). Consequently, we have measured the mechanical properties of the as-prepared fibers, and the results are shown in **Figure 4**. As can be seen from **Figure 4**, the addition of graphene to alginate led to an increase in tensile strength

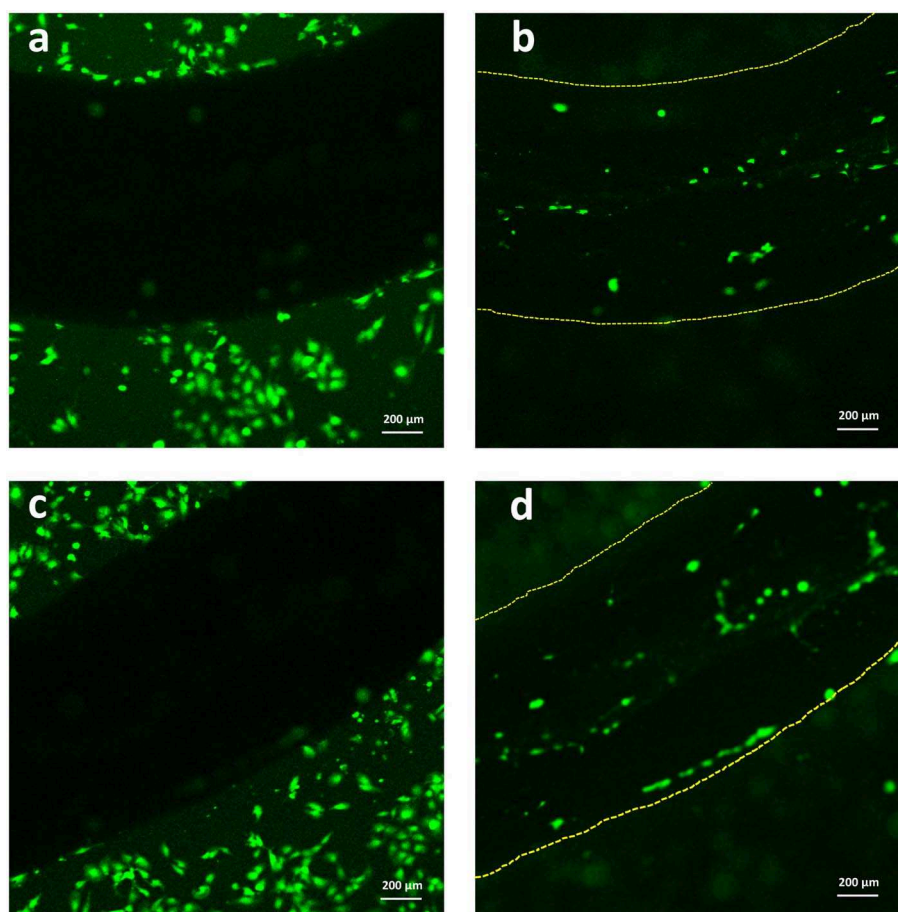


**FIGURE 9** | Live staining of C2C12 cells after 2 days of culture (**a,c**) around the Alg/G fibers and (**b,d**) on the surface of Alg/G fibers.

(from 68 to 98 MPa) and modulus (from 1.26 to 2.77 GPa) of the resulting fibers. This could be a result of graphene–alginate interactions (functional groups on the edges of graphene sheets and the hydroxyl groups on the alginate backbone) that enable the load transfer from the matrix to single-layer graphene sheets enhancing tensile strength and also helping to absorb more energy before fracture (Li et al., 2014; Hu et al., 2016). The tensile strength and modulus values obtained in this study were slightly lower than the reported value in the literature for similar fibers (tensile strength and modulus normally ranging from 50 to 600 MPa and 1–40 GPa, respectively), which could be result from low concentration of alginate as well as graphene nanosheets in our fibers (Xu and Gao, 2014; Ma et al., 2015). Most remarkably, Alg/G fibers in this study exhibited an elongation at break of 25%, which put these fibers among the most flexible graphene-containing fibers in the literature. Wet-spun graphene-containing fibers normally possess an ultimate tensile strain of <10%, which further distinguishes our work from similar studies (Cong et al., 2012; Chen et al., 2013; Xu and Gao, 2014; Hu et al., 2016; Fu et al., 2019). Also, Alg/G fibers exhibited a lower strain at break than did Alg fibers, which was due to contribution of graphene in the load bearing.

The practical application of hydrogels is often hindered by the difficulty in controlling their temporal change in shape after the installation (Kamata et al., 2015; Talebian et al., 2018). Consequently, controlling the swelling of hydrogels appeared as an important step toward their clinical realization. In line with this, we have measured the swelling ratio of the as-spun fibers in SBF, and the results are shown in **Figure 5**.

Accordingly, Alg/G composite fibers possessed a much less swelling ratio (2.9) than did single Alg fibers (33.07). This is probably due to graphene–alginate interactions that also led to an increase in mechanical properties of this composite fiber (Liu S. et al., 2017; Peng et al., 2017). The obtained swelling ratio value for Alg/G fibers in our study is by far among the lowest values reported in the literature (Peng et al., 2017, 2018; Zhao et al., 2017), which made these fibers not easily destroyable by the swelling force.

Electrical conductivity and electrochemical properties of the as-prepared Alg/G nanocomposite fibers have been investigated to evaluate their capabilities as a smart biofiber for electrical stimulation. Cyclic voltammetry for the as-prepared Alg/G fibers in SBF was carried out to evaluate their electrochemical performance. It can be seen from **Figure 6** that the CV curve of the Alg/G fibers displayed a box-like shape superimposed with a pair of Faradaic peaks in the potential range of  $-0.45$  to  $+0.15$  mV, which is caused by the reversible redox reaction of oxygen-containing groups on the graphene sheets, and it is an indication that redox reactions are occurring owing to the conducting fibers providing a broad range of energy states (Xu Y. et al., 2013; Ates et al., 2018). In addition, the electrical conductivity of the as-spun Alg/G nanocomposite fiber was 2 S/m. The obtained value for electrical conductivity of our fibers is not comparable with the values reported in other studies (Jalili et al., 2013; Xu et al., 2016), mostly owing to low concentration of graphene in our composite fibers, which was intentionally chosen to yield flexible fibers with an acceptable level of conductivity.

## In vitro Studies

In order to investigate the biocompatibility of hybrid Alg/G fibers, murine myoblast cell line (C2C12) was used and its cell viability and cell morphology were compared with those of single Alg fibers (**Figures 7, 8**, respectively). We have investigated the biocompatibility of the fibers by using a colorimetric CCK-8, and the results are depicted in **Figure 7**. The cell viability results showed that Alg/G fibers maintained a good level of cell viability even after 4 days of culture. At day 1, cells treated with Alg/G (compared with Alg fibers) showed a lower level of viability, which could be a consequence of released graphene nanosheets that can be taken up by the cells, causing low toxicity (Patel et al., 2016). Interestingly, the viability of cells treated with Alg/G fibers started to increase as the time passes, to a point where after 4 days of culture, no significant difference was observed between these cells and the ones treated with Alg fibers. This further proved that Alg/G fibers were not toxic to myoblasts but rather increased their proliferation, a phenomenon reported previously in the literature (Ku and Park, 2013). Furthermore, the Hoechst staining revealed that both Alg and Alg/G fibers had a good level of biocompatibility against the cells, as indicated by the number of viable cell nucleus stained by Hoechst (**Figure 8**). In addition, they did not induce any unwanted morphological features in the C2C12 cells and kept the characteristic spindle-shaped morphology in the growth media, as indicated by phalloidin staining of actin filaments. Furthermore, C2C12 cells treated with Alg/G fibers were fused to a multinucleate elongated shape, an early indication of myogenic differentiation of myoblasts caused by the presence of graphene in these fibers (Kim M. J. et al., 2015; Lee et al., 2016).

Lastly, with the aim of evaluating the adhesion of C2C12 cells onto the Alg/G fibers, we have utilized a live cell staining method (**Figure 9**). The results showed that cells started to migrate onto the surface of fibers only after 48 h of culture. The lower cell density on the fibers (compared with the area adjacent to the fiber) could be due to lack of bioactive functional groups (amines or sulfates) in alginate, which hindered further migration of cells onto the fibers (Dinoro et al., 2019). This shows that these fibers might have the potential to be also used as conductive scaffolds, if modified with proper functional groups, to encourage the regeneration of cells.

## CONCLUSIONS

In this study, with the aim of establishing a flexible, robust, biocompatible, and electrical conducting hydrogel, we have used a simple wet-spinning method to fabricate nanocomposite fibers from a mixture of alginate and graphene nanosheets. The resulting nanocomposite biofibers showed to have better mechanical properties, lower swelling ratio, and higher thermal stability than did single fibers made from pure alginate. Most remarkably, these composite biofibers possessed excellent electrochemical properties, and when tested against C2C12 myoblast cell lines, they showed high level of biocompatibility. Overall, these fibers hold immense

promise for use as soft conductors in tissue engineering, and future work will include the application of these fibers as smart biopolymer scaffolds in multi-component systems to allow electrical stimulation of cells toward their maturation.

## DATA AVAILABILITY STATEMENT

All datasets generated for this study are included in the article/supplementary materials.

## REFERENCES

- Ahadian, S., Naito, U., Surya, V. J., Darvishi, S., Estili, M., Liang, X., et al. (2017). Fabrication of poly(ethylene glycol) hydrogels containing vertically and horizontally aligned graphene using dielectrophoresis: an experimental and modeling study. *Carbon* 123, 460–470. doi: 10.1016/j.carbon.2017.07.082
- Ahadian, S., Ramón-Azcón, J., Estili, M., Liang, X., Ostrovidov, S., Shiku, H., et al. (2014). Hybrid hydrogels containing vertically aligned carbon nanotubes with anisotropic electrical conductivity for muscle myofiber fabrication. *Sci. Rep.* 4:4271. doi: 10.1038/srep04271
- Akbari, M., Tamayol, A., Laforte, V., Annabi, N., Najafabadi, A. H., Khademhosseini, A., et al. (2014). Composite living fibers for creating tissue constructs using textile techniques. *Adv. Funct. Mater.* 24, 4060–4067. doi: 10.1002/adfm.201303655
- Annabi, N., Shin, S. R., Tamayol, A., Miscuglio, M., Bakooshli, M. A., Assmann, A., et al. (2016). Highly elastic and conductive human-based protein hybrid hydrogels. *Adv. Mater.* 28, 40–49. doi: 10.1002/adma.201503255
- Apollo, N. V., Maturana, M. I., Tong, W., Nayagam, D. A., Shivdasani, M. N., Foroughi, J., et al. (2015). Soft, flexible freestanding neural stimulation and recording electrodes fabricated from reduced graphene oxide. *Adv. Funct. Mater.* 25, 3551–3559. doi: 10.1002/adfm.201500110
- Ates, M., El-Kady, M., and Kaner, R. B. (2018). Three-dimensional design and fabrication of reduced graphene oxide/polyaniline composite hydrogel electrodes for high performance electrochemical supercapacitors. *Nanotechnology* 29:175402. doi: 10.1088/1361-6528/aaae44
- Chen, H., Müller, M. B., Gilmore, K. J., Wallace, G. G., and Li, D. (2008). Mechanically strong, electrically conductive, and biocompatible graphene paper. *Adv. Mater.* 20, 3557–3561. doi: 10.1002/adma.200800757
- Chen, J., Dong, R., Ge, J., Guo, B., and Ma, P. X. (2015). Biocompatible, biodegradable, and electroactive polyurethane-urea elastomers with tunable hydrophilicity for skeletal muscle tissue engineering. *ACS Appl. Mater. Interfaces* 7, 28273–28285. doi: 10.1021/acsami.5b10829
- Chen, L., He, Y., Chai, S., Qiang, H., Chen, F., and Fu, Q. (2013). Toward high performance graphene fibers. *Nanoscale* 5, 5809–5815. doi: 10.1039/c3nr01083j
- Cong, H. P., Ren, X. C., Wang, P., and Yu, S. H. (2012). Wet-spinning assembly of continuous, neat, and macroscopic graphene fibers. *Sci. Rep.* 2:613. doi: 10.1038/srep00613
- Dinoro, J., Maher, M., Talebian, S., Jafarkhani, M., Mehrali, M., Orive, G., et al. (2019). Sulfated polysaccharide-based scaffolds for orthopaedic tissue engineering. *Biomaterials* 214:119214. doi: 10.1016/j.biomaterials.2019.05.025
- Dong, Z., Jiang, C., Cheng, H., Zhao, Y., Shi, G., Jiang, L., et al. (2012). Facile fabrication of light, flexible and multifunctional graphene fibers. *Adv. Mater.* 24, 1856–1861. doi: 10.1002/adma.201200170
- Foroughi, J., Antiohos, D., and Wallace, G. G. (2016). Effect of post-spinning on the electrical and electrochemical properties of wet spun graphene fibre. *RSC Adv.* 6, 46427–46432. doi: 10.1039/C6RA07226G
- Foroughi, J., Spinks, G. M., Ghorbani, S. R., Kozlov, M. E., Safaei, F., Peleckis, G., et al. (2012). Preparation and characterization of hybrid conducting polymer-carbon nanotube yarn. *Nanoscale* 4, 940–945. doi: 10.1039/c2nr11580h
- Foroughi, J., Spinks, G. M., and Wallace, G. G. (2009). Effect of synthesis conditions on the properties of wet spun polypyrrole fibres. *Synth. Met.* 159, 1837–1843. doi: 10.1016/j.synthmet.2009.06.006
- Foroughi, J., Spinks, G. M., and Wallace, G. G. (2011). A reactive wet spinning approach to polypyrrole fibres. *J. Mater. Chem.* 21, 6421–6426. doi: 10.1039/c0jm04406g
- Foroughi, J., Spinks, G. M., and Wallace, G. G. (2015). “Conducting polymer fibers,” in *Handbook of Smart Textiles* (Singapore: Springer), 31–62. doi: 10.1007/978-981-4451-45-1\_14
- Fu, X., Liang, Y., Wu, R., Shen, J., Chen, Z., Chen, Y., et al. (2019). Conductive core-sheath calcium alginate/graphene composite fibers with polymeric ionic liquids as an intermediate. *Carbohydr. Polym.* 206, 328–335. doi: 10.1016/j.carbpol.2018.11.021
- Guo, B., Qu, J., Zhao, X., and Zhang, M. (2019). Degradable conductive self-healing hydrogels based on dextran-graft-tetraaniline and N-carboxyethyl chitosan as injectable carriers for myoblast cell therapy and muscle regeneration. *Acta Biomater.* 84, 180–193. doi: 10.1016/j.actbio.2018.12.008
- Han, L., Lu, X., Wang, M., Gan, D., Deng, W., Wang, K., et al. (2017). A mussel-inspired conductive, self-adhesive, and self-healable tough hydrogel as cell stimulators and implantable bioelectronics. *Small* 13:1601916. doi: 10.1002/smll.201601916
- Hu, T., Wu, Y., Zhao, X., Wang, L., Bi, L., Ma, P. X., et al. (2019). Micropatterned, electroactive, and biodegradable poly (glycerol sebacate)-aniline trimer elastomer for cardiac tissue engineering. *Chem. Eng. J.* 366, 208–222. doi: 10.1016/j.cej.2019.02.072
- Hu, X., Rajendran, S., Yao, Y., Liu, Z., Gopalsamy, K., Peng, L., et al. (2016). A novel wet-spinning method of manufacturing continuous bio-inspired composites based on graphene oxide and sodium alginate. *Nano Res.* 9, 735–744. doi: 10.1007/s12274-015-0952-2
- Jalili, R., Aboutaleb, S. H., Esrafilzadeh, D., Shepherd, R. L., Chen, J., Aminorroaya-Yamini, S., et al. (2013). Scalable one-step wet-spinning of graphene fibers and yarns from liquid crystalline dispersions of graphene oxide: towards multifunctional textiles. *Adv. Funct. Mater.* 23, 5345–5354. doi: 10.1002/adfm.201300765
- Jo, H., Sim, M., Kim, S., Yang, S., Yoo, Y., Park, J.-H., et al. (2017). Electrically conductive graphene/polyacrylamide hydrogels produced by mild chemical reduction for enhanced myoblast growth and differentiation. *Acta Biomater.* 48, 100–109. doi: 10.1016/j.actbio.2016.10.035
- Johra, F. T., Lee, J.-W., and Jung, W.-G. (2014). Facile and safe graphene preparation on solution based platform. *J. Ind. Eng. Chem.* 20, 2883–2887. doi: 10.1016/j.jiec.2013.11.022
- Kadumudi, F. B., Jahanshahi, M., Mehrali, M., Zsuzsán, T. G., Taebnia, N., Hasany, M., et al. (2019). A protein-based, water-insoluble, and bendable polymer with ionic conductivity: a roadmap for flexible and green electronics. *Adv. Sci.* 6:1801241. doi: 10.1002/advs.201801241
- Kamata, H., Li, X., Chung, U., and Sakai, T. (2015). Design of hydrogels for biomedical applications. *Adv. Healthc. Mater.* 4, 2360–2374. doi: 10.1002/adhm.201500076
- Kaur, G., Adhikari, R., Cass, P., Bown, M., and Gunatillake, P. (2015). Electrically conductive polymers and composites for biomedical applications. *RSC Adv.* 5, 37553–37567. doi: 10.1039/C5RA01851J
- Kiew, S. F., Kiew, L. V., Lee, H. B., Imae, T., and Chung, L. Y. (2016). Assessing biocompatibility of graphene oxide-based nanocarriers: a review. *J. Control Release* 226, 217–228. doi: 10.1016/j.jconrel.2016.02.015

## AUTHOR CONTRIBUTIONS

All authors listed have made a substantial, direct and intellectual contribution to the work, and approved it for publication.

## FUNDING

This work has been supported by the Australian Research Council under the Discovery Early Career Researcher Award (JF, DE130100517). The authors also acknowledge the University of Wollongong Australia Global Challenges program.



- Kim, M. J., Lee, J. H., Shin, Y. C., Jin, L., Hong, S. W., Han, D.-W., et al. (2015). Stimulated myogenic differentiation of C2C12 murine myoblasts by using graphene oxide. *J. Korean Phys. Soc.* 67, 1910–1914. doi: 10.3938/jkps.67.1910
- Kim, S., Yoo, Y., Kim, H., Lee, E., and Lee, J. Y. (2015). Reduction of graphene oxide/alginate composite hydrogels for enhanced adsorption of hydrophobic compounds. *Nanotechnology* 26:405602. doi: 10.1088/0957-4484/26/40/405602
- Ku, S. H., and Park, C. B. (2013). Myoblast differentiation on graphene oxide. *Biomaterials* 34, 2017–2023. doi: 10.1016/j.biomaterials.2012.11.052
- Kurapati, R., Kostarelos, K., Prato, M., and Bianco, A. (2016). Biomedical uses for 2D materials beyond graphene: current advances and challenges ahead. *Adv. Mater.* 28, 6052–6074. doi: 10.1002/adma.201506306
- Lee, J. H., Lee, Y., Shin, Y. C., Kim, M. J., Park, J. H., Hong, S. W., et al. (2016). *In situ* forming gelatin/graphene oxide hydrogels for facilitated C2C12 myoblast differentiation. *Appl. Spectrosc. Rev.* 51, 527–539. doi: 10.1080/05704928.2016.1165686
- Li, H., Liu, S., and Lin, L. (2016). Rheological study on 3D printability of alginate hydrogel and effect of graphene oxide. *Int. J. Bioprinting* 2, 54–66. doi: 10.18063/IJB.2016.02.007
- Li, J., Ma, J., Chen, S., Huang, Y., and He, J. (2018). Adsorption of lysozyme by alginate/graphene oxide composite beads with enhanced stability and mechanical property. *Mater. Sci. Eng. C. Mater. Biol. Appl.* 89, 25–32. doi: 10.1016/j.msec.2018.03.023
- Li, Y., Sun, J., Du, Q., Zhang, L., Yang, X., Wu, S., et al. (2014). Mechanical and dye adsorption properties of graphene oxide/chitosan composite fibers prepared by wet spinning. *Carbohydr. Polym.* 102, 755–761. doi: 10.1016/j.carbpol.2013.10.094
- Liang, Y., Zhao, X., Hu, T., Chen, B., Yin, Z., Ma, P. X., et al. (2019). Adhesive hemostatic conducting injectable composite hydrogels with sustained drug release and photothermal antibacterial activity to promote full-thickness skin regeneration during wound healing. *Small* 15:e1900046. doi: 10.1002/sml.201900046
- Liu, J., Cui, L., and Losic, D. (2013). Graphene and graphene oxide as new nanocarriers for drug delivery applications. *Acta Biomater.* 9, 9243–9257. doi: 10.1016/j.actbio.2013.08.016
- Liu, S., Bastola, A. K., and Li, L. (2017). A 3D printable and mechanically robust hydrogel based on alginate and graphene oxide. *ACS Appl. Mater. Interfaces* 9, 41473–41481. doi: 10.1021/acsami.7b13534
- Liu, S., and Li, L. (2017). Effect of functionalized graphene oxide on gelation and scaling law of alginate in aqueous solution. *Eur. Polym. J.* 95, 462–473. doi: 10.1016/j.eurpolymj.2017.08.035
- Liu, X., Miller, A. L., Park, S., Waletzki, B. E., Zhou, Z., Terzic, A., et al. (2017). Functionalized carbon nanotube and graphene oxide embedded electrically conductive hydrogel synergistically stimulates nerve cell differentiation. *ACS Appl. Mater. Interfaces* 9, 14677–14690. doi: 10.1021/acsami.7b02072
- Lu, Z., Chao, Y., Ge, Y., Foroughi, J., Zhao, Y., Wang, C., et al. (2017). High-performance hybrid carbon nanotube fibers for wearable energy storage. *Nanoscale* 9, 5063–5071. doi: 10.1039/c7nr00408g
- Luo, Q., Shan, Y., Zuo, X., and Liu, J. (2018). Anisotropic tough poly (vinyl alcohol)/graphene oxide nanocomposite hydrogels for potential biomedical applications. *RSC Adv.* 8, 13284–13291. doi: 10.1039/C8RA00340H
- Ma, Y., Li, P., Sedloff, J. W., Zhang, X., Zhang, H., and Liu, J. (2015). Conductive graphene fibers for wire-shaped supercapacitors strengthened by unfunctionalized few-walled carbon nanotubes. *ACS nano* 9, 1352–1359. doi: 10.1021/nn505412v
- Mehrali, M., Bagherifard, S., Akbari, M., Thakur, A., Mirani, B., Mehrali, M., et al. (2018). Blending electronics with the human body: a pathway toward a cybernetic future. *Adv. Sci.* 5:1700931. doi: 10.1002/advs.201700931
- Mehrali, M., Sadeghinezhad, E., Akhiani, A. R., Latibari, S. T., Talebian, S., Dolatshahi-Pirouz, A., et al. (2016). An ecofriendly graphene-based nanofluid for heat transfer applications. *J. Clean. Prod.* 137, 555–566. doi: 10.1016/j.jclepro.2016.07.136
- Mehrali, M., Thakur, A., Kadumudi, F. B., Pierchala, M. K., Cordova, J. A. V., Shahbazi, M.-A., et al. (2019). Pectin methacrylate (PEMA) and gelatin-based hydrogels for cell-delivery: converting waste-materials into biomaterials. *ACS Appl. Mater. Interfaces* 11, 12283–12297. doi: 10.1021/acsami.9b00154
- Mehrali, M., Thakur, A., Pennisi, C. P., Talebian, S., Arpanaei, A., Nikkhah, M., et al. (2017). Nanoreinforced hydrogels for tissue engineering: biomaterials that are compatible with load-bearing and electroactive tissues. *Adv. Mater.* 29:1603612. doi: 10.1002/adma.201603612
- Mirabedini, A., Foroughi, J., Romeo, T., and Wallace, G. G. (2015). Development and characterization of novel hybrid hydrogel fibers. *Macromol. Mater. Eng.* 300, 1217–1225. doi: 10.1002/mame.201500152
- Mirabedini, A., Foroughi, J., Thompson, B., and Wallace, G. G. (2016a). Fabrication of coaxial Wet-spun graphene–chitosan biofibers. *Adv. Eng. Mater.* 18, 284–293. doi: 10.1002/adem.201500201
- Mirabedini, A., Foroughi, J., and Wallace, G. G. (2016b). Developments in conducting polymer fibres: from established spinning methods toward advanced applications. *RSC Adv.* 6, 44687–44716. doi: 10.1039/C6RA05626A
- Navai, A., Saini, H., Christenson, W., Sullivan, R. T., Ros, R., and Nikkhah, M. (2016). Gold nanorod-incorporated gelatin-based conductive hydrogels for engineering cardiac tissue constructs. *Acta Biomater.* 41, 133–146. doi: 10.1016/j.actbio.2016.05.027
- Patel, A., Xue, Y., Mukundan, S., Rohan, L. C., Sant, V., Stolz, D. B., et al. (2016). Cell-instructive graphene-containing nanocomposites induce multinucleated myotube formation. *Ann. Biomed. Eng.* 44, 2036–2048. doi: 10.1007/s10439-016-1586-6
- Peng, L., Liu, Y., Gong, J., Zhang, K., and Ma, J. (2017). Continuous fabrication of multi-stimuli responsive graphene oxide composite hydrogel fibres by microfluidics. *RSC Adv.* 7, 19243–19249. doi: 10.1039/C7RA01750B
- Peng, L., Liu, Y., Huang, J., Li, J., Gong, J., and Ma, J. (2018). Microfluidic fabrication of highly stretchable and fast electro-responsive graphene oxide/polyacrylamide/alginate hydrogel fibers. *Eur. Polym. J.* 103, 335–341. doi: 10.1016/j.eurpolymj.2018.04.019
- Qu, J., Zhao, X., Liang, Y., Xu, Y., Ma, P. X., and Guo, B. (2019). Degradable conductive injectable hydrogels as novel antibacterial, anti-oxidant wound dressings for wound healing. *Chem. Eng. J.* 362, 548–560. doi: 10.1016/j.cej.2019.01.028
- Sasaki, M., Karikkineth, B. C., Nagamine, K., Kaji, H., Torimitsu, K., and Nishizawa, M. (2014). Highly conductive stretchable and biocompatible electrode–hydrogel hybrids for advanced tissue engineering. *Adv. Healthc. Mater.* 3, 1919–1927. doi: 10.1002/adhm.201400209
- Shin, S. R., Aghaei-Ghareh-Bolagh, B., Gao, X., Nikkhah, M., Jung, S. M., Dolatshahi-Pirouz, A., et al. (2014). Layer-by-layer assembly of 3D tissue constructs with functionalized graphene. *Adv. Funct. Mater.* 24, 6136–6144. doi: 10.1002/adfm.201401300
- Shin, S. R., Shin, C., Memic, A., Shadmehr, S., Miscuglio, M., Jung, H. Y., et al. (2015). Aligned carbon nanotube-based flexible gel substrates for engineering biohybrid tissue actuators. *Adv. Funct. Mater.* 25, 4486–4495. doi: 10.1002/adfm.201501379
- Shin, S. R., Zihlmann, C., Akbari, M., Assawes, P., Cheung, L., Zhang, K., et al. (2016). Reduced graphene oxide-gelMA hybrid hydrogels as scaffolds for cardiac tissue engineering. *Small* 12, 3677–3689. doi: 10.1002/sml.201600178
- Stankovich, S., Dikin, D. A., Dommett, G. H., Kohlhaas, K. M., Zimney, E. J., Stach, E. A., et al. (2006). Graphene-based composite materials. *Nature* 442, 282–286. doi: 10.1038/nature04969
- Stankovich, S., Dikin, D. A., Piner, R. D., Kohlhaas, K. A., Kleinhammes, A., Jia, Y., et al. (2007). Synthesis of graphene-based nanosheets via chemical reduction of exfoliated graphite oxide. *Carbon* 45, 1558–1565. doi: 10.1016/j.carbon.2007.02.034
- Talebian, S., Foroughi, J., Wade, S. J., Vine, K. L., Dolatshahi-Pirouz, A., Mehrali, M., et al. (2018). Biopolymers for antitumor implantable drug delivery systems: recent advances and future outlook. *Adv. Mater.* 30:1706665. doi: 10.1002/adma.201706665
- Wang, L., Wu, Y., Guo, B., and Ma, P. X. (2015). Nanofiber yarn/hydrogel core–shell scaffolds mimicking native skeletal muscle tissue for guiding 3D myoblast alignment, elongation, and differentiation. *ACS Nano* 9, 9167–9179. doi: 10.1021/acs.nano.5b03644
- Wang, L., Wu, Y., Hu, T., Guo, B., and Ma, P. X. (2017). Electrospun conductive nanofibrous scaffolds for engineering cardiac tissue and 3D bioactuators. *Acta Biomater.* 59, 68–81. doi: 10.1016/j.actbio.2017.06.036
- Wang, S., Guan, S., Xu, J., Li, W., Ge, D., Sun, C., et al. (2017). Neural stem cell proliferation and differentiation in the conductive PEDOT-HA/Cs/Gel scaffold for neural tissue engineering. *Biomater. Sci.* 5, 2024–2034. doi: 10.1039/c7bm00633k



- Wu, Y., Wang, L., Guo, B., and Ma, P. X. (2017). Interwoven aligned conductive nanofiber yarn/hydrogel composite scaffolds for engineered 3D cardiac anisotropy. *ACS. Nano* 11, 5646–5659. doi: 10.1021/acsnano.7b01062
- Wu, Y., Wang, L., Guo, B., Shao, Y., and Ma, P. X. (2016). Electroactive biodegradable polyurethane significantly enhanced Schwann cells myelin gene expression and neurotrophin secretion for peripheral nerve tissue engineering. *Biomaterials* 87, 18–31. doi: 10.1016/j.biomaterials.2016.02.010
- Xiang, C., Young, C. C., Wang, X., Yan, Z., Hwang, C. C., Cerioti, G., et al. (2013). Large flake graphene oxide fibers with unconventional 100% knot efficiency and highly aligned small flake graphene oxide fibers. *Adv. Mater.* 25, 4592–4597. doi: 10.1002/adma.201301065
- Xu, Y., Lin, Z., Huang, X., Wang, Y., Huang, Y., and Duan, X. (2013). Functionalized graphene hydrogel-based high-performance supercapacitors. *Adv. Mater.* 25, 5779–5784. doi: 10.1002/adma.201301928
- Xu, Z., and Gao, C. (2014). Graphene in macroscopic order: liquid crystals and wet-spun fibers. *Acc. Chem. Res.* 47, 1267–1276. doi: 10.1021/ar4002813
- Xu, Z., Liu, Y., Zhao, X., Peng, L., Sun, H., Xu, Y., et al. (2016). Ultrastiff and strong graphene fibers via full-scale synergetic defect engineering. *Adv. Mater.* 28, 6449–6456. doi: 10.1002/adma.201506426
- Xu, Z., Sun, H., Zhao, X., and Gao, C. (2013). Ultrastrong fibers assembled from giant graphene oxide sheets. *Adv. Mater.* 25, 188–193. doi: 10.1002/adma.201203448
- Yang, S., Jang, L., Kim, S., Yang, J., Yang, K., Cho, S. W., et al. (2016). Polypyrrole/alginate hybrid hydrogels: electrically conductive and soft biomaterials for human mesenchymal stem cell culture and potential neural tissue engineering applications. *Macromol. Biosci.* 16, 1653–1661. doi: 10.1002/mabi.201600148
- Zhang, X., Yin, J., Peng, C., Hu, W., Zhu, Z., Li, W., et al. (2011). Distribution and biocompatibility studies of graphene oxide in mice after intravenous administration. *Carbon* 49, 986–995. doi: 10.1016/j.carbon.2010.11.005
- Zhang, Y., Nayak, T. R., Hong, H., and Cai, W. (2012). Graphene: a versatile nanoplatfrom for biomedical applications. *Nanoscale* 4, 3833–3842. doi: 10.1039/c2nr31040f
- Zhao, Y., Gong, J., Niu, C., Wei, Z., Shi, J., Li, G., et al. (2017). A new electrospun graphene-silk fibroin composite scaffolds for guiding Schwann cells. *J. Biomater. Sci. Polym. Ed.* 28, 2171–2185. doi: 10.1080/09205063.2017.1386835
- Zheng, H., Yang, J., and Han, S. (2016). The synthesis and characteristics of sodium alginate/graphene oxide composite films crosslinked with multivalent cations. *J. Appl. Polym. Sci.* 133:43616. doi: 10.1002/app.43616
- Zhou, L., Fan, L., Yi, X., Zhou, Z., Liu, C., Fu, R., et al. (2018). Soft conducting polymer hydrogels cross-linked and doped by tannic acid for spinal cord injury repair. *ACS Nano* 12, 10957–10967. doi: 10.1021/acsnano.8b04609

**Conflict of Interest:** The authors declare that the research was conducted in the absence of any commercial or financial relationships that could be construed as a potential conflict of interest.

Copyright © 2020 Talebian, Mehrali, Raad, Safaei, Xi, Liu and Foroughi. This is an open-access article distributed under the terms of the Creative Commons Attribution License (CC BY). The use, distribution or reproduction in other forums is permitted, provided the original author(s) and the copyright owner(s) are credited and that the original publication in this journal is cited, in accordance with accepted academic practice. No use, distribution or reproduction is permitted which does not comply with these terms.



# Fabrication and Specific Functionalisation of Carbon Fibers for Advanced Flexible Biosensors

Zhang Wenrui<sup>†</sup>, Meng Fanxing<sup>†</sup>, Qin Yanan, Chen Fei, Yue Haitao<sup>\*</sup> and Zhang Minwei<sup>\*</sup>

College Life Science & Technology, Xinjiang University, Urumqi, China

## OPEN ACCESS

### Edited by:

Chengyi Hou,  
Donghua University, China

### Reviewed by:

Pengchao Si,  
Shandong University, China  
Yang Hu,  
Technical University of  
Denmark, Denmark

### \*Correspondence:

Zhang Minwei  
zhangmw@xju.edu.cn;  
zhang78089680@sina.com  
Yue Haitao  
yuehaitao@tsinghua.org.cn

<sup>†</sup>These authors have contributed  
equally to this work

### Specialty section:

This article was submitted to  
Polymer Chemistry,  
a section of the journal  
Frontiers in Chemistry

**Received:** 12 July 2020

**Accepted:** 17 August 2020

**Published:** 23 September 2020

### Citation:

Wenrui Z, Fanxing M, Yanan Q, Fei C,  
Haitao Y and Minwei Z (2020)  
Fabrication and Specific  
Functionalisation of Carbon Fibers for  
Advanced Flexible Biosensors.  
Front. Chem. 8:582490.  
doi: 10.3389/fchem.2020.582490

This review aims at offering an up-to-date comprehensive summary of carbon fibers (CFs)-based composites, with the emphasis on smart assembly and purpose-driven specific functionalization for their critical applications associated with flexible sensors. We first give a brief introduction to CFs as a versatile building block for preparation of multi-functional materials and the current status of research studies on CFs. This is followed by addressing some crucial methods of preparation of CFs. We then summarize multiple possibilities of functionalising CFs, an evaluation of some key applications of CFs in the areas of flexible biosensors was also carried out.

**Keywords:** carbon fibers, fabrication, functionalization, compound material, flexible biosensor

## INTRODUCTION

Carbon fibers (CFs) being thin long filaments, contain more than 90 wt% of carbon and exhibit many outstanding properties such as high modulus (200–900 GPa), high compressive strength (up to 3 GPa), high tensile strength (2–7 GPa) (Nitolaksha et al., 2016; Meng et al., 2017), flexibility, and tunable electrochemical performance so that they can be widely used in various fields (Chen et al., 2020), such as aerospace, automobile, chemical industry, transportation, construction, sewage treatment and other fields. In addition, they can also serve as multifunctional hosts by a facile air-annealing process to get higher defective edge/plane sites, more oxygen-containing functional groups, which can load different electrochemical active substances such as noble metals, metal oxides, polymers, metal-organic frames (MOFs). As a result, they can be applied to fabricate electrochemical sensors with high sensitivity and flexibility as well as energy equipment (e.g., supercapacitors, batteries) with high energy/power density. The greatly improved performance has been found via combining pure CFs with the metal materials, metallic oxide materials, metallic sulfide materials, carbon materials and so on. For instance, the enhancement of performance was achieved by decorating CFs with cobalt oxide nanoparticles via solid-state mixing and thermal decomposition steps. As a result, the energy storage capacity of the capacitor is greatly enhanced. Moreover, CFs can be assembled into various structures applied in sensors, e.g., the electrode with porous structure can easily achieve the penetration of electrolyte and the diffusion of ions as well as the continuous conductive network could enable the rapid transfer of charge to active substances and metal ions (Zhang et al., 2019; Yang et al., 2020). CFs have excellent surface areas and can modify as many enzymes as possible, so they are widely used as substrate materials for biosensors. In the review, we also summarize the current research progress of CFs-based biosensors and their applications in flexible and wearable biosensors. **Figure 1** outlines the interest and focus of the present review.

## PREPARATION OF CFS

It has been more than 100 years since the discovery of CFs. With the continuous updating of technology, the current preparation process of CFs has been very matured. Generally, CFs are prepared from synthetic fibers (precursor fibers) and different fiber raw materials need to use different production processes to prepare CFs. However, it is similar in the general process, which is stable precursor fiber pyrolysis and controlled stretching synthesis of CFs. At present, the main raw materials for the manufacture of CFs are polyacrylonitrile (PAN), pitch and rayon. In the actual production process, 90% of the CFs are produced from PAN-based precursors, and the remaining 10% are produced from precursors of asphalt or rayon (Bhatt and Goe, 2017). This is because compared with asphalt fiber and rayon fiber, polyacrylonitrile-based CFs have a higher strength, modulus and failure strain, and a higher yield rate. Carbon fiber (CF) is a kind of high strength material, which plays an important role in the fields of aerospace, automobile, chemical industry, general engineering, missile, nuclear, composite reinforcement and textile (Wazir and Kakakhel, 2009).

## CFS CLASSIFICATION BASED ON PRECURSORS

### PAN-Based CFs

A PAN-based polymer is the best precursor for the production of CFs because of its tensile and compression properties and a carbon yield of up to 68% (Hamid et al., 2017). Wet spinning is used in the commercial production of CFs from most of the precursors of PAN-based polymers. However, wet spinning is

gradually being replaced by the dry-jet-wet spinning, as it exhibits several advantages such as low adhesion between fibers and high specific surface area for improving the interlaminar shear strength of composite materials. Due to the isolation of extrusion expansion and epidermis solidification in dry-wet spinning, the formation mechanism of fiber has changed, so the phenomena such as cortical fracture and epidermis fold basically disappear in the process of wet spinning. The surface and internal defects of dry-wet spinning are reduced, and the density is increased. At the same time, dry-wet spinning also has the characteristics of high spinneret drawing, high spinning speed, easy to obtain high strength and high orientation fiber (Tian et al., 2017), so as to ensure the sufficient strength of CFs, which is the development direction of CFs production.

### Pitch-Based CFs

Pitch is produced by pyrolysing synthetic polymers. The molecular weight of pitch is in the range of 600–1,000 g/mol, and it contains aromatic groups. The diameter of pitch-based CFs ranges between 10 and 12 mm and the tensile strength and modulus of pitch-based CFs are 3 GPa and 960 GPa, respectively. Pitch is easy to be produced in large quantities and is attractive as a precursor for large-scale CFs manufacturing because the cost of pitch is significantly lower than that of other precursor fibers. Pitch-based precursors have other advantages that make them an attractive alternative, such as less energy required to convert aromatic graphitised materials and a lower proportion of hydrogen, nitrogen and other non-carbon elements (Wazir and Kakakhel, 2009; Yoshikawa et al., 2020).

### Rayon-Based CFs

Rayon is a manufactured fiber made up of cellulose extracted mainly from plants (cotton wool and pulp) (Chen X. et al., 2019). Cellulose is a promising raw material for CFs. Also, the cellulose precursor forms strong CFs by pyrolysis, which have high thermal conductivity, high purity, good mechanical toughness and low cost. The new production process requires that rayon fibers be carbonized into high modulus CFs filaments. In addition to the early low-strength fibers, this was followed by significantly increased yarns with high strength and high modulus of elasticity. However, due to the high cost of hot drawing, the production of these CFs has been delayed for many years, the CFs spinning process is low, and the properties of cellulose precursors are also delayed (Lee et al., 2017). Currently, only very few CFs are produced in this way.

### CFs Based on Other Precursors

In addition to the several widely used precursors mentioned above, other natural fibers such as silk and chitosan are also considered to be precursors for CFs manufacturing, which can reduce production costs, but can not provide strong mechanical properties. In addition, some linear and cyclic polymers have also been proved to be suitable for the preparation of CFs, but the results show that their carbon production is very low, thus hindering their further application (Khayyam et al., 2020).

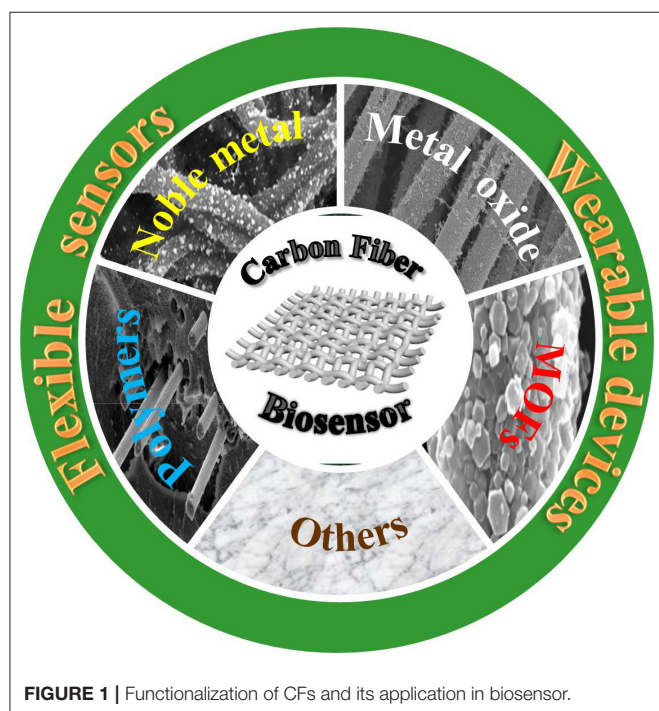


**FIGURE 1** | Functionalization of CFs and its application in biosensor.



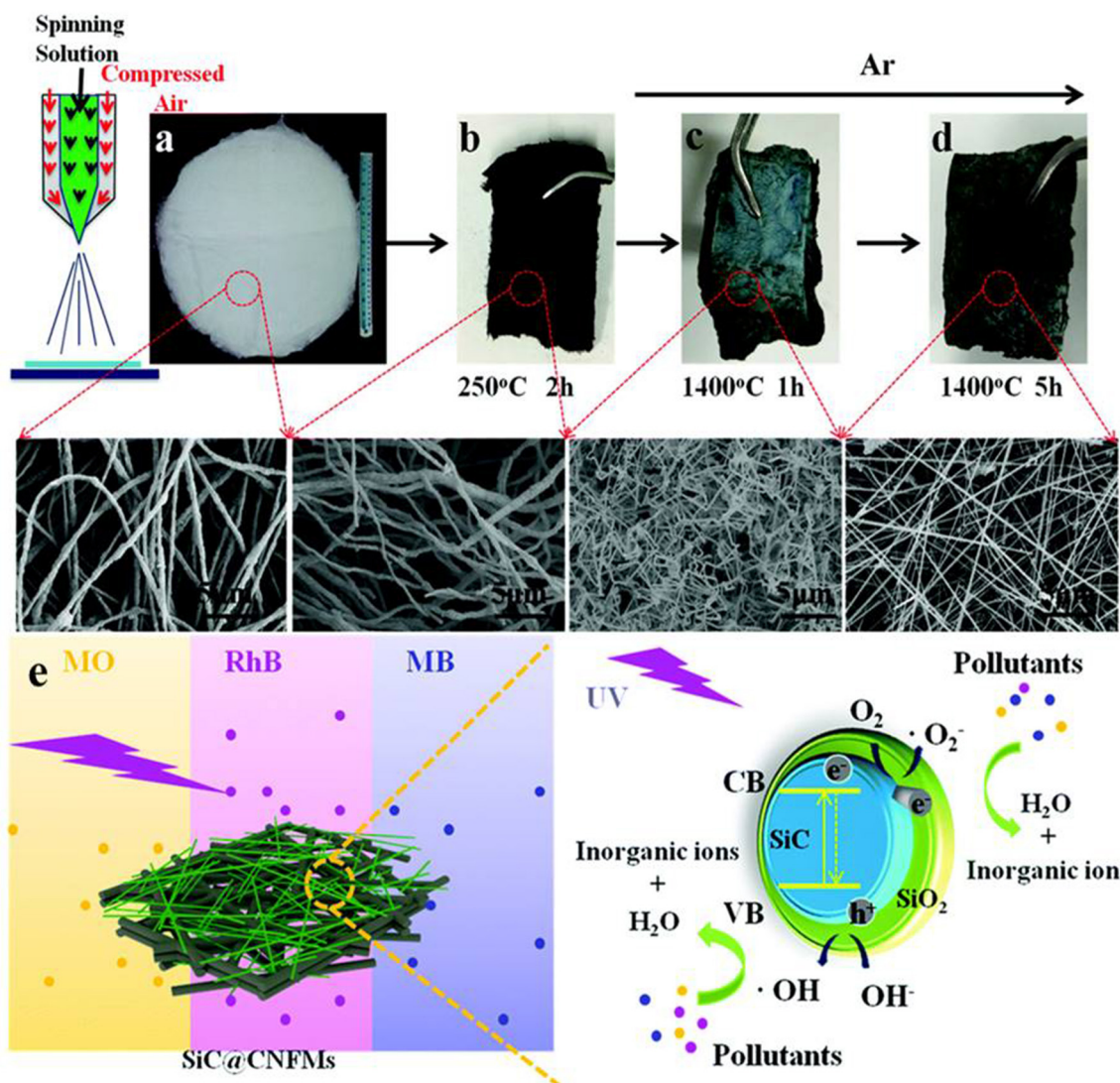


**FIGURE 2 |** (a–d) Schematic illustration of the fabrication process of SiC@CNFMs. (e) Photocatalytic mechanism of the SiC@CNFMs-5. Reproduced with permission from Chen Y. et al. (2019).

## Spinning Classification

Generally speaking, the first step in the production process of CFs is to convert the powder or granular precursor into continuous fibers, that is, the spinning process (Lee et al., 2016). The frequently used spinning techniques can be classified as blow-spinning, electrostatic spinning, and centrifugal spinning depending on the force applied to the precursor solution/melt.

## Blow Spinning

Blow-spinning is a promising method for producing micro-/nano-fibers in large-scale production processes by using high-speed air. The spinning dope is loaded in a syringe with a coaxial single spinneret consisting of an inner nozzle for

the precursor solution and an outer nozzle for the high-speed air used. Blow-spinning is divided into solution spinning and melt spinning. Solution spinning can be divided into dry spinning and wet spinning according to the direction of the spinning solution from the nozzle. For instance, a robust photocatalytic composite SiC@SiO<sub>2</sub>/carbon nanofibre mat is prepared via facile blow-spinning (Figure 2). The spinning dope was fed into a 0.5 mm diameter needle and then stretched by airflow with 0.12 MPa pressure. The synthesized composite exhibited excellent photodegradation of dyes that showed good recycling performance with a dye degradation above 88–95% after 5 cycles, thanks to the utilization of PAN-based carbon nanofibre mats and high chemical stability under both alkaline and acidic environment environments (Chen Y. et al., 2019).



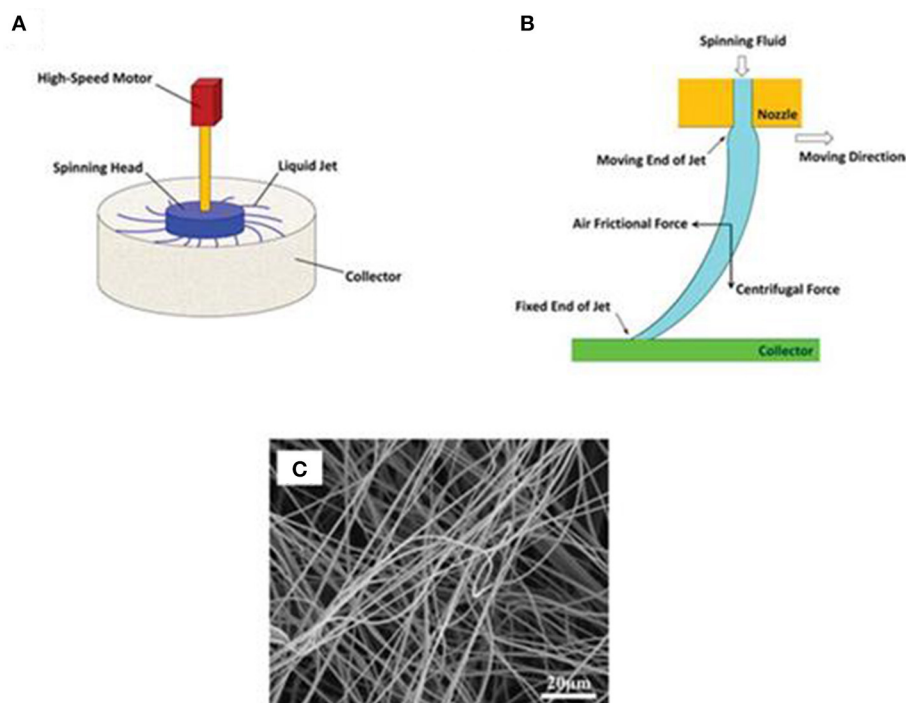


**FIGURE 3 | (A)** Schematic of a basic bench-top centrifugal spinning setup. **(B)** The path of a liquid jet ejected from the nozzle tip during centrifugal spinning. **(C)** SEM image of PAN nanofibers prepared by centrifugal spinning. Reproduced with permission from Zhang and Lu (2014).

## Electrospinning

Electrospinning is a simple and versatile method that can be used to synthesize nanofibres with high porosity, high specific surface area, and excellent mechanical strength. It is a top-down technology where there is a high voltage field between the precursor solution and a conductive substrate. It can make the drop of the solution with the charge in the electric field overcome the surface tension to emit Taylor cone to fabricate ultrafine nanofibres. A porous, free-standing carbon electrode with a high specific surface area was prepared by electrostatic spinning. Jennifer S. Atchison and his group obtained sub-micrometer-sized fibers that were homogeneously composed of nanodomains of metal carbides such as ZrC/C, TiC/C, NbC/C. The range of fiber diameters and the specific surface area is between 294 - 108 nm and  $224 \text{ m}^2 \text{ g}^{-1}$  for ZrC/C, 122 - 28 nm and  $450 \text{ m}^2 \text{ g}^{-1}$  for TiC/C, as well as 65 - 36 nm and  $121 \text{ m}^2 \text{ g}^{-1}$  for NbC/C (Atchison et al., 2015). These metal carbide/carbon nanocomposite fibers were acquired in the form of freestanding non-woven textiles that could serve as an ideal precursor for synthesizing highly porous carbide-derived carbon electrodes for electrochemical applications. However, it is worth noting that the instability of the precursor with a relatively high concentration of inorganic salts often arises during the electrospinning process because the electrical conductivity of the precursor rises with the increase of inorganic salts content and the electrospinning has to bear the risk of high voltage, low productivity, complex operating conditions which limits the application of this technology in large-scale nanofibre production.

## Centrifugal Spinning

As a new spinning method, which is mainly used in the spinning of glass fiber, phenolic and general grade pitch CFs, centrifugal spinning can solve the shortage of electrostatic spinning to some extent. It uses centrifugal force instead of the electrostatic to accomplish the formation of precursor fibers. Therefore, regardless of whether the polymer has good conductivity, it no longer needs the restriction of high voltage, which can sharply reduce the cost of spinning. Moreover, one of the important characteristics is its high production rate (Zhang and Lu, 2014; Song et al., 2019) (Figure 3). The formation mechanism of Ethyl cellulose (EC)/PVP fiber between centrifugal spinning and electrospinning under the same solution and ambient conditions (EC/PVP = 90/10%) was discussed. Through a binary solvent system of ethanol and water (ethanol/water = 70/30%), the micro-porous and nano-porous structures are fabricated by centrifugal spinning with the rotational speed of the spinneret controlled at 3,500 rpm. The wonderful performances of centrifugal spinning may prove that it is not only a novel technique but also a viable alternative for the production of long continuous, non-woven mats of nanofibres at a considerable higher yield.

## Others

Compared with the preparation of single-component fibers, composite fibers have more extensive applications due to their various components and structures. The preparation of composite fibers is mainly based on coaxial spinning by using two

coaxial spinnerets with different inner diameters. This technique can solve the problem of the spinning solution that needs to be a uniform system when preparing composite fibers or the fibers with special structures (e.g., hollow fibers) and it can also properly combine the efficiency and advantages of two kinds of materials to make them deliver excellent properties that they never had when they are used alone (Zhang et al., 2020).

## CARBONIZATION

The main purpose of the carbonization process is to remove most of the oxygen, nitrogen, hydrogen and other elements in precursor fibers by thermal decomposition in order to increase the carbon content (reach at least 90%) and make the coupling reaction between adjacent carbon chains to occur. The whole carbonization process can be summarized into three parts: pre-oxidation, low-temperature carbonization, and high-temperature carbonization (Karacan and Erzurumluoglu, 2015; Byrne et al., 2016; Hameed et al., 2016). The pre-oxidation takes place in an oxygen environment to modify more oxygen-containing functional groups on the surface of precursor fibers and the temperature is controlled within the range of 200–300°C by utilizing oven or muffle furnace as the heating equipment. Through the process, a series of reactions such as dehydrogenation, cyclisation, aromatisation and crosslinking occurred for transforming the linear molecular chain to a conjugated ladder structure thus improving the thermal stability of the precursor fiber as well as the crystallinity of CFs will increase via forming C=C bonding. The whole carbonization process takes place in the nitrogen environment under a temperature of at least 800°C by furnace or tube-furnace to increase the proportion of carbon element. Compared with

untreated CFs, by increasing boron content in the fiber can improve the tensile strength and modulus by 16 and 26%, respectively. Because the substitutional and interstitial diffusion of boron can remove structural defects and relax the distortions in the CF structure to enhance its mechanical properties (Diani et al., 2006; Qin et al., 2012). The stable heating rate during carbonization directly affects the performance of CFs. Too high heating rate will introduce defects, while too low heating rate will waste more nitrogen in the early stage. To avoid thermal shock on CFs, the low-temperature carbonization process mentioned above is very necessary.

## FUNCTIONAL CFS

CFs have been widely studied as nano-materials because of their outstanding chemical and physical properties (Wei and Qu, 2012). However, with the development of technology, in order to meet the research of some specific performance nanomaterials, more and more functional materials are compounded onto the surface of CFs, which significantly improve the properties of composites, such as precious metal nanomaterials, polymers, metal oxides, MOFs and so on. Here, we review the strategies of these common functional CFs.

### Noble Metal Functionalised CFs

Precious metal nanomaterials have empty d-electron orbitals, small energy level gaps, easy to form coordination bonds, and easy to adsorb and desorb groups on their surface, so they form intermediate active compounds easily, thus allowing them to have high catalytic activity. In recent years, precious metal nanomaterials have been often used as nanomaterials to modify the surface of CFs because of their excellent stability, good

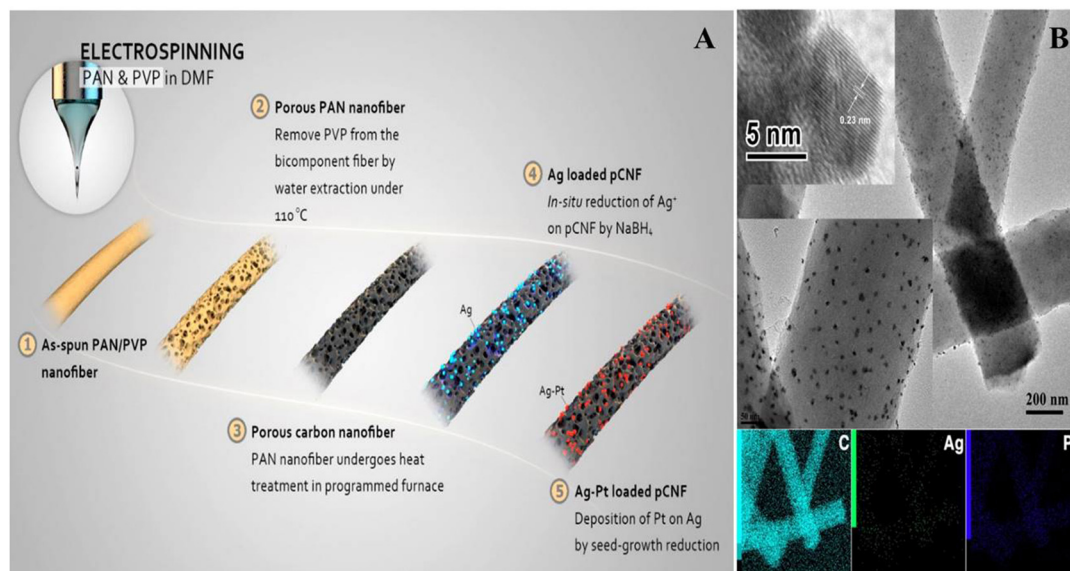


**FIGURE 4 | (A)** Schematic illustration of the preparation of Ag-Pt/pCNFs. **(B)** TEM images of Ag-Pt/pCNFs and the corresponding elemental mappings. Reproduced with permission from Huang et al. (2014).

electrical conductivity and high biocompatibility. At the same time, the production and modification of metal nanoparticles are relatively simple. In order to increase the specific surface area and enhance the electrochemical performance of CFs, gold nanoparticles were used to etch the surface of CFs. The results show that etching not only reduces the diameter of CFs, but also affects the morphology and roughness of CFs surface by producing defects or porous structures. At the same time, it is also found that this etching method will not destroy the  $sp^2$  bonding of graphite, but may focus on grain boundaries or defects (Long et al., 2017). CFs modified by Au NPs are also used to detect cancer cells. Through the preparation of CFs microelectrode with hierarchical nanostructure of Au-MnO<sub>2</sub>/GO/CF, the grapheme-based composite enhanced the specific surface area of CFs and improved the electrical conductivity of the material, and then the MnO<sub>2</sub> on CFs formed porous nanostructures, it provides an excellent matrix for the growth of Au NPs. The results show that the prepared microelectrode can realize real-time, rapid and sensitive detection of hydrogen peroxide secreted by human cervical cancer cells (Abdurhman et al., 2015). At the same time, some researchers directly electrodeposited gold nanoparticles on the surface of CFs to monitor the release of dopamine and to determine the intracellular exocytosis of rats (Barlow et al., 2018). At present, there are few reports on electrochemical detection of dopamine with bimetallic nanomaterials. Based on this, researchers have prepared Ag-Pt bimetallic nanomaterials modified CFs microelectrodes to achieve rapid and sensitive detection of dopamine (Figure 4). The results show that the sensor has the advantages of fast current response, high sensitivity, wide detection range and low detection limit, and can effectively eliminate the effect of interfering substances on the detection results of dopamine (Huang et al., 2014). In conclusion, precious metal composite CFs nanomaterials show the synergistic effect of various components, which further improve the properties of the composites, especially in the application of batteries and capacitors. In the future, precious metals will remain competitive in the application of functional CFs.

## Metal Oxide Functionalised CFs

As the first choice of catalysts, metal oxide nanomaterials are widely used in the catalytic reaction of oxidation-reduction mechanism (Navrotsky et al., 2010), including the fabrication of various sensors and anode materials for batteries, etc., and the combination of metal oxides and CFs is also a common strategy of functionalized CFs. The researchers synthesized a humidity sensor based on bismuth ferrite nanoparticles BiFeO<sub>3</sub> (BFO), and successfully prepared a high-performance humidity sensor by combining BFO with CFs by hydrothermal method. Compared with BFO as humidity sensitive units, composite nanomaterials exhibit high sensitivity, low hysteresis and excellent stability, which proves the potential of BFO in humidity sensing (Douani et al., 2020). With the fine requirements of blasting, the ignition device of detonation has become the focus of researchers' exploration, in which the energy conversion element is the core of the research hotspot. The preparation of high-quality energy conversion elements can enhance the ignition

efficiency, shorten the ignition delay and improve the success rate of detonation. Therefore, taking advantage of the good electrical conductivity and easy surface modification of CFs, the researchers prepared a new type of ignition device by compounding Al/BiO<sub>3</sub> nanomaterials on the surface of CFs, in which Al/BiO<sub>3</sub> can improve the detonation ability and reliability. As the energy conversion element of the ignition device, this is a new application field of CFs materials, and it also develops a new research idea for the ignition device (Yi et al., 2020).

Transition metal oxides are widely used as electrode materials for energy storage devices because of their easy availability and high capacitance. Combining transition metal oxides with CFs has been proved to be an effective method to improve the specific capacitance and energy density of devices. It will still be a hotspot in the research of battery devices in the future (Ma et al., 2017).

## Polymers Modified CFs

CFs composites have excellent tensile properties and stiffness, as well as light and thin, good heat resistance and other advantages, so they are ideal structural materials and are widely used in medical, construction, transportation, aerospace and other fields (Li et al., 2015). Among them, the degree of interfacial adhesion between CFs and matrix is the key to determine the properties and structure of CFs composites (Zhang et al., 2018a). Polymer molecules are often reported to be used to modify CFs to enhance their interfacial stickiness. Based on this, we summarize the research and application of some polymer matrix modified CFs in recent years. They compounded the polydopamine-nickel modified CFs material with rigid polyurethane (RPU) and studied the mechanical and electrochemical properties of the composite (Huang et al., 2020). Compared with the original CFs-RPU composites, the strength, toughness and electrical properties of the modified CFs composites are significantly improved due to the chemical cross-linking between CFs and RPU interface. A green functionalisation method for the modification of CFs in water with polyoxypropylene diamine (D400) as the coupling agent and curing agent was reported (Wang et al., 2017). Through the study of the microstructure and mechanical properties of the modified composites, it was found that D400 not only did not change the surface structure of CFs, but enhanced the polarity, lubricity and roughness of CFs surface.

Polymer reinforced CFs composites have attracted wide attention from researchers because it combines the good electrical conductivity and mechanical properties of CFs and the excellent interfacial adhesion and thermoplasticity of polymers (Liu and Kumar, 2014; Wen et al., 2019). It can not only be used for the preparation of microdevices, such as sensors, energy storage devices but also in aerospace, automotive industry and other heavy industry assembly. CFs reinforced composites still have broad application prospects.

## Metal-Organic Frameworks (MOFs) Functionalised CFs

MOFs are new organic porous materials, also known as porous coordination polymers (PCPs). Generally speaking, they are composed of two main components: metal ions or clusters and organic ligands, both of which are mainly assembled by



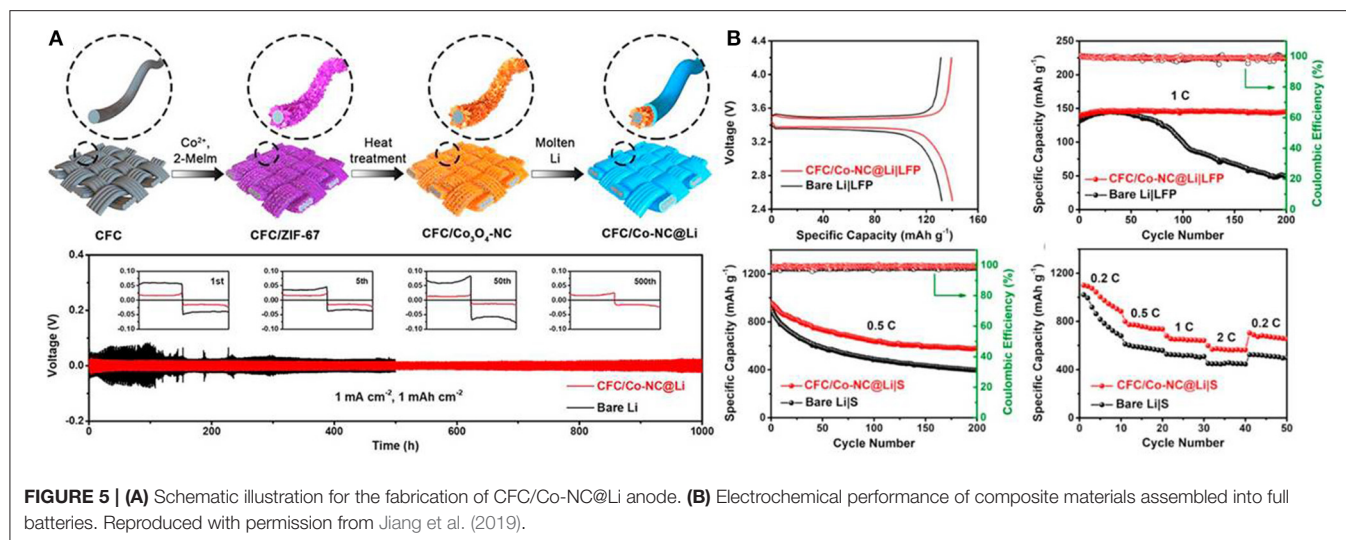


**FIGURE 5 | (A)** Schematic illustration for the fabrication of CFC/Co-NC@Li anode. **(B)** Electrochemical performance of composite materials assembled into full batteries. Reproduced with permission from Jiang et al. (2019).

clear coordination bonds. However, the further application of pure MOFs is limited because of their unique shape, limited function and unsatisfactory performance. In recent years, MOFs composites have become a new research hotspot. For example, inorganic materials, carbon materials, metal nanocrystals, polymers and biomolecules have been proved to be able to combine with MOFs to form new multifunctional composites. MOFs composites are widely used in sensors, batteries, supercapacitors, gas storage and separation, catalysis and so on. In this part, we summarize the applications and challenges of MOFs-CFs composites in these fields in recent years (Li et al., 2017; Jiao et al., 2019; Meng et al., 2020). Lithium-ion batteries and sodium-ion batteries have been widely used in energy storage systems, in which the selection of electrode materials is always the main factor affecting the performance of batteries. CFs have been widely studied as one of the battery anode materials, but their low reversibility in battery manufacturing hinders their further application. For this reason, MOF-derived, Co<sub>3</sub>O<sub>4</sub>-intercalated and nitrogen-doped porous carbon nanoarrays were prepared on CFs sheets (CFC/Co<sub>3</sub>O<sub>4</sub>-NC) as anode materials for lithium-ion batteries for the first time (Jiang et al., 2019). Then the matrix is combined with the molten Li, and the molten Li reacts with the matrix to obtain a composite anode (CFC/Co-NC@Li), which can effectively slow down the volume change and inhibit the growth of Li dendrites (Figure 5). Repeated stripping/plating Li 500 cycles (1,000 h) at low potential (18 mV) still shows excellent stability and long service life.

In addition, MOF modified CFs composites are also used to improve interfacial properties and efficient oxygen evolution reaction. MOFs show remarkable advantages in improving the interfacial properties of composites (Zhu and Xu, 2014). Researchers hope to improve the interfacial properties of CFs/epoxy composites by growing nano-flake MOFs on the surface of CFs (Li et al., 2020). CFs modified by nano-flake MOFs have a uniform surface structure, and the interfacial shear strength and surface energy increase by 70.30 and 69.75%, respectively, under the action of MOF. As a new kind of

porous crystal materials, MOFs have been successfully prepared. However, because of their inherent poor chemical stability and weak conductivity, they are often used as precursors or templates to synthesize various carbon-based structures (Choi et al., 2011). It is still a challenge to build unique MOF-based composites and improve their properties in the future.

## Other Materials Functionalised CFs

In addition to the above-modified materials, nanomaterials such as graphene oxide and carbon nanotubes are also used to functionalise CFs. CFs composites containing carbon nanotubes and graphene have significantly improved mechanical, electrical and thermal properties (Chou et al., 2010; Kong et al., 2013; Rahmadian et al., 2013). By coating the carboxylated carbon nanotubes on the CFs microelectrode, a micron biological electrode with high specific surface area that can be used as the carrier of immobilized enzyme was prepared (Wen et al., 2011). The results show that the CFs electrode modified by carbon nanotubes can make the current density of the electrode show a quantifiable and observable increase, compared with the bare CFs electrode, the modified electrode increases by 2,000 times. At the same time, it is also found that due to the hydrophilicity of carboxylated carbon nanotubes, the biocatalyst precursor enters into the porous structure to form carbon nanotube-hydrogel composites, which can increase the concentration of active media and enzymes. The current density of the modified glucose oxidase electrode can be increased by 6.4 times to 16.63 mA cm<sup>-2</sup>. This study laid a foundation for the preparation and application of bioelectrode and biofuel cell supported by CFs. Carbon nanotubes have greatly improved the sensitivity of the sensor, and this sensor has been successfully applied to the detection of NO release from human venous endothelial cells. Graphene oxide has the characteristics of micron size, high aspect ratio and two-dimensional flake geometry, which can effectively deflect cracks when bending/shearing at the interface of composites (Xu and Buehler, 2010). Sizing agents containing different concentrations of graphene oxide to modify the interface of CFs was reported



(Zhang et al., 2012; Jiang et al., 2017). Through the study and analysis of the morphology, interfacial shear strength and thermomechanical properties of CFs composites, it is proved that the mechanical properties of CFs/epoxy composites can be significantly improved by introducing graphene on the surface of CFs/epoxy composites. The composites with improved mechanical properties may show great application potential in the automotive industry and aerospace industry.

## APPLICATION OF BIOSENSOR BASED ON CFS

As an important technology, an electrochemical biosensor has the advantages of simple operation, rapid analysis, high selectivity, and low cost etc. In recent years, with the rapid development of sensors, the requirements for sensors are increasing. (e.g., high sensitivity, low detection limit, excellent biocompatibility and stability etc.). It has been paid high attention and widely used in environmental detection, food industry, fermentation industry, biomedical research, and other fields. Due to the outstanding properties of CFs such as low relative density, good mechanical strength, high-temperature resistance and their structure can be adjusted into various geometric shapes according to the different needs. With the rapid rise of flexible electrodes and wearable electronic products, biosensors are not limited to the laboratory level. Researchers integrate CFs materials into flexible devices and wearable electronic devices to prepare a new type of miniaturized and portable biosensors. Now, biosensors based on flexible electrodes and wearable devices of CFs nanomaterials have been widely used in environmental analysis, food safety, biomedicine and human health monitoring.

### Conventional Electrochemical Biosensor Based on CFs

The porosity of CFs based electrodes is conducive to the penetration of electrolyte and the diffusion of ions and the continuous conducting network can achieve the rapid transfer of charge between active substances and metal ions. CFs have become a biosensing platform for the detection of biomolecules because of their good biocompatibility, excellent electrical conductivity and robust mechanical properties. Furthermore, thanks to their unique electrochemical properties caused by small size which possess micron size in one dimension, microelectrodes have attracted considerable interests in electrochemical analysis. For instance, the core-shell structure of two-dimension  $\text{VS}_2@\text{VC}@\text{N}$ -doped carbon sheets decorated by ultrafine Pd nanoparticles vertically grown on CFs by a modified template-free hydrothermal method, which assembled into a unique 3D rosette-like array was used to fabricate an  $\text{H}_2\text{O}_2$  electrochemical microsensor (Yuan et al., 2020). This biosensor showed excellent electron transfer ability, electro-catalytic activity, stability and biocompatibility because of the unique rosette-like array structure. It could be used for real-time *in situ* electrochemical detection of  $\text{H}_2\text{O}_2$  in live cancer cells and cancer tissue, exhibiting a high sensitivity of  $152.7 \mu\text{A cm}^{-2} \text{ mM}^{-1}$ , and

a detection limit (LOD) of 50 nM (a signal-to-noise ratio of 3:1) as well as great reproducibility and anti-interference ability. In addition to detecting  $\text{H}_2\text{O}_2$ , the electrode fabricated (Wu et al., 2019) consists of nitrogen-doped cotton carbon fibers (NCFs) modified with silver nanoparticles by electrodeposition has been proposed as a biosensor with excellent catalytic capability for superoxide anion release from cells either under normal or under oxidative stress conditions. The electrochemical sensor operates at a low potential of  $-0.5 \text{ V}$  (vs. SCE), displayed a marvelously wide range that covers 10 orders of magnitude, as well as the detection limit is  $2.32 \pm 0.07 \text{ fM}$ . NCFs were synthesized by a two-step process. The NCFs were prepared via drying in a vacuum oven at  $80^\circ\text{C}$  for 24 h and then directly carbonized at  $800^\circ\text{C}$  below a nitrogen atmosphere to form nitrogen-doped cotton CFs. The silver nanoparticles were grown on the surface of the modified CFs electrode using a one-step electrodeposition technique. CFs-based biosensors are also widely used to monitor human physiological indexes and cellular active components. Cortisol is involved in the regulation of a variety of physiological activities and is considered to be a key factor in stress response and bio-psychology. Researchers (Loaiza et al., 2015) prepared a lactate biosensor based on graphitised carbon nanofibres to detect lactate in wines and ciders. Graphitised carbon nanofibres supported Pt NPs composites (Pt NPs/GCNF) were prepared by chemical reduction of Pt precursors on the surface of GCNF for lactic acid sensing and the lactate oxidase (Lox) was modified by covalent immobilization onto the Pt NPs/GCNF surface using polyethyleneimine (PET) and glutaraldehyde (GA). The lactic acid sensor shows excellent reproducibility (RSD 4.9%,  $n=10$ ) and sensitivity ( $41.302 \pm 546$ )  $\mu\text{A/M cm}^2$ , with a good detection limit ( $6.9 \mu\text{M}$ ). At the same time, it is proved that the activity of the sensor can be preserved about 95% under the storage condition of  $-20^\circ\text{C}$ , which greatly improves the accuracy and sensitivity of lactic acid detection in beverages.

### Flexible or Wearable Biosensor Based on CFs

Flexible electronic devices and wearable smart devices have developed rapidly in recent years. Instead of reducing the detection accuracy and sensitivity, they make the equipment miniaturized, portable and intelligent. Therefore, flexible devices and wearable devices based on CFs biosensors still have broad prospects for development in the future.

The monitoring of brain activity has practical significance for biological physiological health signals. Researchers (Vomero et al., 2019) reported that a flexible biosensor probe based on CFs was implanted into mouse brain tissue (Figure 6). A micromachining technology for embedding flexible, cloth-like and polymer-derived CFs pads in polyimide by selective reactive ion etching is introduced. The whole electrocorticography (ECOG) electrode array is seamlessly composed of a single CF pad, avoiding any joint and metal interconnection. In the process of wafer fabrication, the plane resolution of CFs structure is reduced to  $12.5 \mu\text{m}$  and the height is  $3 \mu\text{m}$ . The prepared superflexible neural device has good electrochemical stability and excellent mechanical properties *in vitro*, and shows good

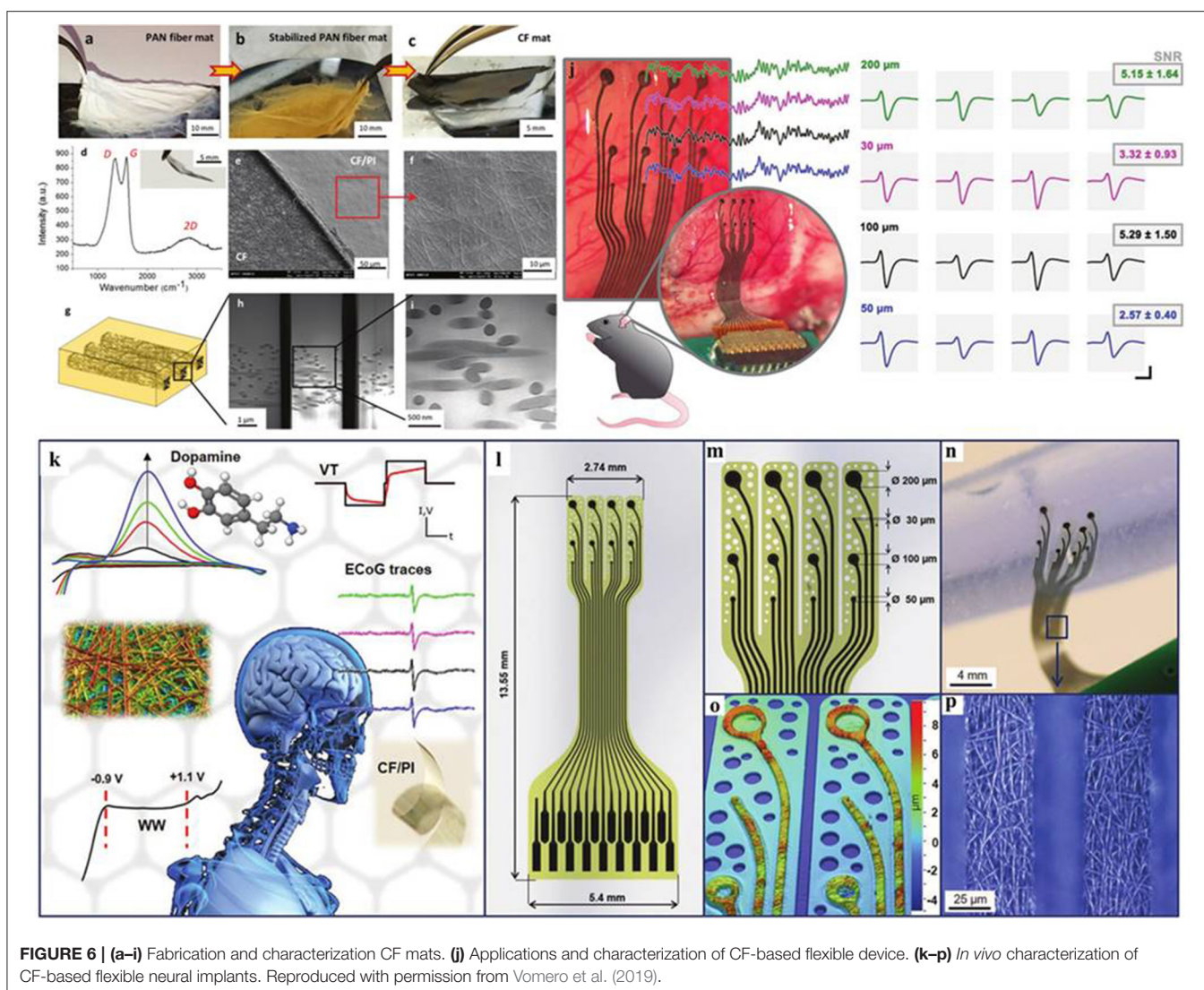


**FIGURE 6 | (a–i)** Fabrication and characterization CF mats. **(j)** Applications and characterization of CF-based flexible device. **(k–p)** *In vivo* characterization of CF-based flexible neural implants. Reproduced with permission from Vomero et al. (2019).

recording performance after implantation *in vivo*. Although this study focuses on the preparation of ECoG electrode, the preparation technique of metal-free implantable probe based on polyimide/CF can also be used in other biomedical monitoring and sensing platforms. Similarly, to monitor the  $\text{H}_2\text{O}_2$  secreted by cancer cells *in vivo* in real-time, researchers (Zhang et al., 2018b) reported a preparation strategy of hybrid flexible microelectrode based on CF through hydrothermal synthesis, which uses CF coated gold nanoparticles modified nitrogen hybrid carbon nanotube arrays (NCNATs). CF is an ideal substrate for *in situ* monitoring because of its nanometer scale and excellent mechanical properties. NCNATs grown on CFs significantly enhanced the electrochemically active surface area and enriched the surface active sites. The gold nanoparticles uniformly distributed on NCNATs provide a guarantee for the electrochemical detection of  $\text{H}_2\text{O}_2$ . In the selective detection of  $\text{H}_2\text{O}_2$ , the detection limit of the composite microelectrode is 50 nM when the signal-to-noise ratio is 3:1, the linear range

is up to 4.3 mM, and the sensitivity is as high as  $142 \mu\text{A cm}^{-2} \text{mM}^{-1}$ . The composite flexible microelectrode for real-time tracking and monitoring of  $\text{H}_2\text{O}_2$  secreted by cancer cells can promote the development of detection and management of early diseases. At present, in the field of biosensors, there are still some challenges in transforming sensing materials into wearable devices. Researchers (Aaron et al., 2018) reported a simple synthesis strategy of biosensors based on CFs to detect peroxides. It provides an effective solution for the application of biosensors in the field of wearable devices. In terms of details, palladium nanostructures were deposited on the surface of CFs by electrodeposition. Through electrodeposition, palladium nanostructures formed nanoneedles and nanorods that were vertically attached to the surface of CFs. Through the detection of peroxide, the flexible electrode shows high sensitivity of  $388 \mu\text{A mM}^{-1} \text{cm}^{-2}$ . This simple preparation strategy provides a reference idea for the development of wearable biosensors.

## SUMMARY AND OUTLOOK

In summary, we review the preparation methods and functional modification of CFs and the application of CFs-based composites in biosensors. In the preparation process of CFs, we introduce the preparation process in detail. Firstly, the raw materials for the preparation of CFs are classified, including i) Natural polymers; ii) Synthetic polymers. In the part of raw material pretreatment and spinning, we list several common spinning methods, which are i) Blow spinning; ii) Electrospinning; iii) Centrifugal spinning; iv) Others. The last step in the preparation of CFs materials is the carbonization process, which is mainly divided into three steps, namely i) pre-oxidation (to improve the thermal stability and crystallinity); ii) low-temperature carbonization; iii) high-temperature carbonization (to enhance the mechanical properties). Next is the review of the functionalisation of CFs. In this part, we generalize four common functionalisation methods and other modified materials, which are i) Precious metal functionalised CFs; ii) Metal oxide functionalized CFs; iii) High molecular polymer-modified CFs; iv) Metal-organic frameworks (MOFs) functionalised CFs; v) Other materials functionalised CFs. Through the functional modification of CFs, the unique properties of each part of the materials have a synergistic effect and show excellent comprehensive properties. As a result, CFs-based composites show a broad application prospect in the fields of sensing, electric energy storage equipment, industrial manufacturing and so on. In the last part, we introduce in detail the application of CFs-based composites in flexible or wearable biosensors.

As we all know, CF, as a very advanced and omnipotent nano-material, has been proved to have a wide range of application prospects. At present, the preparation and production process of CFs has been quite advanced, and its properties have been explored a little bit. In the future research direction, CFs will

still be very popular nano-based materials. When studying the application of CFs in flexible biosensors, we found that the application of CFs in flexible biosensor may be limited due to the complexity and cost in the preparation process of composite materials. On the contrary, CFs are the most preferred materials in the fields of electrical energy storage and industry, because of their excellent mechanical properties. At the same time, it is not uncommon for CFs-based biosensor probes to be implanted in organisms, which shows that CFs-based nanoprobe also have a broad application space in the field of biomedicine (Saito et al., 2011). Therefore, it is still worthy of our attention to explore how to create a balance between the application of CFs in flexible biosensors and the preparation of composites.

## AUTHOR CONTRIBUTIONS

ZW and MF contributed equally to the article and they wrote the article together. QY and CF are responsible for providing the required materials. YH and ZM provided ideas and support for the whole review. All authors contributed to the article and approved the submitted version.

## FUNDING

This work was supported by National Natural Science Foundation of China (No: 31960496), National Natural Science Foundation of Xinjiang (No. 2018D01C040), Tianshan Innovation Team Project in Xinjiang Autonomous Region (2020D14022), and the research start-up fund of Xinjiang University. ZM acknowledges Tianchi doctoral program, Doctoral Innovation program-Tianshan Hundred-Talent Program (Xinjiang Province).

## REFERENCES

- Aaron, M., Ashish, M., and James, D. (2018). Palladium nanoneedles on carbon fiber: highly sensitive peroxide detection for biomedical and wearable sensor applications. *IEEE* 19, 34–38. doi: 10.1109/JSEN.2018.2872895
- Abdurhman, A., Zhang, Y., Zhang, G., and Wang, S. (2015). Hierarchical nanostructured noble metal/metal oxide/graphene-coated carbon fiber: *in situ* electrochemical synthesis and use as microelectrode for real-time molecular detection of cancer cells. *Anal. Bioanal. Chem.* 407, 8129–8136. doi: 10.1007/s00216-015-8989-3
- Atchison, J., Zeiger, M., Tolosa, A., Funke, L., Jackel, N., and Presser, V. (2015). Electrospinning of ultrafine metal oxide/carbon and metal carbide/carbon nanocomposite fibers. *RSC Adv.* 5, 35683–35692. doi: 10.1039/C5RA05409E
- Barlow, S., Louie, M., Hao, R., Defnet, P., and Zhang, B. (2018). Electrodeposited gold on carbon-fiber microelectrodes for enhancing amperometric detection of dopamine release from pheochromocytoma cells. *Anal. Chem.* 90, 10049–10055. doi: 10.1021/acs.analchem.8b02750
- Bhatt, P., and Goe, A. (2017). Carbon fibres: production, properties and potential use. *Mat. Sci. Res. Ind.* 14, 52–57. doi: 10.13005/msri/140109
- Byrne, N., Setty, M., Blight, S., Tadros, R., Ma, Y., Sixta, H., et al. (2016). Cellulose-derived carbon fibers produced via a continuous carbonization process: investigating precursor choice and carbonization conditions. *Macromol. Chem. Phys.* 217, 2517–2524. doi: 10.1002/macp.201600236
- Chen, S., Qiu, L., and Cheng, H. (2020). Carbon-based fibers for advanced electrochemical energy storage devices. *Chem. Rev.* 120, 2811–2878. doi: 10.1021/acs.chemrev.9b00466
- Chen, X., Pang, G., Shen, W., Tong, X., and Jia, M. (2019). Preparation and characterization of the ribbon-like cellulose nanocrystals by the cellulase enzymolysis of cotton pulp fibers. *Carbohydr. Polym.* 207, 713–719. doi: 10.1016/j.carbpol.2018.12.042
- Chen, Y., Wang, N., Jensen, M., Han, S., Li, X., Li, W., et al. (2019). Catalyst-free large-scale synthesis of composite SiC@SiO<sub>2</sub>/carbon nanofiber mats by blow-spinning. *J. Mater. Chem. C* 7, 15233–15242. doi: 10.1039/C9TC05257G
- Choi, K., Jeon, H., Kang, J., and Yaghi, O. (2011). Heterogeneity within order in crystals of a porous metal-organic framework. *J. Am. Chem. Soc.* 133, 11920–11923. doi: 10.1021/ja204818q
- Chou, T., Gao, L., Thostenson, E., Zhang, Z., and Byun, J. (2010). An assessment of the science and technology of carbon nanotube-based fibers and composites. *Compos. Sci. Tech.* 70, 1–19. doi: 10.1016/j.compscitech.2009.10.004
- Diani, J., Liu, Y., and Gall, K. (2006). Finite strain 3D thermoviscoelastic constitutive model for shape memory polymers. *Polym. Eng. Sci.* 46, 486–492. doi: 10.1002/pen.20497
- Douani, R., Lamrani, N., Oughanem, M., Saidi, M., Guhel, Y., Chaouchi, A., et al. (2020). Improvement of humidity sensing performance of BiFeO<sub>3</sub>



- nanoparticles-based sensor by the addition of carbon fibers. *Sensor. Actuat. A Phys.* 307:111981. doi: 10.1016/j.sna.2020.111981
- Hameed, N., Sharp, J., Nunna, S., Creighton, C., Magniez, K., Jyotishkumar, P., et al. (2016). Structural transformation of polyacrylonitrile fibers during stabilization and low temperature carbonization. *Polym. Degrad. Stabil.* 128, 39–45. doi: 10.1016/j.polymdegradstab.2016.02.029
- Hamid, K., Reza, N., Srinivas, N., Gelayol, G., Khashayar, B., Seyed, M., et al. (2017). PAN precursor fabrication, applications and thermal stabilization process in carbon fiber production: Experimental and mathematical modelling. *Prog. Mater. Sci.* 107, 100575. doi: 10.1016/j.pmatsci.2019.100575
- Huang, M., Li, W., Liu, X., Feng, M., and Yang, J. (2020). Study on structure and performance of surface-metallized carbon fibers reinforced rigid polyurethane composites. *Polym. Advan. Technol.* 31, 1805–1813. doi: 10.1002/pat.4907
- Huang, Y., Miao, Y., Ji, S., Tjiu, W., and Liu, T. (2014). Electrospun carbon nanofibers decorated with Ag-Pt bimetallic nanoparticles for selective detection of dopamine. *ACS Appl. Mater. Inter.* 6, 12449–12456. doi: 10.1021/am502344p
- Jiang, D., Liu, L., Wu, G., Zhang, Q., Long, J., Wu, Z., et al. (2017). Mechanical properties of carbon fiber composites modified with graphene oxide in the interphase. *Polym. Composites* 38, 2425–2432. doi: 10.1002/polb.23828
- Jiang, G., Jiang, N., Zheng, N., Chen, X., Mao, J., Ding, G., et al. (2019). MOF-derived porous  $\text{Co}_3\text{O}_4$ -NC nanoflake arrays on carbon fiber cloth as stable hosts for dendrite-free Li metal anodes. *Energy Storage Mater.* 23, 181–189. doi: 10.1016/j.ensm.2019.05.014
- Jiao, L., Seow, J., Skinner, W., Wang, Z. U., and Jiang, H. (2019). Metal-organic frameworks: Structures and functional applications. *Mater. Today* 27, 43–68. doi: 10.1016/j.mattod.2018.10.038
- Karacan, I., and Erzurumluoglu, L. (2015). The effect of carbonization temperature on the structure and properties of carbon fibers prepared from poly(m-phenylene isophthalamide) precursor. *Fiber Polym.* 16, 1629–1645. doi: 10.1007/s12221-015-5030-6
- Khayyam, H., Jazar, R. N., Nunna, S., Golkarnarenji, G., Badii, K., Fakhrhoseini, S., et al. (2020). PAN precursor fabrication, applications and thermal stabilization process in carbon fiber production: experimental and mathematical modelling. *Prog. Mater. Sci.* 107:100575.
- Kong, Y., Qiu, T., and Qiu, J. (2013). Fabrication of novel micro-nano carbonous composites based on self-made hollow activated carbon fibers. *Appl. Surf. Sci.* 265, 352–357. doi: 10.1016/j.apsusc.2012.11.011
- Lee, S., Kim, H., Lee, T., Lee, H., Lee, J., Lee, J., et al. (2017). Synthesis of carbon nanotube fibers from carbon precursors with low decomposition temperatures using a direct spinning process. *Carbon* 124, 219–227. doi: 10.1016/j.carbon.2017.08.064
- Lee, S., Park, J., Kim, H., Lee, T., Lee, J., Im, Y., et al. (2016). Synthesis of carbon nanotube fibers using the direct spinning process based on Design of Experiment (DOE). *Carbon* 100, 647–655. doi: 10.1016/j.carbon.2016.01.034
- Li, F., Liu, Y., Qu, C., Xiao, H., Hua, Y., Sui, G., et al. (2015). Enhanced mechanical properties of short carbon fiber reinforced polyethersulfone composites by graphene oxide coating. *Polymer* 59, 155–165. doi: 10.1016/j.polymer.2014.12.067
- Li, Y., Jiang, B., and Huang, Y. (2020). Constructing nanosheet-like MOF on the carbon fiber surfaces for improving the interfacial properties of carbon fiber/epoxy composites. *Appl. Surf. Sci.* 514:145870. doi: 10.1016/j.apsusc.2020.145870
- Li, Y., Zou, B., Xiao, A., and Zhang, H. (2017). Advances of metal-organic frameworks in energy and environmental applications. *Chin. J. Chem.* 35, 1501–1511. doi: 10.1002/cjoc.201700151
- Liu, Y., and Kumar, S. (2014). Polymer/carbon nanotube nano composite fibers-a review. *ACS Appl. Mater. Inter.* 6, 6069–6087. doi: 10.1021/am405136s
- Loaiza, O., Lamas-Ardiansa, P., Anorga, L., Jubete, E., Ruiz, V., Borghei, M., et al. (2015). Graphitized carbon nanofiber-Pt nanoparticle hybrids as sensitive tool for preparation of screen printing biosensors: detection of lactate in wines and ciders. *Bioelectrochemistry* 101, 58–65. doi: 10.1016/j.bioelechem.2014.07.005
- Long, D., Guo, H., Cui, J., Chen, X., and Lu, M. (2017). Rapid etching of carbon fiber induced by noble metal nanoparticles. *Mater. Lett.* 197, 45–47. doi: 10.1016/j.matlet.2017.03.153
- Ma, W., Chen, S., Yang, S., Chen, W., Weng, W., Cheng, Y., et al. (2017). Flexible all-solid-state asymmetric supercapacitor based on transition metal oxide nanorods/reduced graphene oxide hybrid fibers with high energy density. *Carbon* 113, 151–158. doi: 10.1016/j.carbon.2016.11.051
- Meng, F., McKechnie, J., Turner, T., Wong, K., and Pickering, S. (2017). Environmental aspects of use of recycled carbon fiber composites in automotive applications. *Environ. Sci. Technol.* 51, 12727–12736. doi: 10.1021/acs.est.7b04069
- Meng, J., Liu, X., Niu, C., Pang, Q., Li, J., Liu, F., et al. (2020). Advances in metal-organic framework coatings: versatile synthesis and broad applications. *Chem. Soc. Rev.* 49, 3142–3186. doi: 10.1039/C9CS00806C
- Navrotsky, A., Ma, C., Lilova, K., and Birkner, N. (2010). Nanophase transition metal oxides show large thermodynamically driven shifts in oxidation-reduction equilibria. *Science* 330, 199–201. doi: 10.1126/science.1195875
- Nitilaksha, H., Jimmy, M., and Gajanan, B. (2016). Recent developments in carbon fibers and carbon nanotube-based fibers: a review. *Polym. Rev.* 57, 339–368. doi: 10.1080/15583724.2016.1169546
- Qin, X., Lu, Y., Xiao, H., Wen, Y., and Yu, T. (2012). A comparison of the effect of graphitization on microstructures and properties of polyacrylonitrile and mesophase pitch-based carbon fibers. *Carbon* 50, 4459–4469. doi: 10.1016/j.carbon.2012.05.024
- Rahmanian, S., Thean, K., Suraya, A., Shazed, M., Salleh, M., and Yusoff, H. (2013). Carbon and glass hierarchical fibers: influence of carbon nanotubes on tensile, flexural and impact properties of short fiber reinforced composites. *Mater. Design* 43, 10–16. doi: 10.1016/j.matdes.2012.06.025
- Saito, N., Aoki, K., Usui, Y., Shimizu, M., Hara, K., Narita, N., et al. (2011). Application of carbon fibers to biomaterials: a new era of nano-level control of carbon fibers after 30-years of development. *Chem. Soc. Rev.* 40, 3824–3834. doi: 10.1039/c0cs00120a
- Song, J., Guo, J., Liu, Y., Tan, Q., Zhang, S., and Yu, Y. (2019). A comparative study on properties of cellulose/antarctic krill protein composite fiber by centrifugal spinning and wet spinning. *Fiber Polym.* 20, 1547–1554. doi: 10.1007/s12221-019-8725-2
- Tian, Q., Xu, Z., Liu, Y., Fang, B., Peng, L., Xi, J., et al. (2017). Dry spinning approach to continuous graphene fibers with high toughness. *Nanoscale* 9, 12335–12342. doi: 10.1039/C7NR03895J
- Vomero, M., Gueli, C., Zucchini, E., Fadiga, L., Erhardt, J., Sharma, S., and Stieglitz, T. (2019). Flexible bioelectronic devices based on micropatterned monolithic carbon fiber mats. *Adv. Mater. Technol.* 5:1900713. doi: 10.1002/admt.201900713
- Wang, C., Chen, L., Li, J., Sun, S., Ma, L., Wu, G., et al. (2017). Enhancing the interfacial strength of carbon fiber reinforced epoxy composites by green grafting of poly(oxypropylene) diamines. *Compos. Part. A Appl. Sci. Manuf.* 99, 58–64. doi: 10.1016/j.compositesa.2017.04.003
- Wazir, A., and Kakakhe, L. (2009). Preparation and characterization of pitch-based carbon fibers. *New Carbon Mater.* 24, 83–88. doi: 10.1016/S1872-5805(08)60039-6
- Wei, W., and Qu, X. (2012). Extraordinary physical properties of functionalized graphene. *Small* 8, 2138–2151. doi: 10.1002/smll.201200104
- Wen, H., Nallathambi, V., Chakraborty, D., and Calabrese, B. (2011). Carbon fiber microelectrodes modified with carbon nanotubes as a new support for immobilization of glucose oxidase. *Microchim. Acta* 175, 283–289. doi: 10.1007/s00604-011-0684-2
- Wen, Z., Qian, X., Zhang, Y., Wang, X., Wang, W., and Song, S. (2019). Electrochemical polymerization of carbon fibers and its effect on the interfacial properties of carbon reinforced epoxy resin composites. *Compos. Part. A Appl. Sci. Manuf.* 119, 21–29. doi: 10.1016/j.compositesa.2019.01.014
- Wu, T., Li, L., Song, G., Ran, M., Lu, X., and Liu, X. (2019). An ultrasensitive electrochemical sensor based on cotton carbon fiber composites for the determination of superoxide anion release from cells. *Mikrochim. Acta* 186, 198. doi: 10.1007/s00604-019-3304-1
- Xu, Z., and Buehler, M. J. (2010). Geometry controls conformation of graphene sheets: membranes, ribbons, and scrolls. *ACS Nano* 4, 3869–3876. doi: 10.1021/nn100575k
- Yang, S., Cheng, Y., Xiao, X., and Pang, H. (2020). Development and application of carbon fiber in batteries. *Chem. Eng. J.* 384, 123294. doi: 10.1016/j.cej.2019.123294
- Yi, Z., Cao, Y., Yuan, J., Mary, C., Wan, Z., Li, Y., et al. (2020). Functionalized carbon fibers assembly with  $\text{Al/Bi}_2\text{O}_3$ : A new strategy for high-reliability ignition. *Chem. Eng. J.* 389, 124254. doi: 10.1016/j.cej.2020.124254
- Yoshikawa, Y., Teshima, K., Futamura, R., Tanaka, H., Neimark, A. V., and Kaneko, K. (2020). Structural mechanism of reactivation with steam of



- pitch-based activated carbon fibers. *J. Colloid Inter. Sci.* 578, 422–430. doi: 10.1016/j.jcis.2020.06.002
- Yuan, H., Zhao, J., Wang, Q., Manoj, D., Zhao, A., Chi, K., et al. (2020). Hierarchical core-shell structure of 2D VS<sub>2</sub>@VC@N-doped carbon sheets decorated by ultrafine Pd nanoparticles: assembled in a 3D rosette-like array on carbon fiber microelectrode for electrochemical sensing. *ACS Appl. Mater. Inter.* 12, 15507–15516. doi: 10.1021/acsami.9b21436
- Zhang, M., Shoaib, M., Fei, H., Wang, T., Zhong, J., Fan, L., et al. (2019). Hierarchically porous N-doped carbon fibers as a free-standing anode for high-capacity potassium-based dual-ion battery. *Adv. Energy Mater.* 9:1901663. doi: 10.1002/aenm.201901663
- Zhang, X., Fan, X., Yan, C., Li, H., Zhu, Y., Li, X., et al. (2012). Interfacial microstructure and properties of carbon fiber composites modified with graphene oxide. *ACS Appl. Mater. Inter.* 4, 1543–1552. doi: 10.1021/am201757v
- Zhang, X., and Lu, Y. (2014). Centrifugal spinning: an alternative approach to fabricate nanofibers at high speed and low cost. *Polym. Rev.* 54, 677–701. doi: 10.1080/15583724.2014.935858
- Zhang, X., Wang, A., Zhou, X., Chen, F., and Fu, Q. (2020). Fabrication of aramid nanofiber-wrapped graphene fibers by coaxial spinning. *Carbon* 165, 340–348. doi: 10.1016/j.carbon.2020.04.072
- Zhang, Y., Tao, W., Zhang, Y., Tang, L., Gu, J., and Jiang, Z. (2018a). Continuous carbon fiber/crosslinkable poly(ether ether ketone) laminated composites with outstanding mechanical properties, robust solvent resistance and excellent thermal stability. *Compos. Sci. Technol.* 165, 148–153. doi: 10.1016/j.compscitech.2018.06.020
- Zhang, Y., Xiao, J., Sun, Y., Wang, L., Dong, X., Ren, J., et al. (2018b). Flexible nanohybrid microelectrode based on carbon fiber wrapped by gold nanoparticles decorated nitrogen doped carbon nanotube arrays: *in situ* electrochemical detection in live cancer cells. *Biosens. Bioelectron.* 100, 453–461. doi: 10.1016/j.bios.2017.09.038
- Zhu, Q. L., and Xu, Q. (2014). Metal-organic framework composites. *Chem. Soc. Rev.* 43, 5468–5512. doi: 10.1039/C3CS60472A
- Conflict of Interest:** The authors declare that the research was conducted in the absence of any commercial or financial relationships that could be construed as a potential conflict of interest.

Copyright © 2020 Wenrui, Fanxing, Yanan, Fei, Haitao and Minwei. This is an open-access article distributed under the terms of the Creative Commons Attribution License (CC BY). The use, distribution or reproduction in other forums is permitted, provided the original author(s) and the copyright owner(s) are credited and that the original publication in this journal is cited, in accordance with accepted academic practice. No use, distribution or reproduction is permitted which does not comply with these terms.



# Poly (Glycerol Sebacate)-Based Bio-Artificial Multiporous Matrix for Bone Regeneration

Bo Liang, Qiang Shi, Jia Xu, Yi-Min Chai and Jian-Guang Xu\*

Department of Orthopedic Surgery, Shanghai Jiao Tong University Affiliated Sixth People's Hospital, Shanghai, China

## OPEN ACCESS

### Edited by:

Alfonso Jiménez,  
University of Alicante, Spain

### Reviewed by:

Guoqing Pan,  
Jiangsu University, China  
Linbo Wu,  
Zhejiang University, China

### \*Correspondence:

Jian-Guang Xu  
xjgn6spine@126.com

### Specialty section:

This article was submitted to  
Polymer Chemistry,  
a section of the journal  
Frontiers in Chemistry

**Received:** 08 September 2020

**Accepted:** 26 October 2020

**Published:** 23 November 2020

### Citation:

Liang B, Shi Q, Xu J, Chai Y-M and  
Xu J-G (2020) Poly (Glycerol  
Sebacate)-Based Bio-Artificial  
Multiporous Matrix for Bone  
Regeneration.  
Front. Chem. 8:603577.  
doi: 10.3389/fchem.2020.603577

In recent years, bone repair biomaterials that combine cells and bioactive factors are superior to autologous and allogeneic bone implants. However, neither natural nor synthetic biomaterials can possess all desired qualities such as strength, porosity, and biological activity. In this study, we used poly (glycerol sebacate) (PGS), a synthetic material with great osteogenic potential that has attracted more attention in the field of tissue (such as bone tissue) regeneration owing to its good biocompatibility and high elasticity. It also has the advantage of being regulated by material synthesis to match the bone tissue's strength and can be easily modified to become functional. However, pure PGS lacks functional groups and hydrophilicity. Therefore, we used PGS as the substrate to graft the adhesive ligands RGD and vascular endothelial growth factor mimetic peptide. The bone repair scaffold can be prepared through photo crosslinking, as it not only improves hydrophobicity but also promotes vascularization and accelerates osteogenesis. Simultaneously, we improved the preparation method of hydrogels after freeze-drying and crosslinking to form a sponge-like structure and to easily regenerate blood vessels. In summary, a bone repair scaffold was prepared to meet the structural and biological requirements. It proved to serve as a potential bone-mimicking scaffold by enhancing tissue regenerative processes such as cell infiltration and vascularization and subsequent replacement by the native bone tissue.

**Keywords:** poly (glycerol sebacate), bio-artificial multiporous matrix, regeneration, vascularization, VEGF

## INTRODUCTION

Bone repair following bone damage caused by trauma and disease is a complex process necessitating the need to identify better ways to promote bone regeneration (Shen et al., 2016). Various synthetic biomaterials, such as poly (lactic-co-glycolic acid) and polymethyl methacrylate, were designed to fill bone defects and promote bone regeneration, resulting in its repair. These biomaterials are popular because they circumvent the limited bone resources and avoid the immunological rejections associated with autogenic and allogeneic bone transplantations. They are also easy to design and more economic (Miri et al., 2016). Many studies combine bioactive factors or cells to design these synthetic biomaterials to compensate for the lack of bioactivity in synthetic biomaterials. These studies consider the osteogenic properties of the materials, such as excellent mechanical properties, biodegradability, good biocompatibility, and the osteogenic differentiation ability of stem cells. Several studies consider the relevance of vascularization and osteogenesis as the survival of transplanted cells and tissues in bone regeneration requires a microenvironment with a vibrant vascular network for nutrition delivery and waste removal. The cells in the center

of the scaffold may undergo apoptosis since nutrition and oxygen around the tissue are often limited to a depth of 150–200  $\mu\text{m}$  around the porous scaffold (Suresh and West, 2020). Therefore, novel biomaterials with angiogenic and biodegradable properties to support tissue integration and angiogenesis, with elastic properties to enhance bone tissue repair in a dynamic environment, are required. For better vascularization of biomolecules [e.g., vascular endothelial growth factor (VEGF) (Schnettler et al., 2003) and basic fibroblast growth factor (Stähli et al., 2015)], some metal ions (e.g., copper, cobalt, strontium, magnesium, boron, and calcium) have been used to promote angiogenesis. However, the use of VEGF is the most effective. The VEGF polypeptide not only recapitulates the function of the VEGF factor but also has advantages such as being economic and easily combining with materials through covalent binding to biomaterials (Hung et al., 2019).

VEGF is a potent cytokine secreted by bone cells. It can specifically bind to the VEGF receptor on the surface of endothelial cells to activate the signaling cascade, which eventually leads to the formation of new capillaries, a process called angiogenesis.

Therefore, distributions of VEGF ligands in biomaterials are crucial determinants of angiogenesis. Significant effort is required when combining the VEGF peptide with biomaterials to ensure satisfactory angiogenesis. Hydrogel microspheres covalently bonded peptide derived from vascular endothelial growth factor receptor 2 can mimic the ability of natural extracellular matrix through reversible binding of VEGF. The results showed that VEGF was released in a controlled manner, which promoted the growth and the tube formation of human umbilical vein endothelial cells (HUVECs) (Impellitteri et al., 2012). In another study, the authors designed a proteolytic degradable polyethylene glycol (PEG) hydrogel (García et al., 2016) loaded with VEGF. The hydrogel could achieve protease degradation dependent VEGF protein release while maintaining high VEGF bioactivity. In a critical-sized bone defect model, VEGF's delivery enhanced the infiltration of blood vessels into the defect. Other factors used in combination with VEGF can also promote blood vessels. Rufaihah et al. (2017) demonstrated that PEG-fibrinogen hydrogel provides good mechanical support and simultaneously releases two vascular-related factors, VEGF and angiopoietin 1, in myocardial remodeling to achieve recovery after myocardial infarction.

Poly (glycerol sebacate) (PGS) is a biodegradable synthetic polymer made of the two-block copolymer formed with the polycondensation of glycerol and sebacic acid. PGS elastomers have been successfully used in various biomedical fields because of their good biocompatibility, intentional elastic properties, and their abundant hydroxyl side groups that are easy to be functionalized (Kemppainen and Hollister, 2010; Luginina et al., 2020; Touré et al., 2020; Wang et al., 2020). Multiple osteogenic signals, such as growth factor injection and stem cell

transplantation, have been introduced to PGS systems to achieve better bone recovery. Bioglass® 45S5 porous scaffolds produced via the replica foam technique (Chen et al., 2006) have also been coated with PGS to produce flexible and toughened scaffolds for bone tissue engineering (Chen Q. Z. et al., 2010). Synthesis and fabrication of porous, elastomeric nanocomposite scaffolds using biodegradable PGS and osteoinductive nanosilicates have been reported. The combination of elasticity and tailorable stiffness, tunable degradation profiles, and the osteoinductive capability of the scaffolds offer a promising approach for bone tissue engineering (Kerativitayanan et al., 2017). Lee et al. (2013) described a PGS elastomer containing stromal cell-derived factor 1 alpha, which can enhance the recruitment of endothelial cells and mesenchymal stem cells in the elastic vascular scaffolds by delivering stromal cell-derived factor 1 chemokine, proving that the composite stent has an ability to induce *in situ* vascular regeneration. Lee et al. (2009) reported a type of porous three-dimensional PGS scaffold with high elasticity. The scaffold had good biocompatibility and anticoagulant properties. This scaffold can be used to study the role of endothelial cells and other cells in the development of complex vascular tissue. However, at present, these studies focus on the osteogenic properties of PGS, and few of them combine the osteogenic and vascularization properties of PGS to study the final osteogenic effect. Therefore, it is worth exploring the effect of this combination of VEGF peptide and PGS biomaterials on osteogenesis.

To obtain good angiogenic ability, the material should have a porous sponge structure, which regulates cell ingrowth and makes the blood vessel easily integrated. Fabrication techniques can often determine the physicochemical and biological properties of the scaffold, including porosity, mechanical strength, osteo-conductivity, and bone regenerative potential. Many researchers have opted for electrospinning, salinization, and polymer dissolution methods to obtain porous material. However, these methods' limitations include extremely small pore sizes, complex preparation processes, or harmful dissolved residues. To overcome these problems, numerous investigators have proposed mechanisms for increasing the average pore size of scaffolds. Phipps et al. (2012) used three different technologies to adjust the pore size of PCL/col I/nanoHA hydrogel. Addition of the poly(ethylene oxide) polymer chain before the gel formation resulted in an increased pore diameter. Biological experiments show that this method can promote the regeneration of bone and vascular tissue by increasing cell invasion. Therefore, pore size and architecture play an important role in tissue regeneration. Meanwhile, a previous study has shown that a pore size range of 75–175  $\mu\text{m}$  is believed to be appropriate for the ingrowth of chondrocytes and osteoblasts *in vivo* (Ansari et al., 2019). In light of these biophysical and biochemical cues, we were able to fabricate a PGS-based bio-artificial multiporous matrix via photopolymerization of an acrylate mainly comprising three building blocks: sebacic acid, glycerol, and oligo (acrylic acid) (Nguyen and West, 2002; Browning et al., 2015). Each of the major building blocks has proven to be biocompatible for bone regeneration (Sawhney et al., 1993; Kim et al., 2008). We hypothesized that by adjusting the pore size of PGS hydrogels containing VEGF mimetic peptide, some biological effects such

**Abbreviations:** HUVEC, human umbilical vein endothelial cell; PBS, phosphate-buffered saline; PEG, polyethylene glycol; PGS, poly (glycerol sebacate); rBMSCs, rat bone marrow stromal cells; SEM, scanning electron microscopy; VEGF, vascular endothelial growth factor.

as the speed and location of blood vessels and the quality of bone formation could also be affected, presenting a bone repair material that can rapidly induce the growth of new blood vessels *in vivo* and thereby improve bone repair.

## MATERIALS AND METHODS

### Matrix Synthesis

Acr-PEG-QK peptide (a 15-mer VEGF mimetic peptide: Ac-KLTWQELYQLKYKGI-NH<sub>2</sub>) and Acr-PEG-RGD peptide were custom prepared by a commercial manufacturer (GLS, Shanghai, China) and supplied at 95% purity. Acr-PEG-QK peptide activity was verified by testing endothelial cell activity. PGS hydrogel was fabricated in two steps: (1) the PGS pre-polycondensation step was implemented as previously reported (Samourides et al., 2020), and (2) acrylate was chemically grafted on the PGS prepolymer according to previously published methods (Pashneh-Tala et al., 2020). For the poly condensation process, equimolar mixtures (1 M) of glycerol and sebacic acid were reacted at 120°C under argon for 24 h, followed by pressure reduction from 1 Torr to 40 mTorr for another 5 h. All chemicals were purchased from Sigma Aldrich unless stated otherwise. The PGS prepolymer was acrylated in the following manner: 20 g of PGS prepolymer and 200 mL of anhydrous dichloromethane were added into a dry round bottom flask. After the polymer completely dissolved, the mixture in the reaction bottle was cooled to 0°C under a positive pressure of nitrogen. Acryloyl chloride was slowly added to an equal molar amount of trimethylamine and stirred at 0°C for 24 h. The mixture was filtered, precipitated with ether, dialyzed, and lyophilized.

Hydrogels consisting of adhesive ligands RGD and VEGF mimetic peptide were generated through free radical polymerization of the double bond under ultraviolet light with photoinitiator Irgacure 2959. Non-functional matrices PGS was set as the control. In summary, Acr-PGS was dissolved in phosphate-buffered saline (PBS) at 10% (wt/vol) with 2.8 μM Acr-PEG-RGD, 80 μg/mL Acr-PEG-QK, and 0.05% Irgacure 2959 (Ciba) photoinitiator. Polymer solutions were crosslinked through exposure to a 365-nm ultraviolet light at 10 mW/cm<sup>2</sup> for 10 min.

### Matrix Characterization

The hydrophilicity of PGS could be improved by introducing hydrophilic protein fragments into the polymer network. Therefore, the hydrophilicity of the crosslinked network was determined using the contact angle. The contact angle measuring instrument (Phoenix 300) was used to measure the contact angle of water in two groups, with and without protein fragments (*n* = 3). The samples were then converted into a 0.5 mm-thick film. Pure water (4 μL) was deposited on the surface of the material. The drop image was captured, and the tangent line was measured after the contact angle was stable.

The hydrogel samples were freeze-dried, the initial weight (*W*<sub>0</sub>) was measured, and then they were immersed in PBS buffer at 37°C to measure the swelling ratio. After water swelling, the hydrogel samples were taken out after 24 h, with water on the

surface removed. We also recorded the swelling mass. When the mass was balanced, the weight was set to *W*<sub>s</sub>. The water uptake by these samples was determined with Equation (1):

$$\frac{W_s - W_0}{W_s} \times 100 \quad (1)$$

The evaluation of degradation performance was conducted using the PBS buffer at 37°C and a speed of 80 rpm for 90 days. At specific time intervals, the immersed samples were taken out of the buffer, and weighed (*W*<sub>f</sub>) after overnight lyophilization. The mass loss of samples was calculated with Equation (2):

$$\frac{W_0 - W_f}{W_0} \times 100 \quad (2)$$

### *In vitro* Characterization of rBMSCs and HUVECs in Composite Scaffolds

This study was performed in strict accordance with the National Institutes of Health Guide for the Care and Use of Laboratory Animals. We isolated rat bone marrow stromal cells (rBMSCs) from the femur for *in vitro* experiments. HUVECs were purchased from Shanghai Institutes for Biological Sciences (Shanghai, China). We seeded rBMSCs on different scaffolds to observe the adhesion of cells to the material. Briefly, the 3–5 generations' stem cells were cultured in Minimal Essential Medium supplemented with 10% fetus bovine serum (Gibco) and 1% antibiotics (penicillin/streptomycin, Gibco, USA). The cells were cultured in a moist chamber with 5% CO<sub>2</sub> at 37°C for ~3 days and then digested with trypsin (0.05% trypsin/EDTA, Gibco). Serum was added to the culture medium to stop the digestion, and the cells were re-suspended in the medium. We placed 200 μL of cell suspension comprising 5 × 10<sup>5</sup> cells/mL on different scaffolds in 24-well plates. The cells were cultured on the material for 1 h to adhere, and then 800 μL of the medium was added to submerge the material. rBMSCs were cultured on the scaffold for 3 days to observe the cell morphology. After removing the culture medium, they were rinsed with PBS three times and then fixed with 4% paraformaldehyde for 15 min. After rinsing with PBS three times, the cells were infiltrated with 0.5% Triton X-100 for 10 min and rinsed again with PBS two times. The cells were stained with fluorescein isothiocyanate-labeled phalloidin (Thermo Fisher Scientific, MA, USA) at 25°C for 1 h to mark the cytoskeleton. Cell morphology was observed using three-dimensional reconstruction of confocal images.

The proliferation rate of rBMSCs and HUVECs cultured for 1, 3, and 7 days was obtained using the MTT assay (Invitrogen). TCPS surface was set as the positive control group. Briefly, different scaffolds were placed into a 24-well plate, and 3 × 10<sup>5</sup>/well rBMSCs were seeded on the surface of the scaffold and TCPS.

HUVEC migration on the scaffolds was observed using confocal microscopy 72 h after the initial cell seeding. After rinsing three times in PBS, the hydrogels were fixed in 4% paraformaldehyde at 25°C for 15 min, embedded in paraffin,



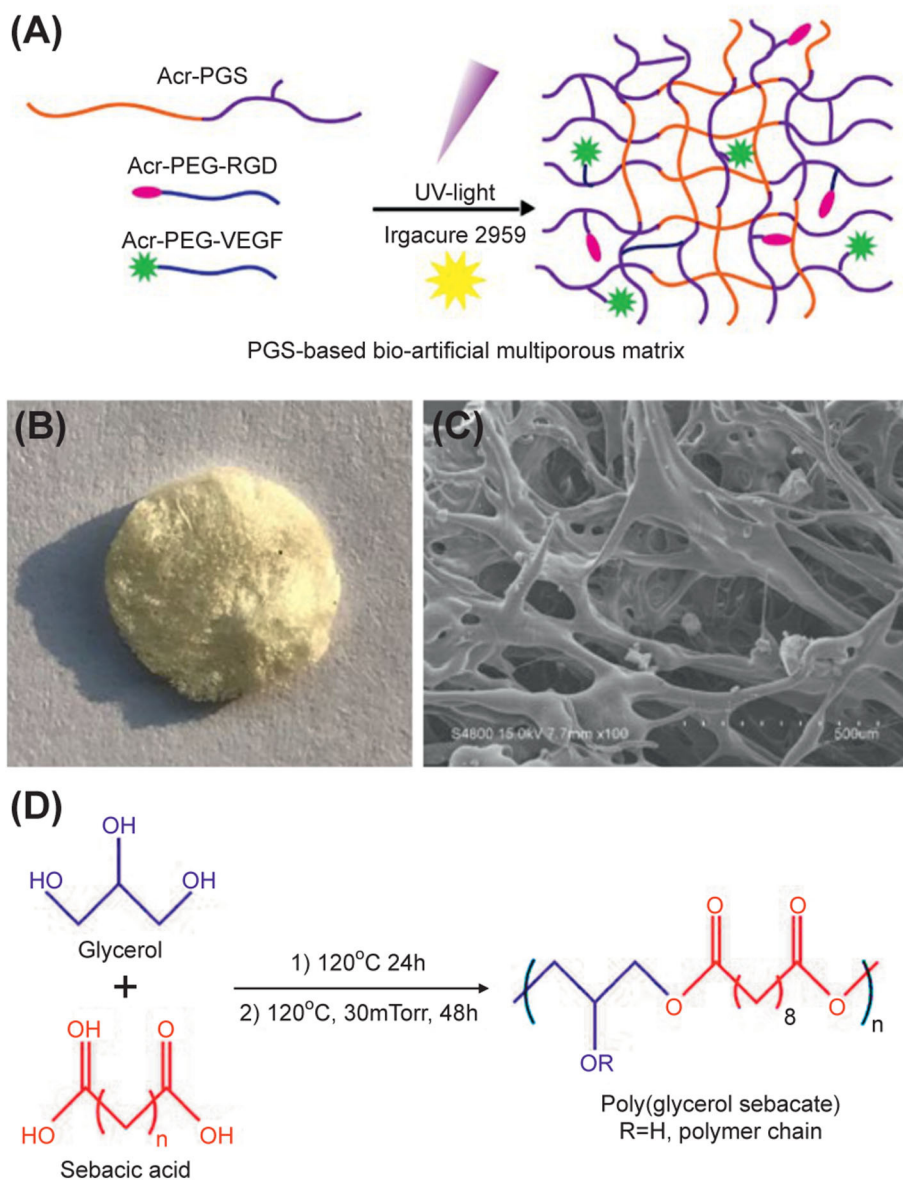


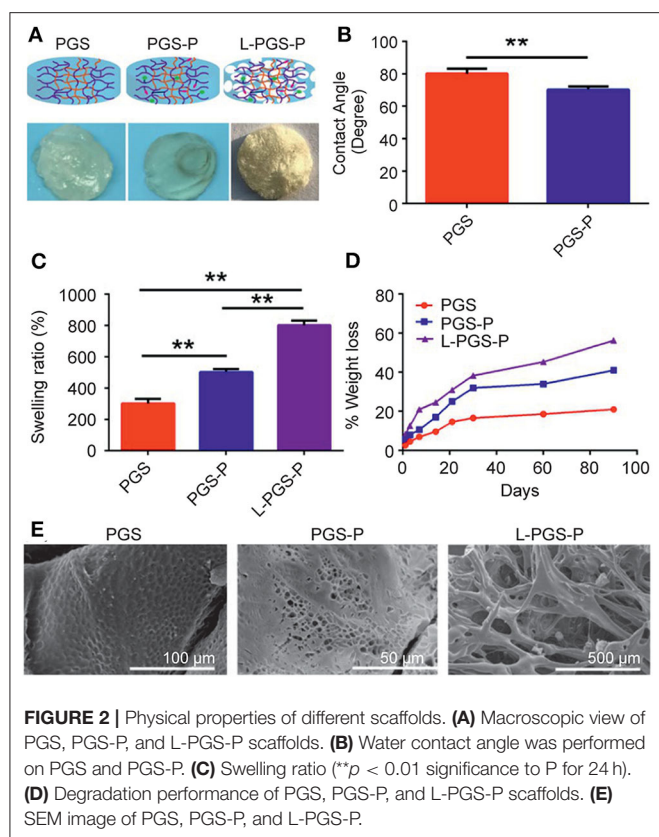
**FIGURE 1 |** Design of PGS-based bio-artificial matrices. **(A)** Bioactive ligands RGD peptide, QK peptide are mono-PEG-acrylated for covalent crosslinking into PGS network. Addition of a photoinitiator to PGS aqueous solution of PGS followed by 10 min UV irradiation results in crosslinking of hydrogel through free radical polymerization of acrylate end groups before and after lyophilization. **(B)** Gross image of L-PGS-P. **(C)** SEM image of L-PGS-P. **(D)** Synthesis of poly (glycerol sebacate) polymer.

and sectioned at 4.5 mm with a microtome. The slides from the middle of the hydrogels were stained with DAPI (Invitrogen) and observed under a laser scanning confocal microscope (Leica, Germany). At least three parallel experiments were conducted for each sample.

## Osteogenic Differentiation

To detect the effect of different materials on the osteogenic differentiation of stem cells, we seeded rBMSCs with a density of  $3 \times 10^4$  cells/well on different materials placed in 24-well plates for 3 and 7 days to detect the expression of osteogenic

related genes. At that point, Trizol method was used to split the cells and extract RNA. The content of RNA was determined using spectrophotometry (Thermo Scientific, MA, USA). For reverse transcription, we used a reverse transcription kit (Takara) and customized primers (Sangon biotech, Shanghai) to perform quantitative polymerase chain reaction tests to analyze the osteogenic differentiation of rBMSCs further. Glyceraldehyde 3-phosphate dehydrogenase was used as the reference gene. The sequence of the primer pairs used was as follows: GAPDH: forward: 5'-CAGG GCTGCCTTCTCTTG-3'; reverse: 5'-AACTTGCC



GTGGGTAGAGTC-3'; RUNX 2: forward: 5'-CCTTCCCT CCGAGACCCTAA-3'; reverse: 5'-ATGGCTGCTCCCTTCT GAAC-3'; ALP: forward: 5'-ACCGCAGGATGTGAACACT-3'; reverse: 5'-GAAGCTGTGGGTTCACTGGT; OCN-3'; forward: 5'-ATTGTGACGAGCTAGCGGAC-3'; reverse: 5'-GCAACACATGCCCTAAACGG-3'. The results were expressed as  $2^{-\Delta\Delta C_t}$ . Alkaline phosphatase (ALP) staining was conducted after 7 days to observe the ALP activity of each group.

### Micro Perfusion, Micro-Computed Tomography Imaging, and Tissue Section Staining

All animal procedures were approved by the Animal Research Committee of the Sixth People's Hospital, Shanghai Jiao Tong University. Distal femoral defect models were established using Sprague-Dawley rats weighing 300–400 g. The surgical operations were conducted on rats anesthetized intraperitoneally with pentobarbital. A 1.0–1.5 cm sagittal incision on the side of the knee joint was made, and a 2.5-mm defect was drilled using a Kirschner wire (American fine science tool company, Fine Science Tool, SFO, USA). The scaffold ( $\varnothing 2.5 \times 3$  mm) was then implanted. Nine rats with 18 defects were allocated to the following three groups: control ( $n = 6$ ), PGS-P ( $n = 6$ ), and L-PGS-P ( $n = 6$ ). Two weeks after the operation, the rats in each group were administered 0.9% saline + 4 mg/mL papaverine (Sigma

Aldrich, Darmstadt, Germany) after inhalation anesthesia, and then 0.9% saline and 10% neutral formalin. After fixation, 30 mL of 80% (vol/vol) diluted mv-122 microfilament (Flowtec) was injected into the aorta with a syringe and an indwelling needle. After polymerization overnight, the samples were removed. The data from the scans were evaluated with a micro-computer tomography reconstructed using the VG studio to establish three-dimensional models. The percentage of new bone volume relative to tissue volume and vascular volume/total implant volume in the bone defect was quantified using the auxiliary histomorphometric software and CTvox software. For microscopic examination of the newly formed bone and vessels, decalcified samples were stained immunohistochemically.

### Statistical Analysis

Data were analyzed using Origin 8.0 (OriginLab, MA, USA). All experiments were performed thrice ( $n = 3$ ), and results are presented as mean  $\pm$  standard deviation. A non-parametric test two-way analysis of variance with multiple comparisons was used for significance testing. The significance was calculated at 95% confidence interval with the two-tail alpha level of 0.05;  $p < 0.05$  was considered significant.

## RESULTS

### PGS-Based Bio-Artificial Multiporous Matrix Fabrication and Characteristics

The first step in the process of *in situ* induced bone regeneration is cell migration and invasion. We engineered bio-artificial multiporous hydrogel matrices consisting of RGD adhesive ligands and the VEGF mimetic peptide for better cell invasion and vascularization (Figure 1A). Hydrogel matrices consisting of Acr-PEG-RGD and Acr-PEG-QK peptides were generated through free radical polymerization of acrylate end-functional groups with low-intensity ultraviolet light using photoinitiator Irgacure 2959 (Figure 1A) (named as PGS-P). We freeze-dried the PGS-P solution before crosslinking (named as L-PGS-P) for the formation of porous structures. We obtained the porous structure from L-PGS-P, as seen in the gross image and scanning electron microscopy image (Figures 1B,C) and the PGS prepolycondensation step was implemented (Figure 1D).

On the macroscopic view of the PGS, PGS-P, and L-PGA-P matrices, we found that the PGS matrix was opaque, while the PGS-P matrix was transparent. L-PGS-P presented as a porous sponge sample after freeze-dried pretreatment (Figure 2A). The hydrophilic property of biomaterials is a very important physical and chemical property. It can directly affect cell adhesion and biocompatibility, hence its application in biomedicine (Chen S. et al., 2010; Gaharwar et al., 2011, 2012). The addition of protein motifs within the PGS crosslinked network promoted hydrophilic characteristics to the PGS prepolymer. We investigated surface hydrophilic characteristics of the PGS and PGS-P matrices using a contact angle measuring instrument (Phoenix 300) (Figure 2B). Pure PGS hydrogels showed a contact angle of  $80 \pm 1.7$  degrees with the water. As expected, the addition of protein motifs (PGS-P)

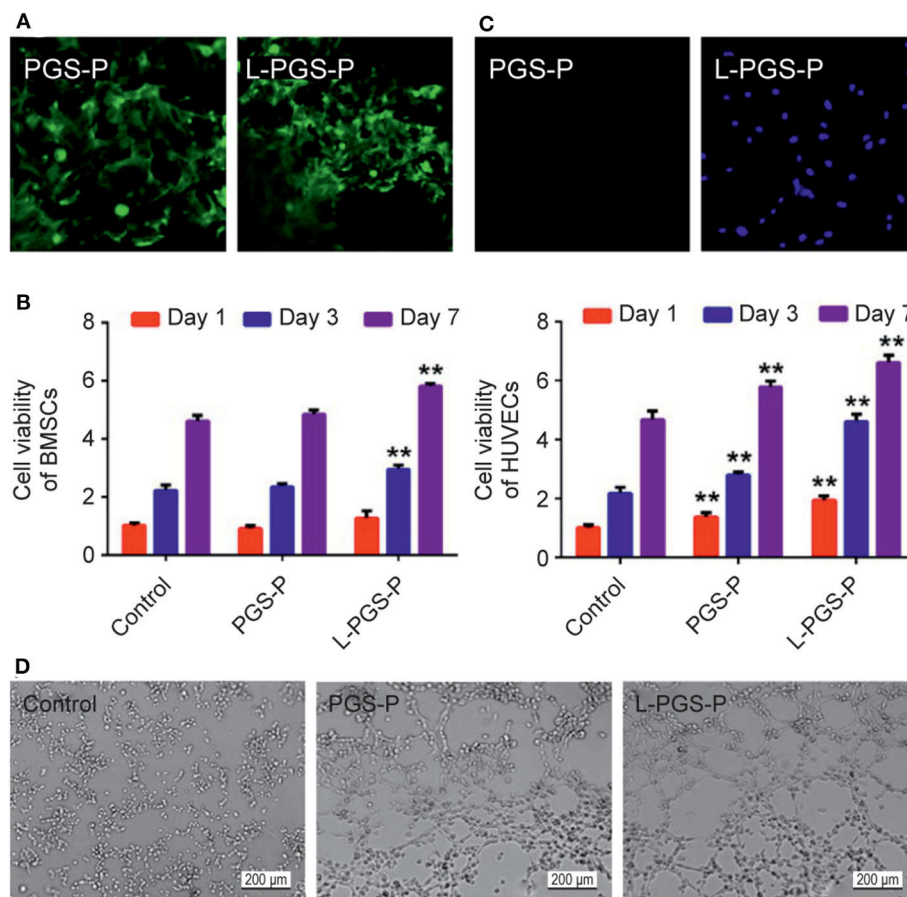


**FIGURE 3 |** Cellular behavior on different scaffolds. **(A)** Cell adhesion activity of PGS-P and L-PGS-P scaffolds illustrated in a 40x magnification picture. **(B)** The proliferation rate of the two kinds of adhered cells on day 1, 3, and 7 was tested using an MTT assay. **(C)** Cell infiltration was observed by DAPI staining. L-PGS-P scaffold supports cell infiltration of HUVECs *in vitro*; 20x magnification picture was captured at cross section. **(D)** Representative images of tube formation for 6 h with different medium from scaffolds soak liquid (soak for 7 days). \*\* $P < 0.01$ , compare with control group at different time point.

increased the hydrophilic nature reducing the contact angle to  $71 \pm 0.1$  degrees. The swelling study was used to further evaluate the bulk hydration characteristic of PGS and PGS-P (Figure 2C). The swelling test revealed the maximum swelling ratio in the L-PGS-P matrix, while PGS water uptake was the least (\*\* $p < 0.01$ ). The degradation rate is very important for tissue regeneration because it needs to match the tissue regeneration rate. Degradation products also need to be non-toxic to tissues. Therefore, the degradation rate was studied to evaluate if the polymeric materials are suitable for biomedical applications (Sheng et al., 2019; Dintcheva et al., 2020). The *in vitro* degradation of the PGS, PGS-P, and L-PGS-P matrices was investigated using the PBS buffer at 37°C over a 90-day period (Figure 2D). The mass loss of all samples was linear and non-sudden disintegration related to erosion degradation of PGS matrix from the surface. The addition of protein motifs and multiporous architecture resulted in a faster degradation rate. Figure 2E shows that the porosity and pore size were improved in the L-PGS-P matrix, with pore sizes being 200–500  $\mu\text{m}$ .

### ***In vitro* Characterization of rBMSCs and HUVECs in Composite Scaffolds**

There is little information about the improvement of L-PGS-P in the angiogenic microenvironment. Through the cytotoxic test, we found that both the PGS-P composite scaffold and L-PGS-P porous composite had good biocompatibility (Figure 3B). rBMSCs adhered well to their surfaces (Figure 3A). For cell infiltration and angiogenic activity, there was more HUVECs entry into L-PGS-P (Figure 3C) and significantly increased endothelial tube formation of HUVECs (Figure 3D) *in vitro*. We speculate that these results may be due to the multiporous architecture of L-PGS-P and more VEGF release after 7 days of soaking in the medium (Figure 2D).

### **Osteogenic Differentiation**

To investigate whether bio-artificial matrix works on the osteogenic potential of rBMSCs, an analysis of its osteogenic ability was performed using RT-qPCR. Compared with the PGS-P scaffold, the mRNA expression levels of Runx2, ALP, and OCN in the L-PGS-P group were significantly higher (Figure 4A).



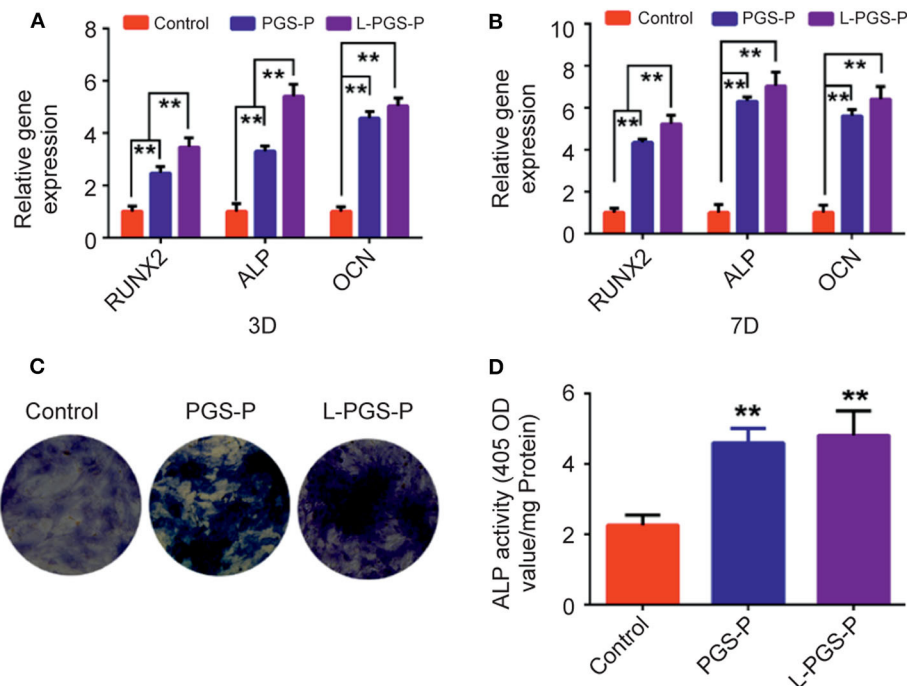


**FIGURE 4 |** The osteogenic effects induced by PGS-P and L-PGS-P on rat bone mesenchymal stem cells. **(A,B)** The statistics of RT-qPCR results for RUNX2, ALP, and OCN gene expression levels which were normalized to GAPDH after 3 and 7 days of osteogenic treating. **(C)** rBMSCs cultured on different scaffolds in osteogenic medium for 7 days were stained for ALP examination. **(D)** ALP activity was assessed by quantitative method.  $^{**}P < 0.01$ , compare with control group.

These results agree with the ALP activity test. The trend of ALP activity on day 7 *in vitro* analysis of BMSCs showed more ALP activity in the L-PGS-P group after ALP staining (Figures 4B,C).

## Micro Perfusion, Micro-Computed Tomography Imaging, and Tissue Section Staining

To inspect the ability of L-PGS-P bio-artificial matrices to improve cell infiltration and vascularization, Microfil perfusion was used to evaluate vessel ingrowth in scaffolds (Figure 5B). By week 2, micro-computed tomography analysis of the scanned constructs showed animals receiving L-PGS-P exhibited an increase in perfusion to the defect compared with the PGS-P and control groups. Importantly, there were a few vessels within the periphery of the PGS-P scaffold. In contrast, larger and more regular vessels were growing into and around the L-PGS-P implants. We also quantified greater blood vessel density in defects treated with L-PGS-P than with PGS and empty controls (Figure 5C). The trends of osteogenic performance were paralleled with the results of vascularization (Figure 5A). These results agree with our *in vitro* test results, indicating better cell invasion in the L-PGS-P group (Figure 2C). Hematoxylin and eosin staining revealed pronounced fibrous tissue around the defect in the control group, and many blood vessels appeared around the defect and a few inflammatory cells around the material in the PGS-P group. In contrast, in the L-PGS-P group,

a large proportion of the trabecular bone was produced in the defect (Figure 5D). The proangiogenic potential of the scaffolds was confirmed with CD31 immunostaining. Compared with limited staining in the control group, there were sufficient CD31-positive cells in the PGS-L and L-PGS-P groups. Interestingly, CD31 positive cells in the PGS-P group formed very narrow tubes but those in the L-PGS-P had very thick tubes (Figure 5E).

## DISCUSSION

Vascularization of biomaterials is an essential step in bone healing and regeneration, as it can provide oxygen and nutrients for osteoblasts to survive and metabolize (Karageorgiou and Kaplan, 2005; Ekaputra et al., 2011). Therefore, tissue engineering pays increased attention to the vascularization ability of biomaterials in design. At the same time, in addition to providing biological clues for vascularization, scaffolds should be designed with pore sizes large enough to allow tissue infiltration and vascular growth. There are many manufacturing technologies to improve the pore size of hydrogels and promote tissue regeneration. However, the pores are not connected and the pore size is not large enough. Therefore, it is very important to adopt new methods to obtain larger pore size hydrogel scaffolds to facilitate vascular ingrowth and osteoblast infiltration in the whole material.

In this study, we chose PGS as the matrix because of its good mechanical properties and biological safety; further, its polymer structure is easy to be functionalized (Chen et al.,



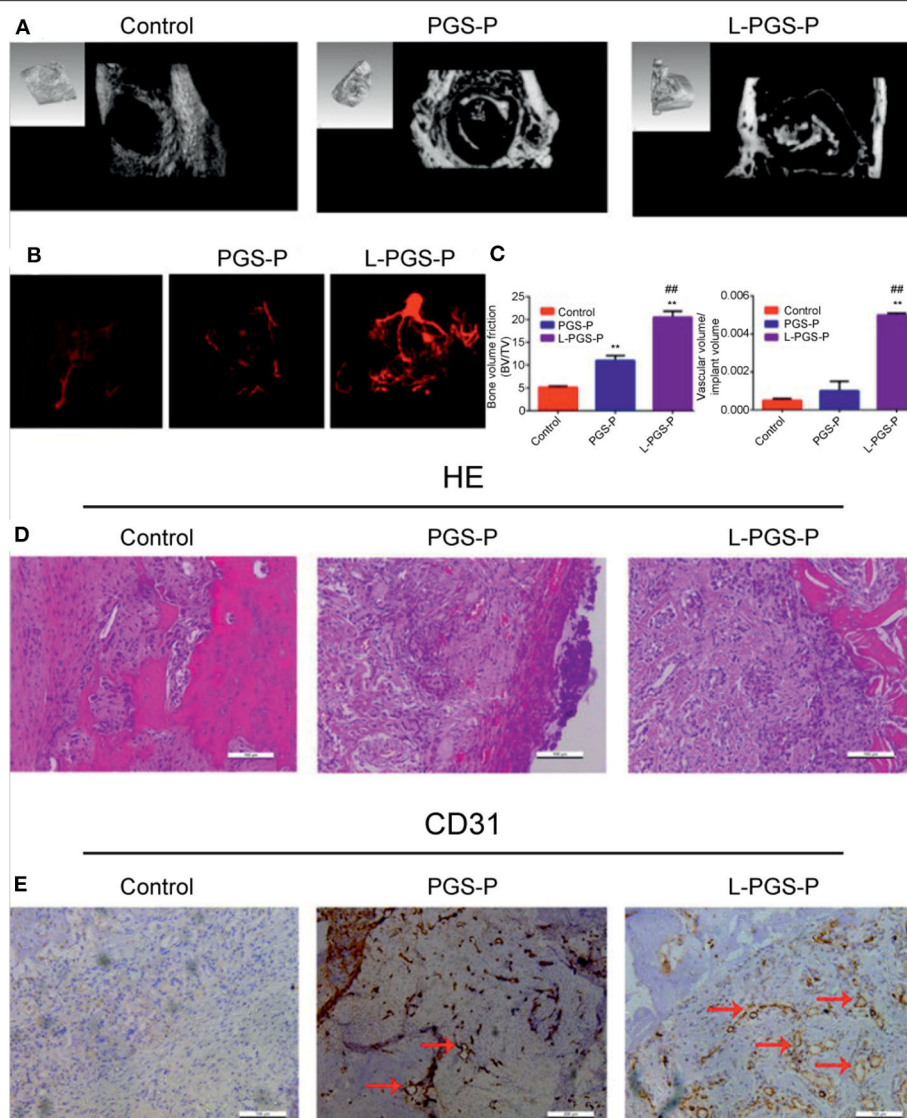


**FIGURE 5 |** The proangiogenic and osteogenic performance of PGS-P and L-PGS-P scaffolds *in vivo*. **(A)** Representative computed tomography reconstruction images of the defects shows abundant mineralized tissues in L-PGS-P than PGS-P at 2 weeks after implantation. **(B)** Micro-computed tomography images of vessel in rat distal femur defects perfused with Microfil radio-opaque contrast agent. L-PGS-P implants showed vasculature in surrounding tissue growing into implant, but not in the PGS-P and control groups. **(C)** Bone volume fraction and quantification of vascular volume/total implant volume. **(D,E)** haematoxylin and eosin **(D)** and CD31 staining **(E)** was performed at 2 weeks after implantation to evaluate the vessel and bone formation. Remarkably, more mineralized tissue and CD31-positive cells were found in L-PGS-P than PGS-P. Red arrows indicate positively stained areas of CD31-positive blood vessels. \*\* $P < 0.01$ , compare with control group; ### $P < 0.01$ , compare with PGS-P group.

2011). Importantly, the ester bond of the PGS backbone can be hydrolyzed and degraded by enzymes *in vivo* (Wang et al., 2003); thus, with the degradation of the main chain, functional groups can be released and used (Phelps et al., 2010). However, the hydrophobicity of PGS is a limiting point and must be solved first (Crapo and Wang, 2010). We found that PGS can improve the hydrophobicity of PGS after functional peptide grafting without additional synthetic modification, which not only functionalizes the scaffold biological but also solves the problem that hydrophobicity makes it impossible to prepare

hydrogels. Second, the hydrogel directly prepared is the same as most hydrogels, i.e., dense and lacking a large pore size facilitated in tissue and blood vessels. Therefore, several traditional methods have been attempted to increase the pore size of hydrogels in the early stage. One is the salting method, but we found that we cannot get the ideal connecting hole. The other method is that the hydrogel is prepared and then freeze-dried. Although the pore size increased with the decrease in polymer content, the hydrogel cannot form after a certain degree of reduction. Therefore, we freeze-dried the polymer solution before gelating to obtain

sponge-like scaffolds and photo crosslinking for the macroporous architecture. Importantly, low polymer concentration will not affect crosslinking. As shown in **Figure 2E**, the pore size of L-PGS-P (200–500  $\mu\text{m}$ ) was larger than that of PGS-P (2–5  $\mu\text{m}$ ). According to the previous consensus on pore classification, pores > 100  $\mu\text{m}$  in tissue regeneration substitutes are defined as macropores. Such a macroporous structure is good for cell attachment, migration, and bone ingrowth into scaffolds (Jones and Hench, 2004).

After successfully preparing functional hydrogels, we needed to inspect the functional properties of the material's cellular level *in vitro* and *in vivo* animal bone defect models. This was done to explore the conceivable clinical applications of bio-artificial multiporous matrices. First, scaffolds were evaluated for the effect of the fabrication method on cellular infiltration *in vitro*. After the endothelial cells were seeded on the surface of the materials, the number of cells entering the interior of the scaffolds was observed using fluorescence staining. Many cells entered the L-PGS-P compared with that in PGS-P, which proved that the macroporous structure produced was sufficient for the cells to enter from the surface to the interior.

Generally, the induction and promotion of the osteogenic ability of stem cells are crucial steps for continuous mineralization (Ramaswamy et al., 2008). In this study, the adhesion, proliferation, ALP activity, and osteogenic gene expression of stem cells were investigated. First, we inspected the adhesion of BMSCs to PGS-P and L-PGS-P scaffolds (**Figure 3A**), which was related to the introduction of RGD. At the same time, the osteogenic gene was significantly up-regulated in the material groups at 3 and 7 days, and the osteogenic properties of the L-PGS-P group were better than those of the PGS-P group (**Figure 4**).

After the scaffolds' implantation, there will be an inflammatory phase, vascular phase, and subsequent bone tissue repair stage. In the process of vascular regeneration, growth starts from the blood vessels around the scaffold. The abundant blood vessels and high perfusion of blood imply that more bone cells will be delivered and nutrient delivery for the new bone will improve, which will accelerate bone regeneration (Liu et al., 2017). *In vitro* tests showed that the tube forming ability of the material group was significantly improved compared with the control group (**Figure 3D**), which was owing to the release of VEGF after grafting, and the tube forming ability of L-PGS-P was more obvious than that of PGS at the same time owing to the accelerated degradation. *In vivo* vascularization experiments confirmed that the PGS-based biological scaffold promotes vascularization compared with the control group. At the same time, as designed in this study, the L-PGS-P scaffold had a faster bone tissue repair rate and more vascular tissue growth. This study verified that a functional biomaterial based on PGS has excellent properties of promoting osteogenesis and angiogenesis.

However, there are some limitations to this study. One is that the *in vivo* experiments are based on a 2.5-mm size defect, which may not be critical enough to fully inspect the

scaffold's abilities since Sprague–Dawley rats may be able to achieve repair without any assistance. Another limitation is that we did not evaluate the effect of different pore sizes on vascularization and bone regeneration. Therefore, it is unclear if the positive effect was achieved by the ingredients of the compound or the specific pore size and structure. In a future study, the PGS-P scaffold should be examined with a more critical bone defect, and scaffolds with different pore sizes should be compared.

## CONCLUSIONS

In previous studies, PGS that supported greater rBMS-C adhesion, signaling, and proliferation was developed, proving its application in tissue engineering. However, the hydrophobicity of PGS makes it difficult to prepare hydrogels. Moreover, even if many methods have been applied to improve hydrophilicity, the pore size of the hydrogel obtained owing to the presence of hydrophobic segments is not conducive to subsequent tissue replacement after cell invasion. In this study, bone-mimetic porous scaffolds consisting of PGS biomaterials and proangiogenic VEGF mimetic peptide caused a significant increase in vascularization and bone regeneration by effectively preparing the interconnected macroporous structure hydrogel and endowing vascular function. Lyophilization before crosslinking through light triggering techniques proved that it could produce macropore structures similar to spinning and has the capability to increase cell infiltration and vascularization. *In vitro* and *in vivo* tests, compared with the control group, showed the material group exhibited better ability of vascularization and osteogenesis. More importantly, L-PGS-P recruited more HUVECs and significantly increased the formation of blood vessels because of promoting cell invasion. Compared with the PGS-P group, the L-PGS-P group produced bone faster, which appeared simultaneously in the center and around the defect. These collective findings support the use of a PGS-based bio-artificial multiporous matrix as potential bone repair materials.

## DATA AVAILABILITY STATEMENT

The original contributions generated for the study are included in the article/Supplementary Material, further inquiries can be directed to the corresponding author/s.

## ETHICS STATEMENT

The animal study was reviewed and approved by the Animal Research Committee of the Sixth People's Hospital, Shanghai Jiao Tong University.

## AUTHOR CONTRIBUTIONS

BL contributed to conceptualization, formal analysis and investigation, methodology and project administration, and writing of the original draft. QS contributed to data curation,

methodology, and project administration. JX curated the data. J-GX and Y-MC contributed to supervision, validation, reviewing, and editing the paper. All authors contributed to the article and approved the submitted version.

## REFERENCES

- Ansari, S., Khorshidi, S., and Karkhaneh, A. (2019). Engineering of gradient osteochondral tissue: From nature to lab. *Acta Biomater.* 87, 41–54. doi: 10.1016/j.actbio.2019.01.071
- Browning, M. B., Cereceres, S. N., Luong, P. T., and Cosgriff-Hernandez, E. M. (2015). Determination of the *in vivo* degradation mechanism of PEGDA hydrogels. *J. Biomed. Mater. Res. A* 102, 4244–4251. doi: 10.1002/jbm.a.35096
- Chen, Q., Liang, S., and Thouas, G. A. (2011). Synthesis and characterisation of poly (glycerol sebacate)-co-lactic acid as surgical sealants. *Soft Matter* 7, 6484–6492. doi: 10.1039/c1sm05350g
- Chen, Q. Z., Quinn, J. M., Thouas, G. A., Zhou, X., and Komesaroff, P. A. (2010). Bone-like elastomer-toughened scaffolds with degradability kinetics matching healing rates of injured bone. *Adv. Eng. Mater.* 12, B642–B648. doi: 10.1002/adem.201080002
- Chen, Q. Z., Thompson, I. D., and Boccaccini, A. R. (2006). 45S5 Bioglass®-derived glass–ceramic scaffolds for bone tissue engineering. *Biomaterials* 27, 2414–2425. doi: 10.1016/j.biomaterials.2005.11.025
- Chen, S., Li, L., Zhao, C., and Zheng, J. (2010). Surface hydration: Principles and applications toward low-fouling/nonfouling biomaterials. *Polymer* 51, 5283–5293. doi: 10.1016/j.polymer.2010.08.022
- Crapo, P. M., and Wang, Y. (2010). Physiologic compliance in engineered small-diameter arterial constructs based on an elastomeric substrate. *Biomaterials* 31, 1626–1635. doi: 10.1016/j.biomaterials.2009.11.035
- Dintcheva, N. T., Infurna, G., Baiamonte, M., and D'Anna, F. (2020). Natural compounds as sustainable additives for biopolymers. *Polymers* 12:732. doi: 10.3390/polym12040732
- Ekaputra, A. K., Prestwich, G. D., Cool, S. M., and Hutmacher, D. W. (2011). The three-dimensional vascularization of growth factor-releasing hybrid scaffold of poly ( $\epsilon$ -caprolactone)/collagen fibers and hyaluronic acid hydrogel. *Biomaterials* 32, 8108–8117. doi: 10.1016/j.biomaterials.2011.07.022
- Gaharwar, A. K., Kishore, V., Rivera, C., Bullock, W., Wu, C. J., Akkus, O., et al. (2012). Physically crosslinked nanocomposites from silicate-crosslinked PEO: mechanical properties and osteogenic differentiation of human mesenchymal stem cells. *Macromol. Biosci.* 12, 779–793. doi: 10.1002/mabi.201100508
- Gaharwar, A. K., Schexnaider, P. J., Kline, B. P., and Schmidt, G. (2011). Assessment of using Laponite® cross-linked poly (ethylene oxide) for controlled cell adhesion and mineralization. *Acta Biomater.* 7, 568–577. doi: 10.1016/j.actbio.2010.09.015
- García, J. R., Clark, A. Y., and García, A. J. (2016). Integrin-specific hydrogels functionalized with VEGF for vascularization and bone regeneration of critical-size bone defects. *J. Biomed. Mater. Res. A* 104, 889–900. doi: 10.1002/jbm.a.35626
- Hung, B. P., Harvestine, J. N., Saiz, A. M., Gonzalez-Fernandez, T., Sahar, D. E., Weiss, M. L., et al. (2019). Defining hydrogel properties to instruct lineage- and cell-specific mesenchymal differentiation. *Biomaterials* 189, 1–10. doi: 10.1016/j.biomaterials.2018.10.024
- Impellitteri, N. A., Toepke, M. W., Levengood, S. K. L., and Murphy, W. L. (2012). Specific VEGF sequestering and release using peptide-functionalized hydrogel microspheres. *Biomaterials* 33, 3475–3484. doi: 10.1016/j.biomaterials.2012.01.032
- Jones, J. R., and Hench, L. L. (2004). Factors affecting the structure and properties of bioactive foam scaffolds for tissue engineering. *J. Biomed. Mater. Res. B* 68, 36–44. doi: 10.1002/jbm.b.10071
- Karageorgiou, V., and Kaplan, D. (2005). Porosity of 3D biomaterial scaffolds and osteogenesis. *Biomaterials* 26, 5474–5491. doi: 10.1016/j.biomaterials.2005.02.002
- Kempainen, J. M., and Hollister, S. J. (2010). Tailoring the mechanical properties of 3D-designed poly (glycerol sebacate) scaffolds for cartilage applications. *J. Biomed. Mater. Res. A* 94, 9–18. doi: 10.1002/jbm.a.32653
- Kerativitayanan, P., Tatullo, M., Khariton, M., Joshi, P., Perniconi, B., and Gaharwar, A. K. (2017). Nanoengineered osteoinductive and elastomeric scaffolds for bone tissue engineering. *ACS Biomater. Sci. Eng.* 3, 590–600. doi: 10.1021/acsbomaterials.7b00029
- Kim, J., Lee, K. W., Hefferan, T. E., Currier, B. L., Yaszemski, M. J., and Lu, L. (2008). Synthesis and evaluation of novel biodegradable hydrogels based on poly (ethylene glycol) and sebacic acid as tissue engineering scaffolds. *Biomacromolecules* 9:149. doi: 10.1021/bm700924n
- Lee, E. J., Vunjak-Novakovic, G., Wang, Y., and Niklason, L. E. (2009). A biocompatible endothelial cell delivery system for *in vitro* tissue engineering. *Cell Transplant.* 18, 731–743. doi: 10.3727/096368909x470919
- Lee, K. W., Johnson, N. R., Gao, J., and Wang, Y. (2013). Human progenitor cell recruitment via SDF-1 $\alpha$  coacervate-laden PGS vascular grafts. *Biomaterials* 34, 9877–9885. doi: 10.1016/j.biomaterials.2013.08.082
- Liu, W. C., Chen, S., Zheng, L., and Qin, L. (2017). Angiogenesis assays for the evaluation of angiogenic properties of orthopaedic biomaterials—A general review. *Adv. Healthc. Mater.* 6:1600434. doi: 10.1002/adhm.201600434
- Luginina, M., Schuhladen, K., Orr, R., Cao, G., Boccaccini, A. R., and Liverani, L. (2020). Electrospun PCL/PGS composite fibers incorporating bioactive glass particles for soft tissue engineering applications. *Nanomaterials* 10:978. doi: 10.3390/nano10050978
- Miri, A. K., Muja, N., Kamranpour, N. O., Lepry, W. C., Boccaccini, A. R., Clarke, S. A., et al. (2016). Ectopic bone formation in rapidly fabricated acellular injectable dense collagen-Bioglass hybrid scaffolds via gel aspiration-ejection. *Biomaterials* 85, 128–141. doi: 10.1016/j.biomaterials.2016.01.047
- Nguyen, K. T., and West, J. L. (2002). Photopolymerizable hydrogels for tissue engineering applications. *Biomaterials* 23, 4307–4314. doi: 10.1016/S0142-9612(02)00175-8
- Pashneh-Tala, S., Moorehead, R., and Claeysens, F. (2020). Hybrid manufacturing strategies for tissue engineering scaffolds using methacrylate functionalised poly (glycerol sebacate). *J. Biomater. Appl.* 34, 1114–1130. doi: 10.1177/0885328219898385
- Phelps, E. A., Landázuri, N., Thulé, P. M., Taylor, W. R., and García, A. J. (2010). Bioartificial matrices for therapeutic vascularization. *PNAS* 107, 3323–3328. doi: 10.1073/pnas.0905447107
- Phipps, M. C., Clem, W. C., Grunda, J. M., Clines, G. A., and Bellis, S. L. (2012). Increasing the pore sizes of bone-mimetic electrospun scaffolds comprised of polycaprolactone, collagen I and hydroxyapatite to enhance cell infiltration. *Biomaterials* 33, 524–534. doi: 10.1016/j.biomaterials.2011.09.080
- Ramaswamy, Y., Wu, C., Zhou, H., and Zreiqat, H. (2008). Biological response of human bone cells to zinc-modified Ca–Si-based ceramics. *Acta Biomater.* 4, 1487–1497. doi: 10.1016/j.actbio.2008.04.014
- Rufaihah, A. J., Johari, N. A., Vaibavi, S. R., Plotkin, M., Kofidis, T., and Seliktar, D. (2017). Dual delivery of VEGF and ANG-1 in ischemic hearts using an injectable hydrogel. *Acta Biomater.* 48, 58–67. doi: 10.1016/j.actbio.2016.10.013
- Samourides, A., Browning, L., Hearnden, V., and Chen, B. (2020). The effect of porous structure on the cell proliferation, tissue ingrowth and angiogenic properties of poly (glycerol sebacate urethane) scaffolds. *Mater. Sci. Eng. C* 108, 110384. doi: 10.1016/j.msec.2019.110384
- Sawhney, A. S., Pathak, C. P., and Hubbell, J. A. (1993). Bioerodible hydrogels based on photopolymerized poly (ethylene glycol)-co-poly (alpha-hydroxy acid) diacrylate macromers. *Macromolecules* 26, 581–587. doi: 10.1021/ma00056a005
- Schnettler, R., Alt, V., Dingeldein, E., Pfeifferle, H. J., Kilian, O., Meyer, C., et al. (2003). Bone ingrowth in bFGF-coated hydroxyapatite ceramic implants. *Biomaterials* 24, 4603–4608. doi: 10.1016/S0142-9612(03)00354-5
- Shen, X., Zhang, Y., Gu, Y., Xu, Y., Liu, Y., Li, B., et al. (2016). Sequential and sustained release of SDF-1 and BMP-2 from silk fibroin-nanohydroxyapatite scaffold for the enhancement of bone regeneration. *Biomaterials* 106, 205–216. doi: 10.1016/j.biomaterials.2016.08.023

## FUNDING

This study was supported by the National Natural Science Foundation of China [grant number NSFC No. 81672217].

- Sheng, D., Li, J., Ai, C., Feng, S., Ying, T., Liu, X., et al. (2019). Electrospun PCL/Gel-aligned scaffolds enhance the biomechanical strength in tendon repair. *J. Mater. Chem. B*, 7, 4801–4810. doi: 10.1039/c9tb00837c
- Stähli, C., James-Bhasin, M., Hoppe, A., Boccaccini, A. R., and Nazhat, S. N. (2015). Effect of ion release from Cu-doped 45S5 Bioglass® on 3D endothelial cell morphogenesis. *Acta Biomater.* 19, 15–22. doi: 10.1016/j.actbio.2015.03.009
- Suresh, V., and West, J. L. (2020). 3D Culture facilitates VEGF-stimulated endothelial differentiation of adipose-derived stem cells. *Ann. Biomed. Eng.* 48, 1034–1044. doi: 10.1007/s10439-019-02297-y
- Touré, A. B., Mele, E., and Christie, J. K. (2020). Multi-layer scaffolds of poly (caprolactone), poly (glycerol sebacate) and bioactive glasses manufactured by combined 3D printing and electrospinning. *Nanomaterials*. 10, 626. doi: 10.3390/nano10040626
- Wang, C. C., Shih, T. Y., Hsieh, Y. T., Huang, J. L., and Wang, J. (2020). l-Arginine grafted poly (glycerol sebacate) materials: an antimicrobial material for wound dressing. *Polymers*. 12:1457. doi: 10.3390/polym12071457
- Wang, Y., Kim, Y. M., and Langer, R. (2003). *In vivo* degradation characteristics of poly (glycerol sebacate). *J. Biomed. Mater. Res. A*. 66A, 192–197. doi: 10.1002/jbm.a.10534

**Conflict of Interest:** The authors declare that the research was conducted in the absence of any commercial or financial relationships that could be construed as a potential conflict of interest.

Copyright © 2020 Liang, Shi, Xu, Chai and Xu. This is an open-access article distributed under the terms of the Creative Commons Attribution License (CC BY). The use, distribution or reproduction in other forums is permitted, provided the original author(s) and the copyright owner(s) are credited and that the original publication in this journal is cited, in accordance with accepted academic practice. No use, distribution or reproduction is permitted which does not comply with these terms.





# Silk Polymers and Nanoparticles: A Powerful Combination for the Design of Versatile Biomaterials

Cristina Belda Marín<sup>1,2</sup>, Vincent Fitzpatrick<sup>3</sup>, David L. Kaplan<sup>3</sup>, Jessem Landoulsi<sup>2</sup>, Erwann Guénin<sup>1\*</sup> and Christophe Egles<sup>4\*</sup>

<sup>1</sup> Laboratory of Integrated Transformations of Renewable Matter (TIRM), Université de Technologie de Compiègne, ESCOM, Compiègne, France, <sup>2</sup> Laboratoire de réactivité de surface (UMR CNRS 7197), Sorbonne Université, Paris, France, <sup>3</sup> Department of Biomedical Engineering, Tufts University, Medford, MA, United States, <sup>4</sup> Biomechanics and Bioengineering, CNRS, Université de Technologie de Compiègne, Compiègne, France

## OPEN ACCESS

### Edited by:

Nan Zhu,  
Dalian University of Technology, China

### Reviewed by:

Arnab Halder,  
Linköping University, Sweden  
Xintai Wang,  
University of Cambridge,  
United Kingdom  
Minwei Zhang,  
Xinjiang University, China

### \*Correspondence:

Christophe Egles  
christophe.egles@utc.fr  
Erwann Guénin  
erwann.guenin@utc.fr

### Specialty section:

This article was submitted to  
Polymer Chemistry,  
a section of the journal  
Frontiers in Chemistry

**Received:** 09 September 2020

**Accepted:** 09 November 2020

**Published:** 01 December 2020

### Citation:

Belda Marín C, Fitzpatrick V,  
Kaplan DL, Landoulsi J, Guénin E and  
Egles C (2020) Silk Polymers and  
Nanoparticles: A Powerful  
Combination for the Design of  
Versatile Biomaterials.  
Front. Chem. 8:604398.  
doi: 10.3389/fchem.2020.604398

Silk fibroin (SF) is a natural protein largely used in the textile industry but also in biomedicine, catalysis, and other materials applications. SF is biocompatible, biodegradable, and possesses high tensile strength. Moreover, it is a versatile compound that can be formed into different materials at the macro, micro- and nano-scales, such as nanofibers, nanoparticles, hydrogels, microspheres, and other formats. Silk can be further integrated into emerging and promising additive manufacturing techniques like bioprinting, stereolithography or digital light processing 3D printing. As such, the development of methodologies for the functionalization of silk materials provide added value. Inorganic nanoparticles (INPs) have interesting and unexpected properties differing from bulk materials. These properties include better catalysis efficiency (better surface/volume ratio and consequently decreased quantity of catalyst), antibacterial activity, fluorescence properties, and UV-radiation protection or superparamagnetic behavior depending on the metal used. Given the promising results and performance of INPs, their use in many different procedures has been growing. Therefore, combining the useful properties of silk fibroin materials with those from INPs is increasingly relevant in many applications. Two main methodologies have been used in the literature to form silk-based bionanocomposites: *in situ* synthesis of INPs in silk materials, or the addition of preformed INPs to silk materials. This work presents an overview of current silk nanocomposites developed by these two main methodologies. An evaluation of overall INP characteristics and their distribution within the material is presented for each approach. Finally, an outlook is provided about the potential applications of these resultant nanocomposite materials.

**Keywords:** natural polymers, silk, nanoparticles, bioactive biomaterials, regenerative medicine

## INTRODUCTION

Silk is a natural polymer originating from various insect and spider species. It is composed of two different proteins, sericin and fibroin, among which fibroin is an FDA-approved material for some medical devices. Due to the remarkable mechanical properties, biocompatibility and biodegradability, fibroin has been shaped into various scaffolds, including sponges, electrospun

mats, microspheres, hydrogels, aerogels, foams, and 3D printed structures. These silk-based scaffolds are particularly investigated in various tissue engineering applications, including for bone, nerve, skin, cartilage or corneal regeneration, but also as vehicles for drug delivery. These materials are also studied in other scientific areas such as for pollution control, electronics, optics, and material science in general.

Moreover, silk fibroin can be blended with different additives to form scaffolds with new properties. Among these, nanocomposites which comprise silk polymers and nanoparticles (NPs) have gained increasing interest due to the outstanding properties of the NPs, which differ in their properties from bulk materials. Accordingly, the development of silk-NPs nanocomposites has triggered growing interest for both academic and industrial research. Combining the assets of silk fibroin materials with those from NPs is appealing to obtain new properties that are unattainable by “classical” composites consisting of the same bulk materials.

In this review, we present an overview of current nanocomposites constituted of silk fibroin and NPs with particular attention to inorganic NPs (INPs), typically metals, oxides, and bioceramics. First, we present current knowledge on silk-based scaffolds and their main applications. We then describe the principal INPs (synthesis, properties) used to produce these composites. Finally, we provide an outlook of the potential applications of the resultant nanocomposite materials and guidelines for tuning their properties and functions.

## SILK

### Silk Structure and Extraction

Silks are protein biopolymers produced by many members of the arthropod family such as spiders, silkworms, flies, and silverfish. Each arthropod produces silk components with a different amino acid composition, resulting in different structural properties (Xiong et al., 2018). Mechanical properties are different, with some spider silks being stronger than silkworms silk. In addition, silk properties are influenced by other parameters, such as the environment and arthropod nutrition, giving rise to different silk types produced by the same species (Koh et al., 2015). Among existing silks, mulberry worm silks are the most commonly used for textiles and biomedical applications. Although some spider silks have greater tensile strength, toughness and extensibility, the cannibalistic nature of spiders makes the development of industrial production of spider silks with high yield impossible. *Bombyx mori* silkworms, on the other hand, were domesticated for industrial silk production centuries ago. As such, silkworm silk is almost exclusively used for medical and related applications, and for this reason only *B. mori* silk is considered in the following sections.

#### *Bombyx mori* Silk Structure

Silk fibers consist of two main proteins from *B. mori* silk: fibroin and sericin. Silk fibers are composed of fibroin microfibrils assembled into filaments. Silk fibers consist of two fibroin filaments each produced by one of the worm's salivary glands during spinning. Both filaments are then covered by sericin, an

adhesive and hydrophilic protein to form the structural unit (Poza et al., 2002).

Fibroin is an hydrophobic protein formed by two chains: a light chain (L-chain, ~26 kDa); and a heavy chain (H-chain, ~390 kDa). The two fibroin chains are covalently linked by a disulfide bond between two cysteines, forming a H-L complex. The formation of this complex is essential for the secretion of silk fibroin from producing cells to the glands. The primary structure of silk fibroin (SF) is formed by highly repetitive sequences composed mainly of glycine (43%), alanine (30%) and serine (12%). Other amino acids such as tyrosine (5%), valine (2%), and tryptophan are present in smaller proportions (Koh et al., 2015). The primary structure of the H-chain contains 12 repetitive hydrophobic domains interspersed with 11 non-repetitive hydrophilic regions. Three different polymorphs of SF (silk I, II, and III) have been reported; Silk I adopts a coiled structure and is found in the silk stored in the arthropods' glands. This conformation is also found in regenerated aqueous dispersions *in vitro*. Silk II corresponds to the antiparallel  $\beta$ -sheet crystal structure obtained once silk has been spun. In the laboratory, this polymorph results from the exposure of silk I to mechanical/physical and chemical treatments, such as stirring, heating, exposure to methanol or water annealing procedures. The formation of the  $\beta$ -sheet structure is possible due to the rearrangement of the repetitive regions that form the H-chain of SF, and the intra and intermolecular interactions by hydrogen bonding, van Der Waals forces and hydrophobic interactions. X-ray diffraction (XRD) analysis of the crystallinity regions of SF found an antiparallel  $\beta$ -sheet structure. The non-repetitive domains adopt a coiled conformation. Silk II excludes water from the structure, giving strength to the protein filament and making it insoluble in water and other solvents like mild acids or bases. The third polymorph, silk III, adopts a helical structure at air-water interfaces (Vepari and Kaplan, 2007).

#### Regenerated Silk Fibroin Extraction

Some studies have shown that sericin may induce an immunogenic response in the human body while SF has been approved by the FDA for medical use in the US (Zhang et al., 2017). Sericin is therefore removed from silk for biomedical applications (Rockwood et al., 2011). *B. mori* silk cocoons are processed to obtain a regenerated SF solution. This procedure differs from that used by the textile industry as the final objective is not to obtain silk fibers but a SF solution. The goal is to bring silk (polymorphs II and III) to the initial state found in the glands of the worm (silk I) before being spun. This transformation can be achieved by denaturing SF proteins, which result in protein solution (Rockwood et al., 2011). Briefly, silk cocoons are boiled in a sodium carbonate ( $\text{Na}_2\text{CO}_3$ ) solution to remove the sericin (soluble in hot water) that glues together the SF filaments. Boiling time is a crucial parameter influencing the properties of SF in solution. Longer times will disrupt SF chains to lower molecular weight. Boiling silk cocoons for 30 min will result in ~100 kDa fibroin proteins (Rockwood et al., 2011). Once boiled, the resulting entangled cotton-like fibers are abundantly rinsed in distilled water (to remove any remaining sericin) to obtain the

SF dispersion prior to solubilization in various, albeit limited, salt and related systems.

Different solvents can be used for complete dissolution of the SF, the most common being lithium bromide (LiBr) (Xiong et al., 2018). Briefly, a LiBr solution is mixed with the extracted and dried SF fibers and heated for a specific time (Rockwood et al., 2011). LiBr allows the destabilization of hydrogen bonds found in silk II polymorph; allowing the shift to the silk I structure (Xiong et al., 2018). LiBr is a chemical hazard that can cause skin and eye irritation, encouraging the search for alternative solutions. Another solvent used to dissolve silk fibroin fibers is a ternary system composed of calcium chloride, ethanol and water (Song et al., 2017). Ionic liquids have also been used to dissolve silk, such as 1-butyl-3-methylimidazolium chloride (BMIM Cl), 1-butyl-2,3-dimethylimidazolium chloride (DMBIM Cl) and 1-ethyl-3-methylimidazolium chloride (EMIM Cl) (Phillips et al., 2004). The solution obtained in the above process must be dialyzed with distilled water to remove the salts. Finally the protein solution is centrifuged twice to remove any solid impurities (Rockwood et al., 2011). The resultant solution is around 6–8% w/v SF and can be further concentrated up to around 30%. Regenerated SF dispersion should be handled with care, as many procedures such as heating, stirring or pH variations will induce protein rearrangement, forming  $\beta$ -sheet structures and resulting in the gelation of the solution. Because of this, regenerated SF dispersion should be stored at 4°C and for no longer than 1 month.

Unlimited storage can be achieved by lyophilizing the SF solution. Lyophilized product can be redissolved in water, formic acid or 1,1,1,3,3,3-hexafluoro-2-propanol (HFIP) (Rockwood et al., 2011) at the desired concentration.

## Silk-Based Materials

Silk is traditionally known for its wide use in the textile industry given its lightweight, soft touch, and luster. The  $\beta$ -sheet structure found in silk II polymorph is responsible for silk's mechanical properties, which are well-beyond most known biopolymers. Because of its unique properties and its versatility, a wide range of materials with various properties can be obtained from a SF dispersion or its lyophilized powder. **Figure 1** shows some of the multiple materials that can be obtained from silk fibroin. Most techniques used to construct SF materials are based on the controlled formation of  $\beta$ -sheet structures. Which enables tailoring mechanical properties, rates of biodegradation, and the degree of solvent dissolution of the silk.

### Silk Fibroin Sponges

Silk fibroin sponges are 3D porous materials for which pore size and interconnectivity can be controlled depending on the production method. Silk fibroin sponges can be produced by mixing the silk solution with a porogen (e.g., salt or sugar crystals, polymer or mineral beads) and subsequently inducing silk gelation. Many different procedures have been described, such as the use of sodium chloride (salt leaching), freeze casting (Cai et al., 2017a), or HFIP solvent (Rockwood et al., 2011). Silk fibroin sponges can be used as scaffolds for bone tissue regeneration due

to their macroporous structure that can be tailored to promote the enhanced formation of new and vascularized bone tissue (Karageorgiou and Kaplan, 2005). Several *in vitro* and *in vivo* studies have demonstrated the potential of cellularized scaffolds or acellular silk materials for bone regeneration (Bhattacharjee et al., 2017).

### Electrospun Mats

Electrospinning is a simple technique that consists of using of an electric field to spin a polymer solution into a non-woven mat composed of nanometer diameter fibers. During electrospinning, the polymer solution is placed in a syringe with a conductive needle connected to a high voltage electric field (5–40 kV). A grounded conductive collector is placed at a distance in front of the needle. While the polymer solution is extruded through the needle, the high voltage electric field induces its stretching, allowing the formation of nanofibers. During the process, the solvent evaporates at rates dependent on its intrinsic properties and experimental conditions, and the fibers are deposited on the collector due to the voltage difference (Rockwood et al., 2011). The nature of the collector used impacts the fiber alignment. If a flat static collector is used, fibers are randomly deposited. A rotating mandrel used as a collector results in alignment of the deposited fibers (Rockwood et al., 2011), useful for some applications, such as direction control of growth in neural regeneration (Belanger et al., 2018).

The fiber diameter obtained by electrospinning can be modulated by adjusting extrinsic parameters: polymer concentration, solvent, polymer extrusion flow rate, needle-to-collector distance, and the applied voltage. The electrospinning procedure may also be sensitive to intrinsic factors such as the molecular weight of the silk. Silk fibroin electrospinning is also dependent on humidity and temperature. A non-controlled variation in one of these parameters will alter the characteristics of final material. Electrospun mats can be used in the field of wound dressings, textiles, wearable electrodes, nerve guides, and other systems (Yukseloglu et al., 2015).

### Microspheres

Silk microspheres can be produced by several methods; encapsulation in fatty acids creating an emulsion, phase separation of silk from another polymer such as poly(vinyl alcohol) (PVA) (Rockwood et al., 2011), or adding potassium phosphate to the aqueous silk solution (Lammel et al., 2010). Silk has been extensively used for drug delivery, both as a vehicle and due to its stabilizing effect on bioactive molecules and enzymes (Li A. B. et al., 2015). Silk microspheres are of interest as an encapsulating material in this field, because modulating their degradation rate results in controlled release of the contents (Lan et al., 2014; Li H. et al., 2017).

### Hydrogels

Hydrogels are of interest due to their mechanical properties akin to soft tissues in the body. In addition, their capacity to swell and retain a high liquid volume renders them interesting for depollution applications, such as in environmental hazard removal (Hou et al., 2018). Hydrogels can be used to replace

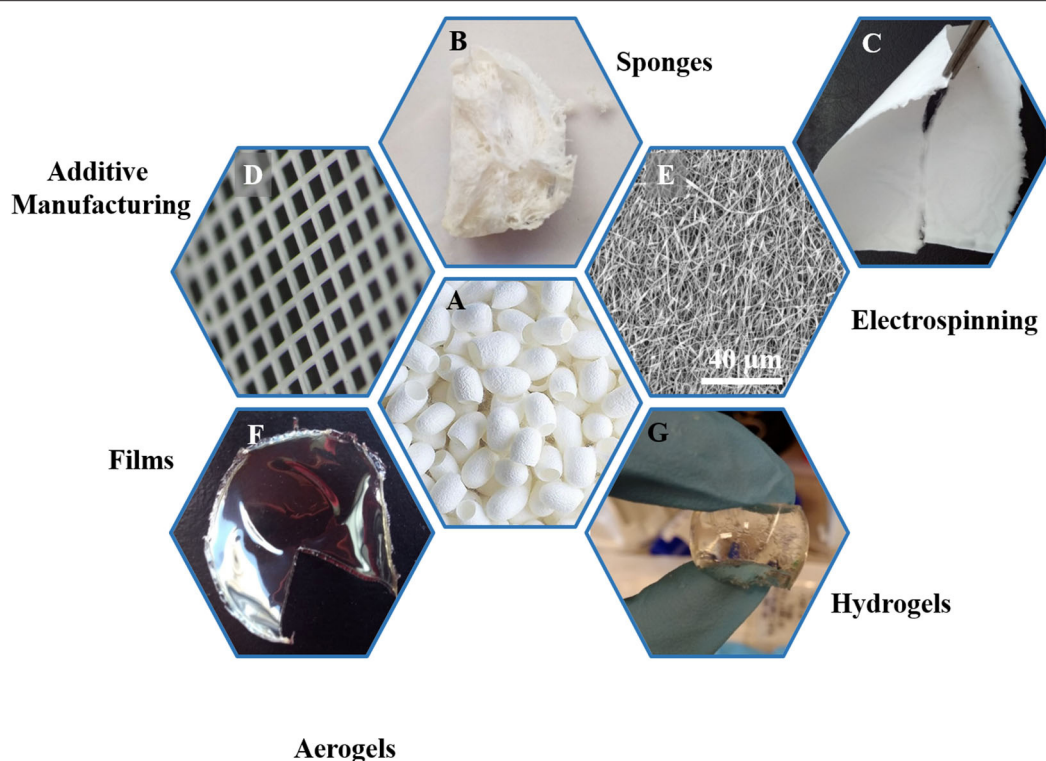


**FIGURE 1 |** Overview of the various biomaterials obtained from of silk fibroin extracted from silk cocoons (A). Silk cocoons (A), sponges (B), macroscopic and microscopic images of electrospun mats (C,E), 3D printed structures (D), films (F), hydrogels (G), and aerogels (H).

damaged soft tissues such as cartilage, the intervertebral disc, cornea and skin, among others. SF hydrogels can be found in applications such as drug delivery (Niu et al., 2019), tissue engineering (Vidal et al., 2019), regenerative medicine (Fernández-García et al., 2016; Frauchiger et al., 2017; Li et al., 2020), and catalysis (Luo and Shao, 2017).

The formation of hydrogels consists of the rearrangement of SF molecules to form crystalline structures as physical crosslinks. For this purpose, many protocols have been described in the literature to control the characteristics of the gels. Physical, photochemical, and chemical-induced gelation methods have been reported. “Physical gelation” occurs through the formation of physical interactions, including electrostatic (coulombic) and van der Waals. Physical gelation protocols include solution sonication (Fernández-García et al., 2016), vortexing, the application of an electrical current or a pH decrease below the pI (Rockwood et al., 2011). “Chemical gelation” consists of the formation of new covalent bonds (crosslinks) via enzymes, chemical catalysts, or other chemical species. Protocols mostly involve the use of enzymes, such as oxidases, phosphatases, transglutaminases, or peroxidases (Nezhad-Mokhtari et al., 2019).

#### Enzyme-assisted crosslinking

Enzymatic crosslinking offers *in situ* crosslinking and interactions with the surrounding extracellular matrix (Nezhad-Mokhtari et al., 2019). Moreover, enzymatic-catalyzed reactions

are specific and their rates are tunable, thus allowing a good control over the reaction products. Although many enzymes have been used to form such hydrogels, horseradish peroxidase (HRP) is the most extensively used.

#### HRP-crosslinked hydrogels

Commercially available horseradish peroxidase is extracted from the roots of *Armoracia rusticana*. In the plant, many different isoenzymes have been identified, although the most common one is HRP C. HRP is an oxidoreductase that catalyzes the conjugation of phenol and aniline derivatives in the presence of hydrogen peroxide ( $H_2O_2$ ). In proteins, the action of HRP results in the formation of dityrosine bonds between the phenol groups present on tyrosine. The incorporation of tyramine in enables crosslinking by HRP (Bang et al., 2017; Bi et al., 2019). The use of this enzyme to crosslink peptides, polysaccharides and polymers has been extensively described in the literature (Hoang Thi et al., 2019; van Loo et al., 2020). In particular, HRP-crosslinked SF hydrogels have been described (Partlow et al., 2014), including the structure, crosslinking kinetics, rheological, and mechanical properties, as well as the cytotoxicity and biocompatibility of the hydrogels formed in the process. The properties of these SF hydrogels were tunable depending on several parameters, including silk fibroin molecular weight and concentration. In addition, the all-aqueous procedure, together with its biocompatibility and *in vivo* tolerance, makes this hydrogel a good candidate for biomedical applications and the



encapsulation of biological factors (growth factors, hormones, cytokines), while preserving their activity.

### Aerogels

Aerogels are open porous materials of very low density that derive from replacing the liquid component of a gel by a gas. Silk aerogels are generally produced by freeze drying a silk solution or hydrogel. Similar to sponge materials, a 3D porous scaffold is obtained (Xiong et al., 2018) and pore size and distribution can be tuned by controlling the rate of freezing. One example of the process is an ice templating technique that consists in controlling ice crystal growth in the silk sample to obtain a desired structure. Microchannel containing silk scaffolds can be obtained by this technique (Qian and Zhang, 2011; Xiong et al., 2018). Aerogels have been used as fire retardant materials, thermal insulators (Maleki and Huesing, 2019), pollution control materials, and as biomaterials (Mandal and Kundu, 2009).

### 3D Printed Structures

The development of 3D printing technologies has made it possible to print polymer dispersions, including silk structures. This approach controls the shape and dimensions of the structures (Mu et al., 2020). Many silk-containing bioinks or 3D printing techniques are being developed with silk inks. Some approaches have focused on the properties of silk to obtain a construct, for example, by printing in a saline bath to induce hierarchical assembly of the silk proteins (Mu et al., 2020), or using freeform printing in a bath of synthetic nanoclay and polyethylene glycol (PEG) for a one-step process of printing and *in situ* physical gelation (Rodríguez et al., 2018). Other strategies have focused on mixing SF with other polymers and thickening agents, such as PEG (Zheng et al., 2018), polyols (Jose et al., 2015) or the polysaccharide Konjac glucomannan (Sommer et al., 2016). 3D printed structures are of interest in the tissue engineering field, as they allow the manufacturing of complex and patient-tailored shapes with controlled macroporosity.

### Silk Foams

Silk memory foams offer a promising and minimally invasive solution for soft tissue regeneration. These materials can be compressed prior to implantation, and then have the ability to recover their volume post-injection or implantation (Brown et al., 2017). *In vivo*, these materials have shown promise as soft tissue fillers, colonized by migrating cells and integrating with the surrounding native tissue (Bellás et al., 2015). These foams can be used as a drug delivery vehicles for bioactive molecules, and their degradation has been tuned using pre-loaded enzymes (Chambre et al., 2020). Likewise, these foams have been loaded with Dinutuximab, a monoclonal antibody with clinical potential for patients with high-risk neuroblastoma (Ornell et al., 2020). These silk foams induced a significant decrease in tumor growth rate in a mouse orthotopic tumor model. Overall, these materials are extremely well-suited for soft tissue regeneration and localized drug-delivery at an injury site.

### Microneedles

The mechanical properties, biocompatibility, biodegradability, benign processing conditions, and stabilizing effect of silk on biological compounds has made it a important candidate

for the fabrication of microneedle systems for drug delivery. The degradation rate of SF and the diffusion rate of the entrained molecules can be controlled by adjusting post-processing conditions (Yin et al., 2018). The microneedles can be further combined with other materials to make composite microneedles and further tune the drug release profile. These microneedles have been prepared with insulin (Wang S. et al., 2019), antibiotics (Tsioris et al., 2012), and vaccines (Demuth et al., 2014; Boopathy et al., 2019). Products based on this technology are currently being developed and commercialized for therapeutic applications.

### Hard Silk Materials

The mechanical properties of regenerated silk materials can be tuned for orthopedic applications requiring hard materials by controlling the fabrication process (Li et al., 2016). Bulk regenerated silk-based materials with excellent mechanical properties were generated through a biomimetic, all-aqueous process. These materials replicated the nano-scale structure of natural silk fibers and demonstrated excellent machinability, allowing the fabrication of resorbable bone screws, intermedullary nails and fixation plates. These devices allowed functionalization with bioactive molecules like antibiotics, morphogens, or micro RNAs (James et al., 2019). Recent work developed a thermal processing method allowing the direct solid-state molding of regenerated silk nanoparticles into bulk “parts” or devices with tunable mechanical properties (Guo et al., 2020). Thus, robust materials that retain biocompatibility, degradability and machinability, without the time, cost, and stability limitations of using silk solution-derived methods represents a significant advance.

### Films

Silk can be processed into thin films by air drying, methanol- or water-annealing, or even electrogelation (Stinson et al., 2020). Glycerol can be added to the formulation to obtain flexible silk films (Lu et al., 2010). While silk films are promising in the field of drug delivery (Zhou et al., 2014), or for the long-term stabilization of vaccines (Stinson et al., 2020), they also have direct applications in tissue engineering. Their interesting optical transparency and thin format make them candidates for corneal tissue models. The films sustain cell adhesion and growth; they can also be physically and chemically patterned to mimic the cellular and ECM organization of the cornea (Lawrence et al., 2009). Pores can also be added in the films to enhance trans-lamellar nutrient diffusion and cell-cell interactions. These films can be further stacked into multi-lamellar, helicoidal structures, and functionalized with RGD-peptides, allowing a biomimetic 3D corneal model (Gil et al., 2010).

## APPLICATIONS

The versatility of silk materials and their tunable properties drive interest for many applications, particularly in tissue engineering (Kundu et al., 2013; Li G. et al., 2015), wearable electronics (Kim et al., 2010), and pollution control (Ling et al., 2017; Gao et al., 2018).

## Silk Fibroin Biocompatibility

Evaluating the biocompatibility of any medical device is a crucial step during its development. Biocompatibility is the fact that a biomaterial is “accepted” by the organism with minimal cytotoxicity and immunogenicity with the aim to prevent any rejection of the biomaterial. However, biocompatibility is dependent on the shape and the time of contact and use of the material. Therefore, every material should be tested in their final form to assess their compatibility. Silk materials have long been used as silk sutures; however, hypersensitivity has been shown in some cases, even it remains scarce. Silk being a foreign body material, when implanted, a mild inflammatory response is generally observed. This immunogenic response has been linked to the presence of sericin (residual or due to the use of non-degummed silk) within the material (Kundu et al., 2013). However, no immunogenicity has been found when using materials composed of a single silk protein, either fibroin or sericin (Bandyopadhyay et al., 2019). Many studies have shown the biocompatibility of alkali heat degummed silk materials, such as SF electrospun mats, films, gels, and microparticles. Interestingly, *in vivo* studies showed that silk induced a lower inflammatory response compared to type I collagen and PLA (Rockwood et al., 2011). Finally, the FDA has approved the use of silk for medical uses in the US (Zhang et al., 2017).

## Biomedical Applications

Silk materials can match most of the challenges in the biomedical field due to their mechanical robustness, biocompatibility, and biodegradability. The various material formats obtained from silk, as described above, can be used in many different medical applications.

Silk sutures have been used in the medical field for a long time, and were patented in 1966, thus establishing the possibility to use silk in medicine. Silk sutures were first developed to overcome the mechanical problems encountered with traditional sutures. Surgical sutures require a great tensile strength to keep both ends of the wound tight together even under physiological movements such as heartbeat, stomach or intestinal peristalsis, or muscle contraction and relaxation. In addition, surgeons should be able to knot sutures. Silk was a suitable candidate fiber as it met all these requirements. Since then, silk materials have been developed for many applications in the biomedical field, such as for wound dressings, skin, bone, cartilage, ocular, vascular, neuronal, and tissue regeneration in general (Kundu et al., 2013).

### Wound Dressing

After sutures, wound dressings are probably the most common application of silk materials in the biomedical field. Several studies have found that silk materials induce faster reepithelization than conventional materials in skin burn wounds. Functionalization of electrospun silk materials has been pursued, such as with epidermal growth factor (EGF) and silver sulfadiazine, improving the overall wound healing process (Gil et al., 2013). Functionalization was also achieved using silk microparticles (Li X. et al., 2017), such as with insulin for chronic wound healing applications. Insulin was chosen because of its contribution to wound healing and its acceleration of

reepithelization. The overall wound healing effect was studied *in vivo* in diabetic rats and the insulin-loaded SF materials resulted in increased wound closure rates compared to non-loaded SF materials and conventional gauze.

### Skin Equivalents

Silk-based materials have emerged in the field of skin equivalents due to the ability to improve wound closure, as well as its biocompatibility and biodegradability properties. One model of artificial skin was produced by silk electrospinning (Sheikh et al., 2015). Three different electrospinning techniques were compared: (i) traditional electrospinning (TE), (ii) salt leaching electrospinning (SLE), and (iii) cold plate electrospinning (CPE). CPE materials provided thicker materials, as ice crystals preserved the conductivity of the deposited material, thus enhancing the deposition of polymer depth. In addition, CPE-obtained materials showed increased cell infiltration and the possibility to generate an artificial skin substitute when culturing keratinocytes at the air-liquid interface. Finally, CPE can be used over curved surfaces, thus, making it easier to produce personalized skin systems.

Cells were included in a silk-based skin equivalent (Vidal et al., 2019). This complex skin equivalent included adipose tissue, endothelial cells, keratinocytes, neural cells, immune cells, and vascularization systems. The hypodermis was constructed on a silk sponge by salt leaching. Dermis and epidermis layers were shaped into a hydrogel containing complete cell culture media, silk, collagen, and fibroblasts. The two layers of materials were then combined to form a full-thickness skin equivalent. The presence of silk in the material was crucial to overcome the concerns about collagen skin equivalents, which is construct contraction over time; this is prevented by the silk due to its stable structure. In addition, the mechanical properties of silk-containing hydrogels were closer to skin than pure collagen materials. Moreover, silk-containing materials were useful for up to 6 weeks *in vitro*, providing the possibility to study patient-specific immune and neuronal responses for a longer period of time.

### Bone Regeneration

Bone tissue engineering materials have been described (Bhattacharjee et al., 2017) with characteristics including: mechanical properties comparable to bone, biocompatibility, bioresorption and the capacity to deliver osteoprogenitor cells and growth factors. In addition, scaffolds should be able to provide mechanical integrity until the bone is completely regenerated, as they have to support high mechanical loads and stimuli. Resorbable materials are preferred as they avoid the need for a second surgery to remove the devices or implant. Collagen is the preferred material; however, a lack of mechanical properties limits its utility, synthetic polymers are used as alternatives. An extended review on silk-based materials for bone tissue engineering has been published (Bhattacharjee et al., 2017), and highlights the potential to exploit the versatility of silk materials as cellularized scaffolds or acellular biomaterials for bone tissue engineering. For example, guided bone regeneration was successfully achieved with silk membranes (Cai et al.,

2017a). The main objective was to generate a material able to avoid connective tissue invasion into a bone defect after surgery. Invasion of the defect by soft tissue makes bone regeneration impossible, resulting in the local loss of function. In their *in vivo* experiments, the material performed as well as commercially available products.

### Vascular Tissue Engineering

The gold standard for cardiovascular disease is autologous transplantation (autografts). However, limited donor tissue availability as well as donor site morbidity drive the need to develop new materials and tissue engineering approaches. Some synthetic materials are already used to construct vascular grafts, namely expanded polytetrafluoroethylene (ePTFE, Teflon®) and polyethylene terephthalate (PET, Dacron®). These materials are largely used for large diameter vessels or artery replacement. However, when replacing small diameter vessels (<6 mm) these materials fail when compared with autografts. Moreover, clinical complications such as aneurysms, intimal hyperplasia and thrombosis are associated with their use. Due to their characteristic mechanical properties and biocompatibility, silk materials have also been used in the field of vascular tissue engineering. Small vessel graft were developed with silk, where the diameter of the tube could be tailored and the graft was rich in  $\beta$ -sheet-structure to confer appropriate mechanical properties (Lovett et al., 2007). The incorporation of polyethylene oxide into the silk dispersion resulted in optimal porosity once the PEO was removed, enabling small protein transport but limiting endothelial cell migration. Vessel grafts were produced by combining two electrospun layers and an intermediate textile layer (Alessandrino et al., 2019). The mechanical properties were similar to native arteries, had biocompatibility, cell adhesion and blood hemocompatibility (no complement activation). However, further optimization is needed to reduce a foreign body response *in vivo* in sheep and minipigs.

### Nerve Regeneration

Neural guidance is a key factor for efficient nerve regeneration. A three-layered silk electrospun material (aligned-random-aligned fibers) was generated to address this need (Belanger et al., 2018). The aligned electrospun silk material induced alignment in Schwann cells in contrast to the random growth found when cultured on glass coverslips. *In vivo* experiments in rats showed successful nerve regeneration after 4 months, with mechanical properties matching the tensile stress of the rat sciatic nerve (ca. 2.6 MPa). The insulating characteristics of silk materials may impair electrical potential for neural action and communication, thus composite approaches may be useful.

### Drug Delivery

The controllable degradation rate of SF materials in the body enables their use as drug delivery devices. Gentamicin sulfate impregnated gelatin microspheres were embedded into silk scaffolds obtained by freeze drying (Lan et al., 2014). The material showed a reduced inflammatory response and accelerated reepithelization *in vivo* while exhibiting antibacterial properties. Similarly, dual drug-loaded silk materials were developed (Li

H. et al., 2017). Silk microspheres containing curcumin were prepared and blended into a silk dispersion with the drug doxorubicin hydrochloride (DOX-HCl). By electrospinning, nanofiber silk materials were obtained containing the hydrophilic DOX-HCl in the shell and the hydrophobic curcumin in the core. Silk hydrogels can also be used for drug delivery. Silk hydrogels were loaded with bevacizumab, an anti-vascular endothelial growth factor antagonist (Lovett et al., 2015). Bevacizumab is a therapeutic agent for the treatment of age-related macular degeneration, an eye disease characterized by the progressive loss of vision. The intravitreal injection of hydrogels in rabbits' eyes showed sustained drug release for up to 90 days.

### Other Applications

Although silk is increasingly being developed in the biomedical field, interesting applications have also emerged in other areas, such as for pollution control (Ling et al., 2017; Gao et al., 2018), electronics (Kim et al., 2010), thermal insulators, and fire retardants (Maleki et al., 2018). For example, silk adsorbs many chemicals and metals, which renders it interesting for water and air pollution. With this objective, electrospinning has been used to develop silk air filters (Gao et al., 2018) that have high efficiency air filtration (up to 99.99%) for particles with mean diameters from 0.3 to 10  $\mu$ m, and a decreased pressure drop in comparison with state-of-the-art materials. In addition, silk filters are biodegradable and can be involved in recycling or sustainability processes.

### NANO-OBJECTS

Nano-objects are objects with at least one of their three dimensions at the nanoscale (smaller than 100 nm). Nano-objects are classified into three groups: nanoplates, nanofibers, and nanoparticles (NPs). According to the IUPAC, NPs are "particles" of any shape with dimensions in the 1–100 nm range. These nano-objects exhibit a high surface-to-volume ratio that is particularly useful in many fields, such as in catalysis and sensing. In addition, unexpected and tunable properties appear at the nanoscale, differing from the bulk material.

NPs are rapidly coated by biomolecules, mostly proteins, when injected into biological fluids, leading to the formation of a "biomolecular corona" (Monopoli et al., 2012). The stability of NPs in solution depends on the equilibrium of attractive and repulsive forces between NPs, influenced by physicochemical conditions including the ionic strength, nature of the ions, pH, temperature, and the presence of bio-organic compounds (e.g., steric effects). Destabilization of the NPs solution may result in aggregation and precipitation. Given these considerations (protein corona formation and stability of NPs solution) it is unlikely that NPs preserve their initial size over time in the body. Large-sized NPs can be easily eliminated from the body through conventional routes. The remaining NPs can be taken up, stored and even degraded by cells to limit bioavailability (Van de Walle et al., 2019; Balfourier et al., 2020; Plan Sangnier et al., 2020).

NPs can be synthesized by top-down or bottom-up methods. Top-down synthesis consists of breaking down the bulk material



until the obtention of nanosized particles, such as ball-milling, laser ablation, and lithography. Bottom-up synthesis is performed by building up the nanomaterial atom by atom or molecule by molecule. Bottom-up methods are liquid synthesis and include chemical precipitation, sol-gel processes and micellar and inverse micellar synthesis, hydro/solvo-thermal methods, etc. (Su and Chang, 2017). Many different synthesis routes are actually used for different materials as a standard and consistent synthesis method for all NPs has not yet been found to our knowledge.

## Noble Metal Nanoparticles

Noble metal NPs are of particular interest in materials because the reduction of material needed allows decreasing costs and lower its environmental impact. Many noble metal NPs are currently used in several applications such as catalysis, biomedicine, environment depollution or electronics.

### Gold NPs

Gold NPs are probably the most well-known type of NPs since the preparation of the colloidal “ruby” gold by Michael Faraday in the 19th century. These NPs are used in many fields, from medicine (imaging, diagnostics, therapeutics) to electronics, essentially due to their unique reactivity and optical properties emerging only at the nanoscale.

Gold NPs have been used for their surface plasmon resonance (SPR) effect that results in an enhancement of the electromagnetic field in the surface of the NPs and optical extinction at the plasmon resonance frequency. SPR allows gold NPs to be used as hyperthermia agents due to their capability to absorb light at a given frequency and transforming the energy into heat (Plan Sangnier et al., 2019; Balfourier et al., 2020). Gold NPs have also been largely used in sensing systems (Zhou et al., 2015; De Crozals et al., 2016; Szekeres and Kneipp, 2019), as contrast agents for computed tomography (CT), as antibacterial agents (Cui et al., 2012), and as catalyst (Alshammari, 2019; Begum et al., 2019).

### Silver NPs

Silver is known for its antibacterial action. The use of silver as an antibacterial agent had decreased with the arrival of antibiotics. However, the widespread use of these powerful molecules has led to the apparition of antibiotic-resistant bacterial strains. Silver NPs have broad spectrum activity against gram positive and gram negative bacteria (Agnihotri et al., 2014), biofilms (Guo et al., 2019), multidrug resistant bacteria (Lara et al., 2010a), fungi (Kim et al., 2009; Chudasama et al., 2011), and even some virus (Lara et al., 2010b). The antibacterial action of silver NPs is dependent on their size and shape (Choi and Hu, 2008).

Silver was initially used in its ionic form for biomedical applications, and, in particular, in surgical cloths and wound dressings (Uttayarat et al., 2012). Although silver ions can be toxic at high concentrations, great controversies exist regarding the toxicity of silver NPs, as this property depends on their size, shape, and surface functionalization. To our knowledge, no silver NP toxicity has been proven except the one resulting from the release of Ag<sup>+</sup> ions. Therefore, silver NPs are actually

being widely used as antibacterial agents (Reidy et al., 2013). Additionally, they can also be used for sensing applications (Annadhasan et al., 2014), as conductive elements in electronics (Cai et al., 2017b) and in environmental remediation applications as they possessed also catalytical properties allowing the degradation of several pollutants in water (Guerra et al., 2018).

### Other Noble Metal NPs (Pd, Pt)

Platinum and palladium NPs are well-known in the catalysis field. Both metals are expensive which drives the industry interests toward the reduction of metal needed to obtain the same result. When used in their nanoparticulate form their catalytic performance increases due to the higher surface-to-volume ratio.

Platinum is mainly used in hydrogenation/dehydrogenation reactions, fuel cell applications, CO, and alcohol oxidations (Martínez-Prieto et al., 2017). On the other hand palladium NPs are used as catalysts mainly in C-C coupling reactions (Suzuki–Miyaura, Sonogashira and Mizoroki–Heck reactions), reduction of nitroarenes, hydrogenation of alkenes and alkynes, and oxidation of primary alcohols (Saldan et al., 2015). Both metal NPs have been used as well for depollution applications (Iben Ayad et al., 2020), photothermal treatments (Samadi et al., 2018; Yang et al., 2019) and as antibacterial/antifungal agents (Dumas and Couvreur, 2015; Pedone et al., 2017).

## Quantum Dots

Quantum dots (QDs) are semiconductor NPs of small size (usually smaller than 10 nm). Because of their tunable fluorescent properties in a large light spectrum (from infrared to visible light), cadmium selenide (CdSe), cadmium telluride (CdTe), and cadmium sulfide (CdS) have been developed. In the biomedical field, QDs are used as biosensors, imaging probes and for diagnostics among others (Pandey and Bodas, 2020). QDs have been also used in photocatalysis applications. For example, the production of hydrogen using QD photocatalysis has been studied. This possibility is interesting for the use of hydrogen as an alternative combustible (Rao et al., 2019).

## Metal Oxide Nanoparticles

### Iron Oxide NPs

Iron oxide NPs are of special interest because of their magnetic properties that differ from the bulk material. Similar to the LSPR effect, iron oxide particles present superparamagnetic behaviors in the nanoscale range (NPs of diameter below 20–30 nm). Because of their small size, these NPs act as single domain particles. They are magnetized in a uniform manner, with all the spins aligned in the same direction when a magnetic field is applied (Cardoso et al., 2018). Again, the magnetic properties of iron oxide NPs strongly depend on their size and shape, as well as their crystalline state (Demortière et al., 2011; Wu et al., 2016). The use of iron oxide NPs in the biomedical field is possible due to their biocompatibility and low toxicity. Because of their magnetic properties and their relaxation times, iron oxide NPs are good candidates for magnetic resonance imaging (MRI) contrast agents. Iron oxide NPs are a type T2 contrast agent resulting in a black contrast. These NPs are also used for protein, molecule or cell separation thanks to their magnetic properties



(Cardoso et al., 2018; Cheng et al., 2019). Iron oxide NPs can be also used for hyperthermia treatments (Liang et al., 2019; Pires et al., 2019), drug delivery (Benyettou et al., 2019), tissue adhesion (Meddahi-Pellé et al., 2014) as magnetic stimulant (Santos et al., 2015), and as pollutant sorbents (Gutierrez et al., 2017).

### Titanium Oxide NPs

Titanium oxide (TiO<sub>2</sub>) is a semiconductor metal used as a white pigment in paints, plastic, papers, cosmetics, food (E171), toothpaste among many others. This white appearance is due to its high refractive index (2.48–2.89) that results in the reflection of 96% of light. In addition, the high opacity of TiO<sub>2</sub> NPs places it as the most used white pigment among industry. TiO<sub>2</sub> is also the active component of sunscreens due to its capacity to absorb UV irradiation. Smaller NPs are preferred in this case as they result in colorless and fluid products (Lan et al., 2013). TiO<sub>2</sub> NPs are also well-known because of their photocatalytic activity. Under ultraviolet irradiation, TiO<sub>2</sub> electrons are excited and can be part of chemical reactions in the surface of the material. This property is mainly used for water hydrolysis to produce hydrogen, pollutant degradation (in air or water) resulting in auto-cleanable surfaces and bactericidal effect due to ROS production. Because of its biocompatibility, low cost, and high photocatalytic activity, TiO<sub>2</sub> NPs are the most used photocatalyst (Haider et al., 2019), even if their reactivity in aqueous media is impacted by aggregation (Degabriel et al., 2018).

In the biomedical field, the photocatalytic activity of TiO<sub>2</sub> NPs has been used for photodynamic treatment of infections, cancers and skin defects as psoriasis (Ahmad et al., 2015). However, this application is limited due to UV irradiation-induced damage in human tissues. To avoid direct use of UV radiation, NP surface modifications can be made, resulting in a shift in light absorption enabling the use of a different light source (Ni et al., 2017; Ziental et al., 2020). TiO<sub>2</sub> NPs have been the subject of a vast literature regarding their toxicity, sometimes polemical (Horváth et al., 2018; Suzuki et al., 2020), and their interaction with proteins impacting cell behavior (Jayaram et al., 2017; Runa et al., 2017).

### Other Metal Oxide NPs (Cu, Zn)

Other metal oxide NPs have been developed and are being used in industry. This group of NPs is used in many applications including antibacterial agents, gas sensors, catalysis, and electronics (Chavali and Nikolova, 2019). Zinc and copper oxide NPs are two of the most important ones aside from titanium oxide, and widely used in catalysis and as antibacterial agents (Stankic et al., 2016). Increasing research in the biomedical field raises the applications of metal oxide NPs as anticancer agents, anti-inflammatory and radiation protection among others (Augustine and Hasan, 2020).

### Hydroxyapatite, Bioactive Glass, and Silica NPs

Bioceramics, including hydroxyapatite (HAP), present low tensile strength and brittleness. This is an issue in bone tissue engineering applications, where biomechanical loads, including torsion, bending, compression, shear stress are frequently applied

to the implanted scaffold. Further, their limited remodeling (Sun et al., 2009) and uncontrolled degradation *in vivo* can lead to changes in the extracellular environment, which can cause adverse effects including cell death (Ge et al., 2008). Polymer/hydroxyapatite nanocomposites offer a promising solution to these issues, by combining the tunable degradability of polymers like silk with the osteoconductivity of ceramic materials (Zhang et al., 2019). The composition of these composites can be tuned to present mechanical properties closer to that of native bone, while preserving biocompatibility and biosorption properties. The nanoscale features of HAP NPs are particularly advantageous because nanotopography modulates cell behaviors like adhesion, differentiation, and proliferation, by promoting greater protein interactions and therefore new bone formation (Van Der Sanden et al., 2010).

Bioactive glasses and glass-ceramics stimulate a beneficial response *in vivo* by bonding to the host bone tissue (Jones, 2013). Further, the controlled release of biologically active calcium and silica ions from these materials leads to the upregulation and activation of genes associated to osteoblastic differentiation, encouraging rapid bone regeneration (Jones, 2013). The controlled release of ions from the dissolution bioactive glasses can induce angiogenesis, opening up further possibilities for enhanced bone or soft tissue regeneration (Hench, 2009). Like with HAP, one of the primary limitations on the clinical use of bioactive glasses is the unpredictable behavior in complex physiological loading conditions. Incorporating them as biologically active phases into composite systems is a promising solution to overcome these challenges.

### Graphene Oxide

Graphene is an interesting nanomaterial owing to its high mechanical strength and outstanding electrical conductivity among others. However, its low solubility reduces its utilization possibilities. Instead, graphene oxide (GO) is easier to synthesize and has better solubility, while matching the mechanical strength of graphene. Further, the presence of chemical groups in GO allows its functionalization and interaction with surrounding molecules (Smith et al., 2019). Because of its electronic configuration, GO nanosheets are impenetrable by many different gases and so can be used as barriers for such molecules. The same molecule exclusion principle together with the high-water permeability of GO has been used to create water filters for wastewater treatment (Thebo et al., 2018). For the same reason, GO is also used as coating to avoid material corrosion (Smith et al., 2019). GO conformation is easily altered when exposed to humidity, light, or heat. This property allows the development of stimuli-responsive materials. For example, the presence of humidity results in GO swelling (Chen et al., 2017).

## SILK-BASED BIONANOCOMPOSITES

The promising potential of combining silk and NPs for the design of bionanocomposites with tailored properties and functions has been pursued. Nanocomposites can present new properties that are not achieved in a classical composite with the same materials. Bionanocomposites are nanocomposites containing a biological

material such as collagen, cellulose, alginate or silk. They have been studied to develop replacement tissues, such as tendon (Yang et al., 2016), corneal stroma (Watanabe et al., 2020), bone (Raja and Yun, 2016) and dermis (Song et al., 2015).

However, these properties are only achieved if the NPs are homogeneously distributed within the resultant material. Therefore, when developing any type of nanocomposite, it is crucial to consider the NP surface chemistry, stabilization within the bulk material and homogeneous distribution. As previously explained, NP stabilization can be easily altered by changing the physicochemical conditions of their environment, such as ionic strength. Mixing NPs with other material results in a new environment so it is not surprising to observe NP aggregation and precipitation within the material. These considerations are particularly important for silk bionanocomposites as in this case silk gelation can easily occur as well due to NP addition to the solution.

Silk bionanomaterials have been generated using at least three different methods. *In situ* synthesis was studied using many different reducing agents (Table 1), including the ability of silk to reduce metal ions (Yu et al., 2017; Zhou et al., 2020). Figures 2B–D show silk electrospun biocomposites obtained by *in situ* synthesis of gold (Au NPs) and iron oxide nanoparticles (IONPs). Although this approach reduces the number of steps needed to produce the bionanocomposite, the resultant NPs can be polydisperse in size and shape. Moreover, the surface chemistry of these NPs is unknown. These issues could result in unpredictable properties and toxicity, which are highly dependent on the characteristics of the NPs. Better control of NP characteristics can be achieved by synthesis upstream and subsequently incorporating them into silk materials. Figure 2 shows an example of silver NPs embedded in silk fibers (Figures 2E–G) and sponges (Figure 2H) obtained by using the latter procedure. However, in these cases it is important to stabilize NPs in solution by controlling their surface chemistry. Therefore, many studies have been conducted to further understand the stability of NPs in the solution (Hotze et al., 2010). Nevertheless, it is shown that, once included within the bulk material, the confinement of NPs enhances their stability by decreasing particle-particle interactions (Chandran et al., 2014). In addition, in many situations, the direct incorporation of NPs into regenerated silk solution induces silk gelation. Some studies have focused on feeding the desired NPs directly to silkworms, with incorporation in the silk cocoons, however, the efficiency of incorporation is low due to the NP biodistribution in the worm (Xu et al., 2019).

## Antibacterial Activity

In the textile world of silk, the incorporation of antibacterial NPs allows for improvement of luxury clothes and reduces odors. In the biomedical field, the presence of such NPs avoids, or at least delays, infections. Silver NPs are used for antibacterial applications and silk materials have been functionalized with silver NPs. UV irradiation was used to synthesize silver NPs directly in silk solutions (Jia et al., 2017), films (Zhou et al., 2019), sponges (Hu et al., 2020), fibers, textiles and electrospun mats (Calamak et al., 2015; Jia et al., 2017; Ribeiro et al.,

2017; Zhou et al., 2019; Hu et al., 2020; Raho et al., 2020). *In situ* synthesis of NPs in silk textiles was not uniform over the fibers, likely due to a different silver ion adsorption depending on the silk chemical groups. Silver ion release was studied for electrospun mats and was dependent on  $\beta$ -sheet content. Electrospun materials with low  $\beta$ -sheet content resulted in cytotoxic effects in mammalian cells. Light was used as a reducing agent for the *in situ* synthesis of silver NPs in silk (Patil et al., 2015) and a gelling agent. The antibacterial activity of the silver NPs demonstrated. However, no tests were performed for the gel nanocomposite. The topical application of this gel in animal skin wound models resulted in faster wound closure in comparison with silk, silver NPs and Carbopol gels and Soframycin gel, a commercially available product (Patil et al., 2015). A difference was observed between silk and silver NPs/silk gels, suggesting a synergistic effect of both components in wound healing.

Silver NP-loaded silk hydrogels have been also used for bone regeneration (Ribeiro et al., 2017). Silver NPs were synthesized *in situ* using light as a reducing agent. Antibacterial activity was found for hydrogels containing more than 0.5% silver NPs. Cytocompatibility was assessed by seeding osteoblast cells on the hydrogels, while a silver NPs concentration-dependent decrease in cell viability was observed.

*In situ* NP synthesis in silk materials has also been developed using caffeic acid, flavonoids, vitamin C, citrate, *Rhizophora apiculata* leaf extracts, *Streptomyces* cell extracts or honeysuckle extracts as reducing agents (Dhas et al., 2015; Meng et al., 2016; Shahid et al., 2017; Zhou and Tang, 2018a,b; Baygar et al., 2019; Gao et al., 2019). The materials acquired antibacterial activities and showed no cytotoxic effects. Interestingly, the materials synthesized using caffeic acid had UV irradiation protection, suggesting applications in sun protective materials.

Silk sponges and films containing silver NPs have been developed (Yu et al., 2012; Das and Dhar, 2014). Silk alone was able to reduce  $\text{Ag}^+$  into  $\text{Ag}^0$  efficiently to form silver NPs. The reduction ability of SF, sericin and peptides has also been shown by others (Zhang et al., 2014; Yu et al., 2017; Zhou et al., 2020). All these *in situ* synthesis procedures resulted in NPs with uncontrolled sizes and shapes, parameters that are crucial to control in order to evaluate NP properties. In addition, no information about NP surface chemistry or the presence of remaining toxic silver ions was described. Altogether, materials obtained by this methodology may not possess the desired antibacterial properties and may also present undesired properties such as toxicity.

Mixing preformed NPs with silk has also been pursued (Gulrajani et al., 2008; Karthikeyan et al., 2011). A two-step functionalization of silk fabrics with silver NPs was reported (Gulrajani et al., 2008). The silk fabric was soaked in silver NPs solution and the effect of pH on NP uptake was assessed, finding greater adsorption in acidic media. Silk uptake of NPs was also temperature dependent, with improved adsorption at 40 vs. 80°C.

A two-step method was developed to functionalize silk fabrics with silver NPs (Zhou and Tang, 2018a). Interestingly the resulting materials were inhibited the growth of both *Escherichia*

**TABLE 1** | Applications, NPs, functionalization method, and silk materials for silk-based bionanocomposites.

Application	NPs type	Functionalization method	Silk material	References
Antibacterial	Ag	<i>In situ</i>	Degummed fibers	Lu et al., 2014b; Meng et al., 2016
			Electrospun	Calamak et al., 2015
			Film	Yu et al., 2012, 2017; Raho et al., 2020
			Silk dispersion	Jia et al., 2017
			Sutures	Baygar et al., 2019
			Textile	Zhang et al., 2014; Shahid et al., 2017; Gao et al., 2019; Velmurugan et al., 2020
		<i>In situ</i> vs. upstream	Degummed fibers	Dhas et al., 2015
		Upstream	Electrospun	Uttayarat et al., 2012
			Fibers	Karthikeyan et al., 2011
			Textile	Gulrajani et al., 2008; Zhou and Tang, 2018a
Yarn	Abbasi et al., 2016			
Antibacterial/catalysis/dyeing	CuO	<i>In situ</i>	Electrospun	Chung et al., 2016
	SeO	<i>In situ</i>	Film	Patil et al., 2018
	ZnO	Upstream	Textile	Zou et al., 2018
	Pt	<i>In situ</i>	Porous films	Zhou et al., 2019
Antibacterial/photocatalysis	Ag/AgCl	<i>In situ</i>	Sponge	Ribeiro et al., 2017
Antibacterial/tissue engineering	Ag Au HAP			Hu et al., 2020
Antibacterial/wound healing	Ag	<i>In situ</i>	Gel	Patil et al., 2015
Antibacterial/UV protection	Au	<i>In situ</i>	Textile	Tang et al., 2014
Antibacterial tissue protection	CeO <sub>2</sub>	Upstream	Degummed fibers	Lu et al., 2014a
	Ag	Upstream	Textile	Zhou and Tang, 2018b
	Au	<i>In situ</i>	Textile	Zhou et al., 2020
	Catalysis	Au	<i>In situ</i>	Sponge
Depollution	Fe <sub>3</sub> O <sub>4</sub>	<i>In situ</i>	Hydrogel	Luo and Shao, 2017
	Pd		Degummed fibers	Ikawa et al., 2005
	CuO		Silk dispersion	Kim et al., 2017
	Fe <sub>2</sub> O <sub>3</sub>		Cocoons	Liu et al., 2018
Hyperthermia	TiO <sub>2</sub>	Upstream	Electrospun	Aziz et al., 2017
	Au	Upstream	Hydrogel	Kojic et al., 2012
			Nanofibers	Wang J. et al., 2019
			Hydrogel	Qian et al., 2020
Imaging	Fe <sub>3</sub> O <sub>4</sub>	Worm feeding	Cocoons	Deng et al., 2020
	NaYF <sub>4</sub> @SiO <sub>2</sub>			Fan et al., 2019
	C nanodots	<i>In situ</i>	Film	Yin et al., 2009a,b
	Au		Silk dispersion	Ranjana et al., 2020
	C nanotubes/Au		hydrogel	Zhang et al., 2020
	CdS		Fibers	Han et al., 2010
	CdTe		Film	Sohail Haroone et al., 2018
	GO		Silk GO paper	Ma and Tsukruk, 2017
	Graphene		Film	Wang et al., 2017
	Ni nanodisc		Textile	Schmucker et al., 2014
Sensing SERS	Au	<i>In situ</i>	Silk textile	Liu et al., 2016
		Upstream	Film	Guo et al., 2015
Tissue engineering	Au	Upstream	Electrospun	Cohen-karni et al., 2012; Das et al., 2015; Sridhar et al., 2015; Akturk et al., 2016
			3D printed	Midha et al., 2018
			Sponge	Bidgoli et al., 2019
			CoFe <sub>2</sub> O <sub>4</sub> /Fe <sub>3</sub> O <sub>4</sub>	Electrospun

(Continued)

TABLE 1 | Continued

Application	NPs type	Functionalization method	Silk material	References
	Cu bioactive glass	<i>In situ</i>	Hydrogel	Wu et al., 2019
	Fe <sub>3</sub> O <sub>4</sub>		Sponge	Aliramaji et al., 2017; Tanasa et al., 2020
	GO		Hydrogel	Wang et al., 2020
	HAP		3D printed	Huang et al., 2019
			Compacted powder	Zakharov et al., 2017
			Silk dispersion	Kong et al., 2004
		Upstream	3D printed	Sun et al., 2012
			Fibers	Heimbach et al., 2018
			Hydrogel	Ding et al., 2017
	HAP TiO <sub>2</sub>	Upstream	Sponge	Kweon et al., 2011; Ye et al., 2017
	Silica		Film	Kim et al., 2016
	Au	Upstream	Film	Mieszawska et al., 2010
Wearable electronics				Tao et al., 2010

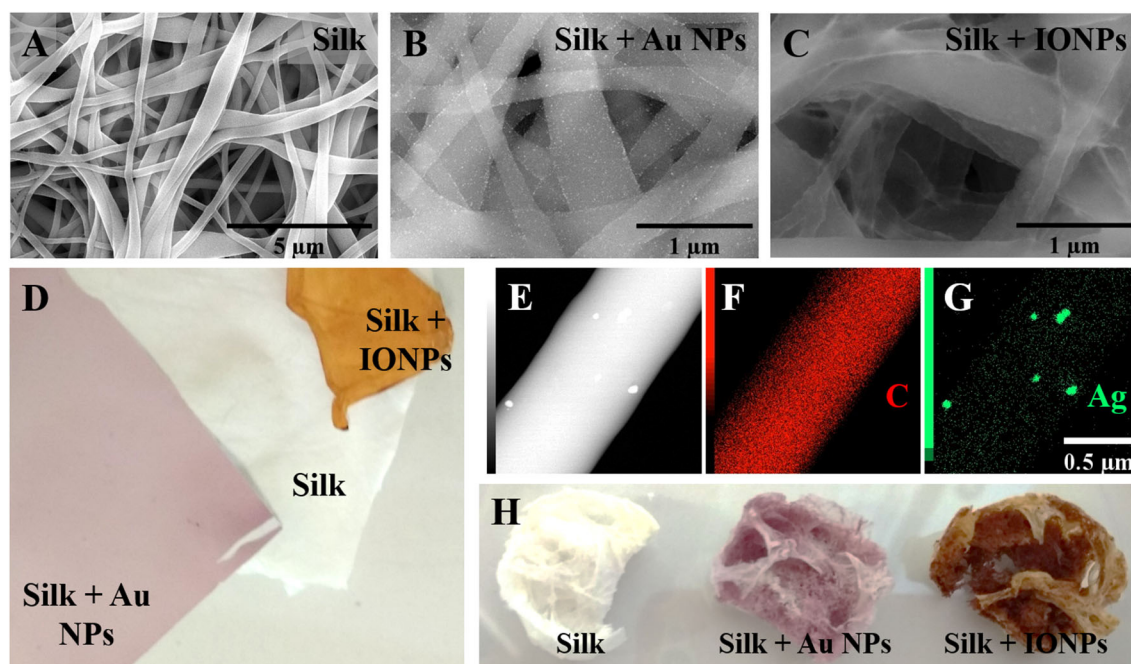


**FIGURE 2 |** Examples of silk bionanocomposites. Scanning Electron Microscopy view of electrospun silk fibers **(A)** with gold nanoparticles (Au NPs) **(B)**, iron oxide nanoparticles (IONPs) **(C)** or silver nanoparticles (Ag NPs) **[(E–G), STEM-EDS with elemental mapping]**. Macroscopic view of electrospun scaffolds **(D)** and sponges **(H)** with gold (Au NPs) and iron oxide nanoparticles (IONPs).

*coli* and *Staphylococcus aureus* even after 30 washes, suggesting a strong bond between the silk and silver NPs.

Other studies have focused on the antibacterial activity of gold (Ribeiro et al., 2017; Zhou et al., 2020), platinum (Zou et al., 2018), copper oxide (Abbasi et al., 2016), zinc oxide (Patil et al., 2018), cerium oxide (Lu et al., 2014a), selenium oxide NPs (Chung et al., 2016) in silk materials.

The *in situ* synthesis of gold NPs in a HAP-containing silk hydrogel was carried out (Ribeiro et al., 2017). Once the hydrogel formed, gold NPs were synthesized by heating the solution to 60°C. Significant antibacterial activity was observed against *S. aureus* (Multidrug sensitive and resistant strains), *E. coli* and *Pseudomonas aeruginosa*, but not against *Staphylococcus epidermidis*.



The *in situ* synthesis of gold NPs in silk fabrics was attained by heating to 85°C (Tang et al., 2014). The result was an antibacterial, UV irradiation blocking and thermal conducting material v for textile applications. However, as for the silver NPs, *in situ* synthesis does not allow tight control of NP size.

## Tissue Engineering

Different NPs containing silk materials have been developed for tissue engineering. Gold NPs can be incorporated into the silk electrospinning solution to obtain silk nanofibers with well-dispersed gold NPs by traditional (Cohen-karni et al., 2012) and wet (Akturk et al., 2016) electrospinning techniques. In both cases, the incorporation of gold NPs into electrospun silk materials resulted in improved mechanical properties. *In vitro* tests showed no cytotoxicity to the materials, and a good cell attachment to the scaffolds. In addition, cell attachment was enhanced by functionalizing the gold NPs with the integrin binding peptides RGD. The resultant materials were tested *in vivo* for wound closure (Akturk et al., 2016). No significant differences were found between silk with or without the gold NPs.

The incorporation of gold NPs into silk scaffolds has been also used to increase material conductivity. Electrical stimuli are crucial for nerve and cardiac tissues, thus, this modification impacts the regeneration process for these tissues. For example, electrospun silk containing gold NPs materials were rolled into conduits to replace sciatic nerves *in vivo* (Das et al., 2015). As a result, gold-containing silk materials outperformed pure silk materials in term of nerve regeneration. The presence of gold NPs in silk materials also supported better mesenchymal stem cell differentiation toward the cardiac lineage (Sridhar et al., 2015).

Most silk-based bionanocomposites developed for biomedical applications have focused on bone tissue regeneration. Because of their osteoconductive properties, silk materials containing HAP, bioactive ceramics and silica NPs have been studied. Nanocomposite scaffolds of silk and HAP are particularly interesting due to the ability of silk to “regulate” the mineralization of calcium phosphates, presumably through chemical interactions involving silk chemical groups (Kong et al., 2004; Zakharov et al., 2017). Silk/HAP scaffolds were manufactured using thermally induced phase separation (TIPS) (Wei and Ma, 2004) or lyophilization (Ye et al., 2017), to generate highly porous silk/nHAP composite scaffolds. Other materials used include silk sponges (Kweon et al., 2011), hydrogels (Ding et al., 2017), or 3D printed constructs (Huang et al., 2019).

Studies with silk/HAP materials for bone regeneration have shown promising results both *in vitro* and *in vivo* due to their biocompatibility, mechanical properties, and chemical composition similar to native bone. In a rabbit radial bone defect the formation of new bone tissue with a density similar to native bone was found using silk/chitosan/HAP biodegradable scaffolds obtained by lyophilization (Ye et al., 2017). A significantly higher rate of bone formation was also found in a rabbit parietal model after 8 weeks using silk sponges loaded with HAP (Kweon et al., 2011). Silk/HAP hydrogels have also been explored for the treatment of irregular bone defects by injection (Ding et al., 2017). *In vitro*, these hydrogels demonstrated good

cytocompatibility and osteogenic differentiation capacity. *In vivo*, in a rat calvarial defect model, these hydrogels were able to support the formation of new bone tissue, suggesting promising applications for bone tissue engineering (Ding et al., 2017).

A bone replacement was developed using a silk hydrogel functionalized with hydroxyapatite NPs (nano-HAP) (Ribeiro et al., 2015). HAP is a calcium phosphate widely used in bone tissue engineering as its composition is close to the mineral phase of bone tissues. *In vitro* experiments showed that the nano-HAP-containing materials enhanced osteoblastic phenotype. The main challenge was to avoid nano-HAP aggregation during silk gelation. The material containing 15 wt% of nano-HAP showed a homogeneous dispersion in the silk hydrogel with no visible aggregation. The aggregation state of nano-HAP remains, however, the main constraint for the design of a silk-based materials with a higher nano-HAP contents.

Adequately matching the morphology of the implant and the surrounding bone is crucial for the proper integration of the implant with the surrounding bone. Recent work has focused on using or tuning the rheological properties of silk/HAP-based pastes for 3D printing applications. These approaches allow the formation of biomimetic and macroporous silk/HAP nanocomposite scaffolds. Using sodium alginate (SA) as a binder, 3D printed scaffolds with large, interconnected pores and relatively high compressive strength were generated and human bone marrow-derived mesenchymal stem cells (hMSCs) seeded on the scaffolds adhered, proliferated and differentiated toward an osteogenic lineage (Huang et al., 2019). Likewise, 3D printed scaffolds composed of a gradient of silk/hydroxyapatite (HA) were generated and supported the growth of hMSCs and human mammary microvascular endothelial cells (hMMECs) (Sun et al., 2012). These cells formed intricate networks of extracellular matrices within the 3D scaffolds with vascular-like structures following the scaffold morphology (Sun et al., 2012).

In addition to scaffold-based applications for bone regeneration, silk/HAP/polylactic acid composites were developed for the fabrication of high strength bioresorbable fixation devices for clinical applications in orthopedics (Heimbach et al., 2018). Bioactive glass NPs have been also used in bone tissue engineering using silk-based materials. For example, SF-bioactive glass composites were fabricated with controlled architecture and interconnected structure by combining indirect three-dimensional (3D) inkjet printing and freeze-drying methods. The silk/bioglass composite scaffolds possessed excellent mechanical properties and stability, and supported the attachment of hMSCs and possessed osteoinductive properties (Bidgoli et al., 2019). 3D printed silk-gelatin-bioactive glass hybrids were generated with the goal of developing patient-specific grafts for bone regeneration (Midha et al., 2018). Two different bioactive glass compositions were tested, with and without strontium, and the strontium-containing constructs induced osteogenic differentiation of MSCs. Further, ion release from bioactive glasses in the silk-gelatin ink triggered the activation of signaling pathways for *in vivo* bone formation (Midha et al., 2018). Bioactive glass nanoparticles can be functionalized with different ions before incorporation into silk matrices. For example, injectable

composite hydrogels of chitosan, silk and glycerophosphate were developed and were highly porous and could be used to administer silica, calcium and copper ions in a sustained and controlled manner (Wu et al., 2019). Further, these materials were suitable for *in situ* injection and underwent rapid gelation under physiological conditions of temperature and pH. *In vitro*, these hydrogels supported the growth of MC3T3-E1 and human umbilical vein endothelial cells, and induced them toward osteogenesis and angiogenesis, respectively. *In vivo*, the copper-functionalized hydrogels restored critical-size rat calvarial bone defects with the newly formed bone tissue vascularized with mineralized collagen deposition in 8 weeks (Wu et al., 2019).

In addition, incorporating silica NPs in silk matrices to confer osteoinductive properties, silica-functionalized silk films were prepared where hMSCs adhered, proliferated, and differentiated toward an osteogenic lineage (Mieszawska et al., 2010). The presence of silica led to upregulation of osteogenic gene expression, including bone sialoprotein and collagen type 1. Collagen fibers and apatite nodules were observed, indicating the formation of new mineralized bone tissue (Mieszawska et al., 2010).

Other NPs have also been incorporated into silk materials for bone tissue engineering. For example TiO<sub>2</sub> NPs or GO have been used to increase the mechanical resistance of silk sponges and hydrogels (Kim et al., 2016; Wang et al., 2020). Magnetic NPs have interesting properties that can be used to apply a magnetic stimuli to cells and tissues (Aliramaji et al., 2017; Brito-Pereira et al., 2018; Tanasa et al., 2020). Recently a silk chitosan magnetite bionanocomposite scaffold was prepared by freeze casting (Aliramaji et al., 2017). They addition of magnetite NPs to the silk/chitosan scaffold did not change the porosity and no magnetite release was detected in a PBS solution after 48 h, to support the stability of NPs in the scaffolds. The combination of magnetite NPs within the scaffolds, together with the static magnetic field applied resulted in no osteosarcoma cell cytotoxicity and increased cell attachment.

Overall, the results described above demonstrate the potential of NP incorporation in silk as a tool for material functionalization; improving mechanical properties, and also to serve as biochemical cues for the surrounding cells toward bone tissue engineering. As our understanding of mechanisms and signaling pathways progresses, the regeneration of complex tissues may benefit from combinations of NPs in silk scaffolding, including spatial patterning, to induce improved and perhaps patterned regeneration outcomes.

## Hyperthermia

Hyperthermia as a therapy for the treatment of cancer uses various external energies, such as microwave, ultrasound, infrared radiations, to locally increase the body temperature and therefore destroy tumor cells. The heaters can be plasmonic or superparamagnetic NPs (Chichef et al., 2007; Kolosnjaj-Tabi et al., 2017). Among hyperthermia modalities, phototherapy is an interesting non-invasive therapy, in which light is used to induce local cell death. Due to the intrinsic light absorption of biological tissues, photothermal therapies can be only achieved in the near infrared region (NIR). State-of-the-art photothermal

agents, namely gold nanorods and nanostars, are not efficient in the NIR II transparency window.

Silk nanofibers containing gold NPs were developed (Wang J. et al., 2019). The specific assembly of NPs results in the broader absorption of light in the NIR and a red shift of the maximum. As a result, gold NP-containing silk nanofibers reached higher temperatures than gold NPs alone under the same conditions. Therefore, the ability to pattern how and where NPs adhere to silk materials result in increased efficiency (Plan Sangnier et al., 2020).

Differently, injectable silk hydrogels containing gold NPs have also been developed for photothermal treatments of infections (Kojic et al., 2012). Silk hydrogels were obtained by vortexing silk solutions in which gold NPs were incorporated. The hydrogels were injected in the infected site and heat was produced by laser exposition. Interestingly heat was produced locally and was able to reduce bacterial populations, thus, reducing infection. The silk hydrogel assured spatial localization of the gold NPs at the injection site. Light penetration limits in biological structures can be overcome by using magnetic fields for hyperthermia treatments. In this case magnetic nanoparticles are placed in the treatment zone and heat is produced in an external magnetic field (Sohail et al., 2017). Injectable silk hydrogels have been formulated for intratumoral injection using this strategy (Qian et al., 2020). The application of a magnetic field successfully enabled deep tumor ablation while no damage was observed in the surrounding healthy tissue. Furthermore, the magnetic field can be used to direct the material to the target spot, reducing systemic distribution of the magnetic NPs.

## Imaging

The possibility to follow silk implants by non-invasive imaging can be achieved by introducing fluorescent or contrast agents into the material. As an example, the introduction of iron oxide NPs into silk materials allows the use of MRI for visualization *in vivo* (Qian et al., 2020). NIR emitting NaYF<sub>4</sub>@SiO<sub>2</sub> NPs were synthesized and silk cocoons were functionalized by directly feeding silk worms with the NPs (Deng et al., 2020). The resultant silk materials were visible by NIR II imaging once implanted into mice. Similarly, silkworms were fed with fluorescent carbon nanodots resulting in fluorescent silk fibers (Fan et al., 2019). Although the materials showed no cytotoxicity, the fluorescent capacity was not evaluated *in vivo*. These results are encouraging for the *in vivo* monitoring of silk implants.

## Electronics and Sensing

The transparency, flexibility, biodegradability and biocompatibility properties of silk materials have been used to develop wearable electrodes and sensors. In many cases, NPs are incorporated to support increased detection sensitivity. As in hyperthermia, gold NPs-containing silk materials have been coupled to thermoelectric chips. By doing so and incorporating the chip into an implantable device, light can be used as an energy source (Tao et al., 2010).

Silk sensors have been developed to detect ammonia (Ranjana et al., 2020) and immunoglobulin G (Sohail Haroone et al., 2018). For example, the detection of ammonia was achieved with *in*

*situ*-synthesized gold NPs in a silk dispersion with UV-B light as reducing agent (Ranjana et al., 2020). Interestingly, the UV absorption of gold NPs decreased as the ammonia concentration increased. However, no control of the size and shape of the NPs was observed, and absorbance is dependent on these features. Silk materials have also been used to protect enzyme-mediated biosensors for the detection of hydrogen peroxide (Yin et al., 2009a), as well as methyl paraoxon, carbofuran and phoxim (Yin et al., 2009b).

Gold NPs-embedded silk films have been developed to enhance Surface-Enhanced Raman Spectroscopy (SERS) signals (Guo et al., 2015). The signal enhancement factor from the silk/gold NP films was around 150-fold. However, the light absorption by the gold NPs was influenced by the presence of the silk and red shifted by 20 nm. This result indicated a silk-induced change in the optical properties of the gold NPs, possibly due to the different refractive indexes of silk and the aqueous solution. The results suggest a capability of these films to be used as biosensors. Similar findings based on *in situ*-synthesized gold NPs in silk fabrics have been reported (Liu et al., 2016).

Silk hydrogels containing carbon nanotubes have been developed to respond to mechanical stimuli (Zhang et al., 2020). The composites were able to sense pressure variations, bending and compression forces. These abilities are interesting for medical applications such as to monitor arterial pressure and intracranial pressure. Gold NPs were integrated into the system, resulting in a laser-mediated degradation due to heat production. Altogether the silk hydrogels were able to trigger a laser exposition-mediated degradation when detecting epileptic episodes (mechanical stimuli). The incorporation of drugs into the hydrogel allows for controlled therapy.

Microcircuits were printed on a silk/GO-based paper (Ma and Tsukruk, 2017). The possibility to have a well-designed circuit structure allows the fine-tuning of electrode responses to external stimuli such as changes in relative humidity or proximity sensing. Silk materials were also used to prevent fluorescence quenching due to QD aggregation (Han et al., 2010). The immobilization of CdTe QDs increased fluorescence lifetime and IgG sensing capability. Silk fibers have also been used to direct the arrangement and *in situ* synthesis of CdS QDs for photoluminescence applications (Han et al., 2010). Surprisingly, physical and chemical nanotags for anti-counterfeiting applications have also been developed where nickel nanodisc structures with or without chromophores were embedded into silk textiles by electrospinning (Schmucker et al., 2014). The unlimited combinations of structure and chromophores enabled the generation of multiple tags identifying different products.

## Catalysis

Currently, nanocatalysts are used for industrial applications due to the increased surface-to-volume ratio, allowing the same catalytic activity as in bulk materials but requiring less catalyst. However, because of their nanometric dimensions, their collection for reutilization is particularly difficult. Therefore, there is an increasing interest in immobilizing nanomaterials into supports, and silk has been used for its biodegradation

and biocompatible features. Catalysis activities of platinum (Zou et al., 2018), gold (Das and Dhar, 2014), palladium (Ikawa et al., 2005), and iron oxide NPs (Luo and Shao, 2017) have been studied in silk materials.

Silk sponges and films containing gold NPs were developed for catalysis using the same preparation methodology used for silk materials containing silver NPs (Das and Dhar, 2014). The reduction of 4-nitrophenol catalyzed by gold NPs containing silk materials was demonstrated. Iron oxide NPs were synthesized *in situ* in silk materials using silk hydrogels (Luo and Shao, 2017). A co-precipitation methodology was used to prepare the embedded NPs-embedded by dipping the hydrogel into a solution containing FeCl<sub>2</sub> and FeCl<sub>3</sub>, and adding ammonium hydroxide to trigger NP synthesis. The magnetic and catalytic activities of magnetite were preserved in the silk materials. Such materials could be used in environmental chemistry applications and be easily separated by their magnetic properties; however, their use in biological applications is compromised by the presence of ammonium hydroxide. Interestingly, the immobilization of palladium nanoparticles into silk materials conserved its catalytic activity and also enhanced the chemoselectivity of the hydrogenation catalyzed reaction (Ikawa et al., 2005).

## Pollution Control

In addition to mechanical strength, biocompatibility and biodegradability of silk, this material is also a good absorbent for aromatic dyes. Therefore, the combination of absorbent properties, dependent on pH and dye concentration, with catalytic activity of several NPs has been explored.

The combination of silk electrospun nanofilters with TiO<sub>2</sub> NPs for anionic dye removal was studied (Aziz et al., 2017). Interestingly, the absorption capacities of the materials increased as the NP content increased, and better absorption was achieved at acidic pH. Similarly, silk iron oxide NPs materials were developed for anionic dye removal (Liu et al., 2018). The photocatalytic activity of CuO<sub>2</sub> NPs embedded in silk for dye removal has also been explored (Kim et al., 2017). These results provide insights into wastewater treatments with biodegradable materials like silk, functionalized with suitable NPs. The combination of SF with hydroxyapatite was efficient for water filtration and purification (Ling et al., 2017). The material was able to remove efficiently dyes and heavy metal ions from solution, a result not achieved with conventional nanofiltration membranes. Silk can also be mixed with silica to form insulating and fire retardant materials (Maleki et al., 2018). These materials can be obtained by a one-step acid catalyzed sol-gel reaction. The resulting silk/silica aerogel showed low density (0.11–0.19 g/cm<sup>3</sup>), high surface area (311–798 m<sup>2</sup>/g), flexibility in compression, and fire retardancy.

## PERSPECTIVES AND FUTURE OUTLOOKS

The great versatility of silk bionanocomposites, due to the possibility to design different material types and embed a variety of inorganic nanomaterials, is at the origin of their outstanding tailored properties and function. Therefore, a better match within the material and the specific requirements for a given

application is possible. In the biomedical field, the development of personalized silk bionanocomposite materials becomes more and more feasible. However, many issues are still to be addressed, particularly the long-term storage and batch-to-batch differences. The fate of the materials for long-term applications deserve, indeed, further investigations, to evaluate the evolution of mechanical properties due to aging, the stability of NPs and their possible release, etc. This requires in-depth physicochemical characterizations, on the one hand, and a great number of clinical trials, on the other hand. For the emerging applications, such as pollution control, silk bionanocomposites are promising as they enable the combination of pollutant adsorption and catalysis procedures.

## CONCLUSIONS

Our walkthrough of the state-of-the-art supports the versatility of silk in a range of materials and applications for these materials. Silk can be shaped into many different material formats in a tunable manner. The versatility allows for easy adaptation to each application, as well as the possibility to combine silk with different NPs for new properties.

However, silk-based bionanocomposites still have some drawbacks to overcome. Two main strategies for silk bionanocomposite preparation are used: *in situ* synthesis and the addition of previously synthesized NPs (upstream) to silk materials. *In situ* synthesis methods are promising by reducing the reaction steps to obtain the final functionalized materials, such as the successful for HAP/silk bionanocomposites obtained by controlled calcium phosphate mineralization. However, silk-based bionanocomposites often fail to control NP size and shape efficiently, which determine the function of the materials. The synthesis of NPs prior to addition to silk materials raises other questions inherent to NP synthesis, control of size, surface functionality and dispersion. Although advances have been made in NP synthesis methodologies, the synthesis of NPs needs to: (i) have control over size and shape; (ii) stabilized

NPs in the surrounding media and avoiding NP aggregation or precipitation; (iii) control of surface chemistry of NPs. Finally, the addition of synthesized NPs can induce silk gelation. Overall, the bionanocomposites should have NPs of controlled size, shape and surface chemistry, and these NPs should be homogeneously distributed within the silk matrix.

Silk bionanocomposites have been largely developed for antibacterial and tissue engineering applications because of their biocompatibility and biodegradation properties. Antibacterial properties allow interesting textile conservation and wound protection from infections. Moreover, the versatility given by different silk materials and the combinations with nanocomponents are well-adapted to many applications in tissue engineering. Emerging applications of silk bionanocomposites have also been described in many other fields such as catalysis, electronics, imaging and sensing devices.

In the future, different combinations of silk/NPs materials may be developed for additional applications. In addition, with the increasing concern on climate change and plastic pollution, biodegradable materials based on silk should remain in the spotlight to provide new materials for new functions in medicine, for the environment, and for a range of additional needs. Improved control of NP dimensions and homogeneity will further drive this innovation in next generation silk-based materials.

## AUTHOR CONTRIBUTIONS

All authors listed have made a substantial, direct and intellectual contribution to the work, and approved it for publication.

## ACKNOWLEDGMENTS

CM acknowledges the financial support of Sorbonne Universités through a Doctoral Fellowship. VF and DK acknowledge the financial support of the NIH (Grant No: P41EB027062).

## REFERENCES

- Abbasi, A. R., Noori, N., Azadbakht, A., and Bafarani, M. (2016). Dense coating of surface mounted Cu<sub>2</sub>O nanoparticles upon silk fibers under ultrasound irradiation with antibacterial activity. *J. Iran. Chem. Soc.* 13, 1273–1281. doi: 10.1007/s13738-016-0841-y
- Agnihotri, S., Mukherji, S., and Mukherji, S. (2014). Size-controlled silver nanoparticles synthesized over the range 5–100 nm using the same protocol and their antibacterial efficacy. *RSC Adv.* 4, 3974–3983. doi: 10.1039/C3RA44507K
- Ahmad, R., Mohsin, M., Ahmad, T., and Sardar, M. (2015). Alpha amylase assisted synthesis of TiO<sub>2</sub> nanoparticles: structural characterization and application as antibacterial agents. *J. Hazard. Mater.* 283, 171–177. doi: 10.1016/j.jhazmat.2014.08.073
- Akturk, O., Kismet, K., Yasti, A. C., Kuru, S., Duymus, M. E., Kaya, F., et al. (2016). Wet electrospun silk fibroin/gold nanoparticle 3D matrices for wound healing applications. *RSC Adv.* 6, 13234–13250. doi: 10.1039/C5RA24225H
- Alessandrino, A., Chiarini, A., Biagiotti, M., Dal Prà, I., Bassani, G. A., Vincoli, V., et al. (2019). Three-layered silk fibroin tubular scaffold for the repair and regeneration of small caliber blood vessels: from design to *in vivo* pilot tests. *Front. Bioeng. Biotechnol.* 7, 1–17. doi: 10.3389/fbioe.2019.00356
- Aliramaji, S., Zamanian, A., and Mozafari, M. (2017). Super-paramagnetic responsive silk fibroin/chitosan/magnetite scaffolds with tunable pore structures for bone tissue engineering applications. *Mater. Sci. Eng. C* 70, 736–744. doi: 10.1016/j.msec.2016.09.039
- Alshammari, A. S. (2019). Heterogeneous gold catalysis: from discovery to applications. *Catalysts* 9:402. doi: 10.3390/catal9050402
- Annadhasan, M., Muthukumarasamyvel, T., Sankar Babu, V. R., and Rajendiran, N. (2014). Green synthesized silver and gold nanoparticles for colorimetric detection of Hg<sup>2+</sup>, Pb<sup>2+</sup>, and Mn<sup>2+</sup> in aqueous medium. *ACS Sustain. Chem. Eng.* 2, 887–896. doi: 10.1021/sc400500z
- Augustine, R., and Hasan, A. (2020). Emerging applications of biocompatible phytosynthesized metal/metal oxide nanoparticles in healthcare. *J. Drug Deliv. Sci. Technol.* 56:101516. doi: 10.1016/j.jddst.2020.101516
- Aziz, S., Sabzi, M., Fattahi, A., and Arkan, E. (2017). Electrospun silk fibroin/PAN double-layer nanofibrous membranes containing polyaniline/TiO<sub>2</sub> nanoparticles for anionic dye removal. *J. Polym. Res.* 24, 0–6. doi: 10.1007/s10965-017-1298-0
- Balfourier, A., Luciani, N., Wang, G., Lelong, G., Ersen, O., Khelifa, A., et al. (2020). Unexpected intracellular biodegradation and recrystallization of gold nanoparticles. *Proc. Natl. Acad. Sci. U.S.A.* 117, 103–113. doi: 10.1073/pnas.1911734116



- Bandyopadhyay, A., Chowdhury, S. K., Dey, S., Moses, J. C., and Mandal, B. B. (2019). Silk: a promising biomaterial opening new vistas towards affordable healthcare solutions. *J. Indian Inst. Sci.* 99, 445–487. doi: 10.1007/s41745-019-00114-y
- Bang, S., Ko, Y. G., Kim, W. Il, Cho, D., Park, W. H., and Kwon, O. H. (2017). Preventing postoperative tissue adhesion using injectable carboxymethyl cellulose-pullulan hydrogels. *Int. J. Biol. Macromol.* 105, 886–893. doi: 10.1016/j.ijbiomac.2017.07.103
- Baygar, T., Sarac, N., Ugur, A., and Karaca, I. R. (2019). Antimicrobial characteristics and biocompatibility of the surgical sutures coated with biosynthesized silver nanoparticles. *Bioorg. Chem.* 86, 254–258. doi: 10.1016/j.bioorg.2018.12.034
- Begum, R., Najeeb, J., Sattar, A., Naseem, K., Irfan, A., Al-Sehemi, A. G., et al. (2019). Chemical reduction of methylene blue in the presence of nanocatalysts: a critical review. *Rev. Chem. Eng.* 0, 749–770. doi: 10.1515/revce-2018-0047
- Belanger, K., Schlatter, G., Hébraud, A., Marin, F., Testelin, S., Dakpé, S., et al. (2018). A multi-layered nerve guidance conduit design adapted to facilitate surgical implantation. *Heal. Sci. Reports* 1:e86. doi: 10.1002/hsr.2.86
- Bellas, E., Lo, T. J., Fournier, E. P., Brown, J. E., Abbott, R. D., Gil, E. S., et al. (2015). Injectable silk foams for soft tissue regeneration. *Adv. Healthc. Mater.* 4, 452–459. doi: 10.1002/adhm.201400506
- Benyettou, F., Prakasham, T., Ramdas Nair, A., Witzel, I. I., Alhashimi, M., Skorjanc, T., et al. (2019). Potent and selective *in vitro* and *in vivo* antiproliferative effects of metal-organic trefoil knots. *Chem. Sci.* 10, 5884–5892. doi: 10.1039/C9SC01218D
- Bhattacharjee, P., Kundu, B., Naskar, D., Kim, H. W., Maiti, T. K., Bhattacharya, D., et al. (2017). Silk scaffolds in bone tissue engineering: an overview. *Acta Biomater.* 63, 1–17. doi: 10.1016/j.actbio.2017.09.027
- Bi, B., Liu, H., Kang, W., Zhuo, R., and Jiang, X. (2019). An injectable enzymatically crosslinked tyramine-modified carboxymethyl chitin hydrogel for biomedical applications. *Colloids Surfaces B Biointerfaces* 175, 614–624. doi: 10.1016/j.colsurfb.2018.12.029
- Bidgoli, M. R., Alemzadeh, I., Tamjidi, E., Khafaji, M., and Vossoughi, M. (2019). Fabrication of hierarchically porous silk fibroin-bioactive glass composite scaffold via indirect 3D printing: effect of particle size on physico-mechanical properties and *in vitro* cellular behavior. *Mater. Sci. Eng. C* 103:109688. doi: 10.1016/j.msec.2019.04.067
- Boopathy, A. V., Mandal, A., Kulp, D. W., Menis, S., Bennett, N. R., Watkins, H. C., et al. (2019). Enhancing humoral immunity via sustained-release implantable microneedle patch vaccination. *Proc. Natl. Acad. Sci. U.S.A.* 116, 16473–16478. doi: 10.1073/pnas.1902179116
- Brito-Pereira, R., Correia, D. M., Ribeiro, C., Francesko, A., Etxebarria, I., Pérez-Álvarez, L., et al. (2018). Silk fibroin-magnetic hybrid composite electrospun fibers for tissue engineering applications. *Compos. Part B Eng.* 141, 70–75. doi: 10.1016/j.compositesb.2017.12.046
- Brown, J. E., Moreau, J. E., Berman, A. M., McSherry, H. J., Coburn, J. M., Schmidt, D. F., et al. (2017). Shape memory silk protein sponges for minimally invasive tissue regeneration. *Adv. Healthc. Mater.* 6:e201600762. doi: 10.1002/adhm.201600762
- Cai, Y., Guo, J., Chen, C., Yao, C., Chung, S. M., Yao, J., et al. (2017a). Silk fibroin membrane used for guided bone tissue regeneration. *Mater. Sci. Eng. C* 70, 148–154. doi: 10.1016/j.msec.2016.08.070
- Cai, Y., Piao, X., Gao, W., Zhang, Z., Nie, E., and Sun, Z. (2017b). Large-scale and facile synthesis of silver nanoparticles: via a microwave method for a conductive pen. *RSC Adv.* 7, 34041–34048. doi: 10.1039/C7RA05125E
- Calamak, S., Aksoy, E. A., Ertas, N., Erdogdu, C., Sagioglu, M., and Ulubayram, K. (2015). Ag/silk fibroin nanofibers: effect of fibroin morphology on Ag<sup>+</sup> release and antibacterial activity. *Eur. Polym. J.* 67, 99–112. doi: 10.1016/j.eurpolymj.2015.03.068
- Cardoso, V. F., Francesko, A., Ribeiro, C., Bañobre-López, M., Martins, P., and Lanceros-Mendez, S. (2018). Advances in magnetic nanoparticles for biomedical applications. *Adv. Healthc. Mater.* 7, 1–35. doi: 10.1002/adhm.201700845
- Chambre, L., Parker, R. N., Allardyce, B. J., Valente, F., Rajkhowa, R., Dilley, R. J., et al. (2020). Tunable biodegradable silk-based memory foams with controlled release of antibiotics. *ACS Appl. Bio Mater.* 3, 2466–2472. doi: 10.1021/acsabm.0c00186
- Chandran, S., Begam, N., Padmanabhan, V., and Basu, J. K. (2014). Confinement enhances dispersion in nanoparticle-polymer blend films. *Nat. Commun.* 5, 1–9. doi: 10.1038/ncomms4697
- Chavali, M. S., and Nikolova, M. P. (2019). Metal oxide nanoparticles and their applications in nanotechnology. *SN Appl. Sci.* 1, 1–30. doi: 10.1007/s42452-019-0592-3
- Chen, L., Weng, M., Zhou, P., Zhang, L., Huang, Z., and Zhang, W. (2017). Multi-responsive actuators based on a graphene oxide composite: intelligent robot and bioinspired applications. *Nanoscale* 9, 9825–9833. doi: 10.1039/C7NR01913K
- Cheng, F., Zhu, C., He, W., Zhao, J., and Qu, J. (2019). PSBMA-conjugated magnetic nanoparticles for selective IgG separation. *Langmuir* 35, 1111–1118. doi: 10.1021/acs.langmuir.8b00878
- Chicheł, A., Skowronek, J., Kubaszewska, M., and Kanikowski, M. (2007). Hyperthermia - description of a method and a review of clinical applications. *Reports Pract. Oncol. Radiother.* 12, 267–275. doi: 10.1016/S1507-1367(10)60065-X
- Choi, O., and Hu, Z. (2008). Size dependent and reactive oxygen species related nanosilver toxicity to nitrifying bacteria. *Environ. Sci. Technol.* 42, 4583–4588. doi: 10.1021/es703238h
- Chudasama, B., Vala, A. K., Andhariya, N., Upadhyay, R. V., and Mehta, R. V. (2011). Antifungal activity of multifunctional Fe<sub>3</sub>O<sub>4</sub>-Ag nanocolloids. *J. Magn. Magn. Mater.* 323, 1233–1237. doi: 10.1016/j.jmmm.2010.11.012
- Chung, S., Ercan, B., Roy, A. K., and Webster, T. J. (2016). Addition of selenium nanoparticles to electrospun silk scaffold improves the mammalian cell activity while reducing bacterial growth. *Front. Physiol.* 7, 1–6. doi: 10.3389/fphys.2016.00297
- Cohen-karni, T., Jeong, K. J., Tsui, J. H., Reznor, G., Mustata, M., Wanunu, M., et al. (2012). Nanocomposite gold-silk nano fibers. *Nano Lett.* 12, 5403–5406. doi: 10.1021/nl302810c
- Cui, Y., Zhao, Y., Tian, Y., Zhang, W., Lü, X., and Jiang, X. (2012). The molecular mechanism of action of bactericidal gold nanoparticles on *Escherichia coli*. *Biomaterials* 33, 2327–2333. doi: 10.1016/j.biomaterials.2011.11.057
- Das, S., and Dhar, B. B. (2014). Green synthesis of noble metal nanoparticles using cysteine-modified silk fibroin: catalysis and antibacterial activity. *RSC Adv.* 4, 46285–46292. doi: 10.1039/C4RA06179A
- Das, S., Sharma, M., Saharia, D., Sarma, K. K., Sarma, M. G., Borthakur, B. S., et al. (2015). *In vivo* studies of silk based gold nano-composite conduits for functional peripheral nerve regeneration. *Biomaterials* 62, 66–75. doi: 10.1016/j.biomaterials.2015.04.047
- De Crozals, G., Bonnet, R., Farre, C., and Chaix, C. (2016). Nanoparticles with multiple properties for biomedical applications: a strategic guide. *Nano Today* 11, 435–463. doi: 10.1016/j.nantod.2016.07.002
- Degabriel, T., Colaço, E., Domingos, R. F., El Kirat, K., Brouri, D., Casale, S., et al. (2018). Factors impacting the aggregation/agglomeration and photocatalytic activity of highly crystalline spheroid- and rod-shaped TiO<sub>2</sub> nanoparticles in aqueous solutions. *Phys. Chem. Chem. Phys.* 20, 12898–12907. doi: 10.1039/C7CP08054A
- Demortière, A., Panissod, P., Pichon, B. P., Pourroy, G., Guillon, D., Donnio, B., et al. (2011). Size-dependent properties of magnetic iron oxide nanocrystals. *Nanoscale* 3, 225–232. doi: 10.1039/C0NR00521E
- Demuth, P. C., Min, Y., Irvine, D. J., and Hammond, P. T. (2014). Implantable silk composite microneedles for programmable vaccine release kinetics and enhanced immunogenicity in transcutaneous immunization. *Adv. Healthc. Mater.* 3, 47–58. doi: 10.1002/adhm.201300139
- Deng, Z., Huang, J., Xue, Z., Jiang, M., Li, Y., and Zeng, S. (2020). A general strategy for designing NIR-II emissive silk for the *in vivo* monitoring of an implanted stent model beyond 1500 nm. *J. Mater. Chem. B* 8, 4587–4592. doi: 10.1039/C9TB02685A
- Dhas, S. P., Anbarasan, S., Mukherjee, A., and Chandrasekaran, N. (2015). Biobased silver nanocolloid coating on silk fibers for prevention of post-surgical wound infections. *Int. J. Nanomedicine* 10, 159–170. doi: 10.2147/IJN.S82211
- Ding, Z., Han, H., Fan, Z., Lu, H., Sang, Y., Yao, Y., et al. (2017). Nanoscale silk-hydroxyapatite hydrogels for injectable bone biomaterials. *ACS Appl. Mater. Interfaces* 9, 16913–16921. doi: 10.1021/acsami.7b03932
- Dumas, A., and Couvreur, P. (2015). Palladium: a future key player in the nanomedical field? *Chem. Sci.* 6, 2153–2157. doi: 10.1039/C5SC00070J

- Fan, S., Zheng, X., Zhan, Q., Zhang, H., Shao, H., Wang, J., et al. (2019). Super-strong and intrinsically fluorescent silkworm silk from carbon nanodots feeding. *Nano-Micro Lett.* 11, 1–11. doi: 10.1007/s40820-019-0303-z
- Fernández-García, L., Mari-Buyé, N., Barrios, J. A., Madurga, R., Elices, M., Pérez-Rigueiro, J., et al. (2016). Safety and tolerability of silk fibroin hydrogels implanted into the mouse brain. *Acta Biomater.* 45, 262–275. doi: 10.1016/j.actbio.2016.09.003
- Frauchiger, D. A., Tekari, A., Wöltje, M., Fortunato, G., Benneker, L. M., and Gantenbein, B. (2017). A review of the application of reinforced hydrogels and silk as biomaterials for intervertebral disc repair. *Eur. Cells Mater.* 34, 271–290. doi: 10.22203/ECM.v034a17
- Gao, A., Chen, H., Hou, A., and Xie, K. (2019). Efficient antimicrobial silk composites using synergistic effects of violacein and silver nanoparticles. *Mater. Sci. Eng. C* 103:109821. doi: 10.1016/j.msec.2019.109821
- Gao, X., Gou, J., Zhang, L., Duan, S., and Li, C. (2018). A silk fibroin based green nano-filter for air filtration. *RSC Adv.* 8, 8181–8189. doi: 10.1039/C7RA12879G
- Ge, Z., Jin, Z., and Cao, T. (2008). Manufacture of degradable polymeric scaffolds for bone regeneration. *Biomed. Mater.* 3:022001. doi: 10.1088/1748-6041/3/2/022001
- Gil, E. S., Mandal, B. B., Park, S. H., Marchant, J. K., Omenetto, F. G., and Kaplan, D. L. (2010). Helicoidal multi-lamellar features of RGD-functionalized silk biomaterials for corneal tissue engineering. *Biomaterials* 31, 8953–8963. doi: 10.1016/j.biomaterials.2010.08.017
- Gil, E. S., Panilaitis, B., Bellas, E., and Kaplan, D. L. (2013). Functionalized silk biomaterials for wound healing. *Adv. Healthc. Mater.* 2, 206–217. doi: 10.1002/adhm.201200192
- Guerra, F. D., Attia, M. F., Whitehead, D. C., and Alexis, F. (2018). Nanotechnology for environmental remediation: materials and applications. *Molecules* 23, 1–23. doi: 10.3390/molecules23071760
- Gulrajani, M. L., Gupta, D., Periyasamy, S., and Muthu, S. G. (2008). Preparation and application of silver nanoparticles on silk for imparting antimicrobial properties. *J. Appl. Polym. Sci.* 108, 614–623. doi: 10.1002/app.27584
- Guo, C., Hall, G. N., Addison, J. B., and Yarger, J. L. (2015). Gold nanoparticle-doped silk film as biocompatible SERS substrate. *RSC Adv.* 5, 1937–1942. doi: 10.1039/C4RA11051J
- Guo, C., Li, C., Vu, H. V., Hanna, P., Lechtig, A., Qiu, Y., et al. (2020). Thermoplastic moulding of regenerated silk. *Nat. Mater.* 19, 102–108. doi: 10.1038/s41563-019-0560-8
- Guo, J., Qin, S., Wei, Y., Liu, S., Peng, H., Li, Q., et al. (2019). Silver nanoparticles exert concentration-dependent influences on biofilm development and architecture. *Cell Prolif.* 52, 1–8. doi: 10.1111/cpr.12616
- Gutierrez, A. M., Dziubla, T. D., and Hilt, J. Z. (2017). Recent advances on iron oxide magnetic nanoparticles as sorbents of organic pollutants in water and wastewater treatment. *Rev. Environ. Health* 32, 111–117. doi: 10.1515/reveh-2016-0063
- Haider, A. J., Jameel, Z. N., and Al-Hussaini, I. H. M. (2019). Review on: Titanium dioxide applications. *Energy Procedia* 157, 17–29. doi: 10.1016/j.egypro.2018.11.159
- Han, J., Su, H., Dong, Q., Zhang, D., Ma, X., and Zhang, C. (2010). Patterning and photoluminescence of CdS nanocrystallites on silk fibroin fiber. *J. Nanoparticle Res.* 12, 347–356. doi: 10.1007/s11051-009-9622-1
- Heimbach, B., Tonyali, B., Zhang, D., and Wei, M. (2018). High performance resorbable composites for load-bearing bone fixation devices. *J. Mech. Behav. Biomed. Mater.* 81, 1–9. doi: 10.1016/j.jmbbm.2018.01.031
- Hench, L. L. (2009). Genetic design of bioactive glass. *J. Eur. Ceram. Soc.* 29, 1257–1265. doi: 10.1016/j.jeurceramsoc.2008.08.002
- Hoang Thi, T. T., Lee, Y., Le Thi, P., and Park, K. D. (2019). Engineered horseradish peroxidase-catalyzed hydrogels with high tissue adhesiveness for biomedical applications. *J. Ind. Eng. Chem.* 78, 34–52. doi: 10.1016/j.jiec.2019.05.026
- Horváth, T., Papp, A., Igaz, N., Kovács, D., Kozma, G., Trenka, V., et al. (2018). Pulmonary impact of titanium dioxide nanorods: examination of nanorod-exposed rat lungs and human alveolar cells. *Int. J. Nanomedicine* 13, 7061–7077. doi: 10.2147/IJN.S179159
- Hotze, E. M., Phenrat, T., and Lowry, G. V. (2010). Nanoparticle aggregation: challenges to understanding transport and reactivity in the environment. *J. Environ. Qual.* 39, 1909–1924. doi: 10.2134/jeq2009.0462
- Hou, X., Mu, L., Chen, F., and Hu, X. (2018). Emerging investigator series: design of hydrogel nanocomposites for the detection and removal of pollutants: from nanosheets, network structures, and biocompatibility to machine-learning-assisted design. *Environ. Sci. Nano* 5, 2216–2240. doi: 10.1039/C8EN00552D
- Hu, C., Wu, L., Zhou, C., Sun, H., Gao, P., Xu, X., et al. (2020). Berberine/Ag nanoparticle embedded biomimetic calcium phosphate scaffolds for enhancing antibacterial function. *Nanotechnol. Rev.* 9, 568–579. doi: 10.1515/ntrev-2020-0046
- Huang, T., Fan, C., Zhu, M., Zhu, Y., Zhang, W., and Li, L. (2019). 3D-printed scaffolds of biomaterialized hydroxyapatite nanocomposite on silk fibroin for improving bone regeneration. *Appl. Surf. Sci.* 467–468, 345–353. doi: 10.1016/j.apsusc.2018.10.166
- Iben Ayad, A., Luat, D., Ould Dris, A., and Guénin, E. (2020). Kinetic analysis of 4-nitrophenol reduction by “water-soluble” palladium nanoparticles. *Nanomaterials* 10:1169. doi: 10.3390/nano10061169
- Ikawa, T., Sajiki, H., and Hirota, K. (2005). Highly chemoselective hydrogenation method using novel finely dispersed palladium catalyst on silk-fibroin: its preparation and activity. *Tetrahedron* 61, 2217–2231. doi: 10.1016/j.tet.2004.11.080
- James, E. N., Van Doren, E., Li, C., and Kaplan, D. L. (2019). Silk biomaterials-mediated miRNA functionalized orthopedic devices. *Tissue Eng.* 25, 12–23. doi: 10.1089/ten.tea.2017.0455
- Jayaram, D. T., Runa, S., Kemp, M. L., and Payne, C. K. (2017). Nanoparticle-induced oxidation of corona proteins initiates an oxidative stress response in cells. *Nanoscale* 9, 7595–7601. doi: 10.1039/C6NR09500C
- Jia, M., Chen, Z., Guo, Y., Chen, X., and Zhao, X. (2017). Efficacy of silk fibroin-nano silver against staphylococcus aureus biofilms in a rabbit model of sinusitis. *Int. J. Nanomedicine* 12, 2933–2939. doi: 10.2147/IJN.S130160
- Jones, J. R. (2013). Review of bioactive glass: from Hench to hybrids. *Acta Biomater.* 9, 4457–4486. doi: 10.1016/j.actbio.2012.08.023
- Jose, R. R., Brown, J. E., Polido, K. E., Omenetto, F. G., and Kaplan, D. L. (2015). Polyol-silk bioink formulations as two-part room-temperature curable materials for 3D printing. *ACS Biomater. Sci. Eng.* 1, 780–788. doi: 10.1021/acsbiomaterials.5b00160
- Karageorgiou, V., and Kaplan, D. (2005). Porosity of 3D biomaterial scaffolds and osteogenesis. *Biomaterials* 26, 5474–5491. doi: 10.1016/j.biomaterials.2005.02.002
- Karthikeyan, K., Sekar, S., Pandima Devi, M., Inbasekaran, S., Lakshminarasiah, C. H., and Sastry, T. P. (2011). Fabrication of novel biofibers by coating silk fibroin with chitosan impregnated with silver nanoparticles. *J. Mater. Sci. Mater. Med.* 22, 2721–2726. doi: 10.1007/s10856-011-4462-9
- Kim, D. H., Viventi, J., Amsden, J. J., Xiao, J., Vigeland, L., Kim, Y. S., et al. (2010). Dissolvable films of silk fibroin for ultrathin conformal bio-integrated electronics. *Nat. Mater.* 9, 1–7. doi: 10.1038/nmat2745
- Kim, J., Kim, D., Joo, O., Woo, H., Min, J., Mi, B., et al. (2016). International Journal of Biological Macromolecules Osteoinductive silk fibroin/titanium dioxide/hydroxyapatite hybrid scaffold for bone tissue engineering. *Int. J. Biol. Macromol.* 82, 160–167. doi: 10.1016/j.ijbiomac.2015.08.001
- Kim, J. W., Ki, C. S., Um, I. C., and Park, Y. H. (2017). A facile fabrication method and the boosted adsorption and photodegradation activity of CuO nanoparticles synthesized using a silk fibroin template. *J. Ind. Eng. Chem.* 56, 335–341. doi: 10.1016/j.jiec.2017.07.029
- Kim, K. J., Sung, W. S., Suh, B. K., Moon, S. K., Choi, J. S., Kim, J. G., et al. (2009). Antifungal activity and mode of action of silver nano-particles on *Candida albicans*. *Biomaterials* 22, 235–242. doi: 10.1007/s10534-008-9159-2
- Koh, L. D., Cheng, Y., Teng, C. P., Khin, Y. W., Loh, X. J., Tee, S. Y., et al. (2015). Structures, mechanical properties and applications of silk fibroin materials. *Prog. Polym. Sci.* 46, 86–110. doi: 10.1016/j.progpolymsci.2015.02.001
- Kojic, N., Pritchard, E. M., Tao, H., Brenckle, M. A., Mondia, J. P., Panilaitis, B., et al. (2012). Focal infection treatment using laser-mediated heating of injectable silk hydrogels with gold nanoparticles. *Adv. Funct. Mater.* 22, 3793–3798. doi: 10.1002/adfm.201200382
- Kolosnjaj-Tabi, J., Marangon, I., Nicolas-Boluda, A., Silva, A. K. A., and Gazeau, F. (2017). Nanoparticle-based hyperthermia, a local treatment modulating the tumor extracellular matrix. *Pharmacol. Res.* 126, 123–137. doi: 10.1016/j.phrs.2017.07.010
- Kong, X. D., Cui, F. Z., Wang, X. M., Zhang, M., and Zhang, W. (2004). Silk fibroin regulated mineralization of hydroxyapatite nanocrystals. *J. Cryst. Growth* 270, 197–202. doi: 10.1016/j.jcrysgro.2004.06.007

- Kundu, B., Rajkhowa, R., Kundu, S. C., and Wang, X. (2013). Silk fibroin biomaterials for tissue regenerations. *Adv. Drug Deliv. Rev.* 65, 457–470. doi: 10.1016/j.addr.2012.09.043
- Kweon, H. Y., Lee, K. G., Chae, C. H., Balázs, C., Min, S. K., Kim, J. Y., et al. (2011). Development of nano-hydroxyapatite graft with silk fibroin scaffold as a new bone substitute. *J. Oral Maxillofac. Surg.* 69, 1578–1586. doi: 10.1016/j.joms.2010.07.062
- Lammel, A. S., Hu, X., Park, S. H., Kaplan, D. L., and Scheibel, T. R. (2010). Controlling silk fibroin particle features for drug delivery. *Biomaterials* 31, 4583–4591. doi: 10.1016/j.biomaterials.2010.02.024
- Lan, Y., Li, W., Jiao, Y., Guo, R., Zhang, Y., Xue, W., et al. (2014). Therapeutic efficacy of antibiotic-loaded gelatin microsphere/silk fibroin scaffolds in infected full-thickness burns. *Acta Biomater.* 10, 3167–3176. doi: 10.1016/j.actbio.2014.03.029
- Lan, Y., Lu, Y., and Ren, Z. (2013). Mini review on photocatalysis of titanium dioxide nanoparticles and their solar applications. *Nano Energy* 2, 1031–1045. doi: 10.1016/j.nanoen.2013.04.002
- Lara, H. H., Ayala-Núñez, N. V., del Turrent, L. C. I., and Padilla, C. R. (2010a). Bactericidal effect of silver nanoparticles against multidrug-resistant bacteria. *World J. Microbiol. Biotechnol.* 26, 615–621. doi: 10.1007/s11274-009-0211-3
- Lara, H. H., Ayala-Núñez, N. V., Ixtapan-Turrent, L., and Rodríguez-Padilla, C. (2010b). Mode of antiviral action of silver nanoparticles against HIV-1. *J. Nanobiotechnology* 8, 1–10. doi: 10.1186/1477-3155-8-1
- Lawrence, B. D., Marchant, J. K., Pindrus, M. A., Omenetto, F. G., and Kaplan, D. L. (2009). Silk film biomaterials for cornea tissue engineering. *Biomaterials* 30, 1299–1308. doi: 10.1016/j.biomaterials.2008.11.018
- Li, A. B., Kluge, J. A., Guziewicz, N. A., Omenetto, F. G., and Kaplan, D. L. (2015). Silk-based stabilization of biomacromolecules. *J. Control. Release* 219, 416–430. doi: 10.1016/j.jconrel.2015.09.037
- Li, C., Hotz, B., Ling, S., Guo, J., Haas, D. S., Marelli, B., et al. (2016). Regenerated silk materials for functionalized silk orthopedic devices by mimicking natural processing. *Biomaterials* 110, 24–33. doi: 10.1016/j.biomaterials.2016.09.014
- Li, G., Li, Y., Chen, G., He, J., Han, Y., Wang, X., et al. (2015). Silk-Based Biomaterials in Biomedical Textiles and Fiber-Based Implants. *Adv. Healthc. Mater.* 4, 1134–1151. doi: 10.1002/adhm.201500002
- Li, H., Zhu, J., Chen, S., Jia, L., and Ma, Y. (2017). Fabrication of aqueous-based dual drug loaded silk fibroin electrospun nanofibers embedded with curcumin-loaded RSF nanospheres for drugs controlled release. *RSC Adv.* 7, 56550–56558. doi: 10.1039/C7RA12394A
- Li, X., Liu, Y., Zhang, J., You, R., Qu, J., and Li, M. (2017). Functionalized silk fibroin dressing with topical bioactive insulin release for accelerated chronic wound healing. *Mater. Sci. Eng. C* 72, 394–404. doi: 10.1016/j.msec.2016.11.085
- Li, Z., Song, J., Zhang, J., Hao, K., Liu, L., Wu, B., et al. (2020). Topical application of silk fibroin-based hydrogel in preventing hypertrophic scars. *Coll. Surf. B Biointerf.* 186:110735. doi: 10.1016/j.colsurf.2019.110735
- Liang, B., Yu, K., Ling, Y., Kolios, M., Exner, A., Wang, Z., et al. (2019). An artificially engineered “tumor bio-magnet” for collecting blood-circulating nanoparticles and magnetic hyperthermia. *Biomater. Sci.* 7, 1815–1824. doi: 10.1039/C8BM01658E
- Ling, S., Qin, Z., Huang, W., Cao, S., Kaplan, D. L., and Buehler, M. J. (2017). Design and function of biomimetic multilayer water purification membranes. *Sci. Adv.* 3, 1–12. doi: 10.1126/sciadv.1601939
- Liu, H., Wang, Z., Li, H., Wang, H., and Yu, R. (2018). Controlled synthesis of silkworm cocoon-like  $\alpha$ -Fe<sub>2</sub>O<sub>3</sub> and its adsorptive properties for organic dyes and Cr(VI). *Mater. Res. Bull.* 100, 302–307. doi: 10.1016/j.materresbull.2017.12.030
- Liu, J., Zhou, J., Tang, B., Zeng, T., Li, Y., Li, J., et al. (2016). Surface enhanced Raman scattering (SERS) fabrics for trace analysis. *Appl. Surf. Sci.* 386, 296–302. doi: 10.1016/j.apsusc.2016.05.150
- Lovett, M., Cannizzaro, C., Daheron, L., Messmer, B., Vunjak-Novakovic, G., and Kaplan, D. L. (2007). Silk fibroin microtubes for blood vessel engineering. *Biomaterials* 28, 5271–5279. doi: 10.1016/j.biomaterials.2007.08.008
- Lovett, M. L., Wang, X., Yucel, T., York, L., Keirstead, M., Haggerty, L., et al. (2015). Silk hydrogels for sustained ocular delivery of anti-vascular endothelial growth factor (anti-VEGF) therapeutics. *Eur. J. Pharm. Biopharm.* 95, 271–278. doi: 10.1016/j.ejpb.2014.12.029
- Lu, S., Wang, X., Lu, Q., Zhang, X., Kluge, J. A., Uppal, N., et al. (2010). Insoluble and flexible silk films containing glycerol. *Biomacromolecules* 11, 143–150. doi: 10.1021/bm900993n
- Lu, Z., Mao, C., Meng, M., Liu, S., Tian, Y., Yu, L., et al. (2014a). Fabrication of CeO<sub>2</sub> nanoparticle-modified silk for UV protection and antibacterial applications. *J. Colloid Interface Sci.* 435, 8–14. doi: 10.1016/j.jcis.2014.08.015
- Lu, Z., Meng, M., Jiang, Y., and Xie, J. (2014b). UV-assisted *in situ* synthesis of silver nanoparticles on silk fibers for antibacterial applications. *Colloids Surfaces A Physicochem. Eng. Asp.* 447, 1–7. doi: 10.1016/j.colsurfa.2014.01.064
- Luo, K.-y., and Shao, Z.-z. (2017). A novel regenerated silk fibroin-based hydrogels with magnetic and catalytic activities. *Chinese J. Polym. Sci.* 35, 515–523. doi: 10.1007/s10118-017-1910-0
- Ma, R., and Tsukruk, V. V. (2017). Seriography-guided reduction of graphene oxide biopapers for wearable sensory electronics. *Adv. Funct. Mater.* 27:e201604802. doi: 10.1002/adfm.201604802
- Maleki, H., and Huesing, N. (2019). Silica-silk fibroin hybrid (bio)aerogels: two-step versus one-step hybridization. *J. Sol-Gel Sci. Technol.* doi: 10.1007/s10971-019-04933-4
- Maleki, H., Montes, S., Hayati-Roodbari, N., Putz, F., and Huesing, N. (2018). Compressible, thermally insulating, and fire retardant aerogels through self-assembling silk fibroin biopolymers inside a silica structure - an approach towards 3D printing of aerogels. *ACS Appl. Mater. Interfaces* 10, 22718–22730. doi: 10.1021/acsami.8b05856
- Mandal, B. B., and Kundu, S. C. (2009). Cell proliferation and migration in silk fibroin 3D scaffolds. *Biomaterials* 30, 2956–2965. doi: 10.1016/j.biomaterials.2009.02.006
- Martínez-Prieto, L. M., Cano, I., Márquez, A., Baquero, E. A., Tricard, S., Cusinato, L., et al. (2017). Zwitterionic amidinates as effective ligands for platinum nanoparticle hydrogenation catalysts. *Chem. Sci.* 8, 2931–2941. doi: 10.1039/C6SC05551F
- Meddahi-Pellé, A., Legrand, A., Marcellan, A., Louedec, L., Letourneur, D., and Leibler, L. (2014). Organ repair, hemostasis, and *in vivo* bonding of medical devices by aqueous solutions of nanoparticles. *Angew. Chemie Int. Ed.* 53, 6369–6373. doi: 10.1002/anie.201401043
- Meng, M., He, H., Xiao, J., Zhao, P., Xie, J., and Lu, Z. (2016). Controllable *in situ* synthesis of silver nanoparticles on multilayered film-coated silk fibers for antibacterial application. *J. Colloid Interface Sci.* 461, 369–375. doi: 10.1016/j.jcis.2015.09.038
- Midha, S., Kumar, S., Sharma, A., Kaur, K., Shi, X., Naruphontjirakul, P., et al. (2018). Silk fibroin-bioactive glass based advanced biomaterials: towards patient-specific bone grafts. *Biomed. Mater.* 13:055012. doi: 10.1088/1748-605X/aad2a9
- Mieszawska, A. J., Fourligas, N., Georgakoudi, I., Ouhib, N. M., Belton, D. J., Perry, C. C., et al. (2010). Osteoinductive silk-silica composite biomaterials for bone regeneration. *Biomaterials* 31, 8902–8910. doi: 10.1016/j.biomaterials.2010.07.109
- Monopoli, M. P., Åberg, C., Salvati, A., and Dawson, K. A. (2012). Biomolecular coronas provide the biological identity of nanosized materials. *Nat. Nanotechnol.* 7, 779–786. doi: 10.1038/nnano.2012.207
- Mu, X., Wang, Y., Guo, C., Li, Y., Ling, S., Huang, W., et al. (2020). 3D printing of silk protein structures by aqueous solvent-directed molecular assembly. *Macromol. Biosci.* 20:1900191. doi: 10.1002/mabi.201900191
- Nezhad-Mokhtari, P., Ghorbani, M., Roshangar, L., and Soleimani Rad, J. (2019). Chemical gelling of hydrogels-based biological macromolecules for tissue engineering: Photo- and enzymatic-crosslinking methods. *Int. J. Biol. Macromol.* 139, 760–772. doi: 10.1016/j.ijbiomac.2019.08.047
- Ni, W., Li, M., Cui, J., Xing, Z., Li, Z., Wu, X., et al. (2017). 808 nm light triggered black TiO<sub>2</sub> nanoparticles for killing of bladder cancer cells. *Mater. Sci. Eng. C* 81, 252–260. doi: 10.1016/j.msec.2017.08.020
- Niu, C., Li, X., Wang, Y., Liu, X., Shi, J., and Wang, X. (2019). Design and performance of a poly(vinyl alcohol)/silk fibroin enzymatically crosslinked semi-interpenetrating hydrogel for a potential hydrophobic drug delivery. *RSC Adv.* 9, 41074–41082. doi: 10.1039/C9RA09344C
- Ornell, K. J., Taylor, J. S., Zeki, J., Ikegaki, N., Shimada, H., Coburn, J. M., et al. (2020). Local delivery of dinutuximab from lyophilized silk fibroin foams for



- treatment of an orthotopic neuroblastoma model. *Cancer Med.* 9, 2891–2903. doi: 10.1002/cam4.2936
- Pandey, S., and Bodas, D. (2020). High-quality quantum dots for multiplexed bioimaging: a critical review. *Adv. Colloid Interface Sci.* 278:102137. doi: 10.1016/j.cis.2020.102137
- Partlow, B. P., Hanna, C. W., Rnjak-Kovacina, J., Moreau, J. E., Applegate, M. B., Burke, K. A., et al. (2014). Highly tunable elastomeric silk biomaterials. *Adv. Funct. Mater.* 24, 4615–4624. doi: 10.1002/adfm.201400526
- Patil, P. P., Meshram, J. V., Bohara, R. A., Nanaware, S. G., and Pawar, S. H. (2018). ZnO nanoparticle-embedded silk fibroin-polyvinyl alcohol composite film: a potential dressing material for infected wounds. *New J. Chem.* 42, 14620–14629. doi: 10.1039/C8NJ01675E
- Patil, S., George, T., and Mahadik, K. (2015). Green synthesized nanosilver loaded silk fibroin gel for enhanced wound healing. *J. Drug Deliv. Sci. Technol.* 30, 30–36. doi: 10.1016/j.jddst.2015.09.001
- Pedone, D., Moglianetti, M., De Luca, E., Bardi, G., and Pompa, P. P. (2017). Platinum nanoparticles in nanobiomedicine. *Chem. Soc. Rev.* 46, 4951–4975. doi: 10.1039/C7CS00152E
- Phillips, D. M., Drummy, L. F., Conrady, D. G., Fox, D. M., Naik, R. R., Stone, M. O., et al. (2004). Dissolution and regeneration of *Bombyx mori* silk fibroin using ionic liquids. *J. Am. Chem. Soc.* 126, 14350–14351. doi: 10.1021/ja046079f
- Pires, F., Munhoz, F., Koch, L. M., Tanaka, M., Souza, M., Israelita, H., et al. (2019). Consenso Brasileiro de Nutrição em Transplante de Células-Tronco Hematopoiéticas : Idosos. *Stem Cell Transplant. Elderly* 17, 1–16. doi: 10.31744/einstein\_journal/2019AE4340
- Plan Sangnier, A., Aufaure, R., Cheong, S., Motte, L., Palpant, B., Tilley, R. D., et al. (2019). Raspberry-like small multicore gold nanostructures for efficient photothermal conversion in the first and second near-infrared windows. *Chem. Commun.* 55, 4055–4058. doi: 10.1039/C8CC09476D
- Plan Sangnier, A., Van de Walle, A., Aufaure, R., Fradet, M., Motte, L., Guénin, E., et al. (2020). Endosomal confinement of gold nanospheres, nanorods, and nanoraspberries governs their photothermal identity and is beneficial for cancer cell therapy. *Adv. Biosyst.* 4:1900284. doi: 10.1002/adbi.201900284
- Poza, P., Pérez-Rigueiro, J., Elices, M., and Lorca, J. (2002). Fractographic analysis of silkworm and spider silk. *Eng. Fract. Mech.* 69, 1035–1048. doi: 10.1016/S0013-7944(01)00120-5
- Qian, K.-Y., Song, Y., Yan, X., Dong, L., Xue, J., Xu, Y., et al. (2020). Injectable ferrimagnetic silk fibroin hydrogel for magnetic hyperthermia ablation of deep tumor. *Biomaterials* 259:120299. doi: 10.1016/j.biomaterials.2020.120299
- Qian, L., and Zhang, H. (2011). Controlled freezing and freeze drying: a versatile route for porous and micro-/nano-structured materials. *J. Chem. Technol. Biotechnol.* 86, 172–184. doi: 10.1002/jctb.2495
- Raho, R., Nguyen, N. Y., Zhang, N., Jiang, W., Sannino, A., Liu, H., et al. (2020). Photo-assisted green synthesis of silver doped silk fibroin/carboxymethyl cellulose nanocomposite hydrogels for biomedical applications. *Mater. Sci. Eng. C* 107:110219. doi: 10.1016/j.msec.2019.110219
- Raja, N., and Yun, H. S. (2016). A simultaneous 3D printing process for the fabrication of bioceramic and cell-laden hydrogel core/shell scaffolds with potential application in bone tissue regeneration. *J. Mater. Chem. B* 4, 4707–4716. doi: 10.1039/C6TB00849F
- Ranjana, R., Parushuram, N., Harisha, K. S., Asha, S., and Sangappa, Y. (2020). Silk fibroin a bio-template for synthesis of different shaped gold nanoparticles: characterization and ammonia detection application. *Mater. Today Proc.* 27, 434–439. doi: 10.1016/j.matpr.2019.11.259
- Rao, V. N., Reddy, N. L., Kumari, M. M., Cheralathan, K. K., Ravi, P., Sathish, M., et al. (2019). Sustainable hydrogen production for the greener environment by quantum dots-based efficient photocatalysts: a review. *J. Environ. Manage.* 248:109246. doi: 10.1016/j.jenvman.2019.07.017
- Reidy, B., Haase, A., Luch, A., Dawson, K. A., and Lynch, I. (2013). Mechanisms of silver nanoparticle release, transformation and toxicity: a critical review of current knowledge and recommendations for future studies and applications. *Materials* 6, 2295–2350. doi: 10.3390/ma6062295
- Ribeiro, M., De Moraes, M. A., Beppu, M. M., Garcia, M. P., Fernandes, M. H., Monteiro, F. J., et al. (2015). Development of silk fibroin/nanohydroxyapatite composite hydrogels for bone tissue engineering. *Eur. Polym. J.* 67, 66–77. doi: 10.1016/j.eurpolymj.2015.03.056
- Ribeiro, M., Feraz, M. P., Monteiro, F. J., Fernandes, M. H., Beppu, M. M., Mantione, D., et al. (2017). Antibacterial silk fibroin/nanohydroxyapatite hydrogels with silver and gold nanoparticles for bone regeneration. *Nanomed. Nanotechnol. Biol. Med.* 13, 231–239. doi: 10.1016/j.nano.2016.08.026
- Rockwood, D. N., Preda, R. C., Yücel, T., Wang, X., Lovett, M. L., and Kaplan, D. L. (2011). Materials fabrication from *Bombyx mori* silk fibroin. *Nat. Protoc.* 6, 1612–1631. doi: 10.1038/nprot.2011.379
- Rodriguez, M. J., Dixon, T. A., Cohen, E., Huang, W., Omenetto, F. G., and Kaplan, D. L. (2018). 3D freeform printing of silk fibroin. *Acta Biomater.* 71, 379–387. doi: 10.1016/j.actbio.2018.02.035
- Runa, S., Lakadamyali, M., Kemp, M. L., and Payne, C. K. (2017). TiO<sub>2</sub> nanoparticle-induced oxidation of the plasma membrane: importance of the protein corona. *J. Phys. Chem. B* 121, 8619–8625. doi: 10.1021/acs.jpcc.7b04208
- Saldan, I., Semeniyuk, Y., Marchuk, I., and Reshetnyak, O. (2015). Chemical synthesis and application of palladium nanoparticles. *J. Mater. Sci.* 50, 2337–2354. doi: 10.1007/s10853-014-8802-2
- Samadi, A., Klingberg, H., Jauffred, L., Kjær, A., Bendix, P. M., and Oddershede, L. B. (2018). Platinum nanoparticles: a non-toxic, effective and thermally stable alternative plasmonic material for cancer therapy and bioengineering. *Nanoscale* 10, 9097–9107. doi: 10.1039/C8NR02275E
- Santos, L. J., Reis, R. L., and Gomes, M. E. (2015). Harnessing magnetic-mechano actuation in regenerative medicine and tissue engineering. *Trends Biotechnol.* 33, 471–479. doi: 10.1016/j.tibtech.2015.06.006
- Schmucker, A. L., Dickerson, M. B., Rycenga, M., Mangelson, B. F., Brown, K. A., Naik, R. R., et al. (2014). Combined chemical and physical encoding with silk fibroin-embedded nanostructures. *Small* 10, 1485–1489. doi: 10.1002/smll.201302923
- Shahid, M., Cheng, X. W., Tang, R. C., and Chen, G. (2017). Silk functionalization by caffeic acid assisted *in-situ* generation of silver nanoparticles. *Dye. Pigment.* 137, 277–283. doi: 10.1016/j.dyepig.2016.10.009
- Sheikh, F. A., Ju, H. W., Lee, J. M., Moon, B. M., Park, H. J., Lee, O. J., et al. (2015). 3D electrospun silk fibroin nanofibers for fabrication of artificial skin. *Nanomed. Nanotechnol. Biol. Med.* 11, 681–691. doi: 10.1016/j.nano.2014.11.007
- Smith, A. T., LaChance, A. M., Zeng, S., Liu, B., and Sun, L. (2019). Synthesis, properties, and applications of graphene oxide/reduced graphene oxide and their nanocomposites. *Nano Mater. Sci.* 1, 31–47. doi: 10.1016/j.nanoms.2019.02.004
- Sohail Haroone, M., Li, L., Ahmad, A., Huang, Y., Ma, R., Zhang, P., et al. (2018). Luminous composite ultrathin films of CdTe quantum dots/silk fibroin co-assembled with layered doubled hydroxide: enhanced photoluminescence and biosensor application. *J. Mater.* 4, 165–171. doi: 10.1016/j.jmat.2018.05.002
- Sohail, A., Ahmad, Z., Bég, O. A., Arshad, S., and Sherin, L. (2017). Revue sur le traitement par hyperthermie méditée par nanoparticules. *Bull. Cancer* 104, 452–461. doi: 10.1016/j.bulcan.2017.02.003
- Sommer, M. R., Schaffner, M., Carnelli, D., and Studart, A. R. (2016). 3D Printing of hierarchical silk fibroin structures. *ACS Appl. Mater. Interfaces* 8, 34677–34685. doi: 10.1021/acsami.6b11440
- Song, J., Zhang, P., Cheng, L., Liao, Y., Xu, B., Bao, R., et al. (2015). Nano-silver *in situ* hybridized collagen scaffolds for regeneration of infected full-thickness burn skin. *J. Mater. Chem. B* 3, 4231–4241. doi: 10.1039/C5TB00205B
- Song, W., Muthana, M., Mukherjee, J., Falconer, R. J., Biggs, C. A., and Zhao, X. (2017). Magnetic-silk core-shell nanoparticles as potential carriers for targeted delivery of curcumin into human breast cancer cells. *ACS Biomater. Sci. Eng.* 3, 1027–1038. doi: 10.1021/acsbiomaterials.7b00153
- Sridhar, S., Venugopal, J. R., Sridhar, R., and Ramakrishna, S. (2015). Cardiogenic differentiation of mesenchymal stem cells with gold nanoparticle loaded functionalized nanofibers. *Coll. Surf. B Biointerf.* 134, 346–354. doi: 10.1016/j.colsurfb.2015.07.019
- Stankic, S., Suman, S., Haque, F., and Vidic, J. (2016). Pure and multi metal oxide nanoparticles: synthesis, antibacterial and cytotoxic properties. *J. Nanobiotechnol.* 14, 1–20. doi: 10.1186/s12951-016-0225-6
- Stinson, J. A., Palmer, C. R., Miller, D. P., Li, A. B., Lightner, K., Jost, H., et al. (2020). Thin silk fibroin films as a dried format for temperature stabilization of inactivated polio vaccine. *Vaccine* 38, 1652–1660. doi: 10.1016/j.vaccine.2019.12.062



- Su, S. S., and Chang, I. (2017). "Review of production routes of nanomaterials," in *Commercialization of Nanotechnologies-A Case Study Approach*, eds D. Brabazon, E. Pellicer, F. Zivic, J. Sort, M. Dolores Baró, N. Grujovic, et al. (Cham: Springer International Publishing), 15–29.
- Sun, J., Shen, Q. Y., and Lu, J. X. (2009). Comparative study of microstructural remodification to porous  $\beta$ -TCP and HA in rabbits. *Chinese Sci. Bull.* 54, 2962–2967. doi: 10.1007/s11434-009-0332-y
- Sun, L., Parker, S. T., Syoji, D., Wang, X., Lewis, J. A., and Kaplan, D. L. (2012). Direct-write assembly of 3D silk/hydroxyapatite scaffolds for bone co-cultures. *Adv. Healthc. Mater.* 1, 729–735. doi: 10.1002/adhm.201200057
- Suzuki, T., Miura, N., Hojo, R., Yanagiba, Y., Suda, M., Hasegawa, T., et al. (2020). Genotoxicity assessment of titanium dioxide nanoparticle accumulation of 90 days in the liver of gpt delta transgenic mice. *Genes Environ.* 42:7. doi: 10.1186/s41021-020-00151-5
- Szekeres, G. P., and Kneipp, J. (2019). SERS probing of proteins in gold nanoparticle agglomerates. *Front. Chem.* 7, 1–10. doi: 10.3389/fchem.2019.00030
- Tanasa, E., Zaharia, C., Hudita, A., Radu, I. C., Costache, M., and Galateanu, B. (2020). Impact of the magnetic field on 3T3-E1 preosteoblasts inside SMART silk fibroin-based scaffolds decorated with magnetic nanoparticles. *Mater. Sci. Eng. C* 110, 1–13. doi: 10.1016/j.msec.2020.110714
- Tang, B., Sun, L., Kaur, J., Yu, Y., and Wang, X. (2014). *In-situ* synthesis of gold nanoparticles for multifunctionalization of silk fabrics. *Dye. Pigment.* 103, 183–190. doi: 10.1016/j.dyepig.2013.12.008
- Tao, H., Siebert, S. M., Brenckle, M. A., Averitt, R. D., Cronin-Golomb, M., Kaplan, D. L., et al. (2010). Gold nanoparticle-doped biocompatible silk films as a path to implantable thermo-electrically wireless powering devices. *Appl. Phys. Lett.* 97:123702. doi: 10.1063/1.3486157
- Thebo, K. H., Qian, X., Zhang, Q., Chen, L., Cheng, H. M., and Ren, W. (2018). Highly stable graphene-oxide-based membranes with superior permeability. *Nat. Commun.* 9, 1–8. doi: 10.1038/s41467-018-03919-0
- Tsioris, K., Raja, W. K., Pritchard, E. M., Panilaitis, B., Kaplan, D. L., and Omenetto, F. G. (2012). Fabrication of silk microneedles for controlled-release drug delivery. *Adv. Funct. Mater.* 22, 330–335. doi: 10.1002/adfm.201102012
- Uttayarat, P., Jetawattana, S., Suwanmala, P., Eamsiri, J., Tangthong, T., and Pongpat, S. (2012). Antimicrobial electrospun silk fibroin mats with silver nanoparticles for wound dressing application. *Fibers Polym.* 13, 999–1006. doi: 10.1007/s12221-012-0999-6
- Van de Walle, A., Sangnier, A. P., Abou-Hassan, A., Curcio, A., Hémadi, M., Menguy, N., et al. (2019). Biosynthesis of magnetic nanoparticles from nanodegradation products revealed in human stem cells. *Proc. Natl. Acad. Sci. U.S.A.* 116, 4044–4053. doi: 10.1073/pnas.1816792116
- Van Der Sanden, B., Dhobb, M., Berger, F., and Wion, D. (2010). Optimizing stem cell culture. *J. Cell. Biochem.* 111, 801–807. doi: 10.1002/jcb.22847
- van Loo, B., Salehi, S. S., Henke, S., Shamloo, A., Kamperman, T., Karperien, M., et al. (2020). Enzymatic outside-in crosslinking enables single-step microcapsule production for high-throughput 3D cell microaggregate formation. *Mater. Today Bio.* 6:100047. doi: 10.1016/j.mtbio.2020.100047
- Velmurugan, P., Shim, J., Kim, H. W., Lim, J. M., Kim, S. A., Seo, Y. S., et al. (2020). Bio-functionalization of cotton, silk, and leather using different *in-situ* silver nanoparticle synthesis modules, and their antibacterial properties. *Res. Chem. Intermed.* 46, 999–1015. doi: 10.1007/s11164-016-2481-3
- Vepari, C., and Kaplan, D. L. (2007). Silk as a biomaterial. *Prog. Polym. Sci.* 32, 991–1007. doi: 10.1016/j.progpolymsci.2007.05.013
- Vidal, S. E. L., Tamamoto, K. A., Nguyen, H., Abbott, R. D., Cairns, D. M., and Kaplan, D. L. (2019). 3D biomaterial matrix to support long term, full thickness, immuno-competent human skin equivalents with nervous system components. *Biomaterials* 198, 194–203. doi: 10.1016/j.biomaterials.2018.04.044
- Wang, F., Jyothirmayee Aravind, S. S., Wu, H., Forsy, J., Venkataraman, V., Ramanujachary, K., et al. (2017). Tunable green graphene-silk biomaterials: mechanism of protein-based nanocomposites. *Mater. Sci. Eng. C* 79, 728–739. doi: 10.1016/j.msec.2017.05.120
- Wang, J., Zhang, Y., Jin, N., Mao, C., and Yang, M. (2019). Protein-induced gold nanoparticle assembly for improving the photothermal effect in cancer therapy. *ACS Appl. Mater. Interfaces* 11, 11136–11143. doi: 10.1021/acsami.8b21488
- Wang, L., Lu, R., Hou, J., Nan, X., Xia, Y., Guo, Y., et al. (2020). Application of injectable silk fibroin/graphene oxide hydrogel combined with bone marrow mesenchymal stem cells in bone tissue engineering. *Coll. Surf. A Physicochem. Eng. Asp.* 604:125318. doi: 10.1016/j.colsurfa.2020.125318
- Wang, S., Zhu, M., Zhao, L., Kuang, D., Kundu, S. C., and Lu, S. (2019). Insulin-loaded silk fibroin microneedles as sustained release system. *ACS Biomater. Sci. Eng.* 5, 1887–1894. doi: 10.1021/acsbomaterials.9b00229
- Watanabe, K., Miwa, E., Asai, F., Seki, T., Urayama, K., Nakatani, T., et al. (2020). Highly transparent and tough filler composite elastomer inspired by the cornea. *ACS Mater. Lett.* 2, 325–330. doi: 10.1021/acsmaterialslett.9b00520
- Wei, G., and Ma, P. X. (2004). Structure and properties of nano-hydroxyapatite/polymer composite scaffolds for bone tissue engineering. *Biomaterials* 25, 4749–4757. doi: 10.1016/j.biomaterials.2003.12.005
- Wu, J., Zheng, K., Huang, X., Liu, J., Liu, H., Boccaccini, A. R., et al. (2019). Thermally triggered injectable chitosan/silk fibroin/bioactive glass nanoparticle hydrogels for *in-situ* bone formation in rat calvarial bone defects. *Acta Biomater.* 91, 60–71. doi: 10.1016/j.actbio.2019.04.023
- Wu, W., Jiang, C. Z., and Roy, V. A. L. (2016). Designed synthesis and surface engineering strategies of magnetic iron oxide nanoparticles for biomedical applications. *Nanoscale* 8, 19421–19474. doi: 10.1039/C6NR07542H
- Xiong, R., Grant, A. M., Ma, R., Zhang, S., and Tsukruk, V. V. (2018). Naturally-derived biopolymer nanocomposites: interfacial design, properties and emerging applications. *Mater. Sci. Eng. R Reports* 125, 1–41. doi: 10.1016/j.mser.2018.01.002
- Xu, Z., Shi, L., Yang, M., and Zhu, L. (2019). Preparation and biomedical applications of silk fibroin-nanoparticles composites with enhanced properties - a review. *Mater. Sci. Eng. C* 95, 302–311. doi: 10.1016/j.msec.2018.11.010
- Yang, G., Lin, H., Rothrauff, B. B., Yu, S., and Tuan, R. S. (2016). Multilayered polycaprolactone/gelatin fiber-hydrogel composite for tendon tissue engineering. *Acta Biomater.* 35, 68–76. doi: 10.1016/j.actbio.2016.03.004
- Yang, Y., Chen, M., Wu, Y., Wang, P., Zhao, Y., Zhu, W., et al. (2019). Ultrasound assisted one-step synthesis of Au@Pt dendritic nanoparticles with enhanced NIR absorption for photothermal cancer therapy. *RSC Adv.* 9, 28541–28547. doi: 10.1039/C9RA04286E
- Ye, P., Yu, B., Deng, J., She, R. F., and Huang, W. L. (2017). Application of silk fibroin/chitosan/nano-hydroxyapatite composite scaffold in the repair of rabbit radial bone defect. *Exp. Ther. Med.* 14, 5547–5553. doi: 10.3892/etm.2017.5231
- Yin, H., Ai, S., Shi, W., and Zhu, L. (2009a). A novel hydrogen peroxide biosensor based on horseradish peroxidase immobilized on gold nanoparticles-silk fibroin modified glassy carbon electrode and direct electrochemistry of horseradish peroxidase. *Sens. Actuat. B Chem.* 137, 747–753. doi: 10.1016/j.snb.2008.12.046
- Yin, H., Ai, S., Xu, J., Shi, W., and Zhu, L. (2009b). Amperometric biosensor based on immobilized acetylcholinesterase on gold nanoparticles and silk fibroin modified platinum electrode for detection of methyl paraoxon, carbofuran and phoxim. *J. Electroanal. Chem.* 637, 21–27. doi: 10.1016/j.jelechem.2009.09.025
- Yin, Z., Kuang, D., Wang, S., Zheng, Z., Yadavalli, V. K., and Lu, S. (2018). Swellable silk fibroin microneedles for transdermal drug delivery. *Int. J. Biol. Macromol.* 106, 48–56. doi: 10.1016/j.ijbiomac.2017.07.178
- Yu, K., Lu, F., Li, Q., Chen, H., Lu, B., Liu, J., et al. (2017). *In situ* assembly of Ag nanoparticles (AgNPs) on porous silkworm cocoon-based wound film: enhanced antimicrobial and wound healing activity. *Sci. Rep.* 7, 1–13. doi: 10.1038/s41598-017-02270-6
- Yu, W., Kuzuya, T., Hirai, S., Tamada, Y., Sawada, K., and Iwasa, T. (2012). Preparation of Ag nanoparticle dispersed silk fibroin compact. *Appl. Surf. Sci.* 262, 212–217. doi: 10.1016/j.apsusc.2012.05.084
- Yukseloglu, S. M., Sokmen, N., and Canoglu, S. (2015). Biomaterial applications of silk fibroin electrospun nanofibres. *Microelectron. Eng.* 146, 43–47. doi: 10.1016/j.mee.2015.04.008
- Zakharov, N. A., Demina, L. I., Aliev, A. D., Kiselev, M. R., Matveev, V. V., Orlov, M. A., et al. (2017). Synthesis and properties of calcium hydroxyapatite/silk fibroin organomineral composites. *Inorg. Mater.* 53, 333–342. doi: 10.1134/S0020168517030128
- Zhang, G., Liu, Y., Gao, X., and Chen, Y. (2014). Synthesis of silver nanoparticles and antibacterial property of silk fabrics treated by silver nanoparticles. *Nanoscale Res. Lett.* 9, 1–8. doi: 10.1186/1556-276X-9-216
- Zhang, L., Liu, X., Li, G., Wang, P., and Yang, Y. (2019). Tailoring degradation rates of silk fibroin scaffolds for tissue engineering. *J. Biomed. Mater. Res. Part A* 107, 104–113. doi: 10.1002/jbm.a.36537

- Zhang, S., Zhou, Z., Zhong, J., Shi, Z., Mao, Y., and Tao, T. H. (2020). Body-integrated, enzyme-triggered degradable, silk-based mechanical sensors for customized health/fitness monitoring and *in situ* treatment. *Adv. Sci.* 7, 1–10. doi: 10.1002/advs.202070071
- Zhang, W., Chen, L., Chen, J., Wang, L., Gui, X., Ran, J., et al. (2017). Silk fibroin biomaterial shows safe and effective wound healing in animal models and a randomized controlled clinical trial. *Adv. Healthc. Mater.* 6, 1–16. doi: 10.1002/adhm.201700121**
- Zhang, Z., Wu, J., Liu, M., Wang, H., Li, C., Rodriguez, M. J., et al. (2018). 3D Bioprinting of self-standing silk-based bioink. *Adv. Healthc. Mater.* 7, 1–12. doi: 10.1002/adhm.201701026
- Zhou, H., Wang, X., Wang, T., Zeng, J., Yuan, Z., Jian, J., et al. (2019). *In situ* decoration of Ag@AgCl nanoparticles on polyurethane/silk fibroin composite porous films for photocatalytic and antibacterial applications. *Eur. Polym. J.* 118, 153–162. doi: 10.1016/j.eurpolymj.2019.05.058
- Zhou, J., Zhang, B., Shi, L., Zhong, J., Zhu, J., Yan, J., et al. (2014). Regenerated silk fibroin films with controllable nanostructure size and secondary structure for drug delivery. *ACS Appl. Mater. Interfaces* 6, 21813–21821. doi: 10.1021/am502278b
- Zhou, L., Yu, K., Lu, F., Lan, G., Dai, F., Shang, S., et al. (2020). Minimizing antibiotic dosage through *in situ* formation of gold nanoparticles across antibacterial wound dressings: a facile approach using silk fabric as the base substrate. *J. Clean. Prod.* 243:118604. doi: 10.1016/j.jclepro.2019.118604
- Zhou, W., Gao, X., Liu, D., and Chen, X. (2015). Gold nanoparticles for *in vitro* diagnostics. *Chem. Rev.* 115, 10575–10636. doi: 10.1021/acs.chemrev.5b00100
- Zhou, Y., and Tang, R. C. (2018a). Facile and eco-friendly fabrication of AgNPs coated silk for antibacterial and antioxidant textiles using honeysuckle extract. *J. Photochem. Photobiol. B Biol.* 178, 463–471. doi: 10.1016/j.jphotobiol.2017.12.003
- Zhou, Y., and Tang, R. C. (2018b). Facile and eco-friendly fabrication of colored and bioactive silk materials using silver nanoparticles synthesized by two flavonoids. *Polymers* 10:404. doi: 10.3390/polym10040404
- Ziental, D., Czarczynska-Goslinska, B., Mlynarczyk, D. T., Glowacka-Sobotta, A., Stanisz, B., Goslinski, T., et al. (2020). Titanium dioxide nanoparticles: prospects and applications in medicine. *Nanomaterials* 10:387. doi: 10.3390/nano10020387
- Zou, F., Zhou, J., Zhang, J., Li, J., Tang, B., Chen, W., et al. (2018). Functionalization of silk with *in-situ* synthesized platinum nanoparticles. *Materials* 11, 1–13. doi: 10.3390/ma11101929

**Conflict of Interest:** The authors declare that the research was conducted in the absence of any commercial or financial relationships that could be construed as a potential conflict of interest.

Copyright © 2020 Belda Marín, Fitzpatrick, Kaplan, Landoulsi, Guénin and Egles. This is an open-access article distributed under the terms of the Creative Commons Attribution License (CC BY). The use, distribution or reproduction in other forums is permitted, provided the original author(s) and the copyright owner(s) are credited and that the original publication in this journal is cited, in accordance with accepted academic practice. No use, distribution or reproduction is permitted which does not comply with these terms.

Key articles in our opinion are presented in bold text to help the reader find them within the reference section.

# Advantages of publishing in Frontiers



## OPEN ACCESS

Articles are free to read  
for greatest visibility  
and readership



## FAST PUBLICATION

Around 90 days  
from submission  
to decision



## HIGH QUALITY PEER-REVIEW

Rigorous, collaborative,  
and constructive  
peer-review



## TRANSPARENT PEER-REVIEW

Editors and reviewers  
acknowledged by name  
on published articles

## Frontiers

Avenue du Tribunal-Fédéral 34  
1005 Lausanne | Switzerland

Visit us: [www.frontiersin.org](http://www.frontiersin.org)

Contact us: [frontiersin.org/about/contact](http://frontiersin.org/about/contact)



## REPRODUCIBILITY OF RESEARCH

Support open data  
and methods to enhance  
research reproducibility



## DIGITAL PUBLISHING

Articles designed  
for optimal readership  
across devices



## FOLLOW US

@frontiersin



## IMPACT METRICS

Advanced article metrics  
track visibility across  
digital media



## EXTENSIVE PROMOTION

Marketing  
and promotion  
of impactful research



## LOOP RESEARCH NETWORK

Our network  
increases your  
article's readership